



## Durham E-Theses

---

### *Easy Use Recyclable Functional Cloths for On-Site Water Decontamination in ODA Countries and Humanitarian Crises*

GODDARD, GEORGE,THEODORE,WACKERBARTH

#### How to cite:

---

GODDARD, GEORGE,THEODORE,WACKERBARTH (2025) *Easy Use Recyclable Functional Cloths for On-Site Water Decontamination in ODA Countries and Humanitarian Crises*, Durham theses, Durham University. Available at Durham E-Theses Online: <http://etheses.dur.ac.uk/15956/>

#### Use policy

---

The full-text may be used and/or reproduced, and given to third parties in any format or medium, without prior permission or charge, for personal research or study, educational, or not-for-profit purposes provided that:

- a full bibliographic reference is made to the original source
- a [link](#) is made to the metadata record in Durham E-Theses
- the full-text is not changed in any way

The full-text must not be sold in any format or medium without the formal permission of the copyright holders.

Please consult the [full Durham E-Theses policy](#) for further details.



**EASY USE RECYCLABLE FUNCTIONAL  
CLOTHS FOR ON-SITE WATER  
DECONTAMINATION IN ODA COUNTRIES AND  
HUMANITARIAN CRISES**

**GEORGE THEODORE WACKERBARTH GODDARD**

**PHD THESIS**

**DEPARTMENT OF CHEMISTRY**

**DURHAM UNIVERSITY**

**2024**

## DECLARATION

The experimental work contained within this thesis was carried out at the Department of Chemistry, University of Durham, between September 2019 and June 2023. It is the original work of this author (except where otherwise acknowledged) and has not been submitted by the author for a degree at this or any other higher education establishment. The funding for this thesis was provided by EPSRC up until the end of August 2022, and self-funded thereafter.

## RESEARCHER CONTRIBUTIONS

### Chapter 3:

- DMAM-calixarene was synthesised by Egemen Ozcelik, Mustafa Karaman, and Mustafa Tabakci (Konya Technical University).
- NKD measurements were taken by Harrison Cox and Joe Rawlinson
- The activated carbon cloth was fabricated by Joe Rawlinson

### Chapter 4:

- Whilst COVID regulations were occurring, UV–Vis spectra were recorded by Aileen Congreve
- ICP-OES was performed by Emily Unsworth

### Chapter 5:

- Calixarenes KTU-009, -010, -011, -013, and -014 were synthesised by Egemen Ozcelik, Mustafa Karaman, and Mustafa Tabakci (Konya Technical University).
- ICP-OES was performed by Emily Unsworth
- NKD measurements were taken by Joe Rawlinson

All other practical experiments, as well as all data evaluation was carried out by George T.W. Goddard. The entire text of this thesis was written by George T.W. Goddard. All figures were also created by George T.W. Goddard, except for some figures taken from the internet, for which the original source has been credited in each instance.

## **ACKNOWLEDGEMENTS**

I would like to begin by thanking my supervisor Professor Jas Pal Badyal FRS for providing me with the opportunity to carry out this PhD project, and in particular, for his advice and patience whenever issues arose with the experiments being carried out. Thank you as well to my co-supervisor Dr Simon Beaumont for providing that extra level of feedback and support which was greatly appreciated.

I would like to thank all members of the Lab 98 team, starting with those who made me feel so welcome when I began my research – Dr Harrison Cox, Dr Preeti Garg, and Dr Vera Bieber. I am especially grateful to Harry and Vera for teaching me the required techniques used within this thesis, and their guidance in getting me up and running. And thank you as well to Claire Hatfield, Maya Spence, Jack Crook and Noam Balter for helping make the group a pleasant team to be a part of. To Shuyue Luan, thank you for always being willing to help whenever I asked, and I wish you the best of luck in your career.

I am especially grateful to the following technical staff, who I'm sure will be quite happy to have me no longer requesting various repairs! Without the glassblowers Malcolm Richardson and Aaron Brown; Neil Holmers in the mechanical workshop; and Bryan Denton and—most notably—Kelvin Appleby in the electronic workshop, the work in this thesis would not be at all possible.

Thank you to Dr Emily Unsworth for carrying out the ICP-OES measurements, and for providing the uranium required for my investigation. Thank you also to Dr Aileen Congreve for carrying out the UV–Vis spectroscopy measurements during the pandemic, as well as providing me with any help required during my UV–Vis experiments.

Outside of chemistry, I would like to thank my family for always being there for me; and to the various friends I made through Handball and Debating for providing me with many moments of joy throughout my time in Durham.

Finally, I would like to provide a special thank you to the two people, without whom I am unsure I would be able to complete my work. To Dr Joe Rawlinson, while your continual help during my research was greatly appreciated, your friendship throughout will always mean a great deal to me, and I wish nothing but the best to you and Georgie. And indeed, to my incredible wife, Isobel, words cannot express how grateful I am for all the support you provided, and for putting up with my many weekends and late nights of work. Thank you.

## TABLE OF ABBREVIATIONS

Abbreviation	Definition
AB10B	Amido Black 10B
AR	Alizarin Red
ATR	Attenuated Total Reflectance
CAGR	Compound Annual Growth Rate
CCD	Charge Coupled Device
CD	Cyclodextrin
CR	Congo Red
CTLS	Chrome-tanned leather shavings
CTLT	Chrome-tanned leather trimmings
DMAM	(Dimethylamino)methyl
DMAM-calixarene	5,11,17,23-tetrakis[(dimethylamino)methyl]-25,26,27,28-tetrahydroxycalix[4]arene
DMAM-phenol	2,6-di- <i>tert</i> -butyl-4-(dimethylaminomethyl)phenol
DR1	Disperse Red 1
DTGS	Deuterated triglycine sulfate
FTIR	Fourier Transform Infrared
GI	Gastrointestinal
GO	Graphene oxide
GSM	Grams per square metre
HH	Hydroxylamine Hydrochloride
HP	High purity
ICP	Inductively Coupled Plasma
ICP-OES	Inductively Coupled Plasma Optical Emission Spectroscopy
IR	Infrared
JGB	Janus Green B
KTU-009	5,17-Diformyl-11,23-di- <i>tert</i> -butyl-25,27-dimethoxy-26,28-dihydroxycalix[4]arene
KTU-010	5,17-di(ureaylimino)-11,23-di- <i>tert</i> -butyl-25,27-dimethoxy-26,28-dihydroxycalix[4]arene
KTU-011	5,17-bis((2-8-(quinolinylloxy)acetamidyl)imino)-11,23-di- <i>tert</i> -butyl-25,27-dimethoxy-26-28-dihydroxycalix[4]arene
KTU-013	5,17-bis(4-hydroxy-3-methoxy-5-(2-ureaylimino)phenylazo)-25,27-dimethoxy-26,28-dihydroxycalix[4]arene

Abbreviation	Definition
KTU-014	5,17-bis(2-(phenoxyacetamidyl)imino)-11,23-di-tert-butyl-25,27-dimethoxy-26,28-dimethoxycalix[4]arene
LM	Levenberg-Marquadt
LPO	Lipidperoxidation
MB	Methylene Blue
MCT	Mercury cadmium telluride
MF	Microfiltration
MMM	Mixed matrix membranes
MOF	Metal Organic Framework
NF	Nanofiltration
NIR	Near Infra-red
ODA	Official Development Assistance
PAR	4-(2-Pyridylazo) resorcinol
PDA	Polydopamine
PET	Polyethylene terephthalate
PP	Polypropylene
PTFE	Polytetrafluoroethylene
RAIRS	Reflection-Absorption-Infrared spectroscopy
RF	Radio-frequency
RO	Reverse Osmosis
ROS	Reactive oxygen species
SDG	Sustainable Development Goal
SWR	Standard wave ratio
TAR	4-(2-thiazolylazo) resorcinol
tBu-calixarene	5,11,17,23-tetra-tert-butyl-25,26,27,28-tetrahydroxycalix[4]arene
TPU	Thermoset polyurethane
UF	Ultrafiltration
UN	United Nations
UV	Ultraviolet
VBC	Vinylbenzyl chloride
WHO	World Health Organisation
WPU	Waterborne poly(urethane-urea)



***Easy Use Recyclable Functional Cloths for On-Site Water Decontamination in ODA***

<b><i>Countries and Humanitarian Crises</i></b>	<b><i>i</i></b>
<b><i>Declaration</i></b>	<b><i>ii</i></b>
<b><i>Researcher Contributions</i></b>	<b><i>ii</i></b>
<b><i>Acknowledgements</i></b>	<b><i>iii</i></b>
<b>1 Chapter 1 – Introduction</b>	<b>1</b>
<b>1.1 Water Pollution</b>	<b>1</b>
1.1.1 Causes	1
1.1.2 Dyes	3
1.1.3 Chromium	5
1.1.4 Uranium	10
1.1.5 Filtration Methods	16
1.1.5.1 Filters and Membranes	17
1.1.5.2 Calixarenes	19
1.1.6 Scope	22
<b>1.2 References</b>	<b>23</b>
<b>2 Chapter 2 – Experimental</b>	<b>33</b>
<b>2.1 Introduction</b>	<b>33</b>
2.1.1 Fabrication Techniques	33
2.1.1.1 Plasmachemical Methods	33
2.1.2 Characterisation Techniques	39
2.1.2.1 Fourier Transform Infrared Spectroscopy	39
2.1.2.2 Spectrophotometry	48
2.1.2.3 UV–Vis Spectroscopy	50
2.1.2.4 Inductively Coupled Plasma Optical Emission Spectroscopy	51
2.1.3 Filtration Techniques	56

2.1.3.1	Dynamic Filtration	56
2.1.3.2	Static Filtration	57
<b>2.2</b>	<b>References</b>	<b>61</b>
<b>3</b>	<b>Chapter 3 – Simultaneous and Selective Extraction of Harmful Anionic and Cationic Dyes from Water Solution by Dimethylamino-Phenol Functional Cloths</b>	<b>64</b>
<b>3.1</b>	<b>Introduction</b>	<b>64</b>
<b>3.2</b>	<b>Experimental</b>	<b>68</b>
3.2.1	Preparation of Functionalised Cloths	68
3.2.2	Characterisation	68
3.2.3	Dye Extraction	69
<b>3.3</b>	<b>Results</b>	<b>71</b>
3.3.1	Characterisation of Functional Cloths	71
3.3.2	Extraction of Dyes	73
3.3.2.1	Cationic Dyes	74
3.3.2.2	Anionic Dyes	76
3.3.2.3	Neutral Dye	80
3.3.3	Maximum Adsorption Capacity	80
3.3.3.1	Experimentally Determined Adsorption Capacity	80
3.3.3.2	Isotherm Determined Adsorption Capacity	82
3.3.3.3	Thickness Dependence on Adsorption Capacity	87
3.3.4	Adsorption Kinetics	88
3.3.5	Active Site Determination	94
3.3.6	Cloth Recycling	95
3.3.7	Selectivity of Functional Cloths	100
3.3.7.1	Competing Anions	100
3.3.7.2	Competing Dyes	103
3.3.8	Alternative Substrates	105
3.3.8.1	Activated Carbon Cloth with Dye Mixture	107
3.3.9	Removal of AB10B from a Simulated Real-World Water Sample	111
<b>3.4</b>	<b>Discussion</b>	<b>113</b>
<b>3.5</b>	<b>Conclusions</b>	<b>117</b>
<b>3.6</b>	<b>References</b>	<b>119</b>



<b>4 Chapter 4 – Use of Chloroform Plasma Treatment in the Production of Dimethylaminomethyl-Calixarene Functional Cloths For Selective Capture of Toxic Hexavalent Chromium from Water Solution</b>	<b>124</b>
<b>4.1 Introduction</b>	<b>124</b>
<b>4.2 Experimental</b>	<b>126</b>
4.2.1 Preparation of Functional Cloths	126
4.2.2 Characterisation	127
4.2.3 Dichromate Extraction	128
<b>4.3 Results</b>	<b>129</b>
4.3.1 Characterisation of Functional Cloths	129
4.3.2 Extraction of Chromate Oxyanions	132
4.3.2.1 Plasma Optimisation	132
4.3.2.2 Adsorbent Comparison	133
4.3.3 Adsorption Kinetics	134
4.3.4 Isotherm Determination	137
4.3.5 Active Site Determination	141
4.3.6 Cloth Recycling	142
4.3.7 Cloth Selectivity	144
4.3.7.1 Competing Anions	144
4.3.7.2 Real-World Chromium Samples	145
<b>4.4 Discussion</b>	<b>147</b>
<b>4.5 Conclusion</b>	<b>151</b>
<b>4.6 References</b>	<b>152</b>
<b>5 Chapter 5 – Plasmachemical Preparation of Amidoxime Functionalised Cloths for the Capture and Release of Toxic Uranium from Water Solution</b>	<b>156</b>
<b>5.1 Introduction</b>	<b>156</b>
<b>5.2 Experimental</b>	<b>165</b>
5.2.1 Calixarene and Polyhydroxybenzene Functionalised Cloths	165
5.2.1.1 Preparation of Functionalised Cloths	165
5.2.2 Amidoxime Functionalised Cloths	165
5.2.2.1 Preparation of Functionalised Cloths	165
5.2.3 Characterisation	166
5.2.4 Uranium Extraction	166

<b>5.3 Results</b>	<b>168</b>
5.3.1 Calixarene Functionalised Cloths	168
5.3.1.1 Characterisation	168
5.3.1.2 Extraction of Uranium	169
5.3.2 Polyhydroxybenzene Functionalised Cloths	170
5.3.2.1 Extraction of Uranium	171
5.3.3 Amidoxime Functionalised Cloths	172
5.3.3.1 Deposition of Pulsed Plasma Poly(2-cyanoethyl acrylate)	172
5.3.3.2 Conversion to Amidoxime	175
5.3.3.3 Static Filtration of Uranium	177
5.3.3.4 Dynamic Filtration of Uranium	178
5.3.3.5 Cloth Recycling	179
5.3.3.6 Isotherm Determination	181
5.3.3.7 Adsorption Kinetics	185
5.3.3.8 Cloth Selectivity	189
<b>5.4 Discussion</b>	<b>191</b>
<b>5.5 Conclusion</b>	<b>194</b>
<b>5.6 References</b>	<b>196</b>
<b>6 Chapter 6 – Conclusion</b>	<b>203</b>
6.1 Contaminant Capture	203
6.2 Outlook	208
6.3 References	209

# 1 CHAPTER 1 – INTRODUCTION

## 1.1 Water Pollution

In 2015, all members of United Nations adopted the 2030 Agenda for Sustainable Development, described as “a shared blueprint for peace and prosperity for people and the planet”.<sup>1</sup> The agenda centres around 17 Sustainable Development Goals (SDGs), which intend to unite all countries in tackling poverty whilst attempting to fight climate change and protect the planet. The 6<sup>th</sup> goal, and one of the most important, is to “Ensure Availability and Sustainable Management of Water and Sanitation for all”. Indeed, it is predicted that 1.6 billion people will be unable to access safe drinking water by 2030, while a lack of monitoring means that water quality is unknown for over 3 billion people.<sup>2</sup>

The impact of this water pollution is deadly. The World Health Organisation (WHO) report that 829,000 die annually from diarrhoea, caused by unsafe drinking-water, sanitation and hand hygiene.<sup>3</sup> Indeed, according to a 2008 WHO report, 3.6 million deaths occur annually<sup>4</sup>—or 1.2 million deaths according to the GBD 2017 Risk Assessment Study<sup>5</sup>—from unsafe water sources. This is the twelfth greatest cause of death across all countries and is the cause of 6 % of all deaths in low-income countries.<sup>6</sup>

Consequently, developing methods of decontaminating water should be considered with upmost importance.

### 1.1.1 Causes

Water pollution exhibits the greatest impact in developing countries for three primary reasons: 1) cost; 2) governmental inefficiencies; and 3) susceptibility to natural disasters.

There are several influencing factors which determine the cost of implementing a water filtration system, including the desired quality of the filtrate (and starting quality of effluent), the flow rate of the water, the installation cost, operational expenses, and equipment maintenance. The cost of installation alone for a system designed to treat 8000–10,000 litres of water per day in India is quoted to be a minimum of Rs 2.5 lakhs (£216,735).<sup>7</sup> For comparison, the average per capita water demand is expected to reach 167 litres per day by 2050.<sup>8</sup> These costs contribute to the fact that Punjab, an Indian state with a Gross State Domestic Product (GSDP) of Rs 6.98 lakh crore (£675 billion)<sup>9</sup> and a population of 27.7 million people,<sup>10</sup> only has 101 wastewater treatment plants, capable of treating 1,367 million litres of water per day (sufficient for providing clean water for less than half the population).<sup>11</sup> Furthermore, once the

water has been treated, it must be transported, which gives rise to further costs in developing and utilising means of water transportation.

While countries often have policies designed to regulate the quality of water consumed, these are typically difficult to regulate.<sup>12,13</sup> This difficulty arises through multiple causes. To begin with—and again using India as an example—the standards themselves are somewhat unclear. The specified quality parameters vary depending on where they are being discharged, and by applying approximations that may no longer be true.<sup>14</sup> Indeed, there are different standards for different water uses, including bathing, but not irrigation (which involves significant human contact) or drinking water (other than pre-packaged bottles).<sup>15</sup> Beyond that, there are no standards for ambient waterbodies – instead they are categorised by a “water quality criteria”, which has no legal basis, and does not take into consideration industrial contaminants (including heavy metals). Even with appropriate standards, water still needs to be monitored, and reports have shown that checks are scarce—Gupta et al. reported that more than three quarters of industrial sources in Punjab are investigated less than once every 5 years, while sewage monitoring occurs only at treatment plants, which fails to consider that the majority of sewage never reaches these plants.<sup>15,16</sup> Furthermore, when measuring the quality of rivers, tests often take place far downstream of major water pollution sources – for example, Vrishabawathi river is not monitored, with the most accurate recording occurring 20 km downstream of where it meets the Arkavathy river, despite most of the pollution sources occurring upstream of the confluence.<sup>15</sup> The next problematic aspect is enforcement, as Indian pollution control boards do not have the power to enforce their own fines, meaning that any action taken needs to go through the courts, which are given a low priority, and have a very low conviction rate. Finally, the pollution control boards themselves suffer from a lack of independence—there are a number of representatives for polluters on the state boards, but there is no representation for the polluted (local population), or any independent scientific advisors.<sup>15</sup> Consequently, there is little in the way of incentive for the boards to tackle any large-scale systemic problems regarding water pollution.

Reports have demonstrated that poorer countries are more susceptible to the consequences of natural disasters, even if there is no geographical explanation for an increase in impact—e.g., a cyclone which hits the Caribbean leads to more dire consequences for (less economically developed) Haiti than for (relatively affluent) Jamaica.<sup>17</sup> It has been shown that investing in disaster prevention, decentralising relief, encouraging political accountability and rewarding states for successful management—all of which are far more possible for richer nations—gives rise to lesser impacts. As such, low-income countries are less able to prevent climate-related disasters, meaning that they are at a significantly greater risk.<sup>17,18</sup> Richer countries are better able to construct stable buildings, implement suitable land zoning laws,

and develop accurate warning systems. At a more nuanced level, countries with a high degree of income inequality, rather than necessarily overall wealth, are affected to a greater extent, owing to the increased proportion of economically marginalised people, who are particularly vulnerable.<sup>17</sup> One of the key impacts of natural disasters is an increase in water pollution. It has been shown that in the 10 days after major floods in Taiwan, there was an increase in reported diseases associated with eyes, skin and gastrointestinal (GI) tract.<sup>19</sup> The floods were reported to contaminate drinking water, as well as damage any water treatment plants. Indeed, a number of studies have reported strong links between floods and extreme rainfall with an increase in waterborne diseases.<sup>20,21,22</sup> Other forms of natural disasters exhibit similar effects on water pollution, such as earthquakes, which have been known to damage wastewater networks, leading to drinking water contamination.<sup>23</sup>

This combination of high cost of water treatment, alongside the greater extent of government inefficiencies and impacts imposed by natural disasters, means that lower income countries are at particular risk of water pollution. As such, water decontamination methods, which are cheap, easy to use, and suitable for point-of-use filtration, are essential to be developed in order to meet the needs of individuals within lower income countries. Within this thesis, water filtration methods towards three such contaminants—toxic dyes, chromium, and uranium—are discussed.

### **1.1.2 Dyes**

Dyes have been used in civilization for thousands of years, with humans frequently using natural, readily accessible colours to stain their textiles. Indeed, the oldest known coloured fibres have been radiocarbon dated as being 36,000 years old, while wearing purple clothes was a status symbol in Ancient Greece, owing to the difficulty in extracting Tyrian Purple from shellfish.<sup>24,25</sup> In 1856, Henry Perkin accidentally discovered Mauveine when attempting to synthesise Quinine, using coal tar (an unwanted by-product from coal distillation). Mauveine was able to dye fabrics a deep purple, and its fabrication led to international competition for the production of new, synthetic dyes using the distillation products from coal tar, and with it, an explosion in the number of colours available to be stained.

Nowadays, dyeing is still a significant global industry, valued at USD \$10.68 billion in 2021, and expected to grow at a Compound Annual Growth Rate (CAGR) of 4.7 % during the period of 2021–2030, reaching a value of USD \$16.08 billion by the end of the decade.<sup>26</sup> This corresponds to an annual production of over 700,000 tonnes of dyestuff, of which 1–15 % is lost to wastewater during the dyeing process.<sup>27,28,29,30</sup>

Of the dyes used in industry, approximately 70 % are classified as azo dyes, which are characterised by their containing of at least one N=N group (which is the chromophore), a skeleton (consisting of benzene rings, naphthalenes, aromatic heterocycles, or enolizable aliphatic groups), auxochrome groups, and water solubilising groups.<sup>31,32</sup> There are a large number of azo dyes, the majority of which are anionic (otherwise known as acid dyes, owing to their acidic properties), and the rest being predominantly neutral, with only three cationic (basic) azo dyes.

Basic dyes were originally developed for their dyeing of silk but are nowadays used predominantly for acrylic fibres and paper.<sup>25</sup> Their cationic group helps to provide the colour, with those derived from triphenyl methane giving exceptionally bright colours. They are required for acrylic fibres, as poly(acrylonitrile) carries a negative charge, meaning that it is electrostatically attracted to the cationic dye.<sup>33</sup> The dyes' positive charge is non-localised, resonating within the structure of the dye, giving rise to poor light-fastness (tendency of the colour to fade when exposed to light).<sup>34</sup> Despite their name, the dyes are usually applied in neutral to weakly acidic conditions.

Neutral azo dyes do not contain the water-soluble groups, meaning that they are insoluble. They are classed as disperse dyes, which are synthetic, non-ionic, slightly polar dyes, containing anthraquinone and/or azo groups, originally designed for dyeing cellulose acetate, but now more commonly used for dyeing polyester and hydrophobic fabrics.<sup>25,35,36</sup> They are typically used in industry by boiling at close to 100 °C in conjunction with a dispersion agent, to overcome the poor solubility in water.<sup>37</sup> Alternatively, the dyes are kept in solid form as pigments, and used in paints and food pigments. Indeed, neutral azo pigments, first discovered in 1858, are the oldest and most widely used food pigments.<sup>38</sup>

Acid dyes are routinely used on textiles containing amido groups, as the anionic groups are able to electrostatically interact with the amine groups present, which become acidified under the conditions (pH 2.6) employed.<sup>25</sup> Consequently, they are popular for the dyeing of wool, which contains ~ 20 times as many amino groups as nylon, and ~ five times as many as silk.<sup>39</sup> In addition to the electrostatic interaction, hydrogen bonds and Van Der Waal's forces between the dye and textile can form, however these are less significant than the electrostatic attractions. Azo acid dyes are also particularly popular due to their good light-fastness properties.<sup>39</sup> One such example is Amido Black 10B (AB10B, Figure 1-1) reported to be commonly used in cotton, wool, ink, plastic, and paint industries, but can damage skin, eyes, and the respiratory system.<sup>40</sup> Indeed, aromatic dyes can be carcinogenic, mutagenic, and teratogenic, and so the ability to remove azo dyes such as AB10B from solution is considered

important in a world where rapid industrial development has resulted in a sharp rise in hazardous pollutant discharge.<sup>41</sup>

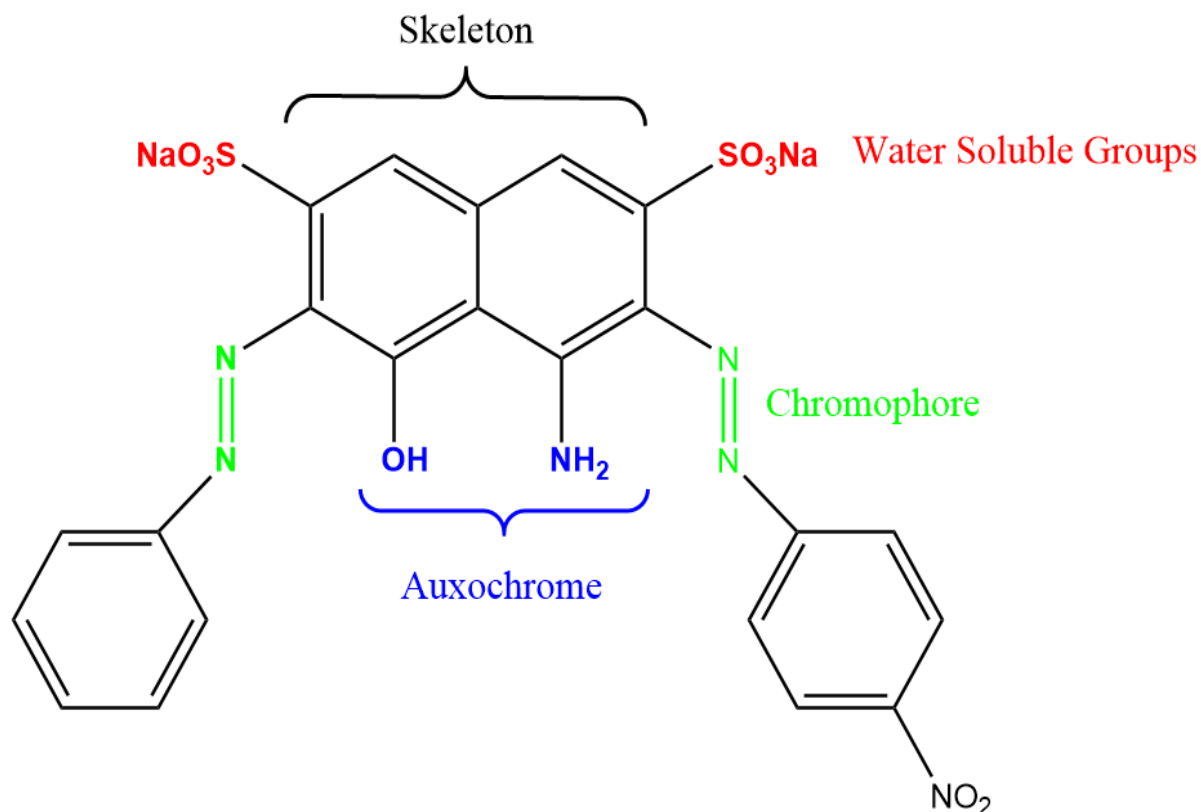


Figure 1-1. Structure of anionic azo dye, Amido Black 10B.

In addition to acid, basic, and disperse dyes, the Colour Index also subdivides dyes into direct dyes, reactive dyes, and vat dyes, however this work does not concern any dyes of these categories.

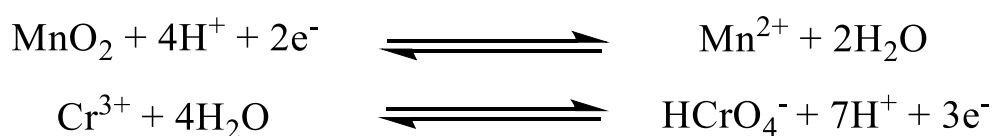
### 1.1.3 Chromium

Chromium, first discovered in 1797 by Louis-Nicolas Vauquelin, has been used in industry since the 19<sup>th</sup> century, although it has been used (unknowingly) since the Qin dynasty (259–210 B.C.E.), who used  $\text{Cr}_2\text{O}_3$  to coat their weapons.<sup>42,43</sup> These applications include textile and pigment mordanting, leather tanning, metallurgy and chromium plating. In modern day, chromium plating is still very common, while chromium is additionally used as industrial catalysts and pigments, while rubies—which exhibit their red colour due to the presence of chromium—are classified as precious stones, and therefore their mining is economically desirable. Furthermore, the majority of leather is tanned—a necessary process, in which animal hides are converted into heat- and microbial-resistant leathers, by forming coordination bonds with multiple carboxyl groups within the collagen fibres—using chromium salts (chrome tanning, which results in leather containing 4–5 % chromium) including potassium

chromium(III) sulfate dodecahydrate (chromium alum),  $\text{KCr}(\text{SO}_4)_2 \cdot 12\text{H}_2\text{O}$  and chromium(III) sulfate dodecahydrate,  $\text{Cr}_2(\text{SO}_4)_3 \cdot 12\text{H}_2\text{O}$ .<sup>43,44,45</sup> Its popularity arises as chrome-tanned leather exhibits excellent hydrothermal stability and reliable mechanical behaviour.

Globally, the leather industry produces 1.7 billion  $\text{m}^2$  of leather at an estimated market value of 34 billion Euros with China and India being the leading producers, alongside notable contributions from Italy, Turkey and Brazil.<sup>46,47</sup> Such a large-scale operation naturally incurs significant waste, with only 20 % (by weight) of starting hides being converted into leather, with a significant proportion of the starting weight contributing to tanned waste, non-tanned waste, and wastewater.<sup>48</sup> Within the wastewater, the chromium concentration has been reported to lie in the 2000–5000  $\text{mg L}^{-1}$  region, far above the permissible limit in Indian wastewater of 2  $\text{mg L}^{-1}$ , and considerably greater than the UN's safe drinking level of 50  $\mu\text{g L}^{-1}$  provided by the WHO.<sup>49,50</sup> This wastewater can be treated, and indeed over the past three decades, the number and efficacy of these plants has improved. However, as discussed in Section 1.1.1, there is still room for improvement.<sup>51</sup> Furthermore, the treatment of the wastewater gives rise to the production of chromium-contaminated waste in the form of sludge, for which countries like India do not have large-scale scientific solid waste disposal. As a result, this sludge is often disposed of in poorly maintained dumping sites. Indeed, it has been reported that 2000–3000 tonnes of chromium are leached into the environment every year in India alone, due to these two contaminant sources.<sup>49</sup>

While the trivalent salts used in the leather tanning process do not possess a particularly significant level of toxicity, the Cr(III) species have been reported to oxidise to Cr(VI) in atmospheric conditions. Furthermore, concentrations as high as 0.6  $\text{mg MnO}_2$  per gram of sludge have been reported.<sup>49</sup> This  $\text{MnO}_2$  is able to act as an oxidising agent, leading to the following redox reactions:



Moreover, the  $\text{Mn}^{2+}$  is capable of reacting with dissolved oxygen, which regenerates the  $\text{MnO}_2$ , meaning that its concentration can be assumed to be effectively constant, and so it is capable of continuously oxidising Cr(III) to Cr(VI). Consequently, the  $\text{MnO}_2$  is described as an electron transporter between Cr(III) and dissolved oxygen. Once oxidised, solid particles containing Cr(VI) are released into the air, and carried by wind into nearby waterbodies, which are then contaminated.<sup>52</sup>



In addition to sludge, the leather industry also produces chrome-tanned leather shavings (CTLS) and chrome-tanned leather trimmings (CTLT). Indeed, an estimated 0.8 million tonnes of CTLS are produced annually across the globe.<sup>48</sup> This waste is typically disposed of in landfills, and where improper lineage of the landfill sites occurs, the leachate can mix with the soil and groundwater. Indeed, previous investigations demonstrated that when the solid residue (CTLS and CTLT) was left in contact with water, a toxic concentration of chromium is released into the water, with chromium concentration increasing with contact time and solid/liquid ratio.<sup>53</sup> Alternatively, these materials can be incinerated, however the heating of the trimmings in an oxygen rich environment readily leads to the production of soluble, toxic Cr(VI)-containing gas.<sup>53</sup>

Chromite mining is an additional contributor to chromium pollution. Within India, the Sukinda Valley contains 90 % of the country's reserves, and owing to the considerable amount of mining waste produced, it has been classified as one of the world's top 10 most polluted places.<sup>54</sup> The mining technique used is open-cast (otherwise known as open-pit), which is a particularly environmentally damaging technique, and the degradation to landscape combined with dumped waste—one ton of mined chromite is reported to produce 10 tons of waste—results in the ready seepage of chromium into air, water and soil.<sup>54</sup> The concentration of chromium found in local surface water has therefore been reported to reach 0.201 mg L<sup>-1</sup>, approximately 4 times the WHO legal safe drinking limit of chromium.<sup>50</sup> Indeed, 24.47 % of people who live within 1 km of the mines suffered from pollution-induced disorders.<sup>54</sup>

In addition to mining and leather tanning, other sources of chromium pollution exist. For example, and as stated previously, chrome tanning is still commonly employed worldwide. This involves submerging a piece of metal in an activation bath (make-up dependent on alloy), to remove oxides from the metal surfaces in order to prepare it for coating. The activated metal is then placed in a chromium bath, containing sulfuric acid and chromic acid (CrO<sub>3</sub>) in a ratio by mass of 1:75–250, with a solution pH of 0. The hexavalent chromic acid is reduced to Cr<sup>3+</sup>, then unstable Cr<sup>2+</sup>, before finally precipitating as Cr<sup>0</sup> onto the activated metal surface.<sup>55</sup> Hexavalent chromium is typically required as the starting material rather than Cr(III), despite its *in situ* production, as too high a concentration of Cr(III) (> 2–3 % of starting chromic acid content) causes issues, owing to its ability to readily form (within 1 s) stable [Cr(H<sub>2</sub>O)<sub>6</sub>]<sup>3+</sup>.<sup>56</sup> In 2017, the European REACH regulation outlawed the use of hexavalent chromium from industrial processes.<sup>57</sup> As such, investigations into chrome plating using Cr(III) (instead of Cr(VI)) baths have been conducted. By using complexing agents such as formate and acetate, the formation of [Cr(H<sub>2</sub>O)<sub>6</sub>]<sup>3+</sup> can be avoided, allowing for the reduction to Cr<sup>0</sup>.<sup>55</sup> However, trivalent chromium baths do exhibit drawbacks. As well as their lower covering power when compared to hexavalent chromium, trivalent baths exhibit a lower conductivity, meaning that

they require greater voltages and hence greater energy consumption.<sup>58</sup> However, trivalent baths do not require as high a temperature as hexavalent baths. Naturally, this EU law does not apply to developing countries, where the easier use of hexavalent baths makes them considerably more popular. Given that concentration of Cr(VI) as high as 5721.95 mg L<sup>-1</sup> have been reported in industrial chrome plating wastewater (approximately 100,000 x the UN safe drinking limit of 0.05 mg L<sup>-1</sup>), if the chromium is not properly contained, then significant harm to the environment may occur.<sup>59</sup>

Furthermore, while industrial processes give rise to chromium pollution when in operation, they can also create long-term contamination once obsolete. Proper shut down and decontamination procedures can be expensive, and so may not be properly performed, especially in countries with weaker regulation. For example, recently there have been 26 abandoned chromate production sites, and 50 abandoned chromium slag dumping grounds in China.<sup>60</sup> Due to mismanagement of these, and other, sites, it has been reported that there are now over 500,000 sites of industrial contamination within China.<sup>61</sup>

Perhaps the most famous case of chromium pollution was in Hinkley, California, where hexavalent chromium was used as a corrosion inhibitor, before chromium polluted water was released into unlined pools, whereupon it could seep into nearby groundwater.<sup>62,63</sup> The subsequent court case and \$333 million lawsuit was brought to life in the 2000 film "Erin Brockovich". Table 1-1 provides a summary of a selection of real-world locations, where chromium pollution has been reported, and the sources responsible.

Table 1-1. Sources of real-world chromium polluted water.

<b>Location; Year</b>	<b>Chromium Concentration / mg L<sup>-1</sup></b>	<b>Pollution Source</b>	<b>Reference</b>
Liaoning Province, China; 1979	0.001–4.33 (depending on distance from factory)	Metallic chromium smelting	64
Hickley, California, US; 1987	Ca. 0.5	Chromium as a corrosion inhibitor	62, 63
Sukinda Valley, India; 2007	0.018–0.201	Chromite Mining	54
Oinofita, Greece; 2007–2009	0.041–0.156	Dumping of processed industrial waste into Asopos river.	65

Location; Year	Chromium Concentration / mg L <sup>-1</sup>	Pollution Source	Reference
Utter Pradesh, India; 2009	16.3	Leather industry waste	66
Andra Pradesh, India; 2010	0.011–0.418	Anthropogenic activities	67
Kerala, India; 2010/11	0.08–1.1	Municipal waste dumping	68
Qujing, Yunan, China; 2011	“...standard of Cr (VI) concentration detected in Nanpan River was about 2000 times”. <i>Unclear what the concentration is 200 times greater than.</i>	Illegal dumping of untreated chromium slag	69
Delhi, India; 2013–2015	0.002–1.98	Improper waste disposal	70
Henan Province, China; 2017	317.65 (total chromium), 163.67 (hexavalent chromium)	N/D	71
Xianxing City, Henan Province, China; 2020	0.0–4.5	Chromium slag waste from a chromate production plant	61

As previously mentioned, Cr(III) salts do not possess a particularly high level of toxicity. However, the Cr(VI) salts—which can be readily formed via oxidation of Cr(III) as discussed above—are known to be toxic and carcinogenic. Furthermore, Cr(VI) salts exhibit a greater hydroxide solubility, meaning that it is more mobile and bioavailable.<sup>48</sup> Hexavalent chromium compounds are readily absorbed by the lungs, digestive tract, and skin.<sup>42</sup> Following inhalation, the chromium compounds induce severe trachea-bronchial irritation, while consuming doses containing 50–80 mg exhibit a caustic effect and give rise to digestive disorders, with specific targeting of the kidney – Cr(VI) has been reported to induce abnormally overactive autophagy in rat kidneys.<sup>72</sup> Within minutes of ingestion, haemorrhagic gastroenteritis occurs, alongside a hepato-cellular deficiency with icterus as well as disseminated intra-vascular coagulation syndrome and acute interstitial tubular nephritis, which leads to acute renal oligo-anuric deficiency.<sup>42</sup> While deaths via skin contact are more rarely reported, an ointment developed in the early 20<sup>th</sup> century, which replaced a sulfur-containing component with a hexavalent

chromium compound, led to the deaths of 12 individuals.<sup>42</sup> Furthermore, frequent contact with hexavalent chromium compounds has been reported to lead to atopic dermatosis.<sup>72</sup>

The carcinogenic effects of Cr(VI) are particularly concerning, with lung cancers arising from chromium compounds having been reported since the 19<sup>th</sup> century.<sup>42</sup> Hexavalent chromium salts are readily able to cross cell membranes, owing to its resemblance of sulfate and phosphate, and hence exhibits a preference of binding to positively charged N7 of guanine on the phosphate backbone of DNA (molecular mimicry),<sup>73</sup> whereupon they are able to oxidise the cell contents (oxidative stress), and in turn produce Cr(III). The Cr(III), which itself is far less able to penetrate a cell membrane, combines with proteins, especially AND and ARN, which are then trapped inside the cell and accumulate. It is the combination of oxidative stress and binding of Cr(III) to DNA that are believed to give rise to the observed mutagenic and genotoxic effects. Furthermore, Cr(VI) is also believed to behave synergistically with other organic carcinogens by inhibiting the repair of benzo(a)pyrene adducts.<sup>74</sup>

#### **1.1.4 Uranium**

An increasing dependence on groundwater has led to a rapid decrease in water reserves – for example, North-Western India has reported that 40 mm/year of water are being lost.<sup>75</sup> In addition, surface runoff and erosion can give rise to contamination. Mining can exacerbate this process, wherein heavy metals from abandoned mines and mine tailings are transported (e.g., by wind), and then seep into groundwater. Uranium is one such heavy metal that has been widely reported to be found in groundwater.<sup>76,77,78</sup> The WHO provides a safe recommended drinking limit of 30  $\mu\text{g L}^{-1}$ ,<sup>79</sup> and the widespread nature of uranium contamination is depicted in Figure 1-2,<sup>80</sup> which portrays the regions of India where the reported concentration of uranium in groundwater is greater than the safe drinking limit. The maximum concentration recorded within this study was 300  $\mu\text{g L}^{-1}$ , with concentrations around 50  $\mu\text{g L}^{-1}$  frequently observed.

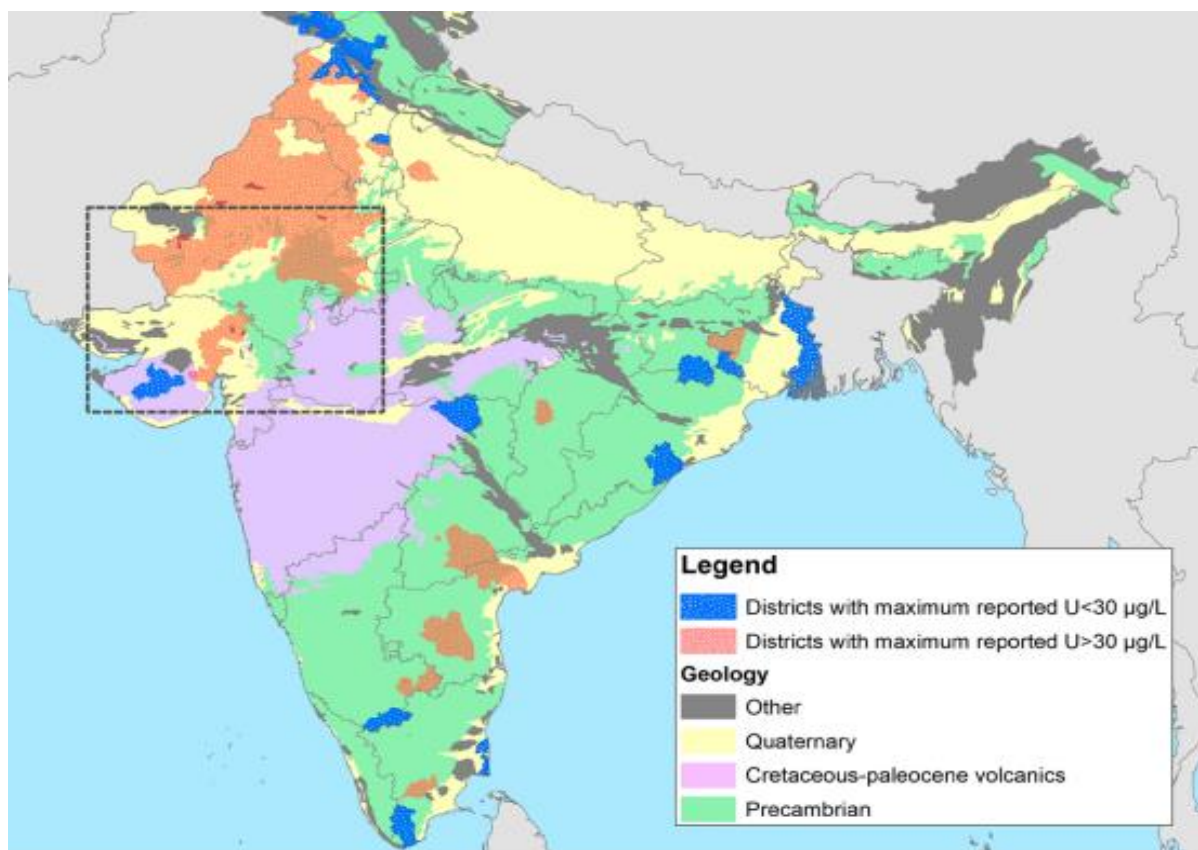


Figure 1-2. Major geological formations in India, and regions where uranium is above (red) and below (blue) the WHO uranium drinking guideline limit, taken from reference 80.

Uranium is a naturally occurring element, 500 times more abundant than gold, with concentrations as high as 15 and 120 mg kg<sup>-1</sup> found in granite and phosphate rock respectively.<sup>76,81</sup> Felsic rock tends to yield greater uranium concentration, owing to the high valence and high ionic radius of uranium being incompatible with silicate magmas.<sup>76</sup> Uranium is most commonly found naturally in the tetravalent U(IV) (reducing conditions) and hexavalent U(VI) (oxidising conditions) forms, however only U(VI) is soluble in water. When water is acidic (for example in nuclear wastewater<sup>82</sup>), U(VI) is found in the free UO<sub>2</sub><sup>2+</sup> state, while under more neutral conditions, uranium forms various hydroxide and carbonate complexes with the components within groundwater (Figure 1-3).<sup>83</sup> As such, all relevant work discussing the removal of uranium from groundwater typically concern interactions with UO<sub>2</sub><sup>2+</sup> species.

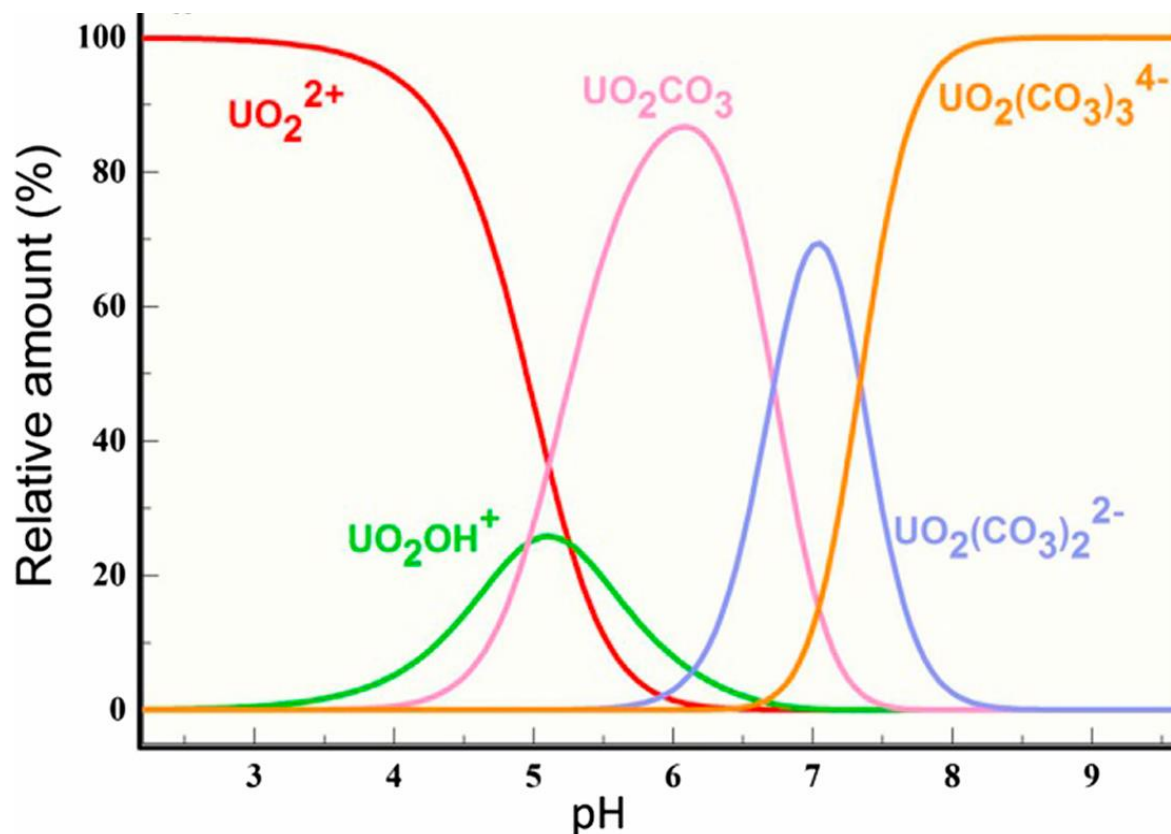


Figure 1-3. Speciation of U(VI). Taken from reference 83.

Uranium does occur naturally in groundwater due to leaching of uranium from U-hosting materials, such as Fe-Mn(oxy) hydroxides within bedrock under oxic conditions.<sup>84</sup> Consequently, uranium can be found in groundwater worldwide, with a greatest concentration of  $12 \text{ mg L}^{-1}$  found in Finnish wells, which are drilled into bedrock (Figure 1-4).<sup>85</sup> As well as leaching from the bedrock, uranium has also been found to occur naturally in groundwater via weathering of surface rocks. For example in north western Punjab, uranium found within the Himalayan Siwaliks can be extracted via rainwater, then dissolve into the surface, before mobilising towards the rivers in the Malma region of Punjab via hydrogeological migration paths (Figure 1-5).<sup>86</sup>

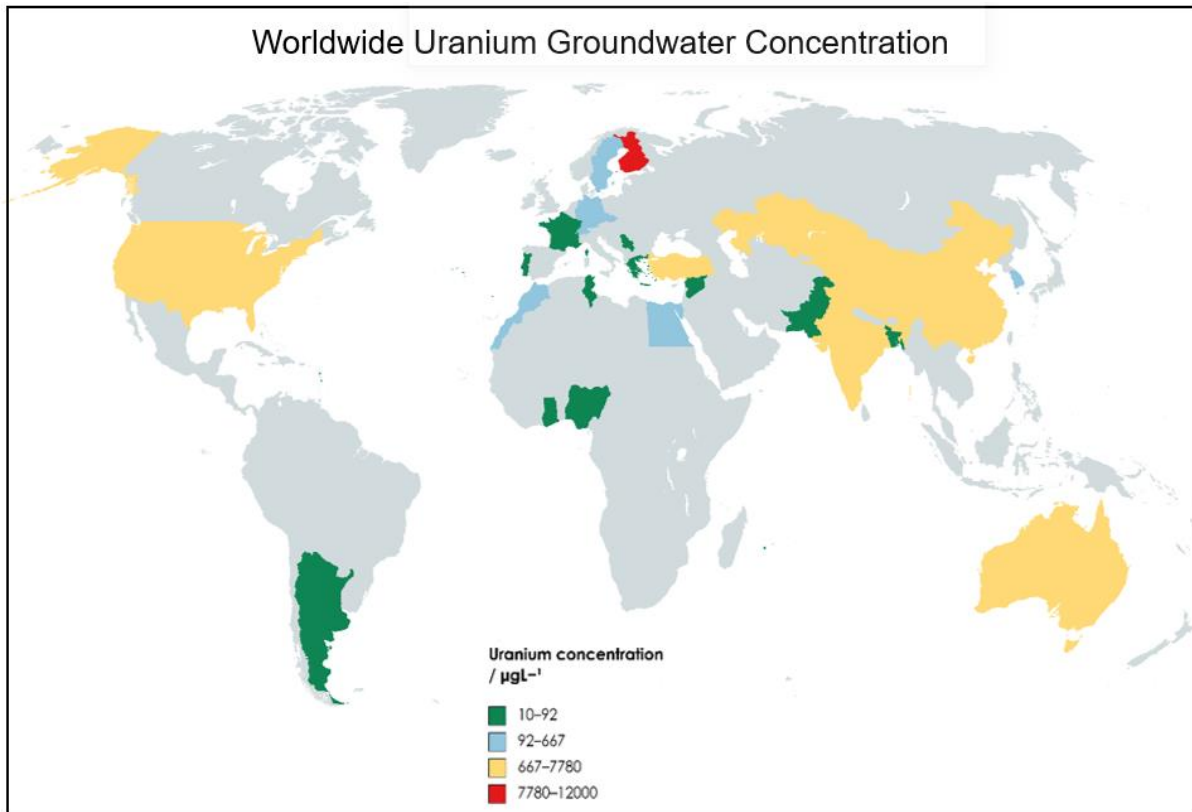


Figure 1-4. Concentration of uranium in groundwater reserves worldwide, using data from references 76 and 87. Where there are multiple data points, the highest U concentration value has been taken.

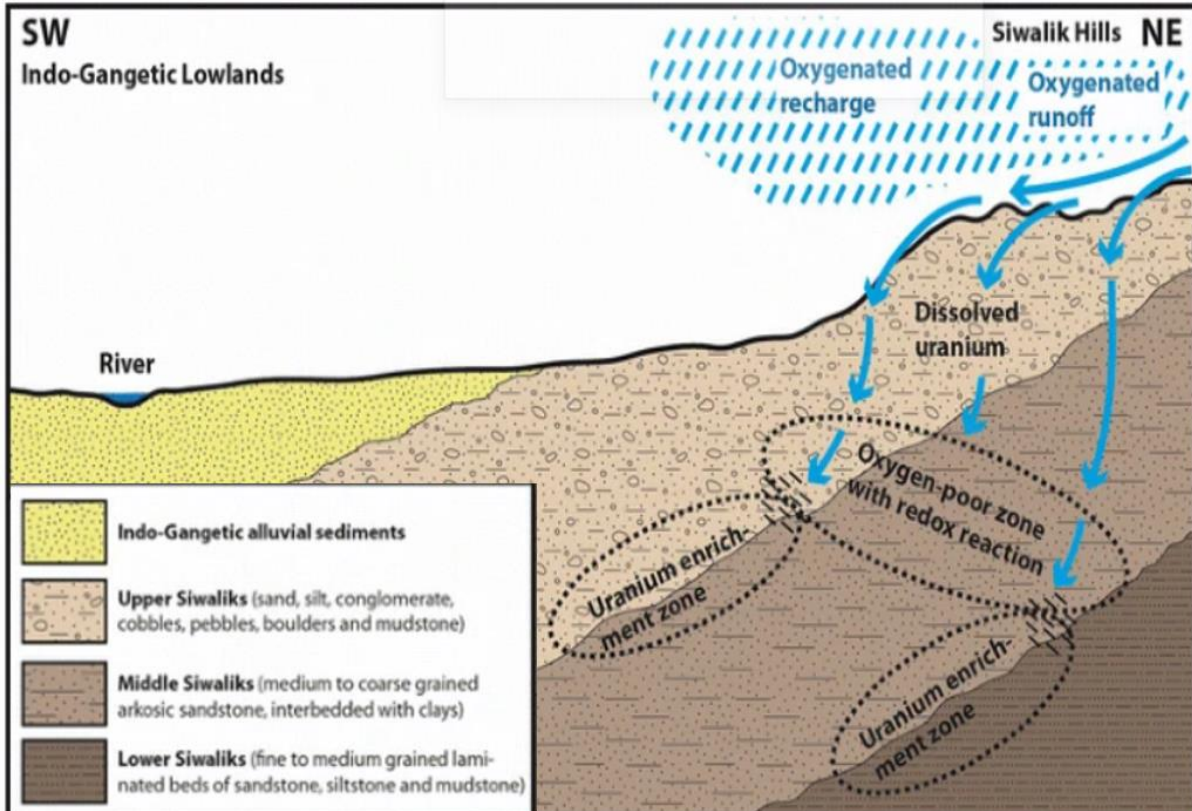


Figure 1-5. Simplified depiction of the mobilization of uranium from the Himalyan Siwaliks to lowland rivers, taken from reference 86.



Unfortunately, uranium has also been found in groundwater due to anthropogenic causes, including pollution from nuclear wastewater,<sup>82,88,89</sup> exacerbating previous uranium levels due to mining,<sup>90,91,92,93,94,95,96,97</sup> and agricultural activities.<sup>77,98,99,100,101,102</sup>

The reliance on nuclear power has grown rapidly over the past few years, with the percentage of the world's power deriving from nuclear power plants rising from 10.3 % in 2020 to 18.9 % in 2021, with the trend expected to increase further.<sup>82</sup> Owing to the vast quantities of water required to cool reactors, significant nuclear wastewater is produced, and needs to be treated. Furthermore, the other processes required to complete the nuclear fuel cycle, including enrichment, fuel fabrication, and treating of spent fuel, all produce their own form of radioactive waste.<sup>89</sup> Additionally, natural disasters, such as the Great East Japan Earthquake, which damaged the Fukushima Daiichi Nuclear Power Plant in March 2012, demonstrate the frailties of powerplants, and the significant hazards associated with radioactive pollution.<sup>88</sup> The conversation regarding nuclear wastewater is particularly topical, as Japan has recently received UN approval to release more than 1.2 million tons of nuclear wastewater from the Fukushima power plant into the Pacific Ocean.<sup>103,104</sup> The wastewater was created by the injection of seawater into the plant to prevent meltdown and has since been stored in the water storage tower, which is now approaching capacity. Despite the UN report claiming that the release was safe according to international safety standards, there has been significant backlash from neighbouring countries, oceanographers, environmental groups, and fishing groups.<sup>105,104</sup> Owing to the particularly long-term radioactive impacts of nuclear waste, storage and disposal of said waste is well regulated worldwide in order to avoid contamination. Very low-level waste and low-level waste are not particularly radioactive, and therefore can be sealed and disposed close to the surface level. However, high-level waste cannot be safely disposed, other than burying in extremely deep repositories which do not yet exist (the US has built a 655 m deep repository suitable for long-lived intermediate waste, but no disposal of high-level waste occurs).<sup>106</sup> High-level waste is instead stored in sealed vats, within pools, ca. 10 m deep for decades, before being converted into solid waste, resealed and restored deep below ground. As such, leaching of uranium from nuclear waste is generally well prevented, however due to the large quantities of nuclear waste in storage (ca. 3 million m<sup>3</sup> of very low-level waste, ca. 1.5 million m<sup>3</sup> of low-level waste, ca. 3 million m<sup>3</sup> intermediate level waste, and 29,000 m<sup>3</sup> of high-level waste)<sup>107</sup>, when events such as the Great East Japan Earthquake do occur, significant pollution is possible.

However, the most widespread form of uranium pollution due to the nuclear fuel cycle is the first stage – the mining and milling of the uranium ore, which releases  $1.8 \times 10^{-2}$  Curies per GWy of uranium (compared to  $2.0 \times 10^{-3}$ ,  $9.9 \times 10^{-4}$ , and  $2.0 \times 10^{-5}$  Curies per GWy for the conversion, enrichment and fabrication processes respectively).<sup>91</sup> For mines which are



open-pit or underground, it is common for uranium-containing water to be released into the ground, while solid waste, such as waste rock and overburden, or uranium mill tailings, can be directly deposited, leading to soil contamination. As with chromium (Section 1.1.3), the greatest levels of contamination can occur when mines are abandoned, even in more developed countries—for example the Midnite Mine in the USA, which was abandoned in 1981, left behind 2.4 million tons of ore and 33 million tons of waste rock in stockpiles.<sup>92</sup> These remnants have been used as gravel for access and haul roads, while two of the original pits have since filled with water, which is capable of draining into Lake Roosevelt. Here, elevated uranium concentrations were observed along the main access road to the mine, and at the original processing mill. Even greater uranium concentrations were determined in stream water close to an abandoned uranium mine in Portugal, which was similarly ill-efficiently decommissioned.<sup>93</sup>

Increased uranium content in soil has been observed in areas where agricultural activities are prevalent. Earlier research attributed an increase in uranium content to the use of phosphate-bearing fertiliser.<sup>98</sup> As phosphate fertilisers contain  $0\text{--}200 \mu\text{g}_{\text{Uranium}}\text{g}_{\text{Fertiliser}}^{-1}$ ,<sup>108</sup> and uranium is known to exchange with calcium ions within apatite,<sup>109</sup> it was theorised that uranium contained within phosphate fertilisers would readily leach into the topsoil. Furthermore, it was claimed that uranium may be found in manure, originating from phosphorous mineral supplements in livestock feeds, which are able to pass through cattle almost completely.<sup>98</sup> Indeed, it has been reported that the use of phosphate fertilisers has led to 14,000 tonnes of uranium being applied to the soil (equivalent to 1 kg U per hectare) over a 60 year period in Germany.<sup>102</sup> This phenomenon was also observed in the US, where uranium concentrations found in groundwater were shown to not derive solely from carbonate lithologies, suggesting an additional source.<sup>101</sup> These authors commented on previous work, which demonstrated a link between uranium and nitrate concentrations in agricultural land groundwater,<sup>110</sup> and suggested an alternative explanation—namely, that the uranium originated from the same sources as the nitrate (the fertiliser). However, research by Banning et al. compared soil samples from land used for agriculture with soil from land without agricultural usage, and could find little difference in uranium concentration, potentially minimising the claim that agriculture leads to anthropogenic input of uranium into soil.<sup>100</sup> This same finding was observed by Lapworth et al., where despite observing elevated levels of uranium in groundwater, no link to fertiliser uranium sources, even in the most aggressively farmed regions, was found.<sup>111</sup> It has been suggested that the presence of nitrate abiotically oxidises U(IV) to the more mobile U(VI), which is then able to permeate into local groundwater, while simultaneously, nitrate-driven Fe(II) oxidation has been reported to produce Fe(III) oxides, that can in turn oxidise U(IV) to U(VI).<sup>110</sup>

Although uranium is classified as a radioactive element, the half-life of  $U^{238}$  (99.284 % abundance) is 4.5 billion years, while the half-life of  $U^{235}$  (0.711 % abundance) is 710 million years.<sup>112</sup> These long half-lives mean that uranium is classified as weakly radioactive. However, uranium is primarily an alpha emitter, and so, while it possesses little radioactive risk when in contact with the skin, uranium can cause damage to internal sensitive tissue if ingested or inhaled. Uranium does also decay through complex chains involving beta, gamma and X-rays, meaning that external radiation can be a problem; however, this is only relevant if directly handling unshielded bulk uranium.<sup>113</sup> More pertinently, both uranium species eventually decay to radium, which in turn decays to radon. Radioactive radon gas has been known to gather in areas of poor ventilation, including mine shafts, where it can be inhaled by workers.<sup>114</sup> Once inhaled, radon and its progeny are able to alpha decay, with the radiation attacking the internal organs, particularly the lungs—radon exposure has been attributed to the second highest number of cases of lung cancer (after smoking).<sup>115</sup>

Rather than radioactive risks, it is the chemical risks associated with uranium as a heavy metal which result in the greatest harm to humans. Uranium is capable of accumulating in people's urine after recent (2–15 days) exposure, nail and hair after several months, and bones after years of uranium exposure, demonstrating that uranium is inefficiently cleared from bodies.<sup>96</sup> Indeed, a study into the retention of uranium by rats following inhalation demonstrated that 78.3 % of the initial uranium was retained in the lungs with a half-life of 141.5 days.<sup>116</sup> Once in the lungs, the presence of uranium generates reactive oxygen species (ROS), which leads to lipidperoxidation (LPO), resulting in cell membrane damage and eventually cell death.<sup>117</sup> As such, in its insoluble form, uranium has been known to cause bone, lung and gastrointestinal cancers.<sup>96</sup>

The renal effects of uranium are particularly significant, with the kidney being the main target organ of uranium following adsorption.<sup>85,118,119</sup> Uranium forms carbonate complexes in the blood, where they are filtered in the kidney at the glomerulus, whereupon they dissociate owing to the acidity of the proximal tubule. The released uranyl ions are then able to react with the filtrate, or parts of the tubular membrane. This binding of uranium has been claimed to alter sodium permeability of the cells, leading to reduced transport and increased excretion of glucose, amino acids and phosphates.<sup>118,119</sup> At sufficiently high levels of uranium accumulation, kidney damage can occur, and is the greatest risk to patient health and chance of survival.

### **1.1.5 Filtration Methods**

There are several different methods of removing contaminants from water. Typically, the first stage in treating water is to use a screen filter, which removes large debris such as leaves,

before inorganic coagulants (e.g., aluminium sulfate<sup>120</sup>) are added, which first serve to neutralise charged contaminants, then adsorb organic species on metal hydroxide precipitates, before entrapping insoluble metal hydroxides (coagulation and flocculation). The particles (floc) are then able to be moved via sedimentation—as the particles settle, a layer of sludge forms on the basin of the tanks, which can be removed mechanically or manually. For particles that do not remove easily, dissolved air flotation is employed. This involves injecting pressurised water into the tank, to produce small bubbles (< 100 µm).<sup>121</sup> The bubbles can become entrapped in large floc structures, nucleate on flocs, or collide with floc when performed. These bubbles then carry the floc to the surface, where it can be removed from the surface of the water. Finally, water is disinfected (e.g., with chlorine,<sup>122</sup> CO<sub>2</sub>,<sup>123</sup> chloramine,<sup>124</sup> ozone,<sup>125</sup> or UV radiation<sup>126</sup>) in order to kill microorganisms including bacteria and viruses, before being filtered (Section 1.1.5.1).

In some countries, and some private supplies, alternative methods of purification are employed. The oldest method involves boiling the water. This is incredibly effective at removing harmful microorganisms, however it is incapable of removing chemical impurities such as dyes, chromium, or uranium.<sup>127</sup> A similar process is distillation, which involves repeated boiling and condensing of water, yielding pure water.<sup>128</sup> This process is particularly important for desalination, which is capable of converting seawater into drinking water.<sup>129</sup>

#### 1.1.5.1 Filters and Membranes

The filtration stage of water purification is the most varied, with the type of filtration required dependent on the contaminants remaining in solution. All of these filtration methods involve passing the water over or through some form of membrane or adsorbate, which removes the target contaminant.

Indeed, some of the methods listed in the previous section can also be combined with membranes to improve efficiency. One such common method is membrane distillation. Water is heated, then comes into contact with a hydrophobic membrane filled with air. At the interface, the feed water evaporates, and the vapour is capable of diffusing through the air trapped in the membrane, whereupon it then condenses on reaching a cool permeate stream at the other side of the membrane.<sup>130</sup> Non-volatile solutes are repelled at the vapour-liquid interface, and so remain in solution. As with conventional distillation, membrane distillation is also employed for desalination.<sup>131</sup>

Mechanical filtration (a.k.a. membrane filtration) is the simplest form of filtration, in which semi-permeable membranes are designed, such that when a fluid passes through the membrane, particles which are too large become ensnared by the membrane, removing it

from the feed. Membrane filtration can be categorised further, depending on the size of the particles it is capable of removing: particle filtration can remove contaminants no smaller than 10  $\mu\text{m}$ ; microfiltration (MF) removes particles between 0.1 and 10  $\mu\text{m}$ ; ultrafiltration (UF) removes particles between 10 nm and 0.5  $\mu\text{m}$ ; nanofiltration (NF) removes particles between 1 and 12.5 nm; and hyperfiltration removes particles between 0.1 and 1.5 nm.<sup>132,133</sup> MF and UF work by similar mechanisms to particle filtration, namely: 1) sieving, in which particles larger than the pores cannot permeate, whereas smaller particles will pass through (the primary mechanism for screen filters, which contain capillary-type pores); and 2) adsorption and mechanical entrapment, which involves non-absolute removal of a range of particle sizes (the primary mechanism for depth filters, which contain a random, torturous porous structure).<sup>134</sup> The only difference is that UF membranes are much denser, with an asymmetric structure, yielding narrower pore sizes, and giving rise to a greater hydrodynamic resistance.<sup>135</sup> As such, the operating pressures of UF are slightly greater (2–5 bar) than for MF (1–3 bar). Nanofiltration is more commonly employed for the removal of dyes and heavy metals.<sup>135</sup> The rejection mechanism is based on size effects for neutral contaminants, as with MF and UF, but also due to Donnan exclusion effects, wherein ionic groups on the membrane dissociate (or ions become adsorbed onto the walls of the pores, inducing an electrical double layer<sup>136</sup>), leading to a charged membrane, which is capable of repelling charged, soluble, molecules. This electric potential means that ions smaller than the pores are able to be rejected.<sup>137</sup> In addition, dielectric and transport effects have also been attributed to contribute to the nanofiltration mechanism. Again, due to the smaller pore size, a greater pressure (5–15 bar) is required to drive the filtration. Reverse-osmosis (RO) falls in the hyperfiltration category and is a commonly employed method for desalination. Here, pressure is applied to the feed water to pass it through a semi-permeable membrane, with the pressure required to be greater than the natural osmotic pressure of the system (e.g., for desalination, seawater has a natural osmotic pressure of 25–33 bar,<sup>138</sup> so pressures up to 80 bar are employed<sup>139</sup>). It has been claimed that the extraction mechanism for RO membranes is the same as for NF membranes.<sup>135,136</sup>

Ion-exchange is another particularly common filtration method. Typically this method does not require membranes (rather, ion-exchange resins are left in contact with the contaminated solution for an extended period of time, such that the ions required to be removed come into contact with the resin, allowing for a substitution reaction to take place).<sup>140</sup> However, it is possible to fabricate ion-exchange membranes.<sup>141</sup> These membranes are made up of highly cross-linked ion-exchange resins, which contain e.g.,  $\text{SO}_3\text{H}$ ,  $\text{PO}_3\text{H}$ ,  $\text{COOH}$  and  $\text{NH}_3\text{OH}$  functional groups. As water, containing a range of ions, passes through the membranes, protons or  $\text{OH}^-$  ions are released from the membrane, substituted by cations and

anions respectively in solution. While ion exchange has been employed to remove poisonous metal ions (e.g., cobalt, copper and nickel)<sup>142</sup>, its most common use is water softening, in which calcium and magnesium ions found in “hard” water are replaced with hydrogen or sodium ions to yield “soft” water.<sup>143</sup>

A final, and popular, non-membrane filtration method, which is particularly relevant to this work, is adsorption. Adsorption is a particularly low-cost and facile water treatment mechanism with high efficiency and flexibility.<sup>144</sup> As with ion-exchange, water is left for a period of time in contact with a solid adsorbent, such that contaminants are transferred from the water to the adsorbent. In order to be effective, adsorbents are required to be chemically and mechanically stable, have a high surface area, be recyclable and exhibit fast kinetics, not all of which are simultaneously possible. Recent developments into novel adsorbents, such as Metal Organic Frameworks (MOFs) (e.g., ZIF-67, which is capable of removing 1683.8 mg<sub>UGMOF</sub><sup>-1</sup>)<sup>145</sup> show significant promise in addressing the drawbacks of adsorption as a filtration method. However, the key fact that adsorption is typically a batch process, and not a continuous process, means that an additional phase-separation step is required. To address this, and to increase flux, large scale adsorption treatments have been known to employ fixed-bed operations, in which the adsorbent is packed in a column, and the contaminated water is passed through the column until the column saturates.<sup>144</sup> Other alternatives, including moving-bed sorption, and fluidized-bed sorption have been employed, however these are considered to be inferior to fixed-bed sorption.<sup>146</sup>

#### 1.1.5.2 Calixarenes

Calixarenes, first discovered in the 1940s by Alois Zinke and Erich Ziegler,<sup>147</sup> are a class of macrocycles, synthesised by linking paraphenolic units with methylene bridges *ortho* to hydroxyl functions. Calixarenes consist of two rims, one of which is wider (Figure 1-6), noting that functionalisation of the rims is also possible.<sup>148</sup> Functionalisation is usually focused on the OR chelating groups (R = H in Figure 1-6), as it is here that the affinity and selectivity can be controlled. Phenolic groups can also be functionalised in the *para* position in order to alter the lipophilicity. This reason, as well as their relatively facile synthesis, has led to interest in using calixarenes for the removal of contaminants from water.

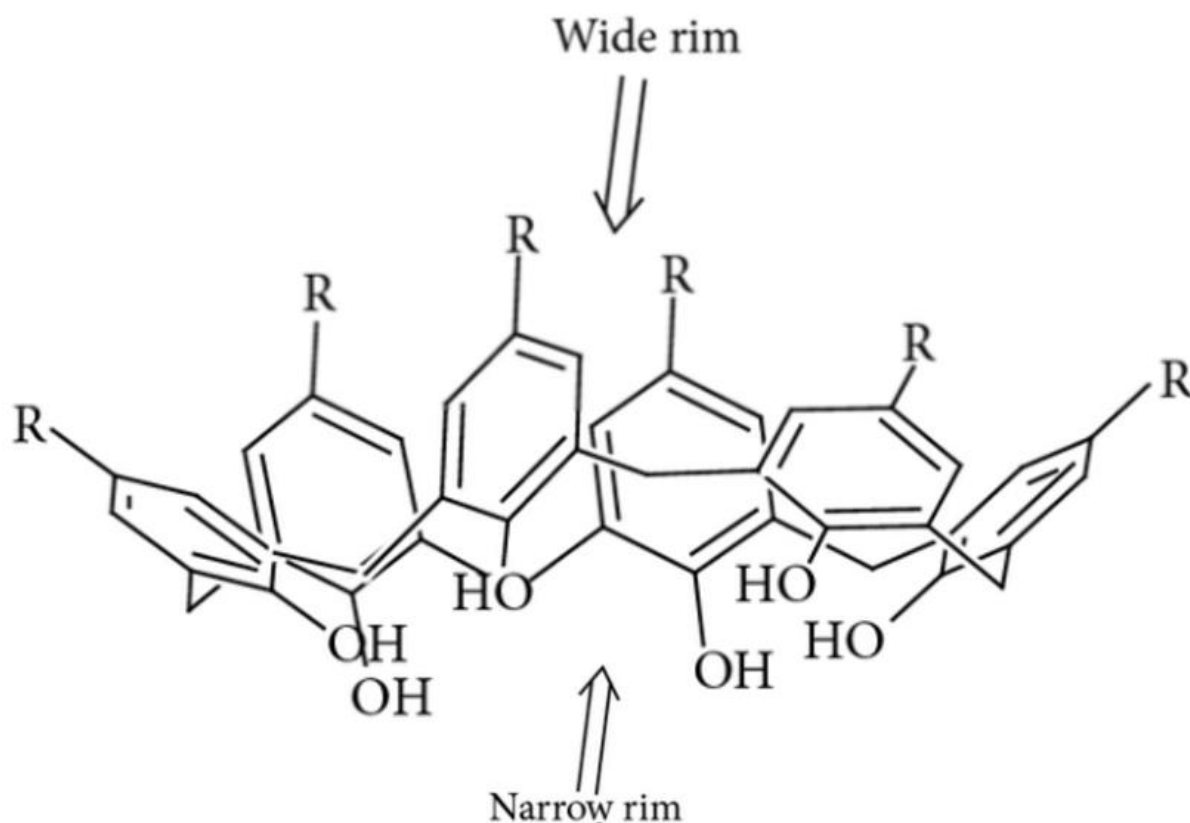


Figure 1-6. Depiction of the structure of a calix[6]arene. Taken from Ref 148.

Calixarenes are routinely used as adsorbents. Their structure is particularly well designed for contaminant removal. Furthermore, their cavities are well suited for the incorporation of target molecules through host-guest interactions in solution, at air-water interfaces, or on solid surfaces (Figure 1-7);<sup>149</sup> dipolar,<sup>150</sup> ion-dipole,<sup>151</sup> hydrogen bonding,<sup>152</sup> or electrostatic<sup>152</sup> interactions with the calixarene rims; non-polar interactions with the hydrophobic cavity;<sup>150</sup> and/or alkyl- $\pi$ ,<sup>153</sup> ion- $\pi$ ,<sup>151</sup> and  $\pi$ - $\pi$  interactions<sup>152,153</sup> with the calixarene rims. As such, calixarenes have been used to extract a range of species, including uranium,<sup>154, 155, 156, 157, 158</sup> chromium,<sup>159, 160, 161, 162, 163, 164</sup> other radionuclides,<sup>163, 164</sup> other toxic metals,<sup>165,166,167</sup> inorganic ions,<sup>168</sup> organic micropollutants,<sup>150</sup> and dyes<sup>152,169,170,171,172</sup> from solution.

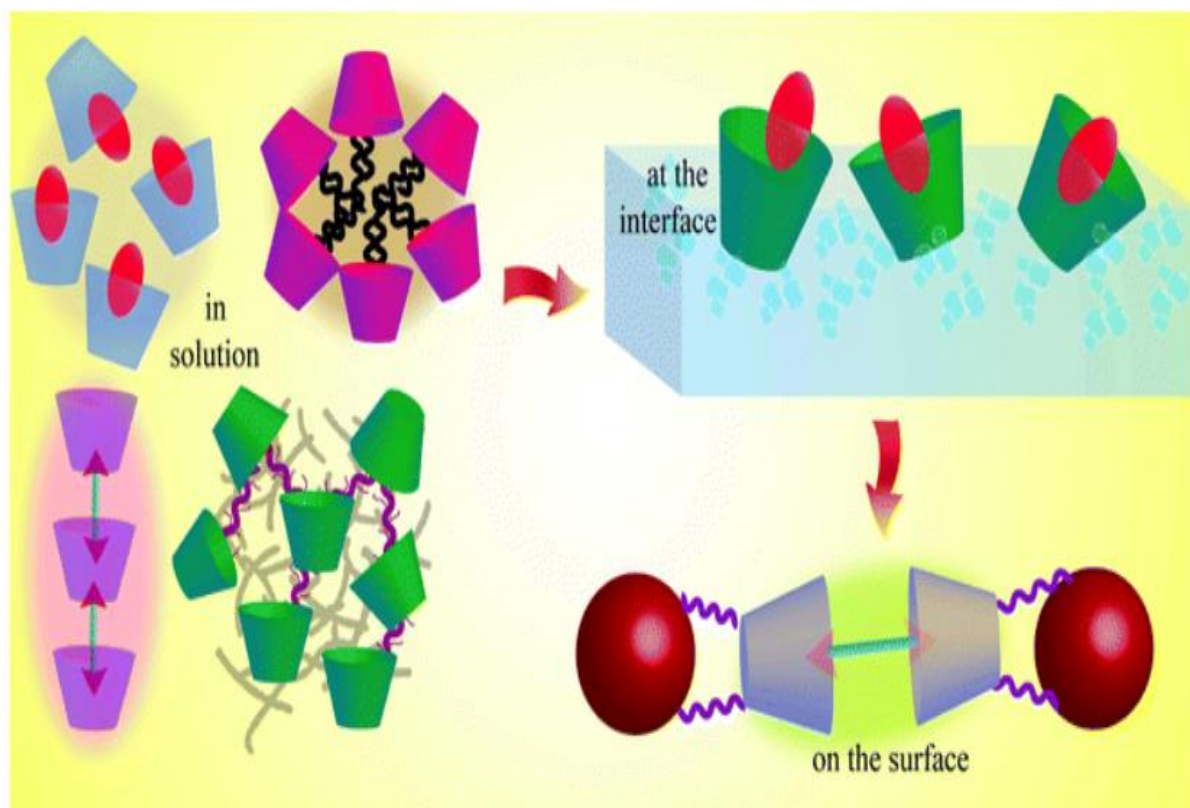


Figure 1-7. Schematic representation of the varying structural morphologies of calixarenes following host-guest interactions with target molecules in solution, at an air-water interface, and on the surface of solids. Taken from reference 149.

Porous nanoparticles have been incorporated into mixed matrix membranes (MMM) and thin-film nanocomposite membranes as a means of improving permeability and selectivity of said membranes.<sup>173</sup> While porous materials such as MOFs and cyclodextrins (CDs) have been utilised, the use of calixarenes provides specific advantages. Namely, that calixarenes exhibit smaller outer dimensions than MOFs, and smaller internal cavity openings than CDs, which allows for greater control over contaminant removal. Additionally, the functional groups on the calixarenes enable it to be well anchored within the membrane (typically between sulfonic acid groups on the calixarene with electron donating groups on the polymeric membranes), providing a greater stability to the membrane. In order to incorporate the calixarenes, the general reaction scheme involves first swelling the membrane using infiltration solvents, before adding the calixarenes, which then become anchored inside the selective layer, and then gatekeeping as the calixarenes are anchored and the membrane dried. As such, the solvents employed, the concentration of calixarene, the type of calixarene, the structure of membranes, and the post-drying conditions are all vital parameters to be controlled during MMM fabrication.

### 1.1.6 Scope

In this thesis, plasma functionalisation techniques have been utilised to prepare cloths, bearing functional groups designed for water purification. Chapter 2 provides a detailed description of the experimental procedures performed, in terms of cloth preparation, characterisation and performance.

Chapter 3 outlines the fabrication of the first of these cloths – a calixarene-based filter, synthesised by depositing pulsed plasma poly(4-vinylbenzyl chloride, 4-VBC) onto a polyurethane cloth, which acts as a linker layer, binding a calixarene to the surface of the cloth. The performance of this cloth towards the removal of aromatic azo dyes was investigated, with particular efficacy towards anionic dyes demonstrated.

The second fabricated cloth, presented in Chapter 4, was also designed such that a calixarene was bound to the surface of a polyurethane cloth. In this case, chloroform plasma was used to functionalise the cloth with chloride groups, which could then be used to bind the calixarene to the filter. In this case, the filter was used to extract Cr(VI) oxyanions from solutions. The use of chloroform to treat the cloths is demonstrated to be a viable alternative to the more cumbersome and harmful pulsed plasma poly(4-VBC) deposition method utilised by Bieber et al.<sup>159</sup>

The final cloth, presented in Chapter 5, was fabricated by depositing pulsed plasma poly(2-cyanoethyl acrylate) onto a polyurethane cloth. The cloth was then reacted with hydroxylamine hydrochloride, which converts the cyano groups to amidoximes.<sup>174</sup> Amidoximes are well known to extract uranium from solution, and so its performance towards uranium filtration was demonstrated.<sup>175</sup>



## 1.2 References

- 1 United Nations Department of Economic and Social Affairs. The 17 Goals. <https://sdgs.un.org/goals> (Accessed 29<sup>th</sup> May 2023)
- 2 World Health Organisation, UNICEF; *Progress on Household Drinking Water, Sanitation and Hygiene 2000-2020: Five Years into the SDGs*. WHO/UNICEF Joint Monitoring Programme for Water Supply, Sanitation and Hygiene, 2021
- 3 World Health Organisation. Drinking-Water. <https://www.who.int/news-room/fact-sheets/detail/drinking-water>. (Accessed 29<sup>th</sup> May 2023)
- 4 Prüss-Üstün, A.; Bos, R.; Gore, F.; Bartram, J. Safer Water, Better Health: Costs, Benefits and Sustainability of Interventions to Protect and Promote Health, *World Health Organization*, Geneva, **2008**
- 5 GBD 2017 Risk Factor Collaborators. Global, Regional, and National Comparative Risk Assessment of 84 Behavioural, Environmental and Occupational, and Metabolic Risks or Clusters of Risks for 195 Countries and Territories, 1990–2017: a Systematic Analysis for the Global Burden of Disease Study. *The Lancet*. **2017**, 392, 1923–1994
- 6 Ritchie, H.; Roser, M. Clean Water and Sanitation. <https://ourworldindata.org/water-access#citation>. (Accessed 29<sup>th</sup> May 2023)
- 7 NetSol Water. What is the approximate cost of a WWTP in India. [netsolwater.com](https://www.netsolwater.com) (Accessed 29<sup>th</sup> May 2023)
- 8 Asian Development Research Institute. Water Resources of India. [https://www.adriindia.org/adri/india\\_water\\_facts](https://www.adriindia.org/adri/india_water_facts) (Accessed 29<sup>th</sup> May 2023)
- 9 Population Census. Punjab Population 2022. <https://www.census2011.co.in/census/state/punjab.html> (Accessed 29<sup>th</sup> May 2023)
- 10 Punjab Budget Analysis 2023/24. <https://prsindia.org/budgets/states/punjab-budget-analysis-2023-24> (Accessed 29<sup>th</sup> May 2023)
- 11 The Times of India. <https://timesofindia.indiatimes.com/city/chandigarh/punjab-to-set-up-63-new-sewage-plants/articleshow/93175359.cms?from=mdr> (Accessed 29<sup>th</sup> May 2023)
- 12 Shah, T. Groundwater Governance and Irrigated Agriculture. In *Global Water Partnership Technical Committee (TEC) Background Paper No.19*. Global Water partnership. Stockholm, Sweden, 2014
- 13 Chindarkar, N.; Grafton, R.Q. India's Depleting Groundwater: When Science Meets Policy. *Asia and the Pacific Policy Studies*. **2019**, 6, 108–124
- 14 Jamwal, P.; Lele, S.; Menon, M. Rethinking Water Quality Standards in the Context of Urban Rivers. Conference Paper in *Eighth INSEE Biennial Conference, 2016, Bengaluru "Urbanization and the Environment"*, 2016
- 15 Lele, S.; Jamwal, P.; Menon, M. Challenges in Regulating Water Pollution in India: Standards, Monitoring, Enforcement and Accountability. *Economic and Political Weekly*. **2021**, 56, 46
- 16 Gupta, S.; Shalini, S.; Omer, F.B. Environmental Enforcement and Compliance in Developing Countries: Evidence from India. *World Development*. **2019**, 117, 313–327
- 17 Tselios, V.; Tompkins, E. Can we Prevent Disasters Using Socioeconomic and Political Policy Tools? *International Journal of Disaster Risk Reduction*. **2020**, 101764
- 18 Ward, P.S.; Shively, G.E. Disaster Risk, Social Vulnerability, and Economic Development. *Disasters*. **2017**, 41, 324–351
- 19 Huang, L-Y.; Wang, Y-C.; Wu, C-C.; Chen, Y-C.; Huang, Y-L. Risk of Flood-Related Diseases of Eyes, Skin and Gastrointestinal Tract in Taiwan: A Retrospective Cohort Study. *PLOS ONE*. **2016**, 11

- 20 Curriero, F.C.; Patz, J.A.; Rose, J.B.; Lele, S. The Association Between Extreme Precipitation and Waterborne Disease Outbreaks in the United States, 1948–1994. *American Journal of Public Health*. **2001**, *91*, 1194–1199
- 21 Auld, H.; Maclever, D.; Klaassen, J. Heavy Rainfall and Waterborne Disease Outbreaks: The Walkerton Example. *Journal of Toxicology and Environmental Health, Part A*. **2004**, *67*, 1879–1887
- 22 Chen, M.J.; Lin, C.Y.; Wu, Y.T.; Wu, P.C.; Lung, S.C.; Su, H.J. Effects of Extreme Precipitation to the Distribution of Infectious Diseases in Taiwan, 1994–2008. *PLOS ONE*. **2012**, *7*, e34651
- 23 Hughes, J.; Cowper-Heays, K.; Olesson, E.; Bell, R.; Stroombergen, A. Impacts and Implications of Climate Change on Wastewater Systems: A New Zealand Perspective. *Client Risk Management*. **2021**, *31*, 100262
- 24 Balter, M. Clothes Make the (Hu) Man. *Science*. **2009**, *325*, 1329
- 25 Abel, A. The History of Dyes and Pigments: From Natural Dyes to High Performance Pigments. In *Colour Design, Theories and Applications, 2<sup>nd</sup> Ed.*; Ed. Best, J. Woodhead Publishing; Duxford, England, 2017; pp. 284–290.
- 26 Polaris Market Research. *Textile Dyes Market Share, Size, Trends, Industry Analysis Report, By Dye Type (Direct, Reactive, Basic, VAT, Disperse, Acid, Others); By Fiber Type (Wool, Polyester, Acrylic, Others); By Region; Segment Forecast, 2022 – 2030*. Report ID: PM2539, 2022.
- 27 Tan, I.A.W.; Hameed, B.H.; Ahmad, A.L. Equilibrium and Kinetic Studies on Basic dye Adsorption by Oil Palm Fibre Activated Carbon. *Chemical Engineering Journal*. **2007**, *127*, 111–119
- 28 El-Sharkawy, E.A.; Soliman, A.Y.; Al-Amer, K.M. Comparative Study for the Removal of Methylene Blue via Adsorption and Photocatalytic Degradation. *Journal of Colloid and Interface Science*. **2007**, *310*, 498–508
- 29 Sauer, T.; Cesconeto, G.; Jose, H.J.; Moreira, R.F.P.M. Kinetics of Photocatalytic Degradation of Reactive Dyes in a TiO<sub>2</sub> Slurry Reactor. *Journal of Photochemistry and Photobiology A: Chemistry*. **2002**, *149*, 147–154
- 30 Khan, I.; Saeed, K.; Zekker, I.; Zhang, B.; Hendi, A.H.; Ahmad, A.; Ahmad, S.; Zada, N.; Ahmad, H.; Shah, L.A.; Khan, I. Review on Methylene Blue: Its Properties, Uses, Toxicity and Photodegradation. *Water*. **2022**, *14*, 242
- 31 Lipskikh, O.I.; Korotkova, E.I.; Khristunova, Y.P.; Berek, J.; Kratochvil, B. Sensors for Voltametric Determination of Food Azo Dyes – a Critical Review. *Electrochimica Acta*. **2018**, *260*, 974–985
- 32 Benkhaya, S.; M'rabet, S.; El Harfi, A. Classifications, Properties, Recent Synthesis and Applications of Azo Dyes. *Heylion*. **2020**, *6*, e03271
- 33 IARC Working Group on the Evaluation of Carcinogenic Risks to Humans. Some Aromatic Amines, Organic Dyes, and Related Exposures. In *IARC Monographs on the Evaluation of Carcinogenic Risks to Human.*, Vol. 99; International Agency for Research on Cancer, Lyon, 2010.
- 34 Yusuf, M.; Shabbir, M.; Mohammed, F. Natural Colorants: Historical, Processing and Sustainable Prospects. *Natural Products and Bioprospecting*. **2017**, *7*, 123–145
- 35 Hamprecht, R.; Westerkamp, A. Disperse Dyes. In *Ullmann's Encyclopaedia of Industrial Chemistry*; Wiley VCH, 2000, pp. 331–342
- 36 Gulrajani, M.L. Disperse Dyes. In *Handbook of Textile and Industrial Dyeing*; Vol. 1; Woodhead Publishing, 2011, pp. 365–394
- 37 Roy Choudhury, A.K. Dyeing of Synthetic Fibres. In *Handbook of Textile and Industrial Dyeing*; Vol. 2; Woodhead Publishing, 2011, pp. 40–128
- 38 Diacu, E. Colors: Properties and Determination of Synthetic Pigments. *Encyclopaedia of Food and Health*. **2016**, 284–290

- 39 Chattopadhyay, D.P. Chemistry of Dyeing. In *Handbook of Textile and Industrial Dyeing*, Vol. 1; Woodhead Publishing, 2011, pp. 150–183
- 40 Kamalabadi, M.; Khalili, S.; Madrakian, T.; Afkhami, A. Facile Synthesis of Magnetic Melamine-Based Covalent Organic Framework for Removal of Amido Black 10B. *European Physical Journal Plus*. **2022**, *137*, 544
- 41 Zereshki, S.; Darei, P.; Shokri, A. Application of Edible Paraffin Oil for Cationic Dye Removal from Water using Emulsion Liquid Membrane. *Journal of Hazardous Materials*. **2018**, *356*, 1–8
- 42 Baruthio, F. Toxic Effects of Chromium and Its Compounds. *Biological Trace Element Research*. **1992**, *32*, 145–153
- 43 Lunk, H-J. Discovery, Properties and Applications of Chromium and its Compounds. *ChemTexts*. **2015**, *1*
- 44 Xiao, Y.; Zhou, J. Wang, C.; Zhang, J.; Radnaeva, V.; Lin, W. Sustainable Metal-Free Leather Manufacture via Synergistic Effects of Triazine Derivative and Vegetable Tannins. *Collagen and Leather*. **2023**, *2*
- 45 Gao, D.; Wang, P.; Shi, J.; Li, F.; Li, W.; Lyu, B.; Ma, J. A Green Chemistry Approach to Leather Tanning Process: Cage-like Octa(aminosilsesquioxane) Combined with Tetrakis(hydroxymethyl) Phosphonium Sulfate. *Journal of Cleaner Production*. **2019**, *229*, 1102–1111
- 46 Parisi, M.; Nanni, A.; Colonna, M. Recycling of Chrome-Tanned Leather and Its Utilization as Polymeric Materials and in Polymer-Based Composites: A Review. *Polymers (Basel)*. **2021**, *13*, 429
- 47 Yamamoto, G.T.; Sekeroglu, O.; Bayramoglu, E.E. Marketing Activities in the Leather Industry: Comparative Country Analysis. *International Journal of Economics and Management Sciences*. **2011**, *1*, 37–48
- 48 Pati, A.; Chaudhary, R.; Subramani, S. A Review on Management of Chrome-tanned Leather Shavings: a Holistic Paradigm to Combat the Environmental Issues. *Environmental Science and Pollution Research*. **2014**, *21*, 11266–11282
- 49 Apte, A.D.; Verma, S.; Tare, V.; Bose, P. Oxidation of Cr(III) in Tannery Sludge to Cr(VI): Field Observations and Theoretical Assessment. *Journal of Hazardous Materials*. **2005**, *B121*, 215–222
- 50 WHO. Chromium in Drinking-water, Background Document for Development of WHO *Guidelines for drinking-water quality*. World Health Organization, Geneva 2020
- 51 United Nations Industrial Development Organization (UNIDO). Tannery Effluent Treatment Plants, India. <https://leatherpanel.org/content/tannery-effluent-treatment-plants-india> (Accessed 20<sup>th</sup> June 2023)
- 52 Arcibar-Orozco, J.A.; Barajas-Elias, B.S.; Baltazar-Campos, H.; Rangel-Mendez, R. Preparation of Carbon Materials from Chromium-tanned Leather Shavings for the Removal of Dyes from Aqueous Solution. *Applied Water Science*. **2022**, *213*
- 53 Erdem, M.; Ozverdi, A. Leaching Behavior of Chromium in Chrome Shaving Generated in Tanning Process and its Stabilization. *Journal of Hazardous Materials*. **2008**, *156*, 51–55
- 54 Prasad, S.; Yadav, K.K.; Kumar, S.; Gupta, N.; Cabral-Pinto, M.M.S.; Rezanian, S.; Radwan, N.; Alam, J. Chromium Contamination and Effect on Environmental Health and its Remediation: A Sustainable Approaches. *Journal of Environmental Management*. **2021**, *285*, 112174
- 55 Del Pianata, D.; Frayret, J.; Gleyzes, C.; Cugnet, C.; Dupin, J.C.; Le Hecho, I. Determination of the Chromium(III) Reduction Mechanism During Chromium Electroplating. *Electrochimica Acta*. **2018**, *284*, 234–241
- 56 Mandich, N.V. Chemistry & Theory of Chromium Deposition 1. Chemistry. *Plating and Surface Finishing*. **1997**, *84*, 108–115
- 57 Council on the Registration, Evaluation, Authorisation and Restriction of Chemicals (REACH). Amendment to Annex XIV of Regulation (EC) No 1907/2006. *Official Journal of the European Union*. **2013**, *108/1–5*

- 58 Protsenko, V.S.; Danilov, F.I. Chromium Electroplating from Trivalent Chromium Baths as an Environmentally Friendly Alternative to Hazardous Hexavalent Chromium Baths: Comparative Study on Advantages and Disadvantages. *Clean Technologies and Environmental Policy*. **2014**, *16*, 1201–1206
- 59 Karegar, S.; Bhargavi, M.; Divekar, S.V. Treatment of Wastewater from Chrome Plating Industry by Ion Exchange Method. *International Journal of Research in Engineering and Technology*. **2015**, *4*
- 60 Wang, X.; Li, L.; Yan, X.; Meng, X.; Chen, Y. Processes of Chromium (VI) Migration and Transformation in Chromate Production Site: A Case Study from the Middle of China. *Chemosphere*. **2020**, *257*, 127282
- 61 Zhang, Y.; Zhang, Q.; Chen, W.; Shi, W.; Cui, Y.; Chen, L.; Shao, J. Hydrogeochemical Analysis and Groundwater Pollution Source Identification based on Self-organizing Map at a Contaminated Site. *Journal of Hydrology*. **2023**, *616*, 128839
- 62 Heath, D. How Industry Scientists Stalled Action on Carcinogen. <https://publicintegrity.org/environment/how-industry-scientists-stalled-action-on-carcinogen/> (Accessed 6<sup>th</sup> July 2023)
- 63 Groundwater Contamination with Chromium-6 in Hinkley, California. <https://ejatlas.org/print/hinkley-groundwater-contamination> (Accessed 6<sup>th</sup> July 2023)
- 64 Zhang, J.; Li, X. Investigation and Study of Chromium Pollution in Jinzhou. *Chinese Journal of Preventive Medicine*. **1987**, *21*
- 65 Linos, A.; Petralias, A.; Christophi, C.; Christoforidou, E.; Kouroutou, P.; Stolidis, M.; Veloudaki, A.; Tzala, E.; Makris, K.; Karagas, M. Oral Ingestion of Hexavalent Chromium Through Drinking Water and Cancer Mortality in an Industrial Area of Greece – An Ecological Study. *Environmental Health*. **2011**, *10*, 50
- 66 Singh, R.K. Sengupta, B.; Bali, R.; Shukla, B.P.; Gurunadharo, V.V.S.; Srivatstava, R. Identification and Mapping of Chromium (VI) Plume in Groundwater for Remediation: A Case Study at Kanpur, Uttar Pradesh. *Journal of the Geological Society of India*. **2009**, *74*, 49–57
- 67 Purushotham, D.; Rashid, M.; Lone, M.A.; Narsing Rao, A.; Ahmed, S.; Nagaiha, E.; Dar, F.A. Environmental Impact Assessment of Air and Heavy Metal Concentration in Groundwater of Maheshwaram Watershed, Ranga Reddy District, Andhra Pradesh *Journal of the Geological Society of India*. **2013**, *81*, 385–396
- 68 Karim, L.R.; Williams, E.S. Accumulation of Heavy Metals in the Surface Water of Asthamudi Lake, Kollam, Kerala. *Nature Environment and Pollution Technology*. **2015**, *14*, 431–434
- 69 Gao, Y.; Xia, J. Chromium Contamination Accident in China: Viewing Environment Policy of China. *Environmental Science and Technology*. **2011**, *45*, 8605–8606
- 70 Bhardwaj, R.; Gupta, A.; Garg, J.K. Evaluation of Heavy Metal Contamination Using Environmetrics and Indexing Approach for River Yamuna, Delhi stretch, India. *Water Science*. **2017**, *31*, 52–66
- 71 Huang, D.; Wang, G.; Shi, Z.; Li, Z.; Kang, F.; Liu, F. Removal of Hexavalent Chromium in Natural Groundwater using Activated Carbon and Cast Iron Combined System. *Journal of Cleaner Production*. **2017**, *165*, 667–676
- 72 Zheng, X.; Li, S.; Li, Y.; Lv, Y.; Wang, X.; Wu, P.; Yang, Q.; Tang, Y.; Liu, Y.; Zhang, Z. Hexavalent Chromium Induces Renal Apoptosis and Autophagy via Disordering the Balance of Mitochondrial Dynamics in Rats. *Ecotoxicology and Environmental Safety*. **2020**, *204*, 111061
- 73 Zhitkovich, A. Importance of Chromium–DNA Adducts in Mutagenicity and Toxicity of Chromium(VI). *Chemical Research Toxicology*. **2005**, *18*, 3–11
- 74 Feng, Z.; Hu, W.; Rom, W.; Costa, M.; Tang, M-S. Chromium(VI) Exposure Enhances Polycyclic Aromatic Hydrocarbon-DNA Binding at the p53 Gene in Human Lung Cell. *Carcinogenesis*. **2003**, *24*, 771–778

- 75 Rodell, M.; Velicogna, I.; Famiglietti, J.S. Satellite-based Estimates of Groundwater Depletion in India. *Nature*. **2009**, *460*, 999–1002
- 76 Pushparaj Gandhi, T.; Sampath, P.V.; Maliyekkal, S.M. A Critical Review of Uranium Contamination in Groundwater: Treatment and Sludge Disposal. *Science of the Total Environment*. **2022**, *825*. 153947
- 77 Lapworth, D.J.; Brauns, B.; Chattopadhyaya, S.; Gooddy, D.C.; Loveless, S.E.; Macdonald, A.M.; MacDonald, A.A.; McKenzie, A.A.; Muddu, S.; Nara, S.N.V. Elevated Uranium in Drinking Water Sources in Basement Aquifers of Southern India. *Applied Geochemistry*. **2021**, *133*, 105092
- 78 Saikia, R.; Chetia, D.; Bhattacharyya, K.G. Estimation of Uranium in Groundwater and Assessment of Age-dependent Radiation Dose in Nalbari District of Assam, India. *SN Applied Sciences*, **2021**, *3*, 21
- 79 World Health Organisation, Guidelines for Drinking-water Quality, 4<sup>th</sup> edition, Incorporating the 1<sup>st</sup> Addendum. **2012**
- 80 Coyte, R. M.; Jain, R. C.; Srivastava, S. K.; Sharma, K. C.; Khalil, A.; Ma, L.; Vengosh, A. Large-Scale Uranium Contamination of Groundwater Resources in India. *Environmental Science & Technology Letters*. **2018**, *5*, 341–347
- 81 Luiz de Souza, A.; Barboza Cotrim, M.E.; Faustino Pires, M.A. An Overview of Spectrometric Techniques and Sample Preparation for the Determination of Impurities in Uranium Nuclear Fuel Grade. *Microchemical Journal*. **2013**, *106*, 194–201
- 82 Kadadou, D.; Said, E.A.; Ajaj, R.; Hasan, S.W. Research Advances in Nuclear Wastewater Treatment using Conventional and Hybrid Technologies: Towards Sustainable Wastewater Reuse and Recovery. *Journal of Water Process Engineering*. **2023**, *52*, 103604
- 83 Xie, Y.; Chen, C.; Ren, X.; Wang, X.; Wang, H.; Wang, X. Emerging Natural and Tailored Materials for Uranium-contaminated Water Treatment and Environmental Remediation. *Progress in Materials Science*. **2019**, *103*, 180–234
- 84 Ulrich, S.; Gillow, J.; Roberts, S.; Byer, G.; Sueker, J.; Farris, K. Hydrogeochemical and Mineralogical Factors Influencing Uranium in Background Area Groundwater Wells: Grants, New Mexico. *Journal of Hydrology: Regional Studies*. **2019**, *26*, 100636
- 85 Kurttio, P.; Auvinen, A.; Salonen, L.; Saha, H.; Pekkanen, J.; Mäkeläinen, I.; Väisänen, S.B.; Penttilä, I.M.; Komulainen, H. Renal Effects of Uranium in Drinking Water. *Environmental Health Perspectives*. **2002**, *110*, 337–342
- 86 Patnaik, R.; Lahiri, S.; Chahar, V.; Naskar, N.; Sharma, P.K.; Avhad, D.K.; Bassan, M.K.T.; Knolle, F.; Schnug, E.; Srivastava, A. Study of Uranium Mobilization from Himalayan Siwaliks to the Malwa Region of Punjab State in India. *Journal of Radioanalytical and Nuclear Chemistry*. **2016**, *308*, 913–918
- 87 Waseem, A.; Ullah, H.; Rauf, M.K.; Ahmad, I. Distribution of Natural Uranium in Surface and Groundwater Resources: a Review. *Critical Reviews in Environmental Science and Technology*. **2015**, *45*, 2391–2423
- 88 Rana, D.; Matsuura, T.; Kassim, M.A.; Ismail, A.F. Radioactive Decontamination of Water by Membrane Processes — A Review. *Desalination*. **2013**, *321*, 77–92
- 89 Zakrzewska-Trznadel, G. Advances in Membrane Technologies for the Treatment of Liquid Radioactive Waste. *Desalination*, **2013**, *321*, 119–130
- 90 Xie, Y.; Chen, C.; Ren, X.; Wang, X.; Wang, H.; Wang, X. Emerging Natural and Tailored Materials for Uranium-contaminated Water Treatment and Environmental Remediation. *Progress in Materials Science*, **2019**, *103*, 180–234
- 91 Gavrilesco, M.; Pavel, L.V.; Cretescu, I. Characterization and Remediation of Soils Contaminated with Uranium. *Journal of Hazardous Materials*. **2009**, *163*, 475–510
- 92 Flett, L.; McLeod, C.L.; McCarty, J.L.; Shaulis, B.J.; Fain, J.J.; Krekeler, M.P.S. Monitoring Uranium Mine Pollution on Native American lands: Insights from Tree Bark Particulate Matter on the Spokane Reservation, Washington, USA, *Environmental Research*. **2021**, *194*, 110619

- 93 Pinto, M.M.S.C.; Silva, M.M.V.G.; Neiva, A.M.R. Pollution of Water and Stream Sediments Associated with the Vale De Abrutiga Uranium Mine, Central Portugal. *Mine Water and the Environment*. **2004**, *23*, 66–76
- 94 Li, R.; Dong, F.; Yang, G.; Zhang, W.; Zong, M.; Nie, X.; Zhou, L.; Babr, A.; Liu, J.; Ram, B.K.; Fan, C.; Zen, Y. Characterization of Arsenic and Uranium Pollution Surrounding a Uranium Mine in Southwestern China and Phytoremediation Potential. *Polish Journal of Environmental Studies*. **2019**, *28*, 1–13
- 95 Zhang, Z.; Tang, Z.; Liu, Y.; He, H.; Guo, Z.; Feng, P.; Chen, L.; Sui, Q. Study on the Ecotoxic Effects of Uranium and Heavy Metal Elements in Soils of a Uranium Mining Area in Northern Guangdong. *Toxics*. **2023**, *11*, 97
- 96 Haakonde, T.; Yabe, J.; Choongo, K.; Chongwe, G.; Nchima, G. Uranium Exposure and Health Risk Implications: A Preliminary Study Among the Residents Living around Uranium Mining Sites in the Southern Province of Zambia. *Environmental Advances*. **2021**, 100098
- 97 Rana, B.K.; Dhumale, M.R.; Lenka, P.; Sahoo, S.K.; Ravi, P.M.; Tripathi, R.M. A Study of Natural Uranium Content in Groundwater around Tummalapalle Uranium Mining and Processing Facility, India. *Journal of Radioanalytical and Nuclear Chemistry*. **2016**, *307*, 1499–1506
- 98 Zielinski, R.A.; Orem, W.H.; Simmons, K.R.; Bohlen, P.J. Fertiliser-Derived Uranium and Sulfur in Rangeland Soil and Runoff: A Case Study in Central Florida. *Water, Air and Soil Pollution*. **2006**, *176*, 163–183
- 99 Lapworth, D.J.; Krishan, G.; MacDonald, A.M.; Rao, M.S. Groundwater Quality in the Alluvial Aquifer System of Northwest India: New Evidence of the Extent of Anthropogenic and Geogenic Contamination. *Science of the Total Environment*. **2017**, *599–600*, 1433–1444
- 100 Banning, A.; Demmel, T.; Rude, T.R.; Wrobel, M. Groundwater Uranium Origin and Fate Control in a River Valley Aquifer. *Environmental Science & Technology*. **2013**, *47*, 13941–13948
- 101 Lyons, W.B.; Gardner, C.B.; Welch, S.A.; Israel, S. Uranium in Ohio, USA Surface Waters: Implications for a Fertiliser Source in Waters Draining Agricultural Lands. *Scientific Reports*. **2020**, *10*, 5151
- 102 Schnug, E.; Lottermoser, B.G. Fertiliser-Derived Uranium and its Threat to Human Health. *Environmental Science & Technology*. **2013**, *47*, 2433–2434
- 103 NPR, The U.N.'s nuclear watchdog says Japan can release nuclear waste water into the ocean. <https://www.npr.org/2023/07/04/1185971497/the-u-n-s-nuclear-watchdog-says-japan-can-release-nuclear-waste-water-into-the-o> (Accessed 12<sup>th</sup> July 2023)
- 104 Guo, J.; Liu, Y.; Wu, X.; Chen, J. Assessment of the Impact of Fukushima Nuclear Wastewater Discharge on the Global Economy Based on GTAP. *Ocean & Coastal Management*. **2022**, *228*, 106296
- 105 International Atomic Energy Agency. Comprehensive Report on the Safety Review of the Alps-treated Water at the Fukushima Daiichi Nuclear Power Station, Vienna, **2023**
- 106 The Guardian, What Should We Do with Radioactive Nuclear Waste. <https://www.theguardian.com/environment/2019/aug/01/what-should-we-do-with-radioactive-nuclear-waste> (Accessed 13<sup>th</sup> July 2023)
- 107 International Atomic Energy Agency. Status and Trends in Spent Fuel and Radioactive Waste Management. IAEA Nuclear Energy Series, No. NW-T-1.14 (Rev. 1), Vienna, 2022
- 108 Zielinski, R.A.; Simmons, K.R.; Orem, W.H. Use of <sup>234</sup>U and <sup>238</sup>U Isotopes to Identify Fertiliser-derived Uranium in the Florida Everglades. *Applied Geochemistry*. **2000**, *15*, 369–383
- 109 Fuller, C. C.; Barger, J. R.; David, J. A.; Piana, M. J. Mechanisms of Uranium Interactions with Hydroxyapatite: Implications for Groundwater Remediation. *Environmental Science & Technology*. **2002**, *36*, 158–165
- 110 Nolan, J.; Weber, K.A.; Natural Uranium Contamination in Major US Aquifers Linked to Nitrate. *Environmental Science & Technology Letters*. **2015**, *2*, 215–220

- 111 Lapworth, D.J.; Brauns, B.; Chattopadhyay, S.; Goody, D.C.; Loveless, S.E.; MacDonald, A.M.; McKenzie, A.A.; Muddu, S.; Nara, S.N.V. Elevated Uranium in Drinking Water Sources in Basement Aquifers of Southern India. *Applied Geochemistry*. **2021**, *133*, 105092
- 112 McClain, D.E.; Miller, A.C.; Kalinich, J.F. Status of Health Concerns about Military Use of Depleted Uranium and Surrogate Metals in Armor-Penetrating Munitions. *NATO RTG-099*, **2005**
- 113 Hartmann, H.M.; Monette, F.A.; Avci, H.I. Overview of Toxicity Data and Risk Assessment Methods for Evaluating the Chemical Effects of Depleted Uranium Compounds. *Human and Ecological Risk Assessment*. **2000**, *6*, 851–874
- 114 Vogianis, E.G.; Nikolopoulos, D. Radon Sources and Associated Risk in Terms of Exposure and Dose. *Frontiers in Public Health*. **2015**, *2*, 207
- 115 Bersimbaev, R.I.; Bulgakova, O. The Health Effects of Radon and Uranium on the Population of Kazakhstan. *Genes and Environment*. **2015**, *37*
- 116 Petitot, F.; Lestaevel, P.; Turlonias, E.; Mazzucco, C.; Jacquinet, S.; Dhieux, B.; Delissen, O.; Tournier, B.B.; Gensdarmes, F.; Beaunier, P.; Dublineau, I. Inhalation of Uranium Nanoparticles: Respiratory Tract Deposition and Translocation to Secondary Target Organs in Rats. *Toxicology Letters*, **2013**, *217*, 217–225
- 117 Periyakaruppan, A.; Kumar, F.; Sarkar, S.; Sharma, C.S.; Ramesh, G.T. Uranium Induces Oxidative Stress in Lung Epithelial Cells. *Archives of Toxicology*. **2007**, *81*, 389–395
- 118 Roszell, L.E.; Hahn, F.F.; Lee, R.B.; Parkhursts, M.A. Assessing the Renal Toxicity of Capstone Depleted Uranium Oxides and Other Uranium Compounds. *Health Physics*. **2009**, *96*, 343–351
- 119 Katz, S. The Chemistry and Toxicology of Depleted Uranium. *Toxics*. **2014**, *2*, 50–78
- 120 Chow, C.W.K.; Van Leeuwen, J.A.; Fabris, R.; Drikas, M. Optimised Coagulation using Aluminium Sulfate for the Removal of Dissolved Organic Carbon. *Desalination*. **2009**, *245*, 120–134
- 121 Edzwald, J.K. Principles and Applications of Dissolved Air Flotation. *Water Science and Technology*. **1995**, *31*, 1–23
- 122 Mazhar, M.A.; Khan, N.A.; Ahmed, S.; Khan, A.H.; Hussain, A.; Rahisuddin, C.F.; Yousefi, M.; Ahmadi, S.; Vambol, V. Chlorination Disinfection By-products in Municipal Drinking Water – A Review. *Journal of Cleaner Production*. **2020**, *273*, 123159
- 123 Vo, H.T.; Imai, T.; Teeka, J.; Sekine, M.; Kanno, A.; Le, T.V.; Higuchi, T.; Phummala, K.; Yamamoto, K. Comparison of Disinfection Effect of Pressurized Gases of CO<sub>2</sub>, N<sub>2</sub>O, and N<sub>2</sub> on *Escherichia Coli*. *Water Research*, **2013**, *47*, 4286–4293
- 124 Lee, W.; Westerhoff, P. Formation of Organic Chloramines During Water Disinfection – Chlorination Versus Chloramination. *Water Research*, **2009**, *43*, 2233–2239
- 125 Kinman, R.N.; Rempel, G. Water and Wastewater Disinfection with Ozone: A Critical Review. *CRC Critical Reviews in Environmental Control*, **1975**, *5*, 141–152
- 126 Song, K.; Mohseni, M.; Taghipour, F. Application of Ultraviolet Light-emitting Diodes (UV-LEDs) for Water Disinfection: A Review, *Water Research*. **2016**, *94*, 341–349
- 127 Ericsson, C.D.; Steffen, R.; Backer, H. Water Disinfection for International and Wilderness Travelers, *Clinical Infectious Diseases*. **2002**, *34*, 355–364
- 128 Saidur, R.; Elcevvadi, E.T.; Mekhilef, S.; Safari, A.; Mohammed, H.A. An Overview of Different Distillation Methods for Small Scale Applications. *Renewable and Sustainable Energy Reviews*. **2011**, *15*, 4756–4764
- 129 Manchanda, H.; Kumar, M. Study of Water Desalination Techniques and a Review on Active Solar Distillation Methods. *Environmental Progress & Sustainable Energy*. **2017**, *37*, 444–464
- 130 Deshmukh, A.; Boo, C.; Karanikola, V.; Lin, S.; Straub, A.; Tong, T.; Warsinger, D.M.; Elimelech, M. Membrane Distillation at the Water-energy Nexus: Limits, Opportunities, and Challenges. *Energy & Environmental Science*. **2018**, *11*, 1177–1196

- 131 Camacho, L.M.; Dumeé, L.; Zhang, J.; Li, J.-D.; Duke, M.; Gomez, J.; Gray, S. Advances in Membrane Distillation for Water Desalination and Purification Applications. *Water*. **2013**, *5*, 94–196
- 132 Baker, R.W. Microfiltration. In *Membrane Technology and Applications, 3rd Ed.*; John Wiley & Sons, Ltd. 2012; pp. 303–324
- 133 Anis, S.F.; Hashaikeh, R.; Hilal, N. Microfiltration Membrane Processes: A Review of Research Trends over the Past Decade. *Journal of Water Process Engineering*. **2019**, *32*, 100941
- 134 Hulsman, I.H. Microfiltration. In *Encyclopaedia of Separation Science*, Elsevier, 2000, 1764–1777
- 135 Singh, R.; Hankins, N.P. Introduction to Membrane Processes for Water Treatment. In *Emerging Membrane Technology for Sustainable Water Treatment*. Elsevier, 2016; pp.15–52
- 136 Lee, P.K.; Arnot, T.C.; Mattia, D. A Review of Reverse Osmosis Membrane Materials for Desalination—Development to Date and Future Potential. *Journal of Membrane Science*. **2011**, *370*, 1–22
- 137 Singh, R.; Bhadouria, R.; Sing, P.; Kumar, A.; Pandey, S.; Kumar Singh, V. Nanofiltration Technology for Removal of Pathogens Present in Drinking Water. In *Waterborne Pathogens, Detection and Treatment*. Eds. Prasad, M.N.V., Grobelak, A. Elsevier, 2020, pp. 463–489
- 138 Nagy, E. Pressure-Retarded Osmosis (PRO) Process. In *Basic Equations of Mass Transport Through a Membrane Layer, 2<sup>nd</sup> Ed.*; Elsevier, 2019; pp. 505–531
- 139 Davenport, D.M.; Deshmukh, A.; Werber, J.R.; Elimelech, M. High-Pressure Reverse Osmosis for Energy-Efficient Hypersaline Brine Desalination: Current Status, Design Considerations, and Research Needs. *Environmental Science & Technology Letters*. **2018**, *5*, 467–475
- 140 Foster, R.I.; Amphlett, J.T.M.; Kim, K.-W.; Kerry, T.; Lee, K.; Sharrad, C.A. SOHIO Process Legacy Waste treatment: Uranium Recovery Using Ion Exchange. *Journal of Industrial and Engineering Chemistry*. **2020**, *81*, 144–152
- 141 Yaroslavtsev, A.B.; Nikonenko, V.V. Ion-Exchange Membrane Materials: Properties, Modification, and Practical Application. *Nanotechnology in Russia*. **2009**, *4*, 137–159
- 142 Botelho Junior, A.B.; Dreisinger, D.B.; Espinosa, D.C.R. A Review of Nickel, Copper, and Cobalt Recovery by Chelating Ion Exchange Resins from Mining Processes and Mining Tailings. *Mining, Metallurgy & Exploration*. **2018**, *36*, 199–213
- 143 Madarasz, D.; Szent, I.; Sapi, A.; Halasz, J.; Kukovecz, A.; Konya, Z. Exploiting the Ion-exchange Ability of Titanate Nanotubes in a Model Water Softening Process. *Chemical Physics Letters*. **2014**, *591*, 161–165
- 144 Dotto, G.L.; McKay, G. Current Scenario and Challenges in Adsorption for Water Treatment. *Journal of Environmental Chemical Engineering*. **2020**, *8*, 103988
- 145 Su, S.; Che, R.; Liu, Q.; Liu, J.; Zhang, H.; Li, R.; Jing, X.; Wang, J. Zeolitic Imidazolate Framework-67: A Promising Candidate for Recovery of Uranium (VI) from Seawater. *Colloids and Surfaces A: Physicochemical and Engineering Aspects*. **2018**, *547*, 73–80
- 146 Patel, H. Fixed-bed Column Adsorption Study: A Comprehensive Review. *Applied Water Science*. **2019**, *9*, 45
- 147 Kappe, T. The Early History of Calixarene Chemistry. *Journal of Inclusion Phenomena and Molecular Recognition in Chemistry*. **1994**, *19*, 3–15
- 148 Kiegel, K.; Steczek, L.; Zakrzewska-Trznadel, G. Application of Calixarenes as Macrocyclic Ligands for Uranium(VI): A Review. *Journal of Chemistry*. **2012**, *2013*, 762819
- 149 Nag, R.; Pulla, Rao, C.P. Calixarene-mediated Host–guest Interactions Leading to Supramolecular Assemblies: Visualization by Microscopy. *Chemical Communications*. **2022**, *58*, 6044–6063



- 150 Shetty, D.; Jahovic, I.; Raya, J.; Asfari, Z.; Olsen, J-C.; Trabolsi, A. Porous Polycalix[4]arenes for Fast and Efficient Removal of Organic Micropollutants from Water. *ACS Applied Materials and Interfaces*. **2018**, *10*, 2976–2981
- 151 Wang, J.; Zhunag, S. Cesium Separation from Radioactive Waste by Extraction and Adsorption Based on Crown Ethers and Calixarenes. *Nuclear Engineering and Technology*. **2020**, *52*, 328–336
- 152 Zhou, S.; Jin, L.; Gu, P.; Tian, L.; Li, N.; Chen, D.; Marcomini, A.; Xu, Q.; Lu, J. Novel Calixarene-based Porous Organic Polymers with Superfast Removal Rate and Ultrahigh Adsorption Capacity for Selective Separation of Cationic Dyes. *Chemical Engineering Journal*. **2022**, *433*, 134442
- 153 Gupta, R.K.; Li, L.; Wang, Z.; Han, B-L.; Feng, L.; Gai, Z-Y.; Tung, C-H.; Sun, D. Regulating the Assembly and Expansion of the Silver Cluster from the Ag<sup>37</sup> to Ag<sup>46</sup> Nanowheel Driven by Heteroanions. *Chemical Science*. **2023**, *14*, 1138–1144
- 154 Shinkai, S.; Koreishi, H.; Ueda, K.; Manabe, O. A New Hexacarboxylate Uranophile Derived from Calix[6]arene. *Journal of the Chemical Society, Chemical Communications*. **1986**, 233–234
- 155 Jain, V.K.; Pillai, S.G.; Pandya, R.A.; Agrawal, Y.K.; Shrivastav, P.S. Molecular Octopus: Octa Functionalized Calix[4]resorcinarene-hydroxamic acid [C4RAHA] for Selective Extraction, Separation and Preconcentration of U(VI). *Talanta*. **2005**, *65*, 466–475
- 156 Ozcan, F.; Bayracker, M.; Ertul, S. Synthesis and Characterization of Novel Nanofiber Based Calixarene and its Binding Efficiency towards Chromium and Uranium Ions. *Journal of Inclusion Phenomena and Macrocyclic Chemistry*. **2016**, *85*, 49–58
- 157 Jaschke, B.A.; Schone, S.; Barthen, R.; Marz, J.; Schmeide, K.; Patzschke, M.; Kersting, B.; Fahmy, K.; Oertel, J.; Brendler, V.; Stumpf, T. Uranium(VI) Complexes with a Calix[4]arene-Based 8-Hydroxyquinoline Ligand: Thermodynamic and Structural Characterization Based on Calorimetry, Spectroscopy, and Liquid-Liquid Extraction. *ChemistryOpen*. **2018**, *7*, 467–474
- 158 Xiao, F-Z.; Pu, Y-Q.; Wang, C.; Xu, Y-L.; Zhang, K.; Ho, C-H.; Peng, G-W.; He, S-Y. Extraction Properties for U(VI) by the 25, 27-dihydroxy-26, 28-dimercaptoethoxy-5, 11, 17, 23-tetra-tert-butyl Calix[4]arene. *Journal of Radioanalytical and Nuclear Chemistry*. **2019**, *321*, 49–55
- 159 Bieber, V.S.; Ozcelik, E.; Cox, H.J.; Ottley, C.J.; Ratan, J.K.; Karaman, M.; Tabakci, M.; Beaumont, S.K.; Badyal, J.P.S. Capture and Release Recyclable Dimethylaminomethyl-Calixarene Functional Cloths for Point-of-Use Removal of Highly Toxic Chromium Water Pollutants. *ACS Applied Materials and Interfaces*. **2020**, *12*, 52136–52145
- 160 Qureshi, I.; Memon, S.; Yilmaz, M. Estimation of Chromium(VI) Sorption Efficiency of Novel Regenerable p-tert-butylcalix[8]areneoctamide Impregnated Amberlite Resin. *Journal of Hazardous Materials*. **2009**, *164*, 675–682
- 161 Sayin, S. Fabrication of Efficient Calix[4]arene-Adorned Magnetic Nanoparticles for the Removal of Cr(VI)/As(V) Anions from Aqueous Solutions. *Polycyclic Aromatic Compounds*. **2022**, *42*, 1023–1034
- 162 Khan, S.; Qureshi, I.; Shifa, M.S.; Waziri, A.H. An Efficient Calixarene-based Functional Material for the Sorption and Recovery of Cr(VI) from Water. *International Journal of Environmental Analytical Chemistry*. **2019**, *99*, 1123–1134
- 163 Smirnov, I.V.; Karavan, M.D.; Efremiva, T.I.; Babain, V.A.; Miroshnichenki, S.I.; Cherenok, S.A.; Kalchenko, V.I. Extraction of Am, Eu, Tc, and Pd from Nitric Acid Solutions with Phosphorylated Calixarenes. *Radiochemistry*. **2007**, *49*, 482–492
- 164 Huang, H.; Ding, S.; Liu, N.; Wu, Y.; Su, D.; Huang, S. Extraction of Trivalent Americium and Europium from Nitric Acid Solution with a Calixarene-based Diglycolamide. *Separation and Purification Technology*. **2014**, *123*, 235–240
- 165 Zhang, A.; Chen, C.; Ji, Y.; Liu, S.; Guo, S. Uptake of Cesium and Some Typical Metals onto Hybrid Calix[4]crown Adsorbent with Silica Carrier by Host–Guest Recognition. *Journal of Chemical & Engineering Data*. **2018**, *63*, 1578–1587

- 166 Shetty, D.; Boutros, S.; Eskhan, A.; De Lena, A.M.; Skorjanc, T.; Asfari, Z.; Traboulsi, H.; Mazher, J.; Raya, J.; Banat, F.; Trabolsi, A. Thioether-Crown-Rich Calix[4]arene Porous Polymer for Highly Efficient Removal of Mercury from Water. *ACS Applied Materials and Interfaces*. **2019**, *11*, 12898–12903
- 167 Supian, F.L.; Richardson, T.H.; Deasy, M.; Kellher, F.; Ward, J.P.; McKee, V. Interaction between Langmuir and Langmuir–Blodgett Films of Two Calix[4]arenes with Aqueous Copper and Lithium Ions. *Langmuir*. **2010**, *26*, 10906–10912
- 168 D’Alonzo, N.J.; Eggers, P.K.; Eroglu, E.; Raston, C. p-Phosphonated Calix[n]arene Stabilizes Superparamagnetic Nanoparticles for Nitrate and Phosphate Uptake, *ChemPlusChem*. **2016**, *82*, 416–422
- 169 Chandran, M.; Mahmood, W.M.A.W.; Omar, F.N.; Lazim, A.M. Removal of Methylene Blue from Aqueous Solution Using Modified Polystyrene-Calixarene (PS-C) Composite. *Water Air & Soil Pollution*. **2022**, *233*
- 170 Zhou, S.; Jin, L.; Gu, P.; Tian, L.; Li, N.; Chen, D.; Marcomini, A.; Xu, Q.; Lu, J. Novel Calixarene-based Porous Organic Polymers with Superfast Removal Rate and Ultrahigh Adsorption Capacity for Selective Separation of Cationic Dyes. *Chemical Engineering Journal*. **2022**, *433*, 134442
- 171 Mohammadi, A.; Abdolvand, H.; Isfahani, A.P. Alginate Beads Impregnated with Sulfonate Containing Calix[4]arene-intercalated Layered Double Hydroxides: In situ Preparation, Characterization and Methylene Blue Adsorption Studies. *International Journal of Biological Macromolecules*. **2020**, *146*, 89–98
- 172 Kamboh, M.A.; Solangi, I.B.; Sherazi, S.T.H.; Memon, S. Synthesis and Application of Calix[4]arene Based Resin for the Removal of Azo Dyes. *Journal of Hazardous Materials*. **2009**, *172*, 234–239
- 173 Chung, T-S.; Lai, J-Y. The Potential of Calixarenes for Membrane Separation. *Chemical Engineering Research and Design*. **2022**, *183*, 538–545
- 174 Mohd Zahri, N.; Md Jamil, S.; Abdullah, L.; Shean Yaw, T.; Nourouzi Mobarekeh, M.; Sim, J.; Mohd Rapeia, N. Improved Method for Preparation of Amidoxime Modified Poly(acrylonitrile-co-acrylic acid): Characterizations and Adsorption Case Study. *Polymers*. **2015**, *7*, 1205–1220
- 175 Tang, N.; Liang, J.; Niu, C.; Wang, H.; Luo, Y.; Xing, W.; Ye, S.; Liang, C.; Guo, H.; Guo, J.; Zhang, Y.; Zeng, G. Amidoxime-based Materials for Uranium Recovery and Removal. *Journal of Materials and Chemistry A*. **2020**, *8*, 7588–7625

## 2 CHAPTER 2 – EXPERIMENTAL

### 2.1 Introduction

Over the course of this work, several experimental techniques have been employed in order to fabricate the functional cloths, characterise their properties, and investigate their contaminant-removal performance. This Chapter provides a summary of each of the techniques used.

#### 2.1.1 Fabrication Techniques

##### 2.1.1.1 Plasmachemical Methods

Plasmas are frequently referred to as the fourth state of matter.<sup>176</sup> Plasmas are gases which contain a mixture of charged species, radicals, and non-reactive species. Despite the presence of the charged species, plasmas contain electrons in roughly equal numbers, such that the resultant space charge is close to zero.<sup>177</sup> The plasmachemical techniques throughout this work use radio-frequency (RF) discharge, whereby a current is passed through a coil, wrapped around a plasma chamber. The RF power interacts inductively with the plasma, whereby energy is transferred from the electric field to the free electrons within the gas.<sup>176</sup> The electrons accelerate, and collide with other species, resulting in excitation, ionisation and dissociation. This ionisation simultaneously generates electrons, which can then undergo the same processes, resulting in a self-sustaining plasma until all monomer molecules have been exhausted.<sup>178</sup> While other methods of producing plasmas exist (e.g., direct current electrical discharges, microwave electric discharges), the method employed is preferable for its characteristics of avoiding contamination with electrodes (direct current) and operating in the ideal frequency for deposition (microwave electric discharge plasmas are typically used to produce gas lasers).<sup>176</sup> While the classical definition of plasmas referred to ionised gas that was fluid, neutral, viscous and “hot” (plasmas formed naturally in stars exist at temperatures greater than 5000 K), these laboratory formed plasmas are considered “cold”, meaning that they are sometimes referred to as “low-temperature plasma”.<sup>179</sup> Furthermore, due the fact that the plasmas employed in this work are luminous (owing to the radiative decay of the excited species to lower levels), they are also known as “glow discharge plasmas”.<sup>180</sup>

The excited species mentioned above are very reactive—not only with each other, but also any surfaces which are in contact with the plasma. Consequently, these glow discharge plasmas can be used to alter the properties of the surface of a substrate, either chemically (deposition or treatment) or physically (etching) without—crucially—affecting the bulk

properties of the substrate (owing to the relatively low-energy energetic particles being unable to penetrate the bulk phase).<sup>179,181</sup>

#### 2.1.1.1.1 *Plasmachemical Deposition*

Depositing a plasma polymer—which typically contains a particular functional group of interest—onto a substrate allows for the introduction of this key functional group onto the surface of a substrate. By using a polymerisable monomer (an organic compound with a sufficiently high vapour pressure, typically containing a ring or olefin group—although nearly all organic compounds can be polymerised under the right conditions<sup>181</sup>), deposition of a plasma polymer onto the surface of the substrate is possible. As opposed to traditional polymers, which are made up of long-chain linear molecules, plasma polymers exist as a three-dimensional network, containing a multitude of short chains.<sup>181</sup> The plasma polymerisation process is system dependent, meaning that the structure of the plasma polymer does not depend solely on the monomer. Rather, the plasma polymer structure depends on a range of factors including temperature, monomer flow rate, input power, and monomer vapour pressure. For example, the use of styrene as the precursor monomer can give rise to a plasma polymer which resembles “typical” polystyrene; or alternatively a hard material which resembles diamond, depending on the reaction conditions.

The mechanism for plasma deposition involves the formation of radical sites on the substrates initiating a radical chain-growth mechanism, wherein polymerisation is terminated by recombination or disproportionation of radicals. Previous research has also claimed that at higher powers, fragmentation of the precursor monomer occurs, followed by recombination and subsequent deposition.<sup>182</sup> Significantly, this (continuous wave) plasma polymerisation is a low-temperature single-step reaction, which is also independent of substrate and does not require solvents, meaning that it is a relatively environmentally friendly means of fabricating functional materials. Furthermore, the deposited films exhibit outstanding adhesion to the substrate surfaces, meaning that they typically do not wash off when in aqueous conditions.<sup>183,184</sup> Due to this range of advantages, plasma processes have been a key part of several industries for many years.<sup>185</sup>

Unfortunately, due to the relatively extreme conditions employed within continuous wave polymerisation, fragmentation readily occurs, leading to a lack of retention of the aforementioned key functional group, meaning that the substrate is not modified to the desired extent. In order to overcome this issue, pulsed plasmas can be employed. Here, a current is passed through the coil for a fractionally short *on*-period before ceasing over a much longer *off*-period. Using time-resolved *in situ* mass spectrometry, Carletto et al. was able to elucidate

the polymerisation mechanism under pulsing conditions. During the brief *on*-period, initiator radical species are formed.<sup>186</sup> Thereafter, conventional stepwise chain polymerisation occurs during the *off*-period, in which monomer units add onto the existing chain, forming a well-defined polymer. As opposed to previous studies where longer (ms range) on-times were used, the shorter ( $\mu$ s range) on-times employed by Carletto et al. narrowed the timeframe for any damaging fragmentation reaction pathways, as well as preventing ion-bombardment damage by preventing the build-up of a plasma sheath.<sup>187</sup> In addition to producing a coating which exhibits a high level of functional group retention, by dint of only passing the current through the coils for a small fraction of the total deposition time, far less energy is used during the process, meaning that pulsed plasma deposition is a particularly environmentally friendly fabrication method.

There are some drawbacks to pulsed plasmas. Most importantly, the polymerisation mechanism described above necessarily relies on the precursor monomer containing a C=C double bond, which means that the aforementioned “right conditions” are not met to produce plasma polymers of non-olefin containing organic materials.<sup>181</sup> Additionally, deposition rates are lower compared to continuous wave deposition, which is problematic if films are required to be a minimum thickness. Finally, pulsed plasma deposited films exhibit weaker adhesion to a substrate than continuous wave plasma deposited films. However, this can be overcome by depositing a continuous wave plasma polymer for a short period of time to attach to the substrate surface, before switching to pulsed plasma, to allow a well-defined plasma polymer with high functional group retention to grow on top of the continuous wave plasma polymer.<sup>183</sup>

#### 2.1.1.1.2 *Plasmachemical Treatment*

The surface of substrates can also be plasmachemically altered without deposition of a thin film. This can occur through etching, wherein the highly energetic species produced in oxygen (or other process gases, such as N<sub>2</sub> or Ar) plasma bombard the substrate surface, breaking it down to volatile and/or smaller molecules, which can then be removed by the vacuum pump under which the systems operate.<sup>188</sup> In doing so, parts of (or the top layer of) the surface are etched away. This process therefore physically changes the properties of the substrate without changing its chemical properties.

More relevantly to this work, surfaces can be chemically modified by plasma treatment. Here, the produced radicals react with the surface leaving behind an activated site which can then interact with gaseous molecules (abstraction and addition), functionalising the surface.<sup>189</sup> For example, treating a surface with ammonia introduces –NH<sub>3</sub> groups,<sup>190</sup> with CF<sub>4</sub> introduces –F groups,<sup>191</sup> and with CO<sub>2</sub> introduces –COOH, –OH, –CHO, and epoxide groups.<sup>192</sup>

### 2.1.1.1.3 Apparatus

The general experimental setup for a plasma deposition/treatment is shown in Figure 2-1. The plasma rig consists of a rotary pump, which attaches to the sealed glassware – a liquid nitrogen cooled cold trap, which is connected to a glass plasma chamber, itself connected to a needle valve and/or a glass monomer tube (cylindrical vessel containing the monomer to deposit). A copper coil surrounds the plasma chamber, which connects to the electronics of the system – a matching unit, used in conjunction with an RF generator, pulse generator and power-meter. An oscilloscope is used to track the signal input and observe the unique plasma pulse shape.

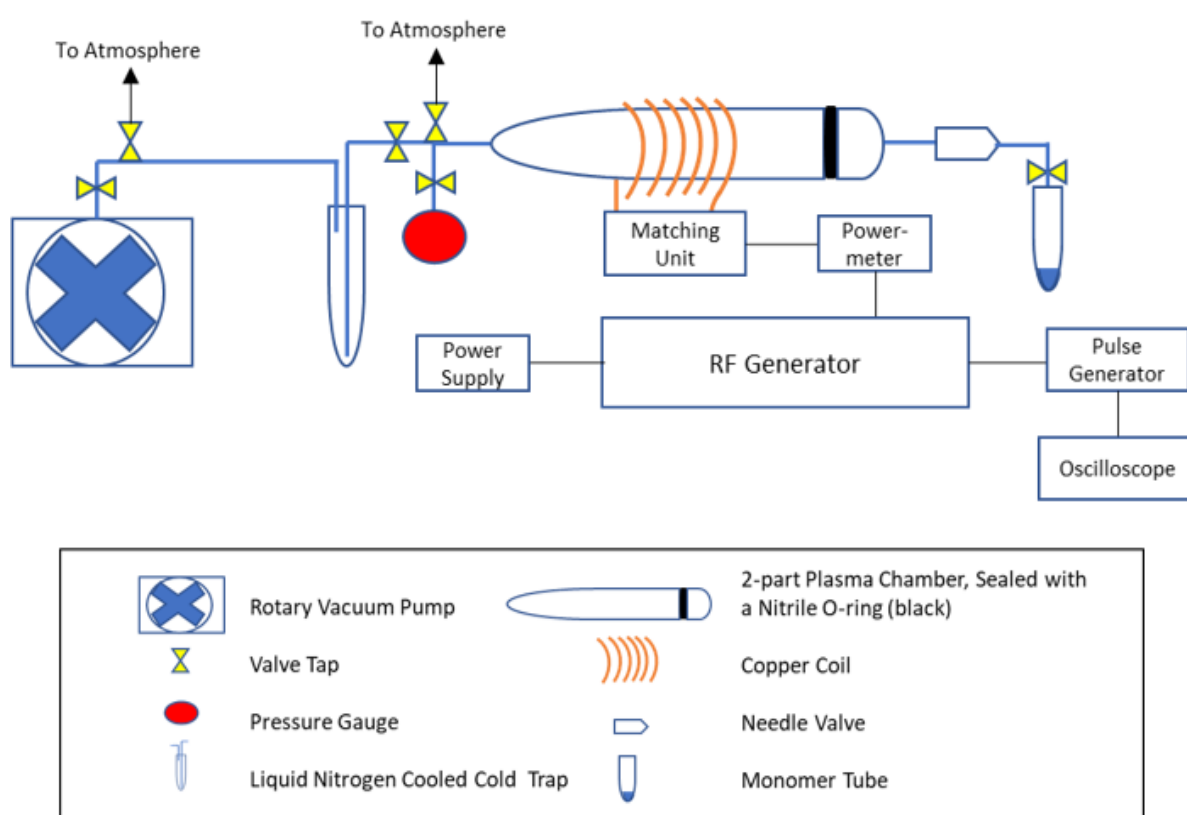


Figure 2-1. Schematic depiction of a plasma rig used in the plasmachemical modification of surfaces.

The rotary pump used is an Edwards Rotary Vane Pump, which houses a circular rotor within a circular pump.<sup>193</sup> There is an offset between the centre of the pump housing and the rotor, which gives rise to eccentric rotation. The rotor is decorated with variable length vanes, meaning that the rotor is in constant contact with the pump housing (oil is used to create a seal). This in turn creates vane chambers, and gas from the system (which is required to be under vacuum) flows into one of the created vane chambers, which then expands as the rotor spins. With this expansion, the gas simultaneously expands to fill the generated cavity. Immediately afterwards, the gas-filled vane chamber enters into the discharge side of the

pump, whereupon it reduces in size. The process repeats rapidly without gas loss until the pressure of the gas, which has become increasingly compressed, is sufficiently high for the gas to be expelled out of the pump outlet.

The valve taps used were Young's taps, which consist of a cylindrical polytetrafluoroethylene (PTFE) plug, equipped with three O-rings—one (also made of PTFE) to form an air-tight seal at the junction of the glassware manifolds, and two more O-rings (one nitrile, one PTFE) which form a seal between the plug and the barrel of the glassware, ensuring that the tap is airtight. By sealing a junction, different sections of the glassware become isolated, meaning that one side can be brought up to atmosphere, while the other remains under vacuum.

The cold trap is designed such that undesirable gases do not get sucked into the pump, which could damage it. The glass tube extending from the chamber leads to the bottom of the cold trap, which is surrounded by liquid nitrogen. Any monomer which has passed through the chamber will condense at this temperature, meaning that once the experiment has ceased, the cold trap can be removed, the condensate disposed of, and the trap cleaned for further use, thus preventing any monomer from reaching the pump. The glass tube connecting the trap to the pump lies at the top of the cold trap, meaning that species which are still gaseous under conditions employed (e.g., nitrogen) can be pumped off.

The pressure gauge used was a thermocouple gauge, which, by means of a thermocouple, records the temperature of a filament which is heated via the constant passage of current.<sup>194,195</sup> The thermocouple consists of two wires of different conductivity, inducing an electrical potential which is related to temperature. In essence, the temperature is a measurement of the thermoconductivity of the surrounding gas, which is itself related to pressure (the greater number of gaseous molecules that contact the filament, the more the heat energy dissipates into the surroundings, lowering the temperature). The thermocouple produces a voltage, which can be calibrated against a known pressure, such that a relationship between voltage output and chamber pressure can be generated.

Needle valves allow the introduction of a gas into the plasma chamber and can administer pressures as low as  $1 \times 10^{-5}$  mbar.<sup>196</sup> The valve consists of a small hole, which is kept closed by a needle using spring pressure. Loosening the adjuster releases the spring, allowing a small leak to enter the valve. The adjuster can be set to a specific value, such that the required gas pressure is allowed to enter the plasma chamber.

The RF generator contains an oscillator circuit, which produces a stable and precise frequency signal. This signal is then modulated, amplified and passed through an output stage.

This output stage involves the signal being passed through a matching unit, which consists of a series of capacitors and inductors in order to match the output impedance of the RF generator with that of the matching unit and chamber coils. The incident and reflected waves are aligned such that the standard wave ratio (SWR) is minimised. SWR is related to reflectance according to Equation (2-1), which shows that reflectance ( $|\Gamma|$ ) must be minimised in order to reduce the SWR. Constructive interference occurs when the load impedance and matching unit impedance are matched, which gives rise to a SWR of 1. The matching unit contains two variable capacitors, whose capacitances can be changed in order to alter the impedance of the circuit according to Equation (2-3)

$$SWR = \frac{1+|\Gamma|}{1-|\Gamma|} \quad (2-1)$$

Where  $\Gamma$  is the reflectance, given by:

$$\Gamma = \frac{Z_L - Z_0}{Z_L + Z_0} \quad (2-2)$$

Where  $z_L$  is the load impedance and  $z_0$  is the characteristic impedance, given by:

$$z_0 = \sqrt{\frac{L}{C}} \quad (2-3)$$

Where  $L$  is the inductance, and  $C$  is the capacitance.

The power-meter is connected to the RF generator and matching unit through coaxial cables, through which the power is transferred prior to impedance matching. As well as displaying the forward power going through the system, the meter also displays the SWR, allowing for ideal adjustment of the matching unit capacitance.

#### 2.1.1.1.4 Cloth Functionalisation

All cloths in this work were functionalised by following a similar method to that performed by Bieber et al.<sup>197</sup> Prior to plasma deposition/treatment, the cloths were washed in a 1:1 by volume mixture of propan-2-ol (+ 99.5 %, Fisher Scientific UK Ltd.) and hexane (fraction from petroleum, laboratory reagent grade, Fisher Scientific UK Ltd.), before being left to dry in air. For experiments involving plasma deposition, silicon wafer substrates (Silicon Valley Microelectronics Inc.) were used as flat, reflective substrates. These were cleaned prior to coating by sonication in a 1:1 by volume mixture of propan-2-ol and hexane, followed by UV/ozone treatment (model UV.TC.EU.003, BioForce Nanosciences Inc.), and finally another sonication step in the propan-2-ol/hexane mixture.



Plasma depositions/treatments were performed using the apparatus described in 2.1.1.1.3 – a cylindrical glass reactor (5 cm diameter, 470 cm<sup>3</sup> volume) is located within a Faraday cage and evacuated using a 30 L min<sup>-1</sup> rotary pump via a liquid-nitrogen cold trap (with a base pressure of less than 1 × 10<sup>-3</sup> mbar and an air leak rate of better than 1 × 10<sup>-9</sup> mol s<sup>-1</sup>). A copper coil is wound around the reactor (5 mm diameter, 10 turns, located 13.1 cm away from the gas inlet) and is connected to a 13.56 MHz RF power supply via an L-C matching network. A signal generator (model TH503, Thurlby Thandar Instruments Ltd.) was used to trigger the RF power supply, and the corresponding pulse shape was monitored with an oscilloscope (model V-252, Hitachi Ltd.). Prior to film deposition, the whole apparatus was thoroughly scrubbed using detergent and hot water, rinsed with acetone, and oven dried at 200 °C, before undergoing further cleaning through exposure to 50 W continuous-wave air plasma at 0.2 mbar for 30 min.

The desired substrate is subsequently placed inside the chamber, resting on the walls with the shorter side lying along the length of the chamber. For plasma deposition experiments, a silicon wafer is also placed at each end of the chamber. The silicon wafer substrates (Silicon Valley Microelectronics Inc.) were used as flat, reflective substrates. These were cleaned prior to coating by sonication in a 1:1 by volume mixture of propan-2-ol and hexane, followed by UV/ozone treatment (model UV.TC.EU.003, BioForce Nanosciences Inc.), and finally another sonication step in the propan-2-ol/hexane mixture. Silicon wafers are not used for plasma treatments.

The monomer is loaded into a sealable glass tube, degassed via several freeze-pump-thaw cycles, then attached to the reactor. The chamber is allowed to pump down to base pressure for at least 3 h, before the monomer vapour is allowed to purge the apparatus at a pressure of 0.2 mbar for 15 min prior to electrical discharge ignition. Following plasma extinction, the monomer is allowed to continue to pass through the chamber for a further 15 min, before pumping back down to base pressure for at least 30 min, followed by venting to atmosphere.

## **2.1.2 Characterisation Techniques**

### *2.1.2.1 Fourier Transform Infrared Spectroscopy*

#### *2.1.2.1.1 Background*

Fourier Transform Infrared (FTIR) Spectroscopy is a particularly useful spectroscopic technique for the elucidation of chemical groups within a sample. Chemical bonds within the sample are capable of absorbing infrared (IR) radiation. In the situation where the energy of

an absorbed photon of IR radiation is equivalent to the energy gap between the initial and excited vibrational energy levels, a vibrational excitation occurs.<sup>198</sup> If the associated stretching/bending vibration results in a change in the overall electric dipole moment, then it is said to be IR active, and the wavelength of this excitation will appear in the final spectrum, as there will be a difference in initial and final energy, due to the absorbance at this wavelength. As different chemical bonds each absorb at their own, specific, wavelength, the chemical bonds present in a sample can be identified by which wavelengths have been absorbed by the sample.

#### *2.1.2.1.2 Interferometer*

FTIR spectrometers contain an interferometer (Figure 2-2), which regulates the IR wavelengths expelled from the IR source and measures the interference pattern between two beams. This signal helps give rise to an interferogram, which is a function of the pathlength between these beams. The collimating mirror transforms the light from the source into parallel rays, and then directs them towards the beamsplitter, which splits the light into two—half is directed towards the moving mirror, and the other half towards the fixed mirror. These beams then reflect back towards the beamsplitter, whereupon they interfere. As the moving mirror is capable of altering the pathlength of the light, differing pathlengths can be created, which gives rise to constructive and destructive interferences for the reflected and transmitted beams respectively. This interference pattern is known as an interferogram. This recombined beam then passes through a sample, and it is the difference in absorbance at each wavelength between the beams that pass through the sample, and the beams found in the interferogram that is recorded by the detector.

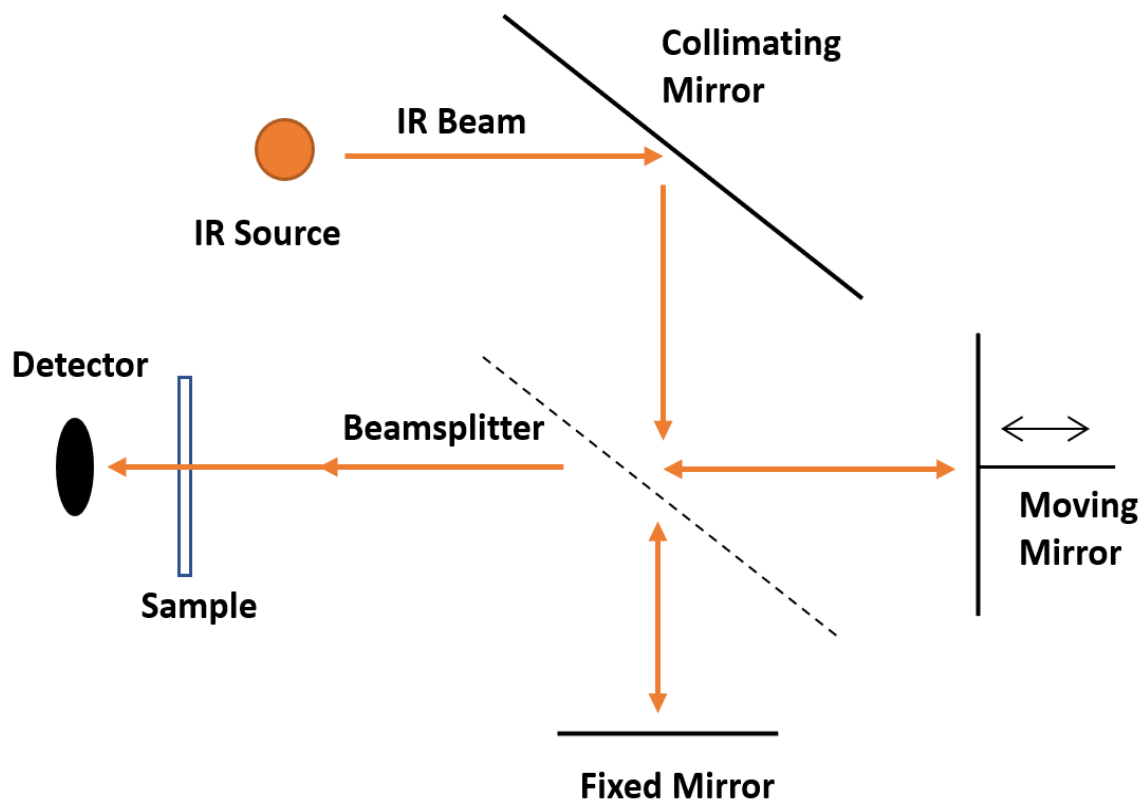


Figure 2-2. Schematic depiction of an interferometer used within a FTIR spectrometer.

#### 2.1.2.1.3 Detectors

There are two types of detectors used by the spectrometer in this work. The first is a pyroelectric detector, and the second is a photoconductive detector. The pyroelectric, deuterated triglycine sulfate (DTGS) detector operates at ambient temperatures.<sup>199</sup> When the IR beams strike the detector, the material changes its temperature, which alters the position of the atoms within the crystal, resulting in a change in the dielectric constant, and in turn, its capacitance.<sup>200</sup> This capacitance change is measured by means of a voltage response, which gives rise to the final spectrum. While the DTGS detector is a cheap and simple detector, it does exhibit a slow response time and poor sensitivity.

In order to obtain a spectrum with greater sensitivity, the photoconductive detector containing mercury cadmium telluride (MCT) can be used. This material is a semiconductor, capable of absorbing IR light, resulting in the excitation of its electrons from the valence band to the conduction band.<sup>200</sup> The excited electrons are then able to create an electrical current proportional to the intensity of IR light absorbed. However, MCT detectors are more fragile, and more expensive, so more care is required when using them. Furthermore, they are very temperature sensitive, and require to be kept under liquid nitrogen temperatures, lest a spectrum with a large signal:noise ratio be generated.

#### 2.1.2.1.4 Monolayer Grazing Angle Specular Reflectance Accessory

There are two types of FTIR measurements featured within this work. The first is Reflection-Absorption-Infrared Spectroscopy (RAIRS) and the second is Attenuated Total Reflectance (ATR). RAIRS spectra are taken by reflecting the incident beam off a film, coated onto a reflective substrate (e.g., gold or silicon), before reaching the detector (Figure 2-3). Molecules within the film are able to absorb the IR light before and after reflection off the substrate. A spectrum is recorded by first recording a background spectrum of the pure reflective surface, which is then subtracted from a spectrum containing the film coated onto the reflective surface.

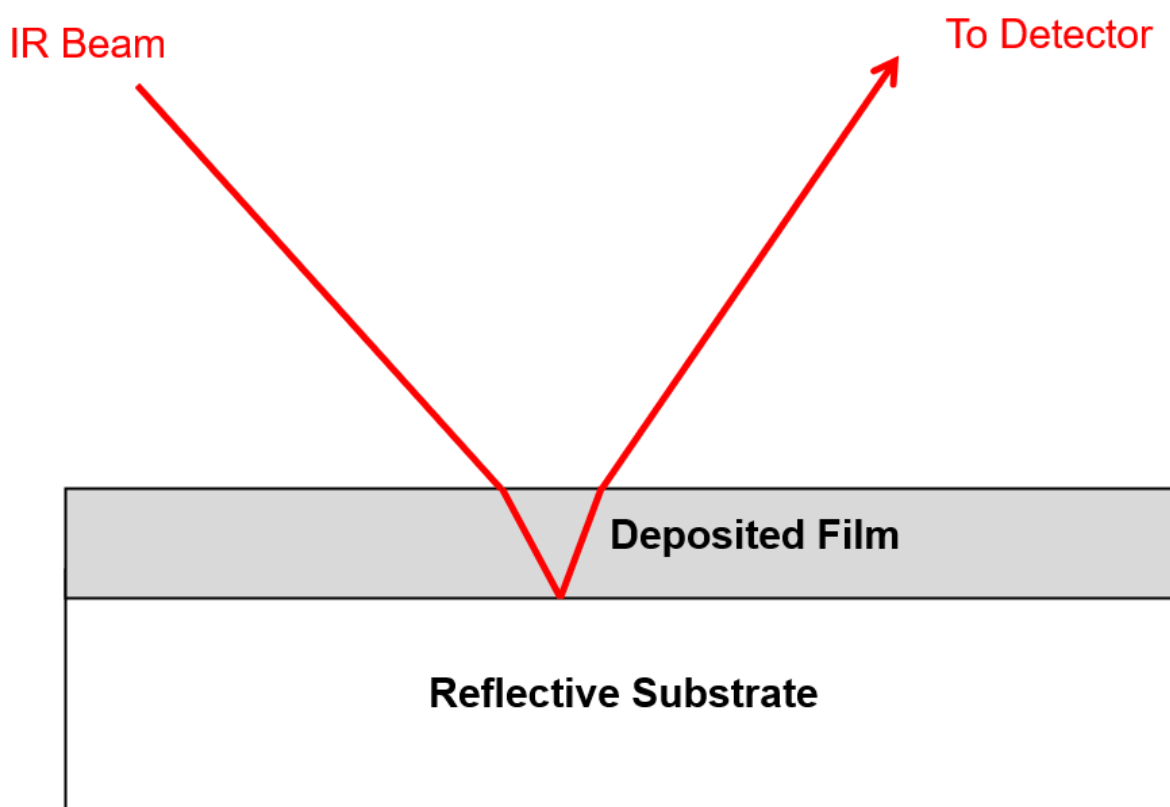


Figure 2-3. Depiction of IR light passing through coating, reflecting off substrate, then passing through coating again, before reaching the detector.

The optimum RAIRS conditions depend on dielectric properties of the substrate and the deposited film.<sup>201</sup> Crucially, the surface selection rule—which states that only vibrations with a component of the transition dipole moment oriented perpendicular to the surface can be observed—determines which vibrational adsorbate modes are IR active.<sup>202</sup> Here, the amplitude and phase of the reflected radiation is dependent on the direction of the electric field vector, which contains parallel and perpendicular polarised light. Parallel light is known as p-polarised light (from the German, parallel), as it lies parallel to the plane of incidence, whereas

perpendicular light is known as s-polarised light (from the German, senkrecht), as it lies perpendicular to the plane of incidence (Figure 2-4).

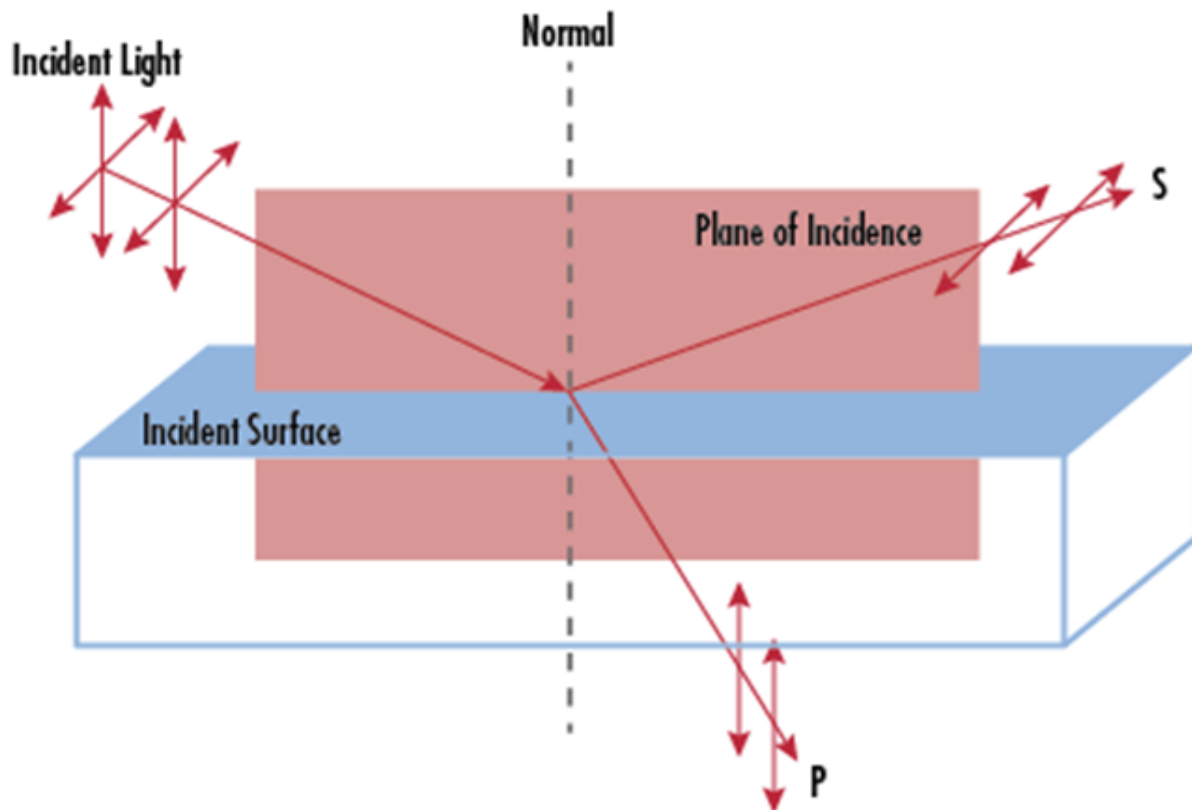


Figure 2-4. p- and s-polarised light, as defined by their relative orientation to the plane of incidence. Taken from reference 203.

When light is reflected from a metal (or Si) surface, it undergoes a phase shift, summarised by Greenlet et al. in Figure 2-5(A).<sup>204</sup> It can be seen that at all angles of incidence, a phase shift of  $180^\circ$  for s-polarised light occurs. As metals (and Si) have high IR reflective capabilities, the magnitudes of the electric vectors post-reflection are very similar to those pre-reflection.<sup>205</sup> As such, the electrical vectors effectively cancel out, yielding a resultant electric field of roughly 0 magnitude or direction. On the other hand, at angles close to grazing, a phase shift of  $90^\circ$  can be obtained for p-polarised light. At this angle, vector addition of the incident and reflected vectors yields an elliptical standing wave, featuring a large component (due to constructive interference, this is almost twice the magnitude of the incident light, Figure 2-5(B)) perpendicular to the surface (parallel to the plane of incidence) and only a small portion parallel to the surface.

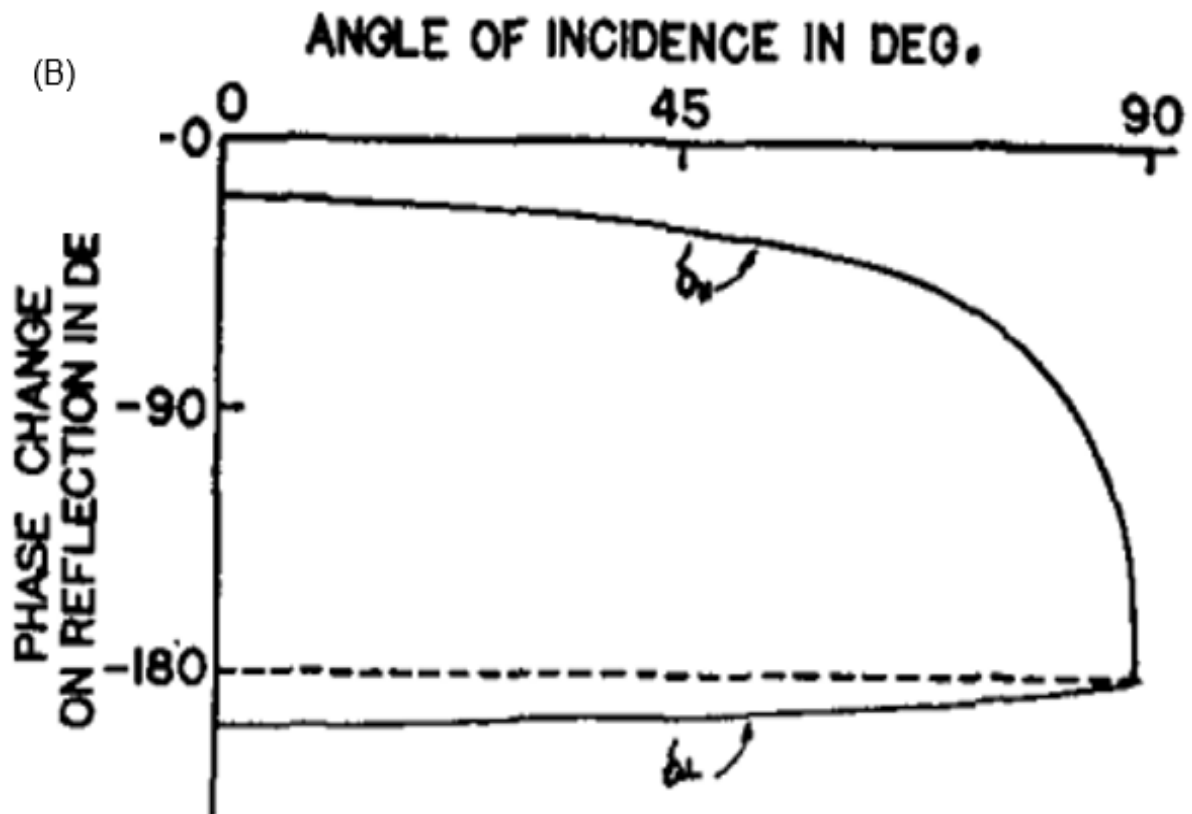
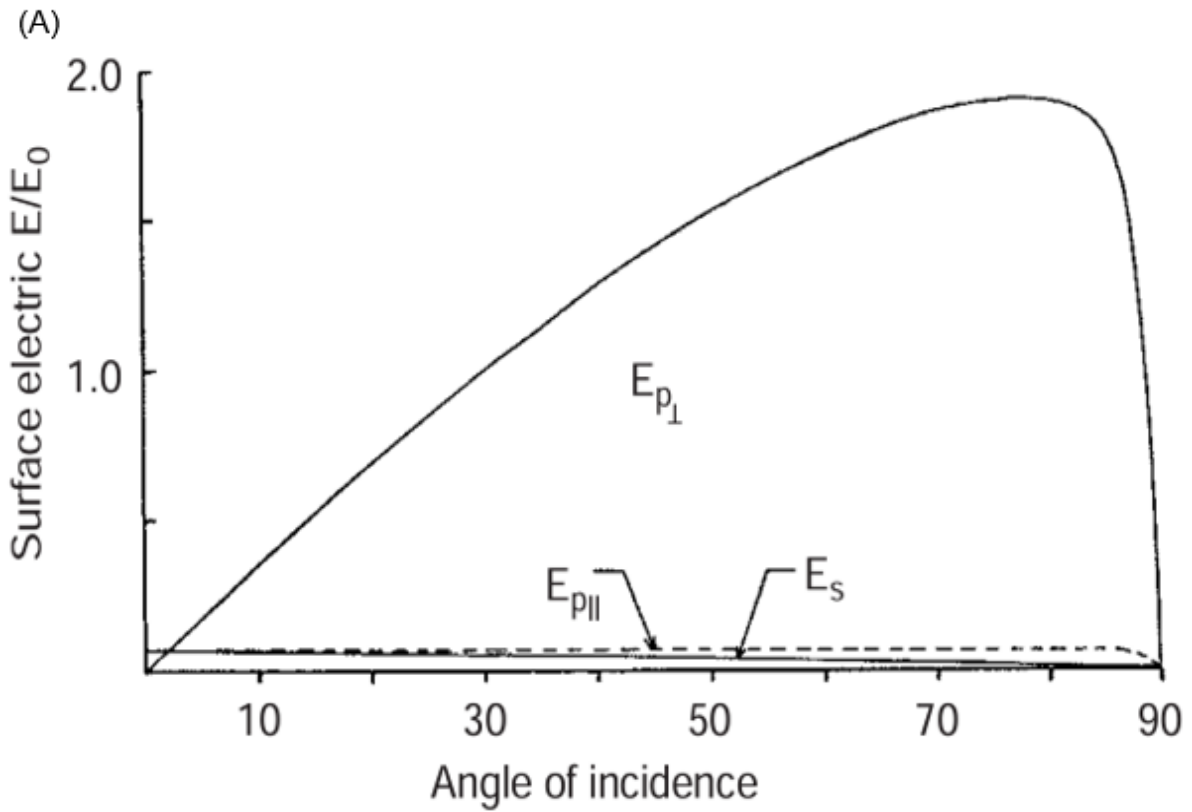
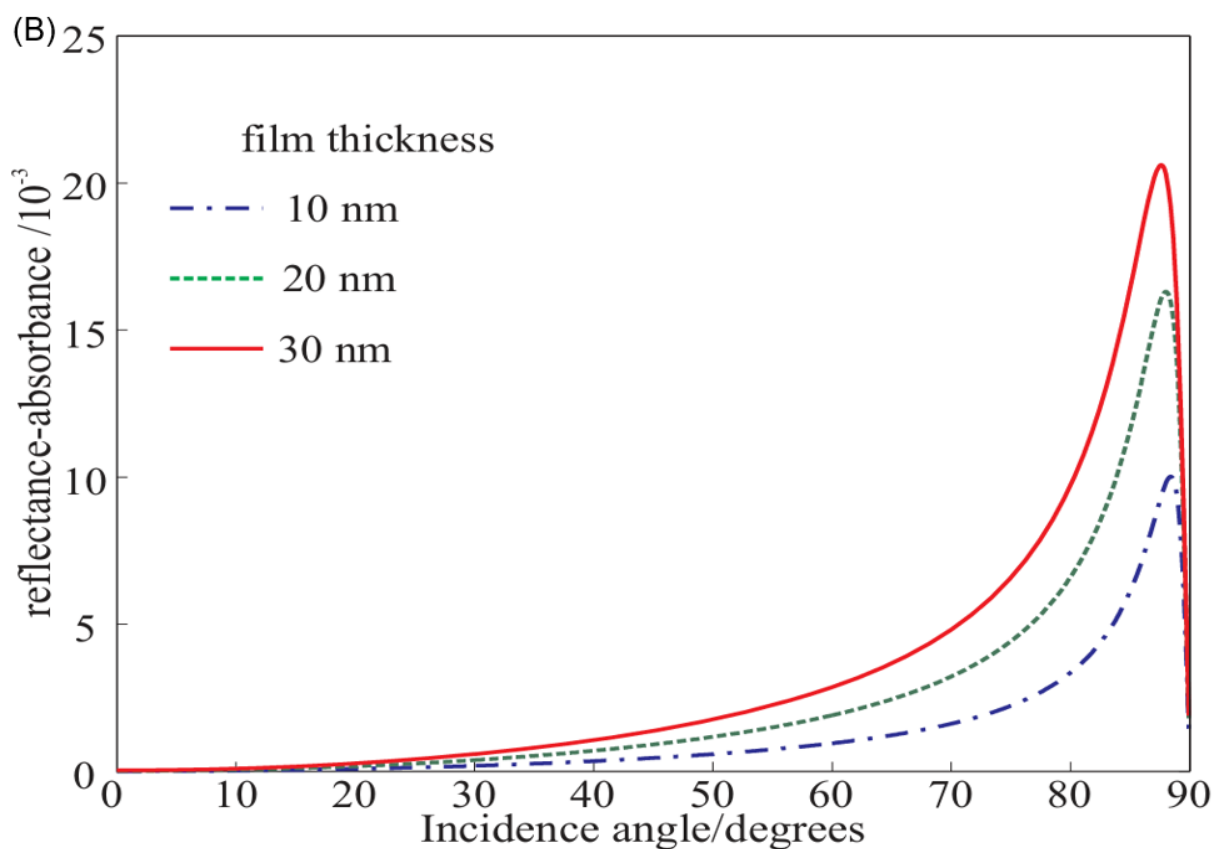


Figure 2-5. (A) Phase change for light reflected from a metal surface for light polarised parallel and perpendicular to the *surface*. Taken from reference 204. (B) Resultant electric fields obtained from p-polarised light, for components parallel and perpendicular to the *surface*. Taken from reference 205. In both images, p-polarised light is depicted by the solid line, while s-polarised light is depicted by the dashed line.

Consequently, it is vital that the s-polarised light is removed from the IR source, before reaching the sample to be investigated. To achieve this, the RAIRS accessory is fitted with a polariser, which is an IR transmitting optical window (in this case thallium bromiodide, KRS-5) lithographically deposited with fine wires, wherein the spacing between the lines is a fraction of the wavelength of light transmitted. In the situation where light is polarised parallel to the metal wires (s-polarised), the wires behave like a typical metal surface, with electrons along the wire length becoming excited, leading to the reflection in almost all s-polarised light. Regarding p-polarised light, only electrons along the wire width (sub-micron range) are excited, meaning that most p-polarised light is transmitted.

Other factors that affect the intensity of the RAIRS spectra include film thickness and substrate material type. Previous work has demonstrated that as the film thickness increases, the optimal grazing angle decreases. While the differences in refractive indices of the film and metal substrate are alluded to as the cause of this effect, minimal explanation is provided.<sup>206</sup> Also included in that work is a demonstration on how band intensity increases with film thickness—the thicker the film, the more radiation can be absorbed—however this is not a linear relationship (Figure 2-6).



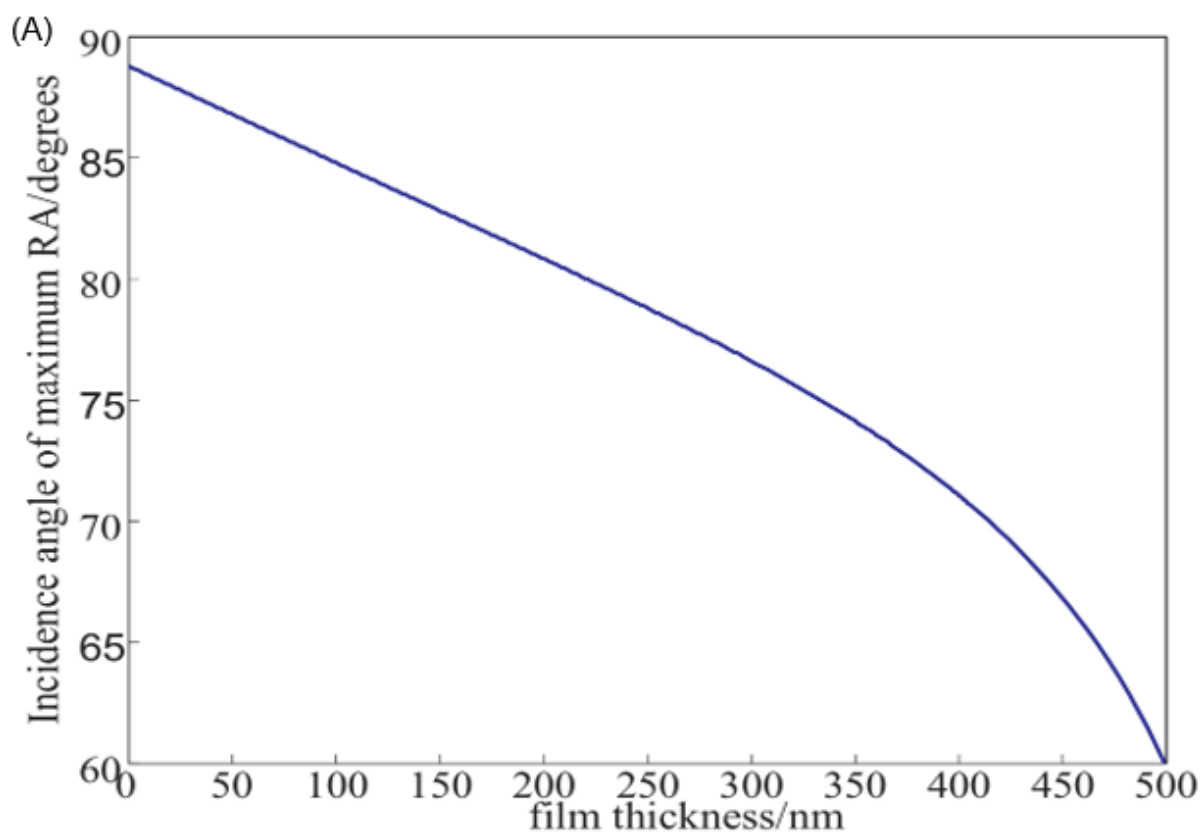


Figure 2-6. (A) Change in optimum grazing angle with film thickness; (B) Change in RAIRS peak intensity with film thickness. Both figures have been taken from reference 206.

As the film thicknesses in this work are typically greater than 300 nm, consideration must be given as to the angle of incidence to employ. Furthermore, significant work using a range of metals as the substrate has led to a range of grazing angles being employed. Given the above, and the fact that previous research has shown that for Si substrates, the lowest signal:noise ratios were observed for grazing angles between  $\sim 60^\circ$  and  $\sim 70^\circ$ ,<sup>207</sup> experiments are performed using a grazing angle of  $66^\circ$ . Attempts to obtain spectra using alternative grazing angles have confirmed that  $66^\circ$  is a suitable angle of incidence for the fabricated films in this work.

#### 2.1.2.1.5 Attenuated Total Reflectance

In situations where the deposited films have not been coated onto a reflective surface, RAIRS will not be able to provide a suitable spectrum. Here, ATR spectroscopy must be employed. This technique utilises total internal reflection, whereby light undergoes several internal reflections when passed through an ATR crystal (typically diamond). This results in the formation of an evanescent wave, assuming that the angle of incidence is greater than critical angle,  $\theta_c$ , which is defined as  $\sin(\theta_c) = \frac{n_2}{n_1}$ , where  $n_1$  and  $n_2$  are the refractive indices of the ATR crystal and sample respectively (Figure 2-7).<sup>208</sup> This wave penetrates the sample at a



depth,  $d_p$ , defined by Equation (2-4).<sup>209</sup> As with RAIRS, a spectrum is created by determining which wavelengths of light have been absorbed after the evanescent waves have passed through the sample, and using the same process of subtracting a background spectrum (typically just the crystal, but using an uncoated substrate + crystal is also possible) from a final spectrum (crystal + sample).

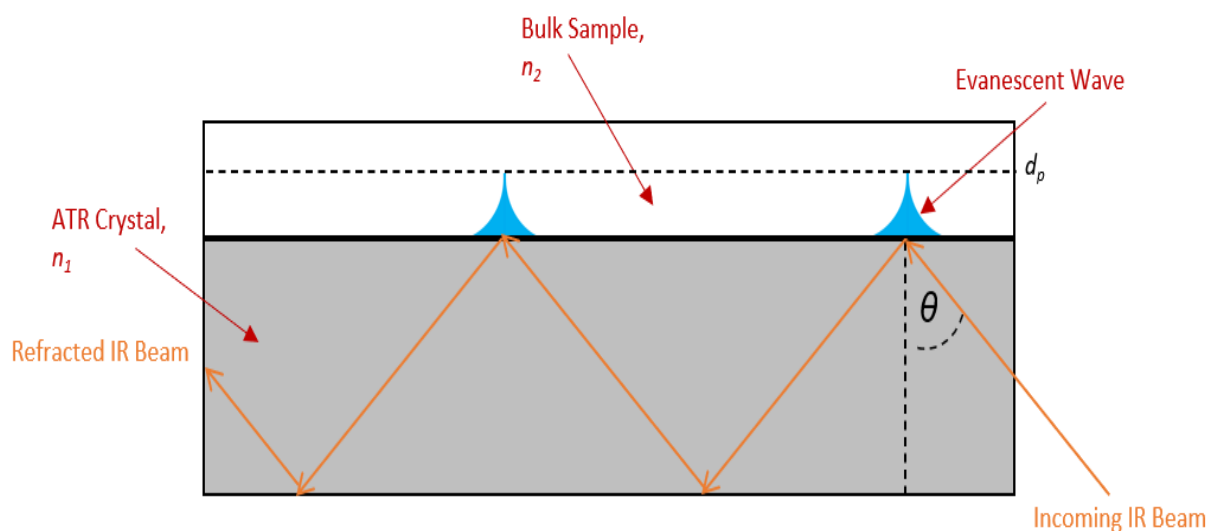


Figure 2-7. Schematic depiction of ATR, showing the induced evanescent wave from total internal reflection.

$$d_p = \frac{\lambda}{2\pi n_1 \sqrt{\sin^2 \theta - \left(\frac{n_1}{n_2}\right)^2}} \quad (2-4)$$

Where  $\lambda$  is the wavelength of incident light in a vacuum,  $n_1$  and  $n_2$  are the refractive indices of the ATR crystal and sample respectively, and  $\theta$  is the angle of incidence.

Consequently, ATR is able to penetrate between 2 and 15  $\mu\text{m}$ , depending on wavelength. Given that this is greater than the thickness of all films fabricated in this work, all ATR samples recorded will observe the absorption bands for the substrate, as well as the deposited film.

#### 2.1.2.1.6 Experimental Conditions

Throughout this thesis, FTIR spectra of the functionalised cloths were acquired using an FTIR spectrometer (SpectrumOne, Perkin Elmer Inc.) fitted with a liquid nitrogen cooled MCT detector. Spectra are an average of 100 scanning accumulations recorded at resolutions of between 1 and 4  $\text{cm}^{-1}$  across the 400–4000  $\text{cm}^{-1}$  range. Attenuated total reflectance (ATR) infrared spectra were obtained using a diamond ATR accessory (Golden Gate, Graseby Specac Ltd.). RAIRS spectra of the coated silicon wafers were obtained using a variable angle

reflection–absorption accessory (Specac Ltd.), adjusted to a grazing angle of  $66^\circ$ , and fitted with a KRS-5 polariser (set to only allow the passage of p-polarised light).

### 2.1.2.2 Spectrophotometry

Spectrophotometry is a useful tool, which can help determine the refractive index ( $n$ ), absorption coefficient ( $k$ ), and thickness ( $d$ ) of a film. The technique involves recording the transmission and/or reflection properties of the surface as a function of wavelength (within the UV–Visible region).

As light (incident beam,  $I_0$ ) passes through a thin film, deposited onto a reflective substrate (e.g., Si), some light will be reflected ( $I_1$ ), and some will be transmitted, before reflecting off the substrate ( $I_2$ ) (Figure 2-8). The two reflected beams will then combine, either constructively or destructively, depending upon the path difference between the two beams. The path difference depends on the thickness and the refractive index—a value which states how fast light travels through the medium when compared to the speed of light in a vacuum—of the film, as well as the angle of transmittance,  $\theta_t$ . Note that although  $\theta_t$  depends on the incident angle,  $\theta_i$ , the two values are not identical, as light bends when passing from one transparent medium to the next according to Snell's law (Equation (2-5)).<sup>210</sup> Equation (2-6) states how  $\theta_i$ ,  $n$ , and  $d$  affect the optical path length.

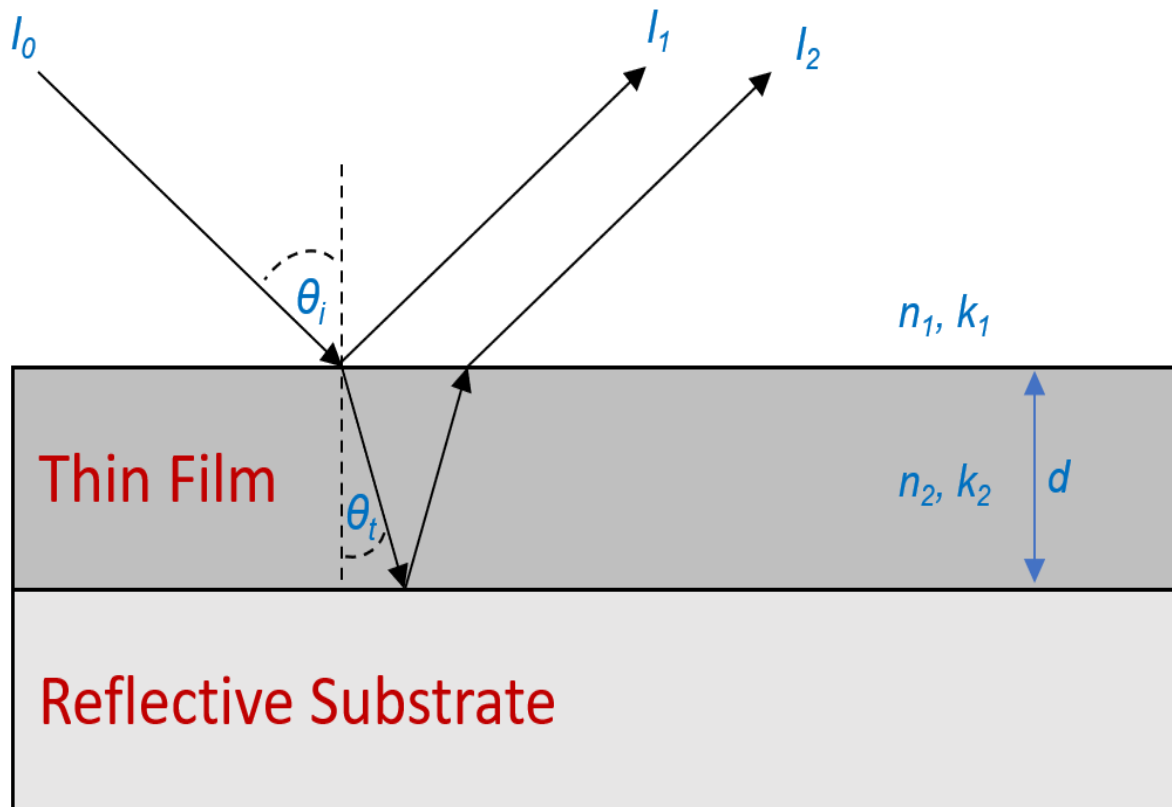


Figure 2-8. Reflection ( $I_1$ ) and transmission of an incident light beam ( $I_0$ ) at the air–film interface. The transmitted light is then reflected ( $I_2$ ) at the film–substrate interface.  $I_1$  and  $I_2$  will interfere, the extent of which dependent on  $n_2$  and  $d$ .

$$\frac{n_1}{n_2} = \frac{\sin(\theta_t)}{\sin(\theta_i)} \quad (2-5)$$

$$\text{Optical Path Difference} = 2n_2d \cdot \cos(\theta_t) \quad (2-6)$$

Consequently, by altering the wavelength of light passed through a coated sample, a reflectance spectrum can be obtained, wherein the intensity of reflectance will oscillate as the wavelengths move from optimal values (e.g.,  $\lambda = d/2$ , leading to constructive interference) to non-ideal values (e.g.,  $\lambda = d/4$ , leading to destructive interference). This oscillating curve can be fitted with a model, and a wellness-of-fit test performed in order to generate a chi-squared value ( $\chi^2$ ). The model is iteratively fitted to the curve until the  $\chi^2$  value is minimised, whereupon a value for  $d$  can be estimated. In this work, the reflectance curves are fitted with a Cauchy model, which assumes that  $k \approx 0$ , using a modified Levenberg-Marquadt (LM) method.<sup>211</sup> The LM method fits non-linear curves by determining the derivatives of the reflectance curves. With the thickness having been calculated, the value of  $n_2$  can then be modelled according to the same method.

### 2.1.2.3 UV–Vis Spectroscopy

UV–Vis spectroscopy is a non-destructive spectroscopic technique, which can be used to help measure the concentration of coloured species. A large range of species contain chromophores, which absorb light in the UV–Vis range, and the absorbance of these transmissions can be measured by a UV–Vis spectrophotometer.

UV–Vis spectrophotometers typically contain two light sources—one for UV light, and one for visible light. For example, the Agilent Cary 5000 spectrometer used in this work contains a deuterium arc lamp and a tungsten-halogen lamp as the UV and visible light sources respectively.<sup>212</sup> The light from these two sources then passes through a monochromator, which contains an entrance slit, which allows the broad-spectrum white light to hit a holographic grating dispersion device. These are glassy optical components containing extremely narrow ( $10^2$  nm scale) etched grooves, coated with a reflective aluminium surface. Diffraction and interference of the light hitting the grating gives rise to linear angular dispersion of wavelengths, meaning that by tuning the grating, specific wavelengths of light can be directed through an exit slit towards the sample and detector. The sample is contained within a black-coloured box, designed to absorb any stray light. Liquid samples are contained within a cuvette, typically made from quartz, as this allows for excellent transmittance of UV light, however cheaper cuvettes made from plastic and glass can be used but are only recommended when measurements within the visible light region are required. Cuvettes are typically 10 mm in diameter (pathlength = 1 cm), as this allows for easy data manipulation, although long pathlength cuvettes can be used for very dilute solutions. Solid samples can be analysed by attaching them to a holder, which is fixed to the sample compartment. UV–Vis spectrophotometers primarily contain either a photomultiplier tube detector, or a silicon photodiode detector, both of which convert the light received from the exit slit into an electrical signal. The photomultiplier allows for small differences in light intensity to be recorded, by means of amplifying the signal received. The photomultiplier contains a cathode, which when struck by a photon, releases an electron, which in turn is accelerated towards the first of a series of dynodes, whereupon secondary emission occurs, releasing several electrons. Each of these electrons can then be accelerated to the next dynode (and so on), giving rise to a cascade effect, until all the electrons (now far larger in number than the number of photons hitting the cathode) hit the final dynode, whereupon the accumulated charge is transferred to the anode, which converts to the electron signal to an electrical current, used to create the spectrum. Photodiode detectors are more commonly used, as they are more robust and have a greater dynamic range. The detector is made of a  $\text{SiO}_2$  semiconductor, which facilitates electrons flowing through it once in contact with the light. These electrons reduce the charge

in a capacitor, which lies across the material. A battery is used to regularly recharge the capacitor, and the amount of charge required is proportional to light intensity.

The spectrometer first records the UV–Vis spectrum of a background sample (e.g., pure solvent), determining the quantity of light transmitted at each wavelength ( $I_0$ ). The spectrum of a sample is then recorded, and the quantity of light transmitted at each wavelength recorded ( $I_1$ ). Transmittance ( $T$ ) is then defined according to Equation (2-7).

$$T = \frac{I}{I_0} \quad (2-7)$$

Usually, the spectra are plotted in terms of absorbance ( $A$ ), which is defined according to Equation (2-8).

$$A = -\log(T) \quad (2-8)$$

Work by Luther at the start of the 20<sup>th</sup> century combined the 18<sup>th</sup> century observations by Pierre Bouguer and Johann Heinrich Lambert—which showed that light intensity depends on pathlength—with the 19<sup>th</sup> century work by August Beer—which discussed the loss in light intensity when it passed through a coloured medium—in order to develop what is commonly known as the Beer-Lambert law, given in Equation (2-9).<sup>213</sup>

$$A = \epsilon \cdot c \cdot l \quad (2-9)$$

Where  $\epsilon$  is the molar extinction coefficient ( $l \text{ dm}^3 \text{ mol}^{-1} \text{ cm}^{-1}$ ),  $c$  is the concentration ( $l \text{ mol dm}^{-3}$ ), and  $l$  is the pathlength ( $l \text{ cm}$ ). Using cuvettes with a pathlength of 1 cm allows for the removal of the  $l$  term, simplifying the equation. Crucially, it can be seen that absorbance is directly proportional to concentration. As such, by recording the absorbance of a sample when compared to the absorbance of a known concentration, the concentration of the unknown sample can be identified.

#### 2.1.2.4 Inductively Coupled Plasma Optical Emission Spectroscopy

Inductively Coupled Plasma Optical Emission Spectroscopy (ICP-OES) is a spectroscopic method, intended to elucidate which metals are present—and in what concentration—in a sample. It is a technique frequently employed in environmental, geological, pharmaceutical and food safety sciences.<sup>214</sup> ICP-OES offers many advantages as a means to determine elemental composition: it is capable of calculating the concentration of a species at a ppb level; delivers results rapidly; and can be used on a wide range of samples, including aqueous, organic, and inorganic liquids, as well as solids.

ICP-OES works by atomising and ionising the molecules using a plasma. As the excited species relax, photons—known as atomic or ionic emission—are released, and are

received by a detector, which is capable of separating the discrete emission wavelengths. The intensity of each wavelength is proportional to the intensity of that element within the sample.

Samples are first converted into liquid form (solid samples are acid digested), and then pumped into the nebulizer, which converts the sample into fine mist. This ensures that the plasma discharge is capable of desolvating, vaporising, atomising and ionising the sample in a consistent manner. The most common type of nebulizer, and indeed, the type used in this work, is a pneumatic nebulizer, in which argon gas rapidly flows past the sample, which is delivered to the nebulizer via a peristaltic pump, then sucked into a glass tube due to the creation of a low-pressure region. The combination of low-pressure and rapid argon flow breaks down the sample into the aerosol (Figure 2-9).

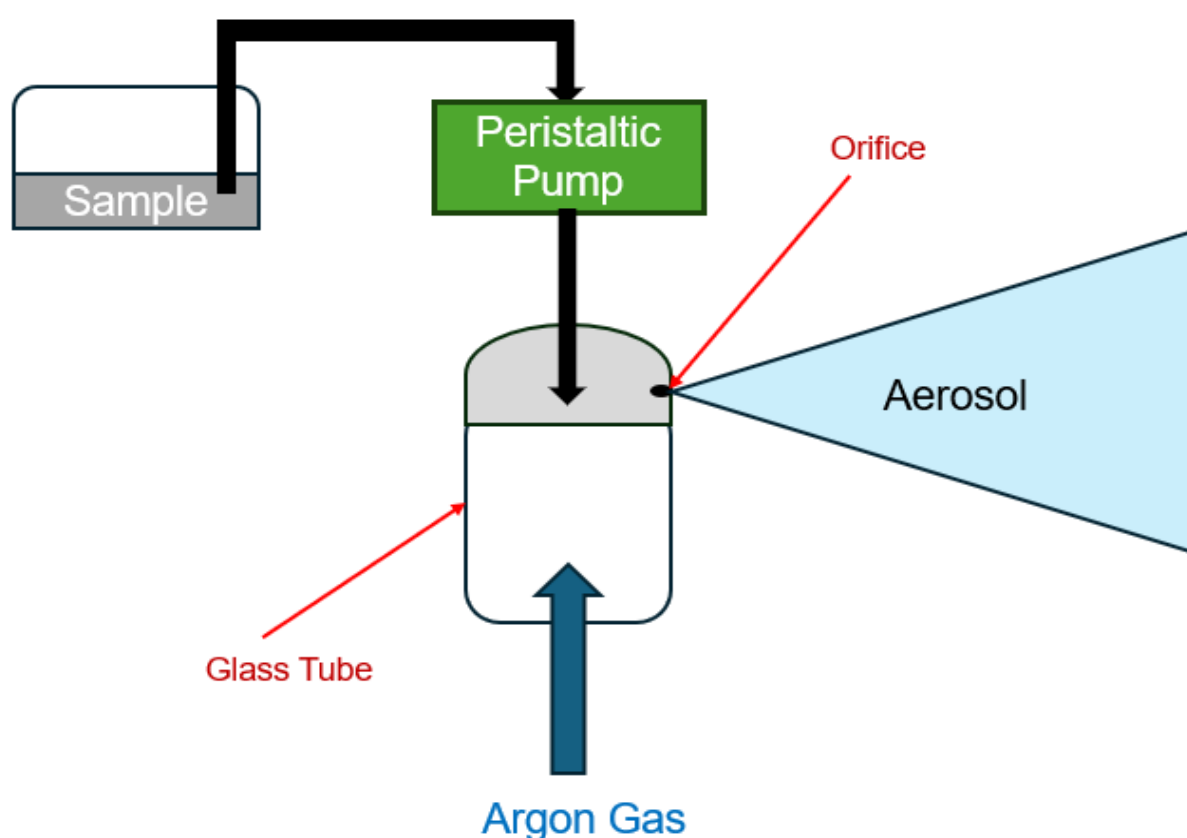


Figure 2-9. Schematic depiction of a pneumatic nebulizer.

The nebulized sample then proceeds into a spray chamber, which is designed to only allow droplets smaller than 10 microns to pass into the plasma (1–5 % of the sample, with the rest drained to waste). In doing so, any pulses generated by the peristaltic pump are smoothed out. Once passed through the chamber, the sample is introduced into the plasma torch by means of a sample injector.

The plasma torch consists of three concentric tubes, through which argon gas flows. The aerosol is supplied in the inner tube, with a tangential flow of argon (auxiliary gas) in a tube concentric to this (Figure 2-10). The argon in the outer tube flows between 7 and 15 L  $\text{min}^{-1}$  and acts as a coolant.<sup>214</sup> A copper coil (load coil) wraps around the end of the torch, and is connected to a RF generator. With argon flowing through the torch, the plasma is ignited, akin to Section 2.1.1.1. The nebulized sample is then swept into the plasma within a stream of argon, whereupon it is ionised. The excited species then relax, and their optical emission can be recorded.

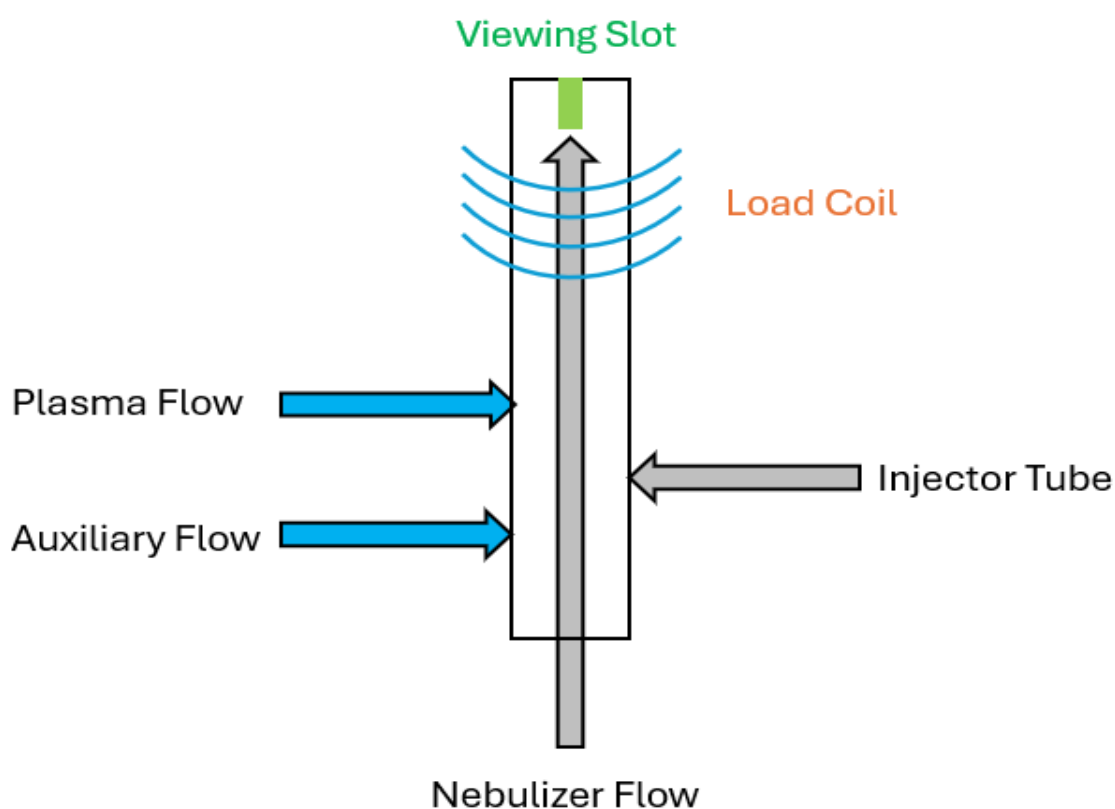


Figure 2-10. Schematic depiction of an ICP-OES plasma torch.

The optical emission of the investigated species is collected by using a convex lens to direct the discharge towards an input slit. In order to determine the emission at each wavelength, individual wavelengths of emission must be sent towards the detector, akin to the UV–Vis spectroscopy discussed in Section 2.1.2.3. Equally similarly, a monochromator can be used, which offers flexibility inasmuch as any particular wavelength can be accessed at any one time.<sup>214</sup> Monochromator based instruments are more suitable for investigations which require complex background corrections. However, consecutively measuring each element means that the machines require a sufficiently large volume of starting sample and exhibit a relative slow sample output rate. Alternatively, the machines can employ polychromators, which utilise several exit slits in order to simultaneously direct multiple wavelengths of light

towards the detector. Consequently, polychromators enable rapid analysis, whereby the whole spectral range can be observed almost within the timeframe of sample introduction.<sup>214</sup> The spectrometer used in this work utilised an Echelle grating and a Charge Coupled Device (CCD) chip detector.

Light passing through an entrance slit is focused onto an Echelle grating (Figure 2-11) by a mirror, which separates the light into its component wavelengths (in a single dimension, Echellogram). Equation (2-10) states the relationship between incident and diffracted light.<sup>215</sup>

$$m\lambda = d(\sin(\alpha) + \sin(\beta)) \quad (2-10)$$

Where  $d$  is the groove spacing (Figure 2-11), and  $m$  is the diffraction order.

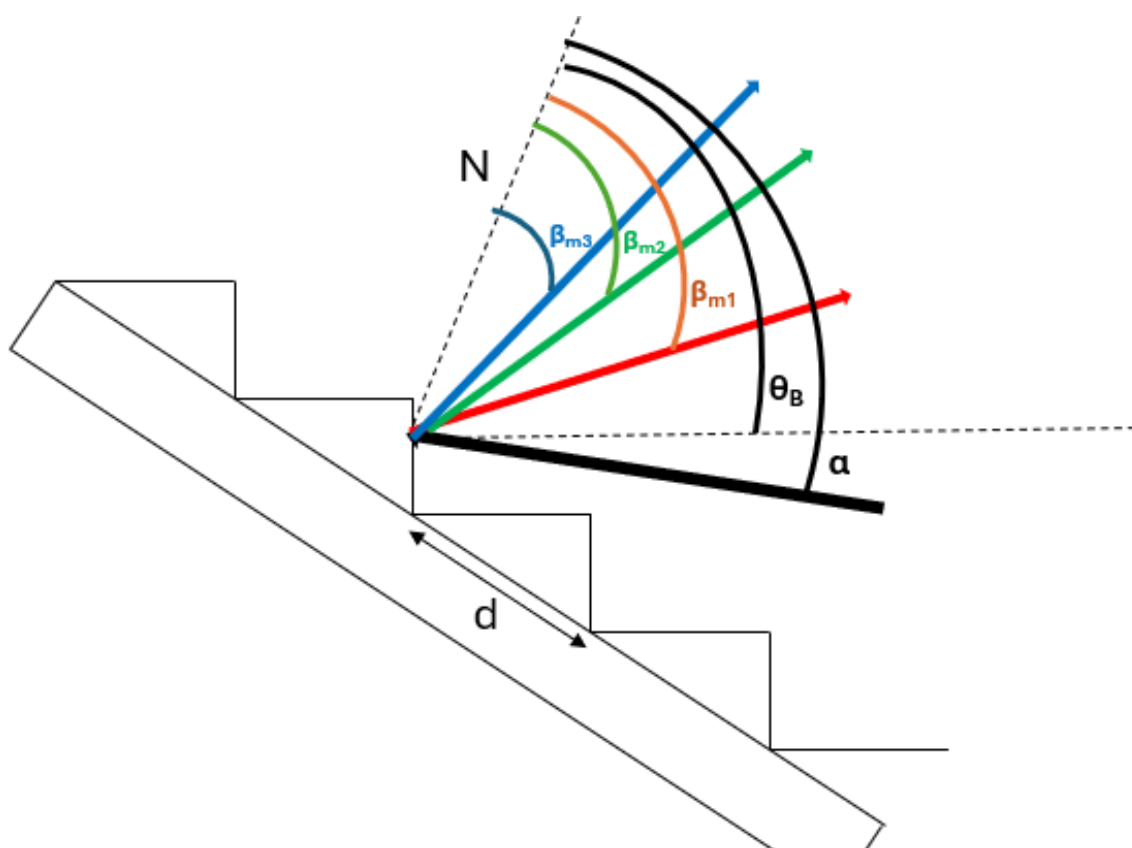


Figure 2-11. Schematic of an Echelle Grating.  $N$  is the grating normal,  $\alpha$  is the angle of incidence,  $d$  is the groove distance,  $\theta_B$  is the blaze angle, and  $\beta_{m1-3}$  are the diffraction angles for order numbers ( $m$ ) 1 through 3.

When  $\alpha + \beta = 2\theta_B$ , the light at the specified wavelength is blazed (maximum diffraction efficiency),<sup>216</sup> and the resolving power ( $R$ ) is defined by Equation (2-11) which shows the resolving power increases with both  $\alpha$  and  $\beta$  ( $0 < \alpha, \beta < \pi/2$ ).

$$R = \frac{\lambda}{\Delta\lambda} = mT = \frac{W}{\lambda} (\sin(\alpha) + \sin(\beta)) \quad (2-11)$$



Where  $T$  is the total number of grooves illuminated on the grating surface, and  $W$  is the illuminated width of the grating. By substituting  $\beta$  with the blazing conditions ( $\alpha + \beta = 2\theta_B$ ), the resolving power at the blazed wavelength ( $\lambda_B$ ) is defined as:

$$R_B = \frac{\lambda_B}{\partial\lambda_B} = \frac{W}{\lambda_B} (\sin(\alpha) + \sin(2\theta_B - \alpha)) \quad (2-12)$$

For which, when  $\alpha = \theta_B$ ,  $R_B$  is at its maximum value, with a resolving power of:

$$R = \frac{2W}{\lambda} \sin(\theta_B) \quad (2-13)$$

Hence, the resolving power at the blazed wavelength depends on the blaze angle of the grating. A common echelle grating exhibits a blaze angle of  $76^\circ$ , with a groove spacing of 79 grooves / mm, while a common grating exhibits groove spacings of 1200 grooves / mm, and a blaze angle of  $22^\circ$ . Assuming that the illuminated width of both gratings is the same, then the echelle grating yields a greater ( $\approx 2.5 \times$  greater) intrinsic resolving power.

Note that, as demonstrated in Figure 2-11, light diffracts in multiple orders. When recording spectra, it is beneficial to attempt to record higher orders, as these also give rise to higher spectral resolution. However, the spectral range becomes very small, as the “red” wavelengths of order  $m$  will overlap with the “blue” wavelengths of order  $m+1$ . This means that in one-dimension, a given pixel on a detector will receive light from several orders of different wavelengths. To overcome this issue, the Echellogram is reflected by a mirror through a “cross disperser”, which is a prism, mounted such that the dispersion direction is perpendicular to the grating. This results in light being diffracted into a second dimension, and hence different orders are offset. As such, the high spectral resolution of the Echelle grating is combined with a large wavelength coverage.

This light is then reflected towards the CCD detector, which is a highly sensitive photon detector. It is a 2D array, divided up into a large number (potentially over one million<sup>217</sup>) of light-sensitive segments (pixels).<sup>218</sup> The chip is sufficiently large that the entire light spectrum can be recorded, while the large pixel number (high resolution) enables excellent wavelength separation, and hence minimises spectral interference.

Within the software built into the spectrometers, optical emission spectra of all possible-to-identify elements are recorded. It is therefore possible to run a spectrum of the sample and allow the software to assign the observed emissions their respective elements. Although the intensity of light observed does provide information on the quantity of each element within the sample, each spectrometer will differ slightly from the next, meaning that the exact concentration cannot be determined. These wide-field scans are therefore useful at

determining which elements are in solution, but should only be used to determine the order of magnitude of elemental composition.

In order to determine an exact concentration of a specific element, known concentrations of the investigated element (made from an ICP stock solution) should be made up, covering the expected concentration range of the element within the sample. A calibration curve between emission intensity and concentration can then be created, and the emission intensity from the sample fit to this curve, enabling an exact concentration to be determined.

### **2.1.3 Filtration Techniques**

Throughout this work, there were two types of filtration employed: 1) Dynamic filtration, in which contaminated water samples permeate through the functionalised cloths, and the contaminants are removed as they pass through; and 2) Static filtration, in which the functionalised cloths are left to shake in a contaminated water solution for an extended period of time.

Following attempted filtration, the extraction percentage (also known as filtration efficiency) of the system towards the investigated contaminant is determined by measuring the concentration of the contaminated solution before ( $C_0$ ) and after ( $C_1$ ) filtration (either by UV-Vis, Section 2.1.2.3, or ICP-OES, Section 2.1.2.4), and performing the calculation in Equation (2-14).

$$\text{Extraction Percentage} = \frac{C_0 - C_1}{C_0} \times 100 \% \quad (2-14)$$

#### **2.1.3.1 Dynamic Filtration**

Dynamic filtration (Figure 2-12) is carried out by cutting a piece of adsorbent into 30 mm x 35 mm sections and compacting a piece into a glass Pasteur pipette (Fisherbrand, 15 cm length, inner diameter 5.6 mm, Fisher Scientific UK Ltd.). 5 mL water samples, spiked with the contaminant of choice are then passed through the pipette in the absence of any externally applied pressure, before the filtrate is collected, and the remaining concentration of contaminant is measured in order to determine extraction percentage. Dynamic filtration best fulfils the requirements for point-of-use water purification, as the setup only requires simple equipment, while the filtrate is obtained comparatively quickly, meaning that drinking water can be obtained in a faster time-period.

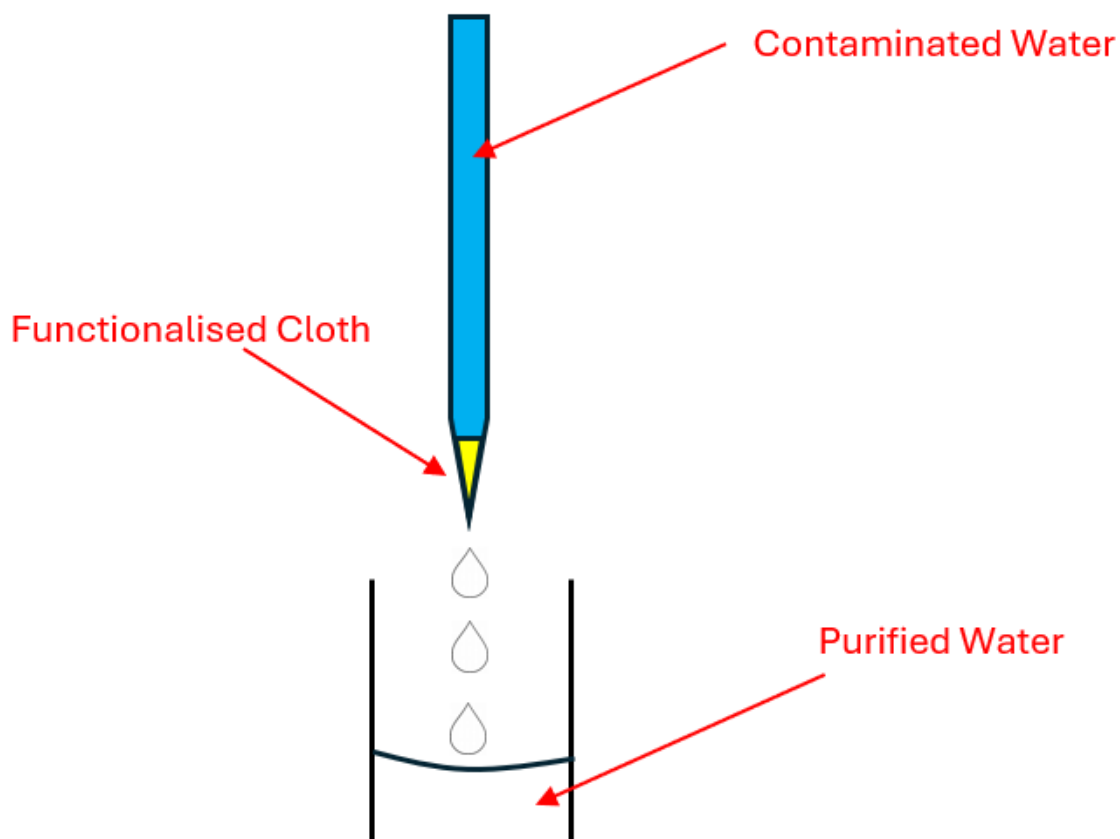


Figure 2-12. Schematic depiction of dynamic filtration.

### 2.1.3.2 Static Filtration

Static (also known as batch) filtration is performed by inserting a 30 mm x 35 mm piece of adsorbent into a vial, adding 5 mL contaminated water solution, sealing the vial, and leaving it to spin at 40 rpm (using a Fisherbrand™ mini-rotator) for an extended period of time. Static filtration best fulfils the requirements of point-of-release water filtration, where the companies who produce the wastewater are more capable of purchasing the equipment required to purify batches of wastewater. Additionally, wastewater at point-of-release will contain a higher concentration of contaminant than downstream, and so the greater adsorption capacities associated with static filtration, attributed to the greater contact time between the contaminant and adsorbent, is a key advantage.

Furthermore, static filtration is required in order to determine various attributes of the adsorption.

#### 2.1.3.2.1 Maximum Adsorption Capacity

Maximum adsorption capacities are determined by performing static filtration of the contaminated solutions at elevated contaminant concentrations. Owing to the limitations of the UV–Vis spectrometer, the highest concentrations of dye and Cr(VI) possible to investigate

were 100 mg L<sup>-1</sup> and 75 mg L<sup>-1</sup> respectively. The highest concentration of U(VI) investigated was impacted by the availability of uranium, and so was also limited to 100 mg L<sup>-1</sup>.

The concentration of dye before and after filtration was measured, and the difference in concentration before and after filtration was converted into mass of dye according to Equation (2-15) Dividing this value by the mass of cloth (Equation 2-16) yields the adsorption capacity.

$$\text{Mass of Dye} = (\Delta c) \times \frac{V}{1000} \quad (2-15)$$

Where  $\Delta c$  = (concentration of dye in starting solution – concentration of dye in filtrate) / mg L<sup>-1</sup>; and  $V$  = volume of dye solution / mL.

$$Q_0 = \text{Mass of Dye} \div \text{Mass of Adsorbent} \quad (2-16)$$

Where  $Q_0$  = maximum adsorption capacity / mg<sub>Dye</sub>g<sub>Adsorbent</sub><sup>-1</sup>

#### 2.1.3.2.2 Isotherm Determination

Adsorption parameters can be estimated by determining whether the observed adsorption follows a Langmuir or Freundlich isotherm.<sup>219</sup> This is performed by recording the adsorption capacity at equilibrium ( $Q_e$  / mg L<sup>-1</sup>) of the system towards contaminated solutions at a range of concentrations, while simultaneously recording the concentration of contaminant remaining in solution at equilibrium ( $C_e$  / mg L<sup>-1</sup>). The non-linear forms of the isotherms are generated by plotting  $Q_e$  against  $C_e$  and fitting the observed data to a modelled fit (Equations (2-17) and (2-19)). The linear Langmuir isotherm is generated by plotting  $C_e/Q_e$  against  $C_e$  (Equation 2-18) while the linear Freundlich isotherm is generated by plotting  $\text{Log}(Q_e)$  against  $\text{Log}(C_e)$  (Equation 2-20).

$$\text{Non-Linear Langmuir:} \quad Q_e = \frac{Q_0 K_L C_e}{1 + K_L C_e} \quad (2-17)$$

$$\text{Linear Langmuir:} \quad \frac{C_e}{Q_e} = \frac{C_e}{Q_0} + \frac{1}{Q_0 K_L} \quad (2-18)$$

$$\text{Non-Linear Freundlich:} \quad Q_e = K_F C_e^{\frac{1}{n}} \quad (2-19)$$

$$\text{Linear Freundlich:} \quad \text{Log}(Q_e) = \text{Log}(K_F) + \frac{\text{Log}(C_e)}{n} \quad (2-20)$$

Where  $Q_0$  = maximum adsorption capacity / mg<sub>Contaminant</sub>g<sub>Adsorbent</sub><sup>-1</sup>;  $K_L$  = Langmuir constant / L<sub>Solution</sub> mg<sub>Adsorbent</sub><sup>-1</sup>; and  $K_F$  and  $n$  are Freundlich constants, known as the distribution coefficient / L<sub>Solution</sub>g<sub>Adsorbent</sub><sup>-1</sup> and the correction factor respectively. Once the correct isotherm has been determined, the values of the constants can be determined for the non-linear plots after fitting the raw data to the non-linear models, as this allows for  $Q_0$  and  $K_L$ , and  $n$  and  $K_F$  to be extracted as constants. For linear plots, the parameters can be estimated from the

gradient ( $Q_0$  and  $n$  for Langmuir and Freundlich respectively) and the intercept ( $K_L$  and  $K_F$  for Langmuir and Freundlich respectively).

Where experimental values for maximum adsorption capacity are obtainable, the parameter  $\theta$  can be calculated according to Equation (2-21):

$$\theta = \frac{\text{Amount of Contaminant Extracted}}{\text{Maximum Adsorption Capacity}} \quad (2-21)$$

This is relevant in the instances of Langmuir adsorption, as the general equation used to describe Langmuir adsorption of gas onto a solid is described by Equation (2-22).<sup>220</sup>

$$\theta = \frac{Kp_A}{1 + Kp_A} \quad (2-22)$$

Where  $K$  is the equilibrium constant, and  $p_A$  is the partial pressure of the gas.

Langmuir adsorptions can also be employed for liquids when the adsorbent is capable of being saturated by a monolayer.<sup>221</sup> Consequently, the equation can be adjusted by converting from pressure to concentration ( $C$ ) (Equation 2-23):

$$\theta = \frac{KC}{1 + KC} \quad (2-23)$$

Consequently, Equation (2-23) demonstrates that a typical adsorption curve will be proportional to concentration at low concentrations (where  $1 + KC \approx 1$ ), before plateauing out at  $\theta$  at high concentrations (where  $1 + KC \approx KC$ ).

Given that Freundlich adsorption (Equation 2-19) follows a  $y = x^{1/n}$  curve, it should be noted that plotting a concentration vs adsorption graph would also give a similar shaped curve for values of  $n > 1$ , with an apparent linear relationship at low concentrations, before forming a convex curve. When  $n < 1$ , the isotherm will form a concave curve, while at  $n = 0$ , adsorption is irreversible.

#### 2.1.3.2.3 Kinetic Modelling

Kinetic modelling of dye and chromium extraction are performed by leaving a vial (containing adsorbent and contaminated water) to spin, then after a designated time, switching off the rotator, lifting the cloth out of solution and stopping the timer. Approximately 3 mL of filtrate is then extracted, and the concentration of contaminant remaining recorded. The filtrate is then returned to the vial, and the cloth moved back into the liquid. The mini-rotator and the stopwatch are then restarted. The observed data can then be plotted using pseudo-first order

and pseudo-second order models in their linear or non-linear forms according to Equations (2-24–27) (Table 2-1).

Table 2-1. Equations and measurements required for determining whether a reaction proceeds via pseudo-first order or pseudo-second order kinetics.  $Q_e$  = concentration of adsorbent adsorbed at equilibrium ( $\text{mg g}^{-1}$ ),  $Q_t$  = concentration of dye adsorbed at time  $t$ ,  $k_1$  and  $k_2$  are pseudo-first and pseudo-second order constants respectively. Linear/non-linear denotations refer to the shape of the graph when plotting the data – non-linear plots are curved, with an asymptote at  $Q_e$ , whereas linear plots are linear, passing through the origin.

Kinetic model	Equation <sup>222</sup>	Measurements required	Equation
Pseudo-first order (non-linear)	$Q_t = Q_e(1 - e^{-k_1 t})$	Plot $Q_t$ against $t$	(2-24)
Pseudo-second order (non-linear)	$Q_t = \frac{Q_e^2 k_2 t}{1 + Q_e k_2 t}$	Plot $Q_t$ against $t$	(2-25)
Pseudo-first order (linear)	$\log(Q_e - Q_t) = \log(Q_e) - \frac{k_1}{2.303} t$	Plot $\log(Q_e - Q_t)$ against $t$	(2-26)
Pseudo-second order (linear)	$\frac{t}{Q_t} = \frac{1}{Q_e^2 k_2} + \frac{t}{Q_e}$	Plot $t/Q_t$ against $t$	(2-27)

## 2.2 References

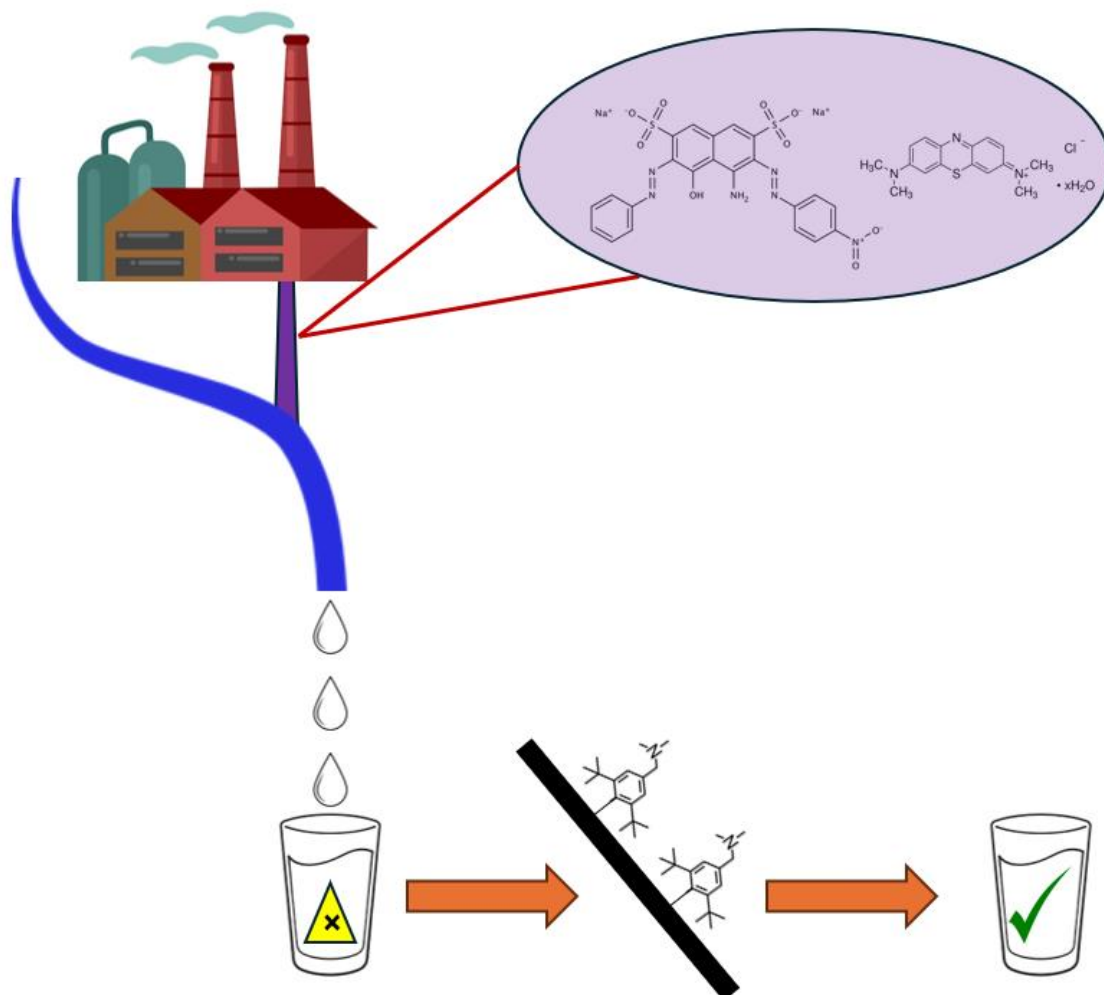
- 176 Eliezer, S.; Eliezer, Y. *The Fourth State of Matter: An Introduction to Plasma Science*, 2<sup>nd</sup> ed.; Institute of Physics Publishing: London, England, 2001
- 177 Langmuir, I. Oscillations in Ionized Gases. *Proceedings of the National Academy of Sciences*. **1928**, *14*, 627–637
- 178 d'Agostino, R., Ed. *Plasma Deposition, Treatment, and Etching of Polymers*; Academic Press, Inc.: London, U.K., 1990
- 179 Yasuda, H. Glow Discharge Polymerisation. *Journal of Polymer Science: Macromolecular Reviews*. **1981**, *16*, 199–293
- 180 Bogaerts, A. The Glow Discharge: An Exciting Plasma! *Journal of Analytical Atomic Spectrometry*. **1999**, *14*, 1375–1384
- 181 Yasuda, H. Plasma Polymerisation and Plasma Modification of Polymer Surfaces. In *New Methods of Polymer Synthesis*; Ebdon, J.R., Eastmond, G.C., Ed.; Springer: Dordrecht, 1995; pp 161–196
- 182 Friedrich, J. Mechanisms of Plasma Polymerization—Reviewed from a Chemical Point of View. *Plasma Processes and Polymers*. **2011**, *8*, 783–802
- 183 Li, L.; Dai, X.J.; Xu, H.S.; Zhao, J.H.; Yang, P.; Maurdev, G.; du Plessis, J.; Lamb, P.R.; Fox, B.L.; Michalski, W.P. Combined Continuous Wave and Pulsed Plasma Modes: For More Stable Interfaces with Higher Functionality on Metal and Semiconductor Surfaces. *Plasma Processes and Polymers*. **2009**, *6*, 615–619
- 184 Zhang, Z.; Chen, Q.; Knoll, W.; Förch, R. Effect of Aqueous Solution on Functional Plasma Polymerized Films. *Surface and Coatings Technology*. **2003**, *174*, 588–590
- 185 Pelletier, J. Distributed ECR Plasma Sources. In *High Density Plasma Sources*; Popov, O. A., Ed.; Noyes Publications: Park Ridge, New Jersey, 1995; pp 380–425
- 186 Carletto, A.; Badyal, J.P.S. Ultra-high Selectivity Pulsed Plasmachemical Deposition Reaction Pathways. *Physical Chemistry Chemical Physics*. **2019**, *21*, 16468–16476
- 187 Mackie, N.M.; Bryant, P.M.; Steele, D.A.; Vasilev, K.; Bradley, J.W.; Short, R.D. Role of Positive Ions in Determining the Deposition Rate and Film Chemistry of Continuous Wave Hexamethyl Disiloxane Plasmas. *Langmuir*. **2011**, *27*, 11943–11950
- 188 Wang, J. H. Surface Preparation Techniques for Biomedical Applications. In *Coatings for Biomedical Applications*; Driver, M., Ed.; Woodhead Publishing Limited, 2012; pp. 143–175
- 189 Levchenko, I.; Xu, S.; Baranov, O.; Bazaka, O.; Ivanova, E.; Bazaka, K. Plasma and Polymers: Recent Progress and Trends. *Molecules*. **2021**, *26*, 4091
- 190 Jiao, Y.; Xu, J.; Zhou, C. Effect of Ammonia Plasma Treatment on the Properties and Cytocompatibility of a Poly(L-Lactic Acid) Film Surface. *Journal of Biomaterial Science, Polymer Edition*. **2012**, *23*, 763–777
- 191 Resnik, M.; Zaplotnik, R.; Mozetic, M.; Vesel, A. Comparison of SF<sub>6</sub> and CF<sub>4</sub> Plasma Treatment for Surface Hydrophobization of PET Polymer. *Materials*. **2018**, *11*, 311
- 192 Bos, G.W.; Scharenborg, N.M.; Poot, A.A.; Engbers, G.H.M.; Terlingen, J.G.A.; Beugeling, T.; Van Aken, W.G.; Feijen, J. Adherence and Proliferation of Endothelial Cells on Surface-Immobilized Albumin-Heparin Conjugate. *Tissue Engineering*. **1997**, *4*, 267–279
- 193 Edwards High Vacuum International, Instruction Manual – Rotary Vacuum Pumps E2M2, E1/E2M5 and 8, E2M12. Issue H.
- 194 LibreTexts. Thermocouples. [https://eng.libretexts.org/Workbench/Materials\\_Science\\_for\\_Electrical\\_Engineering/03%3A\\_Electrical\\_Properties/3.06%3A\\_Electronic\\_Properties/3.6.07%3A\\_Thermocouples#:~:text=A%20thermo](https://eng.libretexts.org/Workbench/Materials_Science_for_Electrical_Engineering/03%3A_Electrical_Properties/3.06%3A_Electronic_Properties/3.6.07%3A_Thermocouples#:~:text=A%20thermo)

- couple%20is%20a%20device%2C%20joined%20together%20from,thermocouple%20is%20not%20an%20absolute%20temperature%20measuring%20device. (Accessed 19<sup>th</sup> May 2023)
- 195 Active Thermocouple Gauges. <https://pdf.directindustry.com/pdf/edwards/active-thermocouple-gauges-datasheet/7014-273859.html>. (Accessed 19<sup>th</sup> May 2023)
- 196 Edwards Vacuum. LV10K Fine Control Leak Valve: Instruction Manual: <http://shop.edwardsvacuum.com/products/C37102000/view.aspx> (Accessed 19<sup>th</sup> May 2023)
- 197 Bieber, V.; Ozcelik, E.; Cox, H.; Ottley, C.; Ratan, J.; Karaman, M.; Tabakci, M.; Beaumont, S.; Badyal, J.P. Capture and Release Recyclable Dimethylaminomethyl-Calixarene Functional Cloths for Point-of-Use Removal of Highly Toxic Chromium Water Pollutants. *ACS Applied Materials and Interfaces*. **2020**, *12*, 52136–52145
- 198 Smith, B. C. *Fundamentals of Fourier Transform Infrared Spectroscopy*, 2<sup>nd</sup> Ed.; CRC Press: Boca Raton, FL, 2011
- 199 Spragg, R.A. IR Spectrometers. In *Encyclopedia of Spectroscopy and Spectrometry*; Elsevier, 2017, pp. 1048–1057
- 200 Subramanian, A.; Rodriguez-Saona, L. Fourier Transform Infrared (FTIR) Spectroscopy. In *Infrared Spectroscopy for Food Quality Analysis and Control*; Sun, D.-W., Ed.; 2009; pp 145–178
- 201 Hinrichs, K. Reflection Absorption IR Spectroscopy (RAIRS). In *Surface and Thin Film Analysis: A Compendium of Principles, Instruments, and Applications*, 2<sup>nd</sup> Ed.; Friedbacher, G., Bubert, H., Eds.; Wiley-VCH Verlag: Weinheim, 2011, pp. 367–375
- 202 Hayden, B.E. *Vibrational Spectroscopy of Molecules on Surfaces*; Plenum Press, New York, London, 1987, pp. 267–344
- 203 Edmund Optics. Introduction to Polarization. <https://www.edmundoptics.eu/knowledge-center/application-notes/optics/introduction-to-polarization>. (Accessed 22<sup>nd</sup> May 2023)
- 204 Greenler, R.G. Infrared Study of Adsorbed Molecules on Metal Surfaces by Reflection Techniques. *J.Chem. Phys.* **1966**, *44*, 310–315
- 205 Hollins, P. Infrared Reflection-Absorption Spectroscopy. In *Encyclopedia of Analytical Chemistry (Applications, Theory and Instrumentation)*; Meyers, R.A., Ed. John Wiley & Sons, Ltd. 2007, pp. 1–17
- 206 Hamilton, M. Applications of Grazing-Angle Reflection Absorption Fourier Transform Infrared Spectroscopy to the Analysis of Surface Contamination. PhD Thesis, University of Canterbury, 2017. [http://www.remspec.com/Papers/Thesis\\_mlh.pdf](http://www.remspec.com/Papers/Thesis_mlh.pdf) (Accessed 22<sup>nd</sup> May 2023)
- 207 Sun, Q.Y.; de Smet, L.; van Lagen, B.; Giesbers, M.; Thune, P.C.; van Engelenburg, J.; de Wolf, F.; Zuilhof, H.; Sudholter, E. Covalently Attached Monolayers on Crystalline Hydrogen-Terminated Silicon: Extremely Mild Attachment by Visible Light. *J. Am. Chem. Soc.* **2005**, *127*, 8, 2514–2523
- 208 Milosevic, M. On the Nature of the Evanescent Wave. *Applied Spectroscopy*. **2013**, *67*, 126–131
- 209 Larkin, P. Instruments and Sampling Methods. In *Infrared and Raman Spectroscopy. Principles and Spectral Interpretation*. Elsevier, 2011, pp. 29–61
- 210 Shrivastava, A. Plastic Properties and Testing. In *Introduction to Plastic Engineering*. 2<sup>nd</sup> Ed., Elsevier, 2018, pp. 49–110
- 211 Lovering, D. NKD-6000 Technical Manual; Aquila Instruments: Cambridge, U.K., 1998.
- 212 Agilent. The Basics of UV-Vis Spectrophotometry. <https://www.agilent.com/cs/library/primers/public/primer-uv-vis-basics-5980-1397en-agilent.pdf> (Accessed 25<sup>th</sup> May 2023)
- 213 Mayerhöfer, T.G.; Pahlow, S.; Popp, J. The Bouguer-Beer-Lambert Law: Shining Light on the Obscure. *ChemPhysChem*. **2020**, *21*, 2029–2046
- 214 Khan, S.R.; Sharma, B.; Chawla, P.A.; Bhatia, R. Inductively Coupled Plasma Optical Emission Spectrometry (ICP-OES): a Powerful Analytical Technique for Elemental Analysis. *Food Analytical Methods*. **2022**, *15*, 666–688



- 215 Becker-Ross, H.; Florek, S.V. Echelle spectrometers and charge-coupled devices. *Spectrochimica Acta Part B*. **1997**, *52*, 1367–1375
- 216 Zhang, Y.; Li, W.; Duan, W.; Huang, Z.; Yang, H. Echelle Grating Spectroscopic Technology for High-Resolution and Broadband Spectral Measurement. *Applied Sciences*. **2022**, *12*, 11042
- 217 Shimadzu Inductively Coupled Plasma Atomic Emission Spectroscopy (ICP-AES) (<https://www.ssi.shimadzu.com/industries/environment/icp-aes/index.html>) (Accessed 27<sup>th</sup> May 2024)
- 218 What is a CCD Detector? <https://www.horiba.com/aut/scientific/technologies/detectors/what-is-a-ccd-detector/> (Accessed 27<sup>th</sup> May 2024)
- 219 Ayawei, N.; Ebelegi, A.N.; Wankasi, D. Modelling and Interpretation of Adsorption Isotherms. *Journal of Chemistry*. **2017**, *2017*, 3039817
- 220 Langmuir, I. The Adsorption of Gases on Plane Surface of Glass, Mica and Platinum. *Journal of the American Chemical Society*. **1918**, *40*, 1361–1402
- 221 Islam, A.; Chowdhury, M.A. Mozumder, S.I.; Uddin, T. Langmuir Adsorption Kinetics in Liquid Media: Interface Reaction Model. *ACS Omega*. **2021**, *6*, 14481–14492
- 222 Ho, Y.S.; Mckay, G. Kinetic Models for the Sorption of Dye from Aqueous Solution by Wood. *Process Safety and Environmental Protection*. **1998**, *76*, 183–191

### 3 CHAPTER 3 – SIMULTANEOUS AND SELECTIVE EXTRACTION OF HARMFUL ANIONIC AND CATIONIC DYES FROM WATER SOLUTION BY DIMETHYLAMINO-PHENOL FUNCTIONAL CLOTHS



#### 3.1 Introduction

Dyeing is a vast global industry, with an expected value of \$16.08 billion by 2030. The vast majority of this market (62 %) lies in textile dyeing, though due to the growing digital ink sector, the printing ink segment is estimated to incur the fastest Compound Annual Growth Rate (CAGR) growth.<sup>223</sup> Owing to strict regulation in North America and Europe, the greatest market for dye production occurs in the Asia Pacific region, which accounts for 63 % of the global revenue share in 2022, centred predominantly around China and India (Figure 3-1). However,

the lack of regulation and insufficient treatment of dye wastewater in these countries has resulted in significant environmental harm and threats to human health.

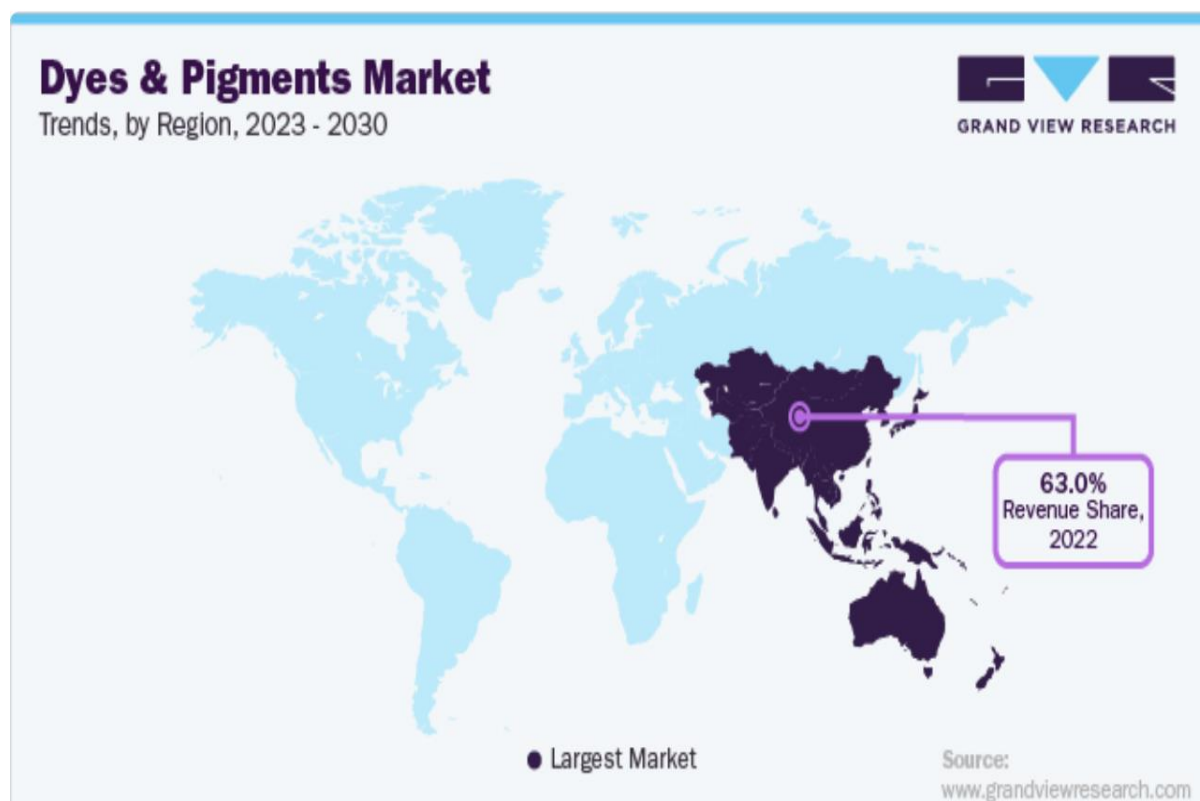


Figure 3-1. Largest market for dyes and pigments, according to revenue share. Taken from reference 223.

Between 7000 and 105,000 tonnes of dye is released into the environment via wastewater each year, which is equivalent to 4900–73,500 tonnes of azo dyes.<sup>224,225,226,227,228</sup> These dyes, such as Amido Black 10B (AB10B; anionic, acid dye), are carcinogenic, mutagenic, and teratogenic, meaning that their removal from drinking water should be considered as a high priority in order to minimise their harm to human health.

There have been a couple of examples of treatment systems which degrade AB10B in solution, in which the azo linkage is broken, yielding a safer, decoloured final product.<sup>229,230</sup> However, these methods can only be used once, and require the use of chemicals which may not be suitable for human consumption, and so it is far more common for systems to adsorb AB10B from solution, which can then be desorbed via extraction with NaOH.<sup>231,232,233,234,235,236,237,238</sup>

Calixarenes are commonly employed as adsorbents, on account of their ability to exhibit host-guest interactions to selectively bind to target molecules, with the host held within the calix of the molecule.<sup>239</sup> Consequently, calixarenes have been frequently employed as

drug-carriers,<sup>240</sup> catalysts,<sup>241</sup> biological mimics,<sup>242</sup> and most pertinently, contaminant extractors.<sup>243,244,245,246</sup> While there are many accounts of substrates being adorned with calixarenes in order to remove the aromatic dyes Congo Red (CR; anionic, acid dye) and Methylene Blue (MB; cationic, basic dye) from solution (Appendix Table 1), only a range of calixarene nanosponges—containing a mixture of solid polymers which yielded a maximum extraction of 97 % AB10B from a 2 mL, 50  $\mu$ M solution, using 4 mg adsorbent (equivalent to an adsorption capacity of  $1.49 \text{ mg}_{\text{AB10B}}\text{g}_{\text{Adsorbent}}^{-1}$ )—have been reported as AB10B adsorbents.<sup>247,248</sup> Instead, a multitude of other adsorbents have been employed to extract AB10B from solution, with a greatest adsorption capacity of  $2647.3 \text{ mg}_{\text{AB10B}}\text{g}_{\text{Adsorbent}}^{-1}$  (Appendix Table 2).<sup>249</sup>

Despite the high adsorption capacities observed, the extraction methods employed are typically static batch adsorption, which lasts several hours, and then requires subsequent filtration of the adsorbent before the reaction can be proceeded.<sup>249</sup> Furthermore, these sorption methods are more suitable for point-of-release decontamination, which can be expensive, and so are often not employed by industries in countries where regulation is sparse or ineffective. Furthermore, the fabrication process for these adsorbents requires the use of non-environmentally friendly solvents—which must be subsequently disposed of—for each synthetic step, and/or utilise a specific substrate, which cannot be interchanged.

Within this work, pieces of cloth functionalised with 5,11,17,23-tetrakis[(dimethylamino)methyl]-25,26,27,28-tetrahydroxycalix[4]arene (DMAM-calixarene), and its phenol analogue, 2,6-di-*tert*-butyl-4-(dimethylaminomethyl)phenol (DMAM-phenol), have been fabricated for the purpose of point-of-use water purification. A range of substrates have been coated with poly(4-vinylbenzyl chloride, 4-VBC) by means of pulsed plasmachemical deposition in order to introduce chloride functionalities, which undergo subsequent nucleophilic substitution with the hydroxyl groups on the lower rim of DMAM-calixarene/phenol (Figure 3-2).<sup>250,251</sup> DMAM-calixarene was selected, owing to its previously demonstrated extraction of alternative contaminants,<sup>245,251</sup> while the cloths chosen as substrates for the point-of-use study (nonwoven polyurethane and nonwoven polyethylene terephthalate/ polypropylene (PET/PP) are cheap, commonly available, more resistant to fungal growth than natural materials (e.g., cotton, biowaste),<sup>252</sup> and can be packed into narrow cartridges such that contaminated water cannot avoid the functionalised surface.

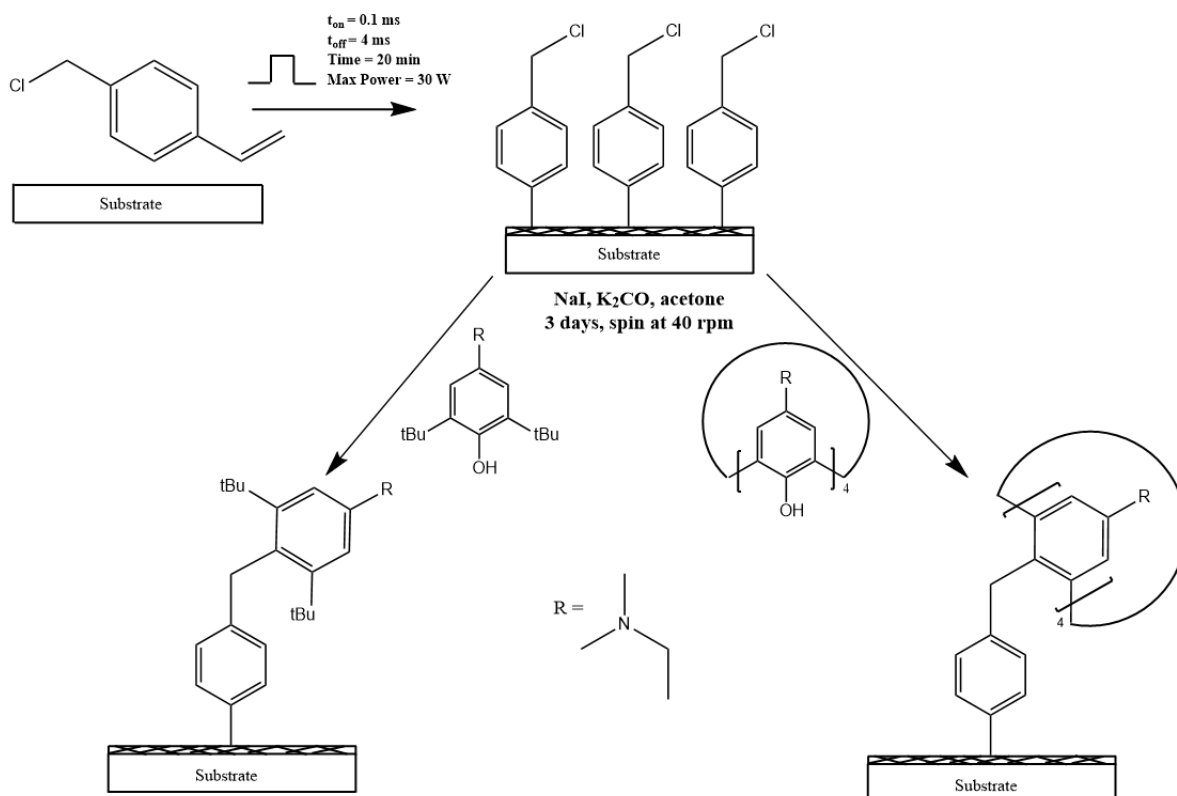


Figure 3-2. Deposition of pulsed plasma poly(4-vinylbenzyl chloride) onto a cloth substrate, followed by functionalisation via nucleophilic substitution with either DMAM-calixarene or DMAM-phenol.

The use of plasmachemical deposition in order to incorporate the chloride functionality onto the substrates addresses two of the aforementioned drawbacks in the previously reported literature. Namely, that this process is substrate independent, and so adsorbents can be fabricated from any accessible porous cloth; while simultaneously no solvents are required for the first stage of the reaction, reducing potentially harmful chemical waste.<sup>253,254</sup> Furthermore, the use of pulsed plasma, combined with a short reaction time, means that this process can be considered to be comparatively low energy. To the best of this author's knowledge, this research is the first to propose the use of pulsed plasmas in order to fabricate an adsorbent designed to extract dye from solution. Furthermore, the adsorbent is designed to be employed at point-of-use, which allows for a cheaper and more targeted approach than systems designed to decontaminate water at point-of-release. The filtration procedure is simple, requiring almost no expertise, meaning that water can be easily purified by consumers without the need for specialised training, which can be time-consuming and challenging to organise.

Following dynamic filtration of an AB10B solution with both DMAM-phenol and DMAM-calixarene functionalised cloths, fast and efficient removal of AB10B is observed. Complete removal of dye at concentrations anticipated at point of use has been demonstrated (concentrations of dye found in dye house effluents range from 10 to 250 mg L<sup>-1</sup>; however,

given that water at point-of-use will be downstream of the dye-houses, it is expected that the dye concentrations will be significantly diluted).<sup>255,256,257</sup> Furthermore, the cloths (especially DMAM-phenol functionalised) also exhibit excellent selectivity, recyclability, and extraction capabilities towards a simulated real-world AB10B contaminated water sample.

## 3.2 Experimental

### 3.2.1 Preparation of Functionalised Cloths

The substrates used for the plasmachemical deposition were: a non-woven polyurethane cloth (TPU; meltblown 35 GSM, M35A1YMO, Don & Low Ltd., 12 cm x 8 cm); a non-woven polyethylene terephthalate/polypropylene blended cloth (PET/PP; thermal bonded, 23 GSM, SBCPPT+23, Warren nonwovens Ltd., 12 cm x 8 cm); and an activated carbon cloth (prepared through pyrolysis of a cotton cloth). The substrates were prepared, the plasma chamber cleaned, and plasmachemical deposition performed using 4-VBC (+ 90 %, 10403053, Fisher Scientific UK Ltd.) as the monomer as described in 2.1.1.1.1. Pulsed plasma deposition was performed using a duty cycle on-period of 100  $\mu$ s and a duty cycle off-period of 4 ms in conjunction with a peak power of 30 W, with the total time for deposition of 20 min.

Following deposition of pulsed plasma poly(4-VBC) onto the first side of the substrate, the cloth was inverted, and placed into a new, clean, chamber, and the process was repeated. Following the second deposition, the non-woven cloths were cut into two 60 mm x 70 mm pieces, leaving a 120 mm x 10 mm strip for characterisation. The coated activated carbon cloth was cut into a 30 mm x 10 mm piece, leaving a 10 mm x 10 mm piece for characterisation.

Each coated cloth piece was placed into separate glass vials (28 mL volume, Fisherbrand™) containing 0.152 g (4 mM)  $K_2CO_3$  (+ 99.0 %, Sigma Aldrich Ltd.) before addition of an acetone (+ 99.8 %, Fisher Scientific UK Ltd.) solution containing 8 mM NaI (+ 99.5 %, Honeywell Fluka™, Fisher Scientific UK Ltd.) and one of: 0.4 mM 5,11,17,23-tetra-tert-butyl-25,26,27,28-tetrahydroxycalix[4]arene (tBu-calixarene; + 99 %, Acros Organics B.V.B.A.), 0.4 mM DMAM-calixarene (Konya Technical University, synthesised according to previous literature<sup>245,246</sup>); 1.6 mM DMAM-phenol (Tokyo Chemical Industry UK Ltd.); or 1.6 mM phenol (BDH Chemicals Ltd.). The vials were sealed and left to spin at 40 rpm for ca. 70 h, before subsequent washing in acetone (15 min), air dried, and finally washed in high-purity (HP) water (15 min) and air dried.

### 3.2.2 Characterisation

The thickness of the pulsed plasma poly(4-VBC) coated silicon wafers was recorded using a spectrophotometer (NKD-6000, Aquila Instruments Ltd.). Transmittance–reflectance curves (350–1000 nm wavelength) were acquired using a parallel p-polarised light source at a 30°

incident angle to the substrate. These curves were fitted to a Cauchy model for dielectric materials using a modified Levenberg–Marquardt algorithm (version 2.2 Pro-Optix software, Aquila Instruments Ltd.).<sup>258,259</sup>

Fourier Transform Infrared (FTIR) spectra were acquired as described in Section 2.1.2.1.6.

Concentrations of all initial dye solutions and dye-containing filtrates were measured using a UV–Vis–NIR spectrophotometer (Cary 5000, Agilent Technologies Inc.) in conjunction with a quartz cell (10 mm light path length, Suprasil high precision quartz 300, Hellma Analytics GmbH & Co.). The concentrations of AB10B (Alfa Aesar, Thermo Fisher Ltd.), Congo Red (CR; RRBD125-T, ACP Pure Ltd.), Alizarin Red (AR; RRBD75-T, ACP Pure Ltd.), Disperse Red 1 (DR1; + 95 %, Sigma Aldrich Ltd.) Janus Green B (JGB; RRBD25598-T, ACP Pure Ltd.), and Methylene Blue (MB; + 70 %, Tokyo Chemical Industry UK Ltd) were determined by recording the absorbance at the absorbance maxima ( $\lambda_{\max}$ ) of 620 nm, 498 nm, 425 nm, 483 nm, 540 nm, 598 nm and 663 nm respectively as performed in prior literature.<sup>260,261,262,263,264</sup> AB10B and CR are anionic azo dyes, AR is an anionic non-azo dye, DR1 is an azo neutral dye, MB is a cationic non-azo dye, and JGB is a cationic azo dye. Dye solutions with concentrations between 0.5 mg L<sup>-1</sup> and 100 mg L<sup>-1</sup> were made up, and calibration curves for absorbance at  $\lambda_{\max}$  against concentration were created. Concentrations of dye found in the filtrates were determined by comparing the absorbance at the appropriate wavelength with the calibration curves.

### 3.2.3 Dye Extraction

200 mg L<sup>-1</sup> stock solutions of AB10B, CR, AR, JGB and MB were made up by dissolving 50 mg dye in 25 mL HP water. As the neutral DR1 dye does not dissolve in water, stock solutions were prepared by dissolving 50 mg DR1 in 25 mL ethanol (+ 99 %, Fisher Scientific UK Ltd.)—neutral disperse dyes are often employed in factories by boiling the desired material at close to 100 °C in conjunction with a dispersion agent, to overcome the poor solubility in water.<sup>265</sup> As these conditions cannot be easily replicated under the experimental conditions, and that the use of alcoholic solvents for disperse dyes has been reported,<sup>266,267</sup> switching the solvent to ethanol ensures minimal changes to the experimental setup. The stock solutions were then diluted with either water or ethanol as required in order to obtain dye solutions of the desired concentration.

Dynamic and static filtration experiments, as well as isotherm determination and kinetic modelling investigations were performed as described in 2.1.3. Mass transfer investigations

were performed by repeating the kinetic modelling investigation, using half the usual spin speed (20 rpm).

In order to calculate the number of amine sites on the surface, and hence determine the ratio of active sites to adsorbed dye molecules, the experimental procedure outlined by Lee et al. was modified and implemented.<sup>268</sup> Pieces of DMAM-phenol functionalised cloths were left to shake at 200 rpm in the presence of 10 mL HCl (approximately 0.05 M) for 24 h. An 8 mL aliquot was extracted and titrated against 0.002 M NaOH. As a reference, 8 mL of the starting HCl solution was titrated against the 0.002 M NaOH solution, and the whole experiment was also repeated using uncoated TPU cloth as a control. If there are far more molecules of dye than adsorption sites, then multi-layers will have formed, implying that the adsorption is dominated by physisorption.<sup>269</sup> If the numbers are similar, then it is likely that a monolayer will have formed, with each amine site binding to one dye molecule. If there are twice as many amine sites as dye molecules, then it is likely that the dyes require two amine sites to bind to them. If there are far more sites than dye molecules, then again, a monolayer will have formed, however there could be a strong degree of hindrance on the surface, wherein the dyes (e.g., due to their size) inhibit a second dye molecule from attaching to a neighbouring binding site.

Cloth recycling experiments were carried out by means of deprotonating the DMAM amine groups, whilst simultaneously displacing captured dye with high concentrations of salt via ion exchange.<sup>251</sup> Regeneration solutions replicating those previously reported as used during the extraction of AB10B, consisting of 1 M NaOH (analytic reagent grade pellets, Fisher Scientific UK Ltd.)<sup>231,232,233,234,235,236,237,238</sup>—as well as one previously employed to regenerate a DMAM-calixarene functionalised absorbent, consisting of 0.5 M NaOH and 2 M NaCl (+ 99.5 %, Sigma Aldrich Ltd.)<sup>251</sup>—were made up. In order to determine the effectiveness of each regeneration solution, 5 mL of a 20 mg L<sup>-1</sup> AB10B solution (a high dye concentration was chosen to ensure that the cloth was fully saturated following each regeneration cycle) was passed through a DMAM-phenol functionalised cloth, followed by 5 mL HP water (after the filtrate had been collected) in order to remove any dye trapped by capillary forces. Then, 5 mL of regeneration solution was passed through the cloth and the eluent collected. The concentration of dye in each filtrate and regeneration eluent was recorded via UV-Vis spectroscopy. It was demonstrated that NaOH has a destructive effect on the AB10B dye, thus the concentration of dye found in the eluent could not be accurately measured, and so the effectiveness of the regeneration solutions was determined by comparing the change in extraction percentage towards 20 mg L<sup>-1</sup> AB10B solution following 10 successive filtration cycles. The experiment was subsequently repeated using 6 mg L<sup>-1</sup> AB10B solutions, which



were filtered with both DMAM-phenol and DMAM-calixarene functionalised cloths, before being regenerated with the optimal regeneration solution—the 0.5 M NaOH/2 M NaCl solution.

Cloth selectivity experiments were performed by passing 5 mL of a 6 mg L<sup>-1</sup> AB10B solution, containing one of: sodium chloride (+ 99.5 %, Sigma-Aldrich Ltd.); monosodium phosphate (+ 99 %, Sigma Aldrich Ltd.); sodium sulfate (+ 99 % anhydrous, Fisher Scientific UK Ltd.); sodium hydrogen carbonate (+ 99 %, Acros Organics B.V.B.A); or magnesium nitrate hexahydrate (+ 99 %, A.C.S. Reagent, Sigma Aldrich Ltd.) in a 1:10 or 1:100 mole ratio of dye:competing anion, through a piece of meltblown TPU cloth, functionalised with either DMAM-calixarene or DMAM-phenol. In addition, solutions were made up containing a 1:1 by mass ratio of AB10B and MB, such that the concentration of each dye was 6 mg L<sup>-1</sup> (for cloths using TPU as the substrate) or 20 mg L<sup>-1</sup> (for cloths using activated carbon as the substrate). The selectivity of an adsorbent towards AB10B was determined by extracting the target dye following dynamic filtration of the 6 mg L<sup>-1</sup> mixed dye solution or static filtration of the 20 mg L<sup>-1</sup> mixed dye solution and calculating the extraction percentage. As the black carbon cloths tended to disintegrate during the filtration process, particulates would remain in solution. These needed to be removed, as the black particulates would otherwise interfere with the UV–Vis spectra. As such, following static filtration, the filtrates were passed through filter paper.

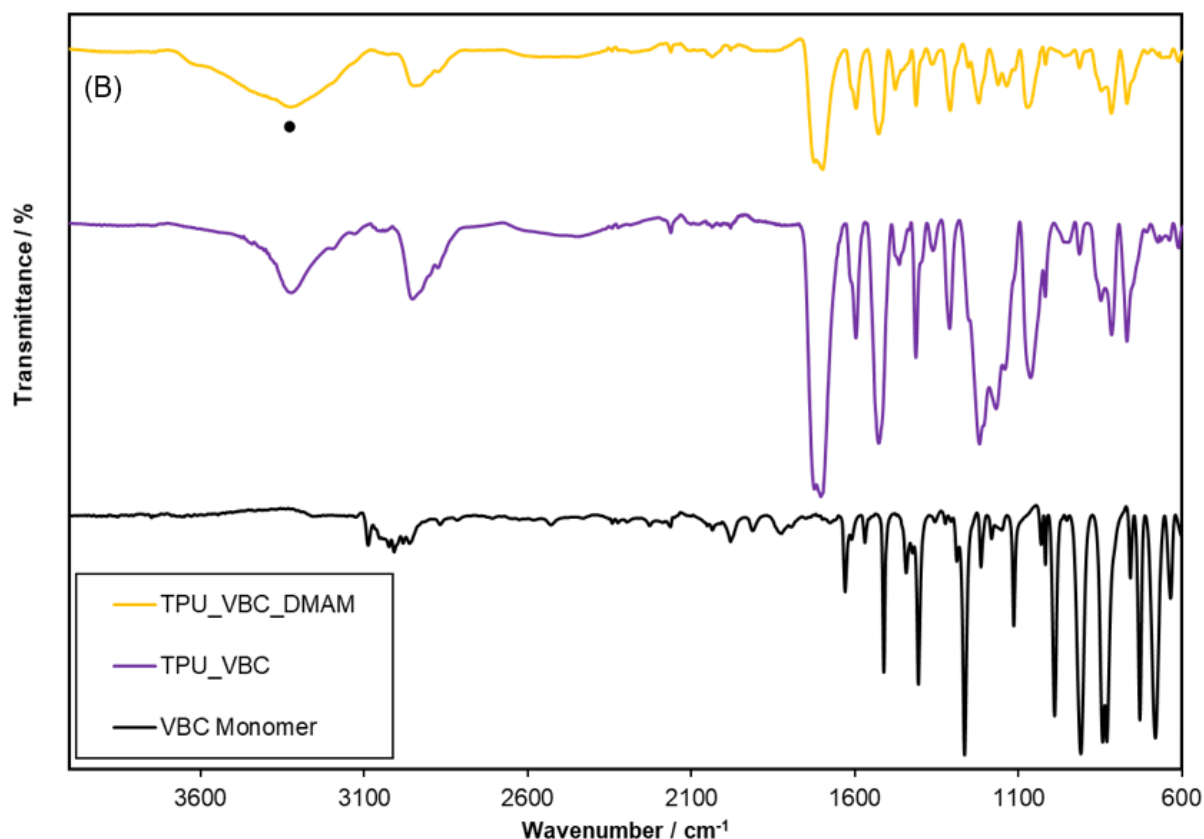
A real-world AB10B contaminated sample was simulated by first collecting water from a vegetated rainwater pond (Durham University, UK)—it is expected that a rainwater pond will contain a wide array of ions and organic matter. The water was first filtered with a membrane filter (Whatman Polydisc GW In-Line polyamide filter with 0.45 µm pore size, GE Healthcare Inc.) in order to remove any solid particulates via mechanical filtration. The particulate-free pond water was then used to make up a solution containing 6 mg L<sup>-1</sup> AB10B, which was then dynamically filtered with TPU cloths functionalised with DMAM-phenol and DMAM-calixarene. The dye solution before and after filtration was analysed by UV–Vis spectroscopy in order to determine the dye extraction percentage. All pond water filtration experiments were performed within 2 h of collection. All experiments have been performed at least three times unless otherwise stated, and error values provided correspond to the standard deviation of the recorded values.

### 3.3 Results

#### 3.3.1 Characterisation of Functional Cloths

The RAIRS spectrum of the pulsed plasma poly(4-VBC) deposited film on the silicon wafer shows a close resemblance to the 4-VBC monomer (Figure 3-3(A), Table 3-1).<sup>253,270,271,272</sup> These characteristic absorption bands include the halide functionality (CH<sub>2</sub> wagging mode of CH<sub>2</sub>–Cl) at 1265 cm<sup>-1</sup>, as well as the phenyl semicircle and quadrant stretches at 1512 and

1605  $\text{cm}^{-1}$  respectively. The disappearance of the C=C stretch at 1619  $\text{cm}^{-1}$  is indicative of successful polymerisation.<sup>253</sup> Unfortunately, the coating washes off the silicon wafers once immersed in the acetone solution, and so tracking the subsequent calixarene derivatisation step must be done using ATR infrared analysis of the coated cloth substrate. The ATR infrared spectrum of a pulsed plasma poly(4-VBC) coated TPU cloth, and the same cloth, following immersion in a DMAM-calixarene solution for three days is shown in Figure 3-3(B). Due to significant overlap with the TPU absorbance bands, it is difficult to identify the peaks associated with the thin pulsed plasma poly(4-VBC) film. However, following derivatisation with DMAM-calixarene, a broad peak at ca. 3220  $\text{cm}^{-1}$  is clearly visible, attributed to the stretching of the intramolecularly hydrogen bonded unreacted O-H groups on the lower rim of DMAM-calixarene.<sup>273</sup> Due to the aforementioned overlap with the TPU absorbance bands, it is not possible to unequivocally assign the tertiary amine C-N stretch (1020–1250  $\text{cm}^{-1}$ ) on the calixarene.



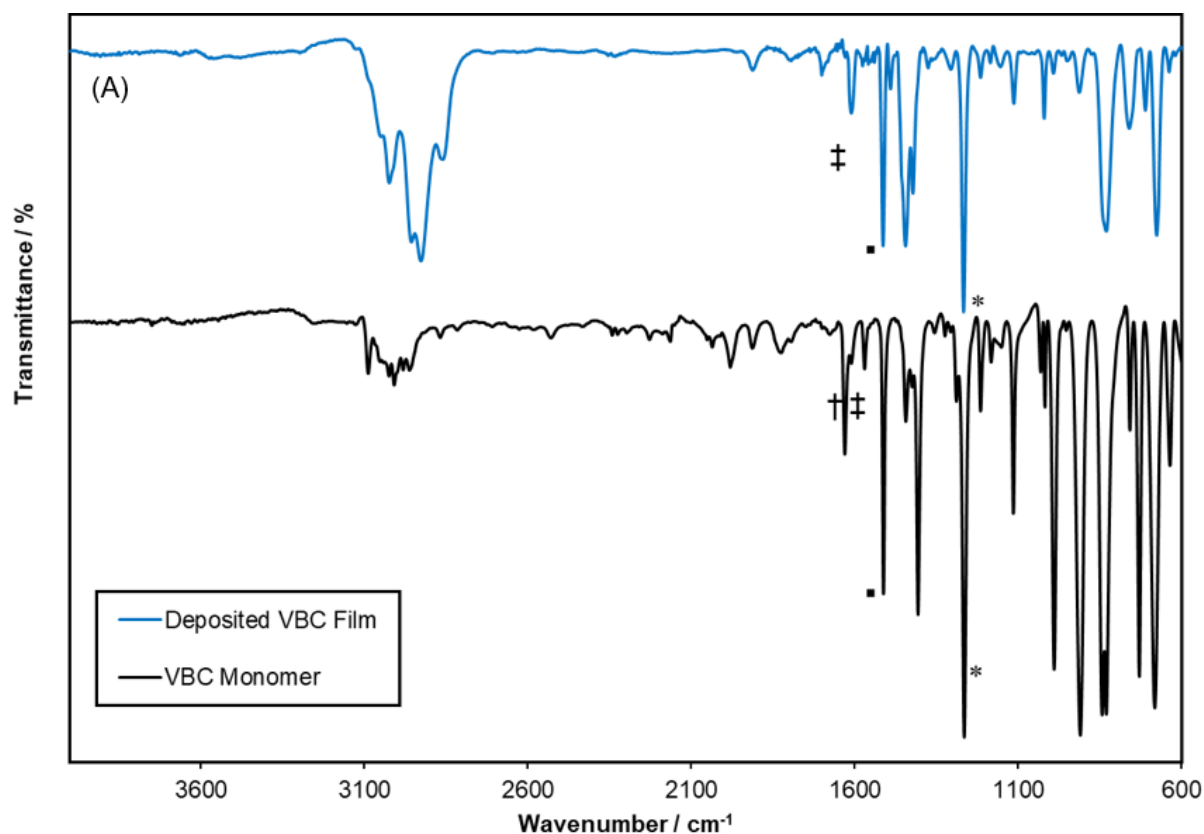


Figure 3-3. (A) ATR–infrared spectrum of 4-VBC monomer (black) and RAIRS–infrared spectrum of pulsed plasma poly(4-VBC) deposited onto a silicon wafer (blue). (B) ATR–infrared spectra of 4-VBC monomer (black), pulsed plasma poly(4-VBC) coated polyurethane cloth (purple) and DMAM-calixarene derivatised, pulsed plasma poly(4-VBC) coated polyurethane cloth (orange).

Table 3-1. Assignment of absorbance bands observed in the FTIR spectra for the 4-VBC monomer, pulsed plasma poly(4-VBC) deposited film, and DMAM-phenol functionalised, pulsed plasma poly(4-VBC) coated TPU Cloth.

Label	Wavenumber / $\text{cm}^{-1}$	Assignment	Reference
•	3220	O–H	251,273,274
†	1619	C=C stretch	253, 274
‡	1605	Phenyl quadrant stretch	253, 274
▪	1512	Phenyl semicircle stretch	274
*	1265	C–H wagging mode of $\text{CH}_2\text{–Cl}$	253, 274

### 3.3.2 Extraction of Dyes

The extraction percentage following dynamic filtration of a meltblown 35 GSM polyurethane cloth; a pulsed plasma poly(4-VBC) coated TPU cloth; a pulsed plasma poly(4-VBC) coated,

phenol functionalised TPU cloth; a pulsed plasma poly(4-VBC) coated, DMAM-calixarene functionalised TPU cloth; a pulsed plasma poly(4-VBC) coated, DMAM-phenol functionalised TPU cloth; and a pulsed plasma poly(4-VBC) coated, tBu-calixarene functionalised TPU cloth towards 6 and 10 mg L<sup>-1</sup> cationic dyes MB and JGB have been determined. In addition, the extraction percentage of the same adsorbents towards the anionic dyes AB10B, AR and CR, and the extraction percentage of the same adsorbents towards the neutral dye DR1, have been determined.

### 3.3.2.1 Cationic Dyes

The uncoated hydrophobic cloth allows the HP water to pass through it in ca. 10 min (Table 3-2). This time increases when extra hydrophobicity is incorporated through deposition of pulsed plasma poly(4-VBC) and subsequent derivatisation with phenol and tBu-calixarene. Similarly, when hydrophilicity is incorporated through derivatisation with DMAM-calixarene or DMAM-phenol, the filtration time decreases. These observations are matched by the dye solutions, although filtration times do differ slightly.

Table 3-2. Extraction efficiencies and filtration time for: uncoated 35 GSM meltblown TPU cloth; pulsed plasma poly(4-VBC) coated TPU cloth; and pulsed plasma poly(4-VBC) coated TPU cloth, derivatised with either phenol, DMAM-phenol, DMAM-calixarene or tBu-calixarene (3 cm x 3.5 cm, inserted into the bottom of the body of a Pasteur pipette (150 mm total length, 100 mm body length, 5.6 mm body internal diameter, Fisher Scientific UK Ltd.)) towards 0, 6 and 10 mg L<sup>-1</sup> cationic dye (JGB and MB) solutions.

Extractant	Dye								
	Cationic Azo Janus Green B				Cationic Non-azo Methylene Blue				No Dye
	Filtration efficiency / %		Filtration time / min		Filtration efficiency / %		Filtration time / min		Filtration time / min
	6 mg L <sup>-1</sup>	10 mg L <sup>-1</sup>	6 mg L <sup>-1</sup>	10 mg L <sup>-1</sup>	6 mg L <sup>-1</sup>	10 mg L <sup>-1</sup>	6 mg L <sup>-1</sup>	10 mg L <sup>-1</sup>	
Uncoated cloth	79.7 ± 9.3	84.5 ± 7.3	Ca. 20	Ca. 30	35.0 ± 5.2	37.9 ± 10.2	Ca. 15	Ca. 15	Ca. 10
Pulsed plasma poly(4-VBC)	77.2 ± 15.3	76.5 ± 11.7	Ca. 60	Ca. 60	39.6 ± 11.1	30.9 ± 8.1	Ca. 60	Ca. 60	> 60
Phenol	80.2 ± 1.2	82.6 ± 6.6	Ca. 45	Ca. 45	52.5 ± 7.9	25.8 ± 8.8	Ca. 30	Ca. 30	Ca. 60
DMAM-phenol	80.9 ± 6.1	81.8 ± 8.8	Ca. 25	Ca. 25	19.8 ± 6.9	26.8 ± 10.7	Ca. 20	Ca. 20	Ca. 5
DMAM-calixarene	83.0 ± 12.3	78.5 ± 6.9	Ca. 25	Ca. 25	25.9 ± 9.8	26.4 ± 10.1	Ca. 15	Ca. 15	Ca. 5

Extractant	Dye								
	Cationic Azo Janus Green B				Cationic Non-azo Methylene Blue				No Dye
	Filtration efficiency / %		Filtration time / min		Filtration efficiency / %		Filtration time / min		Filtration time / min
	6 mg L <sup>-1</sup>	10 mg L <sup>-1</sup>	6 mg L <sup>-1</sup>	10 mg L <sup>-1</sup>	6 mg L <sup>-1</sup>	10 mg L <sup>-1</sup>	6 mg L <sup>-1</sup>	10 mg L <sup>-1</sup>	
tBu-calixarene	84.4 ± 16.6	91.9 ± 8.6	Ca. 45	Ca. 45	55.0 ± 4.5	30.4 ± 6.3	Ca. 45	Ca. 45	Ca. 60

The largest source of error regarding the filtration efficiency of each system is cloth weight, whereby larger cloths will give rise to a greater extraction percentage. Consequently, the data was normalised by means of converting the extraction percentages to adsorption capacities (Table 3-3). The only other potential error source is the unquantifiable filtration procedure, wherein the adsorbent is pushed towards the bottom of the Pasteur pipette. Given that this is performed manually, it is impossible to ensure that each cloth is compressed to the same extent. However, as each cloth is pushed until point of maximum resistance, it is unlikely that severe differences occur between each experiment.

Table 3-3. Adsorption capacities of uncoated 35 GSM meltblown TPU cloth; pulsed plasma poly(4-VBC) coated TPU cloth; and pulsed plasma poly(4-VBC) coated TPU cloth, derivatised with either phenol, DMAM-phenol, DMAM-calixarene or tBu-calixarene (3 cm x 3.5 cm, inserted into the bottom of the body of a Pasteur pipette (150 mm total length, 100 mm body length, 5.6 mm body internal diameter, Fisher Scientific UK Ltd.)) towards 6 and 10 mg L<sup>-1</sup> cationic dye (JGB and MB) solutions.

Extractant	Dye			
	Cationic Azo Janus Green		Cationic Non-azo Methylene Blue	
	Adsorption Capacity / mg <sub>Dye</sub> g <sub>Cloth</sub> <sup>-1</sup>		Adsorption Capacity / mg <sub>Dye</sub> g <sub>Cloth</sub> <sup>-1</sup>	
	6 mg L <sup>-1</sup>	10 mg L <sup>-1</sup>	6 mg L <sup>-1</sup>	10 mg L <sup>-1</sup>
Uncoated cloth	0.64 ± 0.04	1.18 ± 0.06	0.35 ± 0.02	0.45 ± 0.09
Pulsed plasma poly(4-VBC)	0.56 ± 0.12	0.92 ± 0.07	0.31 ± 0.06	0.41 ± 0.09
Phenol	0.50 ± 0.04	0.98 ± 0.07	0.32 ± 0.03	0.31 ± 0.12
DMAM-phenol	0.59 ± 0.06	1.03 ± 0.00	0.14 ± 0.05	0.30 ± 0.08
DMAM-calixarene	0.59 ± 0.10	0.95 ± 0.04	0.21 ± 0.08	0.33 ± 0.12
tBu-calixarene	0.58 ± 0.14	0.90 ± 0.11	0.33 ± 0.07	0.34 ± 0.08

The uptake of JGB was  $0.64 \pm 0.04$  and  $1.18 \pm 0.06$   $\text{mg}_{\text{Dye}}\text{g}_{\text{Cloth}}^{-1}$  for the uncoated TPU cloth for the  $6 \text{ mg L}^{-1}$  and the  $10 \text{ mg L}^{-1}$  solutions respectively. There are insignificant changes in adsorption capacity when the cloth is coated with pulsed plasma poly(4-VBC), and when derivatised with phenol, tBu-calixarene, DMAM-phenol, or DMAM-calixarene. This indicates that the plasma deposition and subsequent derivatisation process exhibit minimal effect on the filtration efficiency. This, in turn, indicates that bulk TPU in the cloth is responsible for the dye removal. For all adsorbents, the capacity of the cloth increases with initial dye concentration, with the increase approximately proportional to the increase in concentration, indicating that capacity is yet to be reached.

The uptake of MB when filtered by the uncoated TPU cloth is  $0.35 \pm 0.02$  and  $0.45 \pm 0.09$   $\text{mg}_{\text{Dye}}\text{g}_{\text{Cloth}}^{-1}$  for the  $6 \text{ mg L}^{-1}$  and  $10 \text{ mg L}^{-1}$  solutions respectively. It is worth noting that the JGB molecules ( $M_r = 511.06 \text{ g mol}^{-1}$ ) are considerably heavier than the MB molecules ( $M_r = 319.85 \text{ g mol}^{-1}$ ), and therefore the adsorption capacity values for the  $6 \text{ mg L}^{-1}$  solutions are more similar when reported in terms of  $\text{mmol}_{\text{Dye}}\text{g}_{\text{Cloth}}^{-1}$  ( $1.27 \pm 0.08 \times 10^{-3} \text{ mmol}_{\text{JGB}}\text{g}_{\text{Cloth}}^{-1}$  vs  $1.09 \pm 0.06 \times 10^{-3} \text{ mmol}_{\text{MB}}\text{g}_{\text{Cloth}}^{-1}$ ), albeit with the capacity towards JGB still slightly higher. However, the disparity in adsorption capacity towards the  $10 \text{ mg L}^{-1}$  dye solutions is greater ( $2.31 \pm 0.12 \times 10^{-3} \text{ mmol}_{\text{JGB}}\text{g}_{\text{Cloth}}^{-1}$  vs  $1.41 \pm 0.22 \times 10^{-3} \text{ mmol}_{\text{MB}}\text{g}_{\text{Cloth}}^{-1}$ ). This has two implications. First, there are greater forces of attraction between the cloth and the JGB dye than between the cloth and the MB dye. Secondly—and combined with the fact that the adsorption capacity does not increase proportionally with dye concentration—it should be stated that the cloth is reaching, or has reached, capacity following filtration of the  $10 \text{ mg L}^{-1}$  solution.

Regarding the functionalised cloths, there is a decrease in adsorption capacity for the extraction of MB from a  $6 \text{ mg L}^{-1}$  solution by the DMAM-functionalised cloths, while the tBu-calixarene and phenol functionalised cloths yield similar extraction percentages to the uncoated and pulsed plasma poly(4-VBC) coated cloths. However, when using a starting MB concentration of  $10 \text{ mg L}^{-1}$ , the adsorption capacity of all extractants reached similar values, indicating that the driving force behind the reduced extraction of the DMAM-functionalised cloths has been overcome at the greater dye concentration.

### 3.3.2.2 Anionic Dyes

For each anionic dye, the general trend in filtration time matches those for the cationic dyes and water solution, whereby the hydrophilic surfaces give rise to the quickest filtration time, followed by the hydrophobic cloth, and then the hydrophobic cloth, with additional hydrophobicity incorporated, yielding the slowest filtration times (Table 3-4). As with the

cationic dyes in Section 3.2.1, the filtration efficiencies have been converted into adsorption capacities (Table 3-5).

Table 3-4. Filtration efficiencies and filtration time for: uncoated 35 GSM meltblown TPU cloth; pulsed plasma poly(4-VBC) coated TPU cloth; and pulsed plasma poly(4-VBC) coated TPU cloth, derivatised with either phenol, DMAM-phenol, DMAM-calixarene or tBu-calixarene (3 cm x 3.5 cm, inserted into the bottom of the body of a Pasteur pipette (150 mm total length, 100 mm body length, 5.6 mm body internal diameter, Fisher Scientific UK Ltd.)) towards 0, 6 and 10 mg L<sup>-1</sup> anionic dyes AB10B (A), CR (B) and AR (C) solutions.

(C)

Extractant	Alizarin Red Dye				
	Filtration efficiency / %		Filtration time / min		
	6 mg L <sup>-1</sup>	10 mg L <sup>-1</sup>	0 mg L <sup>-1</sup>	6 mg L <sup>-1</sup>	10 mg L <sup>-1</sup>
Uncoated cloth	0.0 ± 0.0	0.0 ± 0.0	Ca. 10	Ca. 10	Ca. 15
Pulsed plasma poly(4-VBC)	1.4 ± 2.5	0.8 ± 1.4	> 60	> 60	> 60
Phenol	18.6 ± 10.1	17.7 ± 9.6	Ca. 60	Ca. 60	Ca. 60
DMAM-phenol	96.0 ± 6.9	88.1 ± 8.2	Ca. 5	Ca. 15	Ca. 15
DMAM-calixarene	88.1 ± 18.7	81.7 ± 8.8	Ca. 5	Ca. 15	Ca. 15
tBu-calixarene	12.7 ± 2.1	7.5 ± 2.4	Ca. 60	Ca. 60	Ca. 60

(B)

Extractant	Congo Red Dye				
	Filtration efficiency / %		Filtration time / min		
	6 mg L <sup>-1</sup>	10 mg L <sup>-1</sup>	0 mg L <sup>-1</sup>	6 mg L <sup>-1</sup>	10 mg L <sup>-1</sup>
Uncoated cloth	0.4 ± 0.8	0.0 ± 0.0	Ca. 10	Ca. 10	Ca. 10
Pulsed plasma poly(4-VBC)	7.4 ± 6.3	6.3 ± 4.0	> 60	> 60	> 60
Phenol	11.5 ± 3.0	9.6 ± 2.9	Ca. 60	Ca. 60	Ca. 60
DMAM-phenol	89.8 ± 5.3	76.0 ± 10.2	Ca. 5	Ca. 10	Ca. 10
DMAM-calixarene	88.0 ± 9.3	81.6 ± 2.4	Ca. 5	Ca. 10	Ca. 10
tBu-calixarene	11.0 ± 6.7	13.4 ± 4.0	Ca. 60	Ca. 60	Ca. 60

(A)

Extractant	Amido Black 10B Dye				
	Filtration efficiency / %		Filtration time / min		
	6 mg L <sup>-1</sup>	10 mg L <sup>-1</sup>	0 mg L <sup>-1</sup>	6 mg L <sup>-1</sup>	10 mg L <sup>-1</sup>
Uncoated cloth	1.9 ± 0.7	0.3 ± 0.2	Ca. 10	Ca. 10	Ca. 15
Pulsed plasma poly(4-VBC)	2.0 ± 0.7	6.5 ± 5.2	> 60	> 60	> 60
Phenol	5.8 ± 6.9	3.7 ± 4.7	Ca. 60	Ca. 60	Ca. 60
DMAM-phenol	96.1 ± 5.2	86.3 ± 11.9	Ca. 5	Ca. 15	Ca. 15
DMAM-calixarene	83.9 ± 10.1	66.4 ± 6.3	Ca. 5	Ca. 15	Ca. 15
<i>t</i> Bu-calixarene	7.0 ± 5.0	5.0 ± 6.7	Ca. 60	Ca. 60	Ca. 60

Table 3-5. Adsorption capacities of uncoated 35 GSM meltblown TPU cloth; pulsed plasma poly(4-VBC) coated TPU cloth; and pulsed plasma poly(4-VBC) coated TPU cloth, derivatised with either phenol, DMAM-phenol, DMAM-calixarene or *t*Bu-calixarene (3 cm x 3.5 cm, inserted into the bottom of the body of a Pasteur pipette (150 mm total length, 100 mm body length, 5.6 mm body internal diameter, Fisher Scientific UK Ltd.)) towards 6 and 10 mg L<sup>-1</sup> anionic dye (AB10B, CR and AR) solutions.

Extractant	Dye					
	AB10B		CR		AR	
	Adsorption Capacity / mg <sub>Dye</sub> g <sub>Cloth</sub> <sup>-1</sup>		Adsorption Capacity / mg <sub>Dye</sub> g <sub>Cloth</sub> <sup>-1</sup>		Adsorption Capacity / mg <sub>Dye</sub> g <sub>Cloth</sub> <sup>-1</sup>	
	6 mg L <sup>-1</sup>	10 mg L <sup>-1</sup>	6 mg L <sup>-1</sup>	10 mg L <sup>-1</sup>	6 mg L <sup>-1</sup>	10 mg L <sup>-1</sup>
Uncoated cloth	0.02 ± 0.01	0.00 ± 0.00	0.00 ± 0.01	0.0 ± 0.0	0 ± 0	0 ± 0
Pulsed plasma poly(4-VBC)	0.02 ± 0.00	0.08 ± 0.06	0.09 ± 0.08	0.06 ± 0.04	0.01 ± 0.02	0.01 ± 0.02
Phenol	0.04 ± 0.04	0.04 ± 0.04	0.10 ± 0.02	0.11 ± 0.04	0.13 ± 0.07	0.21 ± 0.11
DMAM-phenol	0.71 ± 0.11	1.12 ± 0.05	0.69 ± 0.13	0.86 ± 0.15	0.60 ± 0.08	0.87 ± 0.08
DMAM-calixarene	0.62 ± 0.14	0.82 ± 0.07	0.57 ± 0.04	0.89 ± 0.12	0.63 ± 0.06	0.87 ± 0.09



Extractant	Dye					
	AB10B		CR		AR	
	Adsorption Capacity / $\text{mg}_{\text{Dye}}\text{g}_{\text{Cloth}}^{-1}$		Adsorption Capacity / $\text{mg}_{\text{Dye}}\text{g}_{\text{Cloth}}^{-1}$		Adsorption Capacity / $\text{mg}_{\text{Dye}}\text{g}_{\text{Cloth}}^{-1}$	
	6 mg L <sup>-1</sup>	10 mg L <sup>-1</sup>	6 mg L <sup>-1</sup>	10 mg L <sup>-1</sup>	6 mg L <sup>-1</sup>	10 mg L <sup>-1</sup>
tBu-calixarene	0.04 ± 0.03	0.06 ± 0.08	0.11 ± 0.05	0.16 ± 0.04	0.09 ± 0.01	0.08 ± 0.1

AB10B is successfully removed by DMAM-calixarene and DMAM-phenol functionalised cloths (DMAM-phenol exhibits a greater adsorption capacity than DMAM-calixarene, particularly at a starting concentration of 10 mg L<sup>-1</sup>, where a capacity of  $1.12 \pm 0.05 \text{ mg}_{\text{Dye}}\text{g}_{\text{Cloth}}^{-1}$  is observed for DMAM-phenol, compared to  $0.82 \pm 0.07 \text{ mg}_{\text{Dye}}\text{g}_{\text{Cloth}}^{-1}$  for DMAM-calixarene). Indeed, the increase in adsorption capacity for the DMAM-phenol functionalised cloth is roughly proportional to concentration of AB10B, which is not the case for DMAM-calixarene, indicating that that system has reached capacity. The AB10B dye is hardly removed by the uncoated TPU cloth; the cloth coated with pulsed plasma poly(4-VBC); and the coated cloth derivatised with either phenol or tBu-calixarene, indicating that the DMAM functionality is responsible for the dye removal.

Just as with AB10B, the DMAM-calixarene and DMAM-phenol functionalised cloths are capable of extracting CR from solution. However, the adsorption capacities of the two systems do not show a noticeable difference. When compared with the uncoated TPU cloth, the pulsed plasma poly(4-VBC) coated cloth, and coated cloths derivatised with either phenol or tBu-calixarene display a slight increase in adsorption capacity towards CR, however these values (ca.  $0.1 \text{ mg}_{\text{Dye}}\text{g}_{\text{Cloth}}^{-1}$ ) are insignificant when compared to adsorption capacity displayed by the DMAM-calixarene and DMAM-phenol functionalised cloths (ca.  $0.6 \text{ mg}_{\text{Dye}}\text{g}_{\text{Cloth}}^{-1}$  at 6 mg L<sup>-1</sup>, and ca.  $0.9 \text{ mg}_{\text{Dye}}\text{g}_{\text{Cloth}}^{-1}$  at 10 mg L<sup>-1</sup>).

AR is a non-azo anionic dye. As with AB10B and CR, excellent extraction of AR is observed by the DMAM-phenol and DMAM-calixarene functionalised cloths, while the other adsorbents are not capable of removing AR to any significant degree. Indeed, the adsorption capacities observed are almost identical to those demonstrated by CR, with insignificant differences observed between DMAM-calixarene and DMAM-phenol functionalised cloths. Similarly, the pulsed plasma poly(4-VBC) coated cloth, and coated cloths, derivatised with either phenol or tBu-calixarene, exhibit a greater adsorption capacity than the uncoated cloth.

### 3.3.2.3 Neutral Dye

The flow-through time for all adsorbents was ca. 15 min for pure ethanol, which did not change when ethanolic dye solutions were employed (Table 3-6). Once more, all extraction percentages have been converted to adsorption capacity, which showed that DR1 could not be removed by any of the reported systems to any reasonable extent. While all adsorption capacity values do lie within error of each other, there does still seem to be a general trend, wherein capacity increases with starting dye concentration.

Table 3-6. Extraction percentage, adsorption capacity and flow-through filtration time for uncoated 35 GSM meltblown TPU cloth, pulsed plasma poly(4-VBC) coated TPU cloth, and pulsed plasma poly(4-VBC) coated TPU cloth, derivatised with either: phenol; DMAM-phenol; DMAM-calixarene; or tBu-calixarene (3 cm x 3.5 cm, inserted into the bottom of the body of a Pasteur pipette (150 mm total length, 100 mm body length, 5.6 mm body internal diameter, Fisher Scientific UK Ltd.)) towards 5 mL of the neutral dye DR1 (dissolved in ethanol) in the absence of any external pressure.

Extractant	Neutral Azo-Disperse Red 1						
	Filtration efficiency / %		Adsorption Capacity / $\text{mg}_{\text{Dye}}\text{g}_{\text{Cloth}}^{-1}$		Filtration time / min		
	6 mg $\text{L}^{-1}$	10 mg $\text{L}^{-1}$	6 mg $\text{L}^{-1}$	10 mg $\text{L}^{-1}$	6 mg $\text{L}^{-1}$	10 mg $\text{L}^{-1}$	No dye
Uncoated cloth	3.4 ±	6.4 ±	0.02 ±	0.08 ±	Ca. 15	Ca. 15	Ca. 15
	4.7	6.6	0.03	0.08			
Pulsed plasma poly(4-VBC)	4.4 ±	2.7 ±	0.03 ±	0.04 ±	Ca. 15	Ca. 15	Ca. 15
	3.8	2.6	0.03	0.04			
Phenol	4.0 ±	4.6 ±	0.02 ±	0.06 ±	Ca. 15	Ca. 15	Ca. 15
	5.9	2.6	0.03	0.04			
DMAM-phenol	2.8 ±	5.9 ±	0.02 ±	0.05 ±	Ca. 15	Ca. 15	Ca. 15
	1.1	3.1	0.01	0.02			
DMAM-calixarene	4.8 ±	3.2 ±	0.03 ±	0.04 ±	Ca. 15	Ca. 15	Ca. 15
	2.6	1.6	0.01	0.01			
tBu-calixarene	4.2 ±	3.0 ±	0.02 ±	0.03 ±	Ca. 15	Ca. 15	Ca. 15
	4.2	4.2	0.02	0.05			

### 3.3.3 Maximum Adsorption Capacity

#### 3.3.3.1 Experimentally Determined Adsorption Capacity

Maximum adsorption capacities towards AB10B were calculated by leaving DMAM-phenol and DMAM-calixarene functionalised cloths to spin in 5 mL dye solutions containing either 10,

25, 50 or 100 mg L<sup>-1</sup> AB10B for at least 6 h, before recording the concentration of dye remaining in solution. 100 % extraction of dye from the 10 mg L<sup>-1</sup> solution was observed, meaning that the final dye concentration will be below the 0.01 mg L<sup>-1</sup> safe limit specified by EU regulation No. 10/2011 for the concentration of primary aromatic amines found in foodstuff.<sup>275</sup> However, this also implies that the cloth has not become fully saturated, and so the value cannot be used in the calculation of maximum adsorption capacity. The calculated maximum adsorption capacities towards the 25, 50 and 100 mg L<sup>-1</sup> AB10B solutions (Figure 3-4) are almost identical ( $1.73 \pm 0.23$ ,  $1.74 \pm 0.31$  and  $1.77 \pm 0.38$  mg<sub>Dye</sub>g<sub>Cloth</sub><sup>-1</sup> for the 25, 50 and 100 mg L<sup>-1</sup> concentrations respectively, yielding a gradient of  $0.0003 \pm 0.0003$  L g<sup>-1</sup> for the dependence of adsorption capacity on starting dye concentration), implying that dye concentration has no effect on adsorption capacity once the saturation limit has been reached. This independence of starting dye concentration on adsorption capacity is similarly observed by the DMAM-calixarene functionalised cloths (dependence gradient =  $-0.00005 \pm 0.00109$  L g<sup>-1</sup>), indicating that this phenomenon is not limited to the DMAM-phenol system. As such, each individual adsorption capacity value can be averaged to yield the experimentally determined adsorption capacities of  $1.74 \pm 0.29$  mg<sub>Dye</sub>g<sub>Cloth</sub><sup>-1</sup> and  $1.37 \pm 0.32$  mg<sub>Dye</sub>g<sub>Cloth</sub><sup>-1</sup> for the DMAM-phenol and DMAM-calixarene functionalised cloths respectively. Although there is an overlap of the error values, the results align with the findings from Section 3.2, where the adsorption capacity of the DMAM-phenol functionalised cloth towards the 10 mg L<sup>-1</sup> AB10B solution was greater than the adsorption capacity of the DMAM-calixarene functionalised cloth towards the same dye solution.

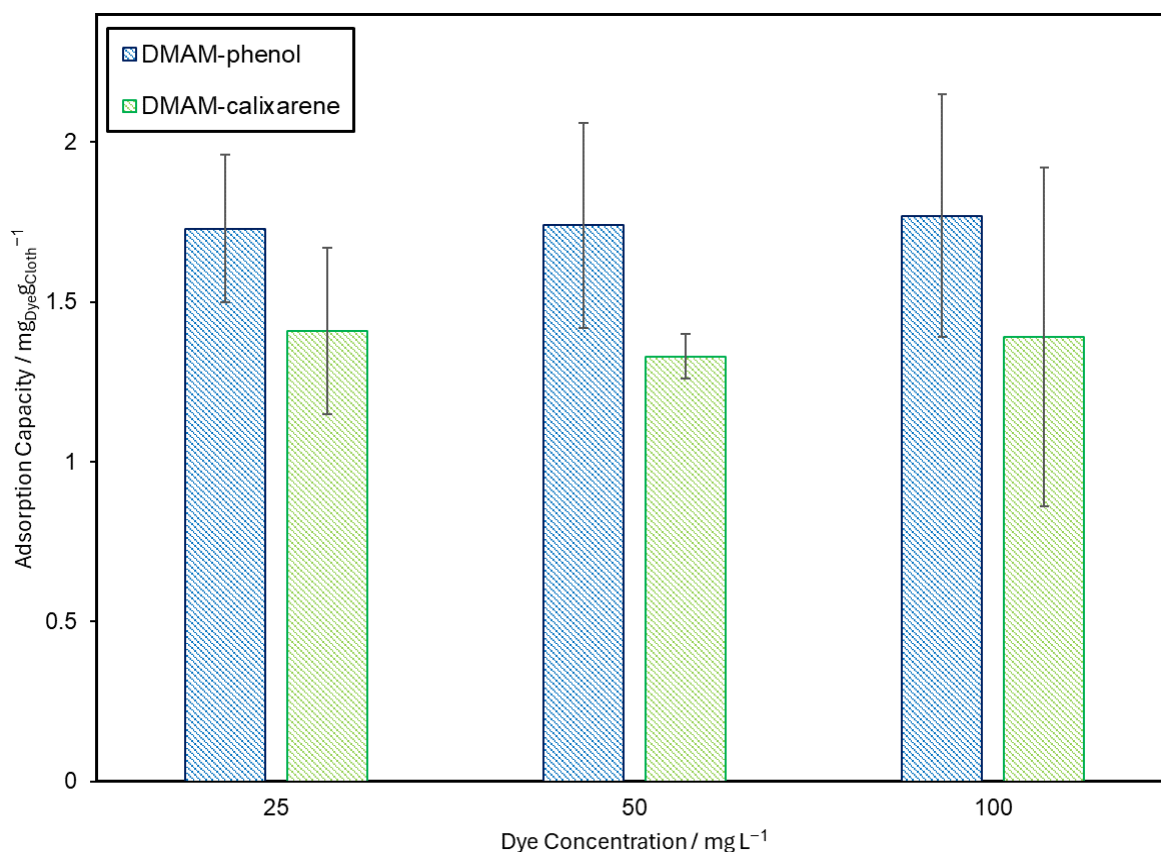


Figure 3-4. Maximum adsorption capacities for DMAM-phenol and DMAM-calixarene functionalised cloths towards 25, 50, and 100 mg L<sup>-1</sup> AB10B (anionic dye) solutions.

### 3.3.3.2 Isotherm Determined Adsorption Capacity

The investigation performed in Section 3.3.1. was expanded for the DMAM-phenol adsorbent to include dye concentrations below the extraction limit. The adsorption capacity values were converted into values of  $\theta$ , according to Equation (2-21) (Section 2.1.3.2.2), where maximum adsorption capacity of the cloth ( $Q_0$ ) =  $1.74 \pm 0.29$  mg<sub>Dye</sub>g<sub>Cloth</sub><sup>-1</sup>.

Values of  $\theta$  were then plotted against  $C$  (Figure 3-5), which yields a clear linear relationship at lower dye concentrations, before the values begin to plateau. This linear relationship is representative of adsorption which follows Henry's law. Henry's law states that the value of  $\theta$  is directly proportional to the concentration of adsorbate.<sup>276</sup> It is frequently observed that at low concentrations, adsorption is often described as belonging to the "Henry region", where the concentration of solute is low, and therefore coverage on the adsorbent is minimal.

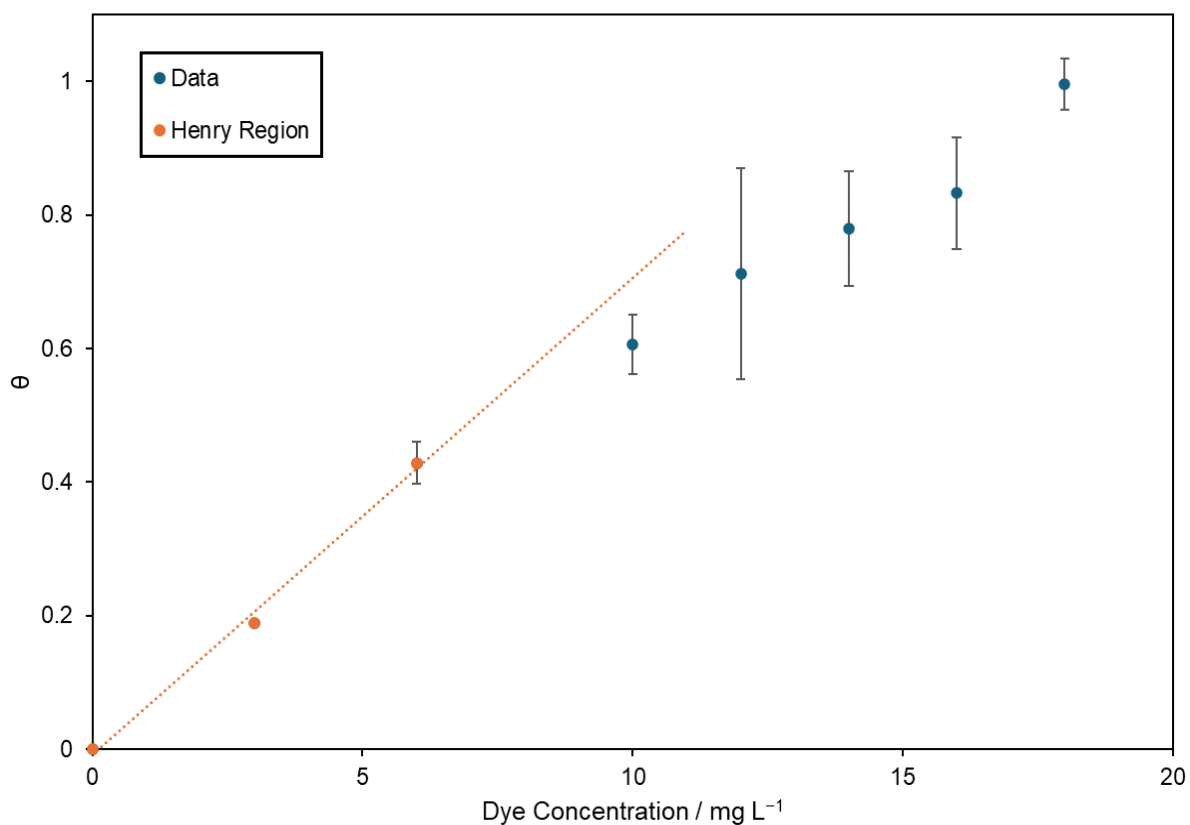


Figure 3-5. Relationship between starting concentration and normalised adsorption capacity. A linear model, which signifies the Henry region, has been overlaid.

In order to convert the data obtained above and in Section 3.3.3.1 into adsorption isotherms, the values of  $\theta$  were converted into the concentration of dye remaining in solution at equilibrium ( $C_e$ ) and the amount of dye adsorbed by the DMAM-phenol functionalised cloth per gram of cloth at equilibrium ( $Q_e$ ), and  $Q_e$  was plotted against  $C_e$  (Figure 3-6).<sup>219</sup> The data could then be modelled by Langmuir and Freundlich isotherms by estimating values for  $Q_0$  (Langmuir adsorption capacity) and  $K_L$  (Langmuir constant) for the Langmuir plot and  $K_F$  (Freundlich adsorption capacity) and  $n$  (Freundlich adsorption intensity) constants for the Freundlich plot. Plots were then generated using the equations for the non-linear isotherms (Section 2.1.3.2.2) and the values of  $Q_0$ ,  $K_L$ ,  $K_F$  and  $n$  were optimised by using the solver function in excel in order to give rise to the lowest  $\chi^2$  value. Additionally,  $C_e/Q_e$  against  $C_e$  and  $\text{Log}(Q_e)$  against  $\text{Log}(C_e)$  were plotted to give the linear forms of the Langmuir and Freundlich isotherms respectively (Figure 3-7).

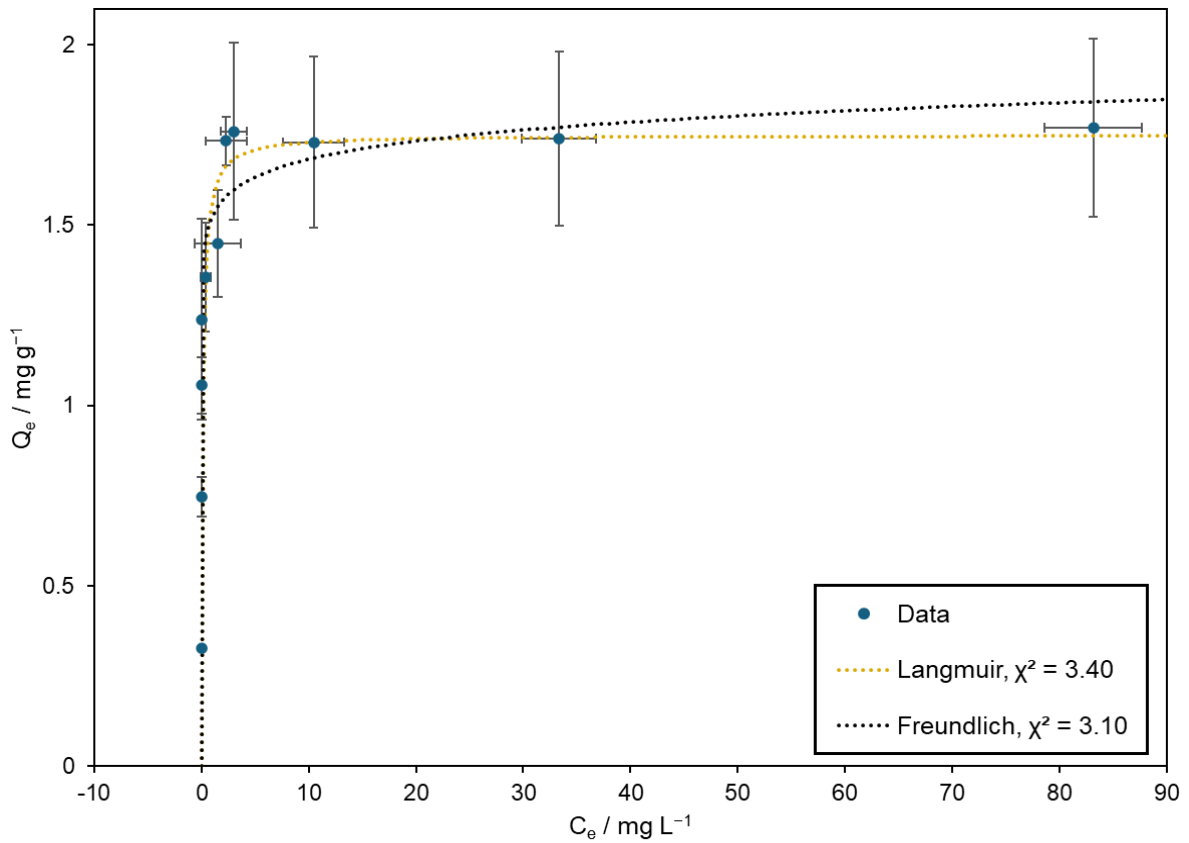
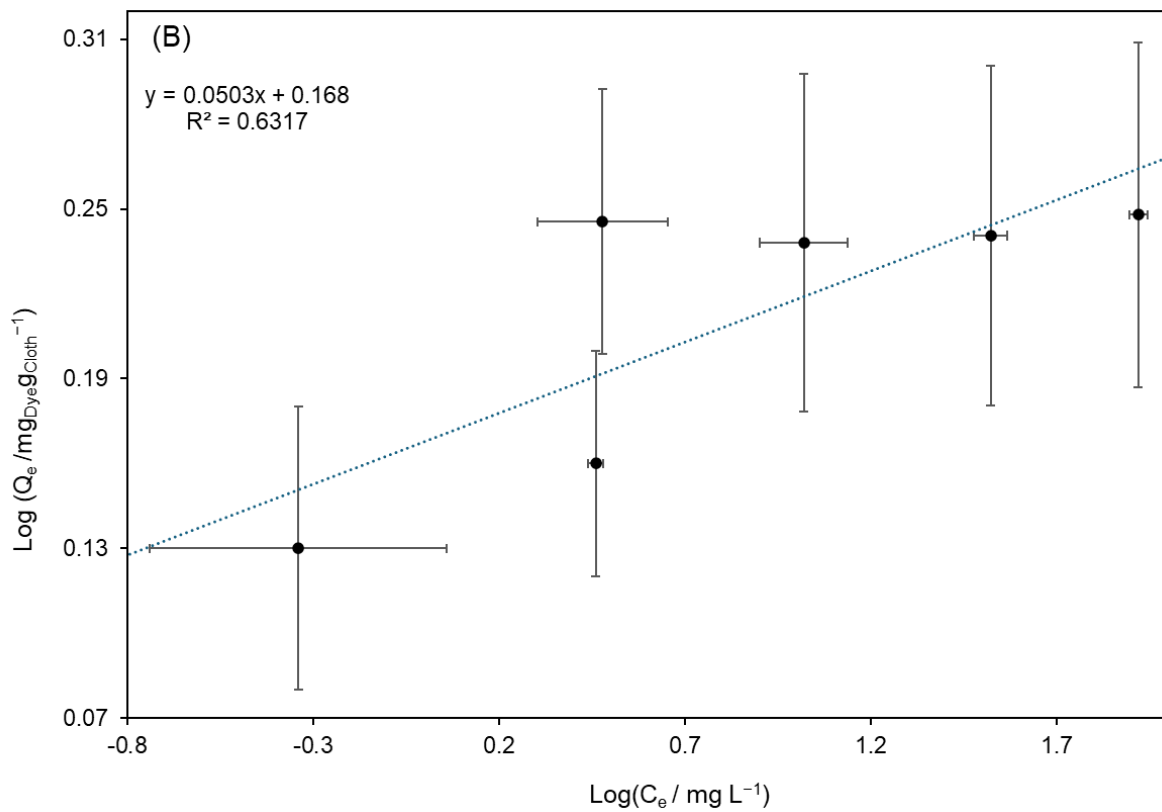


Figure 3-6. Non-linear adsorption isotherm plots for the adsorption of anionic dye AB10B onto DMAM-phenol functionalised cloths, overlaid with Langmuir (orange) and Freundlich (black) isotherms.



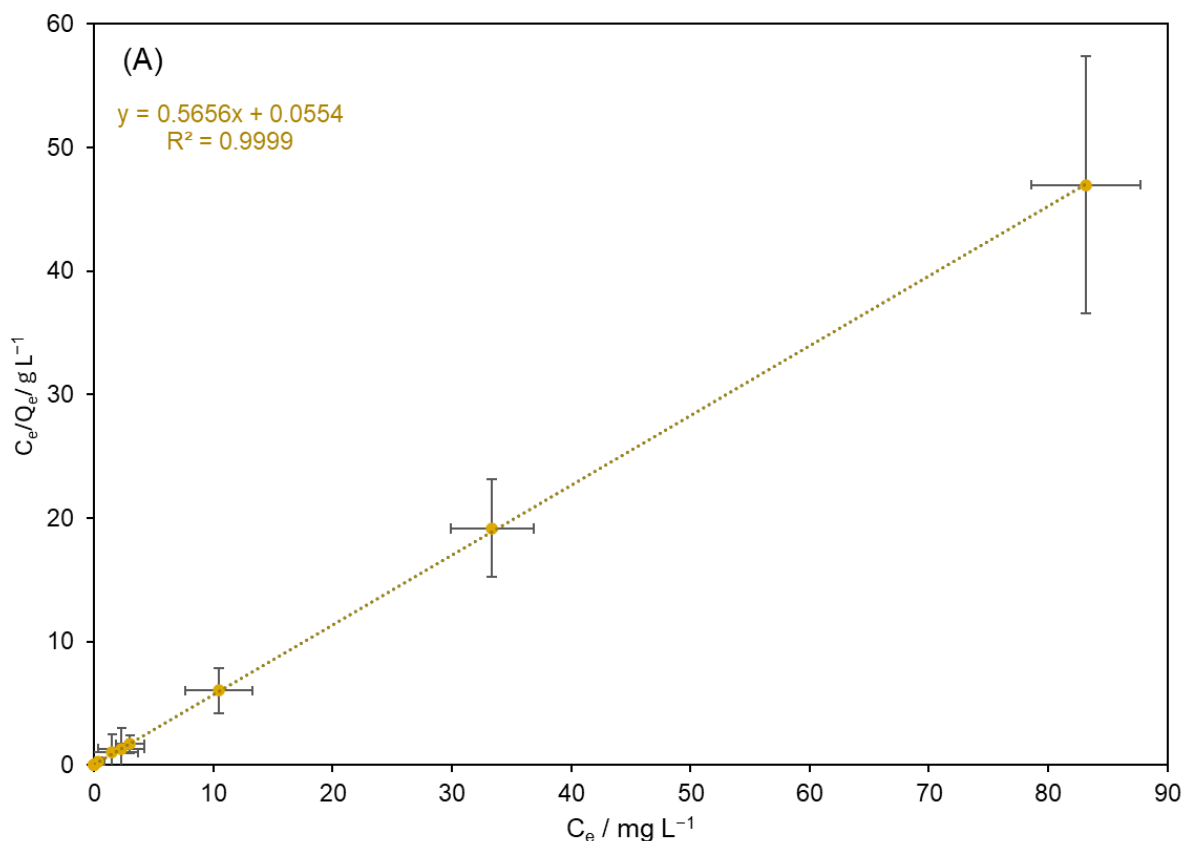


Figure 3-7. (A) Linear Langmuir and (B) Freundlich linear isotherms, associated with the adsorption of anionic dye AB10B from solution onto a DMAM-phenol functionalised cloth.

It can be seen that 100 % dye extraction for concentrations far below the saturation limit give rise to values of  $C_e = 0 \text{ g L}^{-1}$ , which coincides with the Henry region discussed above. Reduced extraction percentages at concentrations just below the adsorption capacity yield the characteristic “L-shape” adsorption curve,<sup>277</sup> before the plot plateaus at a value of  $Q_e \approx 1.74 \text{ mg g}^{-1}$  once the saturation limit has been reached. Indeed, this sharp increase followed by rapid plateau behaviour has been observed previously by Tian et al. and Yu et al. for the adsorption of AB10B.<sup>278,279</sup> In the case of Tian et al., the estimated adsorption capacity from the Langmuir isotherm was identical to the experimentally calculated value. Based on visual appearance, it appears that the Langmuir isotherm does provide a better fit for the adsorption of AB10B onto a DMAM-phenol functionalised cloth. However, despite being similar in value, the  $\chi^2$  value for the Langmuir isotherm (3.40) is greater than the  $\chi^2$  value of the Freundlich isotherm (3.10).

However, by analysing the linear forms of the isotherms, it can be much more clearly seen that the adsorption is modelled by a Langmuir isotherm, with an  $R^2$  value of 0.9998, compared to 0.5312 for the Freundlich isotherm. Consequently, the adsorption can be described as homogenous, with the dye forming a monolayer on the cloth.<sup>280, 281</sup> Each adsorbent site can only bind a single molecule, while being independent from the occupancy

of a neighbouring adsorbent site—each site is equivalent in terms of adsorption energy and adjacent adsorbed molecules do not interact.

Given that adsorption follows a Langmuir isotherm, the Langmuir constant,  $K_L$ , the estimated adsorption capacity,  $Q_0$ , and the dimensionless separation factor,  $R_L$ , can be calculated (Table 3-7 and Table 3-8).<sup>282</sup> The value of  $R_L$  represents the favourability of Langmuir adsorption. Adsorption is determined to be unfavourable if  $R_L > 1$ , favourable if  $0 < R_L < 1$ , and irreversible if  $R_L = 0$ .  $Q_0$  is determined by calculating the inverse of the gradient, and  $K_L$  and  $R_L$  are calculated according to Equations (3-3) and (3-4) respectively, where  $c_i$  is the initial dye concentration. The estimated values of adsorption capacity ( $1.77 \pm 0.09 \text{ mg}_{\text{Dye}}\text{g}_{\text{Adsorbent}}^{-1}$  and  $1.75 \pm 0.67 \text{ mg}_{\text{Dye}}\text{g}_{\text{Adsorbent}}^{-1}$  determined from the linear and non-linear isotherms respectively) are almost identical to the experimentally calculated adsorption capacity ( $1.74 \pm 0.29 \text{ mg}_{\text{Dye}}\text{g}_{\text{cloth}}^{-1}$ ), lending further credence to the suitability of the Langmuir isotherm model. The  $R_L$  values are very low ( $< 1 \times 10^{-2}$  at all investigated concentrations using both non-linear and linear isotherm determined values of  $K_L$ ), indicating that adsorption of AB10B onto the DMAM-phenol functionalised cloths is very favourable. Table 3-7 also shows the estimated Langmuir constants, derived by optimising the constants for the non-linear form of the isotherm.

$$K_L = \frac{1}{\text{Intercept} \times Q_0} \quad (3-3)$$

$$R_L = \frac{1}{1 + K_L c_i} \quad (3-4)$$

Table 3-7. Adsorption capacity ( $Q_0$ ) and Langmuir constant ( $K_L$ ) for the adsorption of anionic dye AB10B by a DMAM-phenol functionalised cloth, determined following fitting of linear and non-linear Langmuir adsorption isotherms. For the linear isotherm, error values for gradient,  $Q_0$  and intercept have been calculated by using the “Data Analysis—Regression” tool in excel, with a confidence interval of 95 %. The error value for  $K_L$  was determined via error propagation. As the value for the intercept lies very close to 0 ( $0.0935 \pm 0.0528$ ), the small error value constitutes a high percentage error. As such, when propagating this error with the error for  $Q_0$ , the error for  $K_L$  is an unrealistically high value. For the non-linear isotherm, the errors were calculated by averaging the percentage error between each data point and the theoretically calculated value and applying this to the determined values of  $Q_0$  and  $K_L$ . Owing to the 100 % error values obtained for when the experimental value of  $Q_e = 0$  was not predicted, these error values are unrealistically high.

Form of isotherm	Gradient / g $\text{mg}^{-1}$	$Q_0 / \text{mg g}^{-1}$	Intercept / g $\text{L}^{-1}$	$K_L / \text{L mg}^{-1}$
Linear	$0.565 \pm 0.002$	(Calculated from inverse of gradient) $1.77 \pm 0.005$	$0.0935 \pm 0.0528$	(Calculated by: $(1/(\text{intercept} \times Q_0)))$ $18.93 \pm 6.09$
Non-Linear	N/A	$1.75 \pm 0.67$	N/A	$8.39 \pm 3.23$



Table 3-8. Values of  $R_L$  dependent on initial dye concentration for the adsorption of AB10B onto DMAM-phenol functionalised cloths, calculated from the  $K_L$  values determined from the linear and non-linear Langmuir isotherms. The error values been calculated from the error in  $K_L$ .

Initial Dye Concentration / mg L <sup>-1</sup>	$R_L$ (linear)	$R_L$ (non-linear)
20	0.0026 ± 0.0008	0.0059 ± 0.0023
25	0.0021 ± 0.0007	0.0047 ± 0.0018
50	0.0011 ± 0.0003	0.0024 ± 0.0009
100	0.0005 ± 0.0002	0.0012 ± 0.0004

### 3.3.3.3 Thickness Dependence on Adsorption Capacity

The experiment was repeated by calculating the adsorption capacity of a meltblown TPU cloth, coated with pulsed plasma poly(4-VBC) for either half (10 min) or double (40 min) the typical reaction time, before derivatisation with DMAM-phenol. The cloths were left to spin in a 50 mg L<sup>-1</sup> AB10B solution, and the concentration of dye removed after > 6 h was calculated (Figure 3-8). The deposition of pulsed plasma poly(4-VBC) was determined to be uniform for the first 20 min of deposition, with a deposition rate of 43.2 ± 3.0 nm min<sup>-1</sup>, which is in line with previous findings.<sup>251</sup> While extending the deposition time to 40 min resulted in a slight loss in proportionality, there are nevertheless large differences in film thickness between those deposited for 10, 20 and 40 min. The adsorption capacities towards following deposition of pulsed plasma poly(4-VBC) for both 10 and 40 min are almost identical (1.91 ± 0.32 and 1.87 ± 0.32 mg<sub>Dye</sub>g<sub>Cloth</sub><sup>-1</sup> respectively) and are within error of the value for 20 min deposition (1.74 ± 0.29 mg<sub>Dye</sub>g<sub>Cloth</sub><sup>-1</sup>). Consequently, it can be implied that dye extraction is independent of film thickness.

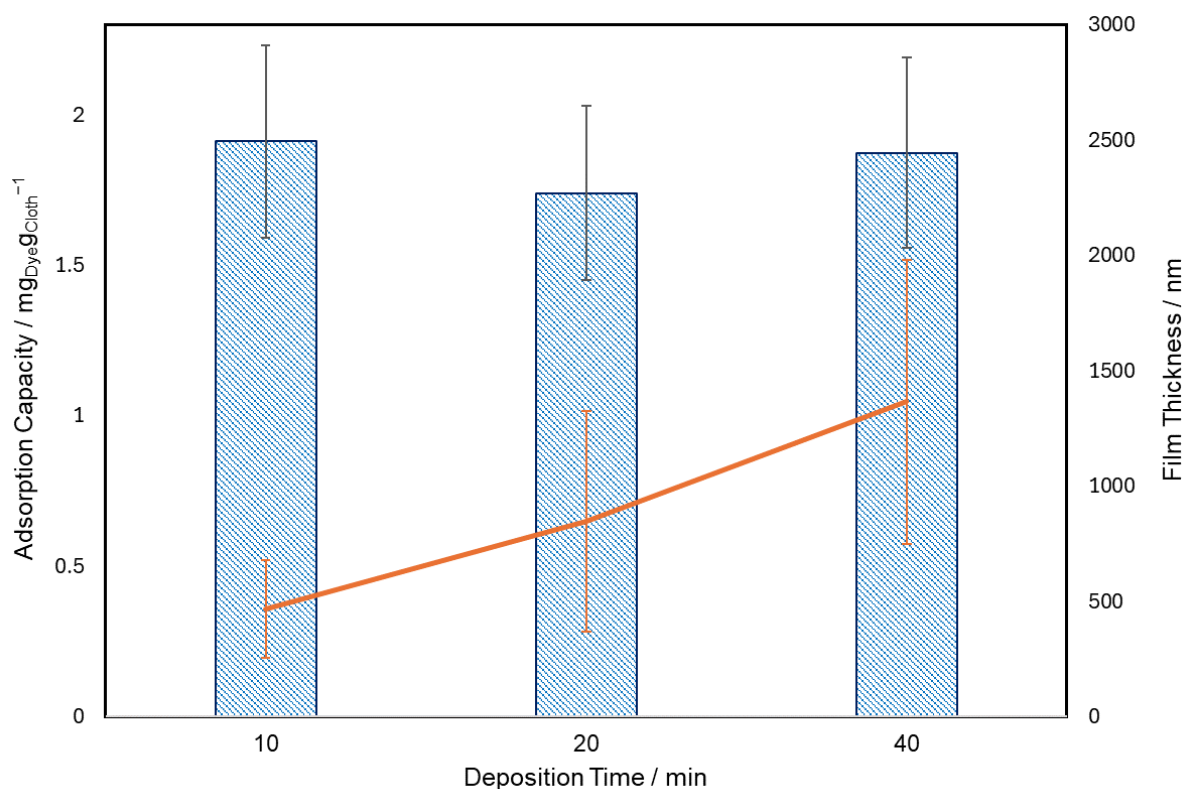


Figure 3-8. Maximum adsorption capacity for a DMAM-phenol derivatised, pulsed plasma poly(4-VBC) coated TPU cloths, following deposition for either 10, 20 or 40 min towards  $50 \text{ mg L}^{-1}$  anionic dye AB10B solutions (blue bars). The thickness of the deposited pulsed plasma poly(4-VBC) films (red line) has been overlain.

### 3.3.4 Adsorption Kinetics

Kinetic studies were performed by recording the concentration of a  $20 \text{ mg L}^{-1}$  AB10B solution removed by a DMAM-phenol functionalised cloth over specific time intervals under static filtration conditions. In pseudo-first order kinetics, one of the reagents is typically found in excess, meaning that its concentration will remain relatively unchanged, and so is adsorbed at a constant rate, proportional to the number of adsorption sites.<sup>283,284,285</sup> Alternatively, pseudo-second order kinetics occur in systems in which the sorption process is described by two competitive reversible second-order reactions at higher sorbate/sorbent ratios alongside a reversible second-order reaction at low sorbate/sorbent ratios.<sup>283</sup> It was determined that equilibrium occurred after ca. 210 min, which was equivalent to a maximum adsorption capacity of  $1.81 \pm 0.14 \text{ mg}_{\text{Dye}} \text{g}_{\text{Cloth}}^{-1}$ , in line with the adsorption capacities obtained in Section 3.3.

From the data obtained, the pseudo-first- and pseudo-second-order kinetic models could be plotted in their linearised form (Figure 3-9). The graphical equations and  $R^2$  values are presented on the graphs, which show that the data appears to be better fit by a pseudo-second order reaction model.

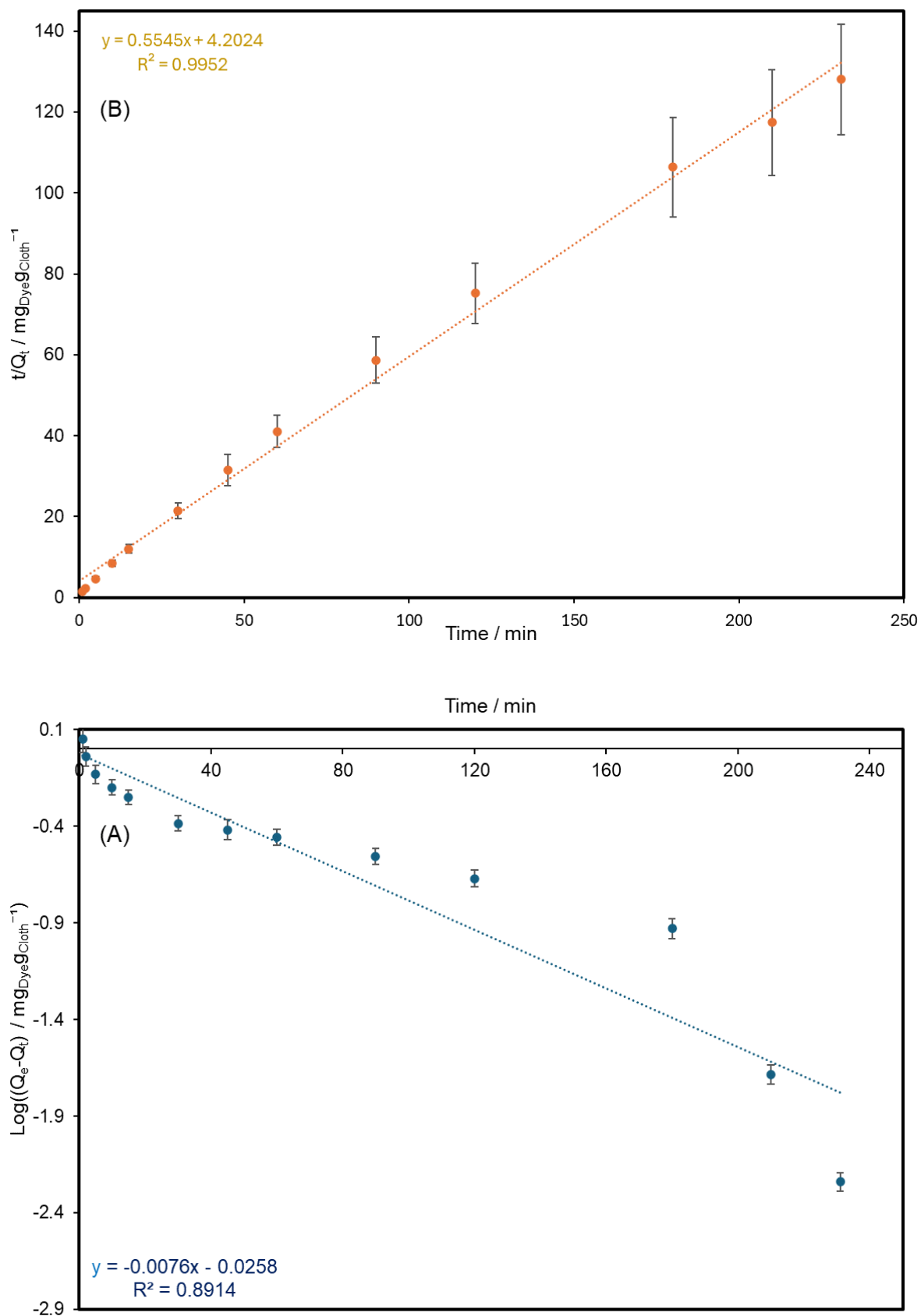


Figure 3-9. Linear forms of the (A) pseudo-first- and (B) pseudo-second-order kinetic models for the adsorption of  $20 \text{ mg L}^{-1}$  AB10B (anionic dye) with a DMAM-phenol functional cloth.

However, several publications have demonstrated the drawbacks behind fitting the data to the linearised forms of the equations, as the assumptions made in linearising the equations give a stronger weighting to values closer to equilibrium, meaning that pseudo-second order kinetics are almost always determined to be the kinetic mechanism, regardless of whether that model is correct.<sup>286, 287, 288, 289</sup> It is therefore recommended that fits are determined for the non-linear form. To that end, the raw data was plotted, and pseudo-first and pseudo-second order kinetic plots were determined, by performing a least-squares analysis on the fit, solved by adjusting values of  $k_1$  and  $k_2$  until the sum of the squares between raw data and fitted data were minimised (Figure 3-10). The determined values of  $k_1$  and  $k_2$  were  $0.154 \pm 0.034 \text{ min}^{-1}$  and  $0.147 \pm 0.020 \text{ g}_{\text{Cloth}}\text{mg}_{\text{Dye}}^{-1}\text{min}^{-1}$  respectively. It can be observed visually that although neither fit appears to be a perfect match, the pseudo-second order model gives rise to a better fit, which is backed up by the least squares data, which yields a value of  $1.13 \text{ mg}_{\text{Dye}}^2\text{g}_{\text{Cloth}}^{-2}$  for the pseudo-first order fit, and  $0.46 \text{ mg}_{\text{Dye}}^2\text{g}_{\text{Cloth}}^{-2}$  for the pseudo-second order fit.

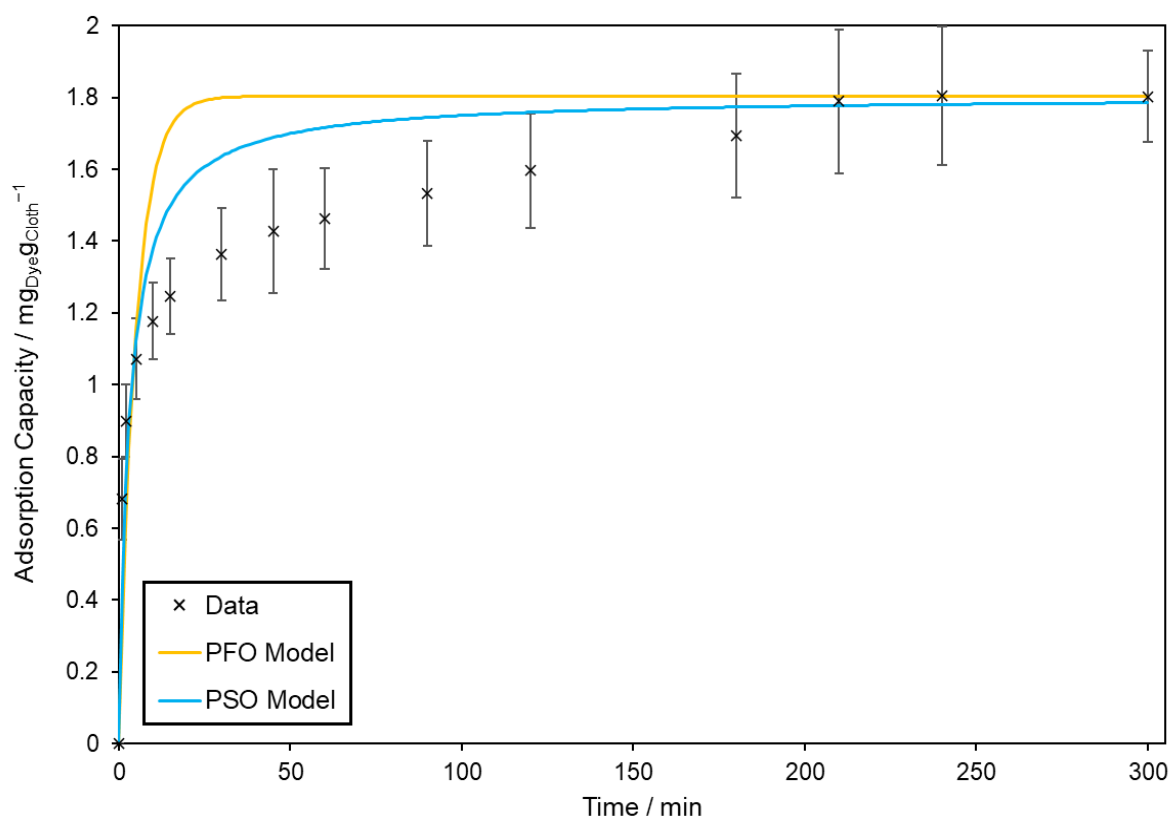


Figure 3-10. Pseudo-first order (orange) and pseudo-second order (blue) kinetic fits for the adsorption of  $20 \text{ mg L}^{-1}$  AB10B (anionic dye) onto a DMAM-phenol functionalised cloth spun at 40 rpm for 5 h.

For the sake of completeness, the rate constant values determined from the linear fits were also determined (Table 3-9)— $k_1$  is determined by multiplying the gradient by  $-2.303$ , and

$k_2$  is determined by taking the inverse of the intercept and dividing that by the square of the maximum adsorption capacity.

Table 3-9. Determined values for rate constants  $k_1$  and  $k_2$ , using non-linear and linear models, for the adsorption of 20 mg L<sup>-1</sup> AB10B (anionic dye) onto a DMAM-phenol functionalised cloth, spun at 40 rpm for 5 h. For the linear plots, the errors were calculated by determining the percentage error in the regression analysis for the gradient and intercept (where appropriate) calculations and applying this to the final rate constant values. For the non-linear plots, the errors were calculated by averaging the percentage error between each data point and the theoretically calculated value and applying this to the final rate constant value.

Variable	Non-Linear / min <sup>-1</sup>	Linear / g <sub>Cloth</sub> mg <sub>Dye</sub> <sup>-1</sup> min <sup>-1</sup>
$k_1$	0.154 ± 0.034	0.0153 ± 0.0005
$k_2$	0.147 ± 0.020	0.0820 ± 0.0181

### 3.4.1. Mass Transfer Investigation

Given the use of the Fisherbrand™ mini-rotator to perform the experiment, it is important to investigate the potential mass-transfer implications of the equipment, in order to ensure that the kinetic data presented is an accurate representation of the chemistry, and not a representation of the ability of the equipment to transfer the dye to the active sites. Therefore, the experiment was repeated using half the usual spin speed (20 rpm), and data for the first hour of filtration was plotted (Figure 3-11). The cloths were left to spin overnight, to ensure that the system had reached equilibrium, which yielded an adsorption capacity of 1.77 ± 0.32 mg<sub>Dye</sub>g<sub>Cloth</sub><sup>-1</sup>, which is very close to the 1.81 ± 0.14 mg<sub>Dye</sub>g<sub>Cloth</sub><sup>-1</sup> value determined for the cloths spun at 40 rpm, demonstrating that adsorption had gone to completion. Once again, the pseudo-second order fit appears to give a superior match to the observed data, which is backed up by a least-squares value of 0.141 mg<sup>2</sup><sub>Dye</sub>g<sub>Cloth</sub><sup>-2</sup>, compared to 0.599 mg<sup>2</sup><sub>Dye</sub>g<sub>Cloth</sub><sup>-2</sup> for the pseudo-first order fit.

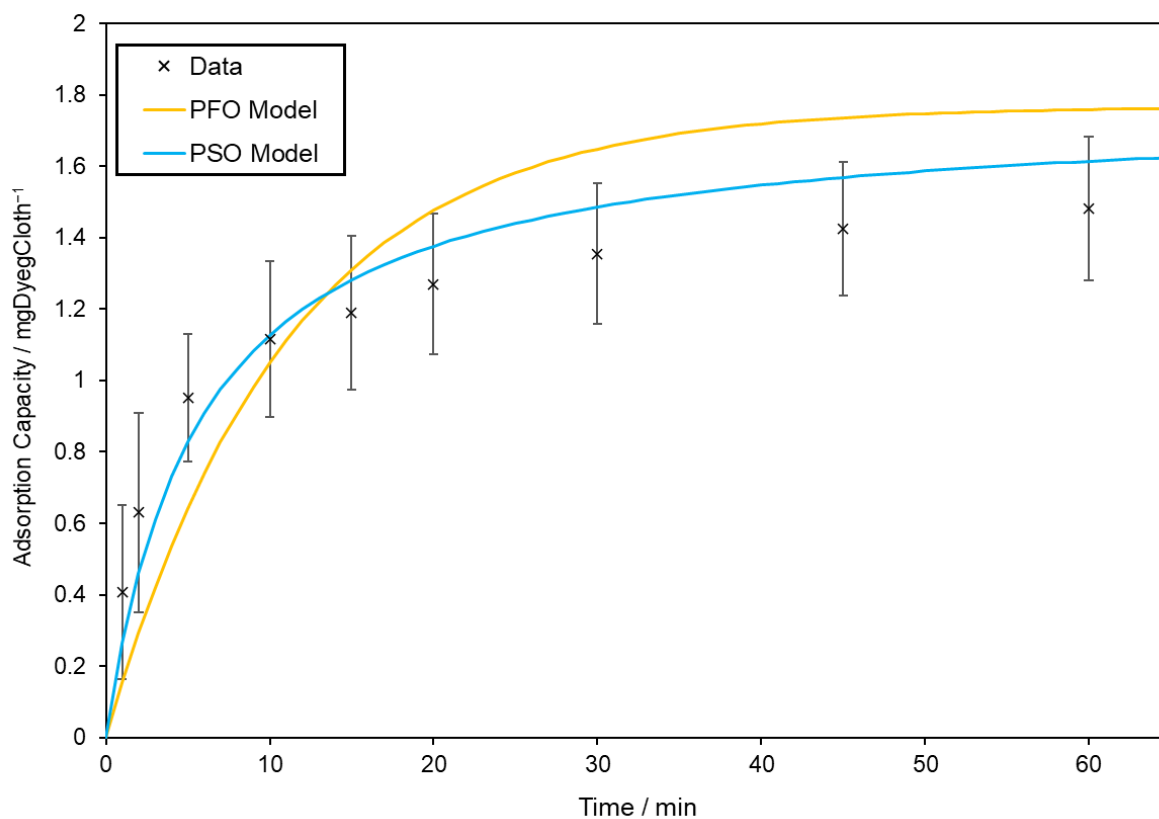


Figure 3-11. Pseudo-first order (orange) and pseudo-second order (blue) kinetic fits for the adsorption of  $20 \text{ mg L}^{-1}$  AB10B (anionic dye) onto a DMAM-phenol functionalised cloth spun at 20 rpm for 1 h.

To further verify this fit, linear forms of the pseudo-first and pseudo-second order kinetic models were plotted, despite their aforementioned limitations (Figure 3-12). Compared to the analysis provided above, a greater portion of the data has been taken away from the equilibrium value, and so the effect of the poor assumptions made in linearising the data will be lessened. Again, it can be seen that the pseudo-second order kinetic model provides a superior fit, with an  $R^2$  value of 0.999 compared to 0.858 for the pseudo-first order kinetic model.

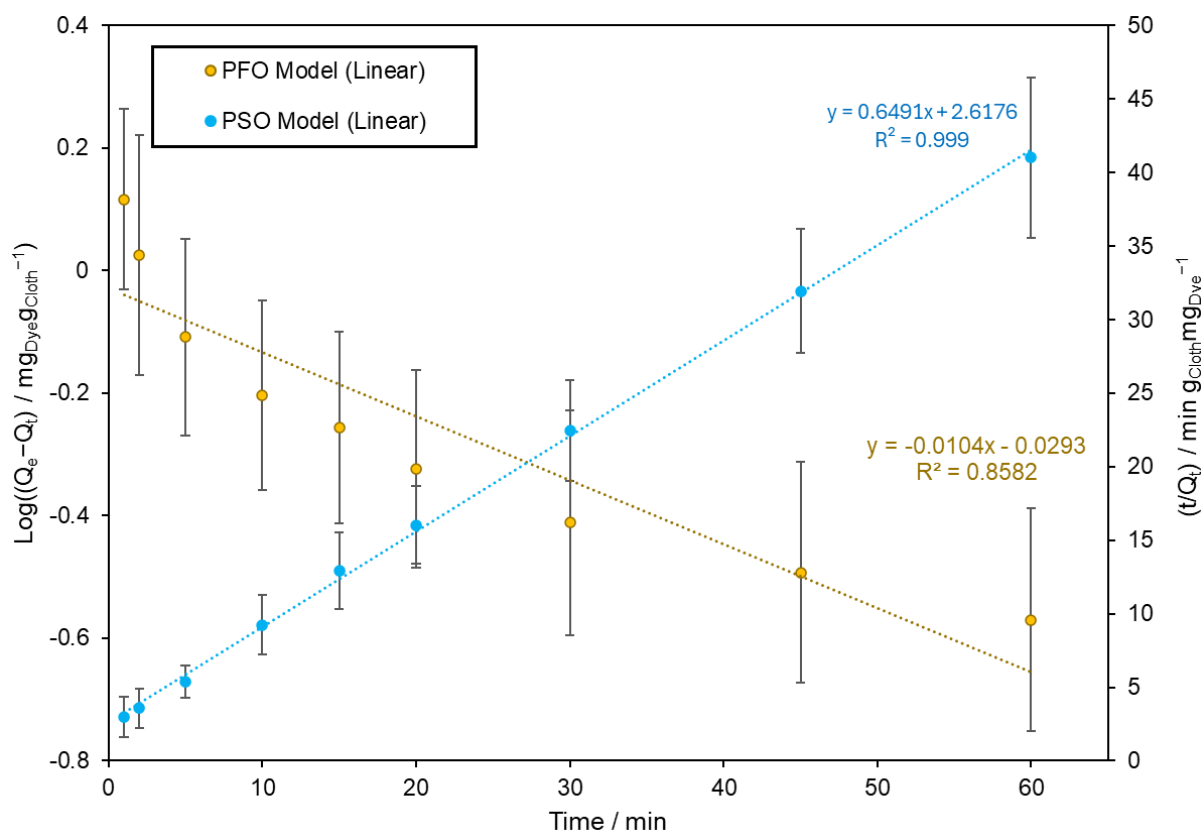


Figure 3-12. Linear fits for the pseudo-first order (orange) and pseudo-second order (blue) kinetic models for the kinetic fits for the adsorption of 20 mg L<sup>-1</sup> AB10B (anionic dye) onto a DMAM-phenol functionalised cloth spun at 20 rpm for 1 h. The pseudo-first order fit has been plotted on the left-hand Y-axis, and the pseudo-second order fit has been plotted on the right-hand Y-axis. Each data point corresponds to the average of three repeats.

Expanding the analysis, the kinetic plots for the cloths spun at 20 rpm and 40 rpm have been superimposed (Figure 3-13). Although the adsorption capacities for the cloth spun at 40 rpm do appear initially greater, the values become very similar after 10 min, and almost identical after 30 min. Furthermore, it should be emphasised that at all time intervals, the calculated adsorption capacities are within error range. As such, it should be stated that the use of the Fisherbrand™ mini-rotator may not give rise to mass-transport issues, but if it does, these only arise during the first 5–10 min. As such, the obtained kinetic plots can be assumed to accurately describe the adsorption behaviour of the AB10B dye onto the DMAM-phenol coated cloth.

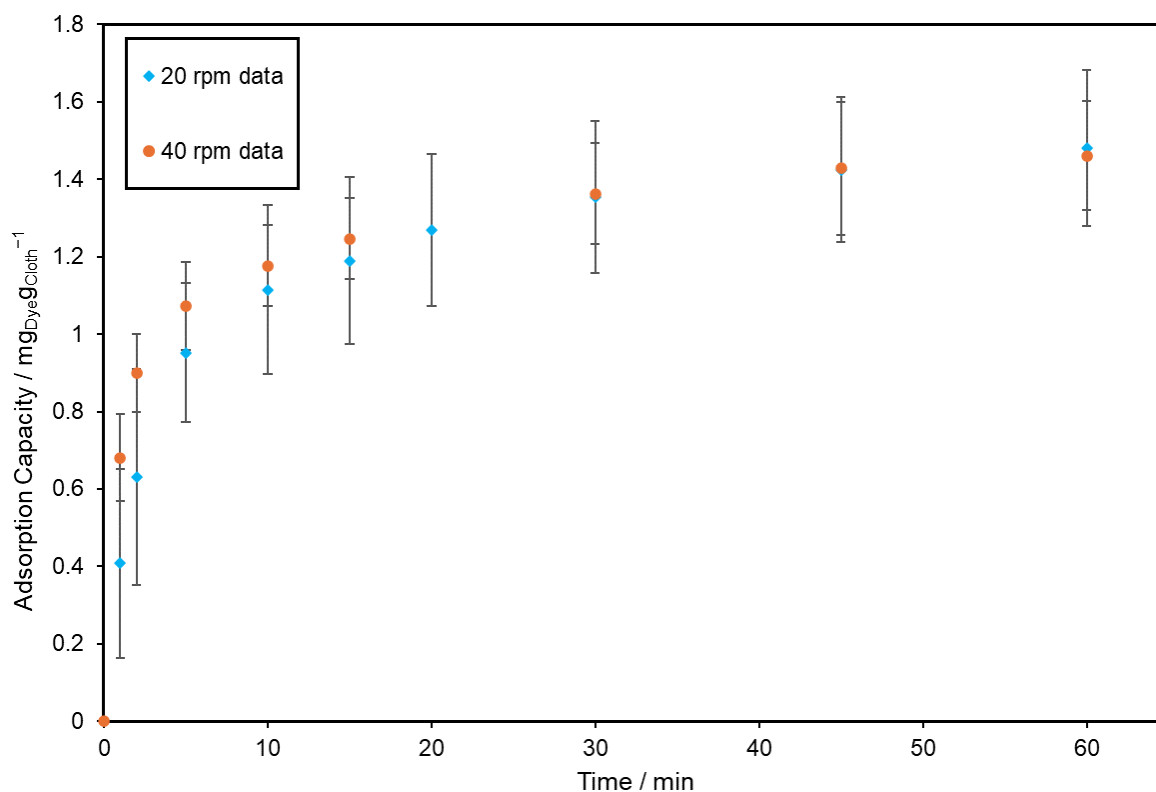


Figure 3-13. Pseudo-second order plots for the first 60 min of the adsorption of 20 mg L<sup>-1</sup> AB10B (anionic dye) onto DMAM-phenol functionalised cloths spun at 20 (blue) and 40 (orange) rpm.

### 3.3.5 Active Site Determination

One method of investigating the adsorption mechanism is by determining the number of amine (adsorption) sites on the surface. By comparing this value with the number of moles of dye adsorbed, the ratio of active sites to adsorbed dye molecules will help elucidate the type of adsorption. If there are far more molecules of dye than adsorption sites, then multi-layers will have formed, implying that the adsorption is dominated by physisorption. If the numbers are similar, then it is likely that a monolayer will have formed, with each amine site binding to one dye molecule. If there are twice as many amine sites as dye molecules, then it is likely that the dyes require two amine sites to bind to them. If there are far more sites than dye molecules, then again, a monolayer will have formed, however there could be a strong degree of hindrance on the surface, wherein the dyes (e.g., due to their size—the dyes in this investigation exhibit a length of ca. 2 nm, which is greater than the 0.6 nm diameter exhibited by phenol, although it is understood that the DMAM functionality will increase this length)<sup>290</sup> inhibit a second dye molecule from attaching to a neighbouring binding site. After acidifying the DMAM-phenol cloths with 0.05 M HCl and back-titrating with NaOH, a slight decrease in volume of NaOH required to neutralise the HCl solution shaken with the DMAM-phenol functionalised cloth (Table 3-10) was observed, when compared to the volume of NaOH



required to neutralise the HCl solution, and the HCl solution, shaken with an unfunctionalised TPU cloth.

Table 3-10. Volume of NaOH required to neutralise a HCl solution, and the same HCl solution, when shaken with an uncoated TPU cloth, and a DMAM-phenol functionalised cloth. By assuming complete dissociation of NaOH, the moles of HCl in solution has been calculated for each system.

Acid Solution	Volume of NaOH required to neutralise / mL	Calculated moles of HCl in solution / mmol
HCl	215.47 ± 0.16	0.4309 ± 0.0003
HCl + TPU Cloth	215.42 ± 0.10	0.4308 ± 0.0002
HCl + DMAM-phenol functionalised cloth	215.05 ± 0.10	0.4301 ± 0.0002

It was determined that the change in number of moles of acid before and after shaking with the DMAM-phenol functionalised cloth was  $0.000733 \pm 0.000289$  mmol, which is equivalent to  $0.0179 \pm 0.0077$  mmol<sub>HgCloth</sub><sup>-1</sup>. As the cloths are capable of extracting  $1.74 \pm 0.29$  mg<sub>AB10BgCloth</sub><sup>-1</sup>, which is equivalent to  $0.0028$  mmol<sub>AB10BgCloth</sub><sup>-1</sup>, this means that there are approximately 6 (~0.018/~0.003) times as many adsorbent sites as dye molecules bound to the surface. However, due to the high observed percentage error of 43.4 % (which is associated with small differences in volume), it is more appropriate to state that there are between 3 and 9 as many adsorbent sites as dye molecules bound to the surface, which is in the ballpark of a 1:1 or fewer amine:dye sites.

### 3.3.6 Cloth Recycling

Many previous studies have used aqueous solutions of NaOH in order to regenerate adsorbents, which have extracted AB10B from solution.<sup>231,232,233,234,235,236,237,238</sup> However, previous research within this group demonstrated that a 0.5 M NaOH/2 M NaCl mixture was superior for the regeneration of a DMAM-calixarene functionalised cloth, designed to remove chromium from solution.<sup>251</sup> Therefore, following dynamic filtration of a 20 mg L<sup>-1</sup> AB10B solution, DMAM-phenol functionalised cloths were regenerated with either 0.5 M NaOH/2 M NaCl or 1 M NaOH and the concentration of dye in the regeneration eluent measured by UV-Vis spectroscopy. Previously, optimising the regeneration fluids has been performed by comparing the concentration of contaminant in the regeneration eluent. However, it was immediately observed by simple visual observation that the concentration of dye found in the eluent never reached the concentration of dye removed. A potential cause of this observation is the destruction (and hence decolouration) of the dye due to NaOH addition. In order to test this hypothesis, 5 mL of 10 mg L<sup>-1</sup> AB10B solutions were mixed with either 3 mL H<sub>2</sub>O or 3 mL 1 M NaOH. It could be observed visually that the solution containing NaOH was notably less

intense in colour—an observation that was supported by the UV–Vis spectra (Figure 3-14) where the shape of the curve following dilution with NaOH has not only changed (implying chemical changes to the system), but the absorption maximum is lower, which explains the paler colour.

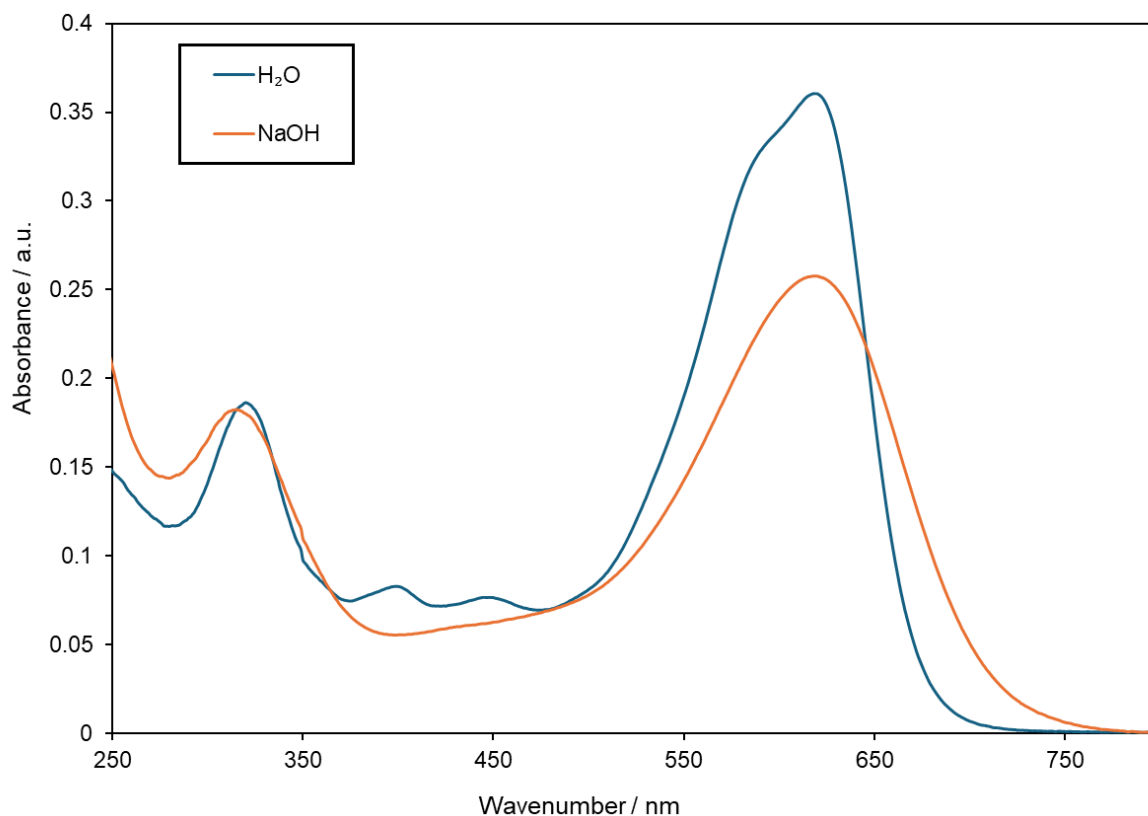


Figure 3-14. UV–Vis spectra of 6.25 mg L<sup>-1</sup> AB10B solution, made up with HP water (blue) or 0.375 M NaOH (orange). This figure demonstrates that the suitability of the regeneration solution cannot be determined by measuring the concentration of dye in the eluant, as the presence of base chemically effects the dye.

Consequently, the optimal regeneration fluid was determined by comparing the drop in dye extraction percentage following repeat cycles. However, post filtration, many of the filtrates following recycling with the 1 M NaOH solution turned pink (Figure 3-15) meaning that not all filtrations could give rise to obtainable extraction percentages following UV-Vis analysis.

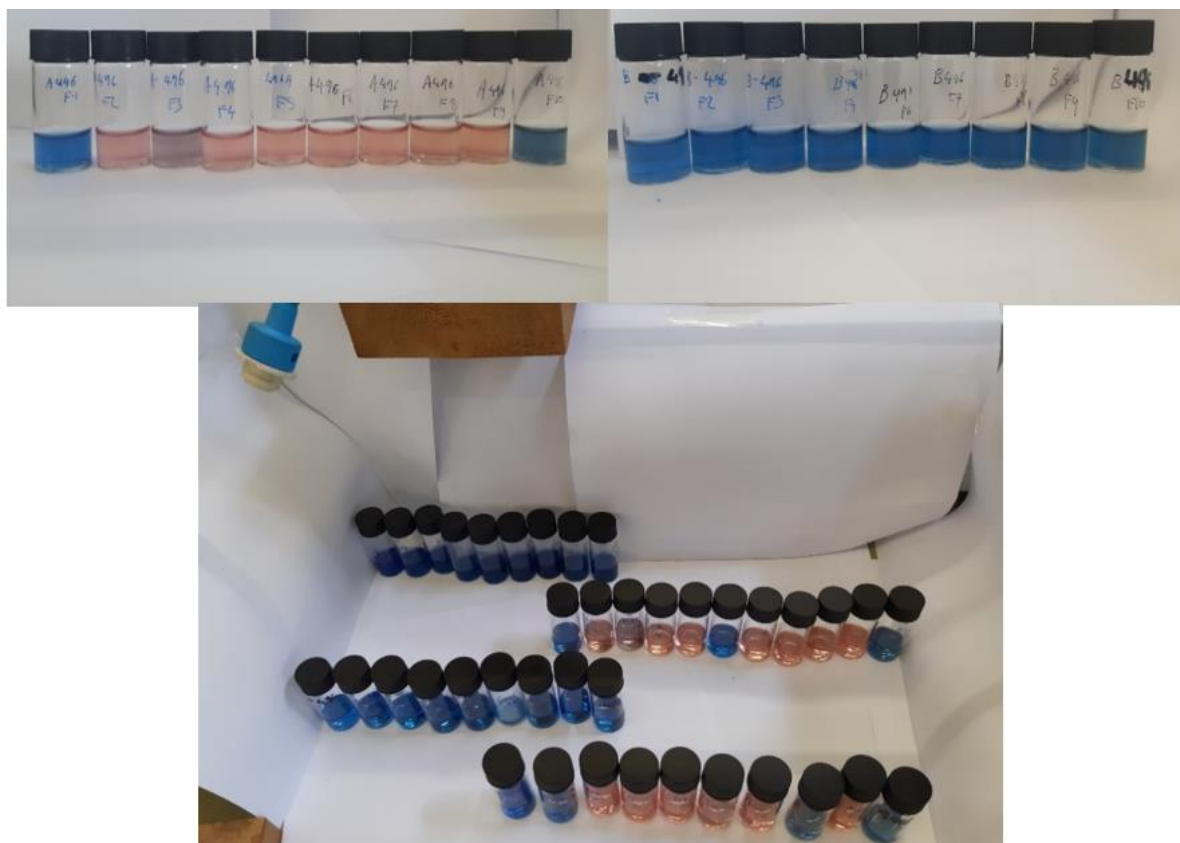


Figure 3-15. Colour of filtrates of a  $20 \text{ mg L}^{-1}$  AB10B (anionic dye) solution after filtration with a DMAM-phenol functionalised cloth following regeneration with 1 M NaOH (top left), 0.5 M NaOH/2 M NaCl (top right). Repeats of both sets of the filtrations have been combined (bottom). It can be seen that the use of the 1 M NaOH recycling solution leads to some of the filtrates of the dye extraction experiments turning pink over time, meaning that filtration efficiency could not be calculated for these samples. The bottom image demonstrates that this was a repeat occurrence.

Despite that, sufficient data has been obtained to plot the change in extraction percentage towards a  $20 \text{ mg L}^{-1}$  AB10B solution following several cycles of filtration and regeneration (Figure 3-16). It can be seen that the extraction percentage drops from 46.1 % to 12.9 % after 10 cycles following cloth regeneration with 1 M NaOH (corresponding to a decrease in adsorption capacity from  $0.94$  to  $0.26 \text{ mg}_{\text{Dye}}\text{g}_{\text{Cloth}}^{-1}$ ). On the other hand, the extraction percentage has only dropped from  $44.4 \pm 11.1$  % to  $34.1 \pm 13.3$  % (corresponding to a decrease in adsorption capacity from  $1.02 \pm 0.26$  to  $0.79 \pm 0.31 \text{ mg}_{\text{Dye}}\text{g}_{\text{Cloth}}^{-1}$ ) after the same number of cycles when using the 0.5 M NaOH/2 M NaCl mixture. The adsorption capacity values obtained are similar to those obtained for the dynamic filtration of  $10 \text{ mg L}^{-1}$  AB10B with a DMAM-phenol functionalised cloth ( $1.12 \pm 0.05 \text{ mg}_{\text{Dye}}\text{g}_{\text{Cloth}}^{-1}$ ), but due to the different extraction method, are much lower than the adsorption capacity towards  $20 \text{ mg L}^{-1}$  AB10B with a DMAM-phenol functionalised cloth following static filtration ( $1.76 \pm 0.19 \text{ mg}_{\text{Dye}}\text{g}_{\text{Cloth}}^{-1}$ ).

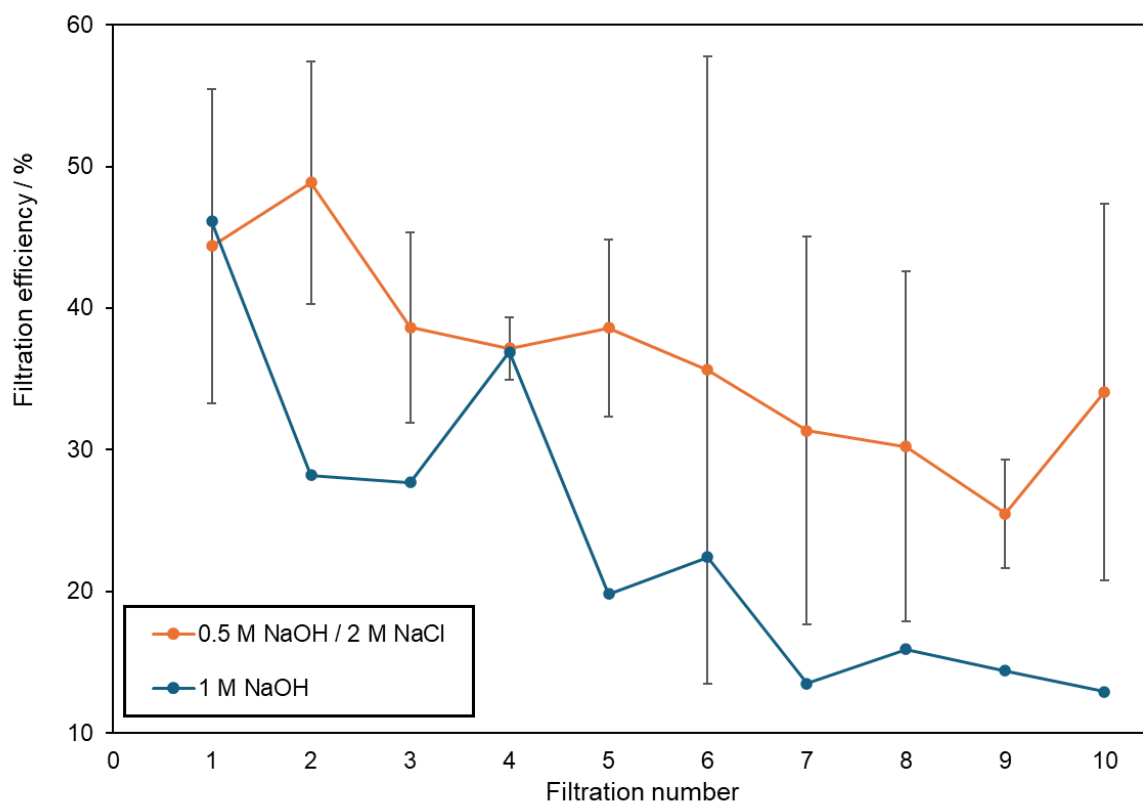


Figure 3-16. Filtration efficiency of a DMAM-phenol functionalised cloth towards  $20 \text{ mg L}^{-1}$  AB10B (anionic dye) following successive regeneration cycles using a  $0.5 \text{ M NaOH} / 2 \text{ M NaCl}$  solution (orange) and a  $1 \text{ M NaOH}$  solution (blue). This graph is comparing the effectiveness of the two regeneration solutions. It shows that despite starting with almost identical extraction percentages, after 10 cycles, the filtration efficiency following regeneration with  $0.5 \text{ M NaOH} / 2 \text{ M NaCl}$  solution is greater than when regenerating with  $1 \text{ M NaOH}$ .

The fact that the filtration percentage exhibited a smaller decrease in efficiency with the  $0.5 \text{ M NaOH} / 2 \text{ M NaCl}$  than with the  $1 \text{ M NaOH}$  solution indicates that the  $0.5 \text{ M NaOH} / 2 \text{ M NaCl}$  solution is the optimal regeneration solution. As such, to test the ability to recycle the DMAM-phenol functionalised cloth for the removal of AB10B at concentrations more likely to occur in real-world solutions, the repeated extraction of  $6 \text{ mg L}^{-1}$  AB10B followed by regeneration with a  $0.5 \text{ M NaOH} / 2 \text{ M NaCl}$  solution was performed (Figure 3-17). Here, it can be seen that extraction percentage remains close to 100 % after 10 successive filtrations, indicating that the DMAM-phenol functionalised cloth is capable of being repeatedly recycled for the purpose of AB10B extraction.

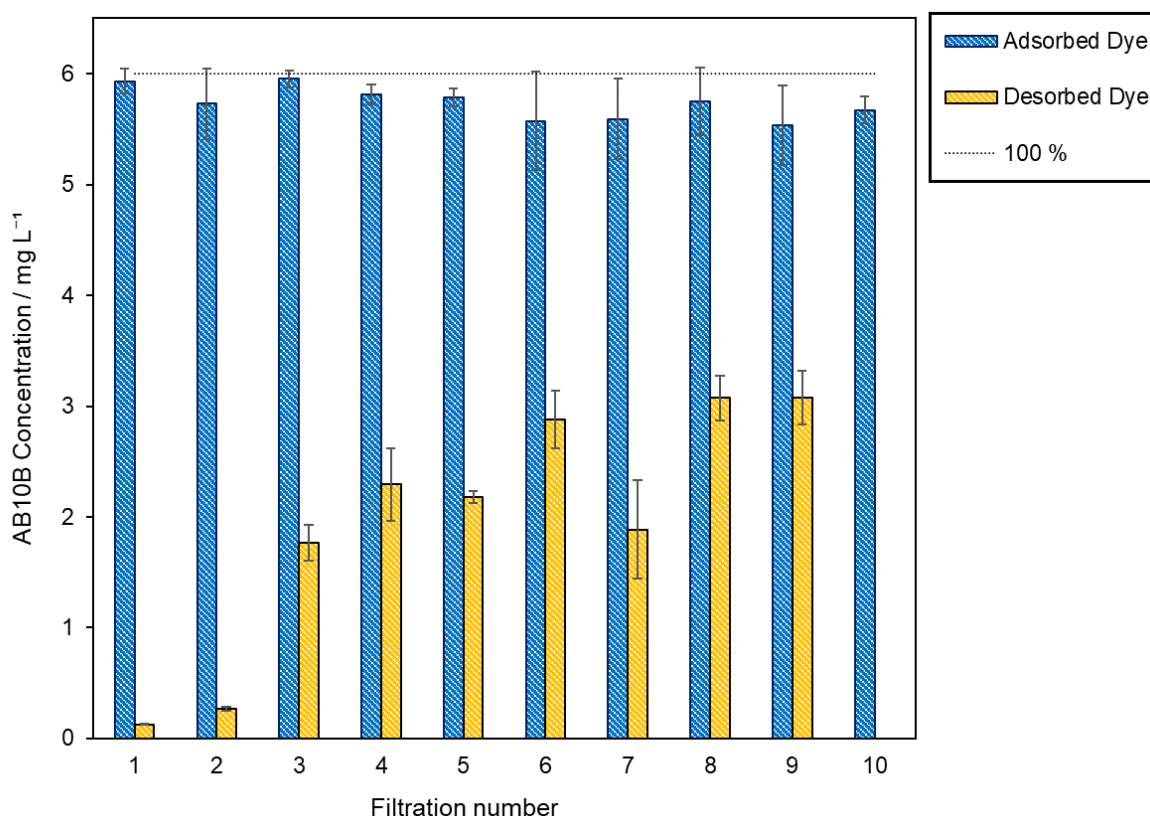


Figure 3-17. Concentration of AB10B removed from a 5 mL 6 mg L<sup>-1</sup> solution after ten successive filtrations by a DMAM-phenol functionalised cloth (blue), after having been regenerated with a 5 mL 0.5 M NaOH/2 M NaCl solution. The concentration of anionic dye AB10B recorded in the subsequent regeneration eluant is shown in orange—note that owing to the reasons provided above, this will not be an accurate measurement of the actual concentration of dye desorbed (but is rather a minimum concentration). The dashed line at 6 mg L<sup>-1</sup> indicates the theoretical 100 % dye removal mark. All concentrations were determined using UV–Vis spectroscopy.

It can also be observed that almost no dye is found in the regeneration eluent following the first two regeneration cycles. Aside from the decolouration of dye due to the NaOH, this was attributed to the adsorption capacity of the cloth not being reached, and so the Cl<sup>-</sup> ions in the regeneration fluid could be bound to the adsorption sites without having to displace the dye. In order to verify this theory, the concentration of dye found in the eluent for the experiment using 20 mg L<sup>-1</sup> AB10B was determined (Figure 3-18). It can be seen that the concentration of dye removed from the cloth was similar following each regeneration cycle, which supports the claim that dye is not seen in the regeneration eluent until cloth adsorption capacity has been reached. Furthermore, the values for concentration of dye desorbed following each cycle are similar to those observed for the experiment using 6 mg L<sup>-1</sup> AB10B (after the first 2 cycles), implying that similar concentrations of dye were released from the cloths each time, regardless of starting concentration during the filtration. Again, due to the reasoning provided above, the values obtained for concentration of dye desorbed will not be the actual value, due to the decolouration caused by the NaOH.

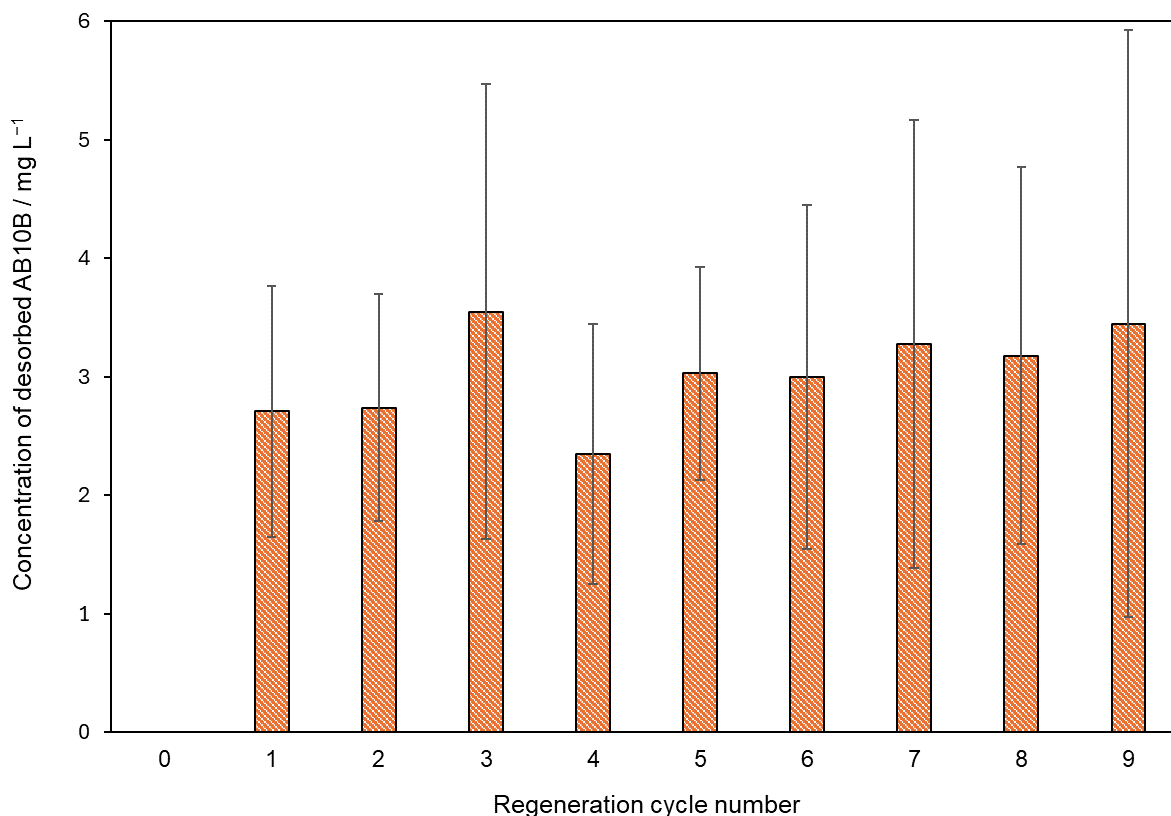


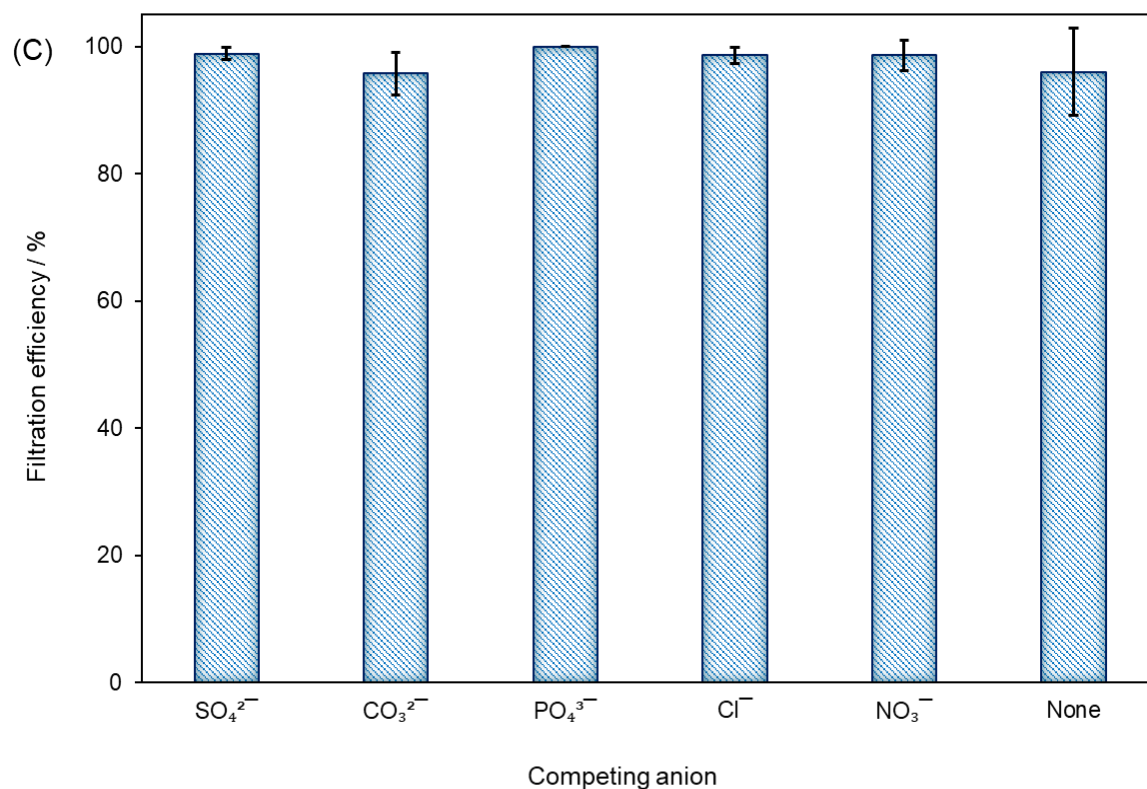
Figure 3-18. Concentration of anionic dye AB10B recorded in the 5 mL eluent following each regeneration cycle of a DMAM-phenol functionalised cloth, used to filter 20 mg L<sup>-1</sup> AB10B from a 5 mL solution.

### 3.3.7 Selectivity of Functional Cloths

#### 3.3.7.1 Competing Anions

The suitability of DMAM-phenol and DMAM-calixarene functionalised cloths for extracting the anionic AB10B from real-world water samples was further investigated by observing the selectivity of the cloths towards AB10B when in competition with other anionic species. The anions chosen—chloride, phosphate, sulfate, carbonate and nitrate—are all commonly found in solution. Solutions were prepared using either a 1:10 or 1:100 mole ratio of dye:competing anion, in order to replicate selectivity studies of anions previously performed.<sup>251,291</sup> For the DMAM-calixarene functionalised cloths (Figure 3-19(A) and (B)), the extraction capabilities towards AB10B are superior in the 1:10 mole ratio solutions than their 1:100 mole ratio counterparts. This is to be expected, as the 1:100 mole ratio solutions contain significantly more competing anions, which can saturate the adsorption sites. The nitrate ions gave rise to the greatest decrease in dye capture ( $64.6 \pm 11.5\%$ ). This is in line with the results obtained by Bieber et al. wherein the presence of nitrate in a 1:100 mole ratio of Cr(VI):NO<sub>3</sub><sup>-</sup> resulted in a decrease in chromium capture from ca. 97 % to ca. 65 % from a 2 mg L<sup>-1</sup> Cr(VI) solution, attributed to the similar size (thermochemical radius of nitrate =  $0.200 \pm 0.019$  nm vs  $0.229 \pm$

0.019 nm for  $\text{CrO}_4^{2-}$ )<sup>292</sup> of the nitrate ion.<sup>251</sup> Here however, no such effect was observed for the DMAM-phenol functionalised cloths (Figure 3-19(C)). The cloths yielded extraction percentages of ca. 100 % for all solutions, which demonstrates that the DMAM-phenol functionalised cloth is highly selective towards AB10B. The 1:10 mole ratio experiments were not performed, as the DMAM-calixarene experiments demonstrate that a lower concentration of competing anion results in greater dye extraction. Owing to the observed superior extraction performance when in the presence of competing anions, it is clear that the DMAM-phenol functionalised cloth is more selective towards AB10B than DMAM-calixarene.





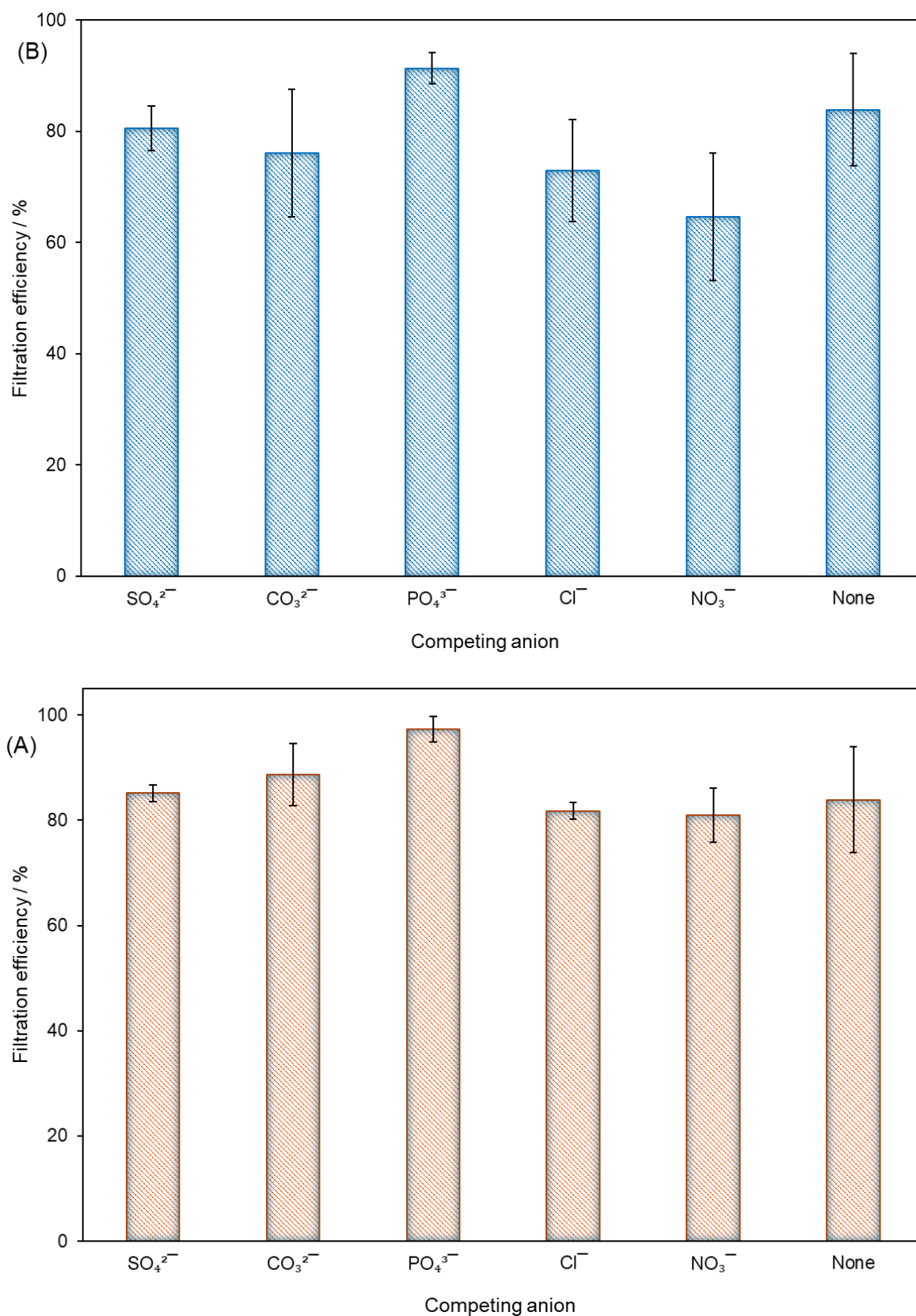


Figure 3-19. Extraction percentage towards  $6 \text{ mg L}^{-1}$  AB10B (anionic dye) when in competition with either a 1:10 (A) or 1:100 mole ratio (B and C) of dye:anion, when passed through a pulsed plasma poly(4-VBC) coated TPU cloth, derivatised with either DMAM-calixarene (A and B) or DMAM-phenol (C).



### 3.3.7.2 Competing Dyes

Having demonstrated selectivity towards AB10B when in competition with common anions, it is also important to demonstrate selectivity when in a mixture of dyes—polluted water will typically contain a number of dye species, rather than one sole contaminant.<sup>293</sup> As such, a solution containing  $6 \text{ mg L}^{-1}$  AB10B and  $6 \text{ mg L}^{-1}$  MB was made up. The solution appears purple in colour, and it can be seen that significant changes in the UV–Vis spectrum of the mixed solution occurs (Figure 3-20), rather than simply being a combination of the two individual dyes. While an absorption maximum at  $663 \text{ nm}$ , attributed to the MB, can be made out, the maximum absorbance of the mixture is significantly lower than for  $6 \text{ mg L}^{-1}$  MB. Furthermore, this maximum absorption occurs at  $552 \text{ nm}$ , which does not exist as a local maximum for either MB or AB10B. These changes in the UV–Vis spectrum imply that the dyes have undergone a chemical reaction, rather than co-existing in solution, and thus making it more difficult to extract the anionic AB10B with the DMAM-phenol functionalised cloth.<sup>294</sup>

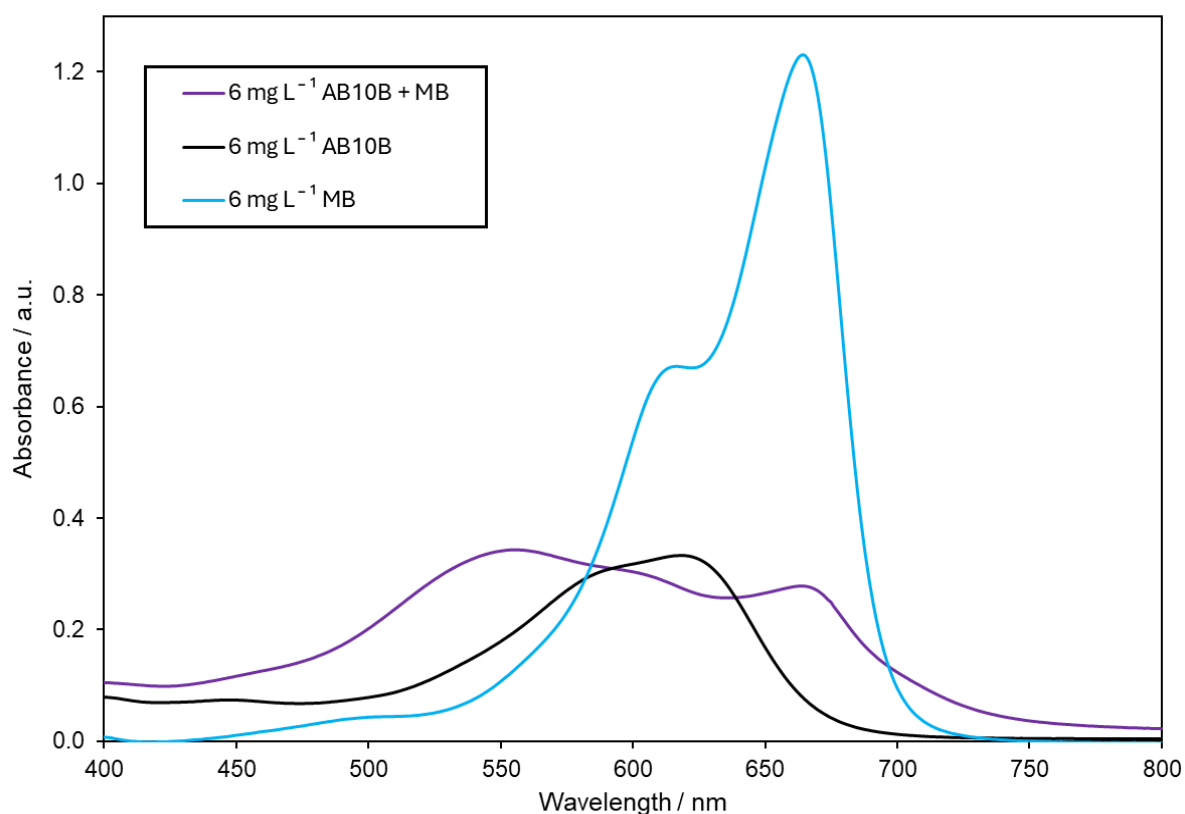


Figure 3-20. UV–Vis spectra of  $6 \text{ mg L}^{-1}$  solutions of cationic dye MB (blue), anionic dye AB10B (black) and a mixture of AB10B and MB (purple).

The UV–Vis spectra of the  $6 \text{ mg L}^{-1}$  mixed solution before and after filtration with an uncoated TPU cloth, a TPU cloth coated with pulsed plasma poly(4-VBC) and a VBC coated TPU cloth, functionalised with DMAM-phenol, are shown in Figure 3-21. It can be seen that when using the uncoated cloth and pulsed plasma poly(4-VBC) coated cloth, the shape of the

UV-Vis spectra of the filtrates remain unchanged. However, the absorbances of both filtrates are lower than the starting mixture, implying that some dye is removed by the control cloths. The absorbance is lower following filtration with the pulsed plasma poly(4-VBC) coated cloth than the uncoated control cloth. On the other hand, the UV-Vis spectrum of the filtrate using the DMAM-phenol functionalised cloths has changed shape, and now matches the shape of the UV-Vis spectrum of MB. This implies that the AB10B has been successfully removed, leaving behind the cationic MB solution. This observation in the UV-Vis spectra is confirmed visually, where the purple mixed starting solution became a light turquoise (the colour of MB) after filtration.

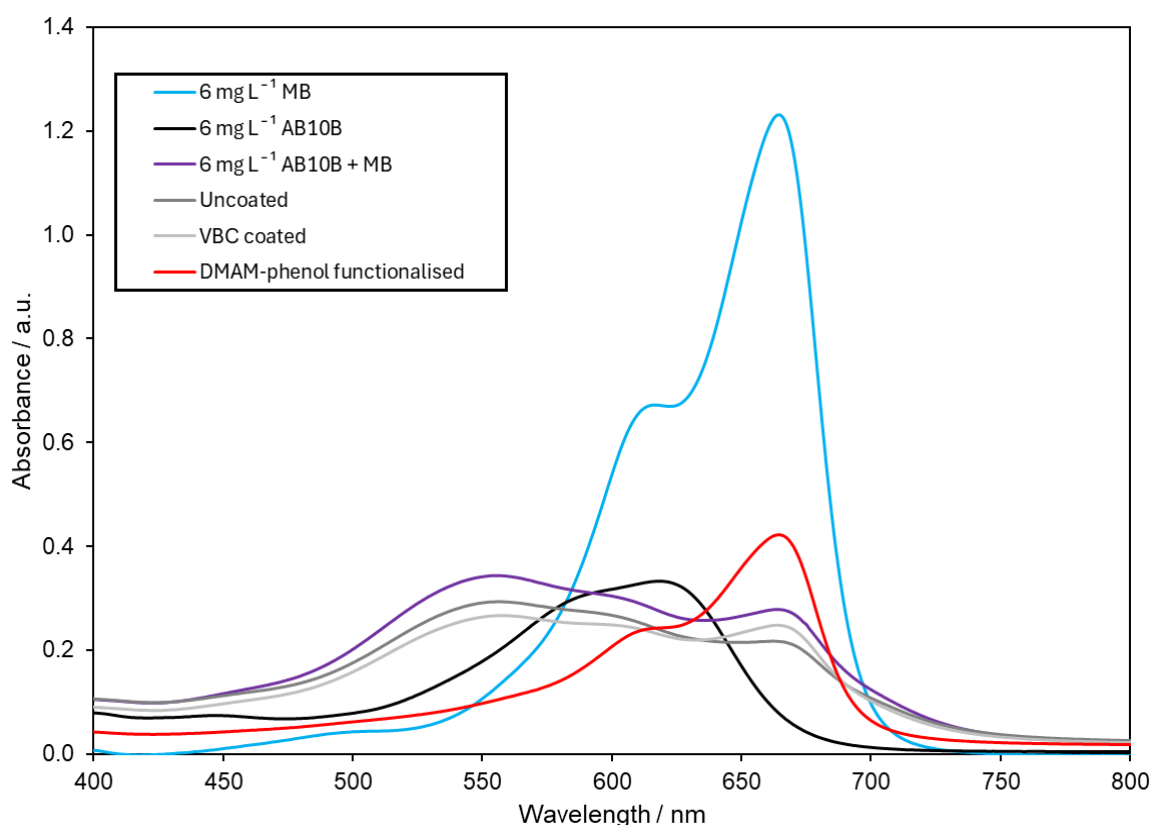


Figure 3-21. UV-Vis spectra of  $6 \text{ mg L}^{-1}$  mixed solution of anionic dye AB10B and cationic dye MB (purple), and the same solution when filtered with an uncoated TPU cloth (dark grey), a pulsed plasma poly(4-VBC) coated cloth (light grey) and a DMAM-phenol functionalised cloth (red). For reference, the UV-Vis spectra of  $6 \text{ mg L}^{-1}$  solutions of cationic dye MB and anionic dye AB10B are shown in blue and black respectively.

A crude calculation can be performed to determine the quantity of dye that has been extracted by the non-functionalised carbon cloths. By comparing the absorption at the new absorbance maximum at 552 nm of the starting mixed solution with the filtrates, an estimated extraction efficiency can be calculated. This method yielded extraction percentages of 22.6 % for the pulsed plasma poly(4-VBC) coated- and 14.7 % for the uncoated-meltblown TPU cloth (Figure 3-22) which does not demonstrate sufficient dye extraction. It is also possible to

determine the concentration of MB removed by the DMAM-phenol functionalised TPU cloths, alongside their complete AB10B extraction. By plotting a calibration curve of concentration of MB against absorbance at 663 nm, the absorbance of the filtrates at 663 nm can be used to determine the final concentration of MB, yielding an extraction percentage towards MB of  $53.5 \pm 9.2\%$ . As such, it should also be stated that a reasonable extraction of the cationic MB dye is also obtained by the DMAM-phenol functionalised meltblown TPU cloth from the 1:1 w/w MB: AB10B solution.

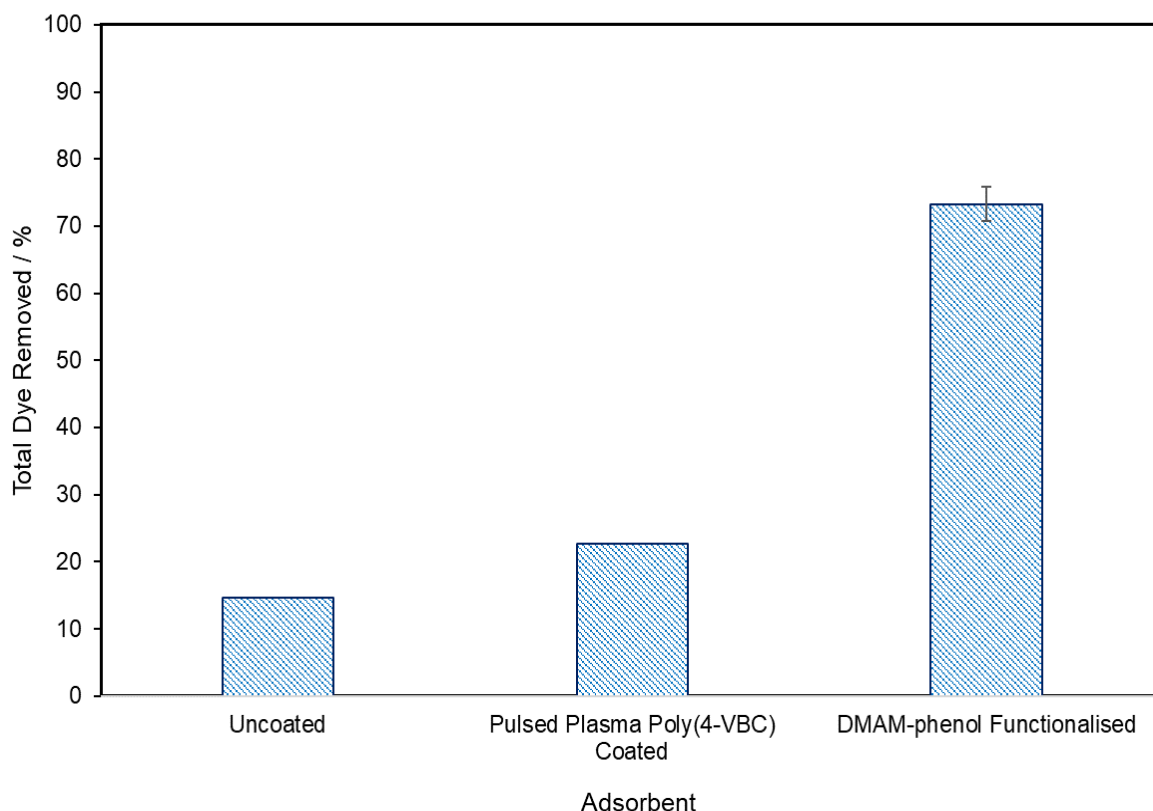


Figure 3-22. Extraction percentage towards a solution containing  $6 \text{ mg L}^{-1}$  AB10B and  $6 \text{ mg L}^{-1}$  MB under dynamic conditions. The adsorbents investigated were an uncoated TPU cloth, a pulsed plasma poly(4-VBC) coated cloth, and a pulsed plasma poly(4-VBC) coated cloth, derivatised with DMAM-phenol (3 cm x 3.5 cm, inserted into the bottom of the body of a Pasteur pipette (150 mm total length, 100 mm body length, 5.6 mm body internal diameter, Fisher Scientific UK Ltd.)). The control experiments (uncoated TPU cloth and pulsed plasma poly(4-VBC) coated cloth) were performed once, while the DMAM-phenol functionalised cloth experiment was repeated 3 times.

### 3.3.8 Alternative Substrates

A key claim of plasma polymerisation is the fact that it is substrate independent. In order to verify this claim, a PET/PP substrate and a carbon cloth derived from cotton pyrolysis have been coated with pulsed plasma poly(4-VBC) and derivatised with DMAM-phenol.

When using the PET/PP substrate it can be seen once again that the extraction percentage towards AB10B is greatest for the DMAM-phenol functionalised substrate (Table

3-11). The extraction percentage is lower for the PET/PP substrate than for the TPU substrate, however the average weight of the PET/PP cloth is roughly half of the TPU cloth. As such, if adsorption capacity experiments were performed, it would be expected that similar values of  $\text{mg}_{\text{Dye}}\text{g}_{\text{Cloth}}^{-1}$  would be obtained.

Table 3-11. Extraction percentage towards anionic dye AB10B with a PET/PP cloth, a pulsed plasma poly(4-VBC) coated cloth, and a pulsed plasma poly(4-VBC) coated cloth, functionalised with DMAM-phenol. The experiment with the DMAM-phenol functionalised substrate has been repeated three times, while the controls have each been performed once. Also included for reference are the results for the DMAM-phenol functionalised TPU cloths. The average mass of the functionalised PET/PP cloths was  $0.0270 \pm 0.0033$  g, compared to ca. 0.05 g for the functionalised TPU cloths.

Adsorbent	Extraction efficiency / %		Filtration time / min	
	6 mg L <sup>-1</sup>	10 mg L <sup>-1</sup>	6 mg L <sup>-1</sup>	10 mg L <sup>-1</sup>
Uncoated PET/PP cloth	0	0	2	3
Pulsed plasma poly(4-VBC) coated	0.3	0	Ca. 40	Ca. 40
DMAM-phenol functionalised	40.6 ± 6.9	26.8 ± 9.0	Ca. 15	Ca. 30
<i>DMAM-phenol functionalised TPU cloth</i>	96.1 ± 5.2	86.3 ± 11.9	Ca. 5	Ca. 5

Unfortunately, the carbon cloth does not fit inside the Pasteur pipette, and so the extraction percentage was determined via static filtration (Table 3-12), where it can be seen that the functionalised carbon cloth gives rise to a significantly greater dye extraction than the uncoated and pulsed plasma poly(4-VBC) carbon cloths, demonstrating that the dye can be successfully removed by a DMAM-phenol functionalised activated carbon cloth. While the extraction percentage is lower than the DMAM-phenol functionalised TPU cloths, it should be noted that the average cloth weight is less than half of the TPU cloth. Calculating the adsorption capacity yields a value of  $2.75 \pm 0.54$   $\text{mg}_{\text{Dye}}\text{g}_{\text{Cloth}}^{-1}$ , which is ca. 1.5 times as large as the  $1.81 \pm 0.14$   $\text{mg}_{\text{Dye}}\text{g}_{\text{Cloth}}^{-1}$  value for the extraction of 20 mg L<sup>-1</sup> AB10B from DMAM-phenol functionalised TPU cloths, indicating that the carbon cloth is a superior substrate for dye removal.

Table 3-12. Extraction percentage towards 20 mg L<sup>-1</sup> AB10B (anionic dye) with an activated carbon cloth, pulsed plasma poly(4-VBC) coated carbon cloth, and a pulsed plasma poly(4-VBC) coated carbon cloth, functionalised with DMAM-phenol. The experiment with the DMAM-phenol functionalised substrate has been repeated three times, while the controls have each been performed once. Also included for reference are the results for the DMAM-phenol functionalised TPU cloths. The average

mass of the functionalised TPU cloths used in this investigation was  $0.0500 \pm 0.0005$  g. The average mass of the functionalised carbon cloths was  $0.0221 \pm 0.0019$  g.

Adsorbent	Extraction efficiency / %	Adsorption Capacity / $\text{mg}_{\text{Dye}}\text{g}_{\text{Cloth}}^{-1}$
Uncoated carbon cloth	27.5	1.18
Pulsed plasma poly(4-VBC) coated	30.4	1.50
DMAM-phenol functionalised	$60.4 \pm 11.7$	$2.75 \pm 0.54$
<i>DMAM-phenol functionalised TPU cloth</i>	$85.0 \pm 6.1$	$1.76 \pm 0.19$

### 3.3.8.1 Activated Carbon Cloth with Dye Mixture

The attempted extraction of a  $20 \text{ mg L}^{-1}$  1:1 solution of AB10B:MB using a DMAM-phenol functionalised, activated carbon cloth was performed. As stated above, the cloth is too thick to fit inside a Pasteur pipette, and so static filtration must be performed.

The UV–Vis spectra of the  $20 \text{ mg L}^{-1}$  mixed solution before and after filtration with an uncoated control carbon cloth, a control carbon cloth coated with pulsed plasma poly(4-VBC) and a pulsed plasma poly(4-VBC) coated carbon cloth, functionalised with DMAM-phenol, are shown in Figure 3-23. As with the filtration of the  $6 \text{ mg L}^{-1}$  mixed solution in 3.3.8., filtration with the control cloths did not result in a significant change in the shape of the UV–Vis spectrum. However, unlike with the  $6 \text{ mg L}^{-1}$  experiments in 3.3.8., the overall absorbance of the filtrate has dramatically reduced compared to the starting solution. As with the dye mixture experiment in 3.3.7.2., the pulsed plasma poly(4-VBC) control cloth gave rise to a greater decrease in absorbance of the mixed dye. In particular, the absorbance at 663 nm for the solution following filtration with the pulsed plasma poly(4-VBC) coated cloth is the lowest of each of the filtrates, which does imply that the pulsed plasma poly(4-VBC) coated carbon cloth is excellent at removing MB from solution.

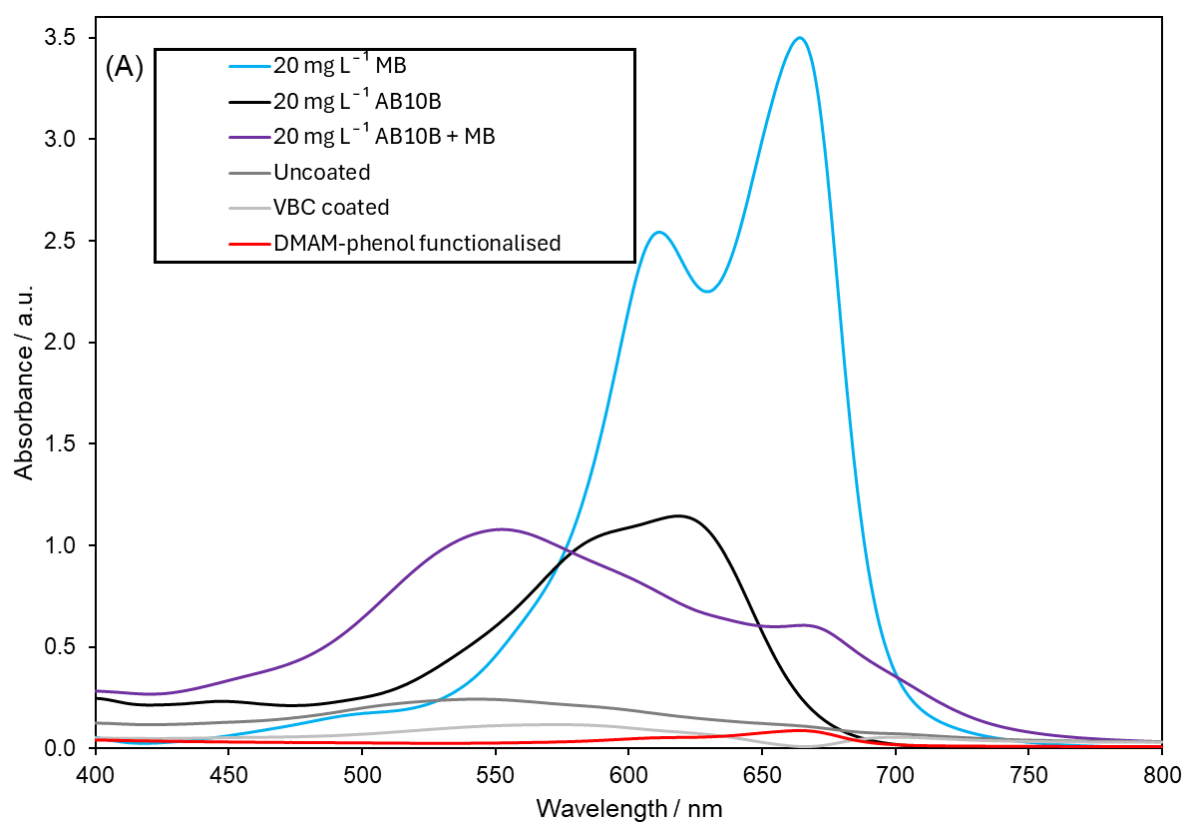
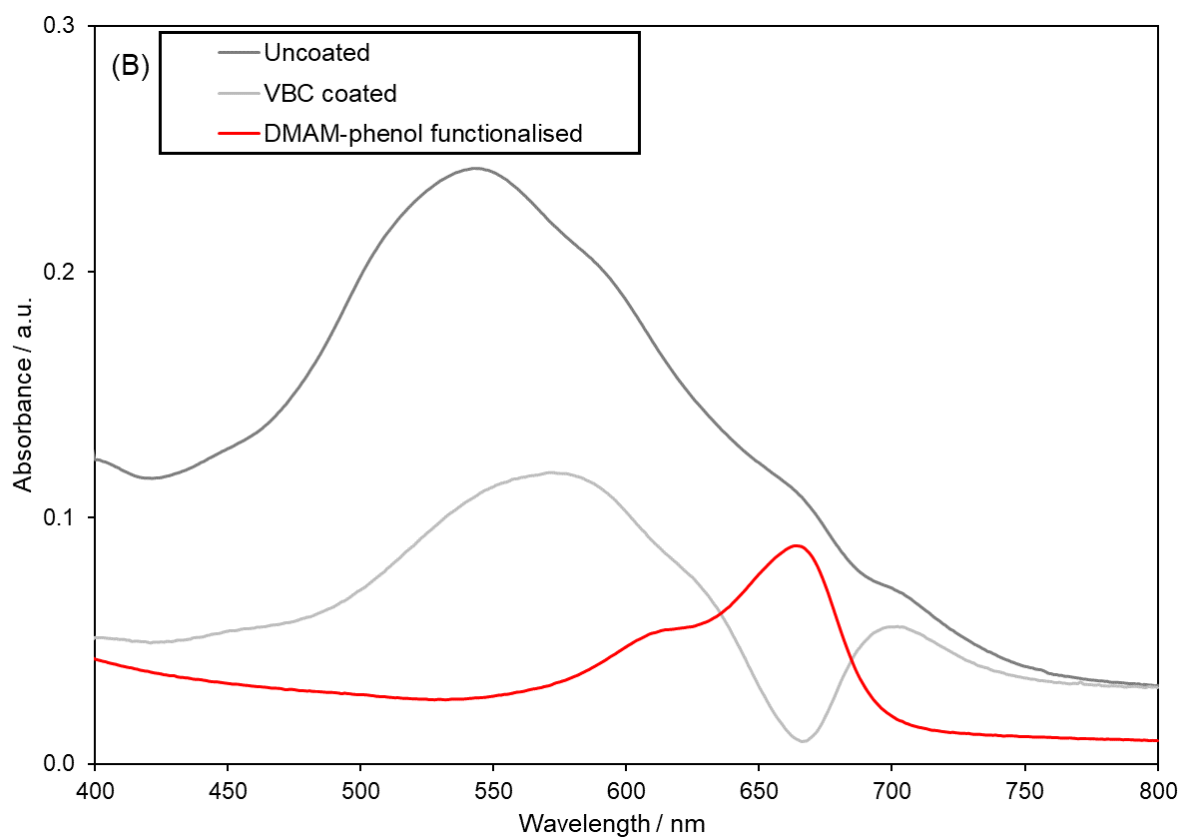


Figure 3-23. (A) UV-Vis spectra of 20 mg L<sup>-1</sup> mixed solution of anionic dye AB10B and cationic dye MB (purple), and the same solution when filtered with an uncoated carbon cloth (dark grey), a pulsed plasma poly(4-VBC) coated cloth (light grey) and a DMAM-phenol functionalised cloth (red). For

reference, the UV–Vis spectra of 20 mg L<sup>-1</sup> solutions of cationic dye MB and anionic dye AB10B are shown in blue and black respectively. (B) is an expansion of (A), in order to allow for easier visualisation of the spectra of the filtrates from the uncoated carbon cloth (dark grey), a pulsed plasma poly(4-VBC) coated cloth (light grey) and a DMAM-phenol functionalised cloth (red).

Using the same method as described in 3.3.7.2, an estimated extraction percentage towards all dyestuff by the non-functionalised carbon cloths was calculated. Values of 89.5 % and 77.8 % were obtained by the pulsed plasma poly(4-VBC) coated- and uncoated-carbon cloths respectively. When compared with the 22.6 % and 14.7 % values with the meltblown TPU cloth towards a mixed dye solution of a much lower concentration, it is clear that the carbon cloth is a significantly superior absorber. Direct comparison should be cautioned however, as the dye filtration methods were different (static for the carbon cloth compared with dynamic for the meltblown cloth).

As with the 6 mg L<sup>-1</sup> experiments in 3.3.7.2, the shape of the UV–Vis spectra of the filtrates, when passed through a DMAM-phenol functionalised carbon cloth has changed, and now once again resembles that of MB. This can be more easily visualised by adjusting the scale, (Figure 3-24, which also displays the UV–Vis spectra of a 2.5 mg L<sup>-1</sup> solution of AB10B and a 1 mg L<sup>-1</sup> solution of MB). This observation demonstrates that the AB10B has been successfully removed from solution following filtration with the DMAM-phenol functionalised carbon cloth.

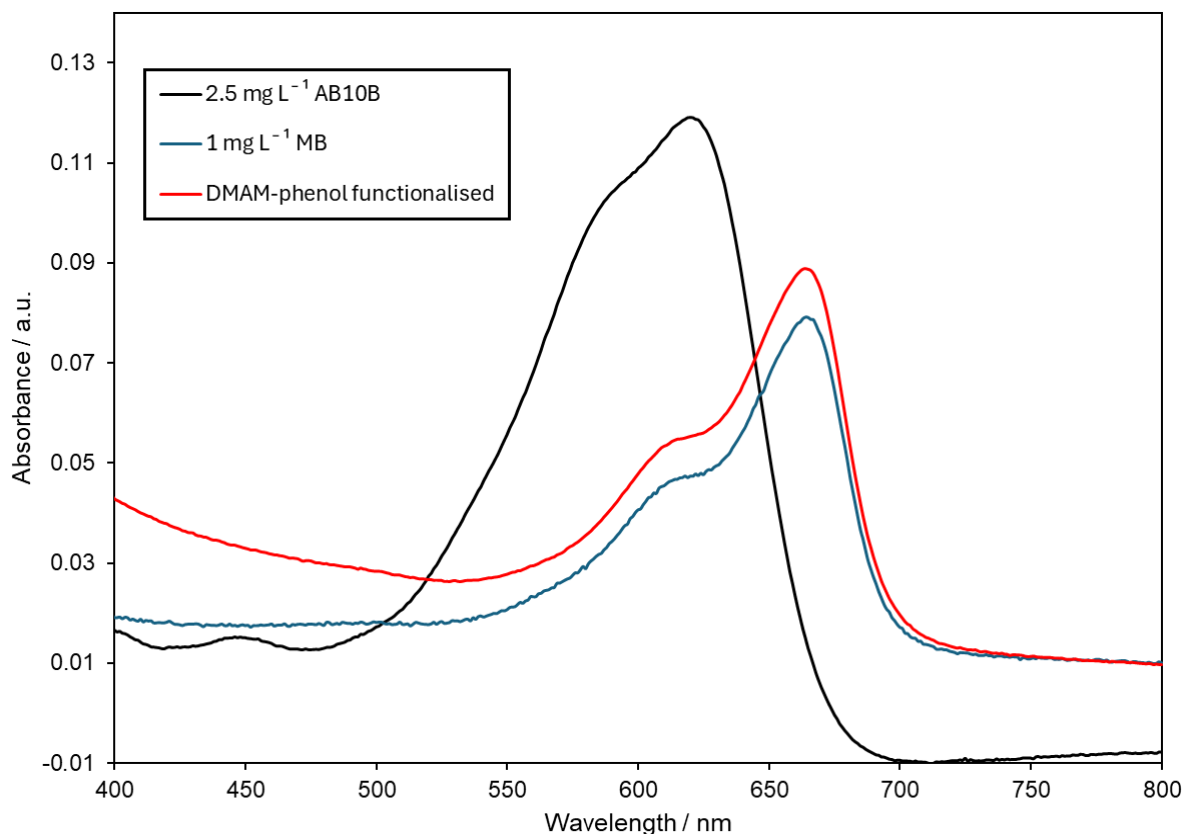


Figure 3-24. UV-Vis spectra of a 20 mg L<sup>-1</sup> mixture of anionic dye AB10B/cationic dye MB, filtered by a DMAM-phenol functionalised cloth (red). For reference, the UV-Vis spectra of a 2.5 mg L<sup>-1</sup> AB10B (black) and 1 mg L<sup>-1</sup> MB (blue) solution have been included.

The other crucial observation from the extraction study is that the final MB concentration is similar to 1 mg L<sup>-1</sup>. Using the calibration curve method as described in 3.3.7.2, the quantity of MB remaining in solution, following filtration with the DMAM-phenol functionalised carbon cloths can be calculated. An extraction percentage towards MB of 96.4 ± 0.8 % was obtained (Table 3-13). As such, it can be stated that a carbon cloth, coated with pulsed plasma poly(4-VBC) and derivatised with DMAM-phenol can be used to efficiently extract both cationic and anionic dyes simultaneously from solution.

Table 3-13. Extraction percentage towards anionic dye AB10B, cationic dye MB, and total dye in a solution containing 20 mg L<sup>-1</sup> AB10B and 20 mg L<sup>-1</sup> MB under dynamic conditions. The adsorbents investigated were an uncoated activated carbon cloth, a pulsed plasma poly(4-VBC) coated carbon cloth, and a pulsed plasma poly(4-VBC) coated carbon cloth, derivatised with DMAM-phenol (3 cm x 1 cm, placed in the bottom of a vial containing 5 mL dye, and left to spin for at least 6 h). The control experiments (uncoated carbon cloth and pulsed plasma poly(4-VBC) coated cloth) were performed once, while the DMAM-phenol functionalised cloth experiment was repeated twice.

Adsorbent	AB10B removed / %	MB removed / %	Total dye removed / %
Uncoated carbon cloth	N/A	N/A	77.8
Pulsed plasma poly(4-VBC) coated cloth	N/A	N/A	89.5



Adsorbent	AB10B removed / %	MB removed / %	Total dye removed / %
DMAM-phenol functionalised cloth	100 ± 0	96.4 ± 0.8	98.4 ± 0.4

### 3.3.9 Removal of AB10B from a Simulated Real-World Water Sample

In order to further investigate the suitability of the system for AB10B removal in real-world environments, a real-world contaminated water sample was simulated. To do this, a water sample was collected from a nearby vegetated rainwater pond, which has a green hue (Figure 3-25(A)). Previous studies have shown that the water contains 4.0 mg L<sup>-1</sup> chloride, < 0.12 mg L<sup>-1</sup> phosphate, 4.4 mg L<sup>-1</sup> sulfate and < 0.7 mg L<sup>-1</sup> nitrate.<sup>251</sup> Further analysis of the water revealed that it contained 0.14 mg L<sup>-1</sup> Ba, 55.63 mg L<sup>-1</sup> Ca, 0.05 mg L<sup>-1</sup> Eu, 0.44 mg L<sup>-1</sup> Fe, 2.21 mg L<sup>-1</sup> K, 2.07 mg L<sup>-1</sup> Mg, 0.35 mg L<sup>-1</sup> Mn, 6.39 mg L<sup>-1</sup> Na, and 1.18 mg L<sup>-1</sup> Si. The water was filtered with a 0.45 µm Whatman membrane filter in order to remove the solid particulates, yielding a colourless sample (Figure 3-25(A)). The mechanically filtered pondwater was then used to make up a 6 mg L<sup>-1</sup> AB10B solution, which was dynamically filtered with either DMAM-phenol or DMAM-calixarene functionalised cloths (Figure 3-25). Following repeats, extraction percentages of 87.2 ± 10.9 % and 87.7 ± 9.5 % for the DMAM-phenol and DMAM-calixarene functionalised cloths respectively were obtained. As such, it can be claimed that the cloths are excellent extractors of AB10B in real-world water samples.

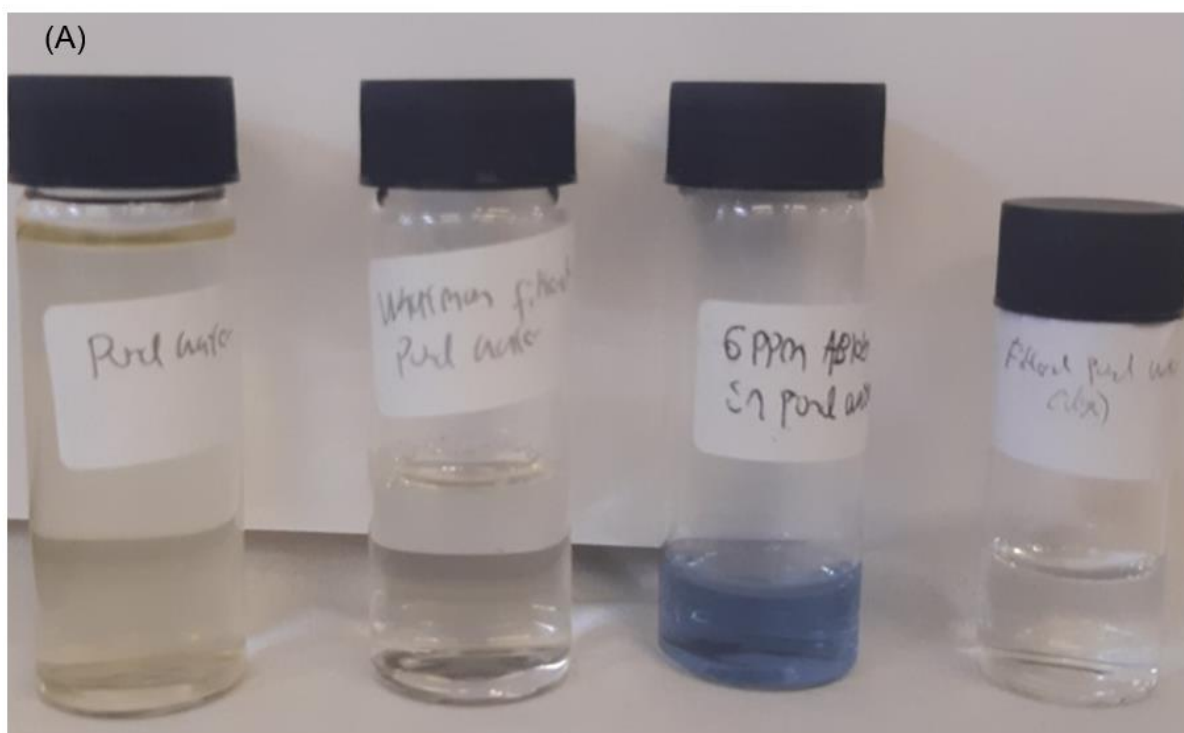
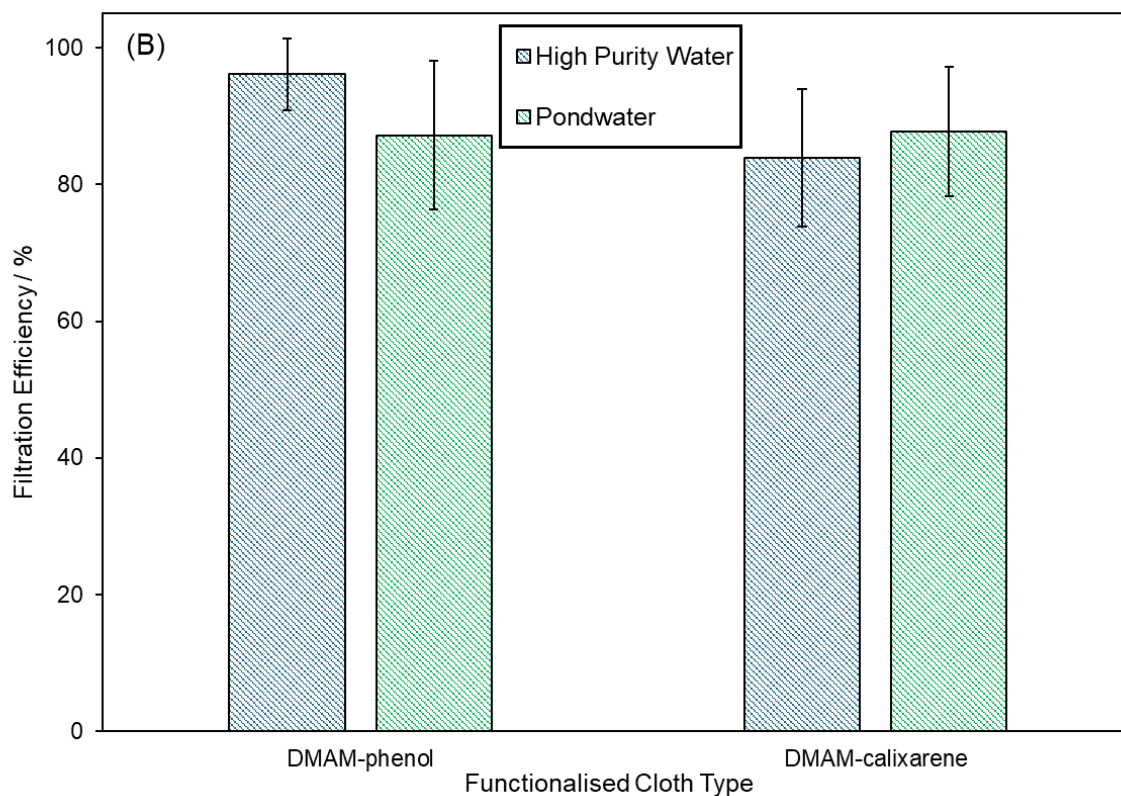


Figure 3-25. (A) Pictorial representation of pondwater (far left) filtered with a Whatman filter (middle left), then spiked with anionic dye AB10B, yielding a  $6 \text{ mg L}^{-1}$  solution (middle right), and then filtered with a DMAM-phenol functionalised cloth (far right). (B) Filtration efficiency of DMAM-phenol and DMAM-calixarene functionalised cloths towards a  $6 \text{ mg L}^{-1}$  AB10B (anionic dye) pondwater (green) and HP water (blue) solution.

### 3.4 Discussion

All prior literature concerning the extraction of AB10B from solution has employed static (batch) adsorption or requires the use of a column with external pressure to force the contaminated water through a sample.<sup>260</sup> In reality, these methods are inappropriate for point-of-use water filtration, requiring expertise to perform, and many hours to complete. Furthermore, many other studies have employed acidic pH conditions, in order to protonate their adsorbents to increase dye capture, however these methods would yield a water sample unfit for human consumption.<sup>231,237,260,262,295,296,297</sup> In this work, an anionic dye adsorbent, capable of decontaminating water at natural pH values and at point-of-use has been investigated. Ca. 100 % filtration of a 6 mg L<sup>-1</sup> AB10B solution with a DMAM-phenol functionalised cloth has been demonstrated, meaning that < 0.01 mg L<sup>-1</sup> will remain in solution—lower than the safe limit specified by EU regulation No. 10/2011 for the concentration of primary aromatic amines found in foodstuff<sup>275</sup>—and so the system is suitable for extracting anionic dye from solution. Given that the extraction percentage of the uncoated cloth and the pulsed plasma poly(4-VBC) coated cloth was insignificant, this excellent dye capture is attributed to the DMAM functionalities on the cloths. The DMAM moieties contain tertiary amine groups, which are protonated under natural pH (the pKa of tertiary amines are ≈ 9–10).<sup>298</sup> Consequently, there are electrostatic interactions between the anionic dyes and the positively charged cloth surface (chemisorption). When determining the number of amine sites, it was found that the ratio of active sites to adsorbed dye molecules was in the ballpark of 1:1 or fewer amine:dye sites. Given that the number of adsorbing sites lies in excess, this indicates that physisorption is unlikely to be the predominant extraction mechanism, as that would give rise to multilayers, meaning that there would be more dye present than adsorbing sites. As the number of adsorbing sites may well be greater than the number of adsorbed dye molecules, this also implies that dye adsorption could be hindered—potentially, the large size of the dye molecules (the dyes in this investigation exhibit a length of ca. 2 nm, which is greater than the 0.6 nm diameter exhibited by phenol)<sup>290</sup> means that neighbouring amine sites are covered, which would sterically hinder the adsorption of dye in those locations.

This adsorption behaviour, which has been shown to be modelled by pseudo-second order kinetics, is found to follow a Langmuir isotherm. Langmuir isotherms imply that the adsorption is homogenous, with the dye forming a monolayer on the cloth. Each adsorbent site can only bind a single molecule, while being independent from the occupancy of a neighbouring adsorbent site – each site is equivalent in terms of adsorption energy and adjacent adsorbed molecules do not interact. The values of  $R_L$ , which are indicative of the favourability of adsorption, lie below  $1 \times 10^{-2}$  for all concentrations employed, which

demonstrates that the adsorption is very favourable, while the system was able to reach equilibrium within ca. 210 min.

This adsorption mechanism aligns with the known behaviour of acid dyes (such as AB10B), which are known to dye amine-containing fibres via electrostatic interaction, and the formation of ionic bonds, between the negatively charged sulphonate groups on the dye with the protonated amine groups on the fibres.<sup>299</sup> Given that the DMAM functionality also contains these amine groups, it is highly likely that the specific chemisorption process in this work is consistent with those exhibited during the dyeing of fabric materials. This mechanistic explanation is also provided by Sun et al., where the amine group on melamine becomes protonated, leading to electrostatic attraction with the negatively charged sulfonate groups on AB10B.<sup>300</sup>

While the uncoated and pulsed plasma poly(4-VBC) coated cloths struggle to extract all negatively charged dyes from solution, the uncoated TPU cloth extracted a noticeable amount ( $1.13 \pm 0.32$  and  $0.58 \pm 0.03$   $\text{mg}_{\text{Dye}}\text{g}_{\text{Cloth}}^{-1}$  of JGB and MB respectively) of both investigated cationic dyes from solution. It is known that some fabrics, such as poly(acrylonitrile), carry a negative charge, and therefore cannot be dyed by anionic dyes, and only yield pale colours with neutral, disperse dyes.<sup>301</sup> For this reason, unnatural dyes had to be synthesised, which could stain the fibres. These dyes are known as “basic dyes” as they carry a positive charge. If the polyurethane cloth behaves similarly to acrylic fibres, then that would explain why it is capable of absorbing (is dyed by) the positively charged dyes. Indeed, work by Chen et al. into textile dyeing of a waterborne poly(urethane-urea) sample demonstrated that the carboxylic groups within the urethane molecules become negatively charged under neutral conditions, which would then electrostatically interact with cationic dyes.<sup>302</sup> There does exist a disparity in adsorption capacity of the uncoated cloth towards JGB and MB ( $2.31 \times 10^{-3}$   $\text{mmol}_{\text{JGB}}\text{g}_{\text{Cloth}}^{-1}$  vs  $1.41 \times 10^{-3}$   $\text{mmol}_{\text{MB}}\text{g}_{\text{Cloth}}^{-1}$  at  $10 \text{ mg L}^{-1}$  dye concentration) indicating that there are greater forces of attraction between the cloth and JGB than between the cloth and MB. The adsorption capacities do not significantly change for all JGB solutions following pulsed plasma poly(4-VBC) deposition and subsequent derivatisation, which demonstrates that the attractive forces between the TPU fibres and the JGB dye is sufficient to overcome any electrostatic repulsion provided by the positively charged DMAM groups. The uptake of MB is unaffected by pulsed plasma poly(4-VBC) deposition and subsequent derivatisation with phenol or tBu-calixarene. However, following derivatisation with DMAM-phenol and DMAM-calixarene, the adsorption capacities towards  $6 \text{ mg L}^{-1}$  MB decreased to  $0.14 \pm 0.05$  and  $0.21 \pm 0.08$   $\text{mg}_{\text{Dye}}\text{g}_{\text{Cloth}}^{-1}$  respectively, showing that the repulsion provided by the positively charged DMAM groups is capable of hindering the (weaker than with JGB) forces of attraction to the cloth. No such decrease is observed for  $10 \text{ mg L}^{-1}$  MB,

which is attributed to the cloth reaching final capacity—unlike with JGB, the adsorption capacity of every adsorbent did not increase proportionally with MB concentration—which allows the DMAM functionalised adsorbents to “catch up” as the amount of MB in solution increases.

The neutral dye DR1 is unable to be extracted by any adsorbent, and all adsorption capacities are within error values of each other, indicating that the pulsed plasma depositions and subsequent derivatisation processes exhibit minimal effect on the dye uptake capabilities. This general lack of uptake of the neutral DR1 by any adsorbent provides further weight to the electrostatic mechanism theory. However, it is worth commenting that an ethanolic solution is not representative of real-world situations, and so the experiment does require upgrading.

The DMAM-calixarene and (in particular) the DMAM-phenol functionalised cloths do exhibit excellent selectivity towards the AB10B dye, which cannot be explained solely by electrostatic interactions (it would be expected that the cloth would preferentially remove the competing anions, owing to their significantly higher concentration in solution). As such, it is likely that there are secondary interactions helping to drive dye capture. As a general trend across all dyes, regardless of charge, the extraction percentage when using the pulsed plasma poly(4-VBC) coated cloth is slightly greater than when using the uncoated TPU cloth, which improves again slightly when using a phenol or tBu-calixarene functionalised cloth. These findings indicate that the cloths are also capable of adsorbing the dye through  $\pi$ - $\pi$  interactions between the  $\pi$ -electron systems of the dyes and the phenyl groups on the TPU cloth, pulsed plasma poly(4-VBC) linker layer, and/or the phenol/calixarene derivatives.<sup>303</sup> These secondary interactions would also explain why some uptake of the neutral and cationic dyes is possible by the adsorbents.

The DMAM-phenol functionalised cloth gives rise to a greater extraction percentage, dye selectivity and superior adsorption capacity than the DMAM-calixarene functionalised cloth. Note that the density of DMAM-phenol groups should not be drastically different to the density of DMAM-calixarene groups on the surface given that the molecular dimensions of the phenol component do not change drastically in calixarene form as opposed to being by itself.<sup>304,305</sup> As DMAM-calixarene will therefore be approximately the same size as four DMAM-phenol molecules, similar densities of DMAM groups *should* reside on the surface (however, no experiment has been performed to calculate the difference in density). This means that, unlike in previous studies,<sup>251</sup> the macrocycle has not aided the dye extraction. Instead, it is possible that the dyes, in particular the bulkier AB10B, are too large to fit inside the calixarene cavity (the diameter of the upper ring of calix[4]arene is 3.8 Å, an order of magnitude smaller than the approximate size of the AB10B dye), as observed similarly by Spinella et al. in their

attempted removal of AB10B by a calixarene nanosponge.<sup>247,290,306,307</sup> As such, this steric repulsion inhibits dye extraction, leading to a slightly reduced extraction efficiency.

The maximum adsorption capacity ( $1.74 \pm 0.29 \text{ mg}_{\text{Dye}}\text{g}_{\text{Cloth}}^{-1}$ ) is lower than in previous studies. However, thickness studies demonstrate that the DMAM-phenol is only present on the very surface of the cloth, meaning that the adsorbent fibres will be very thin, and so the actual value of adsorption capacity in terms of  $\text{mg}_{\text{Dye}}\text{g}_{\text{DMAM-functionalised-fibres}}^{-1}$  will be far higher.

The method has been shown to be successful, regardless of cloth type employed. As such, it should be possible to utilise any cheap and readily available cloths as the substrates for the dye extraction. Furthermore, the elevated adsorption capacity exhibited by the activated carbon cloth helps to demonstrate that utilising substrates with increased surface area could give rise to an even greater degree of dye extraction.

The DMAM-phenol functionalised cloths, designed to be employed for point-of-use dynamic water filtration, demonstrate outstanding capabilities towards real-world water samples. Whereas previous studies tend to show recyclability of adsorbents for five or fewer cycles—and often with a slight decrease in extraction percentage—following dynamic filtration of AB10B solutions of concentrations higher than expected at point-of-use, ca. 100 % extraction was still observed after ten filtrations. Cloth recycling is essential, in order to reduce the environmental impact of the cloth adsorbents, while also allowing for sustainable use in remote locations. Using a regeneration mixture of 0.5 M NaOH and 2 M NaCl was shown to be superior to solely using NaOH to deprotonate the amine groups, as is commonly performed in literature. The use of a significantly higher concentration of chloride anions compared to AB10B enables displacement of the captured dye with chloride, which are then re-displaced by AB10B in the subsequent filtration, owing to the excellent selectivity towards the dye exhibited by the cloth—when using a 1:100 mole ratio of dye: competing anion, ca. 100 % dye extraction is observed for all investigated anions. Furthermore, AB10B is able to be extracted when in a mixture with other dyes, replicating likely real-world conditions, while  $87.2 \pm 10.9 \%$  of  $6 \text{ mg L}^{-1}$  AB10B can be removed from a real-world water sample, laced with the dye contaminant.

The outstanding dye extraction, recyclability, selectivity, and real-world performance all certify that DMAM-phenol functionalised cloths can be used for point-of-use water decontamination, especially in ODA (Official Development Assistance) countries and humanitarian crises, where access to clean water cannot be guaranteed, and large-scale batch filtration of water may not be possible. These adsorbents are easy to use and could be potentially vital to help achieve the 6<sup>th</sup> UN sustainability goal—access to clean water for all.<sup>308</sup> Within this work, three different substrates were coated with pulsed plasma poly(4-VBC) and

subsequently functionalised with DMAM-phenol, thus demonstrating the versatility of the plasmachemical process employed. One of these substrates, an activated carbon cloth, yielded an elevated adsorption capacity of  $2.75 \pm 0.53 \text{ mg}_{\text{Dye}}\text{g}_{\text{Cloth}}^{-1}$ , when attempting to extract  $20 \text{ mg L}^{-1}$  AB10B under static conditions. More potently, when employing the DMAM-phenol functionalised activated carbon cloth as an adsorbent towards the  $20 \text{ mg L}^{-1}$  mixed dye solution, the cloth was able to remove  $98.4 \pm 0.4 \%$  of all dyestuff. While other work has previously demonstrated that close to 100 % dye removal from a system containing a mixture of anionic and cationic dyes is possible<sup>309,310</sup>, this work nevertheless indicates that using plasmachemical techniques to coat a substrate which already demonstrates good extraction of cationic dyes provides significant possibilities with respect to purifying water which might be contaminated with both cationic and anionic dyes. The DMAM-phenol surface layer removes the anionic dyes, before any cationic dye which is able to permeate into the bulk is then extracted. Alternatively, a cloth could be coated, such that one side is derivatised with DMAM-phenol, while the other side is then derivatised with a molecule capable of extracting cationic dyes with high efficiency. While the greatest dye extraction from cationic-anionic binary mixtures this author could find was significantly greater ( $357.1 \pm 8.0 \text{ mg}_{\text{Dye}}\text{g}_{\text{Cloth}}^{-1}$ )<sup>311</sup> than the  $2.75 \pm 0.53 \text{ mg}_{\text{Dye}}\text{g}_{\text{Cloth}}^{-1}$  in this work, no full investigation into dye-mixture adsorption capacity was performed, and so these values cannot be directly compared. However, the same argument as before remains, which states that only the surface fibres of the carbon cloth will be functionalised with DMAM-phenol, meaning that the actual value of adsorption capacity in terms of  $\text{mg}_{\text{Dye}}\text{g}_{\text{DMAM-functionalised-fibres}}^{-1}$  will be far higher.

### 3.5 Conclusions

Pulsed plasma poly(4-VBC) has been successfully deposited onto several cloth substrates and derivatised with phenol, tBu-calixarene, DMAM-phenol, or DMAM-calixarene. The cloths are capable of removing an azo dye (AB10B), which can be damaging to the respiratory system, using point-of-use dynamic filtration with high efficiency (ca. 100 %) at concentrations anticipated in water at point-of-use, and without the need to artificially decrease the pH value. The extraction is modelled by a Langmuir isotherm, and by pseudo-second order kinetics, and the extraction mechanism is primarily electrostatic, however secondary  $\pi$ - $\pi$  interactions also aid dye adsorption. The ratio of adsorbed dye molecules to number of amine sites was in the ballpark of 1:1 or lower, implying that the dye forms a monolayer on the surface of the adsorbent. Higher adsorption capacities are observed by the DMAM-phenol than the DMAM-calixarene functionalised cloth, attributed to macrocycle of the calixarene inhibiting access of the dye to the adsorbent sites. The DMAM-phenol functionalised cloth also demonstrated excellent selectivity when in competition with both commonly found anions (chloride, sulfate, phosphate, carbonate and nitrate), and with another dye (MB). Captured dye can be released

following addition of a small volume of 0.5 M NaOH/2 M NaCl, allowing the cloth to be used at least 10 times without a noticeable drop in extraction efficiency. Even greater dye extraction could be observed by employing static filtration with a DMAM-phenol functionalised activated carbon cloth, which was able to extract ca. 100 % AB10B and  $96.4 \pm 0.8$  % MB from a  $20 \text{ mg L}^{-1}$  solution containing the two dyes in a 1:1 mole ratio. Suitability for real-world use was demonstrated by extracting  $87.2 \pm 10.9$  % of AB10B from a real-world pondwater sample, laced with  $6 \text{ mg L}^{-1}$  AB10B, with a DMAM-phenol functionalised TPU cloth.



### 3.6 References

- 223 Grand View Research. *Dyes And Pigments Market Size, Share & Trends Analysis Report By Product (Dyes (Reactive, Vat, Acid, Direct, Disperse), Pigment (Organic, Inorganic)), By Application, By Region, And Segment Forecasts, 2023 – 2030*. Market Analysis Report, 2021, Report ID: GVR-1-68038-545-8
- 224 Tan, I.A.W.; Hameed, B.H.; Ahmad, A.L. Equilibrium and Kinetic Studies on Basic dye Adsorption by Oil Palm Fibre Activated Carbon. *Chemical Engineering Journal*. **2007**, *127*, 111–119
- 225 El-Sharkawy, E.A.; Soliman, A.Y.; Al-Amer, K.M. Comparative Study for the Removal of Methylene Blue via Adsorption and Photocatalytic Degradation. *Journal of Colloid and Interface Science*. **2007**, *310*, 498–508
- 226 Sauer, T.; Cesconeto Neto, G.; Jose, H.J.; Moreira, R.F.P.M. Kinetics of Photocatalytic Degradation of Reactive Dyes in a TiO<sub>2</sub> Slurry Reactor. *Journal of Photochemistry and Photobiology A: Chemistry*. **2002**, *149*, 147–154
- 227 Khan, I.; Saeed, K.; Zekker, I.; Zhang, B.; Hendi, A.H.; Ahmad, A.; Ahmad, S.; Zada, N.; Ahmad, H.; Shah, L.A.; Khan, I. Review on Methylene Blue: Its Properties, Uses, Toxicity and Photodegradation. *Water*. **2022**, *14*, 242
- 228 Lipskikh, O.I.; Korotkova, E.I.; Khristunova, Ye.P.; Berek, J.; Kratochvil, B. Sensors for Voltametric Determination of Food Azo Dyes – a Critical Review. *Electrochimica Acta*. **2018**, *260*, 974–985
- 229 Sun, J.H.; Sun, S.P.; Wang, G.L.; Qiao, L.P. Degradation of Azo Dye Amido Black 10B in Aqueous Solution by Fenton Oxidation Process. *Dyes and Pigments*. **2007**, *74*, 647–652
- 230 Pagga, U.; Brown, D. The Degradation of Dyestuffs: Part II Behaviour of Dyestuffs in Aerobic Biodegradation Tests. *Chemosphere*. **1986**, *15*, 479–491
- 231 Liu, J.; Chen, T-W.; Yang, Y-L.; Bai, Z-C.; Xia, L-R.; Wang, M.; Lv, X-L.; Li, L. Removal of Heavy Metal Ions and Anionic Dyes from Aqueous Solutions using Amide-functionalized Cellulose-based Adsorbents. *Carbohydrate Polymers*. **2020**, *230*, 115619
- 232 Salih, S.; Mohammed, H.; Abdullah, G.; Kadhom, M.; Ghosh, T. Simultaneous Removal of Cu(II), Cd(II), and Industrial Dye onto a Composite Chitosan Biosorbent. *Journal of Polymers and the Environment*. **2020**, *28*, 354–365
- 233 Tanzifi, M.; Yarak, M.T.; Kiadehi, A.D.; Hosseini, S.H.; Olazar, M.; Bharti, A.K.; Agarwal, S.; Gupta, V.K.; Kazemi, A. Adsorption of Amido Black 10B from Aqueous Solution using Polyaniline/SiO<sub>2</sub> Nanocomposite: Experimental Investigation and Artificial Neural Network Modelling. *Journal of Colloid and Interface Science*. **2018**, *510*, 246–261
- 234 Santosh, C.; Daneshvar, E.; Kollu, P.; Peraniemi, S.; Grace, A.N.; Bhatnagar, A. Magnetic SiO<sub>2</sub>@CoFe<sub>2</sub>O<sub>4</sub> Nanoparticles Decorated on Graphene Oxide as Efficient Adsorbents for the Removal of Anionic Pollutants from Water. *Chemical Engineering Journal*. **2017**, *322*, 472–487
- 235 Huang, R.; Yang, B.; Liu, Q.; Gong, N. Adsorption of a Model Anionic Dye on Protonated Crosslinked Chitosan. *Desalination and Water Treatment*. **2014**, *52*, 7693–7700
- 236 Ahmad, R.; Kumar, R. Conducting Polyaniline/Iron Oxide Composite: A Novel Adsorbent for the Removal of Amido Black 10B. *Journal of Chemical & Engineering Data*. **2010**, *55*, 3489–3493
- 237 Peng, X.; Jia, W.; Lu, D.; Zhang, Q.; Yang, C.; Shuang, S.; Guo, Y.; Dong, C. Preparation and Characterisation of Two-dimensional Magnetic Chitosan Nanosheets for Removal of Azo Dyes from Aqueous Solutions. *Micro & Nano Letters*. **2019**, *14*, 1344–1348
- 238 Afshin, S.; Poureshgh, Y.; Rashtbari, Y.; Fazlzadeh, M.; Bahrami, Asl, F.; Hamzezhadeh, A.; Mahtab Pormazar, S. Eco-friendly Cost-effective Approach for Synthesis of ZnO Nanoparticles and Loaded on Worn Tire Powdered Activated Carbon as a Novel Adsorbent to Remove Organic Dyes from Aqueous Solutions: Equilibrium, Kinetic, Regeneration and Thermodynamic Study. *Desalination and Water Treatment*. **2021**, *227*, 391–403
- 239 Gutsche, C.D. Calixarenes. *Accounts of Chemical Research*. **1983**, *16*, 161–170
- 240 Zhou, Y.; Li, H.; Yang, Y-W. Controlled Drug Delivery Systems Based on Calixarenes. *Chinese Chemical Letters*. **2015**, *26*, 825–828

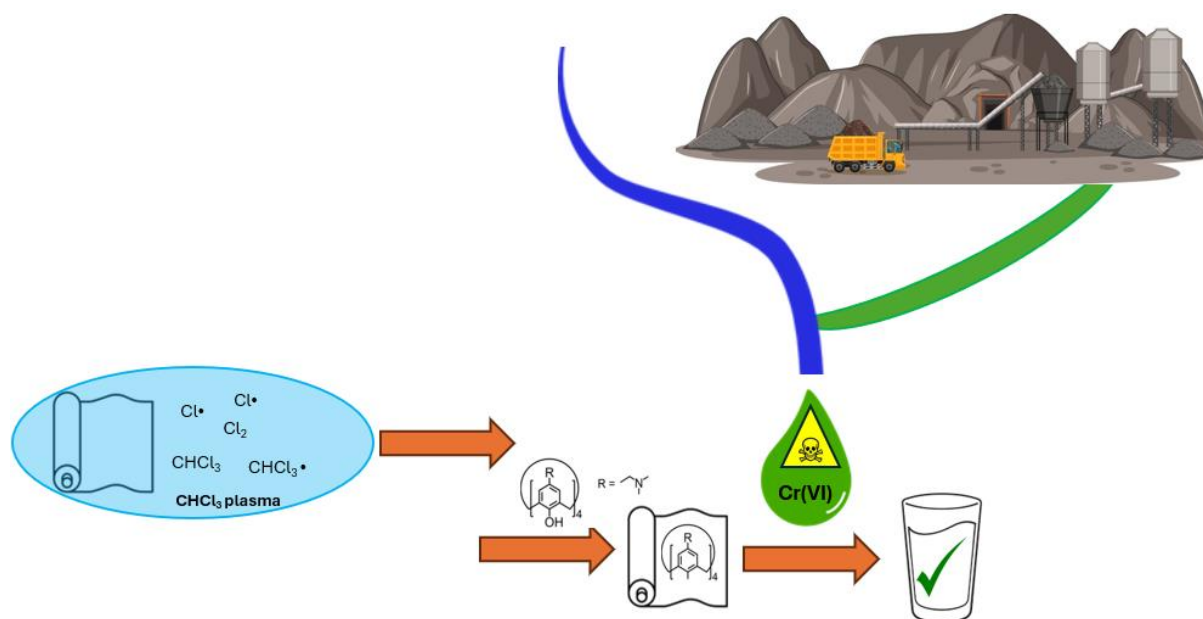
- 241 Homden, D.M.; Redshaw, C. The Use of Calixarenes in Metal-Based Catalysis. *Chemical Reviews*. **2008**, *108*, 5086–5130
- 242 Rebily, J-N.; Reinaud, O. Calixarenes and Resorcinarenes as Scaffolds for Supramolecular Metallo-enzyme Mimicry. *Supramolecular Chemistry*. **2014**, *26*, 454–479
- 243 Tabushi, I.; Kobuke, Y.; Yoshizawa, A. Macrocyclic Tridithiocarbamate as a Specific Uranophile. *Journal of the American Chemical Society*. **1984**, *106*, 2481–2482
- 244 Kiegel, K.; Steczek, L.; Zakrzewska-Trznadel, G. Application of Calixarenes as Macrocyclic Ligands for Uranium(VI): A Review. *Journal of Chemistry*. **2013**, 762819
- 245 Memon, S.; Oguz, O.; Yilmaz, A.; Tabacki, M.; Yilmaz, M.; Ertul, S. Synthesis and Extraction Study of Calix[4]arene Dinitrile Derivatives Incorporated in a Polymeric Backbone with Bisphenol-A. *Journal of Polymers and the Environment*. **2001**, *9*, 97–101
- 246 Gutsche, C. D.; Nam, K. C. Calixarenes. 22. Synthesis, Properties, and Metal Complexation of Aminocalixarenes. *Journal of the American Chemical Society*. **1988**, *110*, 6153–6162
- 247 Spinella, A.; Russo, M.; Di Vincenzo, A.; Martino, D.C; Lo Meo, P. Hyper-reticulated Calixarene Polymers: A New Example of Entirely Synthetic Nanosponge Materials. *The Beilstein Journal of Organic Chemistry*. **2018**, *14*, 1498–1507
- 248 Di Vincenzo, A.; Piccionello, A.P.; Spinella, A.; Martino, D.C.; Russo, M.; Lo Meo, P. Polyaminoazide Mixtures for the Synthesis of pH-Responsive Calixarene Nanosponges. *The Beilstein Journal of Organic Chemistry*. **2019**, *15*, 633–641
- 249 Sun, R.; Wang, S.; Shi, X.; Li, Y.; Yuan, T. Lignin-based Anionic Dye Adsorbent and Preparation Method and Application Thereof. **2020**. Patent No. CN111229179A
- 250 Schofield, W. C. E.; Badyal, J. P. S. Controlled Fragrant Molecule Release from Surface-Tethered Cyclodextrin Host-Guest Inclusion Complexes. *ACS Applied Materials and Interfaces*. **2011**, *3*, 2051–2056
- 251 Bieber, V.; Ozcelik, E.; Cox, H.; Ottley, C.; Ratan, J.; Karaman, M.; Tabakci, M.; Beaumont, S.; Badyal, J.P. Capture and Release Recyclable Dimethylaminomethyl-Calixarene Functional Cloths for Point-of-Use Removal of Highly Toxic Chromium Water Pollutants. *ACS Applied Materials and Interfaces*. **2020**, *12*, 52136–52145
- 252 Lirk, T. K.; Ibach, R.; Mozuch, M. D.; Conner, A. H.; Highley, L. Characteristics of Cotton Cellulose Depolymerized by a Brown-Rot Fungus, by Acid, or by Chemical Oxidants. *Holzforschung*. **1991**, *45*, 239–244
- 253 Teare, D.O.H.; Barwick, D.C.; Schofield, W.C.E.; Garrod, R.P.; Ward, L.J.; Badyal, J.P.S. Substrate-Independent Approach for Polymer Brush Growth by Surface Atom Transfer Radical Polymerization. *Langmuir*. **2005**, *21*, 11425–11430
- 254 Yasuda, H. Plasma Polymerization; Academic Press: New York, 1985.
- 255 Abid, M.F.; Zablouk, M.A.; Abid-Alameer, A.M. Experimental Study of Dye Removal from Industrial Wastewater by Membrane Technologies of Reverse Osmosis and Nanofiltration. *Iranian Journal of Environmental Health Science & Engineering*. **2012**, *9*
- 256 Sivakumar, D. Role of *Lemna minor Lin.* in Treating the Textile Industry Wastewater. *International Journal of Economic and Environmental Geology*. **2014**, *8*, 203–207
- 257 Ghaly, A.E.; Ananthashankar, R.; Alhattab, M.; Ramakrishnan, V.V. Production, Characterization and Treatment of Textile Effluents: A Critical Review. *Journal of Chemical Engineering and Process Technology*. **2014**, *5*
- 258 Dieblod, A. C.; Chism, W. W. Characterisation and Metrology of Medium Dielectric Constant Gate Dielectric Films. In *High Dielectric Constant Materials: VSLI MOSFET Applications*; Huff, H. R., Gilmer, D. C., Eds.; Springer-Verlag: Berlin, 2005; p 486
- 259 Lovering, D. *NKD-6000 Technical Manual*; Aquila Instruments: Cambridge, 1999
- 260 Peng, X.; Jia, W.; Lu, D.; Zhang, Q.; Yang, C.; Shuang, S.; Guo, Y.; Dong, C. Preparation and Characterisation of Two-dimensional Magnetic Chitosan Nanosheets for Removal of Azo Dyes from Aqueous Solutions. *Micro&Nano Letter*. **2019**, *14*, 1344–1348

- 261 Ibrahim, A.G.; Hai, F.A.; Wahab, H.A.; Mahmoud, H. Synthesis, Characterization, Swelling Studies and Dye Removal of Chemically Crosslinked Acrylic Acid/Acrylamide/N,N-Dimethyl Acrylamide Hydrogels. *American Journal of Applied Chemistry*. **2016**, *4*, 221–234
- 262 Fang, R.; He, W.; Xue, H.; Chen, W. Synthesis and Characterization of a High-capacity Cationic Hydrogel Adsorbent and its Application in the Removal of Acid Black 1 from Aqueous Solution. *Reactive and Functional Polymers*. **2016**, *102*, 1–10
- 263 Chen, M.; Chen, Y.; Diao, G. Adsorption Kinetics and Thermodynamics of Methylene Blue onto p-tert-Butyl-calix[4,6,8]arene-Bonded Silica Gel. *Journal of Chemical & Engineering Data*. **2010**, *55*, 5109–5116
- 264 Ghorai, S.; Sarkar, A.K.; Panda, A.B.; Pal, S. Effective Removal of Congo Red Dye from Aqueous Solution using Modified Xanthan Gum/Silica Hybrid Nanocomposite as Adsorbent. *Bioresource Technology*. **2013**, *144*, 485–491
- 265 Roy Choudhury, A.K. *In Handbook of Textile and Industrial Dyeing; Disperse Dyes, Vol. 1; Woodhead Publishing, 2011, pp. 40–128*
- 266 Al-Etaibi, A.M.; Alnassar, H.; El-Asasery, M.A. Dyeing of Polyester with Disperse Dyes: Part 2. Synthesis and Dyeing Characteristics of Some Azo Disperse Dyes for Polyester Fabrics. *Molecules*. **2016**, *21*, 855
- 267 Ferrero, F.; Periolatto, M.; Rovero, G.; Giansetti, M. Alcohol-assisted Dyeing Process: A Chemical Substitution Study. *Journal of Cleaner Production*. **2011**, *19*, 1377–1384
- 268 Lee, T.-J.; Chun, B.C.; Chung, Y.-C. Detoxification of Reactive Compounds by a Cyclic Electrolytic System with Surface-modified Ion-exchange Resin. *Reactive and Functional Polymers*. **2003**, *56*, 37–44
- 269 Bisinella Scheufele, F.; Nivaldo Modenes, A.; Eduardo Borba, C.; Ribeiro, C.; Espinoza-Quinones, F.R.; Bergamasco, R.; Curvelo Pereira, N. Monolayer–multilayer Adsorption Phenomenological Model: Kinetics, Equilibrium and Thermodynamics. *Chemical Engineering Journal*. **2016**, *284*, 1328–1341
- 270 Morsch, S.; Schofield, W.C.E.; Badyal, J.P.S. Surface Actuation of Smart Nanoshutters. *Langmuir*. **2010**, *26*, 12342–12350
- 271 Morsch, S.; Wood, T. J.; Schofield, W. C. E.; Badyal, J. P. S. A Combined Plasmachemical and Emulsion Templating Approach for Actuated Macroporous Scaffolds. *Advanced Functional Materials*. **2012**, *22*, 313–322
- 272 Wilson, M.; Kore, R.; Ritchie, A. W.; Fraser, R. C.; Beaumont, S. K.; Srivastava, R.; Badyal, J. P. S. Palladium-Poly(Ionic Liquid) Membranes for Permselective Sonochemical Flow Catalysis. *Colloids and Surfaces A: Physicochemical and Engineering Aspects*. **2018**, *545*, 78–85.
- 273 Katsyuba, S.; Kovalenko, V.Chernova, A.; Vandyukova, E.; Zverev, V.; Shagidullin, R.; Antipin, I.; Solovieva, S.; Stoikov, I.; Konovalov, A. Vibrational Spectra, Co-operative Intramolecular Hydrogen Bonding and Conformations of Calix[4]arene and Thiacalix[4]arene Molecules and their Para-tert-butyl Derivatives. *Organic & Biomolecular Chemistry*. **2005**, *3*, 2558–2565
- 274 Lui-Vien, D.; Colthup, N. B.; Fateley, W. G.; Grasselli, J. G. *The Handbook of Infrared and Raman Characteristic Frequencies of Organic Molecules*, Academic Press: Boston, 1991
- 275 The European Commission. Commission Regulation (EU) No 10/2011 of 14 January 2011 on Plastic Materials and Articles Intended to Come into Contact with Food Text with EEA Relevance. *Official Journal of the European Union*. **2011**, *12*, 1–89
- 276 Chakraborty, A.; Saha, B.B.; Ng, K.C.; Koyama, K.; Srinivasan, K. Theoretical Insight of Physical Adsorption for a Single Component Adsorbent+Adsorbate System: II. The Henry Region. *Langmuir*. **2009**, *25*, 7359–7367
- 277 Zhu, B.-Y.; Gu, T. Surfactant Adsorption at Solid-liquid Interfaces. *Advances in Colloid and Interface Science*. **1991**, *37*, 1–32
- 278 Tian, S.; Xu, S.; Liu, J.; He, C.; Xiong, Y.; Feng. Highly Efficient Removal of both Cationic and Anionic dyes from Wastewater with a Water-stable and Eco-friendly Fe-MOF via Host-guest Encapsulation. *Journal of Cleaner Production*. **2019**, *239*, 117767

- 279 Yu, C.X.; Chen, J.; Zhang, Y.; Song, W.B.; Li, X.Q.; Chen, F.J.; Zhang, Y.J.; Liu, D.; Liu, L.L. Highly Efficient and Selective Removal of Anionic Dyes from Aqueous Solution by Using a Protonated Metal-Organic Framework. *Journal of Alloys and Compounds*. **2021**, *853*, 157383
- 280 Kholiya, F.; Singh, A.; Gosai, A.; Menna, R. Facile Preparation of Agaraldehyde Chitosan-based Composite Beads as Effectual Adsorbent Especially Towards Amido Black. *Journal of Applied Polymer Science*. **2021**, *138*, 50716
- 281 Langmuir, I. The Adsorption of Gases on Plane Surfaces of Glass, Mica and Platinum. *Journal of the American Chemical Society*. **1918**, *40*, 1361–1403
- 282 Ayawei, N.; Ebelegi, A.N.; Wankasi, D. Modelling and Interpretation of Adsorption Isotherms. *Journal of Chemistry*. **2017**, *2017*, 3039817
- 283 Agbovi, H.; Wilson, L. Adsorption Processes in Biopolymer Systems: Fundamentals to Practical Applications. Elsevier: Amsterdam, 2021, pp.1–51
- 284 Ho, Y.; McKay, G. Kinetic Models for the Sorption of Dye from Aqueous Solution by Wood. *ICChemE, Part B*. **1998**, *76*, 183–191
- 285 Miyah, Y.; Lahrichi, A.; Idrissi, M.; Bouhraf, S.; Taouda, H. Assessment of Adsorption Kinetics for Removal Potential of Crystal Violet Dye from Aqueous Solutions using Moroccan Pyrophyllite. *Journal of the Association of Arab Universities for Basic and Applied Science*. **2017**, *23*, 20–28
- 286 Xiao, Y. Erroneous Application of Pseudo-Second-Order Adsorption Kinetics Model: Ignored Assumptions and Spurious Correlations. *Industrial & Engineering Chemistry Research*. **2018**, *57*, 2705–2709
- 287 Moussout, H.; Ahlafi, H.; Aazza, M.; Maghat, H. Critical of Linear and Nonlinear Equations of Pseudo-first Order and Pseudo-second Order Kinetic Models. *Karbala International Journal of Modern Science*. **2018**, *4*, 244–254
- 288 Revellame, E.D.; Fortela, D.L.; Sharp, W.; Hernandez, R.; Zappi, M.E. Adsorption Kinetic Modeling Using Pseudo-first Order and Pseudo-second Order Rate Laws: A Review. *Cleaner Engineering and Technology*. **2020**, *1*, 100032
- 289 Kostoglou, M.; Karapantsios, T. Why Is the Linearized Form of Pseudo-Second Order Adsorption Kinetic Model So Successful in Fitting Batch Adsorption Experimental Data? *Colloids and Interfaces*. **2022**, *6*
- 290 Prokorov, V.; Petrova, M.; Kovaleva, N.K.; Eugeny, D. Atomic Force and Scanning Near-Field Optical Microscopy Study of Carbocyanine Dye J-aggregates. *Current Nanoscience*. **2014**, *10*
- 291 Memon, S.; Tabakci, M.; Roundhill, D. M.; Yilmaz, M. Synthesis and Evaluation of the Cr(VI) Extraction Ability of Amino/ Nitrile Calix[4]arenes Immobilized onto a Polymeric Backbone. *Reactive and Functional Polymers*. **2006**, *66*, 1342–1349
- 292 Roobottom, H.K.; Jenkins, H.; Donald, B.; Passmore, J.; Glasser, L. Thermochemical Radii of Complex Ions, *Journal of Chemical Education*. **1999**, *76*, 1570
- 293 Kaur, H. Mutagenicity Assessment of Textile Dyes Using AMES Test. *International Journal of Science and Research (IJSR)*. **2020**, *3*, 2581–5997
- 294 Royal Society of Chemistry, Modern Chemical Techniques—Ultraviolet/visible spectroscopy. <https://edu.rsc.org/download?ac=13851> (Accessed 20<sup>th</sup> November 2022)
- 295 Yu, C.X.; Chen, J.; Zhang, Y.; Song, W.B.; Li, X.Q.; Chen, F.J.; Zhang, Y.J.; Liu, D.; Liu, L.L. Highly Efficient and Selective Removal of Anionic Dyes from Aqueous Solution by Using a Protonated Metal-Organic Framework. *Journal of Alloys and Compounds*. **2021**, *853*, 157383
- 296 Rahmayanti, M.; Nurhikmah, I.; Larasati, F. Isolation, Characterization and Application of Humin From Riau, Sumatra Peat Soils as Adsorbent for Naphthol Blue Black and Indigosol Blue Dyes. *Molekul*. **2021**, *16*, 68–74
- 297 Zhang, L.; Hu, P.; Wang, J.; Huang, R. Adsorption of Amido Black 10B from Aqueous Solutions onto Zr (IV) Surface-immobilized Cross-linked Chitosan/bentonite Composite. *Applied Surface Science*. **2016**, *369*, 558–566
- 298 Rayer, A.V.; Sumon, K.Z.; Jaffari, L.; Henni, A. Dissociation Constants (pKa) of Tertiary and Cyclic Amines: Structural and Temperature Dependences. *Journal of Chemical and Engineering Data*. **2014**, *59*, 3805–3813

- 299 Chattopadhyay, D.P. *In Handbook of Textile and Industrial Dyeing; Acid Dyes*, Vol. 1; Woodhead Publishing, 2011, pp. 150–183
- 300 Sun, J.H.; Sun, S.P.; Wang, G.L.; Qiao, L.P. Degradation of Azo dye Amido Black 10B in Aqueous Solution by Fenton Oxidation Process. *Dyes and Pigments*. **2007**, *74*, 647–652
- 301 IARC Working Group on the Evaluation of Carcinogenic Risks to Humans. *In IARC Monographs on the Evaluation of Carcinogenic Risks to Human*, Some Aromatic Amines, Organic Dyes, and Related Exposures, Vol. 99; International Agency for Research on Cancer, Lyon, 2010
- 302 Chen, S.-Y.; Lu, S.-J.; Yen, J.C.; Cuo, Y.J.; Kuo, C.-H.; Rwei, S.-R.; Chen, H.-H. Hydrogen-Bond-Assisted Dye-Incorporated Waterborne Poly(urethane-urea) (WPU) for an Environment-Friendly Textile Dyeing Process. *ACS Applied Polymer Materials*. **2023**
- 303 Kamalabadi, M.; Khalili, S.; Madrakian, T.; Afkhami, A. Facile Synthesis of Magnetic Melamine-Based Covalent Organic Framework for Removal of Amido Black 10B. *European Physical Journal Plus*. **2022**, *137*, 544
- 304 Guerineau, V.; Rollet, M.; Viel, S.; Lepoittevin, B.; Costa, L.; Saint-Aguet, P.; Laurent, R.; Roger, P.; Gimes, D.; Martini, C.; Huc, V. The Synthesis and Characterization of Giant Calixarenes. *Nature Communications*. **2019**, *10*, 113
- 305 Lorenc-Grabowska, E. Effect of Micropore Size Distribution on Phenol Adsorption on Steam Activated Carbons. *Adsorption*. **2016**, *22*, 599–607
- 306 Shinkai S.; Araki K.; Manabe O.J. Does the Calixarene Cavity Recognise the Size of Guest Molecules? On the Hole-size Selectivity in Water-soluble Calixarenes. *Journal of the Chemical Society, Chemical Communications*. **1988**, *3*, 187–189
- 307 Espanol, E.S.; Villamil, M.M. Calixarenes: Generalities and Their Role in Improving the Solubility, Biocompatibility, Stability, Bioavailability, Detection, and Transport of Biomolecules. *Biomolecules*. **2019**, *9*, 90
- 308 Department of Economic and Social Affairs. The 17 Goals. <https://sdgs.un.org/goals> (Accessed 16<sup>th</sup> November 2022)
- 309 Kandil, H.; Ali, H. Simultaneous Removal of Cationic Crystal Violet and Anionic Reactive Yellow Dyes using eco-friendly Chitosan Functionalized by Talc and Cloisite 30B. *Journals of Polymers and the Environment*. **2023**, *31*, 1456–1477
- 310 Chamorro, A.F.; Lerma, T.A.; Palencia, M. CTAB Surfactant Promotes Rapid, Efficient, and Simultaneous Removal of Cationic and Anionic Dyes through Adsorption on Glycerol/Citrate Polyester. *Water*. **2024**, *16*, 1860
- 311 Zhao, X.; Wang, X.; Lou, T. Simultaneous Adsorption for Cationic and Anionic Dyes Using Chitosan/Electrospun Sodium Alginate Nanofiber Composite Sponges. *Carbohydrate Polymers*. **2022**, *276*, 118728

## 4 CHAPTER 4 – USE OF CHLOROFORM PLASMA TREATMENT IN THE PRODUCTION OF DIMETHYLAMINOMETHYL-CALIXARENE FUNCTIONAL CLOTHS FOR SELECTIVE CAPTURE OF TOXIC HEXAVALENT CHROMIUM FROM WATER SOLUTION



### 4.1 Introduction

Chromium is an incredibly valuable metal, essential to a large array of industries, including textile and pigment mordanting, leather tanning, metallurgy and chromium plating. Of these, the leather industry produces 1.7 billion m<sup>2</sup> of leather at an estimated market value of 34 billion €, with China and India being the leading producers, as well as notable contributions from Italy, Turkey and Brazil.<sup>312,313</sup> Unfortunately, a major disadvantage of such widespread use is a large requirement for chromite mining, and the production of significant quantities of waste. Indeed, only 20 % (by weight) of the starting hides are able to be converted into leather, with large quantities of wastewater and solid waste generated<sup>314</sup>—it has been reported that leather wastewater and sludge are responsible for the release of 2000–3000 tonnes of chromium into the environment each year in India alone.<sup>315</sup> Furthermore, the mining technique commonly employed is open-cast, which is a particularly environmentally damaging technique. This degradation to landscape combined with dumped waste—one tonne of mined chromite waste is reported to produce 10 tonnes of waste—results in the ready seepage of chromium into air, water and soil.<sup>316</sup> Consequently, Sukinda Valley in India, which contains 90% of the country's chromite has been classified as one of the world's top 10 most polluted places.

Chromium is typically found in two common oxidation states – trivalent Cr(III) and hexavalent Cr(VI). The leather tanning process requires the use of Cr(III) salts,<sup>317</sup> which are commonly oxidised to Cr(VI) under atmospheric conditions, and in the presence of MnO<sub>2</sub>, which has been reported to occur in chromium-containing sludge at concentrations as high as 0.6 mg g<sup>-1</sup>.<sup>315</sup> Metal plating requires the use of Cr(VI), and concentrations as high as 5721.95 mg L<sup>-1</sup> have been reported in industrial chrome plating wastewater.<sup>318</sup> While Cr(III) does not possess a particularly high level of toxicity, Cr(VI) salts, which are readily absorbed by the lungs, digestive tract, and skin, are known to be toxic and carcinogenic.<sup>319,320</sup> Due to this toxicity, the World Health Organisation (WHO) and United Nations (UN) have provided guidelines to state that chromium concentrations in drinking water higher than 50 µg L<sup>-1</sup> should be classified as unsafe for consumption.<sup>321</sup> Therefore, it is vital to develop methods of removing chromium from water, especially in areas where wastewater treatment is insufficient.

Numerous systems have been employed, with the aim of removing chromium from solution. Of these, a particularly promising one is the use of calixarenes. Calixarenes are macrocycles, with a structure well suited for contaminant removal—their cavities enable the incorporation of target molecules through host-guest interactions, while their rims can be readily functionalised in order to control affinity and selectivity (e.g., by incorporating functional groups with a particular known affinity for a target molecule).<sup>322,323</sup> Consequently, a wide range of calixarenes have been employed with the aim of removing hexavalent chromium from solution (Appendix Table 3).

Of these, adsorption capacities as high as 87.7 mg<sub>Cr</sub>g<sub>Adsorbent</sub><sup>-1</sup> have been observed.<sup>324</sup> However, the filtration methods involved are typically batch adsorption, which may be suitable in large-scale industrial applications before waste is released (point-of-release), but countries where chromium use is at its greatest are typically lesser developed, regulation is often sparse and inefficient, and expensive treating steps may be typically ignored.<sup>325, 326</sup> Rather, consumers require point-of-use filtration, which is able to rapidly produce contaminant free water, without the need for expensive equipment or multiple filtration steps.

For that reason, the Badyal group has recently developed a cloth, designed for point-of-use filtration, which was fabricated by employing plasmachemical deposition of a poly(4-vinylbenzyl chloride, 4-VBC) linker layer onto a polypropylene cloth, before derivatising the pulsed plasma poly(4-VBC) with 5,11,17,23-tetrakis[(dimethylamino)methyl]-25,26,27,28-tetrahydroxycalix[4]arene (DMAM-calixarene).<sup>327</sup> By employing plasmachemical deposition, the use of solvents for the initial functionalisation of the cloth is not required, while plasma processes are independent, and so any porous substrate would be suitable for chromium removal.<sup>328,329</sup> However, plasmachemical deposition does have its drawbacks. In particular,

the apparatus must be disassembled and cleaned between each deposition, which minimises its usefulness in large-scale production. Furthermore, 4-VBC is a toxic and slightly expensive chemical.<sup>330</sup> As such, its use in large-scale production is advised to be avoided, meaning that alternative methods of linking the calixarene onto the surface are desired.

In that work, the calixarene attaches to the cloth by means of nucleophilic substitution of the chloride group on 4-VBC with a hydroxy group on the calixarene.<sup>331,332,333</sup> As such, it was hypothesised that functionalising the cloth with a different chloride group would yield the same result. Previous work has shown that chloroform ( $\text{CHCl}_3$ ), which is a readily available, and relatively safe chemical, can be used to plasma treat substrates, functionalising the surface with chloride groups.<sup>334,335,336,337</sup> Consequently,  $\text{CHCl}_3$  plasma was employed in order to introduce chloride functionality onto a TPU cloth, before substituting the chloride groups with DMAM-calixarene in order to fabricate a cloth capable of removing Cr(VI) from solution. As opposed to the aforementioned work, which used continuous wave  $\text{CHCl}_3$  plasma for extended periods of time, pulsed plasma was employed here, for shorter periods of time. As a result, the process should be considered to be much lower in energy, and therefore cheaper and more environmentally friendly.<sup>338</sup>

Following dynamic filtration of Cr(VI) solutions with DMAM-calixarene functionalised,  $\text{CHCl}_3$  treated cloths, fast and efficient removal of chromium is observed. Concentrations of chromium reported in real-world solutions have been reported to reach  $4.5 \text{ mg L}^{-1}$ ,<sup>339</sup> and near-complete removal at these concentrations following static filtration has been observed. The cloths have also been shown to be able to selectively remove Cr(VI) when in the presence of a range of naturally occurring competing anions, and can be readily recycled for repeated chromium removal.

## 4.2 Experimental

### 4.2.1 Preparation of Functional Cloths

A non-woven polyurethane (TPU; meltblown 35 GSM, M35A1YMO, Don & Low Ltd., 12 cm x 8 cm) cloth was used as the substrate for plasmachemical treatment. The substrate was prepared, and the plasma chamber cleaned as described in 2.1.1.1. Following cleaning with air plasma, the glassware was then exposed to continuous wave  $\text{CHCl}_3$  (+ 99 %, Fisher Scientific Ltd.) plasma at a peak forward power of 30 W for 10 min. Following plasma extinction, the  $\text{CHCl}_3$  vapour was allowed to continue to pass through the chamber for a further 15 min, before pumping back down to base pressure. Once the chamber had reached base pressure, the cloth was inserted into the chamber, and plasma treated as described in Chapter 2 (Experimental). Pulsed plasma treatment was performed using a duty cycle on-period of 100



$\mu\text{s}$  and a duty cycle off-period of 4 ms in conjunction with a peak power of 30 W, with the total time for deposition of 10 min. Following treatment, the cloth was removed and safely stored in a petri dish, while the chamber was re-cleaned with air plasma, before being re-treated with  $\text{CHCl}_3$  plasma. Afterwards, the original cloth was inverted and inserted into the freshly treated chamber, and the process repeated. Following the second treatment, the non-woven cloths were cut into two 60 mm x 70 mm pieces, leaving a 120 mm x 10 mm strip for characterisation.

The treated cloths were then placed into separate glass vials (28 mL volume, Fisherbrand™) containing 0.152 g (4 mM)  $\text{K}_2\text{CO}_3$  (+ 99.0 %, Sigma Aldrich Ltd.) before addition of an acetone (+ 99.8 %, Fisher Scientific UK Ltd.) solution containing 8 mM NaI (+ 99.5 %, Honeywell Fluka™, Fisher Scientific UK Ltd.) and 0.4 mM of one of 5,11,17,23-tetra-tert-butyl-25,26,27,28-tetrahydroxycalix[4]arene (tBu-calixarene; + 99 %, Acros Organics B.V.B.A.) or DMAM-calixarene (Konya Technical University, synthesised according to previous literature). The vials were sealed and left to spin at 40 rpm for ca. 70 h, then washed in acetone (15 min), air dried, and finally washed in high-purity (HP) water (15 min) and air dried.

#### **4.2.2 Characterisation**

Fourier Transform Infrared (FTIR) spectra were acquired as described in Section 2.1.2.1.6.

Concentrations of ideal initial chromate solutions and chromate-containing filtrates were measured using a UV–Vis–NIR (Near infrared) spectrophotometer (Cary 5000, Agilent Technologies Inc.) in conjunction with a quartz cell. The concentrations were determined by recording the absorbance of the chromate isosbestic point at 339 nm.<sup>340</sup> Chromate solutions between 0.2 and 50 mg L<sup>-1</sup> were made up and calibration curves prepared by plotting the change in absorbance at 339 nm with concentration, with the knowledge that absorbance is directly proportional to concentration according to the Beer-Lambert law (Equation 2-9).<sup>341</sup> Extraction percentages were calculated by determining the percentage change in absorbance (Equation 2-14).

Concentrations of real-world initial chromate solutions and chromate-containing filtrates were measured using an Inductively Coupled Plasma–Optical Emission Spectroscopy (ICP-OES) spectrophotometer (iCAP 6500, Thermo Fisher Scientific Inc.). Calibration standards were prepared following serial dilution of a 1000 mg L<sup>-1</sup>  $\text{Cr}(\text{NO}_3)_3$  ICP standard solution (ROMIL Ltd.) Each sample analysis consisted of three replicate measurements for 13 characteristic chromium wavelengths to ensure that the complex environmental matrix was not causing spectral interferences.

### 4.2.3 Dichromate Extraction

Cr(VI) solutions were prepared by first making up a stock solution containing 565.77 mg L<sup>-1</sup> potassium dichromate (+ 99 %, Sigma Aldrich Ltd.) (equivalent to 200 mg L<sup>-1</sup> chromium) in HP water. The stock solution was then diluted to yield Cr(VI) solutions of the desired concentration.

Dynamic and static filtration experiments, as well as isotherm determination and kinetic modelling investigations were performed as described in 2.1.3.2. Mass transfer investigations were performed by repeating the kinetic modelling investigation, using half the usual spin speed (20 rpm).

In order to calculate the number of amine sites on the surface, and hence determine the ratio of active sites to adsorbed chromium molecules, the experimental procedure outlined by Lee et al. was adapted.<sup>342</sup> Pieces of DMAM-calixarene functionalised cloths were left to shake at 200 rpm in the presence of 10 mL HCl (approximately 0.01 M) for 24 h. An 8 mL aliquot was extracted and titrated against 0.002 M NaOH. As a reference, 8 mL of the starting HCl solution was titrated against the 0.002 M NaOH solution, and the whole experiment was also repeated using uncoated TPU cloth as a control. If there are far more molecules of dye than adsorption sites, then multi-layers will have formed, implying that the adsorption is dominated by physisorption.<sup>343</sup> If the numbers are similar, then it is likely that a monolayer will have formed, with each amine site binding to one dye molecule.

Cloth recycling experiments were carried out similarly to Bieber et al.<sup>327</sup> In short, following dynamic filtration of a 20 mg L<sup>-1</sup> Cr(VI) solution, 5 mL of HP water was passed through the cloth to remove any chromium trapped via capillary forces. Then 5 mL of a solution containing 2 M NaCl and 0.5 M NaOH was passed through the cloth and the eluent collected, before being analysed via UV-Vis spectroscopy in order to determine the concentration of Cr(VI) in the regeneration eluent.

Cloth selectivity experiments were performed by passing 5 mL of a 6 mg L<sup>-1</sup> Cr(VI) solution containing one of: sodium chloride (+ 99.5 %, Sigma-Aldrich Ltd.); monosodium phosphate (+ 99 %, Sigma Aldrich Ltd.); sodium sulfate (+ 99 % anhydrous, Fisher Scientific UK Ltd.); sodium hydrogen carbonate (+ 99 %, Acros Organics B.V.B.A.); or magnesium nitrate hexahydrate (+ 99 %, A.C.S. Reagent, Sigma Aldrich Ltd.) in a 1:100 mole ratio of Cr:competing anion.

A simulated real-world Cr(VI) contaminated solution was prepared by first collecting water from a vegetated rainwater pond (Durham University, UK)—it is expected that a rainwater pond would contain a wide array of ions and organic matter. The water was first

filtered with a membrane filter (Whatman Polydisc GW In-Line polyamide filter with 0.45  $\mu\text{m}$  pore size, GE Healthcare Inc.) in order to remove any solid particulates via mechanical filtration. The particulate-free pond water was then used to make up a solution containing 6  $\text{mg L}^{-1}$  Cr(VI), which was then dynamically filtered with TPU cloths functionalised with DMAM-calixarene.

Real-world industrial wastewater samples were collected in polypropylene bottles (Azlon 30 mL round wide neck bottles, Scilab Ltd.) from an industrial zone near Jalandhar, India. Again, the sample was first filtered with a membrane filter (Whatman Polydisc GW In-Line polyamide filter with 0.45  $\mu\text{m}$  pore size, GE Healthcare Inc.) in order to remove any solid particulates via mechanical filtration. The particulate-free industrially polluted water was then dynamically filtered with TPU cloths functionalised with DMAM-calixarene.

Filtrates from both the spiked pond water, and real-world industrially polluted water experiments were analysed via ICP-OES spectroscopy.

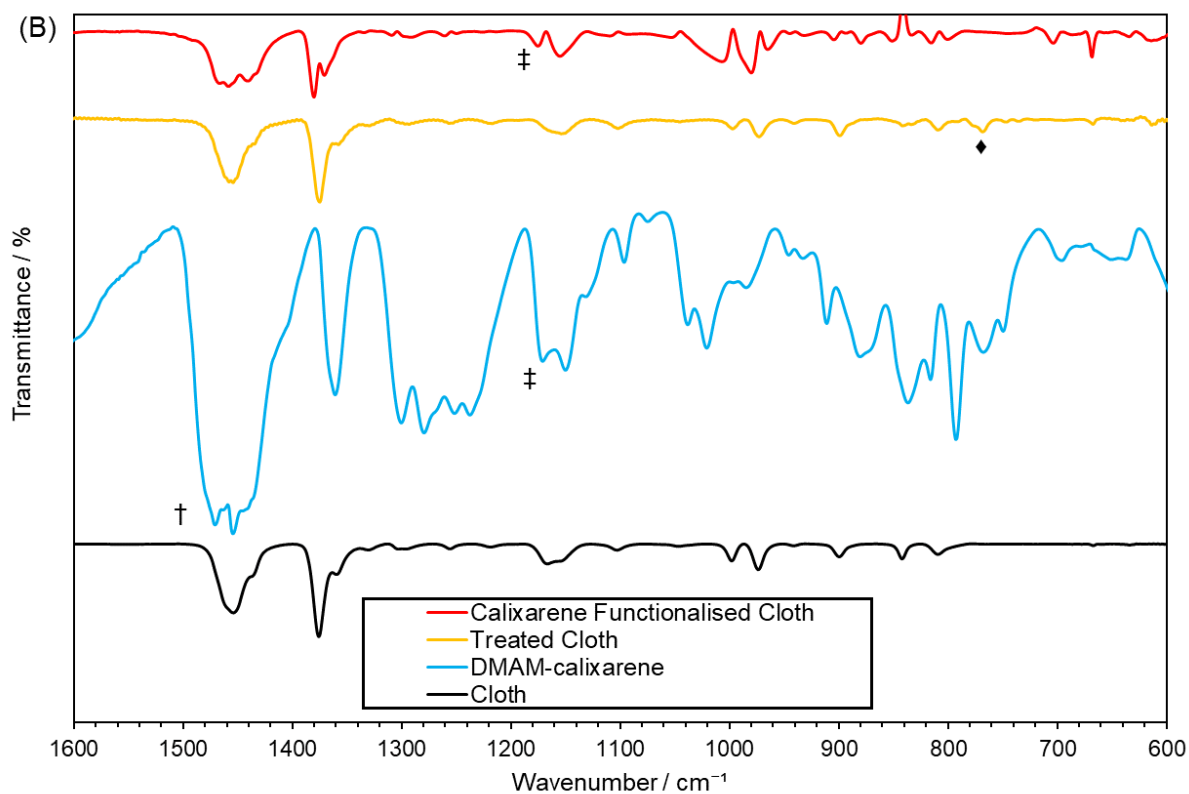
All experiments have been performed at least three times, and error values provided correspond to the standard deviation of the recorded values.

## 4.3 Results

### 4.3.1 Characterisation of Functional Cloths

The ATR spectrum of the TPU cloth, treated with  $\text{CHCl}_3$  plasma, and then the same cloth, left to spin in a DMAM-calixarene solution, revealed little difference in absorbance bands. This can be attributed to the functional groups of the TPU cloth exhibiting significant overlap with the calixarene functional group. Therefore, to aid identification of the key absorbance bands, the experiment was repeated using a polypropylene cloth (meltblown 20 GSM, M020A1WMS, Don&Low Ltd.) as a substrate (Figure 4-1). One key advantage of plasma processes (and as demonstrated in 3.3.8) is that they are substrate independent,<sup>253,329</sup> so carrying out the process with a different cloth should yield the same product on the surface of the substrate. Polypropylene was therefore chosen, owing to its relative lack of absorbance bands in the FTIR spectra. Following treatment with  $\text{CHCl}_3$  plasma, several absorbance bands in the range of 600–800  $\text{cm}^{-1}$  appeared, which are not observable in the ATR spectrum of the untreated cloth. These absorbance bands can be attributed to C–Cl stretches—note that in previous research of chlorine-containing plasma treatment polymer substrates, a wide range of absorbance bands have been attributed to the presence of C–Cl bonds, all of them within this wavelength range (as well as other species which contain C–Cl bonds).<sup>334,335,337, 344, 345</sup> Particularly noticeably, following derivatisation with DMAM-calixarene, the absorbance band at 768  $\text{cm}^{-1}$  is no longer visible, implying that the chloride group has been successfully

substituted. Furthermore, absorbance bands corresponding to various DMAM-calixarene functional groups, including the O–H stretch ( $3240\text{ cm}^{-1}$ ), C–H<sub>3</sub> antisymmetric bend ( $1465\text{ cm}^{-1}$ ), and N–H stretch ( $1175\text{ cm}^{-1}$ ) can be observed following derivatisation with DMAM-calixarene (Figure 4-1, Table 4-1) indicating successful attachment.



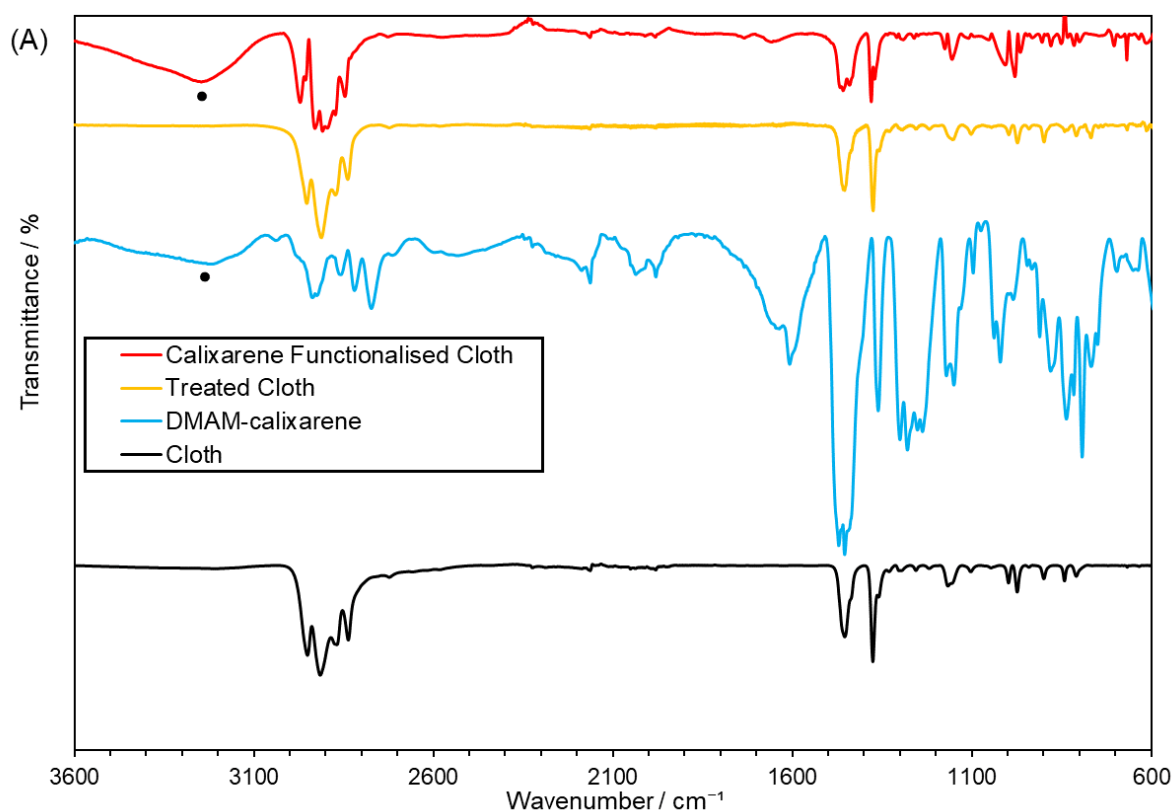


Figure 4-1. (A) ATR-infrared spectrum of untreated polypropylene cloth (black), solid DMAM-calixarene (blue), a polypropylene cloth treated with  $\text{CHCl}_3$  plasma (orange), and the same treated cloth, derivatised with DMAM-calixarene (red). (B) is an expansion of (A), illustrating the absorbance bands between 1600 and 600  $\text{cm}^{-1}$ .

Table 4-1. Assignment of functional groups found in the DMAM-calixarene functionalised,  $\text{CHCl}_3$  treated, polypropylene cloth. \*The absorbance band at 768  $\text{cm}^{-1}$  was observed in the treated cloth, but not in the DMAM-calixarene functionalised cloth.

Label	Absorbance band present in calixarene / $\text{cm}^{-1}$	Absorbance band present in functionalised cloth / $\text{cm}^{-1}$	Assignment	Ref
•	3220	3280	O–H stretch	346, 347
†	1472	1465	C–H <sub>3</sub> antisymmetric bend	346, 347
‡	1171	1175	N–H stretch	346, 347
◆	N/A	768*	C–Cl stretch	344, 345, 347

### 4.3.2 Extraction of Chromate Oxyanions

#### 4.3.2.1 Plasma Optimisation

In order to determine the optimum experimental conditions, pieces of meltblown 35 GSM polyurethane cloth were exposed to  $\text{CHCl}_3$  plasmas consisting of a variety of peak powers, treatment time, and a mixture of continuous wave (C.W.) and pulsed plasma (Table 4-2). The greatest extraction percentage was observed by cloths which were treated with  $\text{CHCl}_3$  plasma under pulsing conditions, with a duty on:off cycle of 100  $\mu\text{s}$ :4 ms. The extraction decreases for both harsher conditions (use of C.W. plasma and longer on-times) and gentler plasma conditions (shorter on times and/or longer off times). While it is generally expected that less harsh plasma conditions give rise to more ideal surfaces,<sup>334,348</sup> it is usual for there to be an optimum “middle ground” plasma power, which results in the most desirable surface.<sup>349</sup> At lower energies, less fragmentation of the monomer occurs, which can lead to fewer anchoring points with the substrate and hence, a lower incorporation of chloride groups.<sup>350</sup> However, at greater powers, chlorine-containing plasmas are known to deposit oligomeric chlorine-containing films.<sup>337</sup> These films may be less susceptible to substitution (e.g., due to their higher degree of cross-linking) than individual chloride groups on the cloth surface, meaning that less calixarene can be incorporated onto the surface.

Table 4-2. Plasma conditions employed during the fabrication of  $\text{CHCl}_3$  treated, DMAM-calixarene functionalised TPU cloths, and their subsequent extraction percentages and filtration times obtained for the dynamic filtration of 20 mg L<sup>-1</sup> Cr(VI). Data presented without errors have been performed one time; both experiments using the 100  $\mu\text{s}$ :4 ms on:off time, and the continuous wave experiments using 30 W plasmas have been performed at least three times; all other experiments have been performed twice.

C.W. or Pulsed Plasma	Peak Power / W	On:Off time / $\mu\text{s}$ :ms	Total time / min	Extraction percentage / %	Filtration Time
Pulsed	30	200:4	1	9.4 $\pm$ 1.5	Ca. 15
Pulsed	30	100:4	10	62.9 $\pm$ 9.2	Ca. 15
Pulsed (Chamber was not pre-treated prior to cloth treatment)	30	100:4	10	14.65 $\pm$ 9.9	Ca.10
Pulsed	30	50:4	10	11.7	Ca.
Pulsed	30	20:20	1	16.8 $\pm$ 12.0	Ca.10
Pulsed	30	2:30	1	1.1 $\pm$ 1.6	Ca. 5
C.W.	30	N/A	5	47.3 $\pm$ 5.6	Ca. 5
C.W.	10	N/A	1	35.0 $\pm$ 10.0	Ca. 5

#### 4.3.2.2 Adsorbent Comparison

The extraction percentage towards Cr(VI) of meltblown TPU cloths, treated with  $\text{CHCl}_3$  plasma for 10 min under the optimised conditions (30 W, 100  $\mu\text{s}$  on, 4 ms off) and derivatised with either DMAM-calixarene, or tBu-calixarene was determined. The extraction percentages following dynamic filtration of a 20 mg  $\text{L}^{-1}$  Cr(VI) solution with each of these adsorbents, and a  $\text{CHCl}_3$  plasma treated cloth were determined (Figure 4-2). Minimal extraction of chromate oxyanions is observed following attempted filtration with both the treated cloth, and the treated cloth functionalised with tBu-calixarene, which demonstrates that attachment of the DMAM moiety is necessary for chromium removal, which aligns with previous results by Bieber et al.<sup>327</sup> In that work, an extraction percentage of  $78 \pm 9\%$  under the same experimental conditions—other than using pulsed plasma poly(4-VBC) as the linker layer—was observed, which is within error range of the  $62.9 \pm 9.2\%$  in this work, indicating that under optimal conditions—note that when using CW plasma at 30 W for 5 min (the next most optimal conditions), the filtration efficiency is no longer within error range of Bieber's findings—the use of  $\text{CHCl}_3$  plasma over VBC does not give rise to a noticeable decrease in chromate extraction.

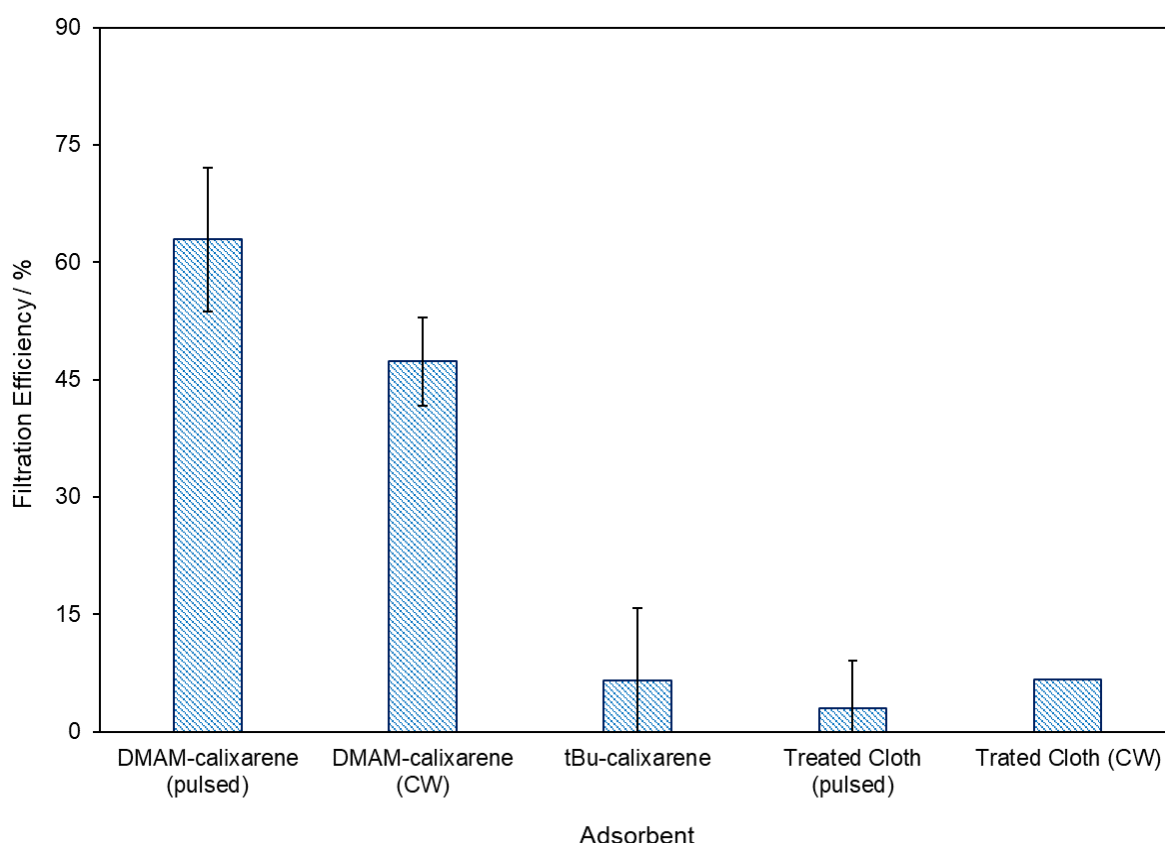


Figure 4-2. Extraction percentages towards 5 mL 20 mg  $\text{L}^{-1}$  Cr(VI) following dynamic filtration with DMAM-calixarene and tBu-calixarene functionalised,  $\text{CHCl}_3$  plasma treated cloths; and  $\text{CHCl}_3$  treated cloths. The treated cloths and DMAM-calixarene functionalised cloths presented were prepared using both using both CW (30 W, 5 min) and pulsed (100  $\mu\text{s}$  on:4 ms off, 30 W, 10 min) plasmas. The tBu-calixarene functionalised cloths were prepared using CW (30 W, 5 min) plasma. The CW treated cloth

was performed once, and the tBu-calixarene functionalised cloth was performed twice. All other experiments were performed at least three times.

### 4.3.3 Adsorption Kinetics

Kinetic studies were performed by recording the concentration of a 30 mg L<sup>-1</sup> Cr(VI) solution, which was adsorbed by a piece of DMAM-calixarene functionalised, CHCl<sub>3</sub> plasma treated TPU cloth, over an extended period of time. Adsorption kinetics are typically described by either pseudo-first order kinetics—in which one of the reagents exists in excess, so its concentration can be modelled as being constant, and so is adsorbed at a constant rate (proportional to the number of adsorption sites)<sup>351,352,353</sup>—or pseudo-second order kinetics, which describes systems which contain two competitive reversible second-order reactions at higher sorbate/sorbent ratios alongside a reversible second-order reaction at low sorbate/sorbent ratios.<sup>283</sup>

Equilibrium was achieved within ca. 10 min (Figure 4-3), which demonstrates that chromium extraction is rapid—an essential requirement for real-world contaminant removal. The experiment was repeated at half the usual spin speed (20 rpm) in order to determine whether the adsorption was affected by mass transfer problems (i.e., whether the kinetic data observed described the transfer of the chromium to the cloth by the Fisherbrand™ mini-rotator, or whether it was an accurate description of the adsorption kinetics). While the adsorption capacity following static filtration at 40 rpm appears initially greater, this disparity only occurs for the first 2.5 min. Furthermore, it should be emphasised that for both spin speeds, the values for adsorption capacity were within error range of each other at all time periods (Figure 4-3). As such, it is unlikely that the use of the Fisherbrand™ mini-rotator to spin the samples at 40 rpm gives rise to mass transfer problems for the adsorption of Cr(VI) with a DMAM-calixarene functionalised cloth.



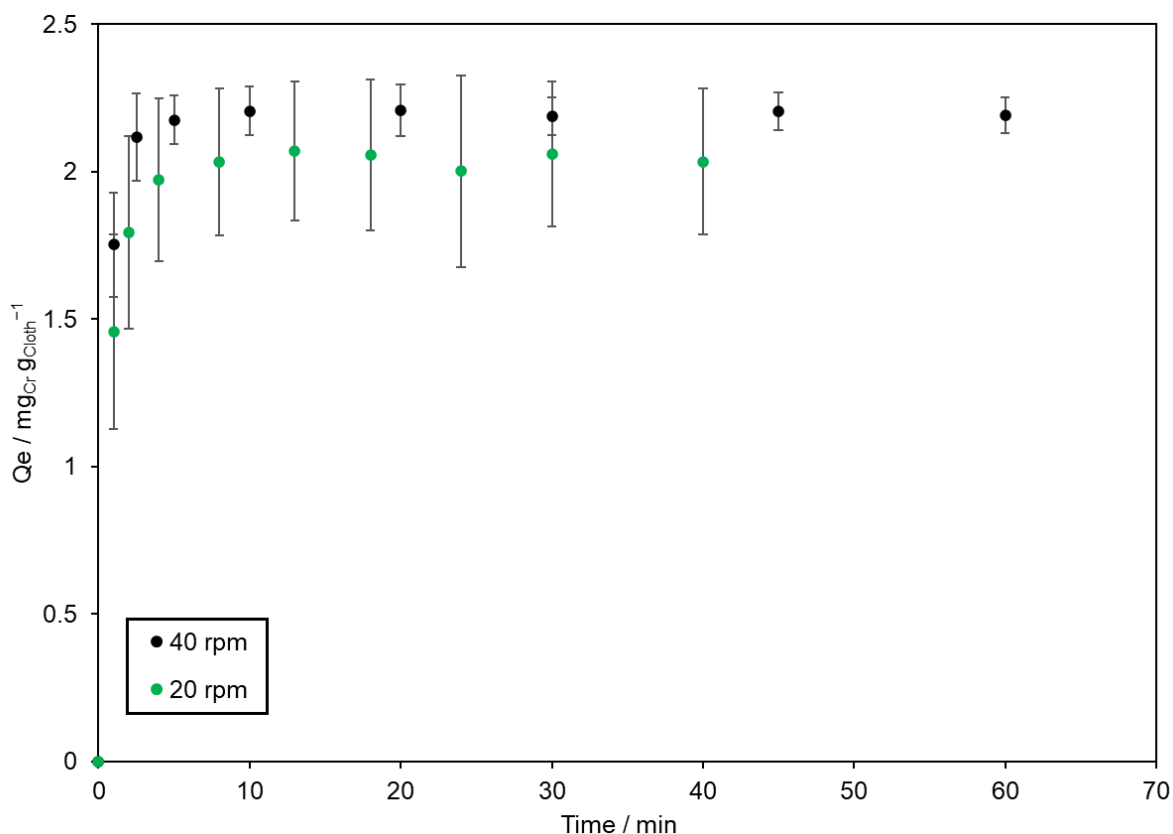


Figure 4-3. Adsorption capacity of a DMAM-calixarene functionalised,  $\text{CHCl}_3$  treated TPU cloth towards a  $30 \text{ mg L}^{-1}$  Cr(VI) solution under static filtration conditions, spinning at 40 rpm (black) and 20 rpm (green).

The data obtained at 40 rpm was modelled with linear and non-linear pseudo-first or pseudo-second kinetic models (Figure 4-4). Following the non-linear fit, the data appears to be well described by both pseudo-first- and pseudo-second-order models, with the error bars for all data points lying within the described adsorption curves. However, the pseudo-first order kinetic model does lie almost exactly on each data point, which would potentially suggest that the pseudo-first order kinetic model is more appropriate. On the other hand, the linear fit gives rise to an almost perfectly proportional relationship under the pseudo-second order kinetic model ( $R^2 = 0.9999$ ), as opposed to the pseudo-first order kinetic model ( $R^2 = 0.9423$ ), which would suggest that the pseudo-second order kinetic model is the more appropriate fit. Several publications have demonstrated the drawbacks behind fitting the data to the linearised forms of the equations, as the assumptions made in linearising the equations give a stronger weighting to values closer to equilibrium, meaning that pseudo-second order kinetics are almost always determined to be the kinetic mechanism, regardless of whether that model is correct.<sup>354, 355, 356, 357</sup> As it has been shown that equilibrium is reached very quickly, this weighting effect will be even more impactful for this calculation.

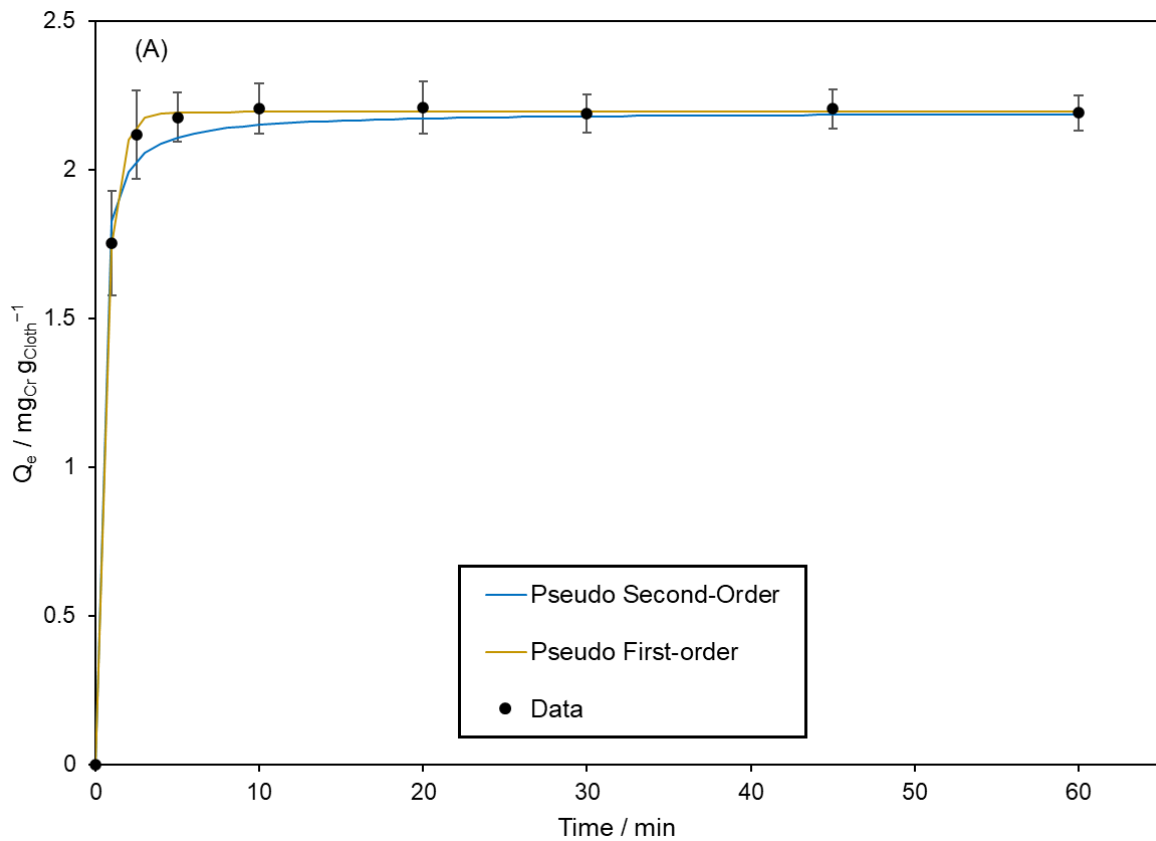
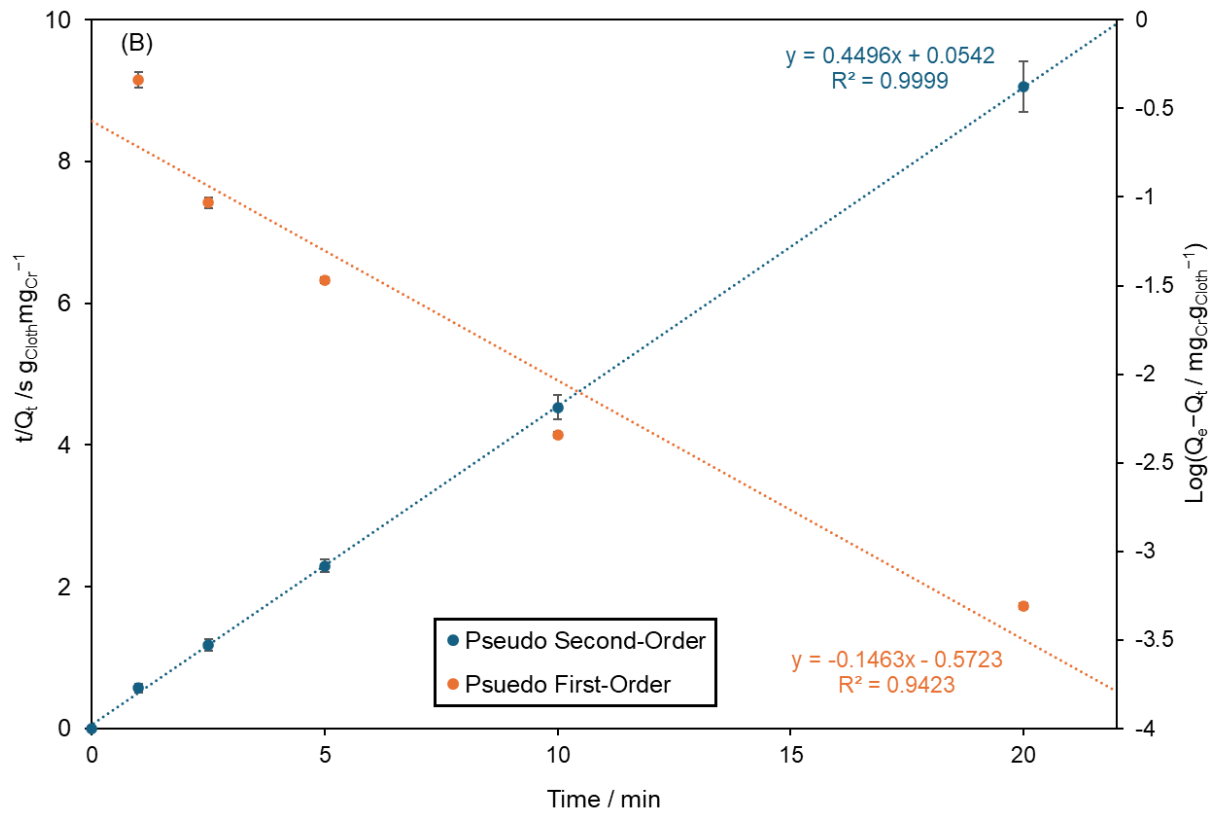


Figure 4-4. Pseudo-first order (orange) and pseudo-second order (blue) kinetic models, determined by following non-linear (A) and linear (B) models.

Consequently, it should be stated that the removal of Cr(VI) from solution by the DMAM-calixarene functionalised cloth does follow adsorption kinetics, however it cannot be confirmed whether pseudo-first order or pseudo-second order kinetics are more appropriate. For the sake of completeness, the determined rate constant values for both non-linear and linear pseudo-first- and second-order kinetic models have been determined (Table 4-3)—the non-linear rate constants are calculated by determining which rate constant values yield the optimal data fit, whereas for the linear rate constants,  $k_1$  is determined by multiplying the gradient by  $-2.303$ , and  $k_2$  is determined by taking the inverse of the intercept and dividing that by the square of the maximum adsorption capacity.

Table 4-3. Determined values for rate constants  $k_1$  and  $k_2$ , using non-linear and linear models, for the adsorption of  $30 \text{ mg L}^{-1}$  Cr(VI) onto a DMAM-calixarene functionalised cloth, spun at 40 rpm. For the linear plots, the errors were calculated by determining the percentage error in the regression analysis for the gradient and intercept (where appropriate) calculations and applying this to the final rate constant values. For the non-linear plots, the errors were calculated by averaging the percentage error between each data point and the theoretically calculated value and applying this to the final rate constant value.

Variable	Non-Linear / $\text{min}^{-1}$	Linear / $\text{g}_{\text{Cloth}}\text{mg}_{\text{Cr}}^{-1}\text{min}^{-1}$
$k_1$	$1.58 \pm 0.01$	$0.0153 \pm 0.0005$
$k_2$	$2.26 \pm 0.05$	$0.0820 \pm 0.0181$

#### 4.3.4 Isotherm Determination

Determining the appropriate adsorption isotherm is a useful tool for elucidating the interactive mechanism between adsorbent and adsorbate.<sup>358</sup> For example, the Langmuir isotherm model describes a monolayer adsorption process wherein adsorption and desorption are equal. On the other hand, the Freundlich isotherm describes a multilayer adsorption system, with no finite adsorption limit when pressure/concentration is sufficiently large. In particular, once the adsorption isotherm has been identified, parameters including the maximum adsorption capacity can be estimated.<sup>359</sup>

DMAM-calixarene functionalised,  $\text{CHCl}_3$  plasma treated cloths were left to spin in 5 mL Cr(VI) solutions for  $> 4$  h at a range of concentrations, their extraction percentages determined, and adsorption capacities (mg of Cr adsorbed per gram of cloth,  $Q_e$ ) calculated.

Calculated values of  $Q_e$  were plotted against  $C$  (Figure 4-5), which demonstrates that at lower concentrations, there is a linear relationship between concentration and  $Q_e$ , which is the adsorption behaviour described by Henry's law.<sup>360</sup> Once the concentration rises, the  $Q_e$  values start to curve off, which is indicative of typical adsorption behaviour.

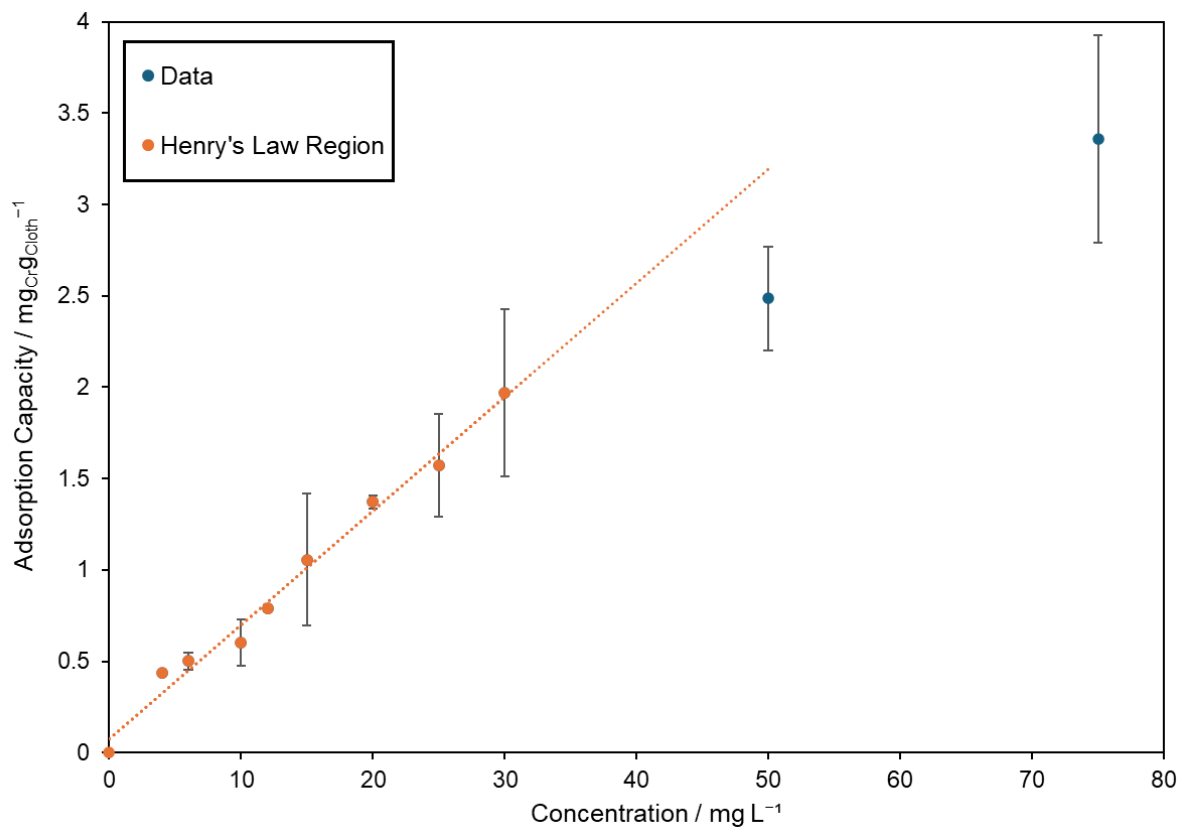


Figure 4-5. Relationship between starting concentration and normalised adsorption capacity. The datapoints in orange represent concentrations at which adsorption can be described by Henry's law.

The obtained data was converted into non-linear (Figure 4-6) and linear (Figure 4-7) Langmuir and Freundlich isotherms by following the process outlined in 2.1.3.2.2.  $X^2$  values for both non-linear plots were calculated, which yielded values of 0.454 and 0.112 for the Langmuir and Freundlich isotherms respectively.

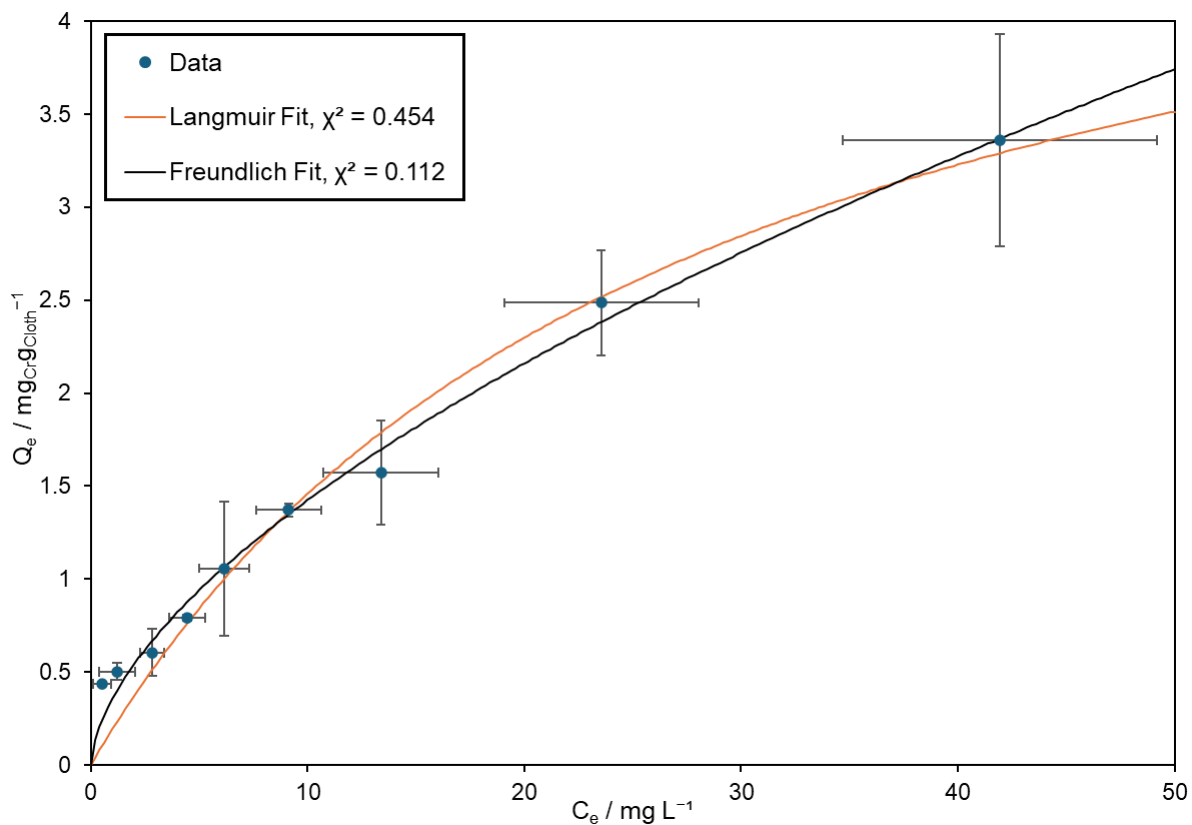
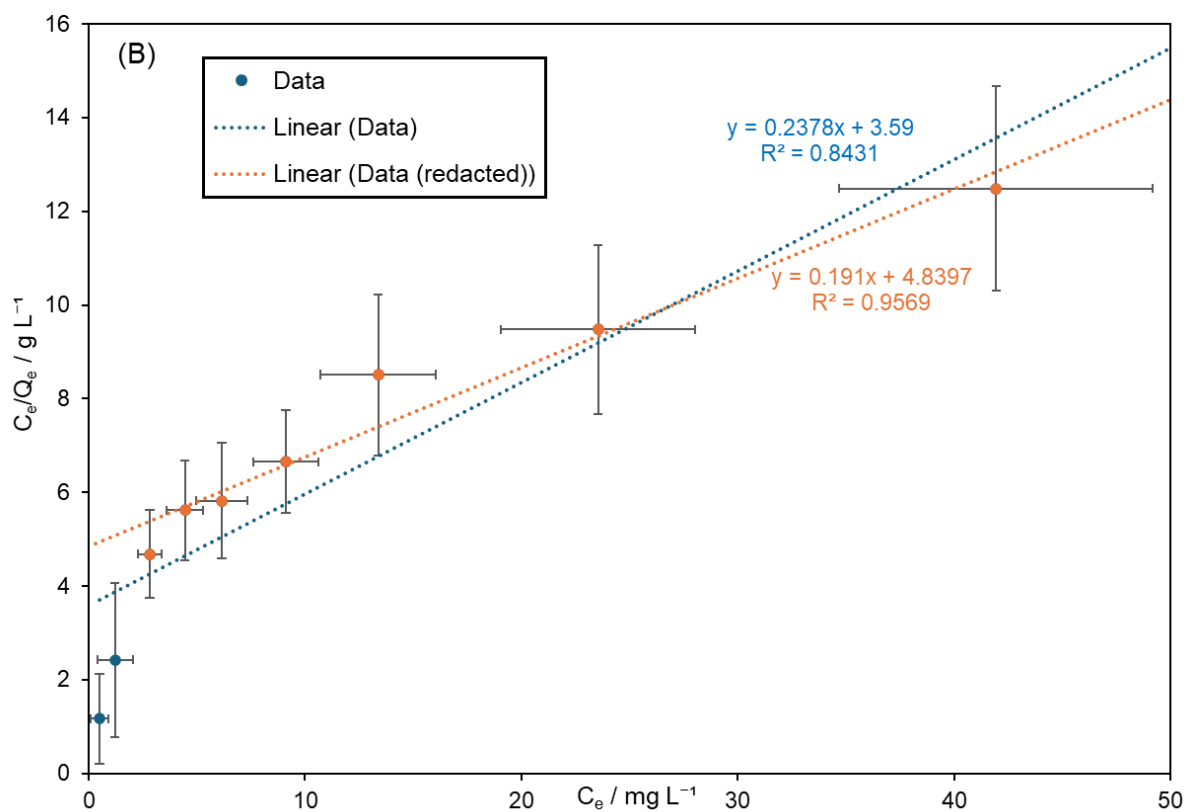


Figure 4-6. Adsorption capacity towards Cr(VI) from solution following static filtration with a DMAM-calixarene functionalised,  $\text{CHCl}_3$  treated, cloth. The raw data has been fitted against non-linear Langmuir (orange) and Freundlich (black) adsorption isotherms.



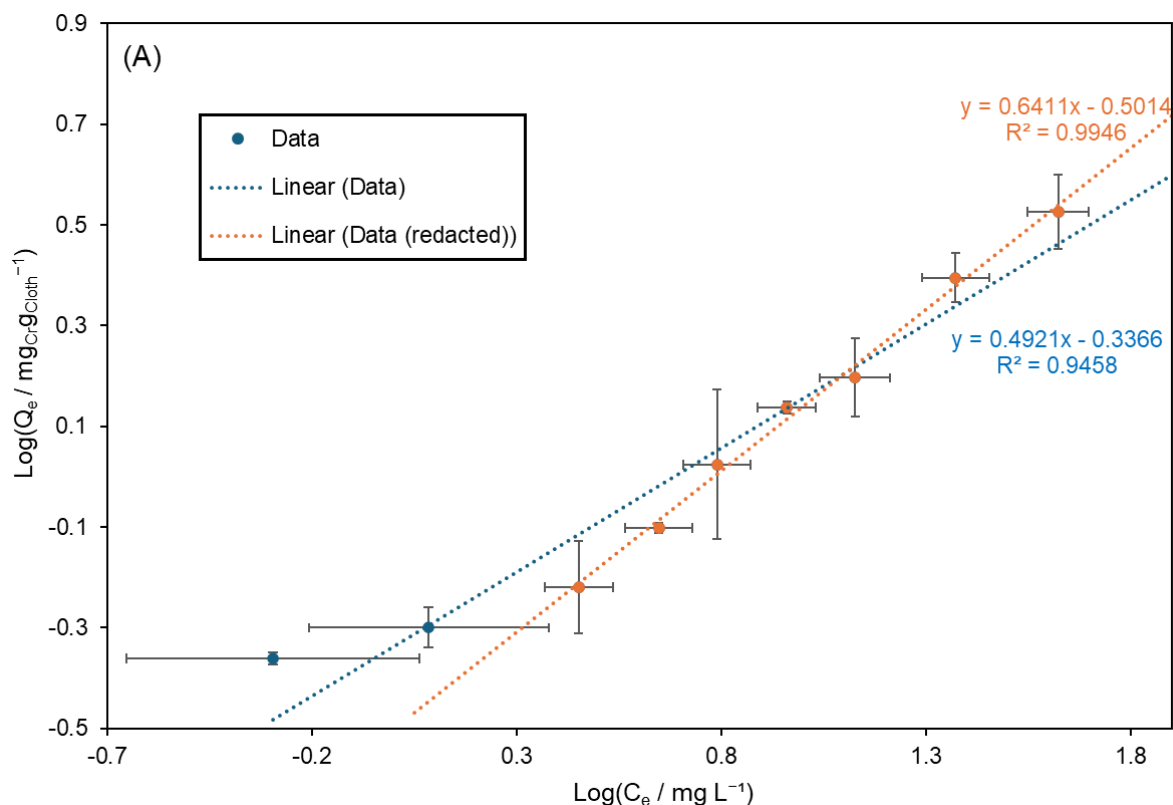


Figure 4-7. (A) Freundlich and (B) Langmuir linear isotherms, associated with the adsorption of Cr(VI) from solution with a DMAM-calixarene functionalised,  $\text{CHCl}_3$  treated, cloth. The blue trendlines correspond to the linear fit incorporating all data points, while the orange trendlines correspond to linear fits omitting the first two data points.

Within the range of concentrations employed, there does not appear to be a Cr(VI) concentration at which 100 % extraction occurs, nor does there appear to be a point at which the amount of Cr(VI) removed from solution remains unchanged, regardless of starting concentration. Note that due to the limitations of the UV-Vis spectrometer employed, concentrations greater than  $75 \text{ mg L}^{-1}$  could not be accurately recorded.

Analysis of the non-linear forms of the isotherms potentially implies that the Freundlich isotherm is a more accurate description of the Cr(VI) adsorption by the DMAM-calixarene functionalised cloths, as the  $\chi^2$  value is lower, which implies a better fit. However, as a visual fit, both models appear suitable, with all data points within error range of both the predicted Freundlich and Langmuir fits.

This determination was solidified by analysing the linear forms of the isotherms. The  $R^2$  value of the linear Freundlich fit was 0.9458, which is much closer to 1 than the 0.8431 value for the Langmuir fit. Furthermore, it can be identified for both fits that the first two data points did not particularly fall in line with the remainder of the data points. As such, linear fits were re-fitted, omitting those two data points. Yet again, the  $R^2$  value for the Freundlich fit (0.9946) lies much closer to 1 than the value for the Langmuir fit (0.9569).

Consequently, it was assumed that the adsorption of Cr(VI) by the DMAM-calixarene functionalised,  $\text{CHCl}_3$  plasma treated cloth could be modelled by a Freundlich adsorption isotherm, for which the values of  $n$  and  $K_F$  could be determined (Table 4-4). According to Equation (2-20), the values of  $n$  and  $K_F$  can be calculated from the linear isotherm by taking the inverse of the gradient and calculating  $10^{\text{Intercept}}$  respectively. Indeed, it can be seen that the values for  $n$  and  $K_F$  determined from the redacted linear isotherm are within error range of the values determined from the non-linear Freundlich isotherms, affirming the validity of the redaction.

Table 4-4. Determined values of  $n$  and  $K_F$  from the non-linear Freundlich plot, as well as both the redacted, and unredacted linear Freundlich plots. The error values for the gradient and intercept from the linear plots were determined by using the “Data Analysis—Regression” tool in excel, with a confidence interval of 95 %. For the non-linear isotherm, the errors were calculated by averaging the percentage error between each data point and the theoretically calculated value and applying this to the determined values of  $n$  and  $K_F$ .

Form of isotherm	Gradient	$n$	Intercept	$K_F / \text{mg L}^{-1}$
Linear	$0.492 \pm 0.045$	$2.03 \pm 0.09$	$-0.337 \pm 0.042$	$0.46 \pm 0.02$
Linear (redacted)	$0.641 \pm 0.021$	$1.56 \pm 0.03$	$-0.501 \pm 0.022$	$0.32 \pm 0.01$
Non-linear	N/A	$1.67 \pm 0.19$	N/A	$0.36 \pm 0.04$

The assignment to a Freundlich isotherm provides information regarding the physical characteristics of the adsorption. Specifically, Freundlich isotherms are representative of adsorptions which are heterogenous, with the formation of multilayers on the cloth.<sup>361</sup> Furthermore, the energy of adsorption is independent of surface coverage, as noted by the (single)  $K_F$  term within Equation (2-19).<sup>362</sup> However the Freundlich isotherm does not allow the determination of an adsorption maximum. Analysis of Equation (2-19) indicates that the variable ( $C_e$ ) is an arithmetic term and given that  $\frac{1}{n} \neq 0$ ,  $C_e^{\frac{1}{n}} \neq 1$ , the value of  $Q_0$  will always increase with  $C_e$ .

#### 4.3.5 Active Site Determination

In order to determine the number of amine groups added to the cloth surface through this procedure, an 8 mL aliquot of HCl (approximately 0.1 M)—before and after immersion of a DMAM-calixarene functionalised cloth—was titrated against a 0.002 M NaOH solution. Determining the number of amine sites can aid in understanding the adsorption mechanism. For example, while the determination of the Freundlich isotherm means that no estimation of the maximum adsorption capacity is possible, if the number of amine sites is found to be smaller than the maximum number of chromate molecules adsorbed to the surface during this investigation (note that the adsorption capacity following static filtration with a  $75 \text{ mg L}^{-1}$  solution was  $3.36 \pm 0.57 \text{ mg}_{\text{Cr}} \cdot \text{g}_{\text{Cloth}}^{-1}$ ), then this would imply that a multilayer is formed. It was

found that after acidifying the DMAM-phenol cloths with 0.1 M HCl and back-titrating with NaOH, a slight decrease in volume of NaOH required to neutralise the HCl solution, shaken with the DMAM-phenol functionalised cloth, was observed (Table 4-5).

Table 4-5. Calculated moles of NaOH required to neutralise a HCl solution, and the same HCl solution, when shaken with an uncoated TPU cloth, and a DMAM-calixarene functionalised cloth.

Acid Solution	Volume NaOH required to neutralise / mL	Calculated moles HCl in solution / mmol
HCl	103.88 ± 0.06	0.2078 ± 0.0001
HCl + TPU Cloth	103.88 ± 0.03	0.2078 ± 0.0001
HCl + DMAM-calixarene functionalised cloth	103.75 ± 0.05	0.2075 ± 0.0001

It was determined that the change in number of moles of acid before and after shaking with the DMAM-calixarene functionalised cloth was  $0.267 \pm 0.004 \mu\text{mol}$ , which is equivalent to  $0.00651 \pm 0.00009 \text{ mmol}_{\text{HCl}} \text{Cloth}^{-1}$ . The greatest chromium adsorption capacity achieved in this investigation was  $3.36 \pm 0.57 \text{ mg}_{\text{Cr}} \text{g}_{\text{Cloth}}^{-1}$ , which is equivalent to  $0.065 \pm 0.011 \text{ mmol}_{\text{Cr}} \text{g}_{\text{Cloth}}^{-1}$ . It can be seen that this is roughly 10 times the number of moles of chromium as amine groups, implying that a multilayer has formed.

However, owing to the small difference (in terms of mL) of NaOH titrated before and after addition of the DMAM-calixarene cloth, the validity of these findings must be questioned. That said, in order for the results to indicate a 1:1 ratio of amine groups to adsorbed chromium, a significantly greater difference in mL of titrated NaOH would need to be observed. As such, it is more than likely that a multilayer of chromate ions does indeed form, which is line with the findings from Section 4.3.4, which indicated that multilayer formation was likely, owing to the adsorption following a Freundlich isotherm.

#### 4.3.6 Cloth Recycling

Recycling of the DMAM-calixarene functionalised,  $\text{CHCl}_3$  plasma treated TPU cloths towards hexavalent chromium was performed by following a recycling procedure similar to that outlined by Bieber et al.<sup>327</sup> Following filtration of a 5 mL  $6 \text{ mg L}^{-1} \text{ Cr(VI)}$  solution, 5 mL of HP  $\text{H}_2\text{O}$  was passed through the used cloth, which was then regenerated with a 5 mL 2 M 0.5 M NaOH/2 M NaCl solution. Nine successive regeneration cycles were performed, with the filtration efficiency decreasing from  $73.9 \pm 5.9 \%$  ( $0.52 \pm 0.07 \text{ mg}_{\text{Cr}} \text{g}_{\text{Cloth}}^{-1}$ ) after the first filtration to  $34.55 \pm 0.8 \%$  ( $0.22 \pm 0.01 \text{ mg}_{\text{Cr}} \text{g}_{\text{Cloth}}^{-1}$ ) after the tenth filtration (Figure 4-8). While a lack of drop-off in chromium extraction would naturally be preferred, the results nonetheless



demonstrate that the same piece of cloth is still capable of removing chromium after 10 repeated uses, which demonstrates good reusability.

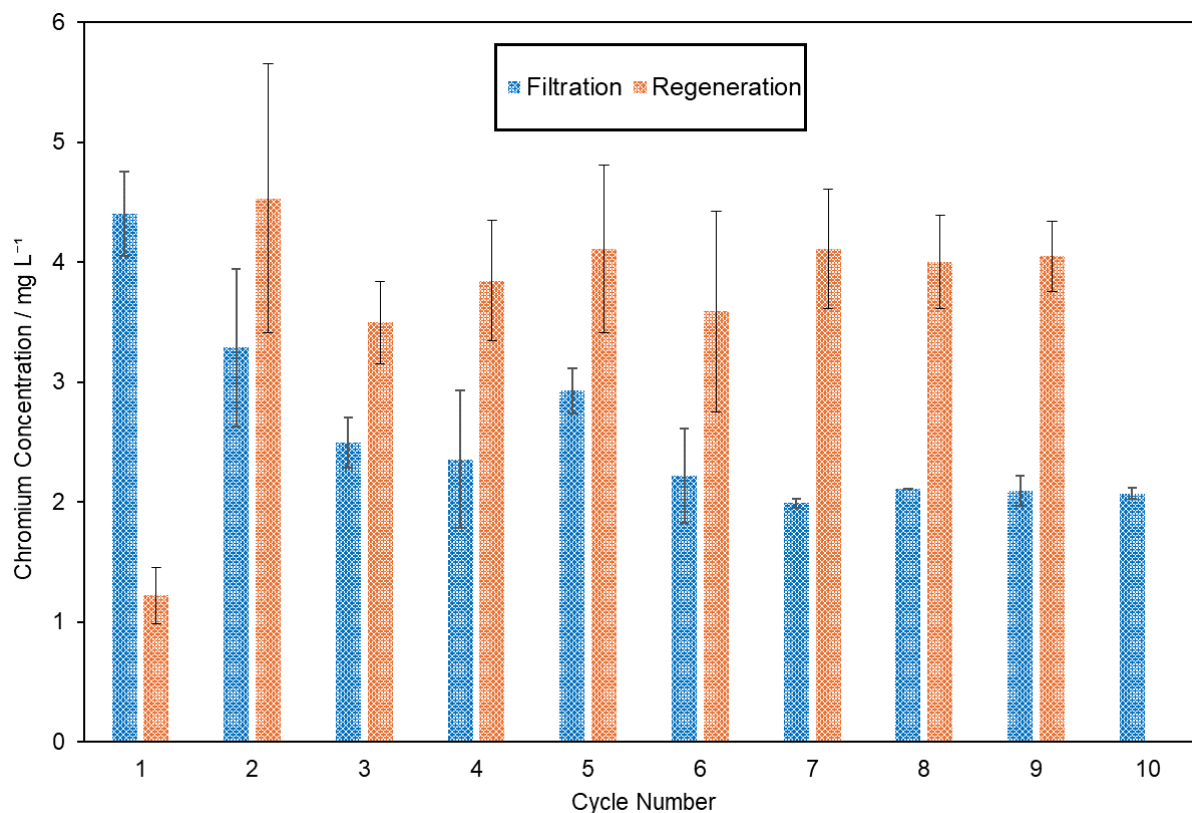


Figure 4-8. Concentration of Cr(VI) removed from a 5 mL 6 mg L<sup>-1</sup> solution after ten successive filtrations by a DMAM-calixarene functionalised, CHCl<sub>3</sub> plasma coated cloth (blue). Also, the concentration of Cr(VI) desorbed by the used cloth following regeneration with a 5 mL 0.5 M NaOH/2 M NaCl solution (orange).

While only a small concentration of Cr(VI) can be observed following the first desorption, a chromium concentration of ca. 4 mg L<sup>-1</sup> is observable in the regeneration eluant from the second desorption onwards. The limited desorption ability performance following the first cycle indicates that the increase in pH only plays a minor role in the cloth recycling—if pH adjustment were the primary driver of cloth recycling, then such an increase in regeneration efficiency in later cycles than earlier cycles would not be expected—meaning that regeneration is predominantly driven by displacement of bound chromate anions with the large excess of chloride ions in the regeneration solution. It was demonstrated in Section 4.3.4 that the maximum adsorption capacity far exceeds the  $0.52 \pm 0.07$  mg<sub>Cr</sub>g<sub>Cloth</sub><sup>-1</sup> observed in this experiment. As such, the cloth is not at capacity following the first regeneration, meaning that the chloride ions in the regeneration solution can bind to the adsorbent sites without needing to displace chromium. This provides a potential explanation for the regeneration behaviour observed, as for each subsequent regeneration—in addition to the chromium adsorbed in the most recent filtration—there is a bank of adsorbed chromate molecules, capable of being displaced by the chloride molecules. By displacing these chromate molecules in addition to

the more recently bound oxyanions, there will be a greater concentration of Cr(VI) in the regeneration eluent than extracted by the adsorbent in that cycle.

### **4.3.7 Cloth Selectivity**

#### *4.3.7.1 Competing Anions*

The suitability of the DMAM-calixarene functionalised,  $\text{CHCl}_3$  plasma treated TPU cloth towards real-world hexavalent chromium extraction was analysed by investigating the filtration efficiency of the cloth towards Cr(VI) contaminated water, containing (one of) a variety of competing anions. The anions chosen—chloride, phosphate, sulfate, carbonate and nitrate—are all commonly found in solution. A 1:100 mole ratio was chosen as the ratio of Cr(VI): competing anion as previous research (and also in Chapter 3 of this thesis) showed that a 1:10 mole ratio was insufficient to demonstrate noticeable changes in extraction percentage upon addition of competing anions.<sup>327</sup>

Following attempted filtration of a  $6 \text{ mg L}^{-1}$  Cr(VI) solution, an extraction percentage of  $68.8 \pm 7.2 \%$  was obtained (Figure 4-9). Following the addition of chloride, phosphate, sulfate and nitrate, little difference in extraction percentage was observed—there is a potential increase to  $80.3 \pm 7.2 \%$  when in the presence of phosphate, and a potential decrease to  $56.9 \pm 11.4 \%$  when in the presence of nitrate, however these extraction percentages are all within error range. The negative impact on extraction percentage by nitrate has been observed previously, with the similar size of nitrate to Cr(VI) used to explain the hindered Cr(VI) extraction (thermochemical radius of nitrate =  $0.200 \pm 0.019 \text{ nm}$  vs  $0.229 \pm 0.019 \text{ nm}$  for  $\text{CrO}_4^{2-}$ ).<sup>327,363</sup> However, a significant decrease in extraction percentage is observed when the filtration was performed in the presence of carbonate ions, yielding an extraction percentage of  $14.6 \pm 4.9 \%$  (Figure 4-9).

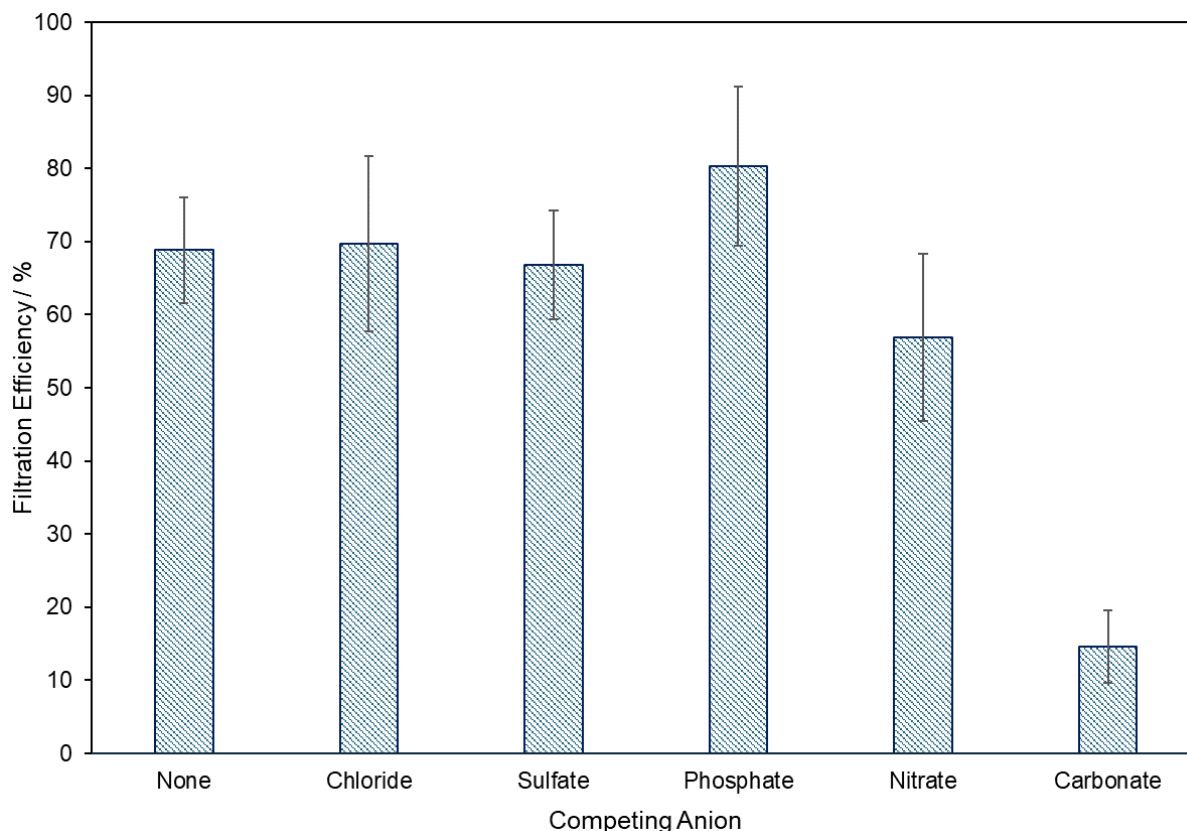


Figure 4-9. Change in extraction percentage for the dynamic filtration of a  $6 \text{ mg L}^{-1}$  Cr(VI) solution with a DMAM-calixarene functionalised cloth, and the same solution, when spiked with either chloride, sulfate, phosphate, nitrate, or carbonate, in a 1:100 mole ratio of chromium:competing anion.

However, it should be noted that the size of sulfate ions ( $0.218 \pm 0.019 \text{ nm}$ ) are more similar to chromate than carbonate ( $0.189 \pm 0.019 \text{ nm}$ ) and nitrate,<sup>363</sup> yet the presence of carbonate ions has a greater (negative) impact on chromate removal. There is an alternative explanation for its poor performance. Sodium hydrogen carbonate is mildly basic, and so its addition to the chromate solution means that, when in contact with the DMAM groups, these groups will become deprotonated, and hence will exhibit a weaker electrostatic attraction to the chromate anions, reducing the filtration efficiency. Furthermore, monosodium phosphate is mildly acidic, and so its addition to the Cr(VI) solution is likely to promote protonation of the amine groups, and hence cause an increased electrostatic attraction with the chromate anions.

#### 4.3.7.2 Real-World Chromium Samples

Attempted filtration of real-world water samples containing hexavalent chromium was performed. The first sample was taken from a nearby duckpond, and spiked with a known ( $6 \text{ mg L}^{-1}$ ) concentration of Cr(VI). A semi quantitative scan of the non-spiked pond water revealed presence of the metal ions shown in Table 4-6. The second sample was taken from

an industrial area in Jalandhar, India, where there is known to be chromium contamination.<sup>327</sup> ICP-OES analysis of the industrial water revealed a chromium concentration of 0.09 mg L<sup>-1</sup>.

Table 4-6. Concentration of elements determined by a semi quantitative ICP-OES scan of non-spiked pond water.

Element	Concentration / mg L <sup>-1</sup>
Ba	0.14
Ca	55.63
Fe	0.44
K	2.21
Mg	2.07
Mn	0.35
Na	6.39
Si	1.18
Sr	0.32

An extraction percentage of  $58.9 \pm 14.1$  % was observed following dynamic filtration of the spiked pondwater sample with a DMAM-calixarene functionalised, CHCl<sub>3</sub> plasma treated cloth, which is within error for the extraction of Cr(VI) from HP water with the same starting concentration ( $68.8 \pm 7.2$  %, Figure 4-10). Therefore, it can be stated that extraction of chromium is still possible, even in the presence of a wide array of organic and inorganic matter. Unfortunately, no extraction from the real-world water sample was observed (Figure 4-10). Section 4.3.4 demonstrated that the capacity towards chromium extraction decreased as concentration reduced, and so the concentration of chromium within the sample may be too dilute to be extracted by the cloth.

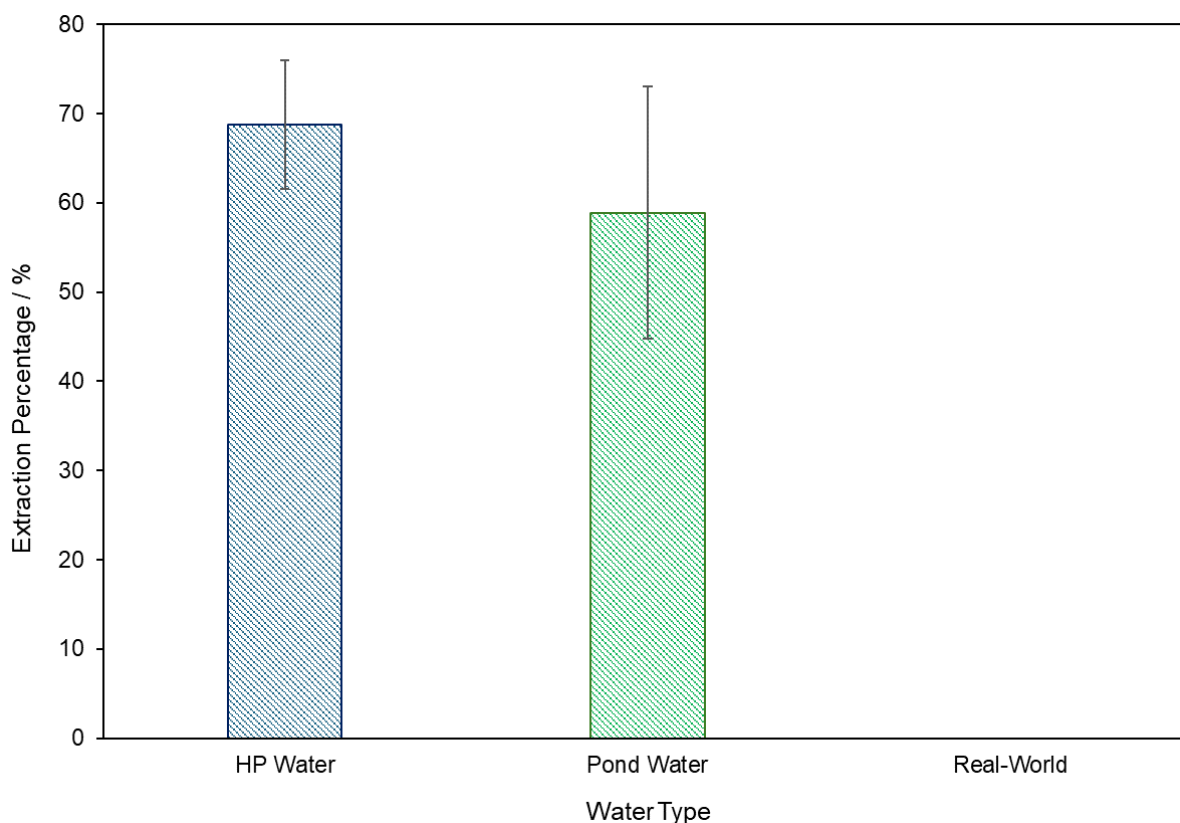


Figure 4-10. Extraction percentage following dynamic filtration of a  $6 \text{ mg L}^{-1}$  Cr(VI) solution, made up with HP water (blue) and pondwater (green), with a DMAM-calixarene functionalised,  $\text{CHCl}_3$  plasma coated TPU cloth. Also, the extraction percentage following dynamic filtration of a real-world chromium contaminated solution, with a DMAM-calixarene functionalised,  $\text{CHCl}_3$  plasma coated TPU cloth (note that this value is 0 %).

#### 4.4 Discussion

This work has built on previous research performed by Bieber et al., who produced a cloth filter, capable of removing hexavalent chromium for solution under dynamic conditions.<sup>327</sup> The need to use dynamic conditions is vital to address contaminated water in point-of-use scenarios, as static conditions—which are most commonly utilised throughout previous research into chromium removal—require expertise and significant timeframes to perform, meaning that they are unsuitable.<sup>324,364,365,366,367,368</sup> Furthermore, previous research into the use of calixarenes to extract Cr(VI) from solution typically uses acidic conditions to protonate the adsorbent, to aid with binding to the chromate anion. Not only is this non-representative of the pH of water typically found in rivers and lakes, but acidifying water to aid with chromium removal would render the water sample unfit for human consumption.<sup>324,364,365,366,367,368,369,370</sup> While the cloth produced by Bieber et al. was capable of extracting  $79 \pm 9 \%$  of Cr(VI) from a  $20 \text{ mg L}^{-1}$  sample under the dynamic filtrations conditions utilised in this work, there are issues associated with their cloth synthesis, specifically with regards to the plasmachemical deposition of pulsed plasma poly(4-VBC): 1) 4-VBC is toxic, and therefore increased levels of

controls are required for safe handling and safe disposal; 2) 4-VBC is relatively expensive, and so manufacturing a large quantity of the cloths would incur costs which may hinder the production; 3) Following plasmachemical deposition, the apparatus must be disassembled and cleaned between each deposition, which takes time, and hence limits the number of cloths that can be manufactured within a given timeframe. In this investigation, a cloth has been synthesised, which addresses each of the aforementioned issues, whilst still being capable of extracting  $62.9 \pm 9.2$  % Cr(VI) under the same conditions used by Bieber. The cloth was synthesised by treating a piece of TPU cloth with  $\text{CHCl}_3$  plasma, before undergoing the same functionalising step performed by Bieber to introduce DMAM-calixarene groups to the cloth surface. Chloroform is  $\sim 100$  times cheaper than 4-VBC and exhibits significantly fewer hazards. Furthermore, the equipment could be used without the need for complete disassembly and cleaning between treatments—the optimal conditions were determined to occur when the chamber was pre-treated with  $\text{CHCl}_3$  plasma prior to cloth insertion, however no scrubbing of the chamber is necessary, meaning that the equipment can be ready-to-use in much faster time periods.

The extraction percentages observed when a  $20 \text{ mg L}^{-1}$  Cr(VI) solution was passed through a  $\text{CHCl}_3$  treated cloth, and a treated cloth, functionalised with tBu-calixarene were minimal, indicating that the DMAM functionalities are responsible for dye extraction. The pKa of tertiary amines are  $\approx 9\text{--}10$ , meaning that under natural pH conditions, the DMAM groups will become protonated,<sup>371</sup> and so an electrostatic interaction between the positively charged cloth surface and negatively charged chromate anions can occur. During Bieber's investigation, no further explanation into the adsorption mechanism was able to be obtained, however greater insight has been found in this investigation. Here, it was discovered that the ratio of adsorbed chromium:active sites was capable of reaching 10:1 for the greatest chromium concentrations investigated. This implies that the adsorbed chromate is capable of forming multilayers. Indeed, this finding aligns with the adsorption behaviour, which has been shown to be modelled by a Freundlich isotherm – Freundlich isotherms imply that the adsorption is heterogeneous and gives rise to the formation of multilayers. Several other pieces of research have also provided adsorbents, which remove Cr(VI) via multilayer adsorption.<sup>372,373,374</sup> There, it is described that initially, electrostatic attractions lead to the formation of a monolayer of Cr(VI) on the adsorbents, before physical interactions between the adsorbed Cr(VI) and Cr(VI) in solution occur, leading to multilayer formation. As such, it is likely that in this work, a monolayer of Cr(VI) forms, owing primarily to the electrostatic interactions between the negatively charged chromate ion, and the positively charged amine groups on DMAM-calixarene, which are protonated under neutral pH, alongside  $\text{N-H}^+ \cdots \text{O}^-_{\text{Chrom}}$  hydrogen bonding. This would then be followed by slightly weaker ion-dipole

interactions and Van Der Waal's forces between the adsorbed chromate species and Cr(VI) species in solution, leading to the formation of multilayers. Multilayer formation is particularly useful as a mechanism of extraction, as it means that the adsorbent does not become exhausted once all the active sites on the cloth surface are saturated, allowing for augmented adsorption capacities.<sup>375,376</sup> Indeed, while the nature of the Freundlich isotherm does not permit the estimation of an adsorption capacity, the experimentally determined adsorption capacity is of the same order of magnitude as most of the adsorbents presented in Appendix Table 3. Given that the adsorbents listed in Appendix Table 3 typically present their optimal results under acidic conditions rather than pH 7, and that the aforementioned adsorbents tend to be high-surface area nanoparticles or resins (rather than a cloth, in which only the surface layer will have been functionalised, meaning that the vast majority of the weight will not be contributing towards the chromium extraction), these findings demonstrate that the DMAM-calixarene functionalised,  $\text{CHCl}_3$  plasma treated TPU cloth should be considered an outstanding adsorbent of hexavalent chromium.

In order to be useful as a point-of-use chromium extractor, an adsorbent also must be able to rapidly extract the contaminant (dynamic filtration implies a short contact-time between the cloth and the chromate, and so slow kinetics would not facilitate sufficient contaminant extraction), be reusable (single use filters would need to be disposed of more rapidly, which if not performed properly, could lead to an increase in pollution), and remove the desired contaminant even when in the presence of a range of competing ions (real-world water will contain a range of substances). Note that in the previous work presented in Appendix Table 3, only three pieces of work contained recycling studies.<sup>324,327,369</sup> Of these, only the work by Qureshi et al. investigated the effectiveness of their filter after ten regeneration cycles, however their work utilised very harsh conditions (4 M HCl) in order to regenerate their resin.<sup>324</sup> Furthermore, in works by Ozcelik et al.<sup>369</sup> and Bieber et al.,<sup>327</sup> the starting extraction percentage is 100 %, meaning that it is unclear whether or not the capacity of the cloth has actually decreased or remained the same for each cycle. Here, ten repeat filtrations of a  $6 \text{ mg L}^{-1}$  Cr(VI) were performed, with the cloth regenerated between each filtration using relatively mild conditions—a 0.5 M NaOH/2 M NaCl mixture. This choice of regeneration solution was based on previous research, where it was stated that base can deprotonate the amine groups, and hence extinguish the electrostatic interaction between the negatively charged chromate ions and the amine groups, while the exceedingly high salt concentration enables chloride ions to displace the chromate groups at the active sites (and hence allows for a lower base concentration to be used). The cloth's recycling behaviour—wherein following completion of the first cycle (where only a small proportion of extracted Cr(VI) is desorbed) more chromium is desorbed each cycle than adsorbed—potentially indicates that the displacement of bound

chromate is the main driving force behind regeneration. Fortunately, the excellent selectivity displayed by the cloth—minimal change in extraction percentage is observed when filtration of a  $6 \text{ mg L}^{-1}$  Cr(VI) solution in a 1:100 mole ratio of Cr(VI):competing anion was performed across a range of anions—means that the adsorbed chloride ions are themselves readily displaced upon addition of a repeat batch of chromium-contaminated water. While a drop-off in chromium extraction was observed, the cloth still demonstrated reasonable adsorption capabilities on the tenth filtration, meaning that it would be able to be used to repeatedly remove chromium from water sources, and hence can be used sustainably in remote locations. Furthermore, the selectivity investigation provides further clarity on the extraction mechanism. The drop-off in extraction percentage following addition of the basic sodium hydrogen carbonate (and potential increase in extraction percentage following addition of mildly acidic monosodium phosphate) lines up with observations illustrated in previous work (Appendix Table 3) whereby extraction percentages decreased with pH, owing to electrostatic interactions between the amine groups on the calixarene and the negatively charged chromate being the primary source of attraction. The relatively small decrease in extraction percentage when attempting Cr(VI) filtration in the presence of nitrate aligns with the research performed by Bieber et al., which stated that the unique cup-shape of the calixarene was able to provide favourable host-guest interactions with the chromate, and hence adsorption over the similarly (but still slightly different) sized nitrate ions was favoured.<sup>327</sup> Finally, under static conditions, equilibrium was reached within 10 minutes, which indicates that uptake is very rapid. Not only does rapid uptake increase the efficacy of dynamic filtration, but if static conditions were to be employed, then short filtration times could be used before cloth recycling, increasing their usefulness as a chromium extractor.

When investigating the filtration efficiency of the cloth towards a real-world water sample, the extraction percentage was in error range of the value determined for HP water, again demonstrating the suitability of the cloth towards real-world chromium removal. Unfortunately, when investigating real-world industrial water samples containing very low concentrations of Cr(VI), insufficient extraction was observed. One solution could be to combine the cloths in this work with a filter which is capable of removing Cr(VI) when in low concentrations (e.g., the filter designed by Bieber et al.<sup>327</sup>). Highly concentrated chromium solutions (e.g., those found in chrome plating wastewaters<sup>318</sup>) could be filtered by the cheaper, and more readily made  $\text{CHCl}_3$  plasma treated, DMAM-calixarene functionalised cloth in this work—whose multi-layer extraction mechanism implies the ability to extract large amounts of chromium—until the concentration is sufficiently low that the more expensive pulsed plasma poly(4-VBC) coated, DMAM-calixarene functionalised cloth can bring the levels of chromium below the  $50 \text{ } \mu\text{g L}^{-1}$  safe drinking level.



## 4.5 Conclusion

A TPU cloth has been successfully treated with  $\text{CHCl}_3$  plasma and functionalised with DMAM-calixarene and tBu-calixarene. The cloth is capable of removing highly-toxic and carcinogenic hexavalent chromium from solution with a high degree of efficacy ( $62.9 \pm 9.2\%$  for a  $20 \text{ mg L}^{-1}$  solution) under dynamic, point-of-use, filtration conditions, without any artificial adjustments in pH. This is appropriate for less affluent, more remote regions, where water contamination is more likely to have occurred. The extraction is modelled by a Freundlich isotherm, although it is unclear whether pseudo-first or -second-order kinetics is the more appropriate kinetic adsorption model. The extraction mechanism is primarily electrostatic, however the host-guest interactions facilitated by the unique shape of the calixarene is likely to support the Cr(VI) adsorption, and provides selectivity for the extraction of Cr(VI) when in competition with anions of similar charge and size in both controlled and real-world solutions. The ratio of adsorbed chromium to number of amine sites was in the ballpark of 10:1, which indicates that the adsorbed chromium forms a multilayer on the cloth, which would enable elevated adsorption capacities – the greatest capacity capable of being recorded under the experimental conditions was  $3.36 \pm 0.57 \text{ mg}_{\text{Cr}}\text{g}_{\text{Cloth}}^{-1}$ , and so increased capacities at elevated starting Cr(VI) concentrations is to be expected. Rapid kinetics were observed, with equilibrium achieved within 10 minutes, and the cloth was still capable of extracting chromium from solution, having been regenerated with a 0.5 M NaOH/2 M NaCl mixture at least 10 times.

## 4.6 References

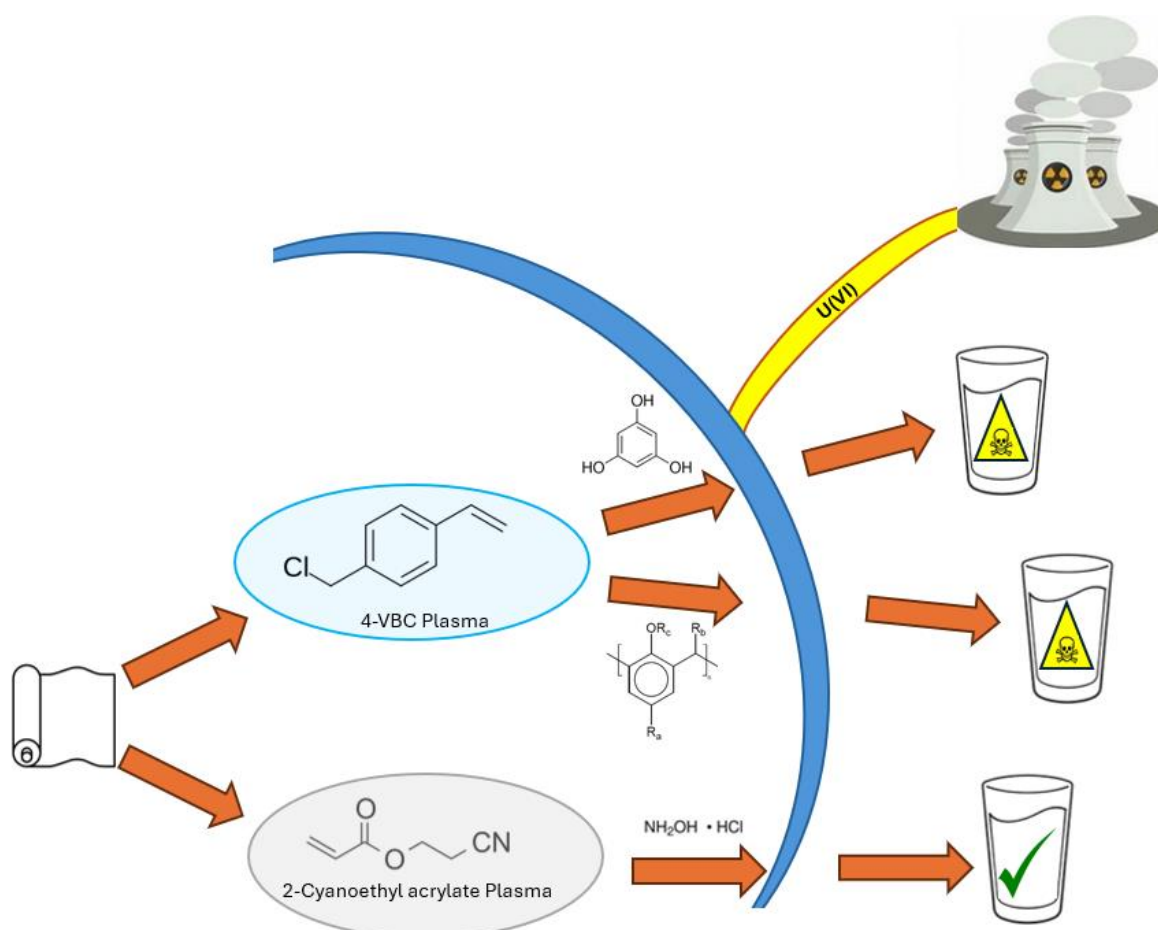
- 312 Parisi, M.; Nanni, A.; Colonna, M. Recycling of Chrome-Tanned Leather and Its Utilization as Polymeric Materials and in Polymer-Based Composites: A Review. *Polymers (Basel)*. **2021**, *13*, 429
- 313 Yamamoto, G.T.; Sekeroglu, O.; Bayramoglu, E.E. Marketing Activities in the Leather Industry: Comparative Country Analysis. *International Journal of Economics and Management Sciences*. **2011**, *1*, 37–48
- 314 Pati, A.; Chaudhary, R.; Subramani, S. A Review on Management of Chrome-tanned Leather Shavings: a Holistic Paradigm to Combat the Environmental Issues. *Environmental Science and Pollution Research*. **2014**, *21*, 11266–11282
- 315 Apte, A.D.; Verma, S.; Tare, V.; Bose, P. Oxidation of Cr(III) in Tannery Sludge to Cr(VI): Field Observations and Theoretical Assessment. *Journal of Hazardous Materials*. **2005**, *B121*, 215–222
- 316 Prasad, S.; Yadav, K.K.; Kumar, S.; Gupta, N.; Cabral-Pinto, M.M.S.; Rezania, S.; Radwan, N.; Alam, J. Chromium Contamination and Effect on Environmental Health and its Remediation: A Sustainable Approaches. *Journal of Environmental Management*. **2021**, *285*, 112174
- 317 Lunk, H-J. Discovery, Properties and Applications of Chromium and its Compounds. *ChemTexts*. **2015**, *1*
- 318 Karegar, S.; Bhargavi, M.; Divekar, S.V. Treatment of Wastewater from Chrome Plating Industry by Ion Exchange Method. *International Journal of Research in Engineering and Technology*. **2015**, *4*
- 319 Baruthio, F. Toxic Effects of Chromium and Its Compounds. *Biological Trace Element Research*. **1992**, *32*, 145–153
- 320 Laulicht, F.; Brocato, J.; Ke, Q.; Costa, M. Carcinogenicity of Metal Compounds. In *Handbook on the Toxicology of Metals Vol 1*. 5<sup>th</sup> Ed. London: Elsevier/Academic Press. 2022
- 321 Chromium in Drinking-water, Background Document for Development of WHO *Guidelines for drinking-water quality*. World Health Organization, Geneva 2020 ([http://www.who.int/water\\_sanitation\\_health/dwq/chemicals/chromium.pdf](http://www.who.int/water_sanitation_health/dwq/chemicals/chromium.pdf)) (Accessed on 12<sup>th</sup> March 2023)
- 322 Nag, R.; Pulla, Rao, C.P. Calixarene-mediated Host–guest Interactions Leading to Supramolecular Assemblies: Visualization by Microscopy. *Chemical Communications*. **2022**, *58*, 6044–6063
- 323 Kiegel, K.; Steczek, L.; Zakrzewska-Trznadel, G. Application of Calixarenes as Macrocyclic Ligands for Uranium(VI): A Review. *Journal of Chemistry*. **2012**, *2013*, 762819
- 324 Qureshi, I.; Memon, S.; Yilmaz, M. Estimation of Chromium(VI) Sorption Efficiency of Novel Regenerable p-tert-butylcalix[8]areneoctamide Impregnated Amberlite Resin. *Journal of Hazardous Materials*. **2009**, *164*, 675–682
- 325 Lele, S.; Jamwal, P.; Menon, M. Challenges in Regulating Water Pollution in India Standards, Monitoring, Enforcement and Accountability. *Economic and Political Weekly*. **2021**, *56*, 46
- 326 Chindarkar, N.; Grafton, R.Q. India's Depleting Groundwater: When Science Meets Policy. *Asia and the Pacific Policy Studies*. **2019**, *6*, 108–124
- 327 Bieber, V.; Ozcelik, E.; Cox, H.; Ottley, C.; Ratan, J.; Karaman, M.; Tabakci, M.; Beaumont, S.; Badyal, J.P. Capture and Release Recyclable Dimethylaminomethyl-Calixarene Functional Cloths for Point-of-Use Removal of Highly Toxic Chromium Water Pollutants. *ACS Applied Materials and Interfaces*. **2020**, *12*, 52136–52145
- 328 Teare, D.O.H.; Barwick, D.C.; Schofield, W.C.E.; Garrod, R.P.; Ward, L.J.; Badyal, J.P.S. Substrate-Independent Approach for Polymer Brush Growth by Surface Atom Transfer Radical Polymerization. *Langmuir*. **2005**, *21*, 11425–11430
- 329 Yasuda, H. *Plasma Polymerization*; Academic Press: New York, 1985.
- 330 Chonde, Y.; Liu, L-J.; Krieger, I.M. Preparation and Surface Modification of Poly(vinylbenzyl Chloride) Lattices. *Journal of Applied Polymer Science*. **1980**, *25*, 2407–2416
- 331 Cai, J.; Wathley, B. A Novel Traceless Solid Phase Tertiary Amine Synthesis Based on Merrifield Resin. *Tetrahedron Letters*. **2001**, *42*, 1383–1385

- 332 Lipschutz, B.; Blomgren, P. Efficient Scavenging of  $\text{Ph}_3\text{P}$  and  $\text{Ph}_3\text{PO}$  with High-Loading Merrifield Resin. *Organic Letters*. **2001**, 3, 1869–1871
- 333 Zhao, X.; Ivanova, N.; Hadzovic, A.; Zimmer-De Liliis; Lough, A.; Morris, R. Use of an Iodide-Modified Merrifield Resin in the Synthesis of Ruthenium Hydride Complexes. The Structure of  $\text{RuHI}((R)\text{-binap})(\text{PPh}_3)$ . *Organometallics*, **2008**, 27, 503–508
- 334 Inagaki, N.; Tasaka, S.; Suzuki Y. Surface Chlorination of Polypropylene Film by  $\text{CHCl}_3$  plasma. *Journal of Applied Polymer Science*. **1994**, 51, 2131–2137
- 335 Chen, S.H.; Chuang, W.H.; Wang, A. Ruan, R.C.; Lai, J.Y. Oxygen/nitrogen Separation by Plasma Chlorinated Polybutadiene/Polycarbonate Composite Membrane. *Journal of Membrane Science*. **1997**, 124, 273–281
- 336 Fernandes, G.F.; Amorim, M.K.M.; Oliveira, P.S.; Graff, I.L.; Rangel, E.C.; Durrant, S.F. Plasma Treatment of Crosslinked Polyethylene Tubes for Improved Adhesion of Water-based Paints. *Journal of Materials Research*. **2018**, 22
- 337 Upadhyay, D.J.; Bhat, N.V. Surface Modification and Characterization of Dichloromethane Plasma Treated Polypropylene Film. *Plasmas and Polymers*. **2003**, 8, 237–257
- 338 Zhang, Q.; Liu, Z.; Lin, D.; Hu, Y.; Zheng, B.; Zhao, T. Analysis of Discharge Characteristics of Pulsed Plasma Power Source in the Microsecond Scale. *Journal of Physics: Conference Series*. **2022**, 2313, 012023
- 339 Zhang, Y.; Zhang, Q.; Chen, W.; Shi, W.; Cui, Y.; Chen, L.; Shao, J. Hydrogeochemical Analysis and Groundwater Pollution Source Identification based on Self-organizing Map at a Contaminated Site. *Journal of Hydrology*. **2023**, 616, 128839
- 340 Xia, L.; Akiyama, E.; Frankel, G.; McCreery, R. Storage and Release of Soluble Hexavalent Chromium from Chromate Conversion Coatings Equilibrium Aspects of  $\text{Cr}^{\text{VI}}$  Concentration. *Journal of the Electrochemical Society*. **2000**, 147, 2556
- 341 Mayerhöfer, T.G.; Pahlow, S.; Popp, J. The Bouguer-Beer-Lambert Law: Shining Light on the Obscure. *ChemPhysChem*. **2020**, 21, 2029–2046
- 342 Lee, T.-J.; Chun, B.C.; Chung, Y.-C. Detoxification of Reactive Compounds by a Cyclic Electrolytic System with Surface-modified Ion-exchange Resin. *Reactive and Functional Polymers*. **2003**, 56, 37–44
- 343 Bisinella Scheufele, F.; Nivaldo Modenes, A.; Eduardo Borba, C.; Ribeiro, C.; Espinoza-Quinones, F.R.; Bergamasco, R.; Curvelo Pereira, N. Monolayer–multilayer Adsorption Phenomenological Model: Kinetics, Equilibrium and Thermodynamics. *Chemical Engineering Journal*. **2016**, 284, 1328–1341
- 344 Stoyanov, E.S.; Bagryanskaya, I.Y.; Stoyanova, I. IR-Spectroscopic and X-ray-Structural Study of Vinyl-Type Carbocations in Their Carborane Salts. *ACS Omega*. **2022**, 7, 27560–27572
- 345 Diem M. Symmetry Properties of Molecular Vibrations. In *Modern Vibrational Spectroscopy and Micro-Spectroscopy. Theory, Instrumentation and Biomedical Applications*. 1<sup>st</sup> Ed. John Wiley & Sons, 2015, pp. 39–70
- 346 Katsyuba, S.; Kovalenko, Y.; Chernova, A.; Vandyukova, E.; Zverev, V.; Shagidullin, R.; Antipin, I.; Solovieva, S.; Stoikov, I.; Konovalov, A. Vibrational spectra, Co-operative Intramolecular Hydrogen Bonding and Conformations of Calix[4]arene and Thiacalix[4]arene Molecules and their para-tert-butyl Derivatives. *Organic and Biomolecular Chemistry*. **2005**, 3, 2558–2565
- 347 Lui-Vien, D.; Colthup, N. B.; Fateley, W. G.; Grasselli, J. G. The Handbook of Infrared and Raman Characteristic Frequencies of Organic Molecules, Academic Press: Boston, **1991**
- 348 Mishra, G.; McArthur, S.L. Plasma Polymerization of Maleic Anhydride: Just What Are the Right Deposition Conditions? *Langmuir*. **2010**, 26, 9645–9658
- 349 Siffer, F.; Ponche, A.; Fioux, P.; Schultz, J.; Roucoules, V. A Chemometric Investigation of the Effect of the Process Parameters During Maleic Anhydride Pulsed Plasma Polymerization. *Analytica Chimica Acta*. **2005**, 539, 289–299
- 350 Carneiro de Oliveira, J.; de Meireles Brioude, M.; Airoudj, A.; Bally-Le Gall, F.; Roucoules, V. Plasma Polymerization in the Design of New Materials: Looking Through the Lens of Maleic Anhydride Plasma Polymers. *Materials Today Chemistry*. **2022**, 23, 100646

- 351 Agbovi, H.; Wilson, L. Adsorption Processes in Biopolymer Systems: Fundamentals to Practical Applications. Elsevier: Amsterdam, **2021**, pp.1–51
- 352 Ho, Y.; McKay, G. Kinetic Models for the Sorption of Dye from Aqueous Solution by Wood. *ICHEM E, Part B*. **1998**, *76*, 183–191
- 353 Miyah, Y.; Lahrichi, A.; Idrissi, M.; Bouhraf, S.; Taouda, H. Assessment of Adsorption Kinetics for Removal Potential of Crystal Violet Dye from Aqueous Solutions using Moroccan Pyrophyllite. *Journal of the Association of Arab Universities for Basic and Applied Science*. **2017**, *23*, 20–28
- 354 Xiao, Y. Erroneous Application of Pseudo-Second-Order Adsorption Kinetics Model: Ignored Assumptions and Spurious Correlations. *Industrial & Engineering Chemistry Research*. **2018**, *57*, 2705–2709
- 355 Moussout, H.; Ahlafi, H.; Aazza, M.; Maghat, H. Critical of Linear and Nonlinear Equations of Pseudo-first Order and Pseudo-second Order Kinetic Models. *Karbala International Journal of Modern Science*. **2018**, *4*, 244–254
- 356 Revellame, E.D.; Fortela, D.L.; Sharp, W.; Hernandez, R.; Zappi, M.E. Adsorption Kinetic Modelling Using Pseudo-first Order and Pseudo-second Order Rate Laws: A Review. *Cleaner Engineering and Technology*. **2020**, *1*, 100032
- 357 Kostoglou, M.; Karapantsios, T. Why Is the Linearized Form of Pseudo-Second Order Adsorption Kinetic Model So Successful in Fitting Batch Adsorption Experimental Data? *Colloids and Interfaces*. **2022**, *6*
- 358 Al-Ghouti, M.A.; Da'ana, D.A. Guidelines for the Use and Interpretation of Adsorption Isotherm Models: A Review. *Journal of Hazardous Materials*. **2020**, *393*, 122383
- 359 Wang, J.; Guo, X. Adsorption Isotherm Models: Classification, Physical Meaning, Application and Solving Method. *Chemosphere*. **2020**, *258*, 127279
- 360 Chakraborty, A.; Saha, B.B.; Ng, K.C.; Koyama, K.; Srinivasan, K. Theoretical Insight of Physical Adsorption for a Single Component Adsorbent+Adsorbate System: II. The Henry Region. *Langmuir*. **2009**, *25*, 7359–7367
- 361 Sun, W.; Selim, M. Fate and Transport of Molybdenum in Solids: Kinetic Modelling. In *Advances in Agronomy*, Ed. Sparks, D.L. Vol 164, Elsevier Inc. 2020, pp. 51–92
- 362 Sparks, D.L.; Singh, B.; Siebecker, M. Sorption of Phenomena on Soils. In *Environmental Soil Chemistry*, 3<sup>rd</sup> Ed. Academic Press, 2023, pp.203–281
- 363 Roobottom, H.K.; Jenkins, H.; Donald, B.; Passmore, J.; Glasser, L. Thermochemical Radii of Complex Ions. *Journal of Chemical Education*. **1999**, *76*, 1570
- 364 Khan, S.; Qureshi, I.; Shifa, M.S.; Waziri, A.H. An Efficient Calixarene-based Functional Material for the Sorption and Recovery of Cr(VI) from Water. *International Journal of Environmental Analytical Chemistry*. **2019**, *99*, 1123–1134
- 365 Tabakci, M.; Erdemir, S.; Yilmaz, M. Preparation, Characterization of Cellulose-grafted with Calix[4]arene Polymers for the Adsorption of Heavy Metals and Dichromate Anions. *Journal of Hazardous Materials*. **2007**, *148*, 428–435
- 366 Bayrakci, M.; Ozcan, F.; Yilmaz, B.; Ertul, S. Electrospun Nanofibrous Polyacrylonitrile/calixarene Mats: an Excellent Adsorbent for the Removal of Chromate Ions from Aqueous Solutions. *Acta Chimica Slovenica*. **2017**, *64*, 679–685
- 367 Ozcan, F.; Bayrakci, M.; Ertul, S. Synthesis and Characterization of Novel Nanofiber Based Calixarene and its Binding Efficiency Towards Chromium and Uranium Ions. *Journal of Inclusion Phenomena and Macrocyclic Chemistry*. **2016**, *85*, 49–58
- 368 Sayin, S. Fabrication of Efficient Calix[4]arene-Adorned Magnetic Nanoparticles for the Removal of Cr(VI)/As(V) Anions from Aqueous Solutions. *Polycyclic Aromatic Compounds*. **2022**, *42*, 1023–1034
- 369 Ozcelik, E.; Mercan, E.S.; Erdemir, S.; Karaman, M.; Tabakci, Calixarene-tethered Textile Fabric for the Efficient Removal of Hexavalent Chromium from Polluted Water. *Colloids and Surfaces A: Physicochemical and Engineering Aspects*. **2021**, *626*, 127045

- 370 Memon, S.; Tabakci, M.; Roundhill, D.M.; Yilmaz, M. Synthesis and Evaluation of the Cr(VI) Extraction Ability of Amino/nitrile Calix[4]arenes Immobilized onto a Polymeric Backbone. *Reactive and Functional Polymers*. **2006**, *66*, 1342–1349
- 371 Rayer, A.V.; Sumon, K.Z.; Jaffari, L.; Henni, A. Dissociation Constants (pKa) of Tertiary and Cyclic Amines: Structural and Temperature Dependences. *Journal of Chemical and Engineering Data*. **2014**, *59*, 3805–3813
- 372 Shobier, A.; El-Said, G.F. Comparative Study of the Effective Removal of Hexavalent Chromium via Calcium Alginate and Calcium Alginate/*Ulva fasciata* Composite. *SN Applied Sciences*. **2023**, *5*
- 373 Dong, H.; Liang, H.; Yang, L.; Yang, X.; Yang, C.; Hu, G.; Zhao, T. Porous Biochar Derived from Waste Distiller's Grains for Hexavalent Chromium Removal: Adsorption Performance and Mechanism. *Journal of Environmental Chemical Engineering*. **2023**, *11*, 110137
- 374 Sun, L.; Wang, M.; Li, W.; Luo, S.; Wu, Y.; Ma, C.; Liu, S. Adsorption Separation of Cr(VI) from a Water Phase Using Multiwalled Carbon Nanotube-Immobilized Ionic Liquids. *ACS Omega*. **2020**, *5*, 22827–22839
- 375 Isah, M.; Adeji, S.; Afagwu, C.; Jamal, S. A Review on Polymer, Gas, Surfactant and Nanoparticle Adsorption Modeling in Porous Media. *Oil & Gas Science and Technology*. **2020**, *75*
- 376 Shi, W.; Wang, Z.; Li, F.; Xu, Y.; Chen, X. Multilayer Adsorption of Lead (Pb) and Fulvic Acid by *Chlorella Pyrenoidosa*: Mechanism and Impact of Environmental Factors. *Chemosphere*. **2023**, *329*, 138596

## 5 CHAPTER 5 – PLASMACHEMICAL PREPARATION OF AMIDOXIME FUNCTIONALISED CLOTHS FOR THE CAPTURE AND RELEASE OF TOXIC URANIUM FROM WATER SOLUTION



### 5.1 Introduction

Uranium is a highly sought-after resource, owing to its exceptional capabilities in both weapons and nuclear fuel.<sup>377</sup> As such, there has been a significant increase in the economic viability of mining for uranium ore—just after the turn of the century, an increase in the price of uranium ore led to a 250 % increase in the global expenditure on uranium exploration (from \$200 million to \$750 million per year), with 5.5 million tonnes of uranium ore estimated to be economically viable.<sup>377, 378</sup> More recently, between January 2023 and January 2024—potentially in response to the percentage of the world’s power derived from nuclear power plants increasing from 10.3 % in 2020 to 18.9 % in 2021, with the trend expected to increase further<sup>379</sup>—the price of uranium more than doubled, from \$40.06 lb<sup>-1</sup> to \$80.36 lb<sup>-1</sup>, indicating that a further rise in uranium mining is imminent.<sup>380</sup> Unfortunately, as a result of extensive

mining, surface runoff and erosion processes have led to the contamination of groundwater with uranium worldwide, while mines that are abandoned, and insufficiently decommissioned, have also been found to result in nearby water-bodies becoming contaminated with uranium.<sup>381, 382</sup> Although uranium is also able to enter groundwater naturally—owing to leaching of uranium from U-hosting materials (such as Fe-Mn(oxy) hydroxides) under oxic conditions, or from weathering of U-containing surface rocks<sup>383, 384</sup>—a significant proportion of uranium content found within groundwater is attributable to human behaviour. As well as the aforementioned mining processes, nitrate-containing fertilisers, used extensively in agriculture, have been suggested to abiotically oxidise U(IV) to the more mobile U(VI), while nitrate driven Fe(II) oxidation gives rise to Fe(III) oxides, which are also capable of oxidising U(IV) into U(VI).<sup>385, 386</sup> Owing to this mobility, U(VI) is then able to permeate into local groundwater. Similarly, reports have stated that the use of phosphate fertilisers—which contain 0–200  $\mu\text{g}_{\text{Uranium}}\text{g}_{\text{Fertiliser}}^{-1}$ , and owing to uranium's ability to exchange with calcium ions in apatite<sup>387, 388</sup>—has led to the introduction of 14,000 tonnes of uranium being applied to the soil (equivalent to 1 kg U per hectare) over a 60 year period in Germany.<sup>389</sup> Finally, natural disasters, such as the Great East Japan Earthquake—in which the Fukushima Daiichi Nuclear Power Plant became damaged, and subsequently has resulted in the release of more than 1.2 million tonnes of nuclear wastewater into the Pacific Ocean<sup>390, 391</sup>—have the potential to damage infrastructure containing uranium waste, and can lead to widespread contamination.

While events, such as the Chernobyl nuclear disaster, tend to mean that people consider the radioactive risks of uranium above all else, it is the chemical risks associated with uranium as a heavy metal which result in the greatest harm to humans. Uranium is inefficiently excreted by bodies and is capable of accumulating in nail and hair after only a few months' exposure. Additionally, research into rats demonstrated that 78.3 % of initial uranium content is retained following inhalation.<sup>392</sup> Once in the lungs, the presence of uranium generates reactive oxygen species (ROS), and lipid peroxidation (LPO) occurs, which leads to cell membrane damage and eventually cell death.<sup>393</sup> Furthermore, uranium is capable of binding to the tubular membrane within the kidney, leading to reduced transport of necessary species (particularly  $\text{Na}^+$ , leading to interference of glucose transport<sup>394</sup>), resulting in kidney damage.<sup>395</sup> Moreover, in its insoluble form, uranium has been found to give rise to gastrointestinal, bone, and lung cancers.<sup>396</sup>

Significant research has been performed to investigate uranium removal from solution, and a wide range of adsorbents have been discovered. These include calixarenes,<sup>397</sup> amidoximes,<sup>398</sup> and polyhydroxybenzenes.<sup>399</sup> In each of these cases, the adsorbent contains an oxygen and/or nitrogen lone pair, which exhibits electrostatic attraction towards the positively charged  $\text{UO}_2^{2+}$  species, removing it from solution.

Calixarenes are particularly attractive, owing not only to their facile synthesis, but also their ability to be functionalised on either the upper or lower rim, thus rendering it easier to control their affinity and selectivity.<sup>400</sup> As such, a range of calixarenes have been used for the attempted removal of uranium from solution (Appendix Table 4). Here, a significant range of calixarenes can be seen, with adsorption capacities as high as  $505.58 \text{ mg}_{\text{Ug}}\text{Adsorbent}^{-1}$  observed,<sup>401</sup> indicating the excellent uranium extraction capabilities of calixarenes. It should be noted that most early work investigating calixarene removal of uranium demonstrated successful removal by determining equilibrium constants, and so these are not reported in Appendix Table 4.<sup>402,403,404,405,406,407,408,409,410,411</sup>

The second class of molecules which demonstrate strong affinity towards uranyl ions is polyhydroxybenzenes, particularly catechols and resorcinols (Figure 5-1).<sup>399</sup> While the calixarenes listed in Appendix Table 4 tended to require functionalisation on the upper rim in order to introduce functional groups that exhibit the strong affinity (typically, groups containing lone pairs and/or a negative charge, e.g., COOH, NH<sub>2</sub>, OH), polyhydroxybenzenes, by their nature of containing (at least) two hydroxy groups which are electrostatically attracted to the positively charge [UO<sub>2</sub>]<sup>2+</sup> ion, already exhibit good affinity towards uranyl.

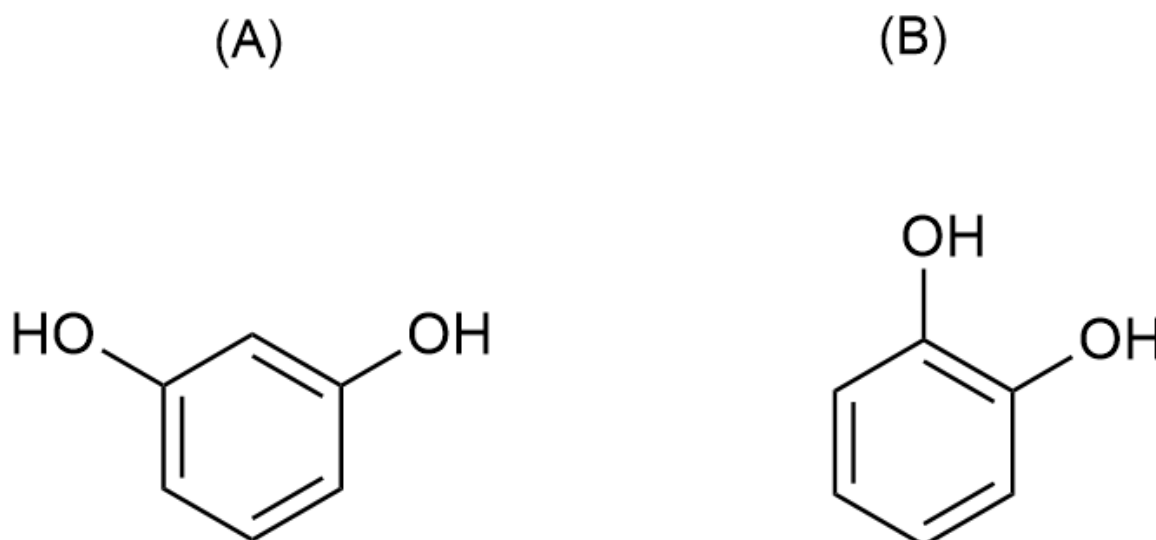


Figure 5-1. Structure of (A) Resorcinol, and (B) Catechol

Consequently, both catechol and resorcinol-type species have been employed as adsorbents for the extraction of uranium from both sea- and freshwater (Appendix Table 5 and Appendix Table 6 for catechol and resorcinol type adsorbents respectively). Note that the list of resorcinol-type adsorbents is significantly shorter, as the majority of uses refer to low-concentration uranium detectors, rather than uranium extraction, owing to the fact that uranium forms coloured complexes when chelated to 4-(2-Pyridylazo) resorcinol (PAR) or 4-(2-



thiazolylazo) resorcinol (TAR).<sup>412,413,414,415,416,417,418,419,420,421,422,423,424,425,426,427,428,429,430,431,432,433,434,435,436,437,438,439,440</sup> The catechol-type adsorbents show particularly promising uranium extraction capabilities, with a crosslinked bayberry tannin being able to remove 307.3  $\text{g}_{\text{Uranium}}\text{g}_{\text{Adsorbent}}^{-1}$ —a value which was surmounted by several of the polydopamine (PDA) type adsorbents, including a salicylaldoxime/PDA mix, tethered to graphene oxide (GO), which could extract 1049  $\text{g}_{\text{Uranium}}\text{g}_{\text{Adsorbent}}^{-1}$ .<sup>441,442</sup> The resorcinol-type adsorbents do still perform well, with PAR tethered to an Amberlite XAD resin capable of removing 115.5  $\text{g}_{\text{Uranium}}\text{g}_{\text{Adsorbent}}^{-1}$ , although this value does still lie below many of the catechol type resins in Appendix Table 5.<sup>443</sup>

The third class of adsorbents relevant to this work, which demonstrate particularly good uranium extraction capabilities, are amidoximes. The synthesis of amidoximes has remained almost unchanged since the 19th century, consisting of nucleophilic attack of the amide with hydroxylamine under basic conditions—although hydroxylamine attack on thioamide, hydrazine imide, iminoether, imidoylbenzo-triazole, and open chain pyrazine derivatives has also been used to produce amidoximes.<sup>444,445</sup> The presence of the two amine groups, as well as the hydroxy group, provide three lone pair sites which are capable of attracting the positively charged uranyl ion—separate spectral studies have given rise to differing conclusions regarding the main active site, potentially indicating that no one particular site dominates uranium binding.<sup>446,447,448</sup>

There exists an extensive amount of literature concerning the use of amidoxime functionalised materials in the removal of uranium from water sources, which has been thoroughly covered in a recent review.<sup>449</sup> Owing to the significant number of pieces of work, only those demonstrating the greatest adsorption capacities have been reported here (Appendix Table 7). Indeed, the excellent uranium capture exhibited by amidoxime-type adsorbents is demonstrated by the fact that—aside from salicylaldoxime/PDA tethered to graphene oxide<sup>442</sup>—the adsorption capacity of the amidoxime type adsorbents in Appendix Table 7 is greater than any of the calixarene-, catechol-, or resorcinol-type adsorbents in Appendix Table 4, Appendix Table 5, or Appendix Table 6 respectively (Figure 5-2).

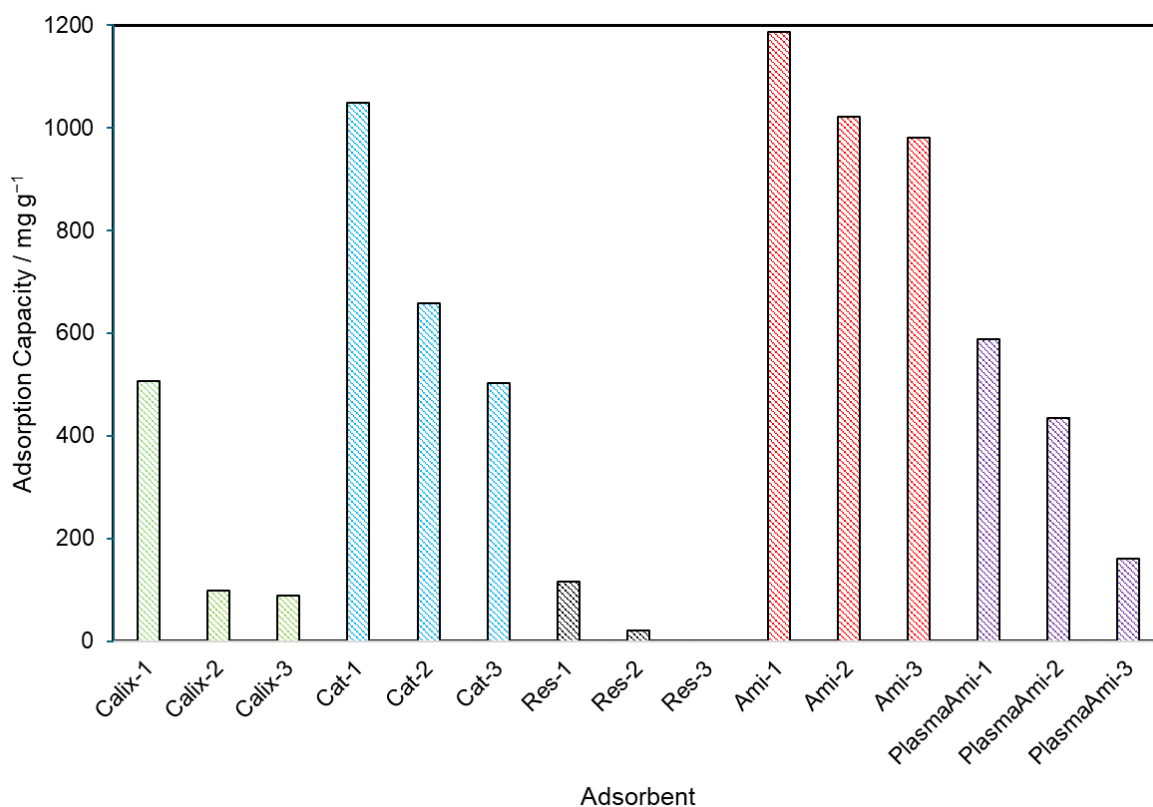


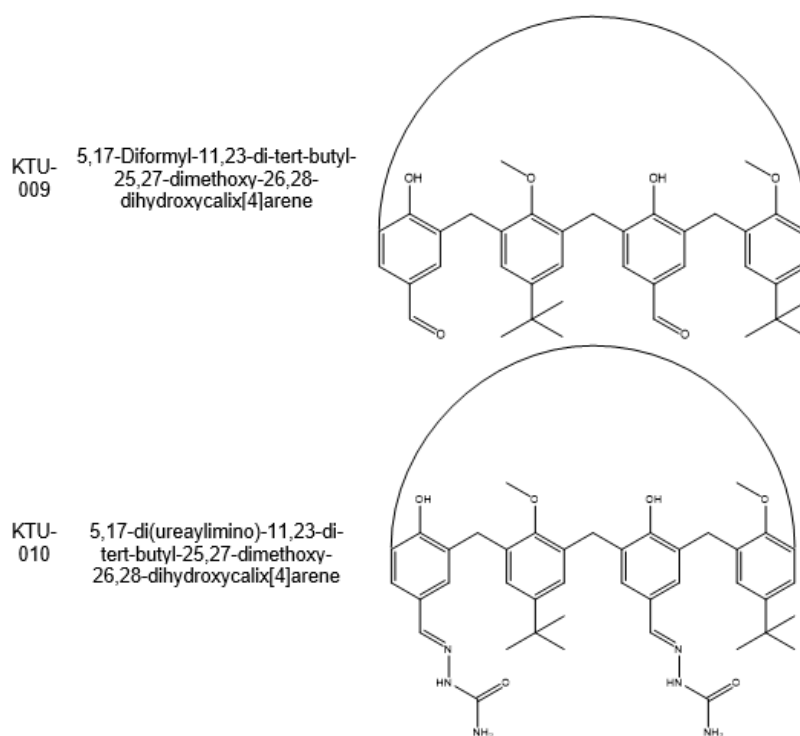
Figure 5-2. Adsorption capacities of the calixarene-based<sup>401,450,451</sup> (green), catechol-based<sup>442,452,453</sup> (blue), resorcinol-based<sup>443,454,455</sup> (black), amidoxime-based<sup>456,457,458</sup> (red), and amidoxime-based, where plasmachemical processes were used as part of the synthesis<sup>459,460,461</sup> (purple) adsorbents, which demonstrated the greatest adsorption capacities towards uranium.

Previous work by the Badyal group has utilised plasmachemical deposition in order to functionalise substrates, so that they are capable of removing contaminants (in this case chromium) from drinking water.<sup>462</sup> As opposed to the various wet chemistry techniques employed in the fabrication of the adsorbents in Appendix Tables 4–7, plasmachemical deposition offers several key advantages: no solvents are required for the initial functionalisation step, reducing material (and monetary) waste; minimal quantities of reagent are required in order to functionalise the substrate; and plasmachemical deposition is substrate independent, meaning that any substrate can be manipulated in order to introduce the key functional group.<sup>463,464</sup> Indeed, no use of plasmas in order to synthesise calixarene-, catechol-, or resorcinol-type adsorbents for the purpose of uranium capture has been found by this author, and only limited literature on the use of plasmas in the synthesis of amidoxime-type adsorbents has been found (Appendix Table 8). However, nearly all of these studies simply used nitrogen/argon plasma in order to activate a surface, so that acrylonitrile could be attached, rather than depositing a cyano-containing group onto the surface. The only deposition involved coating a surface, which already contained amidoxime groups, with an

alternative species whose purpose was to increase the anti-biofouling properties of the adsorbent.<sup>465</sup>

Furthermore, almost all of the extraction conditions stated in Appendix Tables 4–8 utilise batch adsorption, which, although useful when attempting to remove contaminants from large volumes of water (e.g., wastewater treatment prior to release into water bodies), is less appropriate for point-of-use water filtration required by the many thousands of civilians who rely on uranium-contaminated waterbodies for bathing, cooking, and drinking. While some of the systems described above did investigate dynamic filtration, the conditions employed typically involved packing resins into columns and passing through the contaminated water under pressure – conditions which are unlikely to be replicated in the environments where uranium filtration is most needed.

Consequently, the adsorbents synthesised in this work are designed to be used as filters which do not require external pressure, any specialised equipment, nor extended filtration times. To achieve this, polyurethane cloths were initially coated with pulsed plasma poly(4-vinylbenzyl chloride, 4-VBC), as in previous work (and as presented in Chapter 3).<sup>462</sup> Then, the chloride linker layer undergoes nucleophilic substitution with the extractant molecule of choice. In this case, a range of calixarenes containing hydroxy groups on the lower rim, and carboxylic acid, ureayl, ester, and amino moieties—which are designed to bind to uranium—on the upper rim. The calixarenes chosen for this work (KTU-009, KTU-010, KTU-011, KTU-013, KTU-014; all synthesised by Konya Technical University) are shown in Figure 5-3.



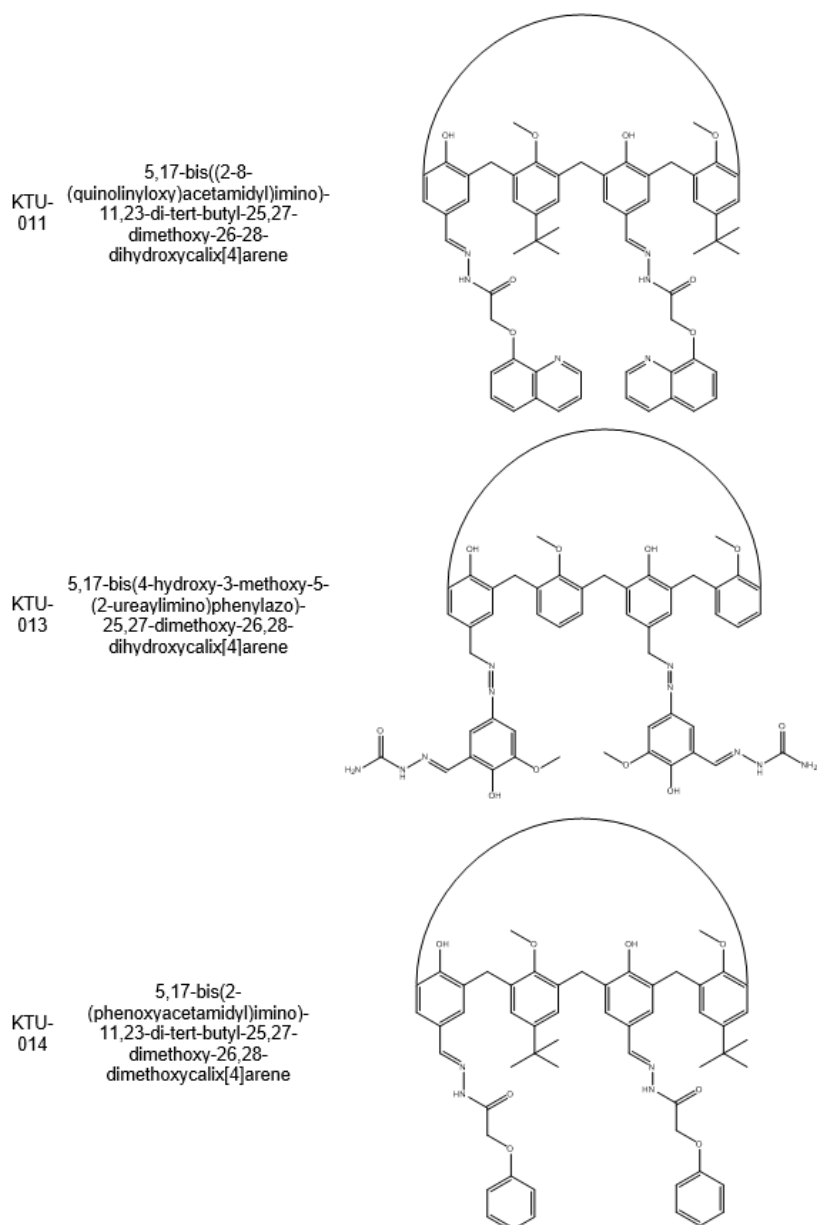
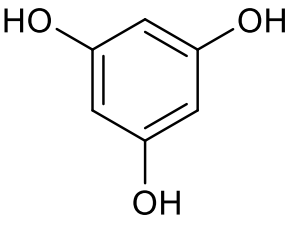
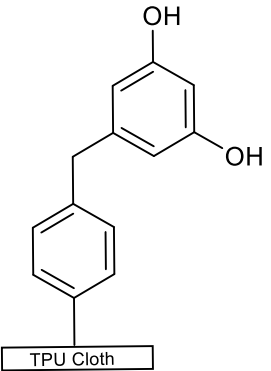
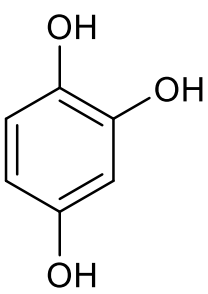
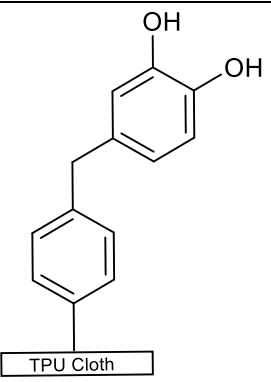


Figure 5-3 - Structures of calixarenes, attempted to be attached to a pulsed plasma poly(4-VBC) coated TPU cloth.

Similarly, hydroxyquinone and phloroglucinol (Table 5-1) were chosen, as nucleophilic substitution between one of the hydroxyl groups and the chloride on the pulsed plasma poly(4-VBC) would give rise to a filter containing catechol and resorcinol groups respectively.

Table 5-1. Structures of polyhydroxybenzene species attempted to graft onto the pulsed plasma poly(4-VBC) linker layer, and the final product synthesised, assuming successful attachment

Reagent	Structure	Final Product
Phloroglucinol		
Hydroxyquinone		

As amidoximes are formed by conversion of a nitrile group,<sup>444,445</sup> it was necessary to functionalise the polyurethane cloth substrate with a nitrile group containing species as the initial step. This was again done using the pulsed plasma deposition technique, here in conjunction with a cyano group monomer.

While previous research has demonstrated that plasma deposition of acrylonitrile, acetonitrile, 2-dicyanoethylene, and tetracyanoethylene in order to produce a cyano-functionalised substrate is possible, the plasma conditions resulted in limited retention of cyano groups, owing to the formation of ketene-imine and conjugated  $-C=N-$  structures.<sup>466, 467, 468, 469, 470, 471</sup> However, the Badyal group has previously deposited pulsed plasma poly(2-cyanoethyl acrylate) (Figure 5-4(A)) onto substrates (PTFE and NaCl plates) in order to fabricate cyano-functionalised solid surfaces with elevated nitrile retention.<sup>472</sup> Consequently, pulsed plasma poly(2-cyanoethyl acrylate) was deposited onto the polyurethane cloths, before reaction with hydroxylamine hydrochloride (HH) in order to give rise to amidoxime functionalised cloths Figure 5-4(B).

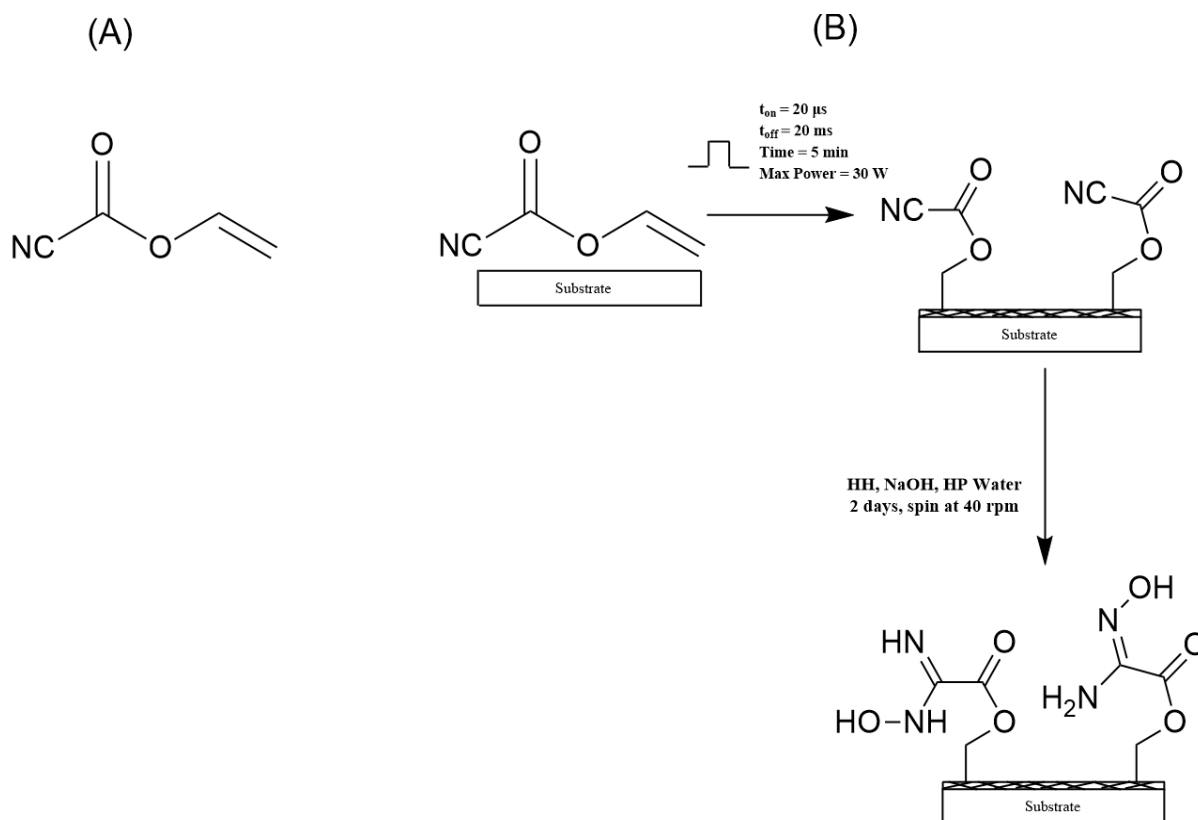


Figure 5-4. (A) Structure of 2-cyanoethyl acrylate. (B) Full scheme for the deposition of pulsed plasma poly(2-cyanoethyl acrylate) onto a polyurethane cloth, followed by amidoximation with hydroxylamine hydrochloride.

Unfortunately, under the conditions used in this research, none of the investigated calixarenes or polyhydroxybenzenes gave rise to successful extraction of uranium. This was potentially attributed to (in part) the inability to tether the target molecules onto the pulsed plasma poly(4-VBC) coated surface, meaning that future studies should investigate alternative attachment mechanisms and/or alternative calixarenes/polyhydroxybenzenes, which would be more susceptible to undergo nucleophilic substitution (whilst leaving the active site available for uranium capture).

However, successful uranium filtration with the amidoxime functionalised cloths was observed, with capture observed under static conditions, achieving an experimentally observed adsorption capacity of  $8.80 \pm 0.85 \text{ mg}_{\text{UG}} \text{Cloth}^{-1}$ . While dynamic filtration occurred rapidly, meaning that a cloth could be able to filter significant quantities of water in a short timescale, the extraction percentage was unfortunately significantly lower than under static conditions ( $22.0 \pm 6.3 \%$  vs  $90.3 \pm 4.5 \%$ ). Furthermore, the cloth was shown to be recyclable, and was capable of selectively removing uranium from solution containing some competing metal ions.

## 5.2 Experimental

### 5.2.1 *Calixarene and Polyhydroxybenzene Functionalised Cloths*

#### 5.2.1.1 *Preparation of Functionalised Cloths*

In order to fabricate the calixarene and polyhydroxybenzene cloths, the cloths first required coating with a pulsed plasma poly(4-VBC) linker layer. This was achieved by following a similar method to that performed previously by the Badyal group.<sup>462, 473, 474, 475, 476</sup> A non-woven polyurethane (TPU; meltblown 35 GSM, M35A1YMO, Don & Low Ltd., 12 cm x 8 cm) cloth was used as the substrate for plasmachemical deposition. The substrates were prepared, the plasma chamber cleaned, and plasmachemical deposition performed using 4-VBC (+ 90 %, 10403053, Fisher Scientific UK Ltd.) as the monomer as described in 2.1.1.1.1. Pulsed plasma deposition was performed using a duty cycle on-period of 100  $\mu$ s and a duty cycle off-period of 4 ms in conjunction with a peak power of 30 W, with the total time for deposition of 20 min.

Following deposition of pulsed plasma poly(4-VBC) onto the first side of the substrate, the cloth was inverted, and placed into a new, clean, chamber, and the process was repeated. Following the second deposition, the non-woven cloths were cut into two 60 mm x 70 mm pieces, leaving a 120 mm x 10 mm strip for characterisation.

Each coated cloth piece was placed into separate glass vials (28 mL volume) containing 0.152 g (4 mM)  $K_2CO_3$  (+ 99.0 %, Sigma Aldrich Ltd.) before addition of an acetone (+ 99.8 %, Fisher Scientific UK Ltd.) solution containing 8 mM NaI (+ 99.5 %, Honeywell Fluka™, Fisher Scientific UK Ltd.) and either 0.8 mM KTU-009, KTU-010, KTU-011, KTU-013, or KTU-014 (to attempt to yield a calixarene functionalised cloth) or 1.6 mM hydroxyquinone (+ 97 %, Fisher Scientific UK Ltd.), or phloroglucinol (+ 99.3 %, APC Pure) (to attempt to yield a polyhydroxybenzene functionalised cloth). The vials were sealed and left to spin at 40 rpm for ca. 70 h, before subsequent washing in acetone (15 min), air dried, and finally washed in high-purity (HP) water (15 min) and air dried.

### 5.2.2 *Amidoxime Functionalised Cloths*

#### 5.2.2.1 *Preparation of Functionalised Cloths*

In order to fabricate the amidoxime functionalised cloths, the cloths first required coating with pulsed plasma poly(2-cyanoethyl acrylate). The polyurethane cloth, glass slide and reflective silicon wafer substrates were prepared, the plasma chamber cleaned, and plasmachemical deposition performed using 2-cyanoethyl acrylate (+ 95 %, Sigma Aldrich Ltd.) as the monomer as described in 2.1.1.1.1. Pulsed plasma deposition was performed using a range of on/off duty cycles in order to determine the optimum conditions, which were established to

be an on/off duty cycle of 20  $\mu$ s on/20 ms off at a peak power of 30 W for 5 min. Following deposition of pulsed plasma poly(2-cyanoethyl acrylate) onto the first side of the substrate, the cloth was inverted, and placed into a new, clean, chamber, and the process was repeated. Following the second deposition, the non-woven cloths were cut into two 60 mm x 70 mm pieces, leaving a 120 mm x 10 mm strip for characterisation.

Amidoximation was performed by following a procedure similar to Zahri et al.<sup>477</sup> HH (+ 99 %, Sigma Aldrich Ltd.) solutions were made up by dissolving the desired mass of HH in a NaOH solution—optimum conditions were determined to be 0.0200 g HH with 5.5 mL NaOH (2 M, + 99.5 %, Fisher Scientific Ltd.) and 94.5 mL HP water. Each piece of pulsed plasma poly(2-cyanoethyl acrylate) coated cloth was placed into separate glass vials (28 mL volume, Fisherbrand™), and 27.5 mL of the HH solution was added. The vials were sealed and left to spin at 40 rpm for ca. 48 h, before subsequent washing in HP water (15 min) and being dried in air.

### 5.2.3 Characterisation

The thickness of the pulsed plasma poly(4-VBC) and pulsed plasma poly(2-cyanoethyl acrylate) coated silicon wafers was recorded using a spectrophotometer (NKD-6000, Aquila Instruments Ltd.). Transmittance–reflectance curves (350–1000 nm wavelength) were acquired using a parallel *p*-polarised light source at 30° incident angle to the substrate. These curves were fitted to a Cauchy model for dielectric materials using a modified Levenberg–Marquardt algorithm (version 2.2 Pro-Optix software, Aquila Instruments Ltd.).<sup>478,479</sup>

Fourier Transform Infrared (FTIR) spectra were acquired as described in Section 2.1.2.1.6.

Concentrations of all uranium-containing solutions were measured using an ICP-OES spectrophotometer (iCAP 6500, Thermo Fisher Scientific Inc.). Calibration standards were prepared following serial dilution of a 1000 mg L<sup>-1</sup> [UO<sub>2</sub>(NO<sub>3</sub>)<sub>6</sub>]<sup>2+</sup> solution (ICP standard solution, ROMIL Ltd.). Each sample analysis consisted of two replicate measurements for three characteristic wavelengths to ensure that the matrix was not causing spectral interferences.

### 5.2.4 Uranium Extraction

A 100 mg L<sup>-1</sup> stock solution of U(VI) was made up following dilution of a 1000 mg L<sup>-1</sup> [UO<sub>2</sub>(NO<sub>3</sub>)<sub>6</sub>]<sup>2+</sup> solution (ICP standard solution, ROMIL Ltd.). Subsequent dilution of this stock solution was performed in order to obtain uranium solutions of the desired concentration.



Dynamic and static filtration experiments, as well as isotherm determination was performed mostly as described in 2.1.3. The only difference occurred under static filtration, where the vials were left to shake (rather than spin) using a VXR Basic Vibrax® shaker at > 200 rpm.

Kinetic modelling experiments were performed following static filtration of several 20 mg L<sup>-1</sup> U(VI) solutions, each with a piece of adsorbent. The vials were left to shake, then after a designated time, the shaker was switched off and the cloth was removed from three (to allow for repetition) of the solutions, which were then submitted to ICP-OES for analysis. The shaker was then restarted, and the next set of the cloths were removed at the next designated time-period. This process was repeated until all cloths had been removed, and the experiment lasted for a duration of 1 h. The adsorption capacity after each time-period was determined and plotted against time. From this, the data was modelled by pseudo-first order and pseudo-second order kinetic models as described in 2.1.3.2.3.

Cloth recycling experiments were carried out similarly to Bieber et al.<sup>462</sup> In short, following dynamic filtration of a 5 mL 20 mg L<sup>-1</sup> U(VI) solution, 5 mL of HP water was passed through the cloth to remove any uranium trapped via capillary forces. Then 5 mL of a regeneration solution was passed through the cloth and the eluent collected, before being analysed via UV-Vis spectroscopy in order to determine the concentration of U(VI) in the regeneration eluent. Two regeneration solutions were investigated: 1 M HNO<sub>3</sub>—this is capable of protonating the amidoxime functional group, removing the electrostatic attraction between the adsorbent and the uranyl ions in solution—and a solution containing 0.5 M HNO<sub>3</sub> and 2 M NaCl—this is similar to the regeneration solution used by Bieber et al., wherein as well as protonating the active sites, captured uranium is displaced owing to the high concentration on salt in solution.

Cloth selectivity experiments were performing via static filtration of a 5 mL 20 mg L<sup>-1</sup> U(VI) solution, containing one of: NaCl (+ 99.5 %, Sigma-Aldrich Ltd.); K<sub>2</sub>CO<sub>3</sub> (+ 99.0 %, Sigma Aldrich Ltd); FeCl<sub>3</sub> (+ 97 %, Sigma Aldrich Ltd.); CaCl<sub>2</sub> (+ 90 %, BDH Laboratory Reagents); MgCl (+ 98 %, Sigma Aldrich Ltd.); or PbNO<sub>3</sub> (+ 99 %, Sigma Aldrich Ltd.) in a 1:50 mole ratio of uranium:competing metal ion, with a piece of functionalised cloth.

A real-world uranium contaminated sample was simulated by first collecting water from a vegetated rainwater pond (Durham University, UK) as it is expected that a rainwater pond will contain a wide array of ions and organic matter. The water was first filtered with a membrane filter (Whatman Polydisc GW In-Line polyamide filter with 0.45 µm pore size, GE Healthcare Inc.) in order to remove any solid particulates via mechanical filtration. The particulate-free pond water was then used to make up a solution containing 20 mg L<sup>-1</sup> U(VI),

which was then statically filtered with functionalised TPU cloths. The uranium solution before and after filtration was analysed by ICP-OES in order to determine the uranium extraction percentage. All pond water filtration experiments were performed within 2 h of collection.

All experiments have been performed at least three times, unless otherwise stated, and error values provided correspond to the standard deviation of the recorded values.

## 5.3 Results

### 5.3.1 Calixarene Functionalised Cloths

#### 5.3.1.1 Characterisation

The deposition rate for the pulsed plasma poly(4-VBC) films coated onto silicon wafers was measured to be  $43.2 \pm 3.0 \text{ nm min}^{-1}$ , giving a coating thickness of  $864 \pm 20 \text{ nm}$  for the deposition time of 20 min.

The FTIR spectra (ATR) of the starting TPU cloth, and pulsed plasma poly(4-VBC) coated cloth (Figure 5-5) demonstrate that pulsed plasma poly(4-VBC) has been successfully deposited on to the TPU cloth, owing to the presence of the C–H wagging mode of  $\text{CH}_2\text{–Cl}$  (from the VBC chloride group) at  $1265 \text{ cm}^{-1}$ , and the VBC benzyl phenyl stretch at  $1512 \text{ cm}^{-1}$ .<sup>464,480</sup> However, following immersion of the coated cloth in calixarene solutions containing one of KTU-009, KTU-010, KTU-011, KTU-013, or KTU-014, the ATR spectra (Figure 5-5) do not provide strong evidence for the presence of any of the calixarenes on the substrate—e.g., through the presence of additional hydroxyl (as seen in Chapter 3, and in previous work<sup>462</sup>), amine or ureayl groups. As such, successful attachment of calixarenes cannot be confirmed.

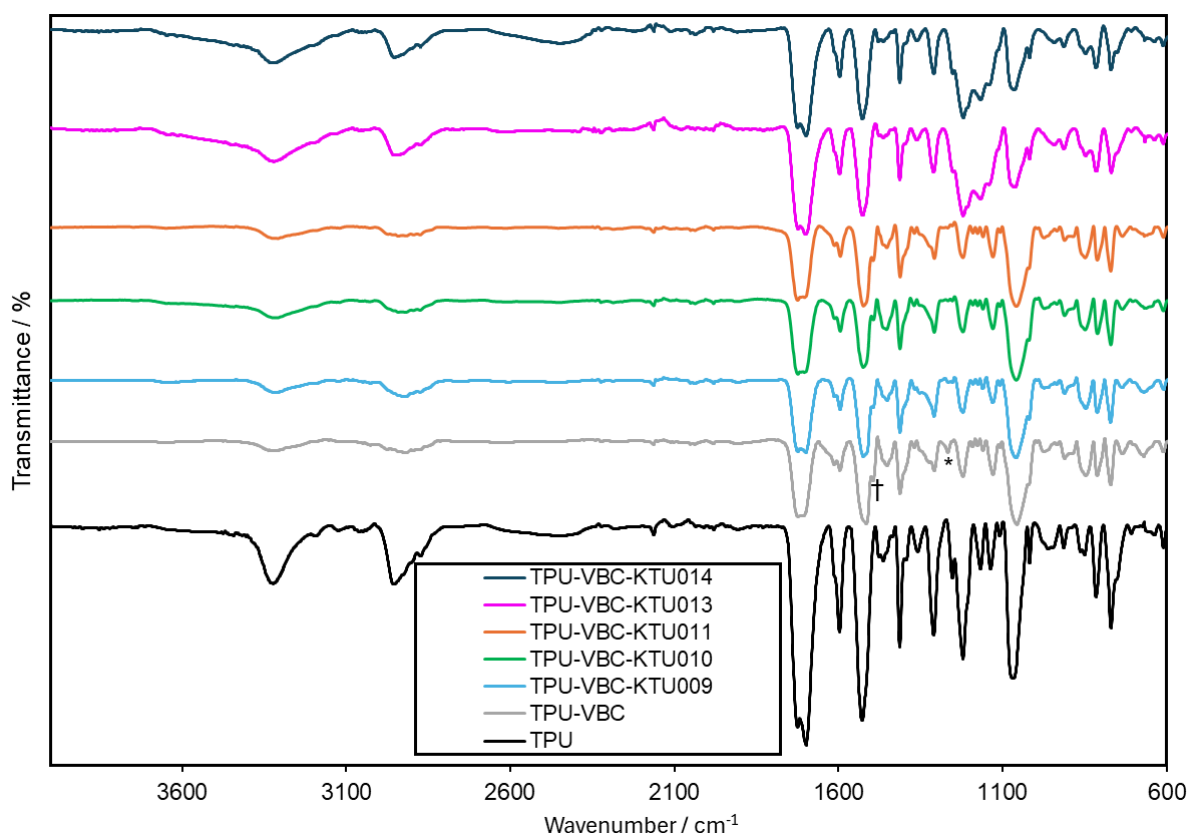


Figure 5-5. ATR-infrared spectrum of uncoated polyurethane (TPU) cloth (black), pulsed plasma poly(4-VBC) coated TPU cloth (grey), and coated TPU cloth, which was then immersed in a solution containing one of the following calixarenes: KTU-009 (pale blue), KTU-010 (green), KTU-011 (orange), KTU-013 (pink), or KTU-014 (dark blue). \* indicates the C–H wagging mode of CH<sub>2</sub>–Cl at 1265 cm<sup>-1</sup>, while † indicates the VBC benzyl phenyl stretch at 1512 cm<sup>-1</sup>.

### 5.3.1.2 Extraction of Uranium

In order to determine whether the adsorbents are suitable for uranium extraction, static filtration of a 10 mg L<sup>-1</sup> U(VI) solution was performed using each of the cloths. Static filtration was employed in order to ensure that sufficient contact between the uranyl ions and the surface occurred. Following static filtration, the uncoated cloth, and the cloth coated with pulsed plasma poly(4-VBC), were unable to remove uranium from solution (extraction efficiency of 2.53 ± 1.47 % and 2.67 ± 0.67 % respectively, Figure 5-6). Following immersion of the coated cloth with each of the investigated calixarenes, an insignificant increase in uranium extraction was observed (Figure 5-6). There are two possible explanations for the lack of uranium capture: (1) None of the investigated calixarenes are capable of binding uranium – this would be surprising, as the upper rim on each of the calixarenes has been functionalised with groups which are known to bind well to uranyl ions. While it is possible that some of the investigated calixarenes may not exhibit affinity to uranium, it is far less likely that none of the calixarenes demonstrate this affinity. Alternatively; (2) The calixarenes did not attach to the surface/only some calixarene molecules attached to the surface. This is the more

likely explanation, owing to the lack of evidence of calixarene attachment demonstrated in 5.3.1.1. Note that each of the investigated calixarenes contain two hydroxy groups and two methoxy groups on the lower rim—as opposed to four hydroxy groups for the investigated calixarene in previous work by the Badyal group and in Chapter 4 of this thesis<sup>462</sup>—meaning that the methoxy groups may a) be less inclined to undergo nucleophilic substitution with the chloride; and/or b) introduce hinderance, inhibiting nucleophilic substitution of the neighbouring hydroxy groups.

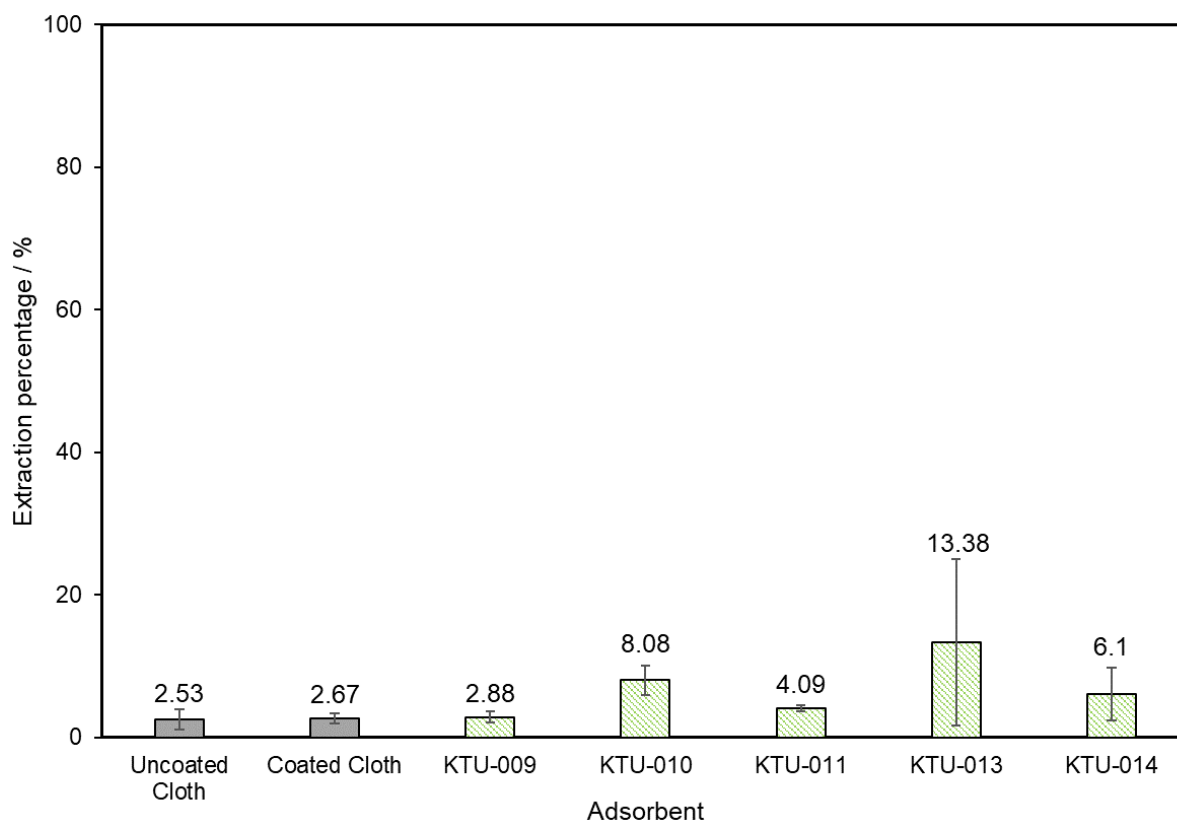


Figure 5-6. Extraction percentage towards uranium, following filtration with an uncoated TPU cloth, a pulsed plasma poly(4-VBC) coated TPU cloth, and a pulsed plasma poly(4-VBC) coated TPU cloth, left to spin in a solution containing one of: KTU-009, KTU-010, KTU-011, KTU-013, or KTU-014. As the uncoated cloth and the coated cloth are control experiments, these are shaded in grey.

### 5.3.2 Polyhydroxybenzene Functionalised Cloths

As with the attempted synthesis of the calixarene functionalised cloths (Section 5.3.1), the ATR spectrum of the pulsed plasma poly(4-VBC) coated cloth demonstrates successful deposition, owing to the presence of absorbance bands at  $1265\text{ cm}^{-1}$  and  $1512\text{ cm}^{-1}$  (Figure 5-7). Following immersion of the cloths in solution containing either phloroglucinol or hydroxyquinone, these functional groups are no longer visible in the ATR spectra—the lack of absorbance band at  $1265\text{ cm}^{-1}$  (attributed to the C–H wagging mode of the  $\text{CH}_2\text{–Cl}$  group) potentially indicates that nucleophilic substitution with the Cl group has successfully occurred, while the lack of visible phenyl absorbance bands attributed to the pulsed plasma poly(4-VBC)

linker layer may occur owing to the presence of the phenyl groups within the polyhydroxybenzenes. Furthermore, there do appear to be broad absorbance bands at ca.  $3200\text{ cm}^{-1}$ , which can be attributed to OH groups found on the polyhydroxybenzenes.

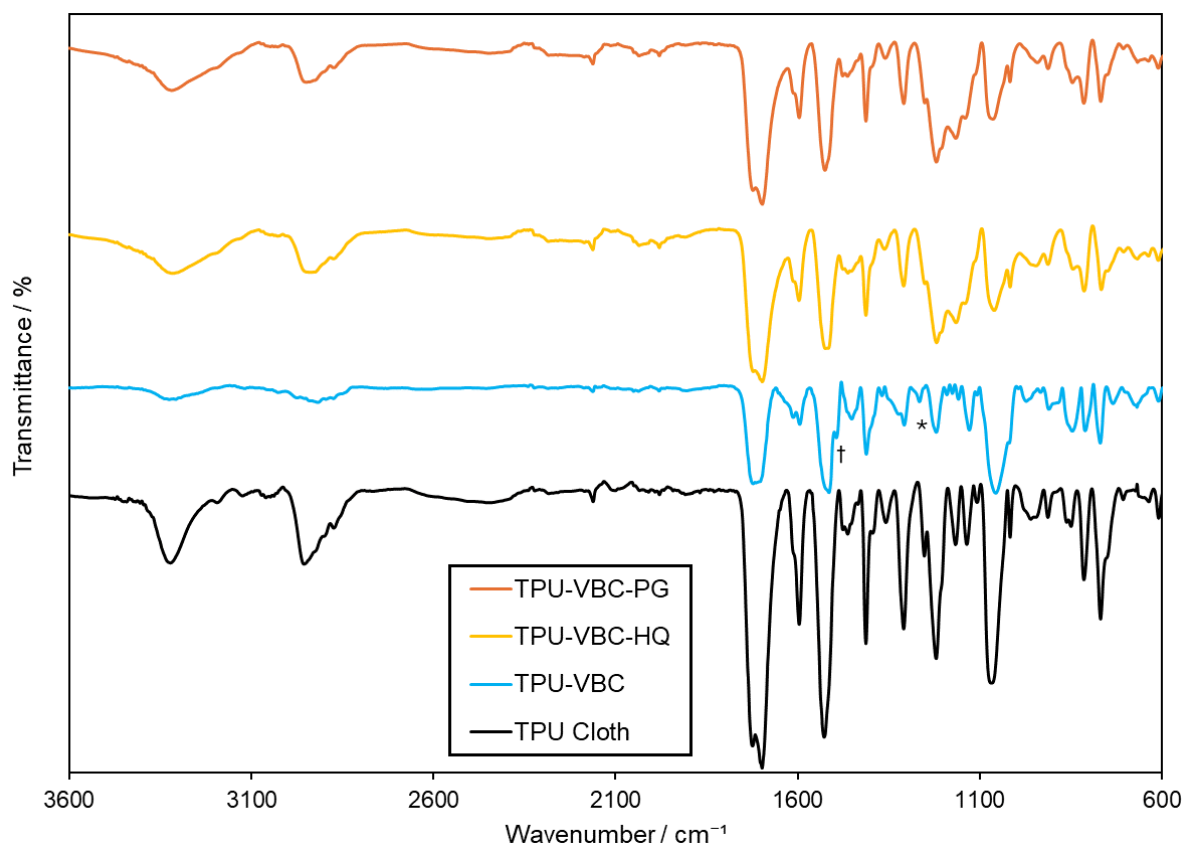


Figure 5-7. ATR-infrared spectrum of uncoated polyurethane (TPU) cloth (black), pulsed plasma poly(4-VBC) coated TPU cloth (blue), and coated TPU cloth, which was then immersed in a solution containing either hydroxyquinone (orange) or phloroglucinol (red). \* indicates the C–H wagging mode of  $\text{CH}_2\text{-Cl}$  at  $1265\text{ cm}^{-1}$ , while † indicates the VBC benzyl phenyl stretch at  $1512\text{ cm}^{-1}$ .

### 5.3.2.1 Extraction of Uranium

Following fabrication of the polyhydroxybenzene functionalised cloths, samples were left to spin for 24 h in a  $10\text{ mg L}^{-1}$  uranium solution, in order to determine their suitability as adsorbents. After attaching the polyhydroxybenzene to the linker layer, very minor increases in uranium extraction were observed (Figure 5-8). While an augmented extraction percentage could lend credence to the incidence of successful derivatisation, the filtered water would still contain  $> 9\text{ mg L}^{-1}$  U(VI), meaning that it remains highly contaminated. As such, the observed affinity towards uranium is insufficient for the synthesised cloths to be considered as useful adsorbents.

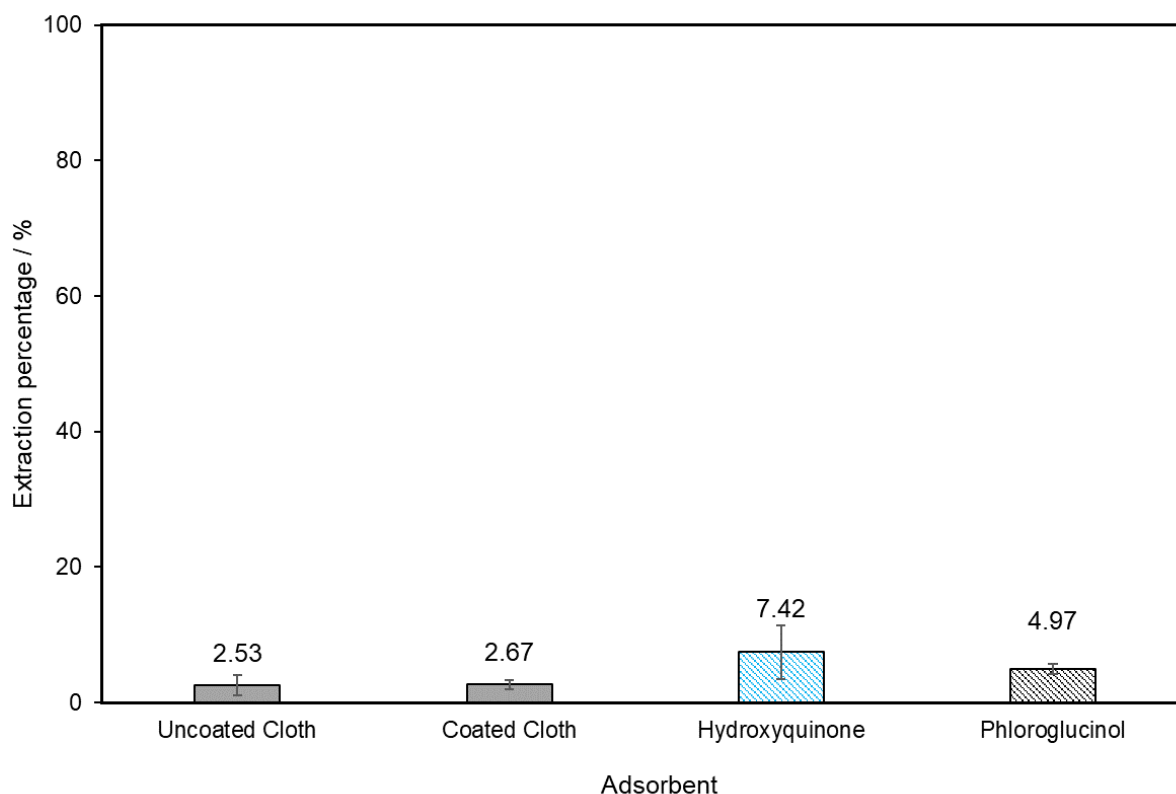


Figure 5-8. Extraction percentage towards uranium, following filtration with an uncoated TPU cloth, a pulsed plasma poly(4-VBC) coated TPU cloth, and a pulsed plasma poly(4-VBC) coated TPU cloth, left to spin in a solution containing one of hydroxyquinone or phloroglucinol. As the uncoated cloth and the coated cloth are control experiments, these are shaded in grey. As hydroxyquinone could give rise to a catechol-type adsorbent, this is coloured in blue. As phloroglucinol could give rise to a resorcinol-type adsorbent, this is coloured in black.

### 5.3.3 Amidoxime Functionalised Cloths

The final type of investigated cloth was amidoxime functionalised cloths. In order to synthesise these cloths, the TPU substrate first had to be coated with a cyano-containing substance, which could then undergo amidoximation. As previous work has successfully deposited poly(2-cyanoethyl acrylate) onto a substrate, this was chosen as the cyano-containing substance.<sup>472</sup>

#### 5.3.3.1 Deposition of Pulsed Plasma Poly(2-cyanoethyl acrylate)

The thickness of the pulsed plasma poly(2-cyanoethyl acrylate) films coated onto silicon wafers was measured to be  $193.9 \pm 51.9$  nm, which yields a deposition rate of  $38.8 \pm 10.4$  nm min<sup>-1</sup> over the course of the 5 min deposition—lower than the value in previous work, which utilised a higher (40 W) peak power.<sup>472</sup>

Pulsed plasma poly(2-cyanoethyl acrylate) was deposited onto a silicon wafer under similar conditions to those previously employed by Tarducci et al.<sup>472</sup> (30 W peak; 20  $\mu$ s on, 20 ms off). Additionally, a duty on:off cycle of 40  $\mu$ s on:8 ms off was utilised, in order to investigate

the effect of a shortened on:off cycle. Unfortunately, a stable plasma could not be obtained with on:off cycles extended beyond 20  $\mu\text{s}$ :20 ms, nor peak powers below 30 W, and so these could not be investigated. Following deposition with the 20  $\mu\text{s}$ :20 ms duty cycle, the key absorbance bands at 2245  $\text{cm}^{-1}$  ( $\text{C}\equiv\text{N}$  stretch) and 1736  $\text{cm}^{-1}$  ( $\text{C}=\text{O}$  stretch) can be observed, while there is no evidence of a  $\text{C}=\text{C}$  stretch at 1637  $\text{cm}^{-1}$ , indicating that deposition and polymerisation have been successful (Figure 5-9, Table 5-2).<sup>472,480</sup> While these absorbance bands are still observable using the shortened duty cycle, the intensity is significantly weakened. This indicates that the more aggressive plasma conditions negatively impact the deposition (e.g., by breaking up the monomer, preventing deposition of the desired coating), and so the more gentle conditions were chosen for all future experiments.

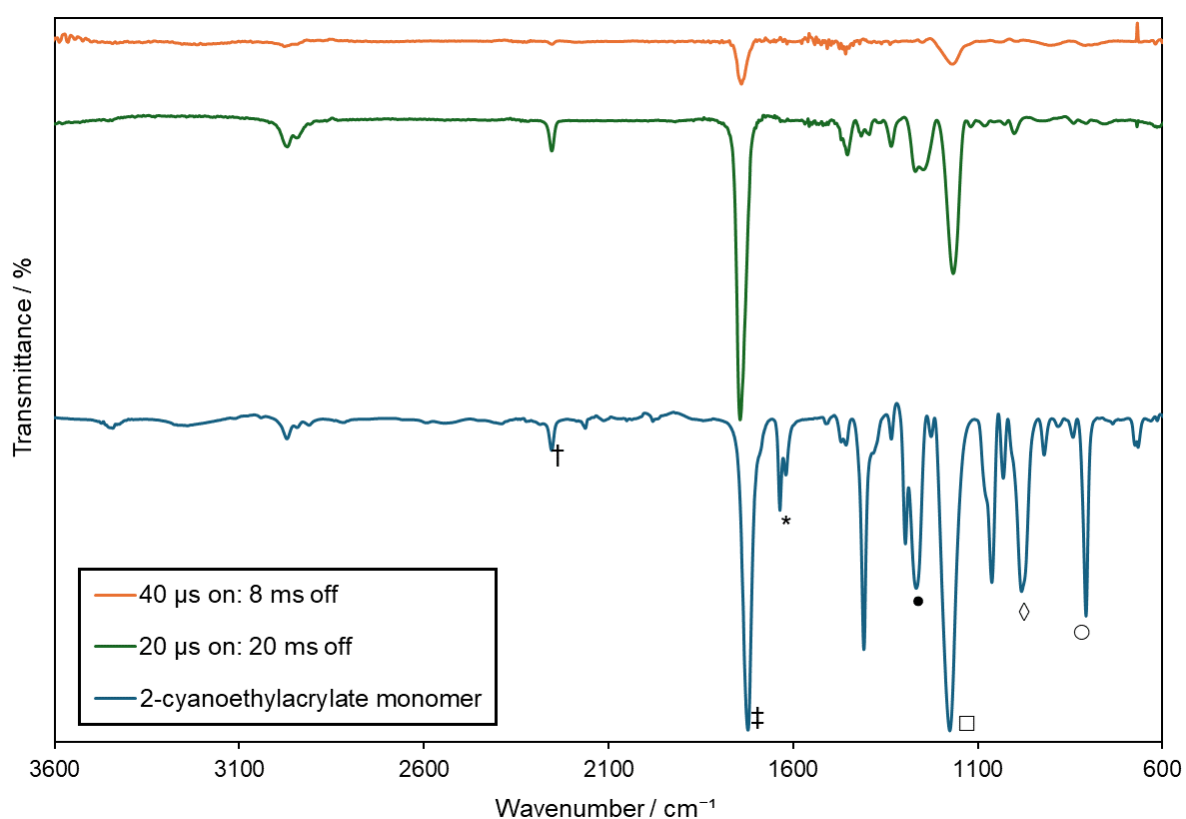


Figure 5-9. FTIR—ATR of 2-cyanoethyl acrylate monomer (blue), and FTIR—RAIRS of pulsed plasma poly(2-cyanoethyl acrylate), deposited with an on:off time of 20  $\mu\text{s}$ :20 ms (green) and 40  $\mu\text{s}$ :8 ms (orange).

Table 5-2. Assignment of the absorbance bands observed in the FTIR spectrum of 2-cyanoethyl acrylate. \*Absorbance bands marked with an Asterix are not present in the spectra of the deposited films.

Label	Wavenumber / $\text{cm}^{-1}$	Assignment	Reference
•	3460	N–H stretch	480
†	2254	$\text{C}\equiv\text{N}$ stretch	472, 480
‡	1736	$\text{C}=\text{O}$ stretch	472, 480

Label	Wavenumber / $\text{cm}^{-1}$	Assignment	Reference
*	1637*	C=C stretch	472, 480
●	1273	C–O stretch	472, 480
□	1175	C–O stretch	472, 480
◇	985*	=CH <sub>2</sub> wag	472, 480
○	810*	=CH <sub>2</sub> stretch	472, 480

Deposition was subsequently performed onto glass slides and a meltblown TPU cloth. Compared to the RAIRS spectra of the deposited film on the Si wafers, several of the pulsed plasma poly(2-cyanoethyl acrylate) peaks are obscured by the substrate absorbance bands (Figure 5-10). This obscuring effect is more notable when using the TPU cloths than the glass slides, however the C≡N stretch at  $2245 \text{ cm}^{-1}$  and C=O stretch at  $1736 \text{ cm}^{-1}$  can still be identified, while there is no evidence of any of the C=C absorbance bands listed in Table 5-2. Consequently, it can be concluded that pulsed plasma poly(2-cyanoethyl acrylate) can be successfully deposited onto a range of substrates.

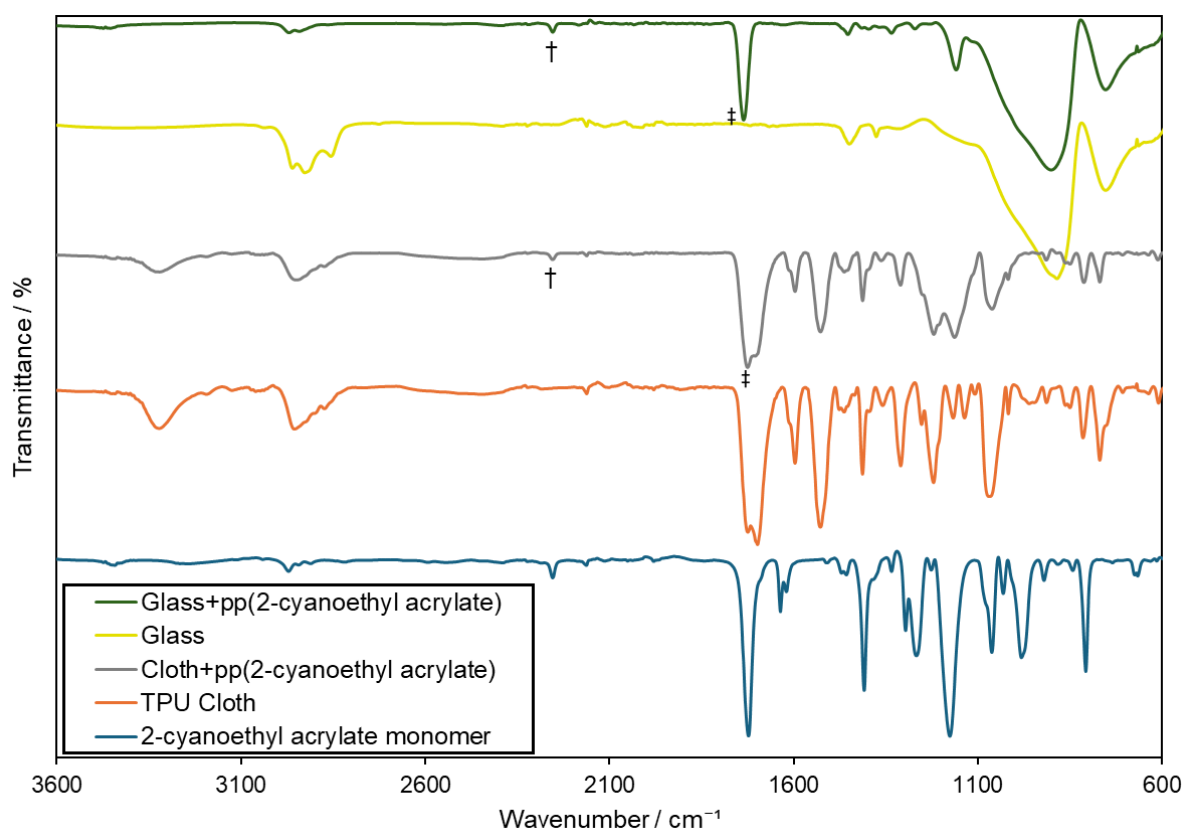


Figure 5-10. FTIR—ATR of 2-cyanoethyl acrylate monomer (blue), TPU cloth (orange), pulsed plasma poly(2-cyanoethyl acrylate) deposited onto a TPU cloth (grey), a glass slide (yellow), and pulsed plasma poly(2-cyanoethyl acrylate) deposited onto a glass slide (dark green). All depositions have been performed with an on:off time of 20  $\mu\text{s}$ :20 ms.



### 5.3.3.2 Conversion to Amidoxime

In order to determine the optimum conditions for amidoxime conversion, varying concentrations NaOH and HH were investigated—the optimum conditions are those which result in successful conversion to the amidoxime whilst using the fewest quantity of materials/energy necessary. Successful conversion to the amidoxime can be demonstrated by the loss of the C≡N stretch at 2245 cm<sup>-1</sup>, and appearance of an N–H stretch at ca. 3460 cm<sup>-1</sup> (Figure 5-11, only visible when using an uncoated TPU cloth as the FTIR background, owing to overlap with TPU absorbance bands). Consequently, in order to determine whether experimental conditions resulted in successful amidoximation, the disappearance/appearance of these respective absorbance bands were tracked (Table 5-3). Here it can be seen that for starting HH concentrations of 0.028 M and above, there is a respective absence and presence of C≡N and N–H absorbance bands, demonstrating successful amidoximation. At lower concentrations, this has not occurred. Therefore, it was determined that a HH concentration of 0.028 M was the minimum requirement for the successful conversion to amidoxime.

Table 5-3. Starting HH and NaOH concentrations for the attempted amidoximation of the deposited pulsed plasma poly(2-cyanoethyl acrylate film), and whether absorbance bands corresponding to N–H and C≡N stretches at 3460 and 2245 cm<sup>-1</sup> respectively could be observed in the final product. \*This solution was left to spin for an extended (4 days) reaction time.

HH Concentration / M	NaOH Concentration / M	N–H absorbance band	C≡N absorbance band
0.006	0.022	×	✓
0.006*	0.022*	×	✓
0.018	0.066	×	✓
0.028	0.110	✓	×
0.043	0.165	✓	×

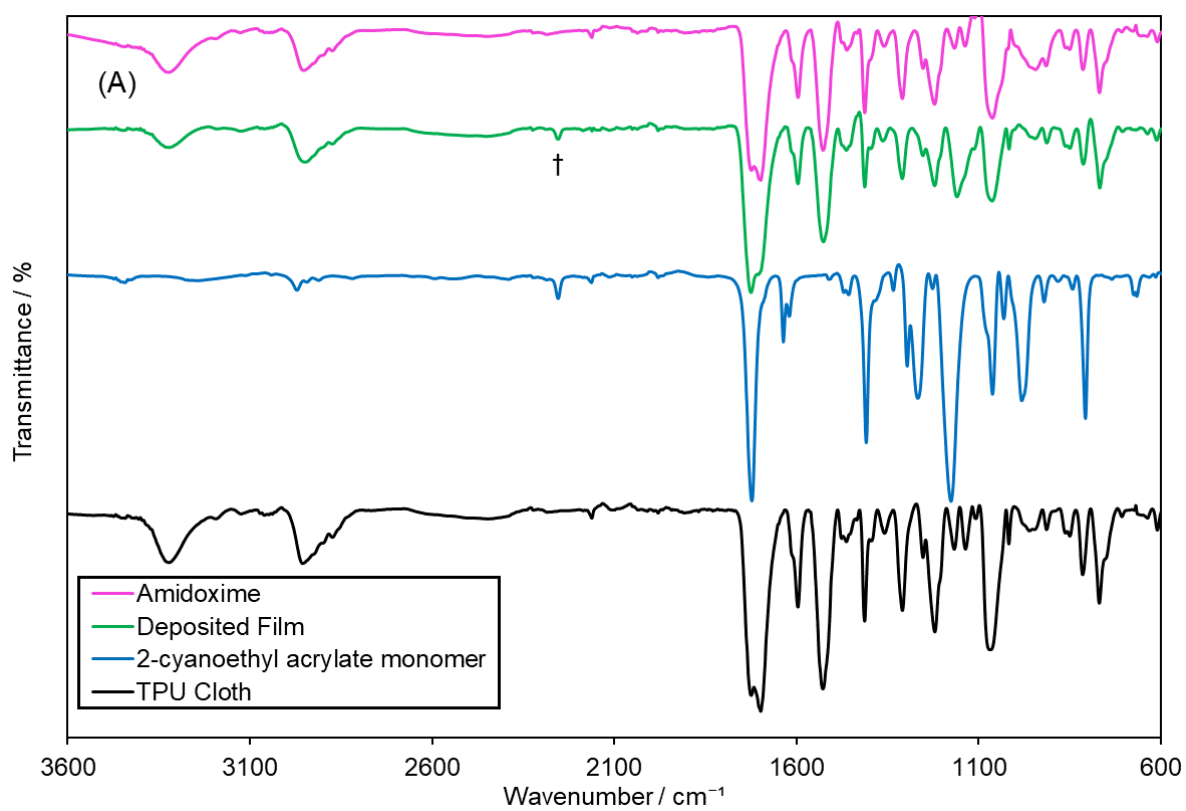
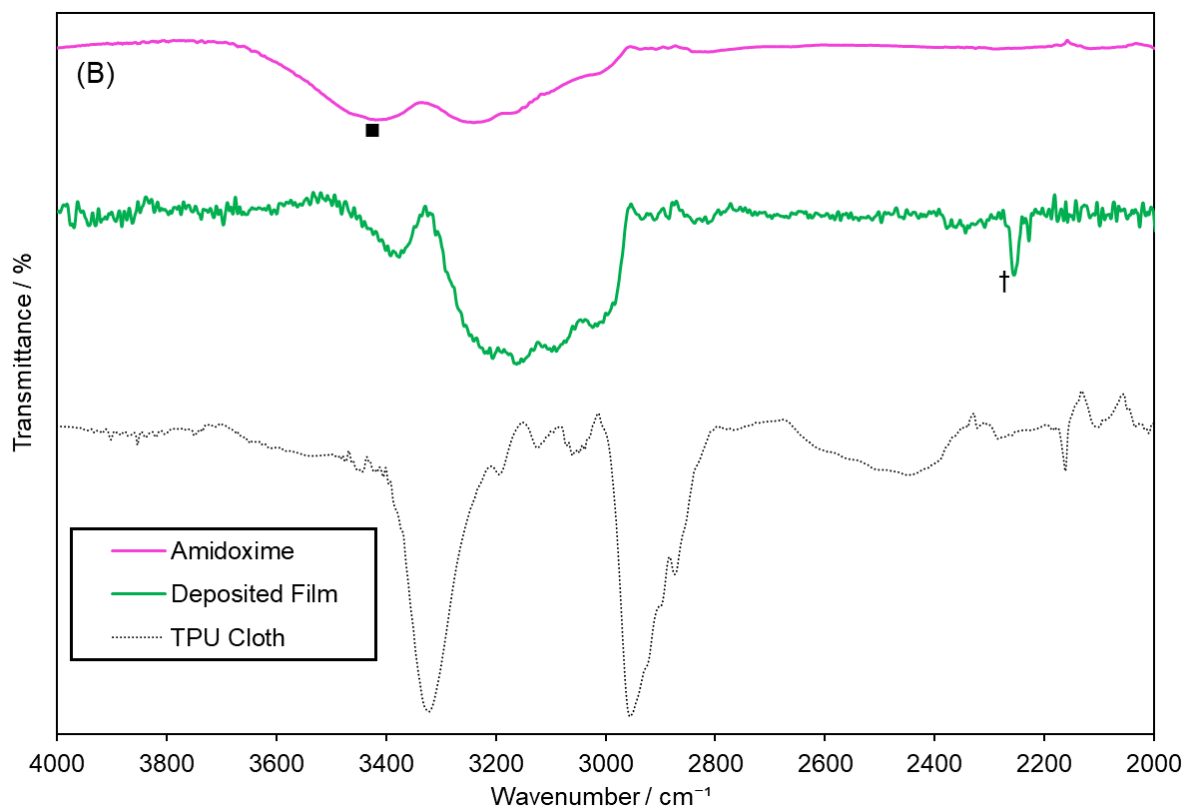


Figure 5-11. FTIR—ATR of (A) the TPU cloth (black), the 2-cyanoethyl acrylate monomer (blue), the pulsed plasma poly(2-cyanoethyl acrylate) film deposited on the TPU cloth (green), and the same film when inserted into a solution containing 0.036 M HH solution (to form the amidoxime) (pink), all using air as the FTIR background; and (B) the TPU cloth (dotted black) using air as the FTIR background, the pulsed plasma poly(2-cyanoethyl acrylate) film deposited on the TPU cloth using an uncoated cloth as the FTIR background (green), and the same film when inserted into a solution containing 0.036 M HH solution (pink), using an uncoated cloth as the FTIR background. ▪ indicates the N–H stretch at 3460  $\text{cm}^{-1}$ , while † indicates the  $\text{C}\equiv\text{N}$  stretch at 2245  $\text{cm}^{-1}$ .

### 5.3.3.3 Static Filtration of Uranium

The cloths which had successfully undergone amidoximation were left to spin in a 10  $\text{mg L}^{-1}$  U(VI) solution for 24 h, in order to determine whether uranium could be removed from solution. Cloths synthesised using different concentrations of HH were investigated to determine whether the concentration of reagent affected uranium capture. Extraction percentages of ca. 90 % for each cloth (Figure 5-12) not only indicated that uranium could be successfully removed from solution, but also that increasing the concentration of HH beyond 0.028 M did not yield improved results (average filtration efficiency =  $90.3 \pm 4.5$  %). As such, concentrations of 0.028 M HH were used for all future experiments.

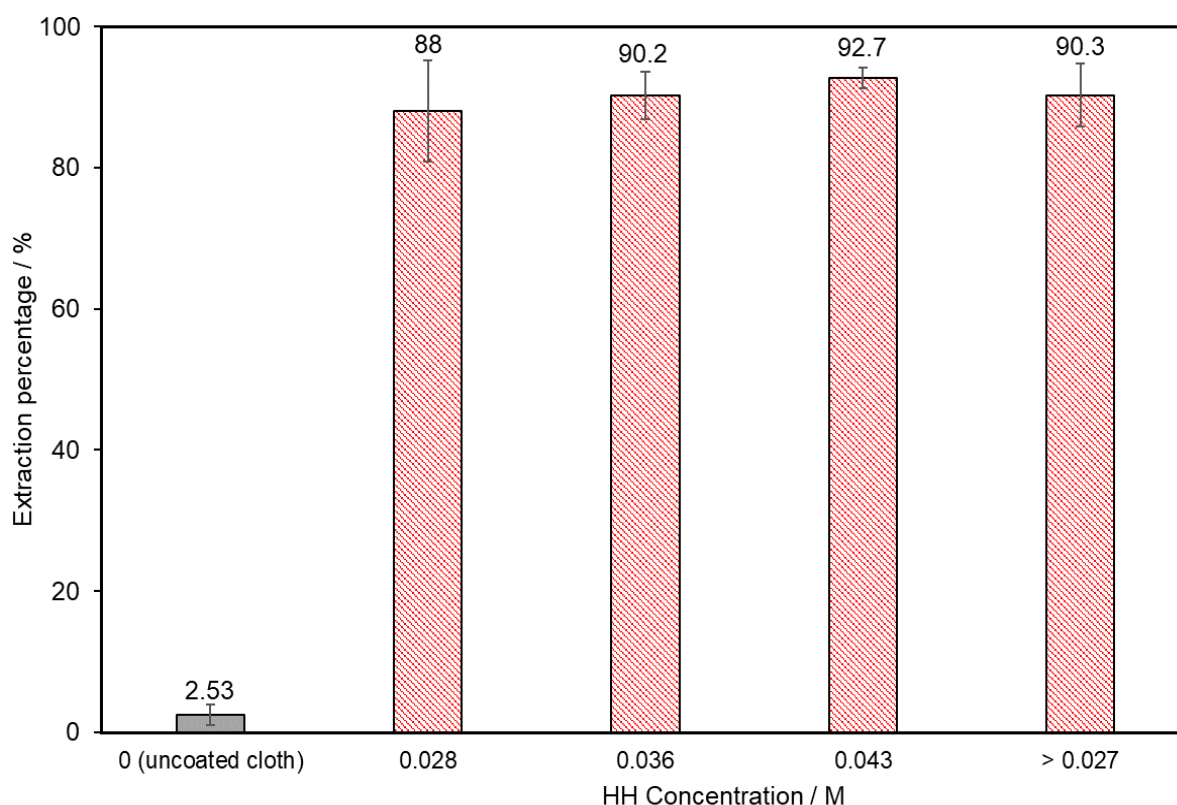


Figure 5-12. Extraction percentages for the static filtration of a 5 mL 10  $\text{mg L}^{-1}$  U(VI) solution with an uncoated TPU cloth, and an amidoxime-functionalised TPU cloth, synthesised using HH concentrations of 0.028 M, 0.036 M, or 0.043 M. Also included is the average extraction percentage for all HH concentrations greater than 0.027 M. As the uncoated cloth is a control experiment, this is shaded in grey.

#### 5.3.3.4 Dynamic Filtration of Uranium

In order to determine the feasibility of utilising the amidoxime functionalised cloths for point-of-use water filtration, dynamic filtration of a  $10 \text{ mg L}^{-1}$  U(VI) solution, using a TPU cloth, coated with pulsed plasma poly(2-cyanoethyl acrylate), as well as the amidoxime functionalised cloths, was performed. The solution rapidly passes through the amidoxime functionalised cloth (filtration time = ca. 90 s for all amidoxime functionalised cloths), as opposed to the pulsed plasma poly(2-cyanoethyl acrylate) coated cloth (filtration time = ca. 15 min). This extraction time, while indicating strong forces of attraction between the cloth and the uranium solution, is particularly useful in real-world environments, as it indicates that substantial quantities of water could be filtered in relatively short periods of time. This short contact time, however, has coincided with significantly reduced extraction percentages ( $22.0 \pm 6.3 \%$  (Figure 5-13) vs  $90.3 \pm 4.5 \%$  (Figure 5-12)). As with the static filtration of U(VI), the filtration efficiency of the amidoxime cloths, synthesised using different concentrations of HH are within error ranges. Finally, it should be noted that the filtration efficiency of the pulsed plasma poly(2-cyanoethyl acrylate) coated cloth towards uranium is even lower than that of the dynamic filtrations with the amidoxime functionalised cloth (filtration efficiency =  $0.9 \%$  vs  $22.0 \pm 6.3 \%$ , Figure 5-13), indicating that, albeit low, under dynamic conditions, removal of *some* uranium with the amidoxime functionalised cloths is possible.

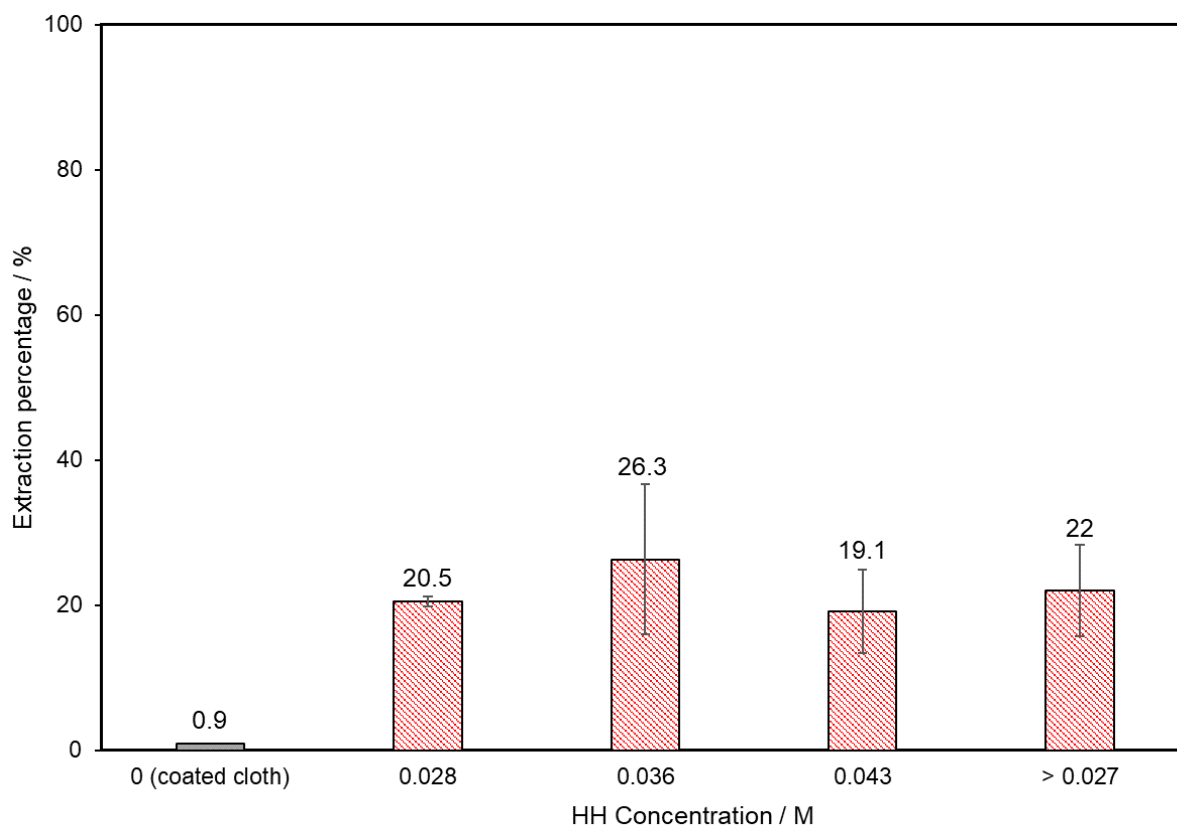


Figure 5-13. Extraction percentages for the dynamic filtration of 5 mL 10 mg L<sup>-1</sup> U(VI) solution with a pulsed plasma poly(2-cyanoethyl acrylate) coated cloth, and amidoxime-functionalised TPU cloths, synthesised using HH concentrations of 0.028 M, 0.036 M, or 0.043 M (3 cm x 3.5 cm, inserted into the bottom of the body of a Pasteur pipette (150 mm total length, 100 mm body length, 5.6 mm body internal diameter, Fisher Scientific UK Ltd.)). Dynamic filtration of U(VI) with the pulsed plasma poly(2-cyanoethyl acrylate) coated cloth has only been performed once. Also included is the average extraction percentage for all HH concentrations greater than 0.027 M. As the coated cloth is a control experiment, this is shaded in grey.

### 5.3.3.5 Cloth Recycling

While previous work has typically used strong acid to protonate the amidoxime sites, and hence remove the electrostatic attraction between the amidoxime and uranyl ion,<sup>458,481,482</sup> previous work by the Badyal group has demonstrated that utilising a large excess of salt in addition to altering the pH results in bound adsorption sites becoming replaced with the respective ion, leading to a greater increase in contaminant being released from a cloth.<sup>462</sup> Consequently, two different regeneration solutions were investigated—one containing 0.5 M HNO<sub>3</sub> and 2 M NaCl, and a second containing 1 M HNO<sub>3</sub>. Owing to the rapid flow-through time, dynamic filtration was chosen as the filtration method, in order to exemplify the difference in performance between the two regeneration solutions. Furthermore, rapid recycling is desirable, and so utilising dynamic filtration better represents real-world conditions. Following dynamic filtration of 10 mg L<sup>-1</sup> solutions, none of the initial filtrations gave rise to successful filtrations (Figure 5-14). However, in each subsequent filtration, the extraction percentage did

increase, before levelling out, indicating that the cloths were certainly not becoming saturated, and indeed may be becoming more suitable extractants following repeat use. It can be seen that the concentration of uranium extracted at each cycle is similar when using both regeneration solutions, and indeed, is similar to the concentration of uranium found in the regeneration eluant when regenerating with the 1 M HNO<sub>3</sub> solution. However, when regenerating with the 0.5 M HNO<sub>3</sub>/2 M NaCl solution, there is a lower concentration of uranium found in the regeneration eluant.

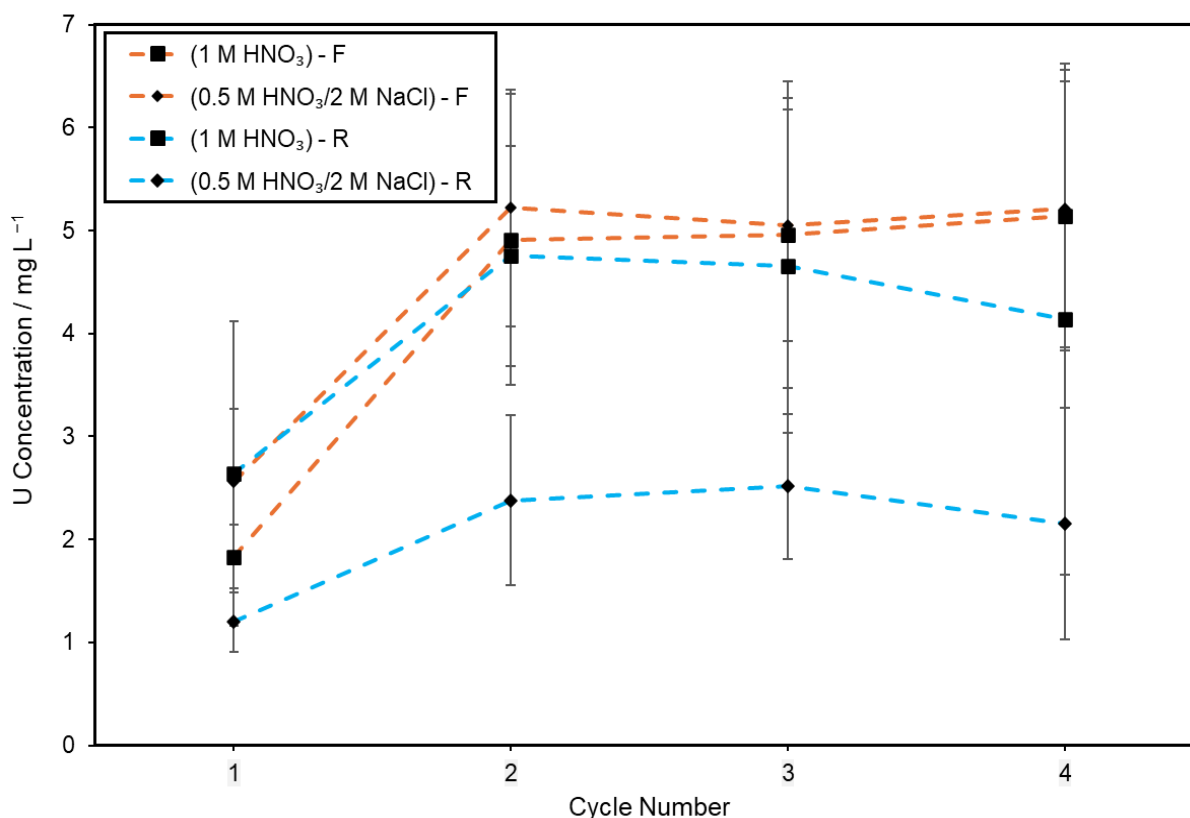


Figure 5-14. Concentration of uranium extracted following dynamic filtration (orange dotted lines) of a 5 mL 10 mg L<sup>-1</sup> U(VI) solution, which was subsequently regenerated using either a 1 M HNO<sub>3</sub> solution (squares) or a 0.5 M HNO<sub>3</sub>/2 M NaCl solution (diamonds). Additionally, concentration of uranium removed from the cloths (blue dotted lines) following recycling with either a 1 M HNO<sub>3</sub> solution (squares) or a 0.5 M HNO<sub>3</sub>/2 M NaCl solution (diamonds).

Obtaining detailed conclusions from Figure 5-14 is difficult, owing to the large error bars—attributable to the relatively large range of concentrations obtained during dynamic filtration. Therefore, it is more appropriate to determine the percentage of uranium desorbed from the cloth following each individual filtration experiment. This was determined by working out the amount of uranium found in the regeneration eluant as a proportion of the amount of uranium extracted in the previous filtration (Figure 5-15). Following each cycle using 1 M HNO<sub>3</sub> as the regeneration solution, > 90 % adsorbed uranium is removed from the cloth, which is indicative of an outstanding ability to recycle the functional cloths. On the other hand, when

using the 0.5 M HNO<sub>3</sub>/2 M NaCl solution, only ca. 50 % adsorbed uranium is removed from the cloth each cycle. This means that—in contrast to the previous work in this group, and indeed earlier in this thesis (3.3.6)—utilising a regeneration solution containing a high concentration of salt does not give rise to a superior ability to recycle the functional cloths.<sup>462</sup> Rather, the superior recycling performance with an increased acid concentration indicates that acidification of the adsorbent sites is the driving force behind cloth regeneration.

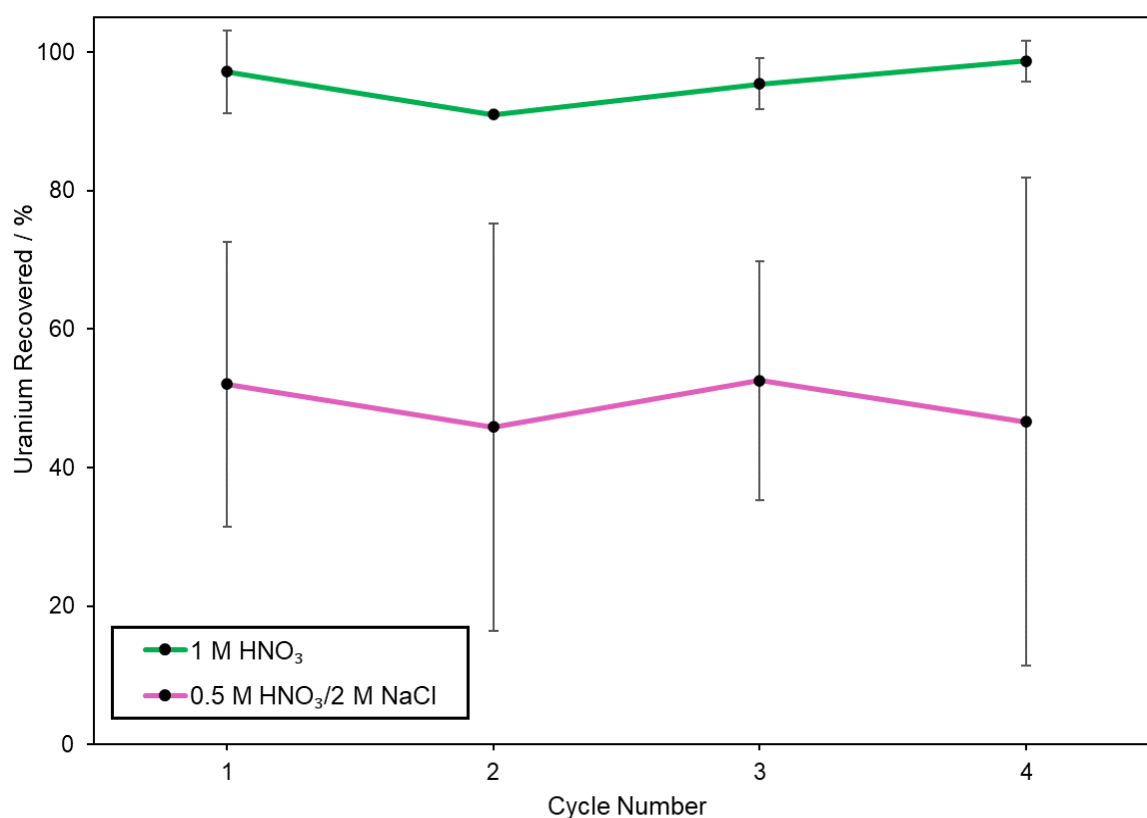


Figure 5-15. Percentage of adsorbed uranium removed from cloths—which had previously been used to dynamically filter a 5 mL 10 mg L<sup>-1</sup> uranyl solution—following regeneration with either a 1 M HNO<sub>3</sub> (green) solution, or a 0.5 M HNO<sub>3</sub>/2 M NaCl solution (pink).

### 5.3.3.6 Isotherm Determination

Determining the appropriate adsorption isotherm is not only a useful tool for elucidating the interactive mechanism between adsorbent and adsorbate, but can also be used to estimate the maximum adsorption capacity of an adsorbent under the investigated conditions, depending of the identified adsorption isotherm.<sup>483, 484</sup> For example, the Langmuir isotherm model describes a monolayer adsorption process wherein adsorption and desorption are equal, with the maximum adsorption capacity occurring when no more adsorbate molecules can be incorporated into the monolayer. On the other hand, the Freundlich isotherm describes a multilayer adsorption system, with no finite adsorption limit.

Amidoxime functionalised, pulsed plasma poly(2-cyanoethyl acrylate) coated cloths were left to spin in 5 mL U(VI) solutions for 24 h under a range of U(VI) concentrations, after which the concentration of uranium remaining in solution was determined. Adsorption capacity ( $Q_e$ ) values were plotted against starting concentration, which demonstrates that initially, adsorption increases linearly with starting concentration (behaviour described by Henry's law,<sup>485</sup> hence concentrations below 25 mg L<sup>-1</sup> can be classified as the Henry region, Figure 5-16). Afterwards, the adsorption capacity ( $Q_e$ ) values begin to curve off, indicative of a typical adsorption curve.

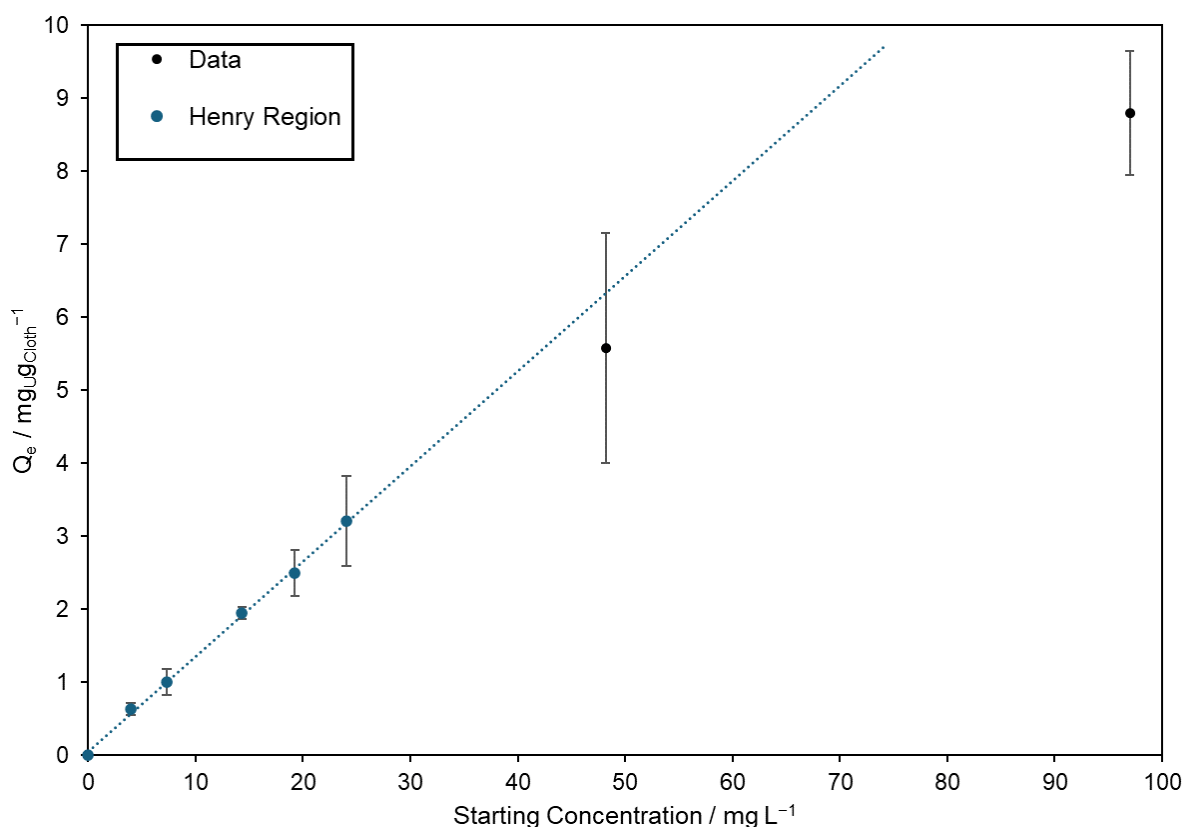


Figure 5-16. Change in adsorption capacity ( $Q_e$ ) of an amidoxime functionalised cloth, following static filtration of U(VI) solutions, with initial concentration of uranium. The blue data points represent concentrations within the Henry region, whereas the black data points represent concentrations greater than the Henry region.

The obtained data was converted into non-linear (Figure 5-17) and linear (Figure 5-18) Langmuir and Freundlich isotherms. The non-linear form of both isotherms (Figure 5-17) are created by plotting  $Q_e$  against  $C_e$ , where  $Q_e$  = adsorption capacity, and  $C_e$  = concentration of U(VI) remaining at equilibrium. It can be seen that within the range of starting uranium concentration employed (0–100 mg L<sup>-1</sup>), there is no concentration at which 100 % uranium extraction occurs ( $C_e = 0$ ), nor (more importantly), is there an observable plateau, in which the adsorption capacity ( $Q_e$ ) is unaffected by increasing the uranium concentration. This means that under the conditions feasible in this experiment, it is not possible to obtain an experimental



value for maximum adsorption capacity – the highest observed adsorption capacity occurs with a starting uranium concentration of  $100 \text{ mg L}^{-1}$ , yielding a value of  $8.80 \pm 0.85 \text{ mg}_{\text{U}}\text{g}_{\text{Cloth}}^{-1}$ . In order to determine whether the data is best fit by either a Langmuir or Freundlich isotherm, the process outlined in 2.1.3.2.2 was followed. The model Langmuir and Freundlich adsorption curves lie within the error values for all observed data points, with the exception of the value determined for the starting uranium concentration of  $100 \text{ mg L}^{-1}$ , wherein the model Langmuir adsorption curve does not pass through the associated error range. This implies that the Freundlich isotherm is a more appropriate isotherm model. This is evidenced through the calculated  $X^2$  values for both plots, which yielded values of 0.775 and 0.040 for the Langmuir and Freundlich isotherms respectively.

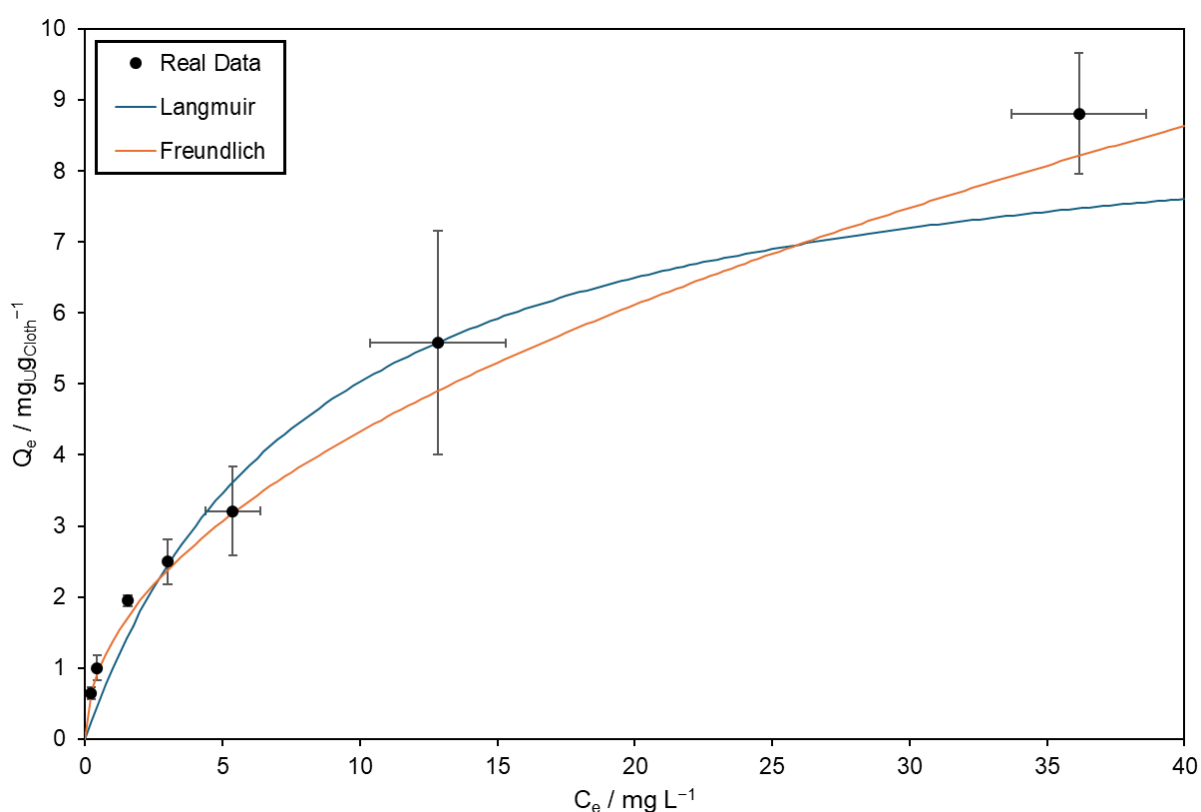


Figure 5-17. Adsorption capacity towards U(VI) from solution following static filtration with a pulsed plasma poly(2-cyanoethyl acrylate) coated, amidoximated cloth. The raw data has been fitted against non-linear Langmuir (blue) and Freundlich (orange) adsorption isotherms.

The linear forms of Langmuir and Freundlich isotherms are determined by plotting  $C_e/Q_e$  against  $C_e$  (Langmuir) and  $\text{Log}(Q_e)$  against  $\text{Log}(C_e)$  (Freundlich) (Figure 5-18). Analysis of the linear forms of the isotherms provide further evidence of the suitability of the Freundlich isotherm, which not only provides a better visual fit to the data, but also exhibits a superior  $R^2$  value of 0.997, compared to 0.944 for the Langmuir fit.

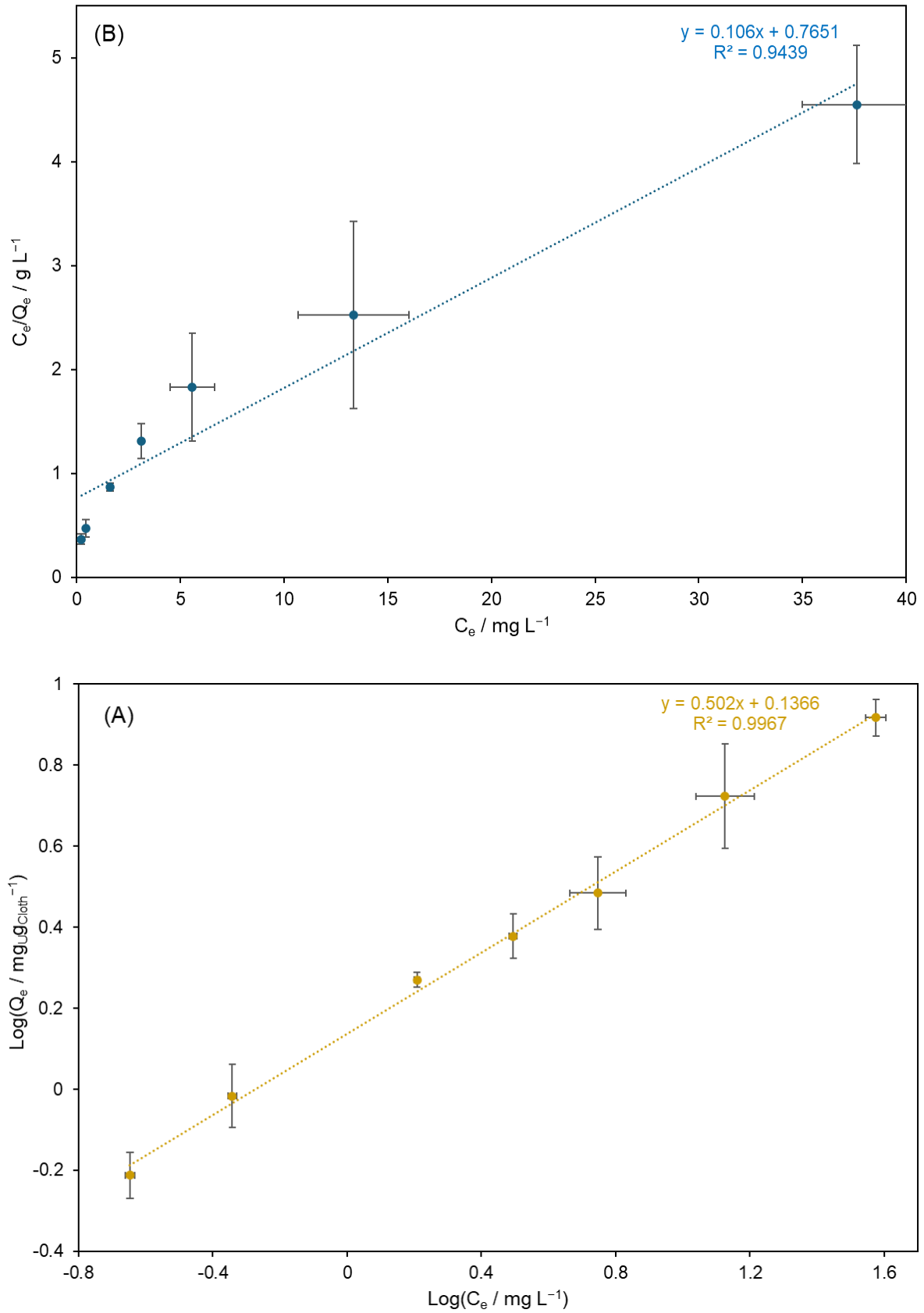


Figure 5-18. Linear Freundlich (A) and Langmuir (B) isotherms, associated with the adsorption of U(VI) from solution with an amidoxime functionalised, pulsed plasma poly(2-cyanoethyl acrylate) coated cloth.

Consequently, it was assumed that the adsorption of U(VI) by the amidoxime functionalised cloths could be modelled by a Freundlich adsorption isotherm, for which the values of  $n$  and  $K_F$  could be determined (Table 4-4). According to Equation (2-20), the values of  $n$  and  $K_F$  can be calculated from the linear isotherm by taking the inverse of the gradient and calculating  $10^{\text{Intercept}}$  respectively. Additionally, it can be seen that the values for  $n$  and  $K_F$  determined from the linear isotherm are within error range of the values determined from the non-linear Freundlich isotherms, validating the accuracy of the determined values, and indeed the fit itself.

Table 5-4. Determined values of  $n$  and  $K_F$  from the non-linear and linear Freundlich plots. The error values for the gradient and intercept from the linear plots were determined by using the “Data Analysis—Regression” tool in excel, with a confidence interval of 95 %. For the non-linear isotherm, the errors were calculated by averaging the percentage error between each data point and the theoretically calculated value and applying this to the determined values of  $n$  and  $K_F$ .

Form of isotherm	Gradient	$n$	Intercept	$K_F / \text{mg L}^{-1}$
Linear	$0.502 \pm 0.013$	$1.99 \pm 0.05$	$0.137 \pm 0.011$	$1.41 \pm 0.07$
Non-linear	N/A	$2.01 \pm 0.08$	N/A	$1.38 \pm 0.06$

The assignment to a Freundlich isotherm provides information regarding the physical characteristics of the adsorption. Specifically, Freundlich isotherms are representative of adsorptions which are heterogenous, with the formation of multilayers on the cloth.<sup>486</sup> Note however, that the Freundlich isotherm does not allow the determination of an adsorption maximum.

### 5.3.3.7 Adsorption Kinetics

Owing to the nature of ICP-OES analysis, it is not feasible to begin a static filtration experiment, pause the experiment in order to remove a sample for uranium concentration determination, then return the extracted uranium and restart the experiment (as would occur during conventional kinetic studies). Subsequently, an alternative technique was required, in order to attempt to establish a suitable kinetic model. One option would be to use a sufficiently large starting volume, so that the removal of small quantities of uranium would leave the remaining volume approximately constant. However, under the conditions required for this to occur, significant safety concerns arise in a laboratory setting. Consequently, a large number of static filtration experiments were set up, and each experiment was stopped after a predetermined length of time, always with three experiments stopped simultaneously. The average adsorption capacity at each time was determined, and these values were used to plot the adsorption curve. As it has been widely reported that fitting kinetic data towards linearised forms of the pseudo-first and pseudo-second order kinetic models provide stronger weighting to values found closer to

equilibrium, it was decided to prioritise filtration times closer to the start of the experiment, owing to the large number of synthesised cloths required for the investigation.

Unfortunately, owing to using different cloths for each data point, there are significant error ranges associated with each time-dependent calculated adsorption capacity ( $Q_t$ ) (Figure 5-19). Furthermore, it can be seen that the data points obtained for the adsorption capacity after 5 and 10 min do not fit the overall adsorption curve (potentially owing to mass transfer effects meaning that adsorption does not occur in earnest until after 10 min). Thus, for the non-linear kinetic model (Figure 5-19), fits were performed with and without including these two data points. Of these kinetic models, the pseudo-second order model (excluding the data points at 5 and 10 min) appears to give the better fit to the observed data, although the pseudo-first order model (excluding the data points at 5 and 10 min) does also pass through the error range of all data points. This was backed up by the  $\chi^2$  values for each of these plots, which were calculated to be 0.560 and 0.707 for the pseudo-first and pseudo-second models, inclusive of all data points respectively; and 0.029 and 0.010 for the pseudo-first and pseudo-second models, excluding the data points at 5 and 10 min respectively.

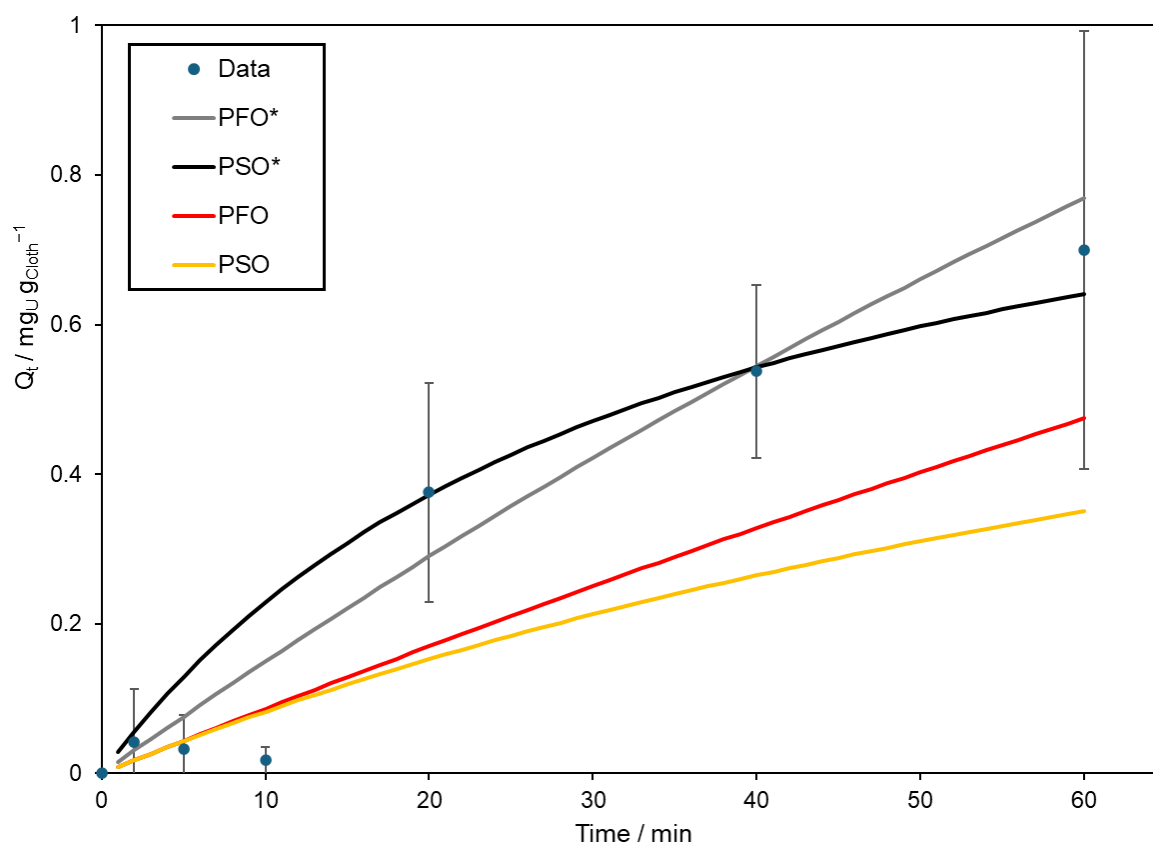
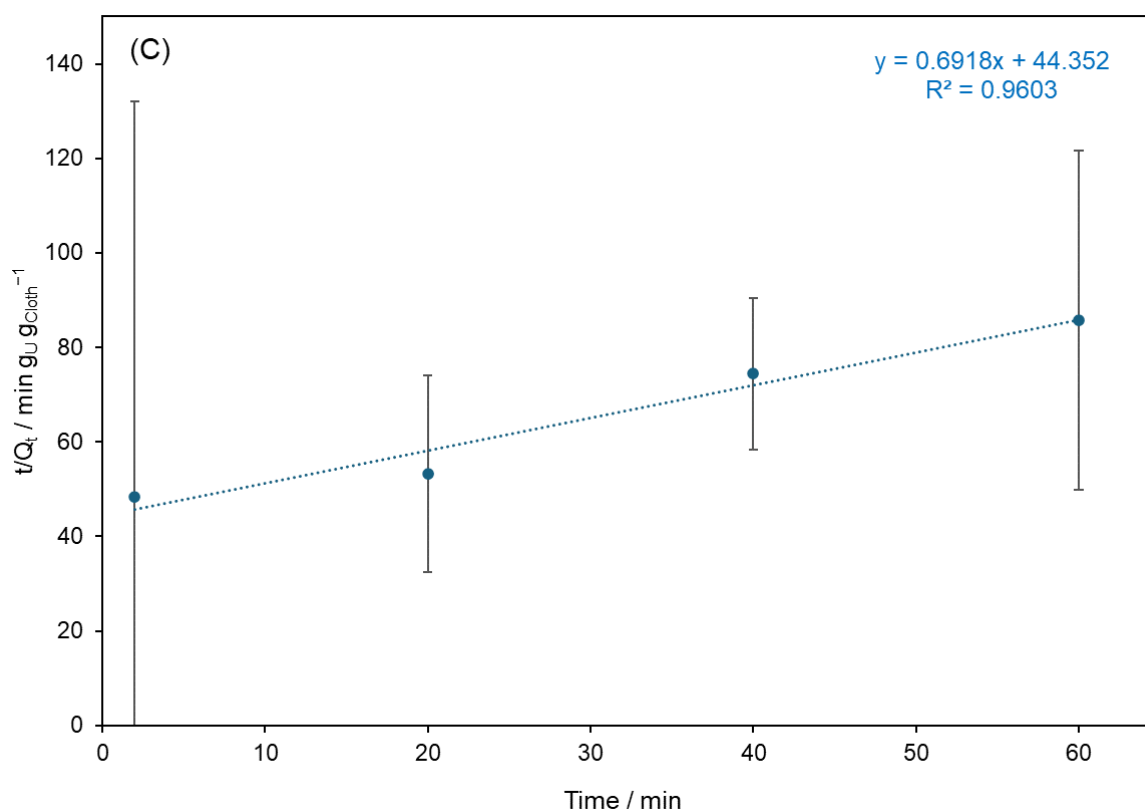


Figure 5-19. Pseudo-first (red) and pseudo-second (orange) order kinetic models for the static adsorption of  $20 \text{ mg L}^{-1}$  U(VI) onto a range of amidoxime-functionalised TPU cloths over the first 60 min of adsorption. Additionally, pseudo-first (grey) and pseudo-second (black) order kinetic models for the adsorption, omitting the data points captured after 5 and 10 min of adsorption.

Similarly, when fitting the data to the linear pseudo-first and pseudo-second order models (Figure 5-20), fits were performed inclusive and exclusive of the data points at 5 and 10 min. In both cases, removing these data points gave rise to better fits to the linear models (indeed, the  $R^2$  value for the linear pseudo-second order kinetic model, inclusive of these points is only 0.0865). As opposed to the non-linear fits, the best fit is the pseudo-first order model, exclusive of the anomalous data points ( $R^2 = 0.9704$ ), followed by the pseudo-second order model, exclusive of the anomalous data points ( $R^2 = 0.9603$ ), then the pseudo-first order model, inclusive of the anomalous data points ( $R^2 = 0.9430$ ), and finally the pseudo-second order model, inclusive of the anomalous data points ( $R^2 = 0.0865$ ).



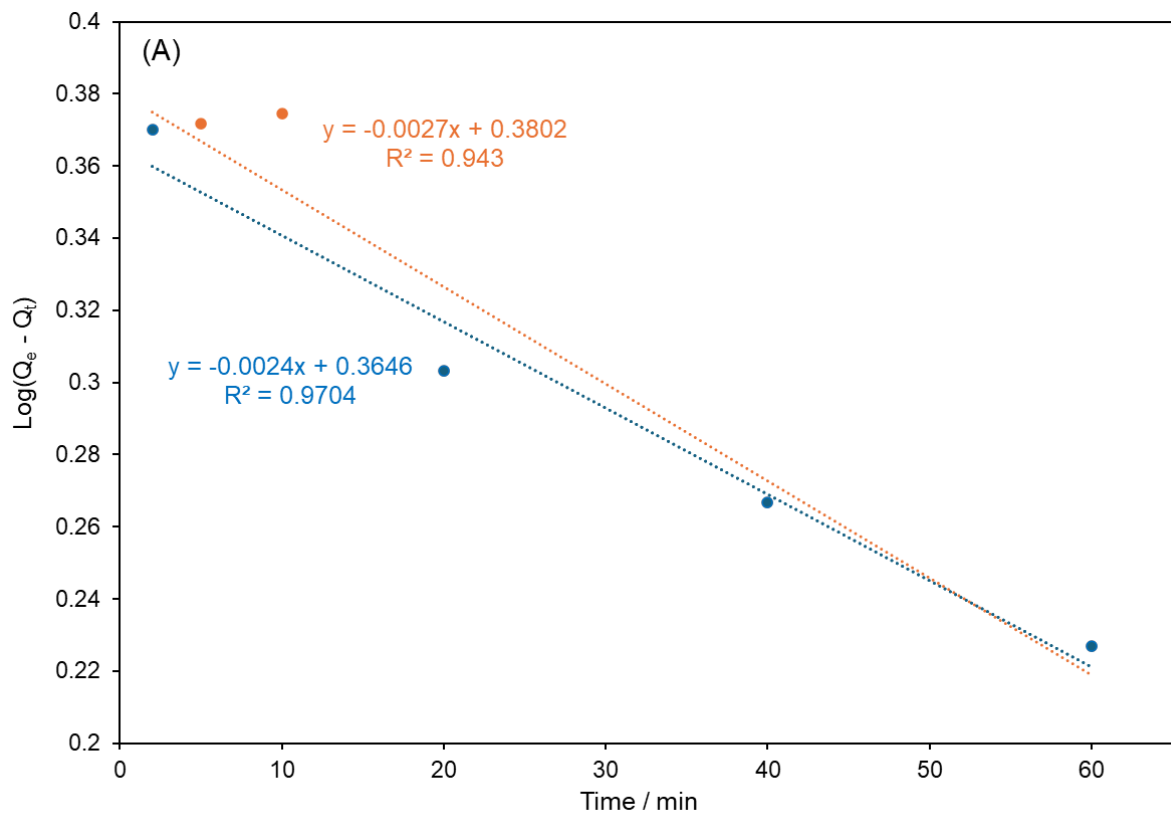
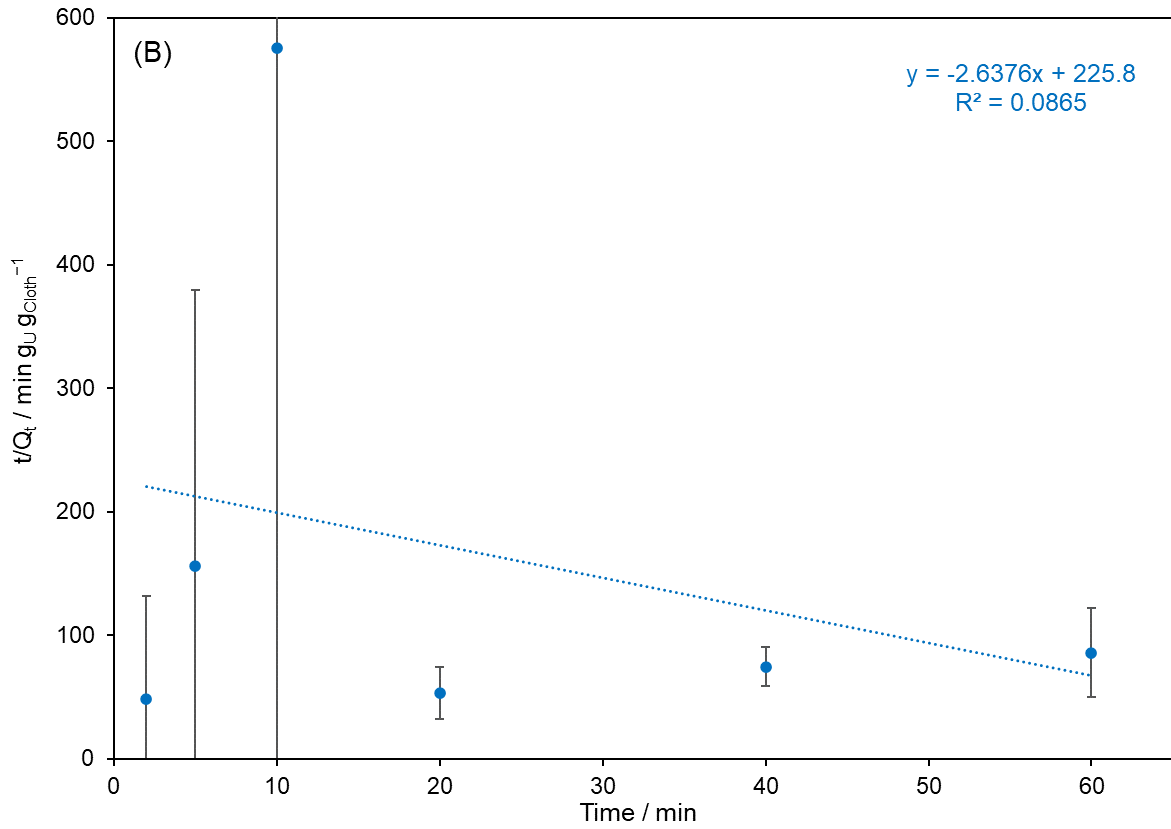


Figure 5-20. (A) Linear plots for the pseudo-first order kinetic model, inclusive of all data points (orange), and excluding the data points at 5 and 10 min (blue). Owing to the extensive error range for all data points, error bars have not been included for ease of viewing. (B) Linear plot for the pseudo-second

order kinetic model, inclusive of all data points, and (C) Linear plot for the pseudo-second order kinetic model, excluding the data points at 5 and 10 min.

Consequently, as the non-linear and linear models give different conclusions as to the appropriate kinetic model, as well as the large error values during the non-linear plots and the similar  $R^2$  values for the linear plots, neither the non-linear, nor the linear kinetic model conclusions, can be considered definitively as the correct model. As such, it is more appropriate to state that the removal of U(VI) from solution follows adsorption kinetics, however it is inconclusive whether these kinetics follow pseudo-first order or pseudo-second order kinetics. For the sake of completeness, the determined rate constant values for both non-linear and linear pseudo-first- and second-order kinetic models have been determined (Table 5-5)—the non-linear rate constants are calculated by determining which rate constant values yield the optimal data fit, whereas for the linear rate constants,  $k_1$  is determined by multiplying the gradient by  $-2.303$ , and  $k_2$  is determined by taking the inverse of the intercept and dividing that by the square of the maximum adsorption capacity ( $2.386 \text{ mg}_{\text{U}}\text{g}_{\text{Cloth}}^{-1}$ ). For each calculation, the models excluding the anomalous data point were utilised.

Table 5-5. Determined values for rate constants  $k_1$  and  $k_2$ , using non-linear and linear models, for the adsorption of  $20 \text{ mg L}^{-1}$  U(VI) onto an amidoxime functionalised cloth under static filtration conditions. The rate constants have been calculated using the redacted data set. For the linear plots, the errors were calculated by determining the percentage error in the regression analysis for the gradient and intercept (where appropriate) calculations and applying this to the final rate constant values. For the non-linear plots, the errors were calculated by averaging the percentage error between each data point and the theoretically calculated value and applying this to the final rate constant value.

Variable	Non-Linear / $\text{min}^{-1}$	Linear / $\text{g}_{\text{Cloth}}\text{mg}_{\text{U}}^{-1}\text{min}^{-1}$
$k_1$	$0.0065 \pm 0.0038$	$0.0055 \pm 0.0003$
$k_2$	$0.0124 \pm 0.0014$	$0.0538 \pm 0.0045$

### 5.3.3.8 Cloth Selectivity

In order to investigate the effectiveness of the synthesised cloth in real-world conditions, static filtration of a  $20 \text{ mg L}^{-1}$  U(VI) solution, in competition with one of several alternative metal ions, in a 1:50 mole ratio of uranium:metal ion was performed. In order to best replicate conditions in which uranium is found in real-world conditions, as well as to investigate a range of metal ion charge and size, the metal ions chosen were  $\text{Na}^+$ ,  $\text{K}^+$ ,  $\text{Mg}^{2+}$ ,  $\text{Ca}^{2+}$ ,  $\text{Pb}^{2+}$ , and  $\text{Fe}^{3+}$ . Following static filtration of the pure U(VI) solution, an adsorption capacity of  $2.50 \pm 0.32 \text{ mg}_{\text{U}}\text{g}_{\text{Cloth}}^{-1}$  was obtained (Figure 5-21). Although the presence of  $\text{Ca}^{2+}$  did not result in a decrease in adsorption capacity, the large excess of  $\text{Pb}^{2+}$ ,  $\text{Mg}^{2+}$ , and  $\text{Na}^+$  did result in lower uranium capture, while the presence of a large excess of  $\text{K}^+$  and  $\text{Fe}^{3+}$  did almost completely inhibit uranium uptake. While it is unlikely that real-world water conditions will contain potassium or

iron concentrations of  $1000 \text{ mg L}^{-1}$ , these results may suggest that in real-world water conditions where there is a large disparity between the concentration of uranium and competing metal ions, the cloth may struggle to extract the contaminating uranyl ions.

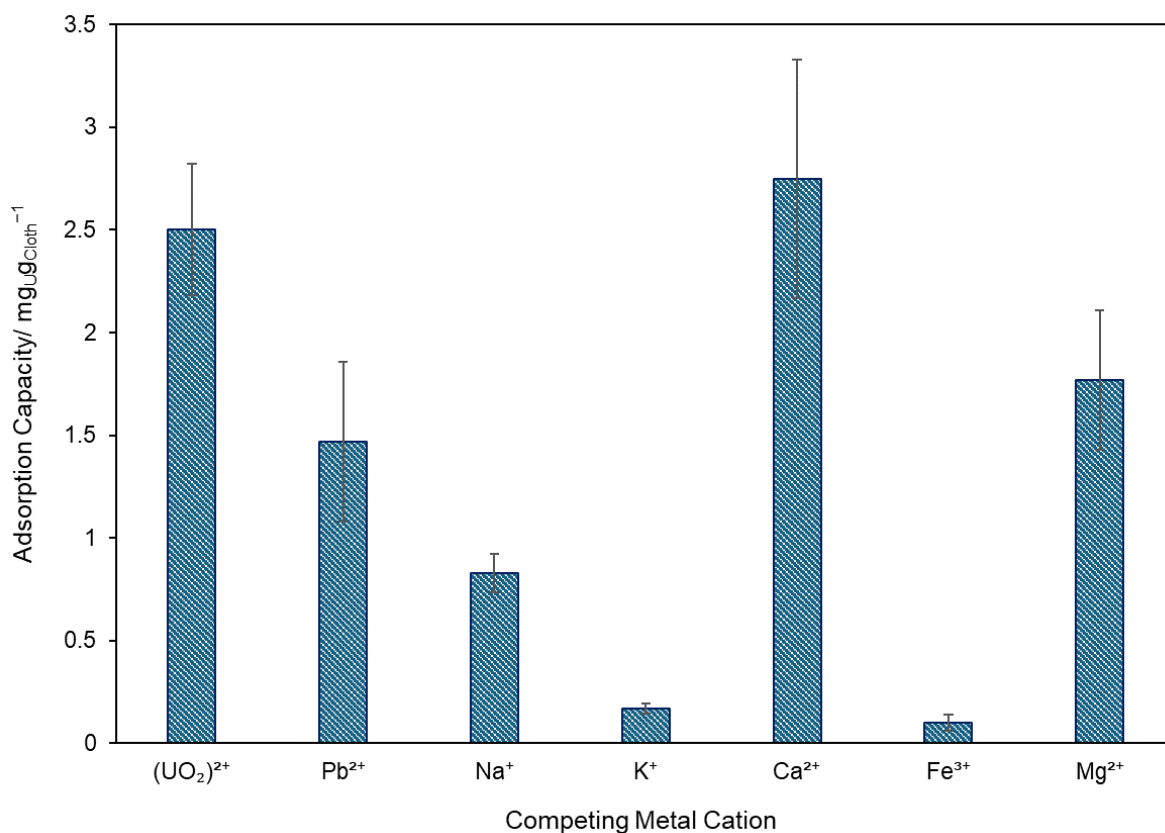


Figure 5-21. Adsorption capacity of an amidoxime functionalised cloth towards a  $5 \text{ mL } 20 \text{ mg L}^{-1} \text{ U(VI)}$  solution, containing a 1:50 mole ratio of U(VI):competing cation, under static conditions.

To further investigate the suitability of the amidoxime functionalised cloths to extract U(VI) under real-world conditions, a  $10 \text{ mg L}^{-1} \text{ U(VI)}$  solution was made up using water taken from a nearby pond. A semi-quantitative scan of the obtained pond water revealed the presence of metal ions shown in Table 5-6, which includes the presence of iron, potassium, magnesium, and sodium. In comparison to the adsorption capacity of  $1.52 \pm 0.29 \text{ mg U g}_{\text{Cloth}}^{-1}$  for the extraction of  $10 \text{ mg L}^{-1} \text{ U(VI)}$  from a  $5 \text{ mL}$  solution made up with HP water, an adsorption capacity of  $0.31 \pm 0.16 \text{ mg U g}_{\text{Cloth}}^{-1}$  was obtained for the extraction of  $10 \text{ mg L}^{-1} \text{ U(VI)}$  from a  $5 \text{ mL}$  solution made up with pond water (Figure 5-22). These findings indicate that while the amidoxime functionalised cloth does display good extraction from water solutions, the cloths may struggle to remove uranium from water solutions containing a range of competing metal ions.



Table 5-6. Concentration of elements determined by a semi-quantitative ICP-OES scan of the obtained pond water.

Element	Concentration / mg L <sup>-1</sup>
Ba	0.14
Ca	55.63
Fe	0.44
K	2.21
Mg	2.07
Mn	0.35
Na	6.39
Sr	0.32

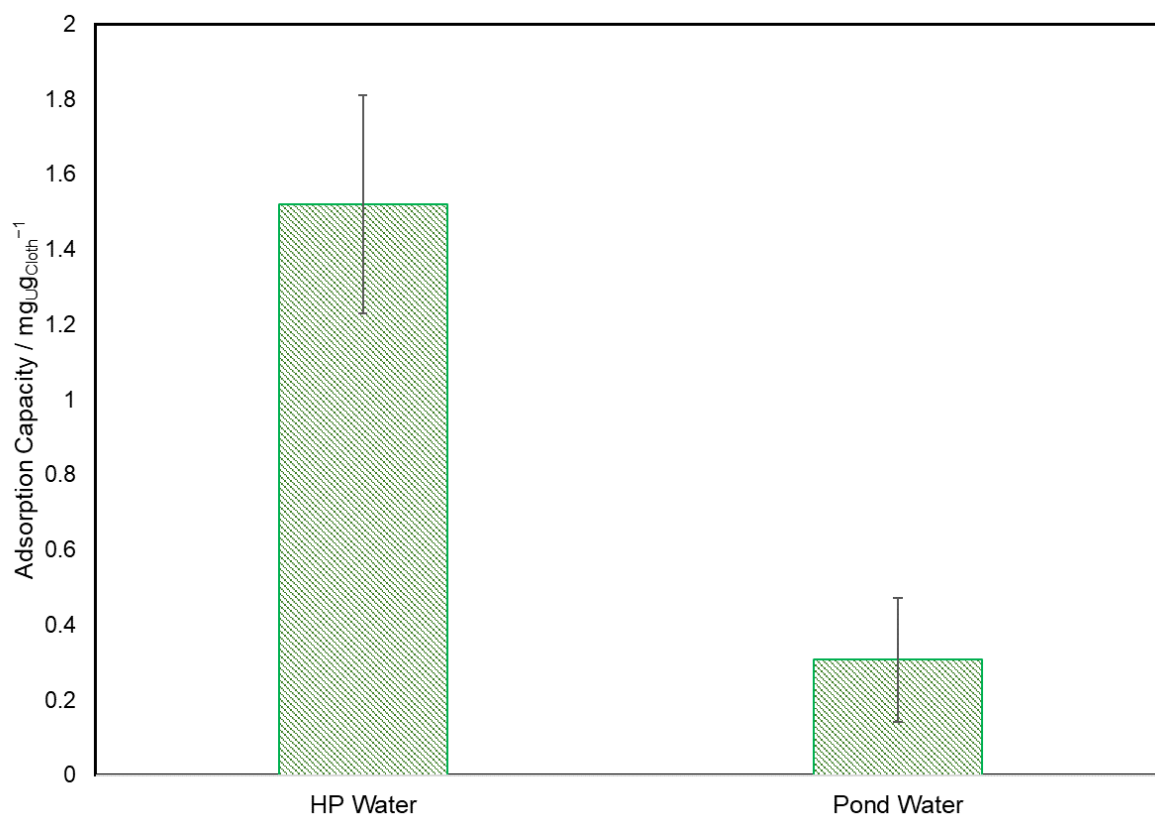


Figure 5-22. Adsorption capacity of an amidoxime functionalised cloth towards 10 mg L<sup>-1</sup> U(VI) solutions, made up with either HP water or pond water.

#### 5.4 Discussion

Attempts were made to synthesise a range of functionalised cloths, including an amidoxime, three polyhydroxybenzene, and five calixarene functionalised cloths. Of these, the amidoxime functionalised cloth yielded the greatest uranium capture, successfully removing  $90.3 \pm 4.5\%$  of uranium from a starting 10 mg L<sup>-1</sup> U(VI) solution under static filtration conditions. Given that neither the uncoated TPU cloth, nor the pulsed plasma poly(2-cyanoethyl acrylate) coated

cloth were able to remove uranium from solution, extraction was attributed to the presence of the amidoxime moieties on the surface. Amidoxime groups behave as weak acids, and so under neutral conditions, will dissociate, before the amidoximate complexes with the positively charged uranyl ion.<sup>487,488</sup> However, no cloth, which was attempted to be functionalised with a calixarene or a polyhydroxybenzene, yielded successful uranium removal. As the calixarenes should behave similarly to amidoximes (weak Lewis acids, with multiple lone pair containing groups), their lack of efficacy towards uranium removal is attributed to the inability to efficiently attach the molecules to the surface, evidenced by the lack of visibility of key absorption bands within the FTIR spectra of the cloths, following attempted grafting of the molecules. Given that there does appear to be some evidence of polyhydroxybenzene attachment, the inefficient uranium extraction is attributed to weaker forces of attraction between the catechol/phloroglucinol molecules and uranyl ions, compared to the amidoxime molecules and uranyl ions. While there has been a plethora of other works utilising amidoxime functionalised substrates in order to extract uranium from solution, these all tend to use batch, static, filtration, which are generally not suitable for point-of-use filtration in real-world conditions. Where dynamic filtration is employed, columns are utilised, with the aid of external pressure, which is not suitable for point-of-use in real-world conditions.<sup>489,490,491</sup> Despite undesirable results (a filtration efficiency of only  $22.0 \pm 6.3$  % could be achieved), dynamic filtration of uranium solutions using the amidoxime functionalised cloth demonstrated potential. The filtration was completed within 2 min, meaning that the system would be able to process large quantities of uranium contaminated water within a short time-frame, which is ideal for point-of-use filtration. It is possible to conclude therefore that, when the methodology for dynamic filtration is optimised to ensure that successful filtration can be guaranteed, the cloth in this work would be a very promising adsorbent for real-world uranium extraction at point-of-use.

Previous work to develop adsorbents designed for the removal of uranium from solution utilise wet chemistry techniques in their synthesis, which often require harmful conditions, long reaction times, and utilise solvents (which necessarily involves material and financial wastage).<sup>463,464</sup> Furthermore, the synthesised adsorbents typically take the form of high surface area adsorbents, such as nanoparticles,<sup>492</sup> silica fibres,<sup>493</sup> or resins,<sup>443</sup> which require more complicated use and handling procedures, and as such, are not suitable for point-of-use conditions. In this work, the adsorbent fabricated was a functionalised cloth, which can be easily handled and readily implemented as a uranium filter. Furthermore, a key stage of the cloth synthesis involved introducing cyano groups onto the surface of the cloth via plasmachemical deposition of pulsed plasma poly(2-cyanoethyl acrylate). Although previous works have used plasma techniques in order to synthesise adsorbents designed for uranium extraction, these techniques involve using Ar/N<sub>2</sub> plasma in order to activate

substances,<sup>460, 494, 495, 496, 497, 498</sup> so that acrylonitrile could be attached, which necessarily involves an additional step to the work presented here. Therefore, this work presents a synthetic route towards fabricating adsorbents, which utilise less energy and solvent than previously employed. Furthermore, the distinct advantage of plasmachemical deposition means that a functional cloth can be synthesised from any starting cloth, meaning that adsorbents can be made from whichever material is readily available.<sup>464</sup> This substrate versatility has been demonstrated here by successfully depositing pulsed plasma poly(2-cyanoethyl acrylate) onto the TPU cloth, silicon wafers, and glass slides.

The adsorption capacity of the cloth shows excellent promise for real-world use. Under the experimental conditions possible, a maximum observed adsorption capacity of  $8.80 \pm 0.85 \text{ mg U g}_{\text{Cloth}}^{-1}$  was observed. While this value is lower than many reported values in prior work, in reality, the cloths will be able to extract a greater quantity of uranium – plotting the adsorption capacity against starting concentration revealed a Henry region (where adsorption is directly proportional to concentration) for starting uranium concentrations up to  $25 \text{ mg L}^{-1}$ , whereupon a shallow adsorption curve became visible. Within the bounds of the experimental conditions, it can be observed that the adsorption curve does not approach plateau, meaning that the actual maximum adsorption capacity of the cloth will be significantly greater than the highest measurable value. Indeed, the adsorption behaviour can be modelled as a Freundlich isotherm, meaning that multilayers of uranyl ions are able to be adsorbed onto the surface, as opposed to the majority of prior work, which models their adsorption as a Langmuir isotherm, and hence monolayer formation. Multilayer formation naturally enables a greater quantity of uranyl ions to be extracted, as uranium adsorption is not limited to the number of adsorption sites directly located on the surface of the adsorbent. Furthermore, plasmachemical deposition results in only the surface layer being functionalised. Therefore, if the adsorption capacity value could be calculated by determining the mass of the functionalised fibres, rather than the mass of the cloth as a whole, this would naturally lead to a significantly greater calculated adsorption capacity. As previous work which resulted in the greatest uranium uptake occurred for adsorbents with high-surface area,<sup>457,458,482,492,499,500,501,502</sup> where the fabrication process applied to a substrate such as GO nanoparticles, it is expected that the observed adsorption capacity would increase dramatically if the processes applied in this work were applied to similar high-surface area substrates.

One distinct advantage of using a cloth as a uranium filter in real-world conditions is its usability, and so it is particularly important that the cloth can be used repeatedly, in order to minimise waste, and to further enhance this benefit over other adsorbents, which may require more complicated regeneration techniques (such as centrifugation<sup>502</sup>). In this work, it was demonstrated that under dynamic filtration conditions, a  $1 \text{ M HNO}_3$  solution is able to remove

> 90 % bound uranium. Given the rapid flow-through time, this demonstrates that the adsorbent can be efficiently, simply and rapidly recycled, and hence would be ideal in real-world conditions.

Unfortunately, there are drawbacks which currently prevent this adsorbent from being able to be utilised in real-world conditions. As well as the inconsistencies with dynamic filtration, the adsorption kinetics under static filtration show that uranium uptake is quite slow – following one hour of adsorption of a 20 mg L<sup>-1</sup> U(VI) solution, only ≈ ¼ of total uranium uptake could be achieved. Furthermore, while uranium removal was shown to be outstanding when in competition with a 1:50 mole ratio of UO<sub>2</sub><sup>2+</sup>:Ca<sup>2+</sup> (and very good when in competition with a 1:50 mole ratio of UO<sub>2</sub><sup>2+</sup>:Pb<sup>2+</sup> and UO<sub>2</sub><sup>2+</sup>:Mg<sup>2+</sup>), there were significant reductions in extraction percentage when the uranyl ions were in a 1:50 mole ratio with Na<sup>+</sup>, and, in particular, K<sup>+</sup> and Fe<sup>3+</sup>. Nevertheless, this is equivalent to a 1000 mg L<sup>-1</sup> concentration of competing metal ion, significantly greater than expected in real-world groundwater. When investigating the uranium extraction abilities of the cloth towards a spiked real-world sample, an adsorption capacity of 0.31 ± 0.16 mg<sub>UgCloth</sub><sup>-1</sup> was obtained, compared to 1.52 ± 0.29 mg<sub>UgCloth</sub><sup>-1</sup> when attempting to extract uranium of the same starting concentration from HP water. While the cloth does still demonstrate some uranium extraction capabilities, it is clear that its capacity has significantly decreased. As such, while the cloth does demonstrate some very promising capabilities towards real-world uranium capture, more work is still required before it would be suitable for point-of-use uranium filtration. However, owing to the cheap and easy production of the cloth, as well as its improved usability as a filter and its rapid regeneration capability, the cloth could be still used as a uranium filter when dealing with water samples containing elevated uranium concentrations (e.g., nuclear wastewater<sup>503,504</sup>).

## 5.5 Conclusion

A TPU cloth has been successfully employed as a substrate for the synthesis of an easy-to-use uranium filter. The cloth was successfully coated with pulsed plasma poly(2-cyanoethyl acrylate), and reacted with hydroxylamine hydrochloride to yield an amidoxime functionalised cloth. While the cloth could be successfully coated with pulsed plasma poly(4-VBC), it was not possible to react it with the range of polyhydroxybenzenes or calixarenes investigated to yield a uranium adsorbent. The amidoxime functionalised cloth is capable of extracting uranium from solution with a high degree of efficacy (90.3 ± 4.5 % from a 10 mg L<sup>-1</sup> under static filtration conditions, and a maximum adsorption capacity capable of being recorded under experimental conditions of 8.80 ± 0.85 mg<sub>UgCloth</sub><sup>-1</sup>). The adsorption mechanism is primarily electrostatic, involving the dissociation of the amidoxime leading to attraction between the positively charged uranyl ions, and the negatively charged amidoxime. The extraction is modelled by a

Freundlich isotherm, meaning that multilayers of uranyl ions are capable of being captured, leading to an elevated estimated adsorption capacity. However, it is unclear whether pseudo-first or -second order kinetics is the more appropriate kinetic adsorption model. Regeneration of the cloths could be achieved rapidly, with > 90 % captured uranium eluted after 5 mL 1 M HNO<sub>3</sub> was passed through the cloth, and good uranium capture was still observed when the uranyl ions were extracted from a solution containing a 1:50 mole ratio of UO<sub>2</sub><sup>2+</sup>:Ca<sup>2+</sup>, Pb<sup>2+</sup>, and Mg<sup>2+</sup>. However, uranium capture did drop dramatically when the uranium was found in solution containing a 1:50 mole ratio of UO<sub>2</sub><sup>2+</sup>:Na<sup>+</sup>, K<sup>+</sup>, and Fe<sup>3+</sup>; and when attempting to extract uranium from solution under dynamic conditions, significantly reduced extraction percentages were observed (22.0 ± 6.3 % from a 10 mg L<sup>-1</sup> U(VI) solution).

## 5.6 References

- 377 Awan, I.Z. Uranium – The Element: Its Occurrence and Uses. *Journal of The Chemical Society of Pakistan*. **2015**, 37, 1056–1080
- 378 OECD Nuclear Energy Agency and International Atomic Energy Agency, Joint Report: Uranium 2005: Resources, Production, and Demand, **2005**
- 379 Kadadou, D.; Said, E.A.; Ajaj, R.; Hasan, S.W. Research Advances in Nuclear Wastewater Treatment using Conventional and Hybrid Technologies: Towards Sustainable Wastewater Reuse and Recovery. *Journal of Water Process Engineering*. **2023**, 52, 103604
- 380 YCharts, Uranium Spot Price (I:USPNM), [https://ycharts.com/indicators/uranium\\_spot\\_price#:~:text=70.06%20USD%2F1b,for%20Dec%202023](https://ycharts.com/indicators/uranium_spot_price#:~:text=70.06%20USD%2F1b,for%20Dec%202023) (Accessed 19<sup>th</sup> February 2024)
- 381 Gavrilesco, M.; Pavel, L.V.; Cretescu, I. Characterization and Remediation of Soils Contaminated with Uranium. *Journal of Hazardous Materials*. **2009**, 163, 475–510
- 382 Flett, L.; McLeod, C.L.; McCarty, J.L.; Shaulis, B.J.; Fain, J.J.; Krekeler, M.P.S. Monitoring Uranium Mine Pollution on Native American lands: Insights from Tree Bark Particulate Matter on the Spokane Reservation, Washington, USA, *Environmental Research*. **2021**, 194, 110619
- 383 Ulrich, S.; Gillow, J.; Roberts, S.; Byer, G.; Sueker, J.; Farris, K. Hydrogeochemical and Mineralogical Factors Influencing Uranium in Background Area Groundwater Wells: Grants, New Mexico. *Journal of Hydrology: Regional Studies*. **2019**, 26, 100636
- 384 Kurttio, P.; Auvinen, A.; Salonen, L.; Saha, H.; Pekkanen, J.; Mäkeläinen, I.; Väisänen, S.B.; Penttilä, I.M.; Komulainen, H. Renal Effects of Uranium in Drinking Water. *Environmental Health Perspectives*. **2002**, 110, 337–342
- 385 Lapworth, D.J.; Brauns, B.; Chattopadhyay, S.; Gooddy, D.C.; Loveless, S.E.; MacDonald, A.M.; McKenzie, A.A.; Muddu, S.; Nara, S.N.V. Elevated Uranium in Drinking Water Sources in Basement Aquifers of Southern India. *Applied Geochemistry*. **2021**, 133, 105092
- 386 Nolan, J.; Weber, K.A.; Natural Uranium Contamination in Major US Aquifers Linked to Nitrate. *Environmental Science & Technology Letters*. **2015**, 2, 215–220
- 387 Zielinski, R.A.; Simmons, K.R.; Orem, W.H. Use of <sup>234</sup>U and <sup>238</sup>U Isotopes to Identify Fertiliser-derived Uranium in the Florida Everglades. *Applied Geochemistry*. **2000**, 15, 369–383
- 388 Fuller, C. C.; Barger, J. R.; David, J. A.; Piana, M. J. Mechanisms of Uranium Interactions with Hydroxyapatite: Implications for Groundwater Remediation. *Environmental Science & Technology*. **2002**, 36, 158–165
- 389 Schnug, E.; Lottermoser, B.G. Fertiliser-Derived Uranium and its Threat to Human Health. *Environmental Science & Technology*. **2013**, 47, 2433–2434
- 390 NPR, The U.N.'s Nuclear Watchdog Says Japan Can Release Nuclear Waste Water into the Ocean. <https://www.npr.org/2023/07/04/1185971497/the-u-n-s-nuclear-watchdog-says-japan-can-release-nuclear-waste-water-into-the-o> (Accessed 21<sup>st</sup> February 2024)
- 391 Guo, J.; Liu, Y.; Wu, X.; Chen, J. Assessment of the Impact of Fukushima Nuclear Wastewater Discharge on the Global Economy Based on GTAP. *Ocean & Coastal Management*. **2022**, 228, 106296
- 392 Petitot, F.; Lestaavel, P.; Tournalias, E.; Mazzucco, C.; Jacquinet, S.; Dhieux, B.; Delissen, O.; Tournier, B.B.; Gensdarmes, F.; Beaunier, P.; Dublineau, I. Inhalation of Uranium Nanoparticles: Respiratory Tract Deposition and Translocation to Secondary Target Organs in Rats. *Toxicology Letters*. **2013**, 217, 217–225
- 393 Periyakaruppan, A.; Kumar, F.; Sarkar, S.; Sharma, C.S.; Ramesh, G.T. Uranium Induces Oxidative Stress in Lung Epithelial Cells. *Archives of Toxicology*. **2007**, 81, 389–395
- 394 Schwartz, J.H.; Flamenbaum, W.. Heavy Metal-induced Alterations in Ion Transport by Turtle Urinary Bladder. *American Journal of Physiology-Legacy Content*. **1976**, 230, 1582–1589.

- 395 Roszell, L.E.; Hahn, F.F.; Parkhurst, M.A. Assessing the Renal Toxicity of Capstone Depleted Uranium Oxides and Other Uranium Compounds. *Health Physics*. **2009**, *3*, 343–351
- 396 Haakonde, T.; Yabe, J.; Choongo, K.; Chongwe, G.; Nchima, G. Uranium Exposure and Health Risk Implications: A Preliminary Study among the Residents Living around Uranium Mining Sites in the Southern Province of Zambia. *Environmental Advances*. **2021**, 100098
- 397 Kiegel, K.; Steczek, L.; Zakrzewska-Trznadel, G. Application of Calixarenes as Macrocyclic Ligands for Uranium(VI): A Review. *Journal of Chemistry*. **2013**, 2013
- 398 Tang, N.; Liang, J.; Niu, C.; Wang, H.; Luo, Y.; Xing, W.; Ye, S.; Liang, C.; Guo, H.; Guo, J.; Zhang, Y.; Zeng, G. Amidoxime-based Materials for Uranium Recovery and Removal. *Journal of Materials Chemistry*. **2020**, *8*, 7588
- 399 Pellet-Rostaing, S.; Arrachart, G.; Mosand, G.; Leydier, A. Novel Formo-phenolic Resins, Process for the Preparation thereof, and Use of the Same in the Extraction of Uranium from Water. Patent Number: WO2022090242A1, **2022**
- 400 Fan, X.; Gua, X. Development of Calixarene-based Drug Nanocarriers. *Journal of Molecular Liquids*. **2021**, *325*, 115246
- 401 Lijia, L.; Chuhong, Z.; Wenda, X.; Chao, W.; Hongxing, D. Porous Polymer Uranium Adsorption Material and Preparation Method Thereof. Chinese Patent No. CN115090270A, **2022**
- 402 Shinkai, S. Calixarenes as New Functionalized Host Molecules, *Pure & Applied Chemistry*. **1986**, *58*, 1523–1528
- 403 Tabushi, I.; Kobuke, Y.; Ando, K.; Kishimoto, M.; Ohara, E. Macrocyclic Hexacarboxylic acid. A Highly Selective Host for Uranyl Ion. *Journal of the American Chemical Society*. **1980**, *102*, 5947–5948
- 404 Tabushi, I.; Kobuke, Y.; Yoshizawa, A. Macrocyclic Tridithiocarbamate as a Specific Uranophile, *Journal of the American Chemical Society*. **1984**, *106*, 2481–2482
- 405 Shinkai, S.; Koreishi, H.; Ueda, K.; Manabe. A New Hexacarboxylate Uranophile Derived from Calix[6]arene. *Journal of the Chemical Society, Chemical Communications*. **1986**, *3*, 233–234
- 406 Nagasaki, T.; Arimura, T.; Shinkai, S. A New Calix[6]arene-based Uranophile with Phosphonate Groups as Ligands. *Bulletin of the Chemical Society of Japan*. **1991**, *64*, 2575–2577
- 407 Nagasaki, T.; Kawano, K.; Araki, K.; Shinkai, S. Kinetic Studies of Calixarene-based Cyclic and Non-cyclic 'Super-uranophiles' *Journal of Chemical Society, Perkin Transactions 2*. **1991**, *2*, 1325–1327
- 408 Felinto, M.; Almeida, V. Solvent Extraction Separation of Uranium (VI) with Acetatecalix[n]arene and  $\beta$ -diketone (HTTA). *Journal of Alloys and Compounds*. **2000**, *303–304*, 524–528
- 409 Leydier, A.; Lecercle, D.; Pellet-Rostaing, S.; Favre-Reguillon, A.; Taran, F.; Lemaire, M. Sequestering Agent for Uranyl Chelation: A New Family of CAMS Ligands. *Tetrahedron*. **2008**, *64*, 6662–6669
- 410 Kalchenko, I. V. Method for Treating Water and Liquid Radioactive Waste from Transuranic Elements and Uranium. Ukraine Patent No. UA28405U, **2006**
- 411 Fang, F.; Liu, Y.; Mo, H.; Pi, A.; Wang, J.; Xie, S.; Zhou, J. Preparation and Use of Hydroxyl Oximated Calix[6]arene Efficient Uranium Extractant. Chinese patent No. CN103242193A, **2013**
- 412 Khan, N.; Tuzen, M.; Kazi, T.G. Simple and Rapid Dual-Dispersive Liquid–Liquid Microextraction as an Innovative Extraction Method for Uranium in Real Water Samples Prior to the Determination of Uranium by a Spectrophotometric Technique. *Journal of AOAC International*. **2017**, *100*, 1848–1853
- 413 Kalyan, Y.; Pandey, A. K.; Naidu, G. R. K.; Reddy, A. V. R. Membrane Optode for Uranium(VI) Ions Preconcentration and Quantification Based on a Synergistic Combination of 4-(2-thiazolylazo)-resorcinol with 8-Hydroxyquinoline. *Spectrochimica Acta, Part A: Molecular and Biomolecular Spectroscopy*. **2009**, *79*, 1235–1241
- 414 El-Sayed, A.; Hamed, M. M. Developed Method for Low Concentration Determination of Uranium. *Eurasian Journal of Analytical Chemistry*. **2009**, *4*, 36–45
- 415 Li, G.; Li, J.; Han, Q. Determination of Trace Uranium by a Photo-catalytic Resonance Fluorescence Method Coupled with Dual Cloud Point Extraction. *Analytical methods*. **2016**, *8*, 5984–5993

- 416 Kallithrakas-Kontos, N. G.; Xarchoulakos, D. C.; Bouladaki, P.; Potiriadis, C.; Kehagia, K. Selective Membrane Complexation and Uranium Isotopes Analysis in Tap Water and Seawater Samples. *Analytical Chemistry*. **2018**, *90*, 4611–4615
- 417 Kaykhail, M.; Ghasemi, E. Room Temperature Ionic Liquid-based Dispersive Liquid–liquid Microextraction of Uranium in Water Samples Before Spectrophotometric Determination. *Analytical Methods*. **2013**, *5*, 5260
- 418 Nazal, M.K.; Albayyari, M.A.; Khalili, F.I. Effect of High Ionic Strength on the Extraction of Uranium(VI) Ions. *Journal of Saudi Chemical Society*. **2014**, *18*, 59–67
- 419 Niazi, A.; Khorshidi, N.; Ghaemmaghami, P. Microwave-assisted of Dispersive Liquid–liquid Microextraction and Spectrophotometric Determination of Uranium after Optimization Based on Box–Behnken Design and Chemometrics Methods. *Spectrochimica Acta, Part A: Molecular and Biomolecular Spectroscopy*. **2015**, *135*, 69–75
- 420 Bagda, E.; Tuzen, M. Determination of Uranium in Water Samples with Chromogenic Reagent 4-(2-thiazolylazo) Resorcinol after Ionic Liquid Based Dispersive Liquid-Liquid Microextraction. *Journal of Radioanalytical and Nuclear Chemistry*. **2016**, *309*, 453–459
- 421 Bosque Sendra, J. M.; Valencia, M. C.; Capitan-Vallvey, L. F. Determination of Uranium in Natural Waters by Solid Phase Spectrometry. *International Journal of Environmental Analytical Chemistry*. **1990**, *38*, 551–559
- 422 Ghosh, A.; Patel, K. S.; Mishra, R. K. Extraction-Spectrophotometric Determination of Uranium(VI) with PAR and N-octylacetamide. *Journal of Radioanalytical and Nuclear Chemistry*. **1991**, *152*, 243–249
- 423 Grudpan, K; Sooksamiti, P.; Laiwraungrath, S. Determination of Uranium in Tin Tailings using 4-(2-pyridylazo)resorcinol by Flow-injection Analysis. *Analytica Chimica Acta*. **1995**, *314*, 51–55
- 424 Mori, I.; Taguchi, K.; Fujita, Y.; Matsuo, T. Improved Spectrophotometric Determination of Uranium(VI) with 4-(2-pyridylazo)resorcinol in the Presence of Benzyltrimethylammonium Chloride. *Fresenius' Journal of Analytical Chemistry*. **1995**, *353*, 174–175
- 425 Lee, C.H.; Suh, M.Y.; Joe, K.S.; Eom, T.Y.; Lee, Won. A Chelating Resin Containing 4-(2-thiazolylazo)resorcinol as the Functional Group. Chromatographic Application to the Preconcentration and Separation of Some Trace Metal Ions Including Uranium. *Analytica Chimica Acta*. **1997**, *351*, 57–63
- 426 Lee, C.H.; Suh, M.Y.; Kim, J.S.; Kim, D.Y.; Kim, W.H.; Eom, T.Y. Separation and Preconcentration of Uranium from Geological Materials with Chelating Resin Containing 4-(2-thiazolylazo)resorcinol Functional Groups. *Analytica Chimica Acta*. **1999**, *382*, 199–203
- 427 Abbas, M. N.; Homoda, A. M.; Mostafa, G. A. E. First Derivative Spectrophotometric Determination of Uranium(VI) and Vanadium(V) in Natural and Saline Waters and some Synthetic Matrices Using PAR and Cetylpyridinium Chloride. *Analytica Chimica Acta*. **2001**, *436*, 223–231
- 428 Grdinic, V. Specific Microdetection of Uranium with 4-(2-pyridylazo)resorcinol on Ion-Exchange Resin Beads. *Fresenius' Journal of Analytical Chemistry*. **1981**, *307*, 205
- 429 Murty, C. R.; Rao, G. S. Detection of Uranium and Thorium with 4-(pyridyl-2'-azo)resorcinol. *Fresenius' Journal of Analytical Chemistry*. **1981**, *308*, 462
- 430 Byerley, J. J.; Scharer, J. M.; Atkinson, G. F. Determination of Uranium(VI) in Process Liquors by Ion Chromatography. *Analyst*. **1987**, *112*, 41–44
- 431 Brcic, I.; Polla, E.; Radosevic, M. Determination of Uranium in Phosphoric Acid Using 4-(2-pyridylazo)resorcinol and 2-(5-bromo-2-pyridylazo)-5-diethylaminophenol Reagents. *Analyst*. **1985**, *110*, 1249–1252
- 432 Perez Trujillo, J. P.; Sosa, Z.; Arias, J. J.; Garcia Montelongo, F. Extraction-spectrophotometric Determination of Uranium with 4-(5'-methyl-3'-isoxazolylazo)resorcinol. *Analytical Letters*. **1988**, *21*, 869–880
- 433 Abbasi, S.A. Atomic Absorption Spectrometric and Spectrophotometric Trace Determination of Uranium in Environmental Samples with N-p-methoxyphenyl-2-furylacrylohydroxamic Acid and 4-(2-pyridylazo)resorcinol. *International Journal of Environmental Analytical Chemistry*. **1989**, *36*, 163–172



- 434 Abe, S.; Okima, K. Preparation of Soluble Ternary Heteroazo Dye Complexes for the Spectrophotometric Determination of Trace Uranium(VI). *Mikrochimica Acta*. **1986**, 3, 309–319
- 435 Brcic, I.; Polla, E.; Radosevic, M. Spectrophotometric Method for the Direct Determination of Uranium in Carbonate Solution. *Mikrochimica Acta*. **1985**, 2, 187–193
- 436 Evans, L.; Collins, G.E. Separation of Uranium(VI) and Transition Metal Ions with 4-(2-thiazolylazo) Resorcinol by Capillary Electrophoresis. *Journal of Chromatography. A*. **2001**, 911, 127–133
- 437 Mori, I.; Taguchi, K.; Fujita, Y.; Matsuo, T. Improved Spectrophotometric Determination of Uranium(VI) with 4-(2-pyridylazo)resorcinol in the Presence of Benzyltrimethylammonium Chloride. *Analytical and Bioanalytical Chemistry*. **1995**, 353, 174–175
- 438 Florence, T. M.; Farrar, Y. Spectrophotometric Determination of Uranium with 4-(2-pyridylazo) Resorcinol. *Analytical Chemistry*. **1963**, 35, 613–616
- 439 Jain, P. C.; Rao, G. S. Resorcinol as an Analytical Reagent for the Spectrophotometric Determination of Uranium. *Analytica Chimica Acta*. **1959**, 20, 171–174
- 440 Pollard, F. H.; Hanson, P.; Geary, W. J. 4-(2-Pyridylazo)resorcinol as a Possible Analytical Reagent for the Colorimetric Estimation of Cobalt, Lead, and Uranium. *Analytica Chimica Acta*. **1959**, 20, 26–31
- 441 Li, B.; Ma, L. Tian, Y.; Yang, X.; Li, J.; Bai, C.; Yang, X.; Zhang, S.; Li, S.; Jin, Y. A Catechol-like Phenolic Ligand-functionalized Hydrothermal Carbon: One-pot Synthesis, Characterization and Sorption Behaviour Toward Uranium. *Journal of Hazardous Materials*. **2014**, 271, 41–49
- 442 Qian, Y.; Yuan, Y.; Wang, H.; Liu, H.; Zhang, J.; Shi, S.; Guo, Z.; Wang, N. Highly Efficient Uranium Adsorption by Salicylaldehyde/Polydopamine Graphene Oxide Nanocomposites. *Journal of Materials Chemistry A*. **2018**, 6, 24676
- 443 Cheira, M.F. Synthesis of Pyridylazo Resorcinol – Functionalized Amberlite XAD-16 and its Characteristics for Uranium Recovery. *Journal of Environmental Chemical Engineering*. **2015**, 3, 642–652
- 444 Tiemann F. Über die Einwirkung von Hydroxylamin auf Nitrile. *Berichten Der Deutschen Chemischen Gesellschaft*. **1884**, 17, 126–129
- 445 Sahyoun, T.; Arrault, A.; Schneider, R. Amidoximes and Oximes: Synthesis, Structure, and Their Key Role as NO Donors. *Molecules*. **2019**, 24, 2470
- 446 Li, W.P.; Han, X.Y.; Wang, X.Y.; Wang, Y.Q.; Wang, X.W.; Xu, H.; Tan, T.S.; Wu, W.S.; Zhang, H.X. Recovery of Uranyl from Aqueous Solutions Using Amidoximated Polyacrylonitrile/exfoliated Na-montmorillonite Composite. *Chemical Engineering Journal*. **2015**, 279, 735–746
- 447 Wang, B.; Zhou, Y.; Li, L.; Wang, Y. Preparation of Amidoxime-functionalized Mesoporous Silica Nanospheres (ami-MSN) from Coal Fly Ash for the Removal of U(VI). *Science of The Total Environment*. **2018**, 626, 219–227
- 448 Zeng, J.; Zhang, H.; Sui, Y.; Hu, N.; Ding, D.; Wang, F.; Xue, J.; Wang, Y. New Amidoxime-based Material TMP-g-AO for Uranium Adsorption Under Seawater Conditions. *Industrial & Engineering Chemistry Research*. **2017**, 56, 5021–5032
- 449 Tang, N.; Liang, J.; Niu, C.; Wang, H.; Luo, Y.; Xing, W.; Ye, S.; Liang, C.; Guo, H.; Guo, J.; Zhang, Y.; Zeng, G. Amidoxime-based Materials for Uranium Recovery and Removal. *Journal of Materials Chemistry*. **2020**, 8, 7588
- 450 Trivedi, U.; Menon, S. Agrawal, Y. Polymer Supported Calix[6]arene Hydroxamic Acid, a Novel Chelating Resin. *Reactive and Functional Polymers*. **2002**, 50, 205–216
- 451 Xu, Y.; Zhang, K.; Wang, C.; Zhu, Q.; Luo, J.; Cheng, F.; Xiao, F.; Peng, G. Fabrication of Magnetic Functionalised *m*-Carboxyphenyl Azo Calix[4]arene Amine Oxime Derivatives for Highly Efficient and Selective Adsorption of Uranium (VI). *Journal of Radioanalytical and Nuclear Chemistry*. **2020**, 323, 1145–1155
- 452 Zhang, F.; Zhang, H.; Chen, R.; Liu, Q.; Liu, J.; Wang, C.; Sun, Z.; Wang, J. Mussel-inspired Antifouling Magnetic Activated Carbon for Uranium Recovery from Simulated Seawater. *Journal of Colloid and Interface Science*. **2019**, 534, 172–182

- 453 Dai, Z.; Sun, Y.; Zhang, H.; Ding, D.; Li, L. Rational Synthesis of Polyamidoxime/Polydopamine-Decorated Graphene Oxide Composites for Efficient Uranium(VI) Removal from Mine Radioactive Wastewater. *Industrial & Engineering Chemistry Research*. **2019**, *58*, 19280–19291
- 454 Pooley, G.; Adel-Hadadi, M.; Li, W.; Dietz, T.; Barkatt, A. Silane coupling and Mordanting as Attachment Techniques for Pyridylazo and Thiazolylazo Ligands in the Synthesis of Adsorbents for Uranium in Seawater. *Adsorption Science and Technology*. **2018**, *36*, 1144–1159
- 455 Lee, C.H.; Kim, J.S.; Suh, M.Y.; Lee, W. A Chelating Resin Containing 4-(2-thiazolylazo)resorcinol as the Functional Group. Synthesis and Sorption Behavior for Trace Metal Ions. *Analytica Chimica Acta*. **1997**, *339*, 303–312
- 456 Wang, D.; Song, J.; Wen, J.; Yuan, Y.; Liu, Z.; Lin, S.; Wang, H.; Wang, H.; Zhao, X.; Fang, M.; Lei, M.; Li, B.; Wang, N.; Wang, X.; Wu, H. Significantly Enhanced Uranium Extraction from Seawater with Mass Produced Fully Amidoximated Nanofiber Adsorbent. *Advanced Energy Materials*. **2018**, *8*, 1802607
- 457 Yang, X.; Li, J.; Liu, J.; Tian, Y.; Li, B.; Cao, K.; Liu, S.; Hou, M.; Li, S.; Ma, L. Simple Small Molecule Carbon Source Strategy for Synthesis of Functional Hydrothermal Carbon: Preparation of Highly Efficient Uranium Selective Solid Phase Extractant. *Journal of Materials Chemistry. A*. **2014**, *2*, 1550–1559
- 458 Wei, X.; Liu, Q.; Zhang, H.; Lu, Z.; Liu, J.; Chen, R.; Li, R.; Li, Z.; Liu, P.; Wang, J. Efficient Removal of Uranium(VI) from Simulated Seawater Using Amidoximated Polyacrylonitrile/FeOOH Composites. *Dalton*. **2017**, *46*, 15746–15756
- 459 Sun, Y.; Lu, S.; Wang, X.; Xu, C.; Lil, J.; Chen, C.; Chen, J.; Hayat, T.; Alsaedi, A.; Alharbi, N.; Wang, X. Plasma-Facilitated Synthesis of Amidoxime/Carbon Nanofiber Hybrids for Effective Enrichment of <sup>238</sup>U(VI) and <sup>241</sup>Am(III). *Environmental Science & Technology*. **2017**, *51*, 12274–12282
- 460 Hu, B.; Guo, X.; Zheng, C.; Song, G.; Chen, D.; Zhu, Y.; Song, X.; Sun, Y. Plasma-enhanced Amidoxime/magnetic Graphene Oxide for Efficient Enrichment of U(VI) Investigated by EXAFS and Modeling Techniques. *Chemical Engineering Journal*. **2019**, *357*, 66–74
- 461 Shao, D.; Wang, X.; Ren, X.; Hu, S.; Wen, J.; Tan, Z.; Xiong, J.; Asiri, A.; Marwani, H. Polyamidoxime Functionalized with Phosphate Groups by Plasma Technique for Effective U(VI) Adsorption. *Journal of Industrial and Engineering Chemistry*. **2018**, *67*, 380–387
- 462 Bieber, V.; Ozcelik, E.; Cox, H.; Ottley, C.; Ratan, J.; Karaman, M.; Tabakci, M.; Beaumont, S.; Badyal, J.P. Capture and Release Recyclable Dimethylaminomethyl-Calixarene Functional Cloths for Point-of-Use Removal of Highly Toxic Chromium Water Pollutants. *ACS Applied Materials & Interfaces*. **2020**, *12*, 52136–52145
- 463 Yasuda, H. *Plasma Polymerization*; Academic Press: New York, 1985.
- 464 Teare, D.O.H.; Barwick, D.C.; Schofield, W.C.E.; Garrod, R.P.; Ward, L.J.; Badyal, J.P.S. Substrate-Independent Approach for Polymer Brush Growth by Surface Atom Transfer Radical Polymerization. *Langmuir*. **2005**, *21*, 11425–11430
- 465 He, Y.; Hou, G.; Lu, X.; Chang, P.; Shao, D. Application of Poly(vinylphosphonic acid) Modified Poly(amidoxime) in Uptake of Uranium from Seawater. *RSC Advances*. **2022**, *12*, 4054
- 466 Jampala S. N., Sarmadi M., Manolache S., Denes F. S., Surface Functionalization by RF plasma Deposition of Ethylene Diamine, Acrylonitrile, and Acetonitrile. *Journal of Applied Polymer Science*. **2007**, *107*, 1686–1695
- 467 Liepins, R.; Campbell, D.; Walker, C. J. 1,2-Dinitrile Polymers. I. Homopolymers and Copolymers of Fumaronitrile, Maleonitrile, and Succinonitrile. *Journal of Polymer Science Part A: Polymer Chemistry*. **1968**, *6*, 3059
- 468 Inagaki, N.; Tasaka, S.; Yamada, Y. Plasma Polymerization of Cyano Compounds. *Journal of Polymer Science Part A: Polymer Chemistry*. **1992**, *30*, 2003–2010
- 469 Lefohn, A. E.; Mackie, N. M.; Fisher, E. R. Comparison of Films Deposited from Pulsed and Continuous Wave Acetonitrile and Acrylonitrile Plasmas. *Plasmas and Polymers*. **1998**, *3*, 197–209
- 470 Panchalingam, V.; Chen, X.; Huo, H-H.; Savage, C. R.; Timmons, R. B.; Eberhart, R. C., Pulsed Plasma Discharge Polymer Coatings. *Polymer Coatings*. **1993**, *39*

- 471 Schneider, V.C.; Herz, J. Die Strahlenchemische Bildung von Ketenimino-Gruppen bei der Tieftemperaturpolymerisation des Acrylnitrils. *Die Makromolekulare Chemie*. **1964**, 73
- 472 Tarducci, C.; Schofield, W.; Badyal J.P.S. Cyano-Functionalized Solid Surfaces. *Chemistry of Materials Journal*. **2001**, 13, 1800–1803
- 473 Morsch, S.; Wood, T. J.; Schofield, W. C. E.; Badyal J. P. S. A Combined Plasmachemical and Emulsion Templating Approach for Actuated Macroporous Scaffolds. *Advanced Functional Materials*. **2012**, 22, 313–322
- 474 Brown P. S.; Wood T. J.; Badyal J. P. S. Combining Plasmachemical Emulsion-Templating with ATRP to Create Macroporous Lipophilic Surfaces. *Journal of Colloid and Interface Science*. *Journal of Colloid and Interface Science*. **2014**, 421, 44–48
- 475 Morsch, S.; Schofield, W.C.E.; Badyal, J.P.S. Surface Actuation of Smart Nanoshutters. *Langmuir*. **2010**, 26, 12342–12350
- 476 Schofield, W.C.E.; Badyal, J.P.S. Controlled Fragrant Molecule Release from Surface-tethered Cyclodextrin Host-guest Inclusion Complexes. *ACS Applied Materials & Interfaces*. **2011**, 3, 2051–2056
- 477 Mohd Zahri, N.; Md Jamil, S.; Abdullah, L.; Shean Yaw, T.; Nourouzi Mobarekeh, M.; Sim, J.; Mohd Rapeia, N. Improved Method for Preparation of Amidoxime Modified Poly(acrylonitrile-co-acrylic acid): Characterizations and Adsorption Case Study. *Polymers*. **2015**, 7, 1205–1220
- 478 Dieblod, A. C.; Chism, W. W. Characterisation and Metrology of Medium Dielectric Constant Gate Dielectric Films. In *High Dielectric Constant Materials: VSLI MOSFET Applications*; Huff, H. R., Gilmer, D. C., Eds.; Springer-Verlag: Berlin, 2005; p 486
- 479 Lovering, D. *NKD-6000 Technical Manual*; Aquila Instruments: Cambridge, 1999
- 480 Lui-Vien, D.; Colthup, N. B.; Fateley, W. G.; Grasselli, J. G. *The Handbook of Infrared and Raman Characteristic Frequencies of Organic Molecules*, Academic Press: Boston, 1991
- 481 Wang, X.; Ji, G.; Zhu, G.; Song, C.; Zhang, H.; Gao, C. Surface Hydroxylation of SBA-15 Via Alkaline for Efficient Amidoxime-functionalization and Enhanced Uranium Adsorption. *Separation and Purification Technology*. **2019**, 209, 623–635
- 482 Zhang, Z.; Dong, Z.; Dai, Y.; Xiao, S.; Cao, X.; Liu, Y.; Guo, W.; Luo, M.; Le, Z. Amidoxime-Functionalized Hydrothermal Carbon Materials for Uranium Removal from Aqueous Solution. *RSC Advances*. **2016**, 6, 102462–102471
- 483 Al-Ghouti, M.A.; Da'ana, D.A. Guidelines for the Use and Interpretation of Adsorption Isotherm Models: A Review. *Journal of Hazardous Materials*. **2020**, 393, 122383
- 484 Wang, J.; Guo, X. Adsorption Isotherm Models: Classification, Physical Meaning, Application and Solving Method. *Chemosphere*. **2020**, 258, 127279
- 485 Chakraborty, A.; Saha, B.B.; Ng, K.C.; Koyama, K.; Srinivasan, K. Theoretical Insight of Physical Adsorption for a Single Component Adsorbent+Adsorbate System: II. The Henry Region. *Langmuir*. **2009**, 25, 7359–7367
- 486 Sun, W.; Selim, M. Fate and Transport of Molybdenum in Solids: Kinetic Modeling. In *Advances in Agronomy*, Ed. Sparks, D.L. Vol 164, Elsevier Inc. 2020, pp. 51–92
- 487 Mehio, N.; Lashely, M.A.; Nugent, J.W.; Tucker, L.; Correia, B.; Do-Thanh, C-L.; Dai, S.; Hancock, R.D.; Bryantsev, V.S. Acidity of the Amidoxime Functionalised Group in Aqueous Solution: A Combined Experimental and Computational Study. *The Journal of Physical Chemistry B*. **2015**, 119, 3567–3576
- 488 Eloy, F.; Lenaers, R. The Chemistry of Amidoximes and Related Compounds. *Chemical Reviews*, **62**, 155–183
- 489 Kuo, L-J.; Janke, C.J.; Wood, J.R.; Strivens, J.E.; Dai, S.; Oyola, Y.; Mayes, R.T.; Gill, G.A. Characterization and Testing of Amidoxime-Based Adsorbent Materials to Extract Uranium from Natural Seawater. *Industrial & Engineering Chemistry Research*. **2016**, 55, 4285–4293
- 490 Astheimer, L.; Schenk, H.J.; Witte, E.G.; Schwochau, K. Development of Sorbers for the Recovery of Uranium from Seawater. Part 2. The Accumulation of Uranium from Seawater by Resins Containing Amidoxime and Imidoxime Functional Groups. *Separation Science and Technology*. **1983**, 18, 307–339

- 491 Kim, J-S.; Tsouris, C.; Oyola, Y.; Janke, C.K.; Mayes, R.T.; Dai, S.; Gill, G.; Kuo, L-J.; Wood, J.; Choe, K-Y.; Schneider, E.; Lindner, H. Uptake of Uranium from Seawater by Amidoxime-Based Polymeric Adsorbent: Field Experiments, Modeling, and Updated Economic Assessment. *Industrial & Engineering Chemistry Research*. **2014**, *53*, 6076–6083
- 492 Yang, P.; Zhang, H.; Liu, Q.; Liu, J.; Chen, R.; Yu, J.; Hou, J.; Bai, X.; Wang, J. Nano-sized Architectural Design of Multi-activity Graphene Oxide (GO) by Chemical Post-decoration for Efficient Uranium(VI) Extraction. *Journal of Hazardous Materials*. **2019**, *375*, 320–329
- 493 Pooley, G.; Adel-Hadadi, M.; Li, W.; Dietz, T.; Barkatt, A. Silane Coupling and Mordanting as Attachment Techniques for Pyridylazo and Thiazolylazo Ligands in the Synthesis of Adsorbents for Uranium in Seawater. *Adsorption Science and Technology*. **2018**, *36*, 1144–1159
- 494 Shao, D.; Wang, X.; Ren, X.; Hu, S.; Wen, J.; Tan, Z.; Xiong, J.; Asiri, A.; Marwani, H. Polyamidoxime Functionalized with Phosphate Groups by Plasma Technique for Effective U(VI) Adsorption. *Journal of Industrial and Engineering Chemistry*. **2018**, *67*, 380–387
- 495 Wang, Y.; Gu, Z.; Yang, J.; Liao, J.; Yang, Y.; Liu, N.; Tang, J. Amidoxime-grafted Multiwalled Carbon Nanotubes by Plasma Techniques for Efficient Removal of Uranium(VI). *Applied Surface Science*. **2014**, *320*, 10–20
- 496 Yu, S.; Sun, C.; Fang, S.; Wang, C.; Alharbi, N.S.; Chen, C. Preparation of Cellulose@amidoxime by Plasma-induced Grafting Technology and its Potential Application for Uranium Extraction. *Applied Surface Science*. **2023**, *637*, 157883
- 497 Shao, D.; Liu, X.; Hayat, T.; Li, J.; Ren, X. Poly(amidoxime) Functionalized MoS<sub>2</sub> for Efficient Adsorption of Uranium(VI) in Aqueous Solutions. *Journal of Radioanalytical and Nuclear Chemistry*. **2019**, *319*, 379–386
- 498 Wang, J.; Zhang, Z.; Gao, Z.; Jiang, Z.; Qiao, Y.; Wang, M.; Fu, Z.; Zhang, Y.; Zhao, D. Uranium Adsorbent and Preparation Method Thereof. Patent No. CN109012586A, **2018**
- 499 Wang, D.; Song, J.; Wen, J.; Yuan, Y.; Liu, Z.; Lin, S.; Wang, H.; Wang, H.; Zhao, X.; Fang, M.; Lei, M.; Li, B.; Wang, N.; Wang, X.; Wu, H. Significantly Enhanced Uranium Extraction from Seawater with Mass Produced Fully Amidoximated Nanofiber Adsorbent. *Advanced Energy Materials*. **2018**, *8*, 1802607
- 500 Wei, X.; Liu, Q.; Zhang, H.; Lu, Z.; Liu, J.; Chen, R.; Li, R.; Li, Z.; Liu, P.; Wang, J. Efficient Removal of Uranium(VI) from Simulated Seawater Using Amidoximated Polyacrylonitrile/FeOOH Composites. *Dalton*. **2017**, *46*, 15746–15756
- 501 Wang, X.; Ji, G.; Zhu, G.; Song, C.; Zhang, H.; Gao, C. Surface Hydroxylation of SBA-15 Via Alkaline for Efficient Amidoxime-functionalization and Enhanced Uranium Adsorption. *Separation and Purification Technology*. **2019**, *209*, 623–635
- 502 Yang, P.; Chen, R.; Liu, Q.; Zhang, H.; Liu, J.; Yu, J.; Liu, P.; Bai, X.; Wang, J. The Efficient Immobilization of Uranium(VI) by Modified Dendritic Fibrous Nanosilica (DFNS) using Mussel Bioglue. *Inorganic Chemistry Frontiers*. **2019**, *6*, 746–755
- 503 Lin, T.; Chen, T.; Jiao, C.; Zhang, H.; Hou, K.; Jin, H.; Liu, Y.; Zhu, W.; He, R. Ion Pair Sites for Efficient Electrochemical Extraction of Uranium in Real Nuclear Wastewater. *Nature Communications*. **2024**, *15*, 4149
- 504 Venturini, M.; Rossen, A.; Silva Paulo, P. Nitrification Process in a Nuclear Wastewater with High Load of Nitrogen, Uranium and Organic Matter under ORP Controlled. *Water*. **2021**, *13*, 1607

## 6 CHAPTER 6 – CONCLUSION

### 6.1 Contaminant Capture

Plasmachemical techniques are a particularly useful way of introducing functionalities to solid materials, in order to tailor their properties as desired. In this thesis, three plasmachemical techniques were employed to introduce a desired functional group to a commonly-occurring polyurethane fabric cloth, in order to facilitate further derivatisation with specific compounds. The compounds chosen were ones designed to extract a contaminant of choice (toxic dye, hexavalent chromium, and uranium), each of which is located readily in groundwater worldwide (Figure 6-1).

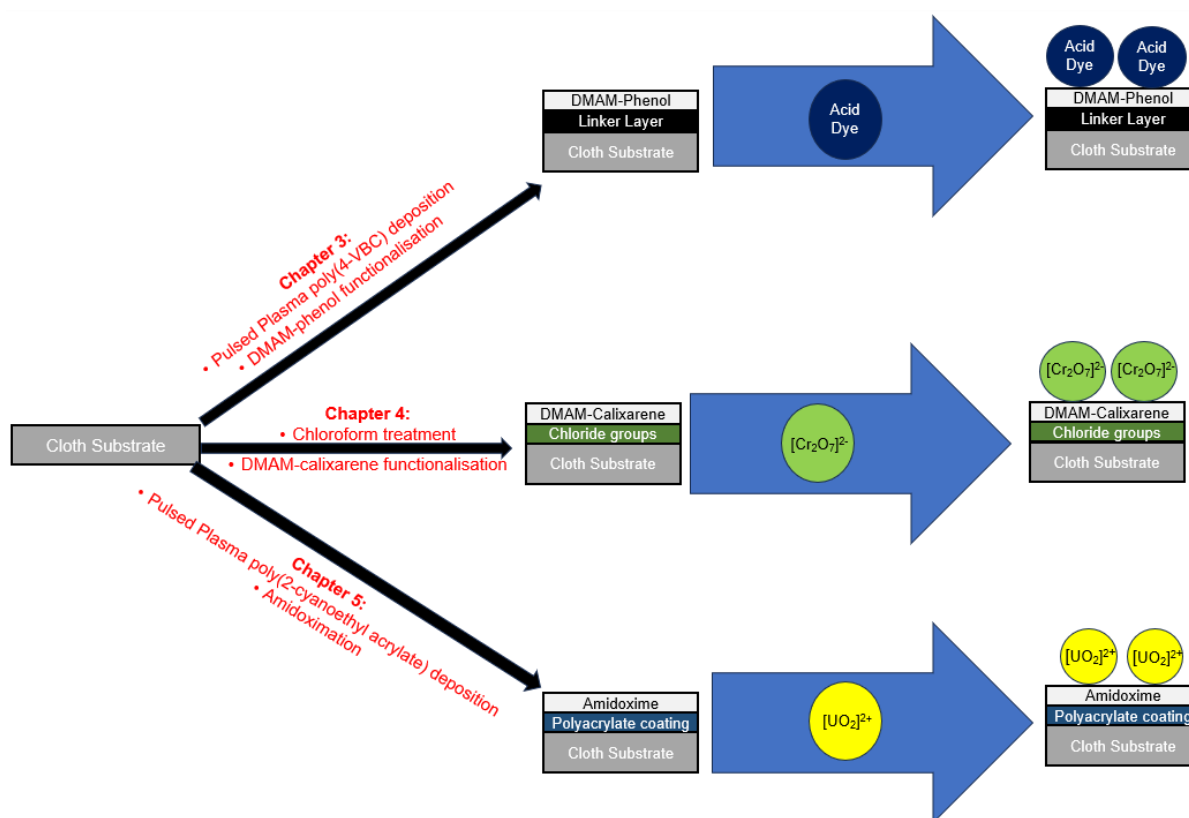


Figure 6-1. Summary of the three cloth adsorbents prepared and characterised in this thesis.

Chapters 3 and 5 utilised plasmachemical deposition to coat the TPU cloth with a pulsed plasma layer (4-vinylbenzyl chloride (4-VBC) and 2-cyanoethyl acrylate respectively) in order to facilitate further functionalisation, while Chapter 4 utilised plasmachemical functionalisation in order to introduce chloride groups directly onto the surface of the TPU cloth. Additionally, in Chapters 3 and 4, the chloride groups introduced to the cloth are used to link the desired molecule to the cloth via nucleophilic substitution, whereas in Chapter 5,

the coated cloth is reacted with hydroxylamine hydrochloride (HH) in order to convert the cyano group into an amidoxime.

Each Chapter focused on the extraction of a different water contaminant. Chapter 3 demonstrated that DMAM-phenol, DMAM-calixarene, tBu-calixarene, and phenol could be incorporated onto the surface of the TPU cloth. Of these, DMAM-phenol and DMAM-calixarene functionalised cloths gave rise to extraction of negatively charged dyes Congo Red (CR), Amido Black 10B (AB10B) and Alizarin Red (AR), but were unable to extract neutral Disperse Red 1 (DR1) or positively charged Methylene Blue (MB) and Janus Green B (JGB) from solution. This indicates that extraction is driven by electrostatic interactions between the negatively charged dye and the DMAM groups (which are positively charged at neutral pH). As stated in previous works—and backed-up by the slightly elevated extraction percentages of the tBu-calixarene and phenol functionalised cloths (compared to the uncoated cloth) towards the anionic dyes—it is likely that the dyes are also bound via  $\pi$ - $\pi$  interactions. Successful dye capture was demonstrated by a PET/PP cloth and an activated carbon cloth, which were both subjected to the same conditions as the TPU cloth, demonstrating that the plasmachemical technique is independent of substrate. Therefore, the process could be used on high-surface area substrates, in order to maximise the adsorption area capable of removing contaminants from solution. Furthermore, the work demonstrated that extraction percentage did not depend on the thickness of the deposited linker layer, indicating that the DMAM-functionalised groups are only incorporated onto the surface layer.

This last finding is important, as it aids in explaining the successful chromium capture demonstrated by the TPU cloth, functionalised with  $\text{CHCl}_3$  plasma, and then reacted with DMAM-calixarene in Chapter 4. While previous work demonstrated that coating a cloth with pulsed plasma poly(4-VBC) and functionalising the coating with DMAM-calixarene (as in Chapter 3) yielded an adsorbent capable of extracting Cr(VI) from solution, utilising plasmachemical functionalisation provides advantages as an alternative to coating with pulsed plasma poly(4-VBC).  $\text{CHCl}_3$  is significantly cheaper and safer-to-handle than VBC, while depositing a plasma polymer means that the equipment must be cleaned between each deposition. Conversely, when functionalising a cloth, the plasma chamber hosting the cloth simply needs re-treating with  $\text{CHCl}_3$  plasma prior to cloth insertion, meaning that functional cloths can be manufactured at an increased rate. The chromium uptake was  $62.9 \pm 9.2 \%$  for a  $20 \text{ mg L}^{-1}$  solution under dynamic conditions, which is within error range of the  $79 \pm 9 \%$  chromium uptake obtained in previous work<sup>505</sup> by the DMAM-calixarene functionalised, pulsed plasma poly(4-VBC) coated cloth under identical conditions, indicating that introducing chloride groups via functionalisation as opposed to deposition does not significantly alter the chromium extraction capabilities of the cloth.

Difficulties in utilising the chloride-containing linker layer were shown in Chapter 5, wherein a range of calixarenes could not be bound to the cloth, attributed to the presence of methoxy groups on the lower rim preventing successful attachment. However, it was possible to deposit a pulsed plasma poly(2-cyanoethyl acrylate) coating on the cloth, which, owing to the presence of the cyano group, was capable of undergoing amidoximation to yield a cloth capable of removing uranium from solution. Both the uncoated TPU cloth, and the TPU cloth coated with pulsed plasma poly(2-cyanoethyl acrylate) were unable to remove uranium from solution, which, as stated in previous works, indicates that electrostatic interactions between the amidoxime group—which dissociates under neutral conditions—and the positively charged uranyl ions, are the driving force behind the observed uranium filtration.

Overall, this work succeeds in demonstrating that plasmachemical techniques can be utilised to manufacture bespoke filters from the same starting substrate, in order to extract the desired contaminant. A key theme in this thesis is ease-of-use. Cloths can be easily handled by lay-users, as opposed to more specific adsorbents commonly found in literature (such as resins or nanoparticles), and dynamic filtration was employed throughout this thesis, in order to replicate conditions required for point-of-use filtration. Furthermore, neutral pH conditions were employed, unlike in most previous work, which tends to artificially adjust the pH in order to increase adsorption capacity. In order to be useful as adsorbents in real-world conditions, adsorption is required to occur rapidly, selectively (especially considering the adsorption mechanisms have been demonstrated to be electrostatic), with a high adsorption capacity, and be readily recycled – factors which are compared in Table 6-1.

Table 6-1. Performance comparison of each of the fabricated cloths towards their desired contaminant. Cells shaded in green designate excellent performance, cells shaded in yellow indicate acceptable performance, and cells shaded in red indicate poor performance. \*ppp = pulsed plasma poly.

Cloth	Dynamic Filtration Performance	Kinetics	Selectivity	Adsorption Capacity	Recyclability
DMAM-phenol functionalised, ppp(4-VBC) coated	<p>&gt; 90 % filtration of AR and AB10B (<math>89.8 \pm 5.3</math> % filtration of CR) from <math>6 \text{ mg L}^{-1}</math> solutions.</p> <p>&gt; 80 % filtration of AR and AB10B (<math>76.0 \pm 10.2</math> % filtration of CR) from <math>10 \text{ mg L}^{-1}</math> solutions.</p>	<p>Dynamic filtration time <math>\approx 5</math> min.</p> <p>Under static filtrations, equilibrium was achieved within 210 min.</p>	<p>Extraction percentage towards <math>6 \text{ mg L}^{-1}</math> AB10B <math>\approx 100</math> %, even when in a 1:100 mole ratio of dye: competing anion.</p> <p>Capable of removing AB10B from a mixture of anionic and cationic dye.</p> <p>Extraction percentage of <math>87.2 \pm 10.9</math> % towards a spiked real-world solution.</p>	<p>Experimentally observed: <math>1.74 \pm 0.29 \text{ mg}_{\text{Dye}}\text{g}_{\text{Cloth}}^{-1}</math>.</p> <p>Adsorption modelling indicated a Langmuir adsorption isotherm (and hence monolayer formation), with an estimated maximum adsorption of <math>1.77 \pm 0.09 \text{ mg}_{\text{Dye}}\text{g}_{\text{Adsorbent}}^{-1}</math>.</p>	<p>After regenerating with a 2 M NaCl/0.5 M NaOH solution, extraction percentage from a <math>20 \text{ mg L}^{-1}</math> solution decreased from <math>44.4 \pm 11.1</math> % to <math>34.1 \pm 13.3</math> %.</p> <p>Extraction percentage remained ca. 100 % following 10 filtration cycles of a <math>6 \text{ mg L}^{-1}</math> solution.</p>



Cloth	Dynamic Filtration Performance	Kinetics	Selectivity	Adsorption Capacity	Recyclability
DMAM-calixarene functionalised, $\text{CHCl}_3$ treated	$68.6 \pm 15.8$ % from a $20 \text{ mg L}^{-1}$ solution.	Dynamic filtration time $\approx 15$ min.  Under static filtrations, equilibrium was achieved within 10 min.	Minor decrease in extraction percentage ( $56.9 \pm 11.4$ %) when in a 1:100 mole ratio of $\text{Cr(VI)}:\text{NO}_3^-$ . Large decrease in extraction percentage ( $14.6 \pm 4.9$ %) when in competition with $\text{CO}_3^{2-}$ , attributed to the associated pH increase.  Minor extraction percentage decrease ( $58.9 \pm 14.1$ %) when removing chromium from a real-world water sample, spiked with Cr(VI), albeit within error of the high-purity water solution.	Experimentally observed: $3.36 \pm 0.57 \text{ mg}_{\text{Cr}}\text{g}_{\text{Cloth}}^{-1}$ .  Adsorption modelling indicated a Freundlich adsorption isotherm (and hence multilayer formation).	Filtration efficiency decreased from $73.9 \pm 5.9$ % after the first filtration to $34.55 \pm 0.8$ % after the tenth.
Amidoximated, ppp(2-cyanoethyl acrylate) coated	Not achieved	Dynamic filtration time $\approx 1.5$ min.  Under static conditions, only $\frac{1}{4}$ total adsorption achieved after 1 h.	Uranyl capture unchanged when in a 1:50 mole ratio of $\text{UO}_2^{2+}:\text{Ca}^{2+}$ ; mildly reduced when in competition with $\text{Pb}^{2+}$ , $\text{Mg}^{2+}$ , and $\text{Na}^+$ ; significantly impeded when in competition with $\text{K}^+$ and $\text{Fe}^{3+}$ .	Experimentally observed: $8.80 \pm 0.85 \text{ mg}_{\text{U}}\text{g}_{\text{Cloth}}^{-1}$ .  Adsorption modelling indicated a Freundlich adsorption isotherm (and hence multilayer formation).	$> 90$ % captured uranium could be desorbed each cycle (4 cycles performed) following regeneration with 1 M $\text{HNO}_3$ .

## 6.2 Outlook

The next stage in this research is to take the functionalised cloths and establish whether they can be applied to real-world polluted water. As demonstrated in Table 6-1, the TPU cloth, coated with pulsed plasma poly(4-VBC) and derivatised with DMAM-phenol provides the greatest performance across the board, with excellent selectivity and recyclability. The only drawbacks of the cloth are the relatively slow time taken for adsorption to reach equilibrium, and the lowest adsorption capacity observed in this thesis. However, dynamic filtration—which is more suitable for point-of-use filtration—of a 5 mL solution could still occur within 5 min, meaning that water could be filtered relatively quickly. Additionally, the adsorption behaviour showed that under anticipated concentrations of dye solutions in water at point-of-use,  $< 0.01 \text{ mg L}^{-1}$  dye will remain in solution, lower than the safe limit specified by EU regulation No. 10/2011 for the concentration of primary aromatic amines found in foodstuff.<sup>506</sup> This ability to fully remove contaminants at lower concentrations is more important in point-of-use environments, which are typically downstream of pollution sources, and hence tend to be more diluted, than an elevated adsorption capacity when exposed to high contaminant concentrations, such as those demonstrated by the DMAM-calixarene functionalised cloth towards Cr(VI) and the amidoxime functionalised cloth towards U(VI).

The DMAM-calixarene and amidoxime functionalised cloths could still be applied to real-world environments. Their adsorption behaviour is more suited to filtering wastewater, which contains elevated concentrations of contaminant, and is typically treated using static filtration. As opposed to nanoparticles and other high-surface area adsorbents, the use of the cloths in this work would provide easier handling, and the scalability of plasmachemical techniques means that cloths of appropriate size to filter the quantities required can be readily manufactured.

In order to build on the research presented in this thesis, the most pressing issue would be to discover a method that allows for dynamic filtration of U(VI) to occur. This may involve adjusting the dynamic filtration procedure, or altering the cloth (e.g., by introducing cyano groups via an alternative method, to increase the number of amidoxime groups on the surface). Furthermore, additional cloths can be synthesised to remove other contaminants—especially those which typically coexist with anionic dyes, hexavalent chromium, and uranium. In Chapter 3, the use of the activated carbon cloth to simultaneously remove positively and negatively charged dyes from solution demonstrates the feasibility of simultaneous contaminant removal, and as cloths are readily stackable, an adsorbent (consisting of several stacked cloths) could be manufactured, which is capable of simultaneously removing a range of contaminants from water.

### 6.3 References

- 505 Bieber, V.; Ozcelik, E.; Cox, H.; Ottley, C.; Ratan, J.; Karaman, M.; Tabakci, M.; Beaumont, S.; Badyal, J.P. Capture and Release Recyclable Dimethylaminomethyl-Calixarene Functional Cloths for Point-of-Use Removal of Highly Toxic Chromium Water Pollutants. *ACS Applied Materials and Interfaces*. **2020**, *12*, 52136–52145
- 506 The European Commission. Commission Regulation (EU) No 10/2011 of 14 January 2011 on Plastic Materials and Articles Intended to Come into Contact with Food Text with EEA Relevance. *Official Journal of the European Union*. **2011**, *12*, 1–89

## APPENDIX A LITERATURE FINDINGS

Appendix Table 1. Adsorption capacity of calixarene-based adsorbents, and the conditions employed to extract the acid dye CR, and the basic dye MB. Where adsorption capacity is not stated within the publication, this has been calculated where possible, with presented data italicised in parentheses.

Dye (Charge)	Calixarene	Substrate	Extraction Conditions	Adsorption Capacity / $\text{mg g}^{-1}$	Additional Information	Ref
CR (Anionic)	1,2,3-triazole-modified thiacalix[4]arene polymers	Polycondensation of 1,2,3-triazole-modified thiacalix[4]arene with an amine bridge.	Add 10 mg polymer to 10 mL dye ( $1 \times 10^{-3}$ M) and stir for 24 h at rtp.	980.3	Dye is desorbed following washes in 10 % HCl and 10 % NaOH. Following five recycling cycles, extraction percentage drops from 96.3 % to 80.4 %.	507
CR (Anionic)	Cationic covalent organic polymers, incorporating a molecular switch and $p\text{TNC4A}$ .	Synthesised following diazo bond formation between $p\text{TNC4A}$ and a viologen-based diamine.	Mix 5 mg polymer with 5 mL dye (25 $\mu\text{M}$ ) for 15 min.	928	Rhodamine B and neutral Nile red dye could be removed by the cationic covalent organic polymers.	508
CR (Anionic)	Poly(calix[4]arene) (CalP2)	N/A	N/D	673	High adsorption was also observed for MB. Total uptake of dye is completed within 15 min.	509

Dye (Charge)	Calixarene	Substrate	Extraction Conditions	Adsorption Capacity / $\text{mg g}^{-1}$	Additional Information	Ref
CR (Anionic)	Amidoamine calix[4]resorcinarene-based polymers	Polycondensation of calix[4]resorcinarenes esters with diethylenetriamine.	Mix dye (unknown concentration) with resin and leave to stir at 360 rpm for 24 h.	625	N/A	510, 511
CR (Anionic)	A) p-tert-butylcalix[8]arene, B) Ester-t-butylcalix[8]arene, and C) Amide-t-butylcalix[8]arene	PAN nanofibers (fabricated through electrospinning).	Mix 50 mL dye (42 ppm) with 0.02 g adsorbent at 160 rpm at pH 7 and rtp for 80 min.	(A) Ca. 22.5* (B) Ca. 19* (C) Ca. 32*  * Capacities were not written down in the publication, so values had to be estimated via reading off figures.	Gold nanoparticles were incorporated into the adsorbent to degrade the captured dye. After five cycles of recycling with water and ethanol, extraction percentage remained unchanged.	512

Dye (Charge)	Calixarene	Substrate	Extraction Conditions	Adsorption Capacity / mg g <sup>-1</sup>	Additional Information	Ref
CR (Anionic)	Tetradodecyloxyphenyl calix[4]arene	None	Pour calixarene into dye (unknown concentration), stir for 1 h at 360 rpm, then separate by centrifuging.	20.3	N/A	513
CR (Anionic)	Calix[4]arene	Amberlite XAD-4	Mix 10 mL dye (2 x 10 <sup>-5</sup> M) containing 0.2 M NaCl with 100 mg resin and stir at 170 rpm at rtp (35 °C) for 1 h at pH 5.8.	1.00 (72 % extraction)	N/A	514
MB (Cationic)	C-3,4,5-trimethoxyphenylcalix[4]-2-methyl resorcinarene	Waste Polystyrene	Batch adsorption of 50 mL MB (10–60 ppm), stirred at 150 rpm at rtp for 2 h.	864.1	N/A	515
MB (Cationic)	Calixarene-based porous organic polymer, POP-8F	None	5 mg of POP-8F added to 15 mL of 100 ppm MB and stirred until equilibrium is reached.	862.07	Excellent selectivity when extracted in competition with Rhodamine Blue (RhB), attributed to smaller size. Excellent extraction after five recycling cycles.	516

Dye (Charge)	Calixarene	Substrate	Extraction Conditions	Adsorption Capacity / mg g <sup>-1</sup>	Additional Information	Ref
MB (Cationic)	Calixarene-based porous organic polymer, POP-10F	None	5 mg of POP-10F added to 15 mL of 100 ppm MB and stirred until equilibrium is reached.	793.65	Excellent selectivity when extracted in competition with Rhodamine B, attributed to smaller size. Excellent extraction after five recycling cycles.	516
MB (Cationic)	Sulfonate containing calix[4]arene-intercalated layered double hydroxide (SuLDH)	Alginate beads, impregnated with unmodified MgAl-NO <sub>3</sub> .	Batch adsorption of 10 mL of a 200 ppm MB solution, shaking at 150 rpm for 30 min at rtp and pH 7.	653.59	Good MB extraction after 5 adsorption/desorption cycles (90 % down to 72.55 %).	517
MB (Cationic)	Porous calix[4]arene polymer	None	120 min for complete removal. No other conditions provided.	625	N/A	509
MB (Cationic)	Calix[4]arene carboxyl derivative	Hydroxyl carbon nanotubes	Batch adsorption, shaking at 200 rpm for 24 h at rtp at pH 7.5.	310	N/A	518

Dye (Charge)	Calixarene	Substrate	Extraction Conditions	Adsorption Capacity / mg g <sup>-1</sup>	Additional Information	Ref
MB (Cationic)	<i>p</i> -nitrobenzyloxy functionalised <i>p</i> - <i>tert</i> -butylcalix[4]arene	Silica Gel	Batch adsorption of a 20 mL, 20 ppm MB solution shaken at 100 rpm for 75 min at pH 12.	212.77	Also investigated textile wastewater, spiked with MB, giving an adsorption yield of 40 % at pH 12.	519
MB (Cationic)	<i>p</i> - <i>tert</i> -butyl-calix[4]arene; <i>p</i> - <i>tert</i> -butyl-calix[6]arene; <i>p</i> - <i>tert</i> -butyl-calix[8]arene	Silica gel	Batch adsorption of 50 mL of a 20 ppm dye solution at pH 8, shaken at 180 rpm at rtp.	23, 87 and 188	N/A	520
MB (Cationic)	<i>p</i> - <i>tert</i> -butylcalix[4]arene and sulfonatocalix[4]arene	Graphene oxide (also use sodium alginate)	Batch adsorption using 10 mL of 100 ppm MB at pH 6 for 1 h at rtp.	170.36	N/A	521
MB (Cationic)	$\beta$ -CD-calix[4]arene coupling products	None	100 mg of calixarene added to 25 mL of MB (20–140 ppm) and shaken for 2 h at pH 9.	22.4	N/A	522



Dye (Charge)	Calixarene	Substrate	Extraction Conditions	Adsorption Capacity / $\text{mg g}^{-1}$	Additional Information	Ref
MB (Cationic)	Thiacalix[4]arene derivative containing multiple aromatic groups	None	Batch adsorption of 10 mL of $2 \times 10^{-5}$ M dye, vigorously agitated for 2 min with 10 mL $1 \times 10^{-3}$ M calixarene in DCM, then magnetically stirred for 1 h at rtp at pH 7.	9.06 (95 % extraction)	N/A	523
MB (Cationic)	Calix[6]arene	PbS	Batch adsorption of 10 mL MB at different concentrations by 44 mg adsorbent. Shaken at 150 rpm for 1 h at pH 6 and 31 °C.	5.495	Good reusability after 3 recycling experiments.	524
MB (Cationic)	1,2,3-triazole-modified thiacalix[4]arene polymers	Polycondensate of 1,2,3-triazole-modified thiacalix[4]arene with an amine bridge.	10 mg of polymer was added to 10 mL of a 1 mM dye solution at pH 7 and left to stir for 24 h at rtp.	0.25 (79.5 % extraction)	Recyclability of the polymer towards CR was performed, but not towards MB.	507

Appendix Table 2. Extraction conditions and adsorption capacity of systems designed to extract AB10B from solution. Where adsorption capacity is not stated within the publication, this has been calculated where possible, with presented data italicised in parentheses.

Adsorbent	Extraction Conditions	Maximum Adsorption Capacity / $\text{mg}_{\text{Dye}}\text{g}_{\text{Adsorbent}}^{-1}$	Additional Information	Ref
Lignin-based adsorbent	10 mg adsorbent added to 100 mL dye (100 ppm) then vibrated at 150 rpm for 24 h.	2647.3	N/A	525
Protonated metal-organic framework	Add 10 mg of adsorbent to 60 mL dye (500 ppm) at pH 4.	2402.82	When investigating other cationic dyes, no removal occurred. Desorption occurred by immersing in DMF for 24 h and placed in a vacuum at 180 °C for 8 h. Removal efficiency dropped from 100 % to 86.87 % after 5 cycles. Tap water and pond water was laced with AB10B, resulting in > 99 % dye extraction.	526
Cationic hydrogel	Add 6 mg hydrogel to 100 mL dye (200 ppm), and stir at 200 rpm at pH 4 for 3 h at 303 K. Continuous adsorption was performed by packing swollen adsorbent into a column and dye (100 ppm) was continuously passed through at flow rates of 4, 8, and 12 mL min <sup>-1</sup> .	1771 (static). 1161.7, 858.4 and 750.1 (dynamic, with flow rates of 4, 8, and 12 mL min <sup>-1</sup> respectively).	N/A	527

Adsorbent	Extraction Conditions	Maximum Adsorption Capacity / $\text{mg}_{\text{Dye}}\text{g}_{\text{Adsorbent}}^{-1}$	Additional Information	Ref
Cationic superadsorbent	0.1 g polymer was added to 400 mL dye (125 ppm) for 24 h.	1697	AB10B was adsorbed to a greater extent than other investigated dyes.	528
Agaraldehyde and chitosan functional beads	50 mg functional beads were added to 10 mL of 5 ppm AB10B at pH 7.4, and left for up to 1440 min.	1506	Higher concentrations of dye could not reach equilibrium until 24 h. Equilibrium was reached in 4 h for the 2 ppm solution.	529
Irradiated Porous Biomass	20 mg of adsorbent is added to 20 mL of dye (1000 ppm) and shaken for 2 h at 200 rpm.	772.4	N/A	530
Amide functionalised cellulose-based adsorbents	0.1 g swollen adsorbent added to 100 mL dye and stirred at 100 rpm for 2 h at pH 2.	751.8	Adsorption percentage increased when the adsorbent was investigated with a complex solution containing AB10B and $\text{Cu}^{2+}$ . Following 5 regeneration cycles with NaOH, the adsorption capacity decreased from 343.8 to 320.2 $\text{mg g}^{-1}$ .	531
Humin	10 mg humin added to 10 mL dye (10 ppm) at pH 5 then shaken for 15 min.	602.93 (0.979 $\text{mmol g}^{-1}$ )	N/A	532
Porous chitosan doped with graphene oxide	Add 15 mg adsorbent to 15 mL dye at pH 7.	573.47	N/A	533

Adsorbent	Extraction Conditions	Maximum Adsorption Capacity / $\text{mg}_{\text{Dye}}\text{g}_{\text{Adsorbent}}^{-1}$	Additional Information	Ref
Zr(IV) surface-immobilised cross-linked chitosan/bentonite composite	0.04 g adsorbent was added to 50 mL dye (100 ppm) and shaken at 200 rpm at pH 2.	418.4	Removal percentage was investigated when in competition with 1:1 ratio NaCl, Na <sub>2</sub> SO <sub>4</sub> , Na <sub>2</sub> CO <sub>3</sub> and Na <sub>3</sub> PO <sub>4</sub> . Extraction percentage decreased reasonably when in competition with carbonate, and substantially when in competition with phosphate.	534
Magnetic chitosan nanosheets	Add 1 mg adsorbent to 5 mL dye (40 ppm) at pH 2 and shake for 24 h.	389.97	Desorption was performed using 0.1 M NaOH. Adsorption capacity decreased from 390 to ca. 250 mg g <sup>-1</sup> after 5 cycles.	535
CMP-97-Fe	Add 10 mg CPM-97-Fe to 15 mL dye (0.022 mM) and stir at 100 rpm at 24 °C.	325	Adsorption mechanism involves ion exchange, electrostatic interactions, $\pi$ - $\pi$ stacking interactions, and pore filling.	536
Magnetically modified <i>Leptothrix</i> sp. sheets	1 mL settled magnetic <i>Leptothrix</i> suspensions (equivalent to 19 mg dried adsorbent) mixed with 10 mL dye solution (100 ppm) at pH 2 and stirred at 27 rpm for 2.5 h at rtp.	339.2	N/A	537
Cross-linked chitosan/bentonite composite	0.05 g adsorbent added to 50 mL dye and shaken at 200 rpm for 480 min at pH 2.	323.6	N/A	538

Adsorbent	Extraction Conditions	Maximum Adsorption Capacity / $\text{mg}_{\text{Dye}}\text{g}_{\text{Adsorbent}}^{-1}$	Additional Information	Ref
Melamine-based covalent organic framework	0.025 g magnetic adsorbent injected into 50 mL dye at pH 4, ultrasonicated for 2 min, then magnetically separated.	228.07	Uptake rate of $920.20 \text{ mg g}^{-1} \text{ s}^{-1}$ . Mechanism involves electrostatic attraction of positively charged amine groups with sulfonic groups on the dye. Also, hydrogen bonding with azo and hydroxyl groups of dye, as well as $\pi$ - $\pi$ stacking interactions occurs. AB10B is desorbed in basic medium, and good extraction is observed following 6 cycles.	539
Polyaniline/SiO <sub>2</sub> composite	Add 10 mg adsorbent to 50 mL dye (30 ppm) and leave for 60 min at pH 6.	149.9 (99.93 % adsorption)	Adsorption efficiency dropped from 99 % to 84.5 % after 4 regeneration cycles using NaOH.	540
Allylamine polymer modified bentonite.	Add 30 mg to 30 mL of dye (200 ppm) and leave to spin for 480 min at 200 rpm.	144.08	Adsorption remained at 95 % following regeneration with dilute NaOH.	541
Polyaniline/Iron Oxide composite	Add 0.015 g adsorbent to 20 mL dye (50 ppm) and shake at 80 rpm for 180 min at pH 2.	135	Also investigated cationic dyes, such as MB, which could not be adsorbed. 94 % desorption occurred when using NaOH. The adsorption capacity decreased from $135 \text{ mg g}^{-1}$ to $110 \text{ mg g}^{-1}$ following 5 cycles.	542

Adsorbent	Extraction Conditions	Maximum Adsorption Capacity / $\text{mg}_{\text{Dye}}\text{g}_{\text{Adsorbent}}^{-1}$	Additional Information	Ref
Composite Chitosan/diatomaceous earth biosorbent	Simultaneous adsorption of $\text{Cu}^{2+}$ , $\text{Cd}^{2+}$ and AB10B. 0.5 g of adsorbent added to 50 mL contaminated solution (50 to 500 ppm).	132.8 (pH 2), 108 (pH 7)	$\text{SO}_4^{2-}$ , $\text{NO}_3^-$ and $\text{PO}_4^{3-}$ all inhibited AB10B extraction (sulphate was the least inhibiting). 0.5 M NaOH was used as a desorption agent. After 10 cycles, adsorption capacity had decreased from 109 $\text{mg g}^{-1}$ to 93 $\text{mg g}^{-1}$ .	543
Magnetic $\text{SiO}_2@\text{CoFe}_2\text{O}_4$ nanoparticles on graphene oxide	Add 0.5 $\text{g L}^{-1}$ adsorbent to a 10 ppm dye solution, and leave for 140 min at pH 2.	130.74	Removed both Cr(VI) and AB10B (separately). When in competition with NaCl, removal efficiency remained unchanged at low (0–10 ppm) NaCl concentrations but dropped slightly at 40 ppm. Following 5 cycles of regenerating with 0.1 M NaOH, the adsorption efficiency only dropped slightly (97 % to 92 %).	544
Carbonised metallised bagasse	6 mg of adsorbent added to 50 ppm dye at pH 3, sonicated for 2 min, then stirred at 250 rpm.	120	95.8 % removed within 5 min. Following 5 cycles, adsorption of AB10B decreased from ca. 98 % to ca. 80 %.	545
ZnO nanoparticles loaded on worn tire powdered activated carbon	1.5 g of adsorbent added to 100 mL solution (100 $\text{mg L}^{-1}$ ) at pH 3, and stirred at 200 rpm for 30 min.	94.36	Regenerated using 0.1 M NaOH, percentage removal dropped from 92.88 % to 66.87 % after 5 cycles. A real-world sample was obtained from Ardabil, Iran. 71.21 % dye was removed (no mention of initial dye concentration).	546

Adsorbent	Extraction Conditions	Maximum Adsorption Capacity / $\text{mg}_{\text{Dye}}\text{g}_{\text{Adsorbent}}^{-1}$	Additional Information	Ref
Smart Metallo-Hydrogels	Add 0.1 mM dye to 7 mL buffer at pH 6.5, then add 25 mg of dry metallo-hydrogel and leave for 24 h.	84	N/A	547
Pumice stone	Add ca. 0.5 g of adsorbent to 250 mL dye (160 ppm), heated at 250 °C and shake at 200 rpm until equilibrium is reached.	72.46	Regeneration studies were performed by rinsing the stone with distilled water several times and heating at 150 °C for 6 h. 99 % of AB10B was desorbed, and 83 % of AB10B was removed on the second cycle.	548
Reduced graphene oxide	Add 5 mg to 15 mL dye (200 ppm) for 12 h under constant shaking at pH 2.	60 (100 % dye extraction)	AB10B was investigated as an addition to neutral red dye, the primary focus. Adsorption capacity of primary investigated dye was < 1300 $\text{mg g}^{-1}$ , but in a mixture of other dyes, total adsorption capacity was > 3500 $\text{mg g}^{-1}$ .	549
Hen feather	Batch adsorption of 25 mL dye with 0.1 g adsorbent at pH 2, shaken for 2.5 h at 303 K.	49.78	N/A	550
Grain Stillage	Add 50 mg modified grains to 20 mL dye (100 ppm) and stir at 120 rpm at 303 K.	> 35.2 (88 % dye extraction)	N/A	551
Polymer/clay nanocomposites	Not provided	28.8	Maximum adsorption (62.74 %) at pH 2.	552

Adsorbent	Extraction Conditions	Maximum Adsorption Capacity / $\text{mg}_{\text{Dye}}\text{g}_{\text{Adsorbent}}^{-1}$	Additional Information	Ref
Vilayti Tulsi plant	Add 100 mg adsorbent to 50 mL dye and stir for 30 min at pH 2, before removal via centrifugation.	Ca. 20	N/A	553
Large adsorbent constituting PVA and glutaric dialdehyde as matrix and activated carbon or crosslinked PAA as adsorptive constituent.	Add 0.2 g adsorbent to 40 mL dye solution (900 ppm) and shake at 200 rpm at pH 6.8.	18	Dyes were dissolved in 6 % v/v methanol in water.	554
ZrO <sub>2</sub> /Pb modified multi-walled carbon nanotube	Stir 0.05 g adsorbent with dye (15 ppm) for 15 min at pH 6.	15.46	Adsorption capacity towards Eosin B was 16.92 $\text{mg g}^{-1}$ . Adsorption isotherm was pseudo-first order.	555
Crosslinked chitosan	Add 0.21 g adsorbent to 50 mL dye (20 ppm) and stir at 200 rpm for 1 h at natural pH.	9.43	90.3 % desorption efficiency occurred with 0.1 M NaOH.	556
Activated carbon from <i>Ricinus Communis</i>	Add 2 g adsorbent to 100 mL dye (100 ppm) and stir at 250 rpm for 80 min.	7.12	Maximum adsorption (95 %) at pH 1. Dropped to 91 % at pH 7.	557
<i>Calotropis procera</i> Weed waste	Add 0.5 g adsorbent to 100 mL dye (30 ppm) and shake at 120 rpm for 60 min at 308.15 K at pH 2.	5.0	With increased ionic strength, the removal percentage increases. Acetic acid is used to regenerate the adsorbent and can be used 5 times. However, the desorption takes 2 h.	558



Adsorbent	Extraction Conditions	Maximum Adsorption Capacity / $\text{mg}_{\text{Dye}}\text{g}_{\text{Adsorbent}}^{-1}$	Additional Information	Ref
Zeolite, synthesised from Fly Ash	Stir the zeolite adsorbent ( $10 \text{ g L}^{-1}$ ) with dye (10 ppm) for 6 h at 300 rpm at pH 4.	0.93 (92.8 % extraction) for 10 ppm 2.43 (48.6 % extraction) for 50 ppm	Following 5 cycles, removal efficiency dropped from 75 % to 60 %, and then to 50 % after 6 cycles.	559
Calixarene nanosponge	Shaking 2 mL of 50 $\mu\text{M}$ AB10B with 4 mg adsorbent for 90 min at rtp.	1.49 (> 97 % extraction)	N/A	560
Calixarene nanosponge	Shaking 2 mL of 50 $\mu\text{M}$ AB10B with 4 mg adsorbent for 90 min at rtp.	0.79 (51 % extraction) at pH 4.4 0.64 (41.5 % extraction) at pH 6.7	N/A	561
Kaolin	Add 0.75 g Kaolin to 20 mL dye (40 ppm) and stir at 200 rpm for 10 min at pH 11.	0.61	N/A	562
Multi Walled Carbon Nanotubes	0.01 g nanotubes were added to 10 mL dye (0.01 mM) and stirred at pH 7.	0.393	N/A	563
Lignocellulosic waste biomass	Batch adsorption of 10 mL dye (unknown concentration) using 100 mg adsorbent at pH 2.3, shaking at 100 rpm at 300 K for 24 h.	95 % dye extraction (unknown adsorption capacity due to unknown concentration).	N/A	564

Adsorbent	Extraction Conditions	Maximum Adsorption Capacity / $\text{mg}_{\text{Dye}}\text{g}_{\text{Adsorbent}}^{-1}$	Additional Information	Ref
<i>L</i> -cysteine-reduced graphene oxide/PVA aerogel	Add 5 mg aerogel to 15 mL dye (20 mL for dye mixture of unknown concentration), then shaken at 303 K.	> 90 % dye extraction (unknown adsorption capacity due to unknown concentration).	N/A	565
Cellulose-based carbon aerogel	Immerse the aerogel in dye solution and stir at rtp.	N/D	Investigated a range of dyes and heavy metal ions. Greatest adsorption capacity was for malachite green ( $1947 \text{ mg g}^{-1}$ ) and $\text{Cu}^{2+}$ ( $801 \text{ mg g}^{-1}$ ).	566

Appendix Table 3. Calixarenes used for the extraction of Cr(VI) from solution, and adsorption capacity towards Cr(VI). Where adsorption capacity is not stated within the publication, this has been calculated where possible, with presented data italicised in parentheses.

Calixarene	Substrate	Extraction Conditions	Adsorption Capacity / $\text{mg g}^{-1}$	Additional Information	Ref
5,11,17,23,29,35,41,47-octa-tert-butyl-49,50,51,52,53,54,55,56-octa-(2-piprazinoethylamino)-carbonylmethoxycalix[8]arene	XAD-4 resin	Add 1 g impregnated resin to a column, and pass through 10 mL Cr (VI) solution at pH 3 ( $1 \times 10^{-4} \text{ M}$ ) at a flow rate of $2 \text{ mL min}^{-1}$ .	87.7	Resin was regenerated by passing through 4 M HCl solution, followed by distilled water. Extraction percentage decreases with pH and flow rate.	567

Calixarene	Substrate	Extraction Conditions	Adsorption Capacity / $\text{mg g}^{-1}$	Additional Information	Ref
25,26,27,28-tetrakis(2-ethoxy-ethoxy)calix[4]arene	XAD-4 Resin	Static: Add 10 mg resin to 25 mL Cr(VI) solution ( $1 \times 10^{-5}$ M) at pH 4 and stir for 1 h. Dynamic: Pack the resin into a column and pass through Cr(VI) solution at various flow rates and concentrations.	85	Column is regenerated via elution with $\text{HNO}_3$ .	568
DMAM-calixarene	PGMA modified cotton	Pass 5 mL Cr(VI) through 1 cm x 1 cm piece of cloth at pH 2.	26.38. Under dynamic filtration at pH 7, an adsorption capacity of ca. $1 \text{ mg g}^{-1}$ was observed.	Cloth was regenerated by passing through 5 mL of 0.1 M NaOH. Adsorption percentage decreased with pH. Extraction was selective in the presence of chloride, nitrate, phosphate and sulfate.	569
DMAM-calixarene	Merrifield Resin	Static: Shake 25 mg adsorbent with 10 mL Cr(VI) ( $1 \times 10^{-4}$ M) at pH 1.5 and stir for 1 h. Dynamic: Pack column with 0.5 g resin, and pass through 50 mL ( $1 \times 10^{-4}$ M) at pH 1.5 at a flow rate of $0.5 \text{ mL min}^{-1}$ .	7.8 (94.5 % extraction)	Adsorption percentage decreased with pH. Liquid-liquid extraction yielded a greater extraction than solid-liquid extraction.	570

Calixarene	Substrate	Extraction Conditions	Adsorption Capacity / $\text{mg g}^{-1}$	Additional Information	Ref
C[4]P-1 and C[4]P-2	Cellulose	Add 25 mg adsorbent to 10 mL Cr(VI) solution ( $1 \times 10^{-4}$ M) and stir at 175 rpm for 1 h at pH 1.5.	2.67 for C[4]P-1 (32.3 % extraction) and 7.52 for C[4]P-2 (91.1 % extraction)	Adsorption percentage decreased with pH.	571
5,17-bis-[(4-benzylpiperidine)-methyl]-calix[4]arene	Electrospun nanofibrous polyacrylonitrile/calixarene mats	Add 25 mg adsorbent to 10 mL Cr(VI) solution ( $1 \times 10^{-4}$ M) and stir at 175 rpm for 1 h at pH 1.5.	7.43 (90 % extraction)	Extraction percentage decreases with pH.	572
5,17-bis[(N-methylglucamine)-methyl]-25,26,27,28-tetrahydrocalix[4]arene	Electrospun calixarene/PAN nanofibres	Add 25 mg adsorbent to 10 mL Cr(VI) solution ( $1 \times 10^{-4}$ M) and stir at 175 rpm for 1 h at pH 1.5.	7.18 (87 % extraction)	Extraction percentage decreases with pH.	573
1,3-distal diphenyl(4-piperidin)methanol-substituted calix[4]arene derivative	$\text{Fe}_3\text{O}_4$ nanoparticles	Add 25 mg adsorbent to 10 mL Cr(VI) solution ( $1 \times 10^{-4}$ M) and stir at 175 rpm for 1 h at pH 2.5.	6.61 (80 % extraction)	Extraction percentage remained similar when in the presence of $\text{SO}_4^{2-}$ , $\text{NO}_3^-$ , and $\text{Cl}^-$ . Extraction percentage decreased with pH.	574

Calixarene	Substrate	Extraction Conditions	Adsorption Capacity / $\text{mg g}^{-1}$	Additional Information	Ref
DMAM-calixarene (Previous work by the Badyal group)	Polypropylene cloth	Static: Spin 16 mL of Cr(VI) ( $20 \text{ mg L}^{-1}$ ) at 40 rpm with 6 cm x 7 cm piece of cloth for 4 h. Dynamic: Pass 10 mL Cr(VI) through a 3 cm x 3.5 cm piece of cloth packed into a pipette.	6.6	Chromium could be removed when in competition with $\text{Cl}^-$ , $\text{NO}_3^-$ , $\text{H}_2\text{PO}_4^{3-}$ , $\text{SO}_4^{2-}$ . Cloth could be recycled by passing through NaCl/NaOH. Successful extraction of real-world chromium was demonstrated.	575
M-DADBP-Calix and M-DABP-Calix	Magnetite nanoparticles	Add 25 mg adsorbent to 10 mL Cr(VI) solution ( $1 \times 10^{-4} \text{ M}$ ) and stir at 175 rpm for 1 h at pH 2.5.	5.37 (65 % extraction) for M-DADBP-Calix; 5.78 (70 % extraction) for M-DABP	Extraction percentage decreases with pH.	576
5,17,di-tert-butyl-11,23-bis[(1,4-dioxa-8-azaspiro[4,5]decanyl)methyl]-25,26,27,28-tetrahydroxy calix[4]arene.	Polymer inclusion membrane	6 h transport of 0.2 mM Cr(VI) (unknown volume) study across the membrane under acidic conditions.	N/D (97.69 % extraction)	N/A	577
25,27-bis[2-N-(4-amiobenzyl)amino-propoxy]-26,28-dihydroxycalix[4]arene	Graphene Quantum Dots	Add $15.6 \text{ mg L}^{-1}$ Cr(VI) (unknown concentration) to adsorbent in a permeation cell for 8 h at pH 5.	N/D (97.23 % extraction)	Extraction was selective in the presence of Fe(III), Ni(II) and Pb(II). Amine groups on calixarene rim were responsible for Cr(VI) removal.	578

Calixarene	Substrate	Extraction Conditions	Adsorption Capacity / $\text{mg g}^{-1}$	Additional Information	Ref
Various calix[4]arene Schiff bases	N/A	Add 10 mL $1 \times 10^{-3}$ M calixarene in DCM to 10 mL $1 \times 10^{-4}$ M Cr(VI) solution at pH 1.5, stirred for 1 h, then left to stand for 30 min.	N/D ( <i>greatest extraction percentage was 91.5 %</i> ).	Cr(VI) removal was selective in the presence of $\text{F}^-$ , $\text{Cl}^-$ , $\text{Br}^-$ , $\text{NO}_3^-$ , $\text{PO}_4^{3-}$ , $\text{SO}_4^{2-}$ .	579
p-sulfonated calix[n]arenes ( $n = 4, 6, 8$ )	Calixarene-composited membrane	Nanofiltration – pumping Cr(VI) ( $1 \times 10^{-4}$ M) contaminated feed through a membrane at pH 9.4.	N/D (77.6 %)	Adsorption percentage increased with pH.	580

Appendix Table 4. Calixarenes used for the extraction of U(VI) from solution, and adsorption capacity towards U(VI). Where adsorption capacity is not stated within the publication, this has been calculated where possible, with presented data italicised in parentheses.

Calixarene	Substrate	Extraction Conditions	Adsorption Capacity / $\text{mg g}^{-1}$	Additional Information	Ref
Calix[4]arene	Phosphoric acid adorned hypercrosslinked calix[4]arene high-efficiency uranium adsorption material	Add 5 mg adsorbent to 50 mL uranyl nitrate ( $60 \text{ mg L}^{-1}$ ) and agitate at 140 rpm for 6 h at pH 6.	505.68	N/A	581

Calixarene	Substrate	Extraction Conditions	Adsorption Capacity / $\text{mg g}^{-1}$	Additional Information	Ref
37,38,39,40,41,42, hydroxy 1,8,13,19,25,31-hexacarboxy calix[6]arene	Resin of calixarene reacted with poly(styrene $\beta$ -hydroxylamine) hexahydroxylamine	Pack a column with 1 g of resin and pass through 25 mL solutions at pH 6 of U(VI) (unknown concentration) at $0.5 \text{ mL min}^{-1}$ .	97.8 (0.411 mmol $\text{g}^{-1}$ )	After passing through 2 M HCl, 99.3 % of extracted uranium was recovered.	582
<i>p</i> -tert-butyl calix[4]arene, modified with <i>m</i> -aminobenzoic acid on the upper rim, and 1,2-dibromoethane, 3,3'-iminodipropio-nitrile and $\text{NH}_2\text{OH}\cdot\text{HCl}$ on the lower rim	$\text{Fe}_3\text{O}_4$ nanoparticles	Mix 8 mg adsorbent with 40 mL U(VI) at 250 rpm for 4 h at pH 5.	88.6	Adsorption followed the pseudo-second order and Freundlich model. Can be recycled through $\text{HNO}_3$ elution, but efficiency decreases with each cycle, dropping to 65 % after the 6th recycle.	583
Calixarene phosphonate derivative	$\text{Fe}_3\text{O}_4$ nanoparticles	Shake adsorbent with 20 mL U(VI) solution at 250 rpm at pH 4.5.	74.11	Equilibrium was reached in 3.5 h. Nitric acid was used as a recycling solution, with adsorption efficiency slightly decreasing each time, but was still greater than 70 % after 5 cycles.	584

Calixarene	Substrate	Extraction Conditions	Adsorption Capacity / $\text{mg g}^{-1}$	Additional Information	Ref
Calix[4]arene-o-vanillinsemi-carbazone	Merrifield chloromethylated resin	Mix 1 g of resin with 500 mL U(VI) solution (100 ppm) at pH 2 at 30 °C.	48.74	Equilibrium was reached after ca. 110 min. Following 20 repeat filtration cycles, following elution with concentrated acid, a 2–3 % decrease in efficiency was observed. After addition of ca. 8 $\text{mg L}^{-1}$ competing cations (compared to 100 $\text{mg L}^{-1}$ U(VI)), reduction in extraction percentage was observed.	585
4-Sulfonylcalix[6]arene	$\text{Fe}_3\text{O}_4@$ Aspergillus Niger	Add 10 mg adsorbent to 100 mL U(VI) solution (5 $\text{mg L}^{-1}$ ) at pH 6 at 30 °C for 8 h.	47.87	Filtration efficiency was unaffected by the presence of $\text{K}^+$ , $\text{Na}^+$ , and $\text{Cu}^{2+}$ . The data was fit towards a pseudo-second order kinetic model and a Langmuir isotherm.	586
<i>p</i> -tert-butylcalix[8]-arene	Silica gel	Pass 50 mL 1 $\text{mg L}^{-1}$ U(VI) solution through the calixarene modified silica gel at pH 6 at 1.5 $\text{mL min}^{-1}$ . Maximum capacity was determined by stirring 25 mL of a 100 $\text{mg L}^{-1}$ U(VI) solution with 100 mg adsorbent for 2 h.	17.14 (0.072 $\text{mmol g}^{-1}$ )	The adsorbent could be regenerated with HCl and used for 15 cycles with no loss in extraction percentage. Ca. 95 % U(VI) removal was determined following extraction from spiked ground water samples.	587



Calixarene	Substrate	Extraction Conditions	Adsorption Capacity / $\text{mg g}^{-1}$	Additional Information	Ref
Para-tert-butyl 1,3-acid-diethyl amide calix[4]arene	Incorporate calixarene into PVC based membrane containing calixarene, plasticiser, and anion excluder. Membranes contained either 0, 1, 2, 4, or 8 wt% calixarene.	Immerse membrane into 10 mL $\text{UO}_2^{2+}$ solutions ( $27.5 \text{ mg L}^{-1}$ ) for 65 h at pH 7. Greatest extractions were observed for membranes containing 8 wt% calixarene.	12.05 (52 % removal)	Extraction percentage decreased as pH divulged from 7. Following elution with 6.5 mL $\text{HNO}_3$ (1 M) for 23 h, 74 % of the adsorbed uranium could be removed. Uranium could not be detected (hence removed) by the fabricated sensor in a simulated wastewater matrix.	588
5,11,17,23-Tetra-tert-butyl-25,27-bis(methoxycarbonylmethoxy)-26,28-dihydroxycalix[4]arene	Grafted onto $\text{Fe}_3\text{O}_4$ nanoparticles	Mix 10 mL $\text{UO}_2^{2+}$ ( $1.15 \times 10^{-5} \text{ M}$ ) with 25 mg sorbent at 180 rpm at pH 5.5.	1.08 (94.2 % removal)	Extraction percentage was not affected by the presence of $\text{Fe}^{3+}$ , $\text{Ca}^{2+}$ , nor $\text{K}^+$ .	589

Calixarene	Substrate	Extraction Conditions	Adsorption Capacity / $\text{mg g}^{-1}$	Additional Information	Ref
Non-tBu[6]CH <sub>2</sub> COOH	PET fabric	Shake 0.5 g textile with 20 mL U(VI) ( $1 \times 10^{-6}$ M) for 6 h at rtp at pH 6.	0.18 ( $7.6 \times 10^{-7}$ mol $\text{g}^{-1}$ )	Equilibrium was obtained after ca. 150 min. Following elution with 0.01 M HCl (and subsequently 0.1 M HCl), ca. 95 % of adsorbed uranium was removed. Following attempted extraction of uranium from three batches of mine water, extraction percentage was unchanged in all bar one experiment.	590
37,38,39,40,41,42-Hexakis(O-carboxymethyl)-p-t-butylcalix[6]-arene	Liquid-liquid extraction	Mix 2.10 mM calixarene with 0.037 M UO <sub>2</sub> <sup>2+</sup> at pH 8 for 15 h at 30 °C.	N/D (100 % removal)	The calixarene was also employed in a membrane which was capable of removing the uranium at 40 °C (but not colder temperatures) and could then release the uranyl ion at lower pH.	591
37,38,39,40,42-Hexakis(O-carboxymethyl)-p-hexylcalix[6]-arene	Liquid-liquid extraction	Mix 2.10 mM calixarene with 0.037 M UO <sub>2</sub> <sup>2+</sup> at pH 8 for 15 h at 30 °C.	N/D (100 % removal)	N/A	591

Calixarene	Substrate	Extraction Conditions	Adsorption Capacity / $\text{mg g}^{-1}$	Additional Information	Ref
37,38,39,40,41,42-Hexakis(N-hydroxycarbamoylmet hoxy)-p-tert-butylcalix[6]-arene	Liquid-liquid extraction	Mix 0.534 mM calixarene in 25 mL chloroform with an aqueous solution containing $\text{UO}_2^{2+}$ (unknown concentration) for 12 h at pH 7 at 30 °C.	N/D (100 % removal)	Extraction percentage towards uranium remained outstanding in a 1:1000 mole ratio of U:Mg <sup>2+</sup> , a 1:1 mole ratio of U:Fe <sup>3+</sup> and 1:10 mole ratios of U:Ni/Zn <sup>2+</sup> . However, extraction percentage dropped to 66 % in a 1:10 mole ratio of U:Fe <sup>3+</sup> . Extraction percentage decreased at pH values below 6.	592
1,3,5-OMe-2,4,6-OCH <sub>2</sub> CONHOH-p-tert-butylcalix[6]-arene	Liquid-liquid extraction	Mix $4.2 \times 10^{-9}$ M $\text{UO}_2^{2+}$ in aqueous buffer with 1 mM calixarene in 1-heptanol over 3 h at 295 K followed by 10 min centrifugation at pH 6.	N/D (100 % removal)	Extraction percentage decreased below pH 6. Ca. 88 % removed U(VI) could be stripped following addition of 0.1 M $\text{HNO}_3$ .	593
Calix[4]resorcinarene-hydroxamic acid	Liquid-liquid extraction	Mix 0.105 mM U(VI) (unknown volume) with 0.105 mM calixarene in 3 mL ethyl acetate for 14 min at pH 8.	N/D (100 % removal)	Extraction in a range of competing cations was investigated, with minimal effect on extraction percentage.	594

Calixarene	Substrate	Extraction Conditions	Adsorption Capacity / $\text{mg g}^{-1}$	Additional Information	Ref
1,3,5-OCH <sub>3</sub> -2,4,6-OCH <sub>2</sub> COOH-p-tertbutyl-calix[6]arene	Nanoemulsion formed by mixing together Myrtraceae plant extract, monostearic acid glycerol ester, paraffin, sorbitol, hydroxyphenyl ester bacteriostatic agent, N,N,N-trimethyl-1-hexadecyl ammonium iodide and calixarene.	First place a full-sized piece of pig skin in a diffusion cell. The skin was kept at 38 °C inside a buffer solution, spiked with 600 $\mu\text{L}$ of a 10 $\text{mg L}^{-1}$ uranyl nitrate solution. 600 $\mu\text{L}$ of the calixarene nanoemulsion treatment was then immediately added, and the diffusion kinetics of uranium through the skin was evaluated for 24 h.	N/D (Prevents up to 95.12 % of the uranium from entering the skin)	N/A	595
5,11,17,23-Tetra-p-tert-butyl-25,27-bis[(8-hydroxy-quinoline-carbaldehyde-hydrazone-carbonyl(methoxy))-26,28-dihydroxycalix[4]arene	Liquid-liquid extraction	Mix $1 \times 10^{-5}$ M U(VI) in aqueous solution with $4 \times 10^{-5}$ M calixarene in organic solution at pH 6.	N/D (ca. 95 % extraction)	N/A	596

Calixarene	Substrate	Extraction Conditions	Adsorption Capacity / $\text{mg g}^{-1}$	Additional Information	Ref
Calix[4]arene bearing N-methyl-glucamine	Electrospinning calixarene with a PAN solution.	Mix $1.15 \times 10^{-5}$ M U(VI) (unknown volume) with 25 mg sorbent and spin at 175 rpm for 1 h at 25 °C at pH 4.5.	N/D (92 % removal)	N/A	597
25,27-dihydroxy-26,28-dimercaptoethoxy-5,11,17,23-tetra-tert-butyl calix[4]arene	Liquid-liquid extraction	Mix 10 mL U(VI) ( $2 \times 10^{-5}$ M) with 10 mL calixarene solution (unknown concentration) at pH 4.5.	N/D (ca. 80 % extraction)	Equilibrium reached in 2 h, and extraction can be modelled as quasi secondary. Extraction percentage reduces with temperature. Extraction decreased in the presence of competing cations, particularly $\text{Ca}^{2+}$ and $\text{Na}^{+}$ .	598
Octaphosphinoylated para-tert-butylcalix[8]-arene	Liquid-liquid extraction	Mix 0.107 mM U(VI) in nitric acid with calixarene (varying concentrations, unknown volume).	N/D (Could remove 0.291 M uranyl ions from 0.299 M starting solution)	The stoichiometry of adsorption ( $\text{UO}_2$ :Calixarene) was determined to be 2:1.	599

Appendix Table 5. Adsorption capacity of catechol-based adsorbents towards uranium. Where adsorption capacity is not stated within the publication, this has been calculated where possible, with presented data italicised in parentheses.

Catechol Species	Substrate	Extraction Conditions	Adsorption Capacity / mg g <sup>-1</sup>	Additional Information	Ref
Salicylaldoxime/PDA	GO	5 mg adsorbent is added to 500 mL uranium solution and shaken at 300 rpm at rtp at pH 5 for 400 min.	1049 (675 for RGO-PDA).	Data is best fit by a Langmuir isotherm. Excellent extraction of uranium from simulated seawater was observed. The adsorbent was regenerated by using 1 M Na <sub>2</sub> CO <sub>3</sub> and 0.1 M H <sub>2</sub> O <sub>2</sub> . 97 % desorption after 30 min was observed, but no repeat cycles were performed.	600

Catechol Species	Substrate	Extraction Conditions	Adsorption Capacity / mg g <sup>-1</sup>	Additional Information	Ref
PDA	Activated Carbon/Ag nanoparticles	10 mg adsorbent was added to 20 mL U(VI) solution and shaken at 180 rpm at pH 8.	657.89. 427.7 µg g <sup>-1</sup> were recovered from a simulated seawater sample.	Data was best described by Langmuir and pseudo-second order models. Mechanistic investigation showed that the catechol units of PDA, metal oxygen and MAC carboxylic acid groups all combined in the removal of uranium, while indole units of PDA may participate in the complexation. Following 5 regeneration cycles using 0.1 M HCl, adsorption decreased from ca. 200 mg g <sup>-1</sup> to 151 mg g <sup>-1</sup> . MACS@PDA-Ag showed excellent selectivity towards uranium when in competition with a range of competing cations, except for V and Pb.	601

Catechol Species	Substrate	Extraction Conditions	Adsorption Capacity / mg g <sup>-1</sup>	Additional Information	Ref
Polyamidoxime/PDA	Graphene Oxide	5 mg adsorbent is added to 150 mL 10 mg L <sup>-1</sup> U(VI) and shaken at 200 rpm at pH 6 for 24 h.	502.5	Data is best fit by a Langmuir isotherm and a pseudo-second order kinetic model. Following regeneration with 0.1 M HCl, extraction percentage dropped from just below 100 % to ca. 90 % after 5 cycles. Adsorption of uranium mine wastewater was performed (pH = 5.87), and an extraction percentage of ca. 95 % was observed, yielding a uranium concentration below the WHO recommended level.	602
Polydopamine (PDA)	N/A	10 mL U(VI) solution was added to 20 mg adsorbent at pH 6.5 for 200 h.	480	N/A	603
PDA	Graphene oxide/chitosan aerogel	Adsorbent was added to a U(VI) solution to yield a 0.3 g L <sup>-1</sup> solution and stirred for 24 h at 120 rpm at pH 7.	Ca. 160 experimentally. Maximum adsorption of 415.9 according to Langmuir.	Aerogel was recycled by immersing in 0.5 M HNO <sub>3</sub> for 120 min at 120 rpm, before rinsing with deionised water. Extraction percentage was almost unchanged following 6 cycles. The adsorption follows a Langmuir isotherm and pseudo-second order kinetics.	604



Catechol Species	Substrate	Extraction Conditions	Adsorption Capacity / mg g <sup>-1</sup>	Additional Information	Ref
PDA	Wastepaper derived carbon.	Add WPC@PDA (unknown quantity) to 50 mg L <sup>-1</sup> U(VI) at pH 6 for 100 min.	384.6. > 85 % adsorption in simulated seawater, even at 1 µg L <sup>-1</sup> concentration.	Data is best fit by a Langmuir isotherm and a pseudo-second order kinetic model. Adsorbent was regenerated with 0.1 M HNO <sub>3</sub> , and desorption efficiency is almost unchanged following 5 cycles. Excellent selectivity compared to a range of metal ions was demonstrated.	605
PDA	Mesoporous silica	Mix together solutions of U(VI) (60 mg L <sup>-1</sup> ), NaNO <sub>3</sub> (1 M) and adsorbent (1 g L <sup>-1</sup> ) at pH 5.5.	332.3	Data is best fit by a Langmuir isotherm and a pseudo-second order kinetic model. 0.01 M HNO <sub>3</sub> was used to regenerate the adsorbent, and adsorption capacity decreases each cycle.	606

Catechol Species	Substrate	Extraction Conditions	Adsorption Capacity / mg g <sup>-1</sup>	Additional Information	Ref
PDA	Graphene oxide	0.01 g adsorbent was added into 20 mL U(VI) solution.	314	<p>The kinetics best follow a pseudo-second order model.</p> <p>The GO-PDA system was further functionalised with polyethylene imine (PEI), and the GO-PDA-PEI system gave rise to an adsorption capacity of 530.6 mg g<sup>-1</sup>. Elution efficiency decreased slightly following 5 regeneration cycles using 0.8 M NaCl. GO-PDA-PEI showed excellent selectivity towards U(VI), except for when in the presence of Pb. &gt; 90 % adsorption from simulated seawater over a range of uranium concentrations was observed.</p>	607

Catechol Species	Substrate	Extraction Conditions	Adsorption Capacity / mg g <sup>-1</sup>	Additional Information	Ref
Crosslinked bayberry tannin	N/A	Add 10 mg adsorbent to 25 mL U(VI) solution (300 mg L <sup>-1</sup> ) at pH 4.5 and stir for 10 min.	307.3	Competitive sorption capacity was performed with a range of metal ions. Uranium was removed to a significantly greater degree than all other ions, 4 times greater than Gd, the next most effectively removed ion.  The phenolic hydroxyl groups were stated to be the primary force of attraction in the removal of uranium.	608
PDA	<i>A.niger</i> mycelium	40 mg adsorbent was added to U(VI) solution and stirred at 150 rpm at pH 5 at 303.15 K.	257.7	Data is best fit by a Langmuir isotherm and a pseudo-second order kinetic model. The adsorbent was regenerated by immersing in a solution containing 0.05 M HCl and 0.05 M NaOH for 2 h. Several ions significantly reduced the adsorption percentage towards U(VI). The uranium percentage removal decreased from 87.41 % in deionised water to 75.21 % in tap water to 61.71 % in lake water.	609

Catechol Species	Substrate	Extraction Conditions	Adsorption Capacity / mg g <sup>-1</sup>	Additional Information	Ref
PDA	SBA-15	Add the adsorbent (0.2 g L <sup>-1</sup> ) to 50 mL uranium solution (30 mg L <sup>-1</sup> ) and stir at 200 rpm at rtp at pH 6.	196	Data best fits a Langmuir model. Adding Na <sup>+</sup> or K <sup>+</sup> resulted in a slight decrease in adsorption capacity.	610
PDA	Attapulgate/chitosan aerogel	0.02 g adsorbent is added to 50 mL 50 mg L <sup>-1</sup> U(VI) and shaken for 24 h at 120 rpm at pH 5 and 25 °C.	175.1	Data is best fit by a Langmuir isotherm and a pseudo-second order kinetic model. Adsorbent was regenerated by washing with distilled water and then shaking for 120 min in 0.5 M HNO <sub>3</sub> .	611
PDA	Halloysite nanotubes	Add a 0.5 g L <sup>-1</sup> nanotube to 50 mL 20 mg L <sup>-1</sup> U(VI) solution and leave to spin for 8 h at pH 6.	72.51	Data is best fit by a Freundlich isotherm and a pseudo-second order kinetic model. Adsorbent was regenerated with 0.1 M Na <sub>2</sub> CO <sub>3</sub> , and adsorption percentage dropped from 93.11 % to 76.67 % after 5 cycles.	612

Catechol Species	Substrate	Extraction Conditions	Adsorption Capacity / mg g <sup>-1</sup>	Additional Information	Ref
PDA	OMC/GFC/Fe <sub>3</sub> O <sub>4</sub> nanoparticles	Add nanoparticles to a solution containing 100 mg L <sup>-1</sup> U(VI) at pH 6 and mix for 200 h.	45.5	<p>Selectivity studies were performed with a range of ions commonly found in seawater. The adsorbent was selective towards uranium in all cases except zinc and molybdenum. XPS photoelectron spectroscopic analysis demonstrated that the catechol functionality was the dominant group behind uranium adsorption.</p> <p>100 % removal from un-purified seawater, and seawater laced with additional uranium up to 2000 ppb occurred for PDA modified Fe<sub>3</sub>O<sub>4</sub> and CMK-3.</p>	613

Catechol Species	Substrate	Extraction Conditions	Adsorption Capacity / mg g <sup>-1</sup>	Additional Information	Ref
Catechol, salicylic acid, and 7-dichloroquinoline-8-ol (DCQ)	Vinylated chelating ligand, VP	Add 0.02 g adsorbent to a 1 L solution containing 10 µg U for 10 min at pH 7.	Catechol-VP = ca. 19 (80 µmol g <sup>-1</sup> ) Salicylic acid = ca. 26 (110 µmol g <sup>-1</sup> ) DCQ = ca. 31 (130 µmol g <sup>-1</sup> )	Decent selectivity compared to Th(IV) and Fe(III) were observed, and excellent selectivity was observed over a range of other metals in the +2 oxidation state. The system was used to determine uranium concentration found in Arabian seawater. DCQ-VP could remove 83 % from synthetic seawater, and 99 % from Na <sub>2</sub> CO <sub>3</sub> , whereas SA-VP could only remove 25 % from the solutions. > 99 % removal from Arabian seawater was observed.	614
Catechol	Aminopropyl silica gel	0.2 g CASG was packed into a column, and a solution containing 2–100 µg U(VI) was diluted 100-fold, adjusted to pH 5, and passed through the column at a rate of 2 mL min <sup>-1</sup> (dynamic). 0.2 g CASG was mixed with U(VI) (2–100 µg, 10–1000 mL) at pH 5 for 10 min (static).	15.94 (static)	Metal ions were eluted with 10 mL of 1 M HCl, which enabled extraction to be performed 25 times with only a 2 % loss in adsorption capacity. (Unclear whether static or dynamic).	615

Catechol Species	Substrate	Extraction Conditions	Adsorption Capacity / mg g <sup>-1</sup>	Additional Information	Ref
Persimmon Tannin	Glutaraldehyde	Suspend 2 mg adsorbent in 100 mL U(VI) solution (10 mg L <sup>-1</sup> ) for 1 h at 30 °C at pH 5.	7.2	Of the tannins, this exhibits the highest adsorption capacity. Several other tannins have also been investigated but have not been included. Selectivity was performed by comparing uranium adsorption in competition with Mn, Co, Ni, Cu, Zn and Cd. Uranium was selectively removed, with Cu offering the strongest competition.	616
<i>Myrica rubra</i>	Collagen fibres	0.5 g adsorbent, sealed in filter cloth was suspended in 100 mL U(VI) solution (0.5–2.5 mM) at pH 5 and stirred for 24 h.	1.2	The tannin is weakly bound to the collagen, and so in solution, the tannin is released.	617
Pine bark (and pine bark modified by conversion to amidoxime).	N/A	100 mg adsorbent is added to 50 mL uranium solution (10 mM) at pH 6 and shaken at 350 rpm for 50 h at 298 K.	0.36 (and 1.05)	A greater adsorption capacity towards Cu <sup>2+</sup> and Hg <sup>2+</sup> were observed.	618

Catechol Species	Substrate	Extraction Conditions	Adsorption Capacity / mg g <sup>-1</sup>	Additional Information	Ref
Catechol, iminodiacetic acid, imidodimethylphosphonic acid, phenylarsonic acid or serine	Chitosan	Add 80 mL of 2 M nitric acid to the wet resin (mass not stated) and stir for 6 h. Then filter and pack the wet resin into a polypropylene mini column. 10 mL uranium solution is then passed through the column at a flow rate of 1 mL min <sup>-1</sup> .	N/D (100 % adsorption at pH > 4 for catechol-type 1 resin. 100 % adsorption at pH > 3 for catechol-type 2 resin IDP-type resin gave 100 % adsorption at all pH levels.)	10 mL of 1 M nitric acid is used to elute the uranium from the resin.	619



Catechol Species	Substrate	Extraction Conditions	Adsorption Capacity / mg g <sup>-1</sup>	Additional Information	Ref
Various polyhydroxybenzenes: phenol, catechol, resorcinol, hydroquinone, pyrogallol, hydroxyhydroquinone, phloroglucinol, protocatechualdehyde and gallic aldehyde	4-Aminopolystyrene	12 mg of adsorbent in 100 mL seawater, containing 10 mg L <sup>-1</sup> uranium at pH 8. Mixture was stirred for 1 h at 30 °C.	N/D (All values are given as mM / mol ligand: <i>Phenol</i> = 6.0 <i>Catechol</i> = 55.4 <i>Resorcinol</i> = 9.5 <i>Hydroquinone</i> = 9.9 <i>Pyrogallol</i> = 98.6 <i>Hydroxy-hydroquinone</i> = 61.5 <i>Phloroglucinol</i> = 11.0)	Selectivity experiments were performed by stirring 20 mg adsorbent with 0.04 mM Mn <sup>2+</sup> , Co <sup>2+</sup> , Ni <sup>2+</sup> , Cu <sup>2+</sup> , Zn <sup>2+</sup> , Cd <sup>2+</sup> and UO <sub>2</sub> <sup>2+</sup> at pH 5.  Catechol adsorbed 89.7 % starting uranium, and pyrogallol adsorbed 78.7 %, however catechol also adsorbed 49.8 % starting Cu and pyrogallol adsorbed 64.6 %. Mn, Co, Ni, Zn and Cd all gave rise to < 10 % extraction.  Assumed binding mechanisms were provided. Catechol gives rise to a chelate ring, whereas pyrogallol gives rise to two chelate rings, with one molecule binding to 2 uranyl ions.	620

Catechol Species	Substrate	Extraction Conditions	Adsorption Capacity / mg g <sup>-1</sup>	Additional Information	Ref
Catechol-3,6-bis(methyleneimino-diacetic acid) (CBMIDA)	N/A	Rats were injected with depleted uranium (range of pH values) and then with CBMIDA.	N/D <i>(Measurements were performed by comparing the percentage of injected uranium that was excreted. Ca. 40 % was excreted after the first day, and ca. 50 % was excreted after the sixth day, compared to 20 % and 25 % for the sample without CBMIDA addition).</i>	N/A	621

Appendix Table 6. Adsorption capacity of resorcinol-based adsorbents towards uranium. Where adsorption capacity is not stated within the publication, this has been calculated where possible, with presented data italicised in parentheses.

Resorcinol Species	Substrate	Extraction Conditions	Adsorption Capacity / $\text{mg g}^{-1}$	Additional Information	Ref
PAR	Amberlite XAD resin	Add 0.05 g adsorbent to 50 mL 125 ppm U(VI) solution and stir at 200 rpm for 3 h at rtp and pH 4.5.	115.5	Data is best fit by a Langmuir isotherm and a pseudo-second order kinetic model. 0.1 g uranium loaded resin can be desorbed with 5 mL 0.5 M nitric acid. Tolerance ratios of at least 100 were observed for all investigated competing metal ions. Almost complete uranium adsorption occurs for 30 consecutive cycles, dropping to 95 % after the 35 <sup>th</sup> .	622
PAR and TAR	Silica fibres	Add 15 mg adsorbent to uranyl acetate in Atlantic Ocean seawater (0.2–1.0 ppm) and spin for 7 days at 30 rpm.	20	N/A	623
TAR	Amberlite XAD-16 resin	Add 1 mL U(VI) (0.5 mM) to a solution containing 50 mg of TAR-XVI in 99 mL 0.1 M acetate buffer and leave to shake for 1 day at pH 6.	0.17 ( <i>0.71 mmol g<sup>-1</sup></i> )	Complete desorption with 0.1 M HNO <sub>3</sub> was observed.	624

Resorcinol Species	Substrate	Extraction Conditions	Adsorption Capacity / $\text{mg g}^{-1}$	Additional Information	Ref
TAR	N/A	Add 200 $\mu\text{L}$ TAR (0.025 mM) to 15 mL $60 \mu\text{g L}^{-1}$ U(VI) alongside 80 $\mu\text{L}$ chloroform at pH 6.	N/D (Ca. 85 %)	In selectivity experiments, the sensor tolerated element-to-interference ratios of 1:50 for nickel, aluminium and cadmium. However, ratios were greater than 1:500 for all other investigated metals.	625

Appendix Table 7. Adsorption capacity of a selection of amidoxime-based adsorbents towards uranium.

Amidoxime	Substrate	Extraction Conditions	Adsorption Capacity / $\text{mg g}^{-1}$	Additional Information	Ref
Amidoximated PAN	Nanofibers	Mix 15 mg adsorbent with 5 mL 8 mg $\text{L}^{-1}$ U(VI) at pH 7 at rtp for 24 h.	1187.05	Uranium uptake in simulated seawater was achieved, even with the addition of competing metal ions at elevated concentrations (though a significant quantity of vanadium was also extracted). Following regeneration with a carbonate-peroxide solution, adsorption capacity decreased by ca. 5 % from the 3 <sup>rd</sup> adsorption, and each subsequent adsorption.	626
Amidoximated Hydrothermal carbon	N/A	Mix 10 mg adsorbent with 50 mL 300 mg $\text{L}^{-1}$ U(VI) at pH 4.5 for 2 h at rtp.	1021.6	N/A	627

Amidoxime	Substrate	Extraction Conditions	Adsorption Capacity / $\text{mg g}^{-1}$	Additional Information	Ref
Amidoximated PAN	FeOOH	Mix 20 mg adsorbent with 50 mL U(VI) (unknown concentration) at pH 8 for 4 h.	980.39	The adsorption process followed the pseudo-second order model and Langmuir isotherm. Following regeneration with 0.1 M HCl, the extraction percentage towards uranium dropped by only 6.91 % on the 5 <sup>th</sup> adsorption cycle. The distribution coefficient of uranium is significantly higher than a range of competing metal ions, indicating a strong selectivity towards U(VI).	628
Amidoxime functionalised diamino-maleonitrile	Graphene Oxide	Mix 10 mg adsorbent with 20 mL 500 $\text{mg L}^{-1}$ U(VI) at pH 8 for 6 h at rtp.	935	Following 5 adsorption-desorption cycles, the extraction efficiency was almost unaffected.	629

Amidoxime	Substrate	Extraction Conditions	Adsorption Capacity / $\text{mg g}^{-1}$	Additional Information	Ref
Amidoximated Hydrothermal carbon	N/A	Mix 10 mg adsorbent with 10 mL U(VI) at pH 5 for 4 h at 308.15 K.	724.6	Following regeneration with HCl, the adsorption capacity decreases slightly on each of the first five adsorption-desorption cycles. Adsorption capacity towards U(VI) was significantly greater than a range of competing metal ions. Adsorption followed pseudo-second order kinetics and extraction efficiency decreased with pH below pH 5.	630
Amidoximated mesoporous silica SBA-15	N/A	Mix adsorbent with 10 mL U(VI) at pH 6 for 3 h at rtp with a mass/volume ratio of $0.1 \text{ g L}^{-1}$ .	709	Adsorption capacity was significantly reduced with increasing and decreasing pH. Following regeneration, a slight decrease in uranium capture was observed in each of the subsequent three adsorption cycles.	631

Amidoxime	Substrate	Extraction Conditions	Adsorption Capacity / $\text{mg g}^{-1}$	Additional Information	Ref
Amino-amidoxime bifunctional poly-acrylonitrile	Dendritic fibrous nanosilica	Mix 10 mg adsorbent with 20 mL 500 $\text{mg L}^{-1}$ U(VI) at pH 8 for 12 h at rtp.	678	Following regeneration via centrifugation, the extraction efficiency dropped by 15 % following the 5 <sup>th</sup> adsorption-desorption cycle. Good selectivity in competition with a range of competing metal ions.	632

Appendix Table 8. Adsorption capacity of amidoxime-based adsorbents—synthesised using plasma-based methods—towards uranium.

System	Use of Plasma	Extraction Conditions	Adsorption Capacity / $\text{mg g}^{-1}$	Additional Info	Ref
Suspension of amidoxime/ carbon nanofiber hybrids in deionised water	$\text{N}_2$ plasma activation of the carbon nanofibers, in order to attach acrylonitrile (which is then converted to an amidoxime).	Liquid-liquid extraction: pH = 3.5, 273 K (solution); pH = 7.8, 293 K (groundwater); pH = 8.1, 293 K (seawater).	588.24 (solution), 398.41 (groundwater), 248.14 (seawater)	Adsorption was modelled by pseudo-second order kinetics and a Langmuir isotherm model. Adsorption capacity decreases at pH > 6.5.	633



System	Use of Plasma	Extraction Conditions	Adsorption Capacity / $\text{mg g}^{-1}$	Additional Info	Ref
PAO/Magnetic Graphene Oxide (mGO)	$\text{N}_2$ plasma activation of mGO, in order to attach acrylonitrile (which is then converted to an amidoxime).	Mix 5 mg PAO/mGO with 10 mL U(VI) ( $10 \text{ mg L}^{-1}$ ) for 2 days at pH 6.	435	Adsorption capacity towards uranium was significantly higher than alternative radionuclides. Adsorption was modelled by pseudo-second order kinetics and a Langmuir isotherm model.	634
$\text{PO}_4/\text{PAO}$	Reaction between PAO and $\text{H}_3\text{PO}_4$ under Ar plasma in order to obtain $\text{PO}_4/\text{PAO}$ .	Shaken for 24 h at pH 7.	161.5	Adsorbent was regenerated with $\text{Na}_2\text{CO}_3$ and was capable of removing uranium following 8 successive adsorption-desorption cycles. Adsorption percentage increased with pH until pH 7, before decreasing.	635
Polyamidoxime/poly (vinylphosphonic acid) (PAO/PVPA)	Polymerising PAO onto PAN. Primary purpose is to increase the anti-biofouling properties.	Shaken for 24 h at pH 8.2 at rtp.	145	Equilibrium was reached after 24 h, and adsorption follows a Langmuir isotherm.	636

System	Use of Plasma	Extraction Conditions	Adsorption Capacity / $\text{mg g}^{-1}$	Additional Info	Ref
Amidoximated multiwalled carbon nanotubes	$\text{N}_2$ plasma activation of the carbon nanotubes, in order to attach acrylonitrile (which is then converted to an amidoxime).	Mix 20 mg adsorbent with 20 mL U(VI) ( $100 \text{ mg L}^{-1}$ ) at pH 4.5 at rtp for 4 h.	145	System can only operate at pH 4.5 or below. Adsorption was modelled by pseudo-second order kinetics and a Langmuir isotherm model. Uranium capture was greater than the removal of a range of competing metal ions. Adsorption capacity decreased by 10 % in a 1:1000 mole ratio of U:V.	637
Cellulose@amidoxime	Plasma activation of cellulose samples, in order to attach acrylonitrile (which is then converted to an amidoxime).	Add 0.25 mg adsorbent to a 250 mL simulated seawater sample containing various U(VI) concentrations and leave for 15 days.	101.15	Adsorption was modelled by pseudo-second order kinetics and a Langmuir isotherm model.	638
Suspensions of PAO/MoS <sub>2</sub>	Ar plasma activation of MoS <sub>2</sub> , in order to attach acrylonitrile (which is then converted to an amidoxime).	Liquid-liquid extraction (pH 5).	47.4	Adsorption was modelled by pseudo-second order kinetics and a Langmuir isotherm model. Extraction percentage decreased when U(VI) was in competition with K, Na, Mg, and Ca metal ions.	639

System	Use of Plasma	Extraction Conditions	Adsorption Capacity / $\text{mg g}^{-1}$	Additional Info	Ref
PAO/carbon nanotubes	Reacting carbon nanotubes with dimethylamine under $\text{N}_2$ plasma, in order to introduce cyano groups onto the surface.	N/D	Ca. 4	N/A	640



## REFERENCES

- 507 Lai, J.; Yang, F.; Guo, H.; Jiao, Z. Novel Effective Dye Sorbents: Synthesis and Properties of 1,2,3-triazole-modified Thiocalix[4]arene Polymers Based on Click Chemistry. *Iran Polymer Journal*. **2014**, *23*, 899–906
- 508 Skorjanc, T.; Shetty, D.; Sharma, S.K.; Raya, J.; Traboulsi, Han, D.S.; Lalla, J.; Newlon, R.; Jagannathan, R.; Kirmizialtin, S.; Olsen, J.C.; Trabolsi, A. Redox-Responsive Covalent Organic Nanosheets from Viologens and Calix[4]arene for Iodine and Toxic Dye Capture. *Chemistry – A European Journal*. **2018**, *24*, 8648–8655
- 509 Abubakar, S.; Skorjanc, T.; Shetty, D.; Trabolsi, A. Porous Polycalix[n]arenes as Environmental Pollutant Removers. *ACS Applied Materials and Interfaces*. **2021**, *13*, 14802–14815
- 510 Shalaeva, Y. V.; Morozova, J. E.; Mironova, D. A.; Kazakova, E. K.; Kadirov, M. T.; Nizameev, I. R.; Kononov, A. I. Amidoamine Calix[4]resorcinarene-based Oligomers and Polymers as Efficient Sorbents of Azo Dyes from Water. *Supramolecular Chemistry*. **2015**, *27*, 595–605
- 511 Morozova, J.E.; Mironova, D.A.; Kazakova, E.K. Calix[4]arene Composition for Sorption of Azo Dyes from Aqueous Solution. Patent No. RU2489205C1, **2013**
- 512 Chen, M.; Wang, C.; Fang, W.; Wang, J.; Zhang, W.; Jin, G.; Diao, G. Electrospinning of Calixarene-Functionalized Polyacrylonitrile Nanofiber Membranes and Application as an Adsorbent and Catalyst Support. *Langmuir*. **2013**, *29*, 11858–11867
- 513 Ehrnestovna, M.J.; Khatibovna, K.E. Tetradodecyloxyphenyl Calix[4]arene for Sorption of Azo-Dyes from Aqueous Solution. Patent No. RU2428411C1, **2011**
- 514 Kamboh, M.A.; Solangi, I.B.; Sherazi, S.T.H.; Memon, S. Synthesis and Application of Calix[4]arene Based Resin for the Removal of Azo Dyes. *Journal of Hazardous Materials*. **2009**, *172*, 234–239
- 515 Chandran, M.; Mahmood, W.M.A.W.; Omar, F.N.; Lazim, A.M. Removal of Methylene Blue from Aqueous Solution Using Modified Polystyrene-Calixarene (PS-C) Composite. *Water Air & Soil Pollution*. **2022**, *233*
- 516 Zhou, S.; Jin, L.; Gu, P.; Tian, L.; Li, N.; Chen, D.; Marcomini, A.; Xu, Q.; Lu, J. Novel Calixarene-based Porous Organic Polymers with Superfast Removal Rate and Ultrahigh Adsorption Capacity for Selective Separation of Cationic Dyes. *Chemical Engineering Journal*. **2022**, *433*, 134442
- 517 Mohammadi, A.; Abdolvand, H.; Isfahani, A.P. Alginate Beads Impregnated with Sulfonate Containing Calix[4]arene-intercalated Layered Double Hydroxides: In situ Preparation, Characterization and

- Methylene Blue Adsorption Studies. *International Journal of Biological Macromolecules*. **2020**, *146*, 89–98
- 518 Hong, B.; Wang, W.; Yang, F. Calix[4]arene-Modified Multi-Walled Carbon Nanotubes: Novel High-Efficient Sorbent for Organic Dyes. *Fullerenes, Nanotubes and Carbon Nanostructures*. **2015**, *23*, 1077–1085
- 519 Temel, F.; Turklimaz, M.; Sezen, K. Removal of Methylene Blue from Aqueous Solutions by Silica Gel Supported Calix[4]arene Cage: Investigation of Adsorption Properties. *European Polymer Journal*. **2020**, *125*, 109450
- 520 Chen, M.; Chen, Y.; Diao, G. Adsorption Kinetics and Thermodynamics of Methylene Blue onto p-tert-Butyl-calix[4,6,8]arene-Bonded Silica Gel. *Journal of Chemical & Engineering Data*. **2010**, *55*, 5109–5116
- 521 Mohammadi, A.; Doctorsafaei, A.H.; Zia, K.M. Alginate/calix[4]arenes Modified Graphene Oxide Nanocomposite Beads: Preparation, Characterization, and Dye Adsorption Studies. *International Journal of Biological Macromolecules*. **2018**, *120*, 1353–1361
- 522 Zhang, X.; Shi, L.; Xu, G.; Chen, C. Synthesis of  $\beta$ -cyclodextrin-calix[4]arene Coupling Product and its Adsorption of Basic Fuchsin and Methylene Blue from Water. *Journal of Inclusion Phenomena and Macrocyclic Chemistry*. **2013**, *75*, 147–153
- 523 Yang, C.; Wang, Z.; Guo, H.; Jiao, Z.; Yang, F. Thiocalix[4]arene Derivatives Containing Multiple Aromatic Groups: High Efficient Extractants for Organic Dyes. *Journal of Chemical Sciences*. **2015**, *127*, 1383–1388
- 524 Rosly, N.Z.; Abdullah, A.H.; Kamarudin, M.A.; Ashari, S.E.; Ahmad, S.A.A. Adsorption of Methylene Blue Dye by Calix[6]Arene-Modified Lead Sulphide (PbS): Optimisation Using Response Surface Methodology. *International Journal of Environmental Research and Public Health*. **2021**, *18*, 397
- 525 Sun, R.; Wang, S.; Shi, X.; Li, Y.; Yuan, T. Lignin-based Anionic Dye Adsorbent and Preparation Method and Application Thereof. Patent number CN111229179A, **2020**
- 526 Yu, C.X.; Chen, J.; Zhang, Y.; Song, W.B.; Li, X.Q.; Chen, F.J.; Zhang, Y.J.; Liu, D.; Liu, L.L. Highly Efficient and Selective Removal of Anionic Dyes from Aqueous Solution by Using a Protonated Metal-Organic Framework. *Journal of Alloys and Compounds*. **2021**, *853*, 157383
- 527 Fang, R.; He, W.; Xue, H.; Chen, W. Synthesis and Characterization of a High-capacity Cationic Hydrogel Adsorbent and its Application in the Removal of Acid Black 1 from Aqueous Solution. *Reactive and Functional Polymers*. **2016**, *102*, 1–10

- 528 Sharma, T.; Madras, G. Effect of Crosslinker on the Swelling and Adsorption Properties of Cationic Superabsorbent. *Bulletin of Materials Science*. **2016**, 39, 613–626
- 529 Kholiya, F.; Singh, A.; Gosai, A.; Menna, R. Facile Preparation of Agaraldehyde Chitosan-based Composite Beads as Effectual Adsorbent Especially Towards Amido Black. *Journal of Applied Polymer Science*. **2021**, 138, 50716
- 530 Li, L.; Lv, X.; Zhang, Y.; Chen, T.; Yang, Y. Porous Biomass Adsorbing Material, and Preparation Method and Application Thereof. Patent No. WO2020052502A1, **2020**
- 531 Liu, J.; Chen, T-W.; Yang, Y-L.; Bai, Z-C.; Xia, L-R.; Wang, M.; Lv, X-L.; Li, L. Removal of Heavy Metal Ions and Anionic Dyes from Aqueous Solutions using Amide-functionalized Cellulose-based Adsorbents. *Carbohydrate Polymers*. **2020**, 230, 115619
- 532 Rahmayanti, M.; Nurhikmah, I.; Larasati, F. Isolation, Characterization and Application of Humin From Riau, Sumatra Peat Soils as Adsorbent for Naphthol Blue Black and Indigosol Blue Dyes. *Molekul*. **2021**, 16, 68–74
- 533 Wang, Y.; Xia, G.; Wu, C.; Sun, J.; Song, R.; Huang, W. Porous Chitosan Doped with Graphene Oxide as Highly Effective Adsorbent for Methyl Orange and Amido Black 10B. *Carbohydrate Polymers*. **2015**, 115, 686–693
- 534 Zhang, L.; Hu, P.; Wang, J.; Huang, R. Adsorption of Amido Black 10B from Aqueous Solutions onto Zr (IV) Surface-immobilized Cross-linked Chitosan/bentonite Composite. *Applied Surface Science*. **2016**, 369, 558–566
- 535 Peng, X.; Jia, W.; Lu, D.; Zhang, Q.; Yang, C.; Shuang, S.; Guo, Y.; Dong, C. Preparation and Characterisation of Two-dimensional Magnetic Chitosan Nanosheets for Removal of Azo Dyes from Aqueous Solutions. *Micro&Nano Letter*. **2019**, 14, 1344–1348
- 536 Tian, S.; Xu, S.; Liu, J.; He, C.; Xiong, Y.; Feng, P. Highly Efficient Removal of both Cationic and Anionic dyes from Wastewater with a Water-stable and Eco-friendly Fe-MOF via Host-guest Encapsulation. *Journal of Cleaner Production*. **2019**, 239, 117767
- 537 Angelova, R.; Baldikova, E.; Pospiskova, K.; Safarikova, M.; Safarik, I. Magnetically Modified Sheaths of *Leptothrix* sp. as an Adsorbent for Amido Black 10B Removal. *Journal of Magnetism and Magnetic Materials*. **2017**, 427, 314–319
- 538 Liu, Q.; Zhang, L.; Yang, B.; Huang, R. Adsorption of an Anionic Azo Dye by Cross-Linked Chitosan /bentonite Composite. *International Journal of Biological Macromolecules*. **2015**, 72, 1129–1135

- 539 Kamalabadi, M.; Khalili, S.; Madrakian, T.; Afkhami, A. Facile Synthesis of Magnetic Melamine-Based Covalent Organic Framework for Removal of Amido Black 10B. *European Physical Journal Plus*. **2022**, *137*, 544
- 540 Tanzifi, M.; Yaraki, M.T.; Kiadehi, A.D.; Hosseini, S.H.; Olazar, M.; Bharti, A.K.; Agarwal, S.; Gupta, V.K.; Kazemi, A. Adsorption of Amido Black 10B from Aqueous Solution using Polyaniline/SiO<sub>2</sub> Nanocomposite: Experimental Investigation and Artificial Neural Network Modelling. *Journal of Colloid and Interface Science*. **2018**, *510*, 246–261
- 541 Guo, W.; Xia, T.; Pei, M.; Du, Y.; Wang, L. Bentonite Modified by Allylamine Polymer for Adsorption of Amido Black 10B. *Polymers*. **2019**, *11*, 502
- 542 Ahmad, R.; Kumar, R. Conducting Polyaniline/Iron Oxide Composite: A Novel Adsorbent for the Removal of Amido Black 10B. *J. Chem. Eng. Data*. **2010**, *55*, 3489–3493
- 543 Salih, S.; Mohammed, H.; Abdullah, G.; Kadhom, M.; Ghosh, T. Simultaneous Removal of Cu(II), Cd(II), and Industrial Dye onto a Composite Chitosan Biosorbent. *Journal of Polymers and the Environment*. **2020**, *28*, 354–365
- 544 Santosh, C.; Daneshvar, E.; Kollu, P.; Peraniemi, S.; Grace, A.N.; Bhatnagar, A. Magnetic SiO<sub>2</sub>@CoFe<sub>2</sub>O<sub>4</sub> Nanoparticles Decorated on Graphene Oxide as Efficient Adsorbents for the Removal of Anionic Pollutants from Water. *Chemical Engineering Journal*. **2017**, *322*, 472–487
- 545 Sai Rashmi, R.; Akhila, S.; Duas, V.; Singh, A.; Samal, A.K.; Devan, R.S.; Saxena, M. Cobalt-Iron Alloy Nanoparticles Impregnated Partially Graphitized Carbon Adsorbent from Metallized Bagasse for Organic Pollutants Removal. *ChemRxiv Preprint*. **2020**
- 546 Afshin, S.; Poureshgh, Y.; Rashtbari, Y.; Fazlzadeh, M.; Bahrami, Asl, F.; Hamzezadeh, A.; Mahtab Pormazar, S. Eco-friendly Cost-effective Approach for Synthesis of ZnO Nanoparticles and Loaded on Worn Tire Powdered Activated Carbon as a Novel Adsorbent to Remove Organic Dyes from Aqueous Solutions: Equilibrium, Kinetic, Regeneration and Thermodynamic Study. *Desalination and Water Treatment*. **2021**, *227*, 391–403
- 547 Ray, S.; Das, A.; Banerjee, A. pH-Responsive, Bolaamphiphile-Based Smart Metallo-Hydrogels as Potential Dye-Adsorbing Agents, Water Purifier, and Vitamin B12 Carrier. *Chemistry of Materials*. **2007**, *19*, 1633–1639
- 548 Samarghandi, M.R.; Zarrabi, M.; Amrane, A.; Soori, M.M.; Sepehr, M.N. Removal of Acid Black Dye by Pumice Stone as a Low-Cost Adsorbent: Kinetic, Thermodynamic and Equilibrium Studies. *Environmental Engineering and Management Journal*. **2013**, *12*, 2137–2147



- 549 Xiao, J.; Lv, W.; Xie, Z.; Tan, Y.; Song, Y.; Zheng, Q. Environmentally Friendly Reduced Graphene Oxide as a Broad-spectrum Adsorbent for Anionic and Cationic Dyes via  $\pi$ - $\pi$  Interactions. *Journal of Materials Chemistry A*. **2016**, *4*, 12126–12135
- 550 Mittal, A.; Thaku, V.; Gajbe, V. Adsorptive Removal of Toxic Azo Dye Amido Black 10B by Hen Feather. *Environmental Science and Pollution Research*. **2013**, *20*, 260–269
- 551 Li, C.; Wu, N.; Zhang, M. Cationic Adsorbent Prepared from Grain Stillage, Preparation Method for Cationic Adsorbent and Application of Cationic Adsorbent. Patent No. CN107433188A, **2017**
- 552 Saravana Sundaram, E.J.; Dharmalingham, P. Synthesis and Characterization of PMMA Polymer/Clay Nanocomposites for Removal of Dyes. *Asian Journal of Chemistry*. **2019**, *31*, 2589–2595
- 553 Salunke, A. S.; Gund, N. N.; Marmat, B. M.; Sonar, J. P.; Dokhe, S. A.; Zine, A. M.; Thore, S. N.; Pardeshi, S. D. Adsorptive Removal of Amido Black from Aqueous Solution Using Economical Adsorbent: Kinetic and Isotherm Study. *International Journal of Chemical and Physical Sciences*. **2020**, *9*, 1–7
- 554 Ruckenstein, E.; Sun, Y. Preparation and Characteristics of Polymer-Based large Adsorbent Particles. *Journal of Applied Polymer Science*. **1996**, *61*, 1949–1956
- 555 Sheibani, M.; Zare-Shahabadi, V.; Ghaedi, M.; Asfaram, A.; Anaraki-Ardakani, H. Designing, Modelling, and Optimising Amido Black and Eosin B dyes Adsorption on MWCNT/ZrO<sub>2</sub>/Pb Nanocomposites from Aqueous Solution by Response Surface Methodology. *International Journal of Environmental Analytical Chemistry*. **2021**, *103*, 8032–8050
- 556 Huang, R.; Yang, B.; Liu, Q.; Gong, N. Adsorption of a Model Anionic Dye on Protonated Crosslinked Chitosan. *Desalination and Water Treatment*. **2014**, *52*, 7693–7700
- 557 Kaur, R.; Kaur, H. Adsorptive Removal of Amido Black 10B from Aqueous Solution using Stem Carbon of Ricinus communis as Adsorbent. *Asian Journal of Chemistry*. **2019**, *31*, 1071–1076
- 558 Kaur, R.; Kaur, H. Adsorption of Amido Black 10B from Aqueous Solution using Weed Waste as Adsorbent: Characterization, Equilibrium, Kinetic and Thermodynamic Studies. *Asian Journal of Chemistry*. **2017**, *29*, 441–446
- 559 Garg, A.; Mainrai, M.; Vijaya Kumar, B.; Barman, S. Experimental Investigation on Adsorption of Amido Black 10B Dye onto Zeolite Synthesised from Fly Ash. *Chemical Engineering Communications*. **2015**, *202*, 123–130

- 560 Di Vincenzo, A.; Piccionello, A.P.; Spinella, A.; Martino, D.C.; Russo, M.; Lo Meo, P. Polyaminoazide Mixtures for the Synthesis of pH-Responsive Calixarene Nanosponges. *Beilstein J. Org. Chem.* **2019**, *15*, 633–641
- 561 Spinella, A.; Russo, M.; Di Vincenzo, A.; Martino, D.C.; Lo Meo, P. Hyper-reticulated Calixarene Polymers: A New Example of Entirely Synthetic Nanosponge Materials. *Beilstein J. Org. Chem.* **2018**, *14*, 1498–1507.
- 562 Ayanda, O.S.; Nelana, S.M.; Sodeine, K.; Naidoo, E.B. Adsorptive Behaviour of Kaolin for Amido Black Dye in Aqueous Solution. *Oriental Journal of Chemistry.* **2018**, *34*, 1233–1239
- 563 Kumar, S.; Kumar, R.; Bhanjana, G.; Dilbaghi, N. Removal of Anionic Dye Amido Black by Multi-Walled Carbon Nanotubes. *Journal of Nanoengineering and Nanomanufacturing.* **2014**, *4*, 1–6
- 564 Nethaji, S.; Sivasamy, A. Adsorptive Removal of an Acid Dye by Lignocellulosic Waste Biomass Activated Carbon: Equilibrium and Kinetic Studies. *Chemosphere.* **2011**, *82*, 1367–1372
- 565 Xiao, J.; Lv, W.; Xie, Z.; Song, Y. L-cysteine-reduced Graphene Oxide/poly(vinyl alcohol) Ultralight Aerogel as a Broad-spectrum Adsorbent for Anionic and Cationic Dyes. *Journal of Materials Science.* **2017**, *52*, 5807–5821
- 566 Wang, H.; Gong, Y.; Wang, Y. Cellulose-based Hydrophobic Carbon Aerogels as Versatile and Superior Adsorbents for Sewage Treatment. *RSC Advances.* **2014**, *4*, 45753–45759
- 567 Qureshi, I.; Memon, S.; Yilmaz, M. Estimation of Chromium(VI) Sorption Efficiency of Novel Regenerable p-tert-butylcalix[8]areneoctamide Impregnated Amberlite Resin. *Journal of Hazardous Materials.* **2009**, *164*, 675–682
- 568 Khan, S.; Qureshi, I.; Shifa, M.S.; Waziri, A.H. An Efficient Calixarene-based Functional Material for the Sorption and Recovery of Cr(VI) from Water. *International Journal of Environmental Analytical Chemistry.* **2019**, *99*, 1123–1134
- 569 Ozcelik, E.; Mercan, E.S.; Erdemir, S.; Karaman, M.; Tabakci, Calixarene-tethered Textile Fabric for the Efficient Removal of Hexavalent Chromium from Polluted Water. *Colloids and Surfaces A: Physicochemical and Engineering Aspects.* **2021**, *626*, 127045
- 570 Memon, S.; Tabakci, M.; Roundhill, D.M.; Yilmaz, M. Synthesis and Evaluation of the Cr(VI) Extraction Ability of Amino/nitrile Calix[4]arenes Immobilized onto a Polymeric Backbone. *Reactive and Functional Polymers.* **2006**, *66*, 1342–1349
- 571 Tabakci, M.; Erdemir, S.; Yilmaz, M. Preparation, Characterization of Cellulose-grafted with Calix[4]arene Polymers for the Adsorption of Heavy Metals and Dichromate Anions. *Journal of Hazardous Materials.* **2007**, *148*, 428–435

- 572 Bayrakci, M.; Ozcan, F.; Yilmaz, B.; Ertul, S. Electrospun Nanofibrous Polyacrylonitrile/calixarene Mats: An Excellent Adsorbent for the Removal of Chromate Ions from Aqueous Solutions. *Acta Chimica Slovenica*. **2017**, *64*, 679–685
- 573 Ozcan, F.; Bayrackci, M.; Ertul, S. Synthesis and Characterization of Novel Nanofiber Based Calixarene and its Binding Efficiency Towards Chromium and Uranium Ions. *Journal of Inclusion Phenomena and Macrocyclic Chemistry*. **2016**, *85*, 49–58
- 574 Sayin, S. Fabrication of Efficient Calix[4]arene-Adorned Magnetic Nanoparticles for the Removal of Cr(VI)/As(V) Anions from Aqueous Solutions, *Polycyclic Aromatic Compounds*. **2022**, *42*, 1023–1034
- 575 Bieber, V.; Ozcelik, E.; Cox, H.; Ottley, C.; Ratan, J.; Karaman, M.; Tabakci, M.; Beaumont, S.; Badyal, J.P. Capture and Release Recyclable Dimethylaminomethyl-Calixarene Functional Cloths for Point-of-Use Removal of Highly Toxic Chromium Water Pollutants. *ACS Applied Materials and Interfaces*. **2020**, *12*, 52136–52145
- 576 Sayin, S.; Yilmaz, M.; Tavasli, M. Syntheses of Two Diamine Substituted 1,3-distal Calix[4]arene-based Magnetite Nanoparticles for Extraction of Dichromate, Arsenate and Uranyl Ions. *Tetrahedron*. **2011**, *67*, 3743–375
- 577 Kaya, A.; Onac, C.; Alpoguz, H.K.; Yilmaz, A.; Atar, N. Removal of Cr(VI) through Calixarene Based Polymer Inclusion Membrane from Chrome Plating Bath Water. *Chemical Engineering Journal*. **2016**, *283*, 141–149
- 578 Onac, C.; Kaya, A.; Alpoguz, H.K.; Yola, M.L.; Eriskin, S.; Atar, N.; Sener, I. Recovery of Cr(VI) by Using a Novel Calix[4]arene Polymeric Membrane with Modified Graphene Quantum Dots. *International Journal of Environmental Science and Technology*. **2017**, *14*, 2423–2434
- 579 Sap, A.; Tabacki, B.; Yilmaz, A. Calix[4]arene-based Mannich and Schiff Bases as Versatile Receptors for Dichromate Anion Extraction: Synthesis and Comparative Studies. *Tetrahedron*. **2012**, *68*
- 580 Tabakci, M.; Erdemir, S.; Yilmaz, M. Removal of Chromium Anions with Nanofiltration Complexation by Using p-Sulfonated Calix[4]arene. *Supramolecular Chemistry*. **2008**, *20*, 587–591
- 581 Lijia, L.; Chuhong, Z.; Wenda, X.; Chao, W.; Hongxing, D. Porous Polymer Uranium Adsorption Material and Preparation Method Thereof. Chinese Patent No. CN115090270A, **2022**
- 582 Trivedi, U.; Menon, S. Agrawal, Y. Polymer Supported Calix[6]arene Hydroxamic Acid, a Novel Chelating Resin. *Reactive and Functional Polymers*. **2002**, *50*, 205–216
- 583 Xu, Y.; Zhang, K.; Wang, C.; Zhu, Q.; Luo, J.; Cheng, F.; Xiao, F.; Peng, G. Fabrication of Magnetic Functionalised *m*-Carboxyphenyl Azo Calix[4]arene Amine Oxime Derivatives for Highly Efficient and

- Selective Adsorption of Uranium (VI). *Journal of Radioanalytical and Nuclear Chemistry*. **2020**, 323, 1145–1155
- 584 Xiao, F-Z.; Wang, C.; Yu, L-M.; Pu, Y-Q.; Xu, Y-L.; Zhang, K.; Luo, J-Q.; Zhu, Q-Q.; Chen, F.; Liu, Y.; Ho, C-H.; Peng, G-W.; He, S-Y. Fabrication of Magnetic Functionalised Calix[4]arene Composite for Highly Efficient and Selective Adsorption Towards Uranium (VI). *Environmental Chemistry*. **2019**, 16, 577–586
- 585 Jain, V.K.; Panday, R.A.; Pillai, S.G. Simultaneous Preconcentration of Uranium(VI) and Thorium(IV) from Aqueous Solutions Using a Chelating Calix[4]arene Anchored Chloromethylated Polystyrene Solid Phase. *Talanta*. **2006**, 70, 257–266
- 586 Li, L.; Liao, Q.; Cao, C.; Tang, S.; Ding, D.; Yuang, Y.; Cheng, B.; Dai, Z.; Ma, D.; Lu, W.; Hou, S. 4-Sulfonylcalix[6]arene Modified Fe<sub>3</sub>O<sub>4</sub>@Aspergillus Niger Biosorbents for Effective Removal of Uranium (VI) from Aqueous Solutions. *Journal of Nanoscience and Nanotechnology*. **2019**, 19, 6978–6986
- 587 Ayata, S.; Merdivan, M. P-tert-Butylcalix[8]arene Loaded Silica Gel for Preconcentration of Uranium(VI) via Solid Phase Extraction. *Journal of Radioanalytical and Nuclear Chemistry*. **2010**, 283, 603–607
- 588 Duncan, D.M.; Cockayne, J.S. Application of Calixarene Ionophores in PVC Based ISEs for Uranium Detection. *Sensors and Actuators B: Chemical*. **2001**, 73, 228–235.
- 589 Ozcan, F.; Bayrackci, M.; Ertul, S. Synthesis and Preparation of Novel Magnetite Nanoparticles Containing Calix[4]arenes With Different Chelating Group Towards Uranium Anions. *Journal of Macromolecular Science, A*. **2015**, 52, 599–608.
- 590 Schmeide, K.; Heise, K.H.; Bernhard, G.; Keil, D.; Jansen, K.; Praschak, D. Uranium(VI) Separation from Aqueous Solution by Calix[6]arene Modified Textiles. *Journal of Radioanalytical and Nuclear Chemistry*. **2004**, 261, 61–67
- 591 Shinkai, S.; Shiramama, Y.; Satoh, H.; Manabe, O. Selective Extraction and Transport of UO<sub>2</sub><sup>2+</sup> with Calixarene-based Uranophiles. *Journal of the Chemical Society, Perkin Transactions*. **1989**, 2, 1167–1171
- 592 Nagasaki, T.; Shinkai, S. Synthesis and Solvent Extraction Studies of Novel Calixarene-based Uranophiles Bearing Hydroxamic Groups. *Journal of the Chemical Society, Perkin Transactions 2*. **1991**, 7, 1063–1066
- 593 Boulet, B.; Bouvier-Capely, C.; Cossonnet, C.; Cote, G. Solvent Extraction of U(VI) by Calix[6]arenes. *Solvent Extraction and Ion Exchange*. **2006**, 24, 319–330

- 594 Jain, V.L.; Pillai, S.G.; Pandya, R.A.; Agrawal, Y.K.; Shrivastav, P.S. Molecular Octopus: Octa Functionalized Calix[4]resorcinarene-hydroxamic Acid [C4RAHA] for Selective Extraction, Separation and Preconcentration of U(VI). *Talanta*. **2005**, *65*, 466–475
- 595 Gu, X.; Xue, X.; Su, L.; Yang, X.; Wu, B.; Wu, Z.; Ru, S.; Zhan, J.; Yang, K. Type of Skin Stain Uranium Detergent and Preparation Method Thereof. Chinese Patent No. CN202111232240A, **2022**
- 596 Bauer, A.; Jachke, A.; Schone, S.; Barthen, R.; Marz, J.; Schmeide, K.; Patzschke, M.; Kersting, B.; Fahmy, K.; Oertel, J.; Brendler, V.; Stumpf, T. Uranium(VI) Complexes with a Calix[4]arene-Based 8-Hydroxyquinoline Ligand: Thermodynamic and Structural Characterization Based on Calorimetry, Spectroscopy, and Liquid–Liquid Extraction. *ChemistryOpen*. **2018**, *7*, 467–474
- 597 Ozcan, F.; Bayrackci, M.; Ertul, S. Synthesis and Characterization of Novel Nanofiber Based Calixarene and its Binding Efficiency Towards Chromium and Uranium Ions. *Journal of Inclusion Phenomena and Macrocyclic Chemistry*. **2016**, *85*, 49–58
- 598 Xiao, F-Z.; Pu, Y-Q.; Wang, C.; Xu, Y-L.; Ho, C-H.; Peng, G-W.; He, S-Y. Extraction Properties for U(VI) by the 25,27-dihydroxy-26,28-dimercaptoethoxy-5,11,17,23-tetra-tert-butyl Calix[4]arene. *Journal of Radioanalytical and Nuclear Chemistry*. **2019**, *321*, 49–55
- 599 Ramirez, F.D.M.; Serrano-Valero, E.; Verbanov, S. Octaphosphinoylated para-tert-butylcalix[8]arene as an Extracting Agent for Uranyl Ions in an Acidic Nitrate Medium: Study of the Extracted Uranyl Calixarene Compound. *Journal of Radioanalytical and Nuclear Chemistry*. **2020**, *323*, 651–662
- 600 Qian, Y.; Yuan, Y.; Wang, H.; Liu, H.; Zhang, J.; Shi, S.; Guo, Z.; Wang, N. Highly Efficient Uranium Adsorption by Salicylaldoxime/Polydopamine Graphene Oxide Nanocomposites. *Journal of Materials Chemistry A*. **2018**, *6*, 24676
- 601 Zhang, F.; Zhang, H.; Chen, R.; Liu, Q.; Liu, J.; Wang, C.; Sun, Z.; Wang, J. Mussel-inspired Antifouling Magnetic Activated Carbon for Uranium Recovery from Simulated Seawater. *Journal of Colloid and Interface Science*. **2019**, *534*, 172–182
- 602 Dai, Z.; Sun, Y.; Zhang, H.; Ding, D.; Li, L. Rational Synthesis of Polyamidoxime/Polydopamine-Decorated Graphene Oxide Composites for Efficient Uranium(VI) Removal from Mine Radioactive Wastewater. *Industrial & Engineering Chemistry Research*. **2019**, *58*, 19280–19291
- 603 Bliznyuk, V.; Kolacinska, K.; Pud, A.; Ogurtsov, N.; Noskov, Y.; Powell, B.; DeVol, T. High Effectiveness of Pure Polydopamine in Extraction of Uranium and Plutonium from Groundwater and Seawater. *RSC Advances*. **2019**, *9*, 30052

- 604 Liao, Y.; Wang, M.; Chen, D. Preparation of Polydopamine-Modified Graphene Oxide/Chitosan Aerogel for Uranium(VI) Adsorption. *Industrial & Engineering Chemistry Research*. **2018**, *57*, 8472–8483
- 605 Zhu, J.; Liu, Q.; Liu, J.; Chen, R.; Zhang, H.; Zhang, M.; Liu, P.; Li, R.; Wang, J. Investigation of Uranium (VI) Adsorption by Poly(dopamine) Functionalized Wastepaper Derived Carbon. *Journal of Taiwan Institute of Chemical Engineers*. **2018**, *91*, 266–273
- 606 Bai, L.; Duan, S.; Jian, W.; Liu, M.; Wang, S.; Sang, M.; Gong, X.; Li, J.; Xuan, S. High Performance Polydopamine-Functionalized Mesoporous Silica Nanospheres for U(VI) Removal. *Applied Surface Science*. **2017**, *426*, 1121–1132
- 607 Li, S.; Yang, P.; Liu, X.; Zhang, J.; Wei, X.; Wang, C.; Liu, C.; Guo, Z. Graphene Oxide Based Dopamine Mussel-like Cross-linked Polyethylene Imine Nanocomposite Coating with Enhanced Hexavalent Uranium Adsorption. *Journal of Materials Chemistry A*. **2019**, *7*, 16902
- 608 Li, B.; Ma, L. Tian, Y.; Yang, X.; Li, J.; Bai, C.; Yang, X.; Zhang, S.; Li, S.; Jin, Y. A Catechol-like Phenolic Ligand-functionalized Hydrothermal Carbon: One-pot Synthesis, Characterization and Sorption Behaviour Toward Uranium. *Journal of Hazardous Materials*. **2014**, *271*, 41–49
- 609 Yang, H.; Ding, H.; Zhang, X.; Luo, X.; Zhang, Y. Immobilization of Dopamine on *Aspergillus niger* Microspheres (AM/PDA) and its Effect on the U(VI) Adsorption Capacity in Aqueous Solutions. *Colloids and Surfaces A: Physicochemical and Engineering Aspects*. **2019**, *583*, 123914
- 610 Gao, J-K.; Hou, L-A.; Zhang, G-H.; Gu, P. Facile Functionalized of SBA-15 Via a Biomimetic Coating and its Application in Efficient Removal of Uranium Ions from Aqueous Solution. *Journal of Hazardous Materials*. **2015**, *286*, 325–333
- 611 Liao, Y.; Wang, M.; Chen, D. Production of Three-dimensional Porous Polydopamine-functionalized Attapulgite/Chitosan Aerogel for Uranium(VI) Adsorption. *Journal of Radioanalytical and Nuclear Chemistry*. **2018**, *316*, 635–647
- 612 Ou, T.; Wu, Y.; Han, W.; Kong, L.; Song, G.; Chen, D.; Su, M. Synthesis of Thickness-controllable Polydopamine Modified Halloysite Nanotubes (HNTs@PDA) for Uranium (VI) Removal. *Journal of Hazardous Materials*. **2022**, *424*, 127208
- 613 Wu, F.; Pu, N.; Ye, G.; Sun, T.; Wang, Z.; Song, Y.; Wang, W.; Huo, X.; Lu, Y.; Chen, J. Performance and Mechanism of Uranium Adsorption from Seawater to Poly(dopamine)-Inspired Sorbents. *Environmental Science & Technology*. **2017**, *51*, 4606–4614

- 614 Metilda, P.; Gladis, M.; Venkateswaran, G.; Prasada Rao, T. Investigation of the Role of Chelating Ligand in the Synthesis of Ion-imprinted Polymeric Resins on the Selective Enrichment of Uranium(VI). *Analytica Chimica Acta*. **2007**, 587, 263–271
- 615 Metilda, P.; Mary Gladis, J.; Prasada Rao, T. Catechol Functionalized Aminopropyl Silica Gel: Synthesis, Characterization and Preconcentrative Separation of Uranium(VI) from Thorium(IV). *Radiochimica Acta*. **2005**, 93, 219–224
- 616 Sakaguchi, T.; Nakajima, A. Accumulation of Uranium by Immobilized Persimmon Tannin. *Separation Science and Technology*. **1994**, 29, 205–221
- 617 Liao, X.; Lu, Z.; Du, X.; Liu, X.; Shi, B. Collagen Fiber Immobilized *Myrica rubra* Tannin and its Adsorption to  $UO_2^{2+}$ . *Environmental Science & Technology*. **2004**, 38, 324–328
- 618 Sung, P.M.; Chang, S.K. Adsorption of Metal and Uranyl Ions onto Amidoximated Pinus Densiflora Bark. *Wood Science and Technology*. **2010**, 44, 283–299
- 619 Oshita, K.; Sabarudin, A.; Takayanagi, T.; Oshima, M.; Motomizu, S. Adsorption Behavior of Uranium(VI) and Other Ionic Species on Cross-linked Chitosan Resins Modified with Chelating Moieties. *Talanta*. **2009**, 79, 1031–1035
- 620 Nakajima, A.; Sakaguchi, T. Recovery of Uranium using Immobilized Polyhydroxybenzene. *Journal of Radioanalytical and Nuclear Chemistry*. **1994**, 178, 319–326
- 621 Fukuda, S.; Ikeda, M.; Nakamura, M.; Yan, X.; Xie, Y. Effects of pH on DU Intake and Removal by CBMIDA and EHBP. *Health Physics*. **2007**, 92, 10–14
- 622 Cheira, M.F. Synthesis of Pyridylazo Resorcinol – Functionalized Amberlite XAD-16 and its Characteristics for Uranium Recovery. *Journal of Environmental Chemical Engineering*. **2015**, 3, 642–652
- 623 Pooley, G.; Adel-Hadadi, M.; Li, W.; Dietz, T.; Barkatt, A. Silane Coupling and Mordanting as Attachment Techniques for Pyridylazo and Thiazolylazo Ligands in the Synthesis of Adsorbents for Uranium in Seawater. *Adsorption Science and Technology*. **2018**, 36, 1144–1159
- 624 Lee, C.H.; Kim, J.S.; Suh, M.Y.; Lee, W. A Chelating Resin Containing 4-(2-thiazolylazo)resorcinol as the Functional Group. Synthesis and Sorption Behavior for Trace Metal Ions. *Analytica Chimica Acta*. **1997**, 339, 303–312
- 625 Abbas, M. N.; Homoda, A. M.; Mostafa, G. A. E. First Derivative Spectrophotometric Determination of Uranium(VI) and Vanadium(V) in Natural and Saline Waters and some Synthetic Matrices Using PAR and Cetylpyridinium Chloride. *Analytica Chimica Acta*. **2001**, 436, 223–231

- 626 Wang, D.; Song, J.; Wen, J.; Yuan, Y.; Liu, Z.; Lin, S.; Wang, H.; Wang, H.; Zhao, X.; Fang, M.; Lei, M.; Li, B.; Wang, N.; Wang, X.; Wu, H. Significantly Enhanced Uranium Extraction from Seawater with Mass Produced Fully Amidoximated Nanofiber Adsorbent. *Advanced Energy Materials*. **2018**, *8*, 1802607
- 627 Yang, X.; Li, J.; Liu, J.; Tian, Y.; Li, B.; Cao, K.; Liu, S.; Hou, M.; Li, S.; Ma, L. Simple Small Molecule Carbon Source Strategy for Synthesis of Functional Hydrothermal Carbon: Preparation of Highly Efficient Uranium Selective Solid Phase Extractant. *Journal of Materials Chemistry. A*. **2014**, *2*, 1550–1559
- 628 Wei, X.; Liu, Q.; Zhang, H.; Lu, Z.; Liu, J.; Chen, R.; Li, R.; Li, Z.; Liu, P.; Wang, J. Efficient Removal of Uranium(VI) from Simulated Seawater Using Amidoximated Polyacrylonitrile/FeOOH Composites. *Dalton*. **2017**, *46*, 15746–15756
- 629 Yang, P.; Zhang, H.; Liu, Q.; Liu, J.; Chen, R.; Yu, J.; Hou, J.; Bai, X.; Wang, J. Nano-sized Architectural Design of Multi-activity Graphene Oxide (GO) by Chemical Post-decoration for Efficient Uranium(VI) Extraction. *Journal of Hazardous Materials*. **2019**, *375*, 320–329
- 630 Zhang, Z.; Dong, Z.; Dai, Y.; Xiao, S.; Cao, X.; Liu, Y.; Guo, W.; Luo, M.; Le, Z. Amidoxime-Functionalized Hydrothermal Carbon Materials for Uranium Removal from Aqueous Solution. *RSC Advances*. **2016**, *6*, 102462–102471
- 631 Wang, X.; Ji, G.; Zhu, G.; Song, C.; Zhang, H.; Gao, C. Surface Hydroxylation of SBA-15 Via Alkaline for Efficient Amidoxime-functionalization and Enhanced Uranium Adsorption. *Separation and Purification Technology*. **2019**, *209*, 623–635
- 632 Yang, P.; Chen, R.; Liu, Q.; Zhang, H.; Liu, J.; Yu, J.; Liu, P.; Bai, X.; Wang, J. The Efficient Immobilization of Uranium(VI) by Modified Dendritic Fibrous Nanosilica (DFNS) using Mussel Bioglue, *Inorganic Chemistry Frontiers*. **2019**, *6*, 746–755
- 633 Sun, Y.; Lu, S.; Wang, X.; Xu, C.; Lil, J.; Chen, C.; Chen, J.; Hayat, T.; Alsaedi, A.; Alharbi, N.; Wang, X. Plasma-Facilitated Synthesis of Amidoxime/Carbon Nanofiber Hybrids for Effective Enrichment of <sup>238</sup>U(VI) and <sup>241</sup>Am(III). *Environmental Science & Technology*. **2017**, *51*, 12274–12282
- 634 Hu, B.; Guo, X.; Zheng, C.; Song, G.; Chen, D.; Zhu, Y.; Song, X.; Sun, Y. Plasma-enhanced Amidoxime/magnetic Graphene Oxide for Efficient Enrichment of U(VI) Investigated by EXAFS and Modeling Techniques. *Chemical Engineering Journal*. **2019**, *357*, 66–74
- 635 Shao, D.; Wang, X.; Ren, X.; Hu, S.; Wen, J.; Tan, Z.; Xiong, J.; Asiri, A.; Marwani, H. Polyamidoxime Functionalized with Phosphate Groups by Plasma Technique for Effective U(VI) Adsorption. *Journal of Industrial and Engineering Chemistry*. **2018**, *67*, 380–387



- 636 He, Y.; Hou, G.; Lu, X.; Chang, P.; Shao, D. Application of Poly(vinylphosphonic acid) Modified Poly(amidoxime) in Uptake of Uranium from Seawater. *RSC Advances*. **2022**, *12*, 4054
- 637 Wang, Y.; Gu, Z.; Yang, J.; Liao, J.; Yang, Y.; Liu, N.; Tang, J. Amidoxime-grafted Multiwalled Carbon Nanotubes by Plasma Techniques for Efficient Removal of Uranium(VI). *Applied Surface Science*. **2014**, *320*, 10–20
- 638 Yu, S.; Sun, C.; Fang, S.; Wang, C.; Alharbi, N.S.; Chen, C. Preparation of Cellulose@amidoxime by Plasma-induced Grafting Technology and its Potential Application for Uranium Extraction. *Applied Surface Science*. **2023**, *637*, 157883
- 639 Shao, D.; Liu, X.; Hayat, T.; Li, J.; Ren, X. Poly(amidoxime) Functionalized MoS<sub>2</sub> for Efficient Adsorption of Uranium(VI) in Aqueous Solutions. *Journal of Radioanalytical and Nuclear Chemistry*. **2019**, *319*, 379–386
- 640 Wang, J.; Zhang, Z.; Gao, Z.; Jiang, Z.; Qiao, Y.; Wang, M.; Fu, Z.; Zhang, Y.; Zhao, D. Uranium Adsorbent and Preparation Method Thereof. Patent No. CN109012586A, **2018**